UNIVERSIDADE FEDERAL DO RIO GRANDE DO SUL
INSTITUTO DE GEOCIÊNCIAS
PROGRAMA DE PÓS-GRADUAÇÃO EM GEOCIÊNCIAS

METASSOMATISMO POLIFÁSICO EM ROCHAS CARBONÁTICAS: EVOLUÇÃO E METALOGÊNESE DOS ESCARNITOS ASSOCIADOS À INTRUSÃO DO COMPLEXO GRANÍTICO CAÇAPAVA DO SUL (RS, BRASIL)

GUILHERME SONNTAG HOERLLE

ORIENTADOR – Prof. Dr. Marcus Vinicius Dorneles Remus

Porto Alegre, 2021

UNIVERSIDADE FEDERAL DO RIO GRANDE DO SUL
INSTITUTO DE GEOCIÊNCIAS
PROGRAMA DE PÓS-GRADUAÇÃO EM GEOCIÊNCIAS

METASSOMATISMO POLIFÁSICO EM ROCHAS CARBONÁTICAS: EVOLUÇÃO E METALOGÊNESE DOS ESCARNITOS ASSOCIADOS À INTRUSÃO DO COMPLEXO GRANÍTICO CAÇAPAVA DO SUL (RS, BRASIL)

GUILHERME SONNTAG HOERLLE

ORIENTADOR – Prof. Dr. Marcus Vinicius Dorneles Remus

BANCA EXAMINADORA:

Profa. Dra. Gláucia Nascimento Queiroga – Departamento de Geologia, Universidade Federal de Ouro Preto

Prof. Dr. Léo Afraneo Hartmann – Instituto de Geociências, Universidade Federal do Rio Grande do Sul

Prof. Dr. Moacir José Buenano Macambira – Instituto de Geociências, Universidade Federal do Pará

Tese de doutorado apresentada como requisito parcial para obtenção do título de Doutor em Ciências

Porto Alegre, 2021

CIP - Catalogação na Publicação

Hoerlle, Guilherme Sonntag
Metassomatismo polifásico em rochas carbonáticas: evolução e metalogênse dos escarnitos associados à intrusão do Complexo Granítico Caçapava do Sul (RS, Brasil) / Guilherme Sonntag Hoerlle. -- 2021.
340 f.
Orientador: Marcus Vinicius Dorneles Remus.

Tese (Doutorado) -- Universidade Federal do Rio Grande do Sul, Instituto de Geociências, Programa de Pós-Graduação em Geociências, Porto Alegre, BR-RS, 2021.

1. metassomatismo. 2. metamorfismo. 3. escarnito. 4. Complexo Granítico Caçapava do Sul. 5. Complexo Metamórfico Passo Feio. I. Remus, Marcus Vinicius Dorneles, orient. II. Título.

Elaborada pelo Sistema de Geração Automática de Ficha Catalográfica da UFRGS com os dados fornecidos pelo(a) autor(a).

AGRADECIMENTOS

Agradeço ao Conselho Nacional de Desenvolvimento Científico e Tecnológico (CNPq) pela concessão de bolsa de doutorado (Proc. 141333/2017-0) e à Coordenação de Aperfeiçoamento de Pessoal de Nível Superior (CAPES) pela concessão de bolsa de doutorado sanduíche através do Programa Institucional de Internacionalização (Proc. 88887.467220/2019-00).

Agradeço ao Prof. Marcus Remus pela excelente orientação, apoio e atenção ao longo do desenvolvimento do doutorado. Agradeço pelo apoio nos trabalhos de campo, pelas claras explicações sobre metamorfismo, geologia estrutural, geoquímica, e geologia do Escudo Sul-riograndense. Agradeço pelas longas conversas, com discussões de alto nível científico presenciais ou por videoconferências realizadas durante o período no exterior e pandêmico, estando sempre disponível e aberto às diferentes propostas mirabolantes e hipóteses para as questões científicas que surgiram ao longo do desenvolvimento da pesquisa. Além disso, agradeço ao Prof. Remus pela busca na disponibilização de laboratórios e fundos para desenvolvimento da pesquisa.

Agradeço ao Prof. Norberto Dani pelo auxílio na obtenção de dados geoquímicos, pelas discussões geológicas e incentivo. Agradeço à Profa. Lidia Vignol pela disponibilidade, auxílio na preparação de amostras e bons ensinamentos sobre o mundo das apatitas. Agradeço ao Prof. Cristiano Lana e ao geólogo Marco Silva por me receberem na Universidade Federal de Ouro Preto e pelo apoio na obtenção de dados geocronológicos e geoquímicos. Agradeço a Profa. Márcia Gomes, Susan, Lucas e Rafael pelo suporte na preparação de amostras e operação da microssonda eletrônica. Agradeço à Denise e o Lucas do Laboratório de Preparação de Amostras pela ajuda na preparação das várias e várias lâminas, seções polidas e concentrados. Agradeço ao Gabriel Mônaco pelo apoio e companhia em trabalho de campo.

Agradeço ao Prof. Thomas Müller, pelo acolhimento na Universidade de Leeds e na Universidade de Göttingen e pelo imenso esforço em viabilizar diversas análises em plena pandemia e mudança de universidade. Agradeço também ao Prof. Müller pelos ensinamentos sobre interação fluido-rocha, frentes de reação e dinâmica de isótopos estáveis. Agradeço à Profa. Sandra Piazolo pelas orientações e ensinamentos sobre metamorfismo e deformação, interação fluido-rocha e, pelos muitos questionamentos que levaram a respostas importantes e principalmente pelas dicas de redação de

artigos científicos e elaboração de projetos de pesquisa. Agradeço aos colegas Anthony Ramirez-Salazar, Felix Boschetty e Rafael Schmitz pelo acolhimento e parceria durante a estadia em Leeds.

Por fim, agradeço o incentivo e apoio incondicional da família e amigos e principalmente à minha companheira Lidia por estar sempre ao meu lado nessa longa caminhada que está apenas começando.

RESUMO

Múltiplos estágios de fluxo de fluido localizado associados à intrusão do Complexo Granítico Caçapava do Sul em mármores do Complexo Metamórfico Passo Feio resultaram em escarnitos magnesianos prógrados e retrógrados. Os mármores foram intrudidos por apófises máficas e félsicas entre *ca.* 578 a 557 Ma, gerando reações metassomáticas em três estágios principais. Os escarnitos representam indicadores das condições e dos caminhos dos fluidos ígneos ao infiltrar os carbonatos. O primeiro estágio resultou em diopsídio escarnitos que foram formados em contatos litológicos e ao longo de planos de foliação pré-existentes, sugerindo infiltração localizada e limitada de fluidos derivados de apófises félsicas e máficas, incluindo lamprófiros. O segundo estágio é registrado na formação sin-cinemática de forsterita escarnitos causada por fluidos ricos em H_2O derivados de intrusões félsicas. Geocronologia U-Pb em zircão com *ca.* 578 Ma obtidas para um granodiorito diretamente associado a fo escarnito define a idade deste estágio. O calor de repetidas intrusões tabulares e transpressão resultou no metamorfismo e deformação das apófises máficas e félsicas previamente formadas. Neste estágio, o fluxo de fluidos foi localizado e heterogêneo ao longo dos contatos litológicos e controlado estruturalmente, concentrado em zonas de charneira e planos axiais. O fluxo de fluidos nos dois primeiros estágios foi canalizado e em altas temperaturas (~ 581 a 628°C) e profundidades entre 14 e 17 km. As mudanças das assembleias minerais foram controladas por pulsos distintos com XCO_2 e $aSiO_2$ variáveis. O terceiro estágio é caracterizado pela serpentinização dos escarnitos anteriores, cloritização de fases ígneas e formação de escarnitos retrógrados entre ~270 e 310°C. O regime de fluxo neste estágio foi controlado pela porosidade criada devido ao hidrofraturamento relacionado ao resfriamento do complexo granítico. Apatita e titanita de diferentes apófises máficas registram idades U-Pb de *ca.* 557 Ma que marcam o efeito térmico das últimas intrusões ígneas e resfriamento do complexo granítico. Finalizando, conclui-se que as reações metassomáticas comumente observadas nas rochas hospedeiras e apófises de um complexo magmático fornecem informações úteis sobre a deformação, atividade de fluido e história de formação de corpos ígneos complexos.

Palavras-chave: metassomatismo; interação fluido-rocha; escarnito; Complexo Granítico Caçapava do Sul; Complexo Metamórfico Passo Feio

ABSTRACT

Multistage localized and episodic fluid flux associated with the intrusion of the Caçapava do Sul Granitic Complex into marbles of the Passo Feio Metamorphic Complex resulted in prograde and retrograde magnesian skarns. The marbles were intruded by mafic and felsic intrusions from *ca.* 578 to 557 Ma, triggering a set of metasomatic reactions at three main stages. The skarns represent useful indicators of the pathways used by the magmatic fluids when infiltrating the carbonates. The first stage resulted in diopside-skarns. They were formed at lithological boundaries and along pre-existing foliation planes suggesting spatially-limited infiltration of fluids released from felsic and mafic apophyses, including lamprophyres. A second stage is recorded by the synkinematic formation of forsterite-skarns during transpression triggered by H_2O-rich fluids derived from felsic apophyses. Zircon U-Pb age of c. 578 Ma obtained for a granodiorite directly associated to fo-skarns define the age of the second stage. Heat supply from repeated intrusions and transpression resulted in deformation and metamorphism of the prior mafic and felsic apophyses. Fluid pathways recorded by reaction textures were localized and characterized by heterogeneous flow along lithological boundaries and structurally controlled focused flow in fold hinges and axial planes. Fluid flux in the first two stages was highly localized and at high temperatures (~581 to 628°C) and depths between 14 and 17 km in which the changes of the skarn assemblages were controlled by variable XCO_2 and $aSiO_2$ of distinct pulses. The third stage is mainly characterized by serpentinization of previous skarn assemblages, chloritization of igneous phases and formation of retrograde skarns between ~270 and 310°C. Fluid flow regime at this stage was controlled by the porosity and permeability created due to brittle fracturing related to the cooling of the granitic complex. Apatite and titanite from different mafic apophyses record consistent U-Pb ages of *ca.* 557 Ma that mark the thermal effect of the last igneous intrusions and subsequent cooling of the Caçapava do Sul Granitic Complex. The metasomatic reactions commonly observed in the host rocks and apophyses of a magmatic complex provide useful insights on timing of the pluton assembly, deformation and associated fluid activity.

Keywords: metasomatism; fluid-rock interaction; skarn; Caçapava do Sul Granitic Complex; Passo Feio Metamorphic Complex

LISTA DE ABREVIAÇÕES

ÓRGÃOS, INSTITUIÇÕES E PROGRAMAS

CAPES: Coordenação de Aperfeiçoamento de Pessoal de Nível Superior

CNPq: Conselho Nacional de Desenvolvimento Científico e Tecnológico

CPGeo-USP: Centro de pesquisas geocronológicas da Universidade Federal de São Paulo

DEGEO-UFOP: Departamento de Geologia da Universidade Federal de Ouro Preto

IGEO-UFRGS: Instituto de Geociências da Universidade Federal do Rio Grande do Sul

IGL-UFOP: Laboratório de Geologia Isotópica da Universidade Federal de Ouro Preto

IMA: *International Mineralogy Association*

IUGS-SSMR: União Internacional de Ciências Geológicas, Subcomissão de Sistemática de Rochas Metamórficas

PPGGEO: Programa de Pós-Graduação em Geociências

PRINT: Programa Institucional de Internacionalização da CAPES

UNIDADES GEOLÓGICAS E TECTÔNICAS

CSGC: Complexo Granítico Caçapava do Sul; *Caçapava do Sul Grantic Complex*

PFMC/PFC: Complexo Metamórfico Passo Feio; *Passo Feio Metamorphic Complex*

CB: Bacia do Camaquã; *Camaquã Basin*

DFB: Cinturão Dom Feliciano; *Dom Feliciano Belt*

SGT: Terreno São Gabriel; *São Gabriel Terrane*

LSSA: Associação Shoshonítica de Lavras do Sul; *Lavras do Sul Shoshonitic Association*

CSMD: Distrito de mineração de mármore de Caçapava do Sul; *Caçapava do Sul marble district*

MÉTODOS, EQUIPAMENTOS E PADRÕES

BSE: elétrons retroespalhados; *back-scattered electron*

CL: catodoluminescência; *cathodoluminescence*

EMPA: microssonda eletrônica; *electron-microprobe analyzer*

HREE: elementos terras-rara pesados; *heavy rare-earth elements*

ICP-MS: espectrômetro de massa com plasma indutivamente acoplado; *Inductively Coupled Plasma mass spectrometer*

ICP-OES: espectrômetro de emissão ótica com plasma indutivamente acoplado

LA: ablação de laser; *Laser ablation*

LOI: perda ao fogo; *loss on ignition*

LREE: elementos terras-rara leves; *light rare-earth elements*

MS: espectrômetro de massa; *mass spectrometer*

MSWD: desvio médio quadrático ponderado; *mean squared weighted deviation*

Pbc: chumbo comum; *common lead*

PPL: luz plano polarizada; *plane-polarized light*

RL: luz refletida; *reflected light*

SE: elétrons secundários; *secondary electrons*

SHRIMP: Microssonda Iônica de Alta Resolução e de Alta Sensibilidade; *Sensitive high-resolution ion microprobe*

SMOW / VSMOW: *Vienna Standard Mean Ocean Water*

VPDB: *Pee Dee Belemnite*

W/R: razão fluido-rocha; *water-to-rock ratio*

WDS: espectroscopia por comprimento de onda dispersive; *Wavelength-dispersive spectroscopy*

XPL: luz polarizada com nicóis cruzados; *cross-polarized light*

XRF: fluorescência de raios-X; X-*ray fluorescency*

MINERAIS

Act: actinolita; *actinolite*

Aln: alanita; *allanite*

Ap: apatita; *apatite*

Atg: antigorita; *antigorite*

Bt: biotite; *biotite*

Cal: calcita; *calcite*

Ccp: calcopirita; *chalcopyrite*

Chl: clorita; *chlorite*

Cv: covelita; *covellite*

Di: diopsídio; *diopside*

Dol: dolomita; *dolomite*

Fo: forsterita; *forsterite*

Grt: granada; *garnet*

Hbl: hornblenda; hornblende

Hst: hastingsita; *hastingsite*

Kfs: feldspato alcalino; K-feldspar

Mol: molibdenita; *molybdenite*

Ol: olivina; *olivine*

Phl: flogopita; *phlogopite*

Pl: plagioclásio; *plagioclase*

Po: pirrotita; *pyrrhotite*

Py: pirita; *pyrite*

Qz: quartzo; *quartz*

Srp: serpentina; *serpentine*

Tr: tremolita; *tremolite*

Ttn: titanita; *titanite*

SUMÁRIO

ESTRUTURA DA TESE

Esta tese está estruturada em três artigos submetidos a periódicos internacionais e um manuscrito. Os artigos são precedidos por um capítulo inicial (Capítulo 1) contendo: (i) introdução com formulação do problema e hipóteses; (ii) objetivos da pesquisa, (iii) área de estudo, matérias e métodos; (iv) contexto geológico; (v) estado da arte; (vi) resumo dos principais resultados obtidos, interpretações e discussão integradora dos resultados; (vii) conclusões e (viii) referências.

O Capítulo 2 apresenta o contexto geológico da área de estudo. Os artigos e respectivas classificações conforme os estratos Qualis-CAPES/PPGGEO estão dispostos a seguir.

Artigo I (A1) **Metasomatic reactions triggered by localized and episodic fluid flux record multistage intrusion history: An example from the syntectonic Caçapava do Sul Granitic Complex, Southern Brazil.**

Autores: Hoerlle, G.S., Remus, M.V.D., Müller, T., Piazolo, S., Lana., C.C., Sorger, D.

Artigo submetido à Journal of Metamorphic Geology

Artigo II (A1) **Metalamprophyres in the Dom Feliciano Belt: insights for the development of strike-slip tectonics and localized metamorphism during the post-collisional stage.**

Autores: Hoerlle, G.S., Remus, M.V.D., Dani, N.

Artigo submetido à Precambrian Research.

Artigo III (A1) **Post-collisional magmatic-hydrothermal mineralization in the São Gabriel Terrane (southern Brazil): insights from mineral chemistry, stable isotopes, and sulfide trace-elements of the Caçapava do Sul skarns.**

Autores: Hoerlle, G.S., Remus, M.V.D., Silva, M., Lana, C.

Artigo submetido à Ore Geology Reviews.

Artigo IV **Mechanisms of fluid infiltration and reaction front controls during synkinematic contact metamorphism: a stable isotope and mineral chemistry study of Mg-skarns of the Caçapava do Sul aureole (Dom Feliciano Belt, southern Brazil)**

Autores: Hoerlle, G.S., Remus, M.V.D., Müller, T., Piazolo, S., Ramirez-Salazar, A., Sorger, D.

Manuscrito a ser submetido à Chemical Geology.

CAPÍTULO 1 – INTRODUÇÃO

1. INTRODUÇÃO

O fluxo de fluidos possui papel fundamental para transferência de calor e massa na crosta, influenciando diretamente as reações metamórficas e formações de depósitos minerais (*e.g.*, Ferry, 1978; Bucher-Nurminen, 1982; Ferry & Dipple, 1991; Yardley *et al*. , 1991; Baumgartner & Valley, 2001; Putnis & Austrheim, 2010; Ague, 2014; Koehn *et al*., 2021). A infiltração e percolação de fluidos afetam as rochas desde escalas microscópicas, controlando reações no contato entre os grãos (*e.g.*, Putnis, 2009; Bégué *et al*., 2019), até escala litosféricas, gerando metamorfismo e deformação a nível regional (*e.g.*, McCaig, 1988; Ferry, 1992; Piccoli *et al*., 2021). Portanto, decifrar a evolução espacial e temporal do fluxo de fluidos é crucial para compreender processos geológicos em diversos ambientes e escalas.

Durante as interações fluido-rocha, a adição e remoção de componentes químicos e modificações na composição mineral ou de rocha-total estão diretamente ligadas aos processos metassomáticos. Diante disso, os fluidos desempenham um papel importante, fornecendo um mecanismo de transporte muito mais eficiente do que a difusão no estado sólido. Apesar da dificuldade de observação direta do fluido ígneo ou metamórfico, seus efeitos são registrados pela dissolução de minerais pré-existentes, reprecipitação ou precipitação de novas fases (*e.g.*, Nabelek *et al*., 2013; Ducoux *et al*., 2017; Engvik *et al*., 2018). Sendo assim, as rochas metassomáticas são as principais fontes de informação para o entendimento das condições em que a interação fluido-rocha ocorreu.

Em particular, as rochas carbonáticas e seus equivalentes metamórficos são tipicamente muito reativos a fluidos externos ou mudanças nas condições

metamórficas (*e.g.*, Bucher-Nurminen, 1981; Ferry, 1991; Müller *et al*., 2004; 2009 Bégué *et al*., 2020). Quando intrudidas por rochas magmáticas, as reações geradas a partir da interação entre os fluidos ígneos e os carbonatos comumente resultam na formação de rochas cálcio-silicáticas, denominadas de escarnitos. Estas rochas registram as condições de pressão, temperatura e composição dos fluidos envolvidos durante as interações metassomáticas. Além disso, há uma relação direta entre a sequência de intrusão, cristalização, alteração e resfriamento de um plúton e a evolução espacial e temporal dos escarnitos associados (Brown *et al*., 1985; Meinert *et al*., 2005).

Dentre os vários ambientes geológicos, as auréolas de metamorfismo de contato são tipicamente influenciadas por grandes quantidades de fluidos derivados de intrusões magmáticas (*e.g.*, Roselle *et al*., 1999; Cook & Bowman, 2000). Nestes casos, além do efeito termal da intrusão, o fluxo de fluidos pode afetar as propriedades reológicas das rochas encaixantes (*e.g.*, Ducoux *et al*., 2017) e levar à formação de depósitos minerais (*e.g.*, Meinert *et al*., 2005). No entanto, apesar do crescente número de estudos nesta temática (*e.g.*, Harlov & Austrheim, 2013; Ague, 2014), diversas questões referentes ao significado e efeitos da infiltração dos fluidos ígneos durante o metamorfismo seguem amplamente debatidas. Dentre elas, a distinção e a caracterização de fluxos contínuos ou pulsos episódicos seguem relativamente pouco entendidas, especialmente porque muitas rochas metassomáticas carecem de geocronômetros adequados (Villa & Williams, 2013). Contudo, a distinção entre fluxos contínuos ou episódicos pode ser particularmente útil para decifrar a história das intrusões associadas e é crucial para compreensão da evolução metamórfica da auréola de contato. Além disso, os mecanismos, taxas e durações da formação de complexos magmáticos permanece amplamente debatida, o que afeta significativamente a compreensão dos processos metassomáticos associados. Por exemplo, diversos autores propuseram que os plútons ascendem como grandes diápiros em pulsos únicos (*e.g.*, Buddington, 1959; Clarke, 1992; Miller & Paterson, 1999). Outros autores consideram esse processo lento e ineficiente e sugerem que grandes corpos magmáticos ígneos são formados pelo suprimento incremental de magma através de estruturas semelhantes a diques e soleiras que podem construir um corpo magmático ao longo de milhões de anos (*e.g.*, Clemens & Mawer, 1992; Petford *et al*., 2000; Coleman *et al*., 2004). No entanto, o reconhecimento de plútons

formados incrementalmente é problemático já que o sistema permanece em altas temperaturas por um longo período de tempo, potencialmente obliterando os contatos originais entre incrementos individuais (*e.g.*, Bartley *et al.*, 2008). Ainda, pulsos magmáticos intervalados com períodos sem atividade ígnea podem durar dezenas de milhões de anos e resultar em batólitos graníticos sobreimpressos (*e.g.*, He *et al.*, 2018; Pivarunas & Meert, 2019; Tichomirowa *et al.*, 2019). Embora os modelos acima sejam conceitualmente plausíveis, eles são caracterizados por histórias de resfriamento e infiltração de fluido fundamentalmente diferentes. Neste caso, o estudo das rochas metassomáticas formadas pela interação de fluidos magmáticos com rochas hospedeiras tem o potencial de fornecer informações relevantes sobre a história da intrusão e padrão de infiltração de fluidos durante a formação de um complexo ígneo.

2. OBJETIVOS

Considerando as questões abordadas acima, esta tese tem como objetivo principal contribuir com o entendimento dos controles e efeitos da infiltração de fluidos ígneos em rochas carbonáticas e seus significados para a história magmática e metamórfica das rochas envolvidas. Neste contexto, a pesquisa tem como objetivos específicos:

- Caracterizar a gênese e evolução dos escarnitos magnesianos de Caçapava do Sul, identificando os principais estágios de formação, respectivas idades e condições físico-químicas de cada estágio;
- Identificar controles e mecanismos de fluxo de fluidos associados à intrusões ígneas em rochas carbonáticas, principalmente em relação à geração de porosidade e estruturas de infiltração e circulação de fluidos;
- Verificar o potencial do estudo das rochas metassomáticas para obtenção de informações sobre a história evolutiva e modo de intrusão de corpos ígneos complexos;
- Contribuir com as discussões sobre evolução crustal e metalogênese associadas ao estágio pós-colisional do Cinturão Dom Feliciano no Escudo Sul-riograndense.

3. MÉTODOS E ÁREA DE ESTUDO

A principal área de estudo desta pesquisa está localizada no contato entre o Complexo Granítico Caçapava do Sul (CSGC) e o Complexo Metamórfico Passo Feio (PFMC) onde afloram mármores dolomíticos, apófises ígneas e escarnitos associados (Figuras 1 e 2). A área foi selecionada devido à ampla exposição das rochas carbonáticas, magmáticas e metassomáticas em função das atividades de mineração no local, facilitando a observação de diferentes estruturas e litologias. Para fins de simplificação, esta área é denominada de forma geral como distrito mineiro de Caçapava do Sul ou *marble district* (*MD area*) e está subdividida em localidades (Figura 2b). Além disso, uma segunda área no PFMC localizada na porção mais distante do contato entre o batólito granítico do CSGC (Figura 1c) foi selecionada visando obter amostras de apófises ígneas análogas àquelas encontradas cortando os mármores. Esta área contempla enxames de diques félsicos e máficos pouco deformados ou metamorfizados, expostos em lajeados ao longo do Arroio das Pedras (*AP area*).

Os métodos e técnicas utilizados no desenvolvimento desta tese incluem (i) levantamento de campo; (ii) análises petrográficas; (iii) mapeamento composicional por microfluorescência de raios-X; (iv) análises químicas de elementos maiores, menores e traço de rocha total; (v) análises de química mineral; (vi) datações radiométricas em zircão, titanita e apatita; (vii) análises de isótopos estáveis de carbono e oxigênio; (viii) análises de elementos traço em sulfetos e (ix) microscopia eletrônica de varredura. A relação de técnicas, laboratórios e equipamentos utilizados está resumida na Tabela 1. O detalhamento dos métodos empregados, condições analíticas e padrões utilizados em cada um dos quatro estudos que compõe esta tese estão descritos nas seções de materiais e métodos dos respectivos artigos científicos (Capítulos 2 a 5). O resumo das amostras analisadas, técnicas e laboratórios utilizados em cada artigo, juntamente com as coordenadas da localização das amostras está demonstrado no Anexo A.

Técnica	**Laboratório**	**Instituto**	**Universidade**	**Equipamento**
Microssonda eletrônica (EMPA)	Laboratório de Microssonda Eletrônica	Instituto de Geociências	UFRGS	CAMECA SX Five
Microssonda eletrônica (EMPA)	*Electron Microprobe Laboratory*	*Geoscience Center*	*Uni-Göttingen*	JEOL JXA 8900

Técnica	Laboratório	Instituto	Universidade	Equipamento
Fluorescência de raios-X (FRX)	Laboratório de Fluorescência de Raios-X	Instituto de Geociências	UFRGS	RIGAKU RIX 2000
Micro-fluorescência de raios-X (microFRX)	*Micro-XRF laboratory*	*Department of Mineralogy*	*Uni-Göttingen*	Brucker M4 Tornado
Datação U-Pb por LA-ICP-MS	Laboratório de Geoquímica Isotópica	Departamento de Geologia	UFOP	TF Element II; Neptune Plus
Microscopia eletrônica de varredura (MEV)	Laboratório de Microscopia e Microanálises	Departamento de Geologia	UFOP	JEOL 6510
Microscopia eletrônica de varredura (MEV)	Laboratório de Geologia Isotópica	Instituto de Geociências	UFRGS	JEOL JSM-6610LV
Elementos traço por LA-ICP-MS	Laboratório de Geoquímica Isotópica	Departamento de Geologia	UFOP	Thermo-Finnigan Element II
Petrografia ótica	Laboratório de Petrografia Metamórfica	Instituto de Geociências	UFRGS	LEICA DM4500 e S6D
Isótopos estáveis de C e O em carbonatos	Laboratório de Geologia Isotópica	Instituto de Geociências	UFRGS	IRMS Delta V Advantage
Isótopos estáveis de C e O em carbonatos	Laboratório de Geoquímica e Geologia Isotópica	Geoscience Center	Uni-Göttingen	Thermo KIEL VI com Finnigan Delta+
Isótopos estáveis de O em silicatos	Laboratório de Geoquímica e Geologia Isotópica	Geoscience Center	Uni-Göttingen	ThermoElectron MAT 253
ICP-OES/MS	SGS Geosol	-	-	-

Tabela 1: Resumo de técnicas, laboratórios e equipamentos empregados no desenvolvimento da tese.

4. CONTEXTO GEOLÓGICO

Esta seção apresenta de maneira geral o contexto geológico no qual os escarnitos de Caçapava do Sul estão inseridos. As particularidades da geologia regional que estão relacionadas aos assuntos abordados em cada artigo (*e.g.*, metalogênese; tectônica pós-colisional) são apresentadas e discutidas em cada artigo nos capítulos 2 a 5.

Os escarnitos de Caçapava do Sul são encontrados no contato entre as intrusões do Complexo Granítico Caçapava do Sul e os mármores dolomíticos do Complexo Metamórfico Passo Feio. Ambos pertencem ao Cinturão Dom Feliciano (DFB)

4.1. CINTURÃO DOM FELICIANO

O Cinturão Dom Feliciano (DFB) representa a porção austral da Província Mantiqueira e ocorre desde o Uruguai até o sul do Brasil (Figura 1a). Este cinturão corresponde a um orógeno Neoproterozoico formado pela colagem tectônica de domínios oceânicos e fragmentos continentais entre os crátons Rio de la Plata, Congo e Kalahari. Na porção central do DFB (setor Sul-riograndense), três eventos orogênicos ocorreram durante a evolução do orógeno, sendo eles: Passinho (890 a 860 Ma), São Gabriel (770 a 680 Ma) e Dom Feliciano (650 a 540 Ma) (Fernandes *et al*., 1992; Chemale, 2000, Hartmann *et al*., 2000; 2007, Saalmann *et al*. 2011).

Estes eventos resultaram numa distribuição de domínios tectônicos divididos entre: Terreno São Gabriel, Terreno Tijucas (ou Cinturão Porongos) e Batólito de Pelotas (ou Cinturão Dom Feliciano Leste; Terreno Pelotas) (Figura 1b).

4.2. TERRENO SÃO GABRIEL

O Terreno São Gabriel (SGT) está localizado na porção oeste do Cinturão Dom Feliciano e é composto por sequências supracrustais metavulcano-sedimentares que foram metamorfizadas em condições de fácies anfibolito e subsequentemente intrudidas por magmas cálcico-alcalinos juvenis, agora presentes como ortognaisses, ofiolitos e complexos máfico-ultramáficos (Chemale *et al*., 1995; Babinski *et al*., 1996; Hartmann *et al*., 2000; 2011; Saalmann *et al*., 2005; Arena *et al*., 2016; Philipp *et al*., 2018; Pertille *et al*., 2017; Cerva-Alves *et al*., 2020). Além disso, o SGT hospeda diversas intrusões graníticas neoproterozóicas (*e.g.*, CSGC) e é parcialmente coberto por sequências vulcano-sedimentares pós-colisionais (*i.e.*, Bacia do Camaquã).

4.2.1. Complexo Metamórfico Passo Feio

O Complexo Metamórfico Passo Feio (PFMC) está localizado na borda leste do SGT e consiste em uma associação supracrustal de rochas metapelíticas, anfibolitos, mármores, rochas cálcio-silicáticas, metavulcânicas, entre outras, que foram intrudidas pelo Complexo Granítico Caçapava do Sul e carbonatitos (Leinz *et al*., 1941; Ribeiro *et al*., 1966; Bitencourt, 1983; Hartmann *et al*., 1990; Remus *et al*., 2000; Cerva-Alves *et al*., 2017; Bicalho *et al*., 2019; Souza, 2020; Tennholm, 2019; Costa, 2021). Os eventos metamórficos que formaram o PFMC foram interpretados de

maneira distinta e discutidos principalmente ao longo da década de 1980 (*e.g.*, Bitencourt, 1983; Silva-Filho & Matsdorf, 1987; Bortollotto, 1988; Hartmann *et al.*, 1990).

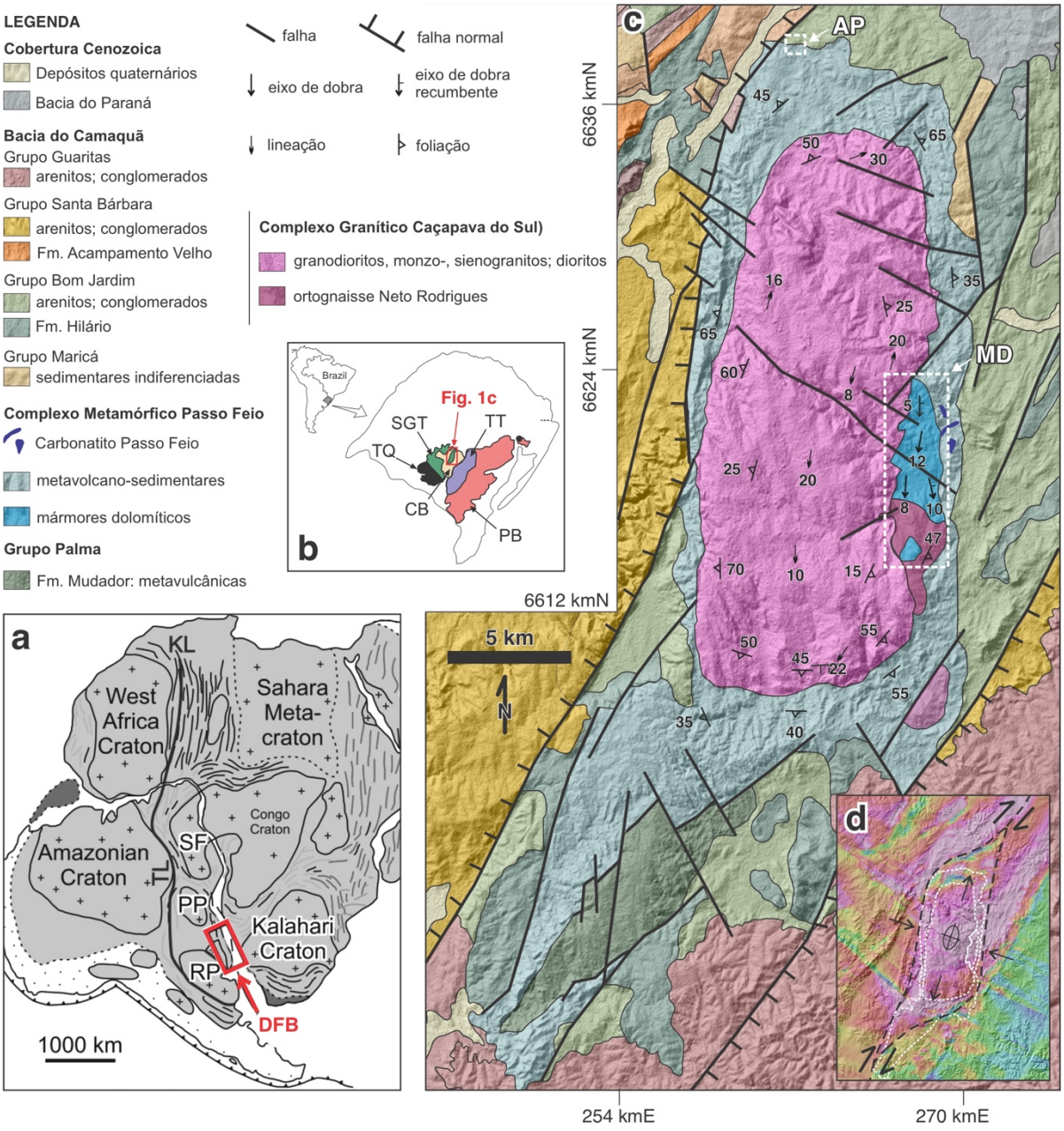

Figura 1: Localização do Complexo Granítico Caçapava do Sul e do Complexo Metamórfico Passo Feio no escudo Sul-riograndense, sul do Brasil. a) Localização do Cinturão Dom Feliciano (DFB) no Gondwana Ocidental (RP: cráton Rio de la Plata; PP: bloco Paranapanema, SF: cráton São Francisco; KL: lineamento Kandi; TL: lineamento Transbrasiliano) b) Domínios tectônicos do Escudo Sul-riograndense (TT: Terreno Tijucas; SGT: Terreno São Gabriel; PB: Batólito de Pelotas; CB: Bacia do Camaquã; TQ: Cráton Taquarembó). c) Mapa geológico da área do Complexo Metamórfico Passo Feio e do Complexo Granítico Caçapava do Sul (Modificado de UFRGS, 1998 e Porcher & Lopes, 2000); d) Magnetometria e mapa de relevo

sombreado da região de Caçapava do Sul mostrando estrutura plana de forma sigmoidal em torno de CSGC e PFMC (CPRM, 2010).

Embora haja um consenso de que o PFMC registra pelo menos dois eventos metamórficos exibindo um grau metamórfico crescente em direção ao CSGC, ideias contrastantes foram propostas a respeito do efeito térmico da intrusão no registro metamórfico. Alguns autores descreveram rochas de fácies hornblenda-cornubianito e piroxênio-hornblenda-cornubianito circundando o granito até algumas centenas de metros do contato, que foram gradualmente seguidas por rochas de fácies albita-epidoto-hornfels e xisto verde mais distantes do contato com base em extenso mapeamento da área (Leinz *et al*., 1941; Ribeiro *et al*., 1966; Ribeiro, 1970; Silva-Filho & Matsdorf, 1987; Bortolotto, 1988).

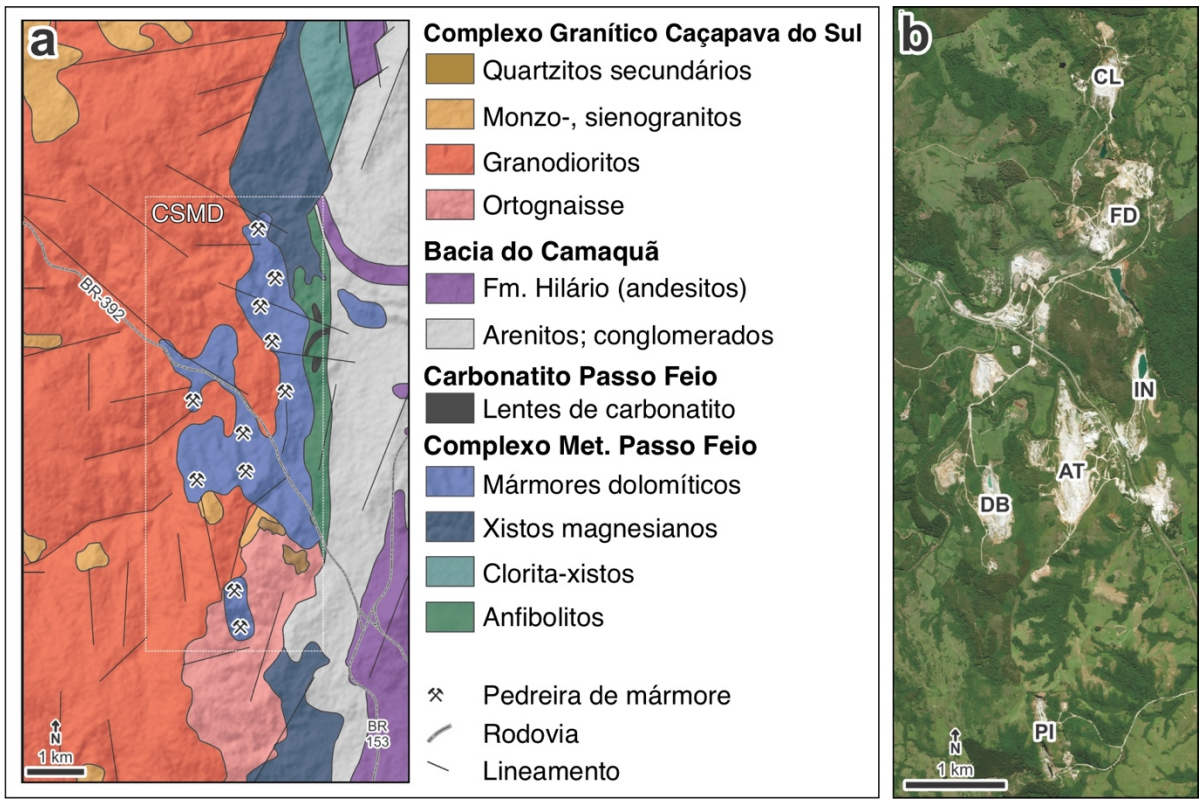

Figura 2: a) Mapa geológico do entorno do Distrito Mineiro de Mármore de Caçapava do Sul (CSMD). b) localização das principais áreas de coleta de amostras (CL: Coronel Linhares; FD: Fida; IN: Inducal; AT: Ativa Minerais; DB: Dagoberto Barcelos; PI: Pinheiro) (Adaptado de Cerva-Alves *et al*., 2017; imagem de satélite: Google Earth).

Esses autores interpretaram a distribuição das fácies metamórficas como sendo o resultado de um evento metamórfico regional primário variando de fácies xisto verde a anfibolito, seguido por um segundo evento metamórfico de contato associado à

intrusão do CSGC. Por outro lado, outros autores interpretam ambos os eventos metamórficos como regionais, com o primeiro atingindo condições de fácies anfibolito (zona da estaurolita) e o segundo, síncrono à intrusão, como fácies xisto verde (zona da clorita) com efeitos térmicos e de infiltração restritos à borda de algumas apófises graníticas (Bitencourt, 1983; Hartmann *et al*., 1990). Estudos recentes com base em equilíbrio de fases e pseudoseções na porção sul do PFMC indicaram que o pico metamórfico para as amostras estudadas atingiu temperaturas entre 535 e 590°C e pressões entre 4.7 e 7.6 kbar (Tennholm, 2019; Costa, 2021). Além disso, as autoras indicaram que o metamorfismo de contato é evidente nas proximidades do CSGC e sugeriram que o evento termal ocorreu após o complexo atingir as condições de pico metamórfico regional.

Estudos de proveniência de zircão em metapelitos e xistos revelaram populações arqueanas, paleoproterozóicas e neoproterozóicas (3637 a 774 Ma), sugerindo áreas-fonte de origem continental complexas (Lopes *et al*., 2015; Remus *et al*., 2000; Souza, 2020). Químioestratigrafia baseada em isótopos de C, O e Sr dos mármores dolomíticos indica que a deposição dos carbonatos ocorreu provavelmente entre 770 e 750 Ma (Goulart *et al*., 2013; Neis, 2017). Datações em monazitas de xistos pelíticos do PFMC por LA-ICP-MS resultou em uma série de idades entre 650 e 620 Ma, que foram atribuídas ao primeiro evento metamórfico (Remus *et al*., 2010). O segundo evento metamórfico foi então relacionado à idade obtida para uma apófise granodiorítica do CSGC de 562 ± 8 Ma com base em datação de zircão SHRIMP U-Pb (Remus *et al*., 2000).

4.2.2. Complexo Granítico Caçapava do Sul

O Complexo Granítico Caçapava do Sul (CSGC) exibe uma ampla variedade composicional, sendo principalmente composto por granodioritos, monzogranitos, leucogranitos, dioritos, tonalitos e quartzo-dioritos de afinidade metaluminosa e cálcio-alcalina (Leinz *et al*., 1941; Ribeiro *et al*., 1966; Sartori & Kawashita, 1985; Nardi & Bitencourt, 1989; UFRGS, 1998). Modelos de posicionamento contrastantes foram propostos incluindo (i) um modelo diapírico (Nardi & Bitencourt, 1989); (ii) uma intrusão em forma de alongada sub-horizontal (Fragoso César, 1991); (iii) um mega-porfiroblasto em forma de lente (Fernandes *et al*., 1992) ou (iv) uma intrusão ao longo

de uma zona de cisalhamento de deslizamento lateral direito (Costa *et al*., 1995; Costa, 2021).

As primeiras tentativas de datar o CSGC foram feitas por meio de isócronas Rb/Sr e datações K/Ar e, que resultaram em idades entre 520 a 640 Ma (Cordani *et al*., 1974; Sartori & Kawashita, 1985; 1989; Soliani, 1986). Estudos de U-Pb SHRIMP em zircão foram realizados em apófises graníticas, revelando uma distribuição complexa de idades que indicaram quantidades significativas de perda de chumbo incluindo idades inversamente discordantes (Leite *et al*., 1998; Remus *et al*., 2000). Os dois estudos relataram idades concordantes dentro do mesmo erro de 561 ± 6 Ma (MSWD = 1,04; n = 4; Leite *et al*., 1998) e 562 ± 8 Ma (MSWD = 0,56; n = 18; Remus *et al*., 2000) e outra idade de 540 ± 11 Ma (MSWD = 0,89; n = 3; Leite *et al*., 1998). A idade mais jovem de *ca.* 540 Ma foi reinterpretada como resultado da perda de chumbo comum de zircões mais antigos (Remus *et al*., 2000). Populações herdadas de zircões paleoproterozoicos com idades variando de 1,7 a 2,4 Ga foram relatadas em ambos os estudos. As grandes variações nos valores iniciais de $^{87}Sr/^{86}Sr$ e εNd, isótopos de chumbo e idades de zircão sugerem que o CSGC foi gerado a partir de uma fonte crustal complexa e heterogênea de composição e idade variáveis (Sartori & Kawashita, 1989; Babinski *et al*., 1996; Remus *et al*., 2000).

5. ESTADO DA ARTE

5.1. METASSOMATISMO

O termo metassomatismo foi introduzido por Naumann (1826) e atualmente é definido pela IUGS-SSMR (União Internacional de Ciências Geológicas - Subcomissão de Sistemática de Rochas Metamórficas) como o processo metamórfico pelo qual a composição de uma rocha é modificada de maneira pervasiva contemplando a adição ou remoção de componentes químicos como resultado da interação entre a rocha e fluidos penetrantes. Durante o metassomatismo a rocha permanece essencialmente no estado sólido (Zharikov *et al*., 2007). As principais características do metassomatismo incluem:

1. Substituição íon-por-íon em minerais;
2. Substituição das rochas no estado sólido, diferindo dos processos de interações magma-rocha ou cristalização de fusões;

3. Mudanças substanciais na composição das rochas que ocorrem tanto pela adição como pela subtração de elementos maiores, além de H_2O e CO_2;
4. Formação de zonas ou zonações regulares, representando equilíbrio químico entre duas rochas ou entre uma rocha e um fluido infiltrante.

O metassomatismo pode ocorrer por dois processos principais: difusão e infiltração. O primeiro é caracterizado pela difusão de um soluto através de um fluido, gerada pelos gradientes de atividade química na solução rocha-poro. As rochas metassomáticas formadas por difusão contemplam corpos finos zonados (franjas) ao longo de fraturas, veios e superfícies de contato e a composição dos minerais pode variar gradualmente através de cada zona metassomática. Já o metassomatismo de infiltração ocorre pela movimentação dos fluidos e a transferência de material em solução através das rochas hospedeiras, motivada pela pressão e por gradientes de concentração entre os fluidos infiltrantes e as soluções rocha-poro. Neste caso, os elementos são transportados passivamente na solução. Além disso, as rochas metassomáticas formadas por infiltração ocupam volumes maiores (comparados ao processo de difusão) e a composição dos minerais tende a ser constante ao longo de cada zona metassomática.

A formação regular de conjuntos de zonas é típica do metassomatismo. Estas zonas formam um padrão característico ao longo do corpo metassomático. O padrão zonal representa o equilíbrio químico entre duas rochas ou entre uma rocha e o fluido. No caso de difusão, as mudanças minerais ocorrem de maneira transicional ao longo das zonas e no caso de infiltração as mudanças ocorrem em etapas. O número de zonas metassomáticas depende das condições físico-químicas do meio. O caso mais simples pode ser representado por uma única zona. Todas as zonas numa coluna metassomática são geradas e crescem concomitantemente, com aumento de espessura na direção à principal superfície de infiltração ou transporte de massa.

O metassomatismo é um processo importante na evolução de uma grande variedade de sistemas geológicos, porém ainda relativamente pouco estudado devido à complexidade dos sistemas que envolvem reações químicas e processos físicos em condições de pressão e temperatura onde informações básicas sobre as propriedades dos fluidos comumente está ausente (Yardley, 2013). Entretanto, os estudos do metassomatismo têm evoluído de especulações petrológicas para investigações e avaliações mais rigorosas. O metassomatismo tem sido discutido como um braço da

petrologia, principalmente no contexto das rochas metamórficas, mas também como um braço da geologia econômica, em função dos diversos depósitos minerais formados por processos metassomáticos (mais comumente denominada de “alteração” na Geologia Econômica). No entanto, o estudo isolado do metassomatismo nestas duas áreas do conhecimento acabou resultando em algumas terminologias distintas para os mesmos processos.

5.1.1. Controles e Tipos de Metassomatismo

Os principais controles do metassomatismo estão relacionados a origem, concentração e abundância de fluidos. Em relação à origem, os fluidos metassomáticos podem ser (i) fluidos pré-existentes entre poros (água de formação) que são expulsos das rochas hospedeiras; (ii) fluidos metamórficos gerados por reações de desvolatilização, ou (iii) fluidos magmáticos liberados durante a cristalização do magma. Em relação à concentração e abundância de fluidos, a magnitude do metassomatismo depende tanto da concentração de sólidos dissolvidos no fluido quanto à quantidade dele que flui para formar uma rocha metassomática. Em ambientes rasos da crosta, onde grandes fluxos de fluido são possíveis (*e.g.*, ambientes geotermais), muitas mudanças podem ocorrer mesmo que os fluidos sejam muito diluídos. Já em ambientes da crosta inferior, os fluidos são tipicamente mais concentrados e podem causar metassomatismo intenso com quantidade de fluidos reduzida (Yardley, 2013).

Dentre os processos metassomáticos formados por fluidos pré-existentes, o mais conhecido é o metassomatismo de fundo oceânico. Neste processo há interação das rochas basálticas com a água do mar, modificando a composição dos basaltos e da própria água oceânica.

A cristalização de uma rocha ígnea intrusiva pode gerar uma variedade de processos metassomáticos que afetam a própria rocha (autometassomatismo), gerando fenitos ou greisens, ou que afetam as rochas encaixantes (metassomatismo de contato), formando escarnitos, por exemplo. Entretanto, nem todas as intrusões são acompanhadas por metassomatismo, o que já fornece informações sobre as condições físico-químicas da intrusão e quantidade e composição de fluidos liberados durante o processo de cristalização.

A liberação e migração de fluidos metamórficos, que ocorre principalmente a partir de reações de desvolatilização, pode gerar metassomatismo associado a estruturas sin-metamórficas (*e.g.*, Huang & Rubenach, 1995), escarnitos no contato entre xistos e mármores (Yardley *et al.*, 1991), entre outros. Entretanto, muitos exemplos de metassomatismo associado ao metamorfismo e falhas profundas ou zonas de cisalhamento, deixam dúvidas em relação à fonte dos fluidos pela falta de evidências que confirmem a origem metamórfica dos fluidos. Os efeitos do metassomatismo durante o metamorfismo progressivo ainda continuam controversos, pois a documentação deles é complexa quando não há feições óbvias de metassomatismo e há um número reduzido de fases (Yardley, 2013). Além disso, os fluidos metamórficos são gerados muito lentamente, pois as reações de desvolatilização são fortemente endotérmicas, enquanto o fluxo de calor na crosta é muito baixo (tipicamente entre 30 e 100 Wm^{-2}), gerando baixas taxas de fluxo de fluidos apesar das altas pressões. Os fluidos gerados pelo metamorfismo regional também são limitados pela dificuldade de recircular, já que se movem para regiões de menor pressão e como resultado, é provável que continuem a reequilibrar com as rochas que atravessam sem produzir uma assinatura química bem definida. Apesar das dificuldades em evidenciar que as reações de desidratação possam gerar um fluxo de fluidos suficiente para acarretar metassomatismo, alguns autores propõem que volumes significativos de fluidos metamórficos podem afetar grandes volumes de rocha, resultando em metassomatismo local durante o metamorfismo regional (*e.g.* Ferry, 1994; Ague, 1994).

5.1.2. Mecanismos de fluxo de fluidos durante o metamorfismo

O fluxo dos fluidos pode ser pervasivo ou canalizado e está distinção varia de acordo com a escala de observação. No geral, o conceito é principalmente utilizado a nível regional ou em escala de afloramento. O fluxo pervasivo é aquele que afeta todo volume de rocha, controlado por microestruturas criadas por diversos processos (*e.g.*, deformação, mudanças de volume por reações de desvolatização, entre outros; Ferry, 1994). O fluxo pervasivo ocorre principalmente na escala do grão mineral e os principais controles microestruturais incluem os ângulos diedros (von Bargen & Waff, 1986), anisotropia mineral e microfraturas. Em agregados minerais isotrópicos com ângulos diedros menores que 60° forma-se uma rede de porosidade estável (Bulau *et*

al., 1979). Os ângulos diedros normalmente são menores em baixas temperaturas e alcança 60° em aproximadamente 450°C para fluidos compostos por H_2O pura (Holness, 1993). Ainda assim, fluxos pervasivos são observados em rochas metamórficas de temperaturas muito mais elevadas, portanto, outros mecanismos foram propostos. Processo de dissolução e precipitação é um modo formador de porosidade amplamente aceito no qual os fluidos infiltram gradativamente pelos contatos dos grãos gerando reações de dissolução e precipitação que formam uma rede de porosidade através da rocha (*e.g.*, Putnis & Putnis, 2007; Putnis & Ruiz-Agudo, 2013). Além disso, a deformação comumente produz uma série de microfraturas nos grãos que resulta em uma rede de porosidade utilizada pelos fluidos gerando um fluxo pervasivo onde a porosidade era praticamente inexistente (*e.g.*, Ferry, 1994).

O fluxo canalizado normalmente afeta somente as porções de rocha no entorno de estruturas de circulação preferenciais de fluido. A canalização dos fluidos em terrenos metamórficos normalmente se dá ao longo de fraturas, falhas, zonas de cisalhamento, litologias permeáveis, zonas de charneira, contatos litológicos ou descontinuidades paralelas a acamamento ou foliação (Figura 3; Ague, 2003). Esta canalização de fluidos resulta em veios e suas respectivas “ouréolas” (*i.e.*, halos, zonas de reação; *selvedges*).

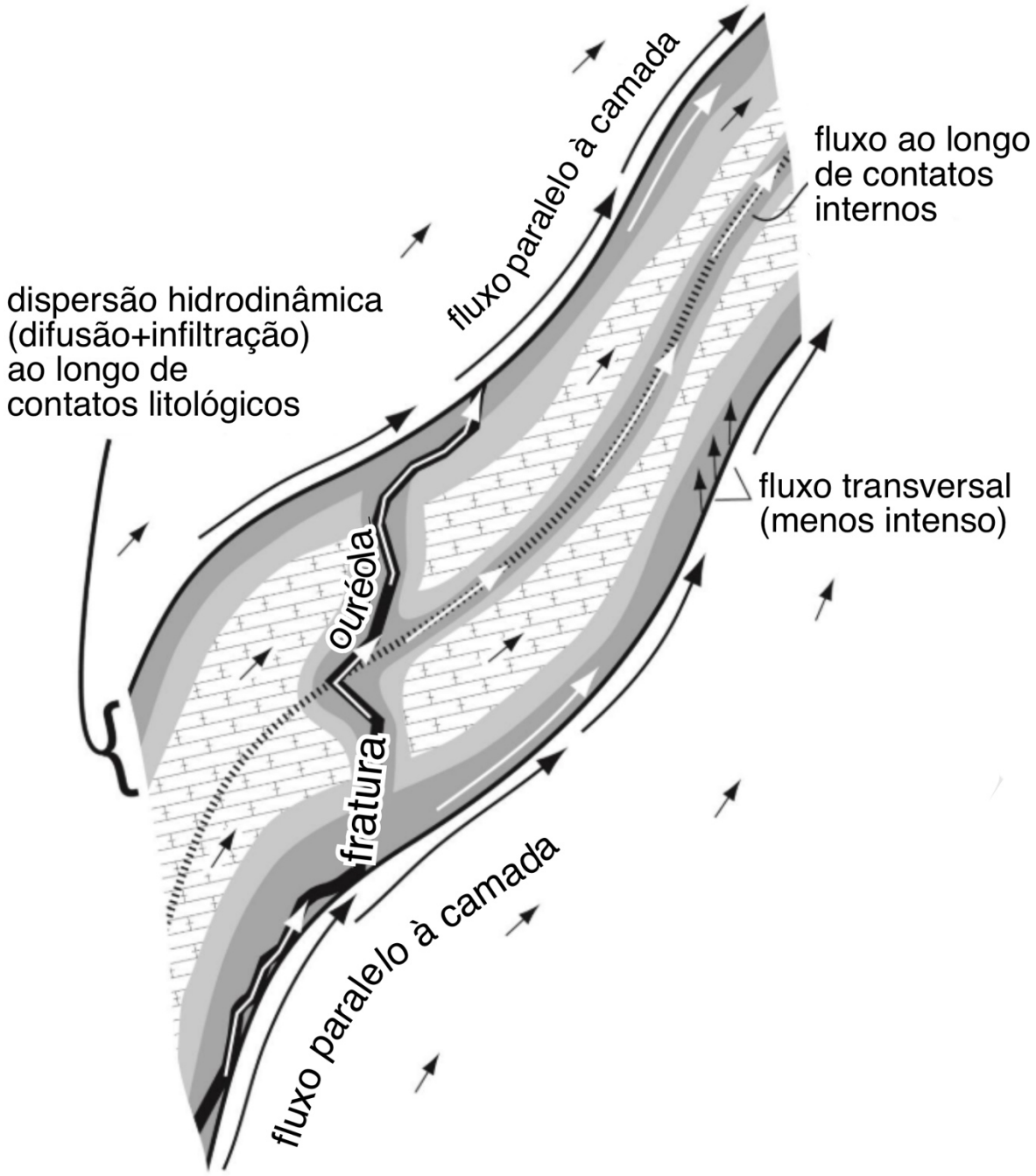

Figura 3: Resumo de alguns tipos de fluxos canalizados de fluidos durante o metamorfismo (traduzido de Ague, 2003). A dispersão hidrodinâmica e o fluxo transversal representam componentes menores induzidos por reações de desvolatização ou formacão de ouréolas. Fluidos originados destes processos tendem a ser canalizados a superficies de maior permeabilidade como contatos litológicos, fraturas ou discontinuidades internas.

5.1.3. Fluidos crustais e fluidos metassomáticos associados a intrusões

O sistema H_2O–CO_2–NaCl é utilizado para representar as principais relações de fases dos sistemas metassomáticos. Entretanto, ainda que haja grande solubilidade entre H_2O e NaCl e entre H_2O e CO_2, fluidos ricos nos três componentes só existem em condições extremas de pressão e temperatura e segregam durante o resfriamento ou despressurização. Uma sequência representativa de diagramas de fase para este sistema está demonstrada na Figura 4. Em altas temperaturas a água reage com as rochas silicáticas para produzir fusões hidratadas. Portanto, fluidos aquosos não são comuns em temperaturas acima de 700ºC. Contudo, em altas pressões, os fluidos com alta salinidade diminuem a atividade da água fazendo com que ela permaneça na fase fluida mesmo submetida a altas temperaturas. Na maioria das condições de pressão da crosta, a química dos fluidos é descrita pelo conteúdo de sais dissolvidos. O ânion predominante é o cloro enquanto o sódio é o principal cátion, mesmo que em concentrações menores que o Cl. A troca do Na por outros cátions é possível, principalmente em altas temperaturas. O Ca, K, e o Fe são componentes importantes nas salmouras crustais (Yardley, 2013).

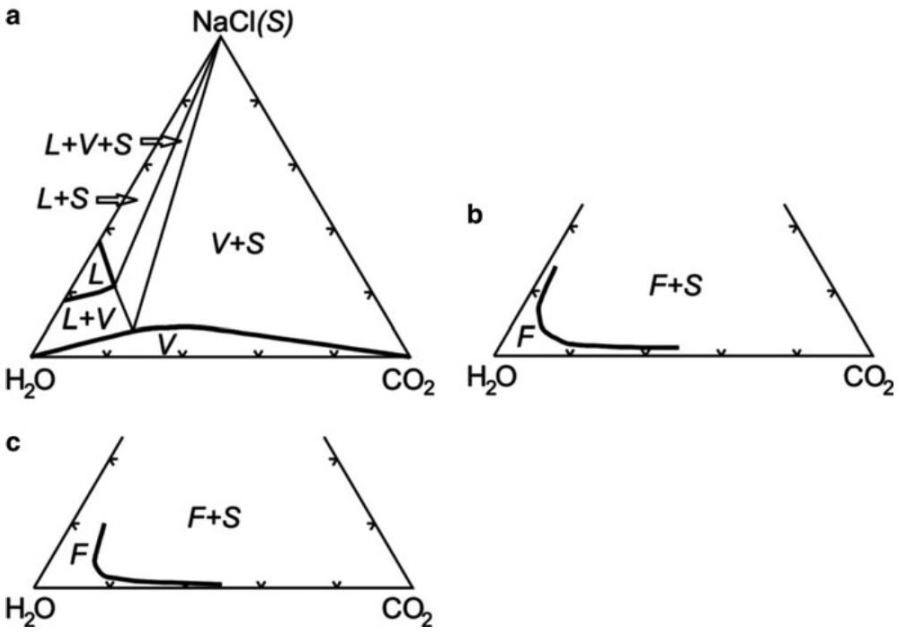

Figura 4: Relações de fase no sistema NaCl-H2O-CO2 . (a) 500°C e 50 MPa (b) 800°C e 200 MPa (c) 500°C e 500 MPa. F=fluido, L=liquido, S=sólido, V=vapor (Extraído de Yardley, 2013).

A composição dos fluidos gerados pela cristalização magmática varia bastante em função da química do magma inicial e das condições de cristalização, principalmente relacionadas à profundidade. Os fluidos podem ser gerados nos estágios iniciais de cristalização e interagirem com as fusões silicáticas ou surgirem somente nos estágios finais e afetarem as encaixantes e a própria rocha intrusiva já cristalizada. Além de serem enriquecidos em elementos incompatíveis, os fluidos gerados também podem produzir reações com as hospedeiras em função das diferenças no pH ou no estado de oxidação.

Os fluidos podem ser exsolvidos dos magmas como salmouras, fluidos ricos em CO_2 ou ricos em H_2O. A evolução na composição dos fluidos depende principalmente das condições de pressão no momento da segregação destes fluidos da fusão (Cline & Bodnar, 1991). Ainda que haja uma ampla gama de rochas metassomáticas associadas com intrusões, as mais comuns são os fenitos, greisens e escarnitos.

5.2. ESCARNITOS

O termo *skarn* surgiu na Suécia, sendo utilizado na mineração para referir-se às rochas cálcio-silicáticas de granulação grossa associadas ao minério de ferro (Törnebohm, 1875). No Brasil, a maioria dos autores tem utilizado o termo “escarnito” como tradução livre para o termo *skarn* (*e.g.* Jordt-Evangelista *et al*., 2000; Creach *et al*., 2011; Remus *et al*., 2011; Parente *et al*., 2015; Mesquita, 2016).

As definições de escarnito variam de acordo com o autor, desde classificações mais abrangentes que consideram apenas características mineralógicas, até as mais restritas que incluem aspectos genéticos ou metalogenéticos (Kerrick, 1977; Burt, 1982; Meinert, 1992; Pirajno, 2013). Para fins de simplificação, neste trabalho o termo escarnito será utilizado como: rocha metassomática composta por silicatos e carbonatos formada pela interação entre uma rocha ou fluido de origem ígnea e uma rocha carbonática, independente da presença ou não de mineralização associada. Neste caso, o termo escarnito se sobrepõe a classificações mais abrangentes como “alteração” ou “veios hidrotermais”. Diversos autores optam por utilizar estes termos em estudos envolvendo escarnitos (*e.g.*, Bégué *et al*., 2019; Guo *et al*., 2021).

A gênese dos escarnitos está comumente associada ao metarmorfismo de contato e por vezes ao metamorfismo regional. São rochas encontradas adjacentes a plútons,

ao longo de falhas, zonas de cisalhamento, sistemas geotermais rasos, no topo do assoalho oceânico ou em terrenos metamórficos na crosta inferior. As assembleias minerais dos escarnitos fornecem informações sobre as condições de temperatura, pressão e as composições da rocha hospedeira e do fluido. Em geral, são rochas de grande interesse econômico, pois são tipicamente exploradas para uma vasta variedade de elementos como ferro, cobre, ouro, prata, estanho, zinco, molibdênio, tungstênio, urânio, flúor, boro e elementos terras-rara (Meinert *et al*., 2005). Os escarnitos ocorrem em todos os continentes e em rochas de praticamente todas as idades. Os escarnitos não devem ser confundidos com cornubianitos cálcio-silicáticos. Enquanto que essas rochas são relativamente homogêneas formadas por metamorfismo isoquímico (podendo incluir reações de desvolatização) de rochas carbonáticas impuras, os escarnitos envolvem a transferência de massa entre as rochas e fluidos envolvidos.

5.2.1. Classificação dos Escarnitos

Neste trabalho adotamos termos descritivos para distinguir os escarnitos com base em sua posição espacial e assembleia mineral. Utilizamos os termos descritivos amplamente empregados, como endo- vs. exoescarnito; escarnito cálcico vs. magnesiano e prógrado vs. retrógrado (*e.g.*, Meinert *et al*., 2005; Winter, 2013). Endoescarnitos contemplam as substituições que ocorrem na rocha intrusiva envolvida na reação. Em geral, são os que substituem os granitoides formando rochas ricas em epidoto ou granada grossulária, geralmente de volume limitado. Os exoescarnitos são mais comuns e são aqueles formados pela substituição das rochas carbonáticas. Os exoescarnitos que substituem rochas magnesianas (dolomitos ou mármores dolomíticos) são denominados escarnitos magnesianos, enquanto que os que substituem rochas ricas em cálcio (calcários ou mármores calcíticos) são classificados como escarnitos cálcicos.

Os escarnitos predominantemente compostos de carbonatos e minerais anidros tipicamente de alta temperatura (i.e, diopsídio, forsterita e espinélio) são classificados como escarnitos prógrados, enquanto aqueles com carbonatos e assembleias hidratadas de baixa temperatura (*i.e.*, clorita, antigorita e talco) são denominados escarnitos retrógrados. Em termos de posição espacial, os escarnitos são divididos em escarnitos de contato e de veio. Escarnitos de contato ocorrem nas interfaces entre

apófises ígneas e mármores devido ao metassomatismo de difusão e/ou infiltração ao longo dos contatos litológicos. Os escarnitos de veio referem-se àqueles formados pela infiltração de fluidos ígneos em fraturas, descontinuidades ou contatos internos dos mármores, levando à substituição de carbonatos por associações de cálcio-silicáticas (± sulfetos). Ainda, neste trabalho utilizamos o termo "veio" para nos referirmos às assembleias formadas no preenchimento de fraturas e às respectivas zonas de reação associadas que substituem a rocha hospedeira (*i.e.*, ouréola ou *selvdge*).

5.2.2. Profundidade de formação dos escarnitos

Um dos controles mais fundamentais do tamanho e geometria dos escarnitos é a profundidade de formação do corpo escarnítico. As estimativas de profundidade são tipicamente realizadas através de estudos de geobarometria com base em equilíbrio mineral (*e.g.*, Anovitz & Essene, 1990), inclusões fluidas (*e.g.*, Guy *et al*., 1988) ou combinações desses métodos (*e.g.*, Hames *et al*., 1989). Os métodos qualitativos incluem reconstruções estratigráficas, modelos geológicos e interpretações de texturas ígneas ou geobarometria de assembleias ígneas. Observações simples de margens resfriadas, morfologia de plútons, tamanho de pórfiros, presença de brechas e fraturas permitem distinguir entre ambientes mais rasos ou mais profundos.

A profundidade influencia diretamente os processos formadores dos escarnitos, principalmente em função do contraste de temperatura entre a intrusão e as rochas hospedeiras. Assumindo um gradiente geotermal médio de aproximadamente 35ºC/km (*e.g.*, Blackwell *et al*., 1990), a temperatura das rochas hospedeiras a 2 km seria de 70ºC, enquanto que a 12 km seria de 420ºC. Com o fluxo de calor proveniente da intrusão, o volume de rocha afetado por temperaturas entre 400 e 700ºC é consideravelmente maior e com efeitos mais prolongados que em baixas profundidades. Portanto, os ambientes de maior profundidade e temperatura afetam a história de cristalização de um plúton (neste caso de um pulso único) e podem reduzir a quantidade de minerais formados por retrometamorfismo. Isso ocorre porque em maiores profundidades e temperaturas, o escarnito pode não resfriar abaixo da zona de estabilidade da granada e do piroxênio se não houver soerguimento ou outras mudanças tectônicas.

A profundidade de formação dos escarnitos também afeta as propriedades mecânicas das rochas hospedeiras. Em ambientes mais profundos, as rochas tendem a deformar-se ductilmente ao invés de ruptilmente. Contatos intrusivos com rochas sedimentares em maior profundidade tendem a ser sub-paralelos ao acamamento ou foliação pré-existente. Nestes casos, o plúton intrude ao longo de planos de acamamento ou as rochas sedimentares dobram-se e/ou fluem até que estejam alinhadas com o contato intrusivo. Em contraste, as rochas hospedeiras em sistemas mais rasos tendem a deformar-se formando fraturas ou falhas ao invés de dobras. Sendo assim, os contatos são tipicamente discordantes para sistemas formados em baixas profundidades e os escarnitos comumente cortam o acamamento ou foliação pré-existente. O hidrofraturamento que ocorre em sistemas mais rasos aumenta a permeabilidade das rochas hospedeiras não só para os fluidos ígneos, mas também para fluidos posteriores, como a água meteórica, por exemplo. A introdução de água meteórica e subsequente alteração da mineralogia escarnítica de alta temperatura é uma característica típica dos escarnitos formados em ambientes rasos.

5.2.3. Mineralogia dos escarnitos

A identificação e classificação de depósitos minerais dos escarnitos são tradicionalmente baseados na sua mineralogia (Einaudi *et al*., 1981; Meinert, 1992; Meinert *et al*., 2005). Mesmo que alguns minerais sejam típicos minerais formadores de rocha, alguns são menos abundantes e a maioria possui variações composicionais que carregam informações importantes sobre o ambiente de formação da rocha. Minerais como o quartzo e a calcita podem estar presentes em praticamente todos os tipos de escarnitos. Outros como forsterita, humita, periclásio, flogopita, talco, serpentina e brucita são típicos de escarnitos magnesianos, por exemplo. Nos tipos cálcicos predominam as granadas (principalmente grossulária e/ou andradita) e a wollastonita. Além disso, muitos minerais com estanho, boro, berílio ou flúor na sua estrutura que são de ocorrência restrita, são localmente importantes. A utilização da microssonda eletrônica torna relativamente fácil a determinação precisa da composição dos minerais e, assim, das variedades específicas dos minerais. No entanto, apesar da série de piroxênios envolver várias composições e nomes específicos, é comum na literatura utilizar somente os termos finais das séries, tal como diopsídio, quando só o que se sabe é que se trata de um piroxênio, por exemplo.

Contudo, os minerais mais úteis para classificação e estudo dos escarnitos utilizados são aqueles que estão presentes na maioria dos escarnitos e possuem ampla variedade composicional, como as granadas, anfibólios e piroxênios. A Figura 5 ilustra as composições mais comuns das granadas e piroxênios relacionados a diferentes tipos de escarnitos mineralizados.

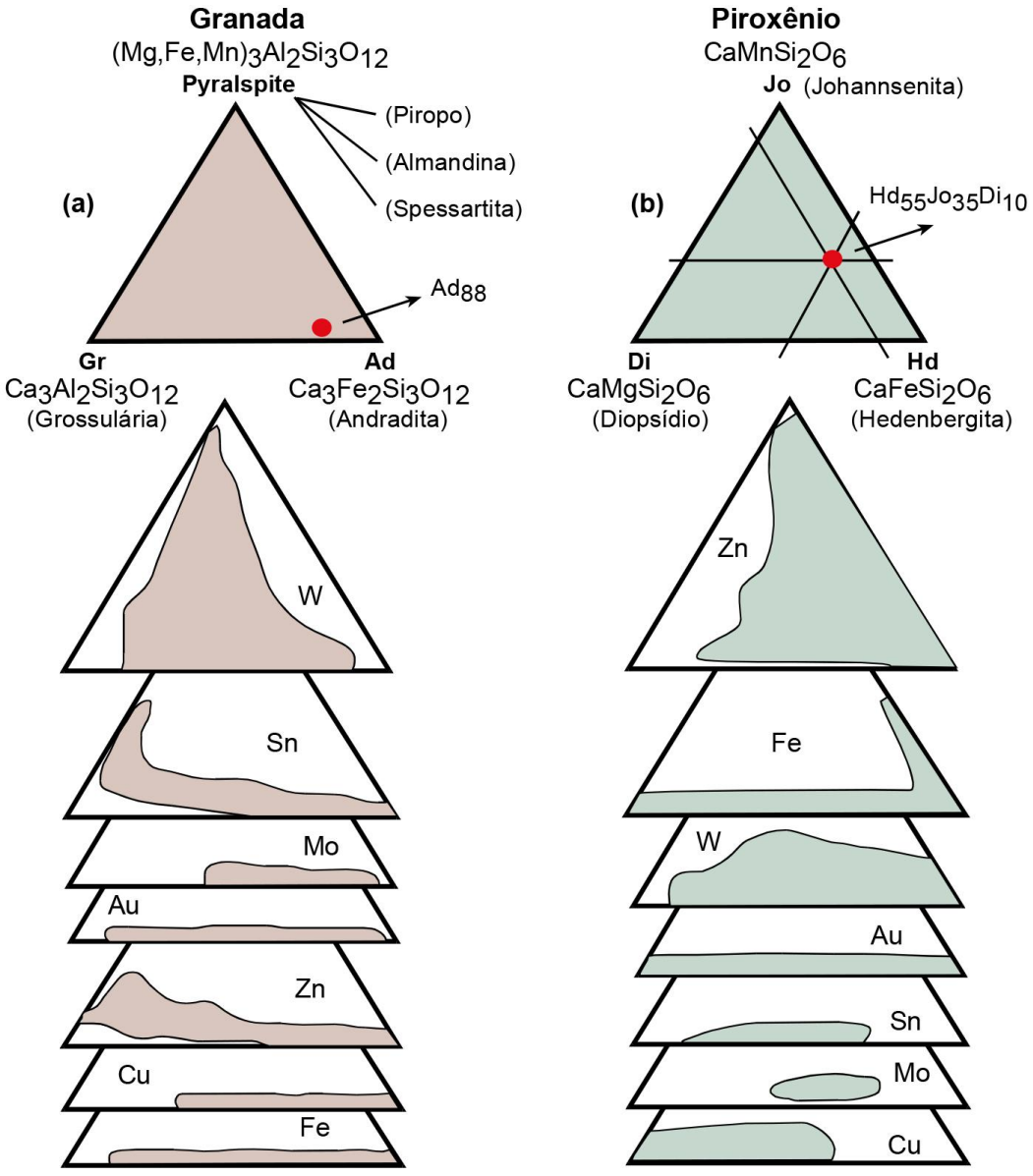

Figura 5: Variações composicionais das granadas e piroxênios relacionadas aos diferentes tipos de depósitos escarníticos (traduzido de Einaudi *et al*., 1981).

Os escarnitos magnesianos contém principalmente diopsídio, forsterita, serpentina, magnetita e talco em locais com pouca sílica, e talco, tremolita-actinolita em ambientes mais ricos em sílica. Além destes, é comum a presença de espinélio, periclásio,

clinohumita, flogopita e pargasita. Quando mineralizados, tipicamente hospedam minérios de ferro, cobre, ouro, boratos de Fe-Mg e flogopita (Meinert *et al*., 2005). Estes escarnitos desenvolvem-se tanto em estágios magmáticos como pós-magmáticos. Os escarnitos cálcicos consistem principalmente de granada grossulária, diopsídio (salita, ferrosalita ou johannsenita), wollastonita, vesuvianita, rodonita, bustamita, epidoto, escapolita e plagioclásio. Comumente hospedam minério de ferro, metais base, cobre, tungstênio, molibdênio, berílio, boro, urânio e elementos terras-rara. Praticamente todos escarnitos cálcicos ocorrem no estágio pós-magmático (Zharikov *et al*. 2007).

5.2.4. Estágios de Formação dos Escarnitos

Apesar das diferenças entre os tipos de escarnitos em diferentes ambientes tectônicos e distintas composições da rocha intrusiva e da rocha hospedeira, a maioria dos escarnitos passa por três processos principais: (i) metamorfismo de contato isoquímico com ou sem infiltração de fluidos ígneos nos estágios iniciais da intrusão; (ii) metassomatismo e alteração durante a saturação dos fluidos magmáticos e (iii) soerguimento e mistura com fluidos meteóricos durante resfriamento do plúton (Einaudi *et al*., 1981; Meinert, 1992).

Na fase inicial da intrusão ígnea, a rocha hospedeira pode desenvolver texturas cornubianíticas e a assembleia mineral formada nesta etapa tende a refletir a composição da litologia original. A produção de fluidos neste estágio comumente está associada às reações metamórficas de desvolatilização, envolvendo principalmente H_2O e CO_2. O desenvolvimento da zonação metamórfica com a sequência granada-clinopiroxênio-tremolita-talco/flogopita é comum em unidades dolomíticas. Geralmente não há mineralização associada a este estágio, ainda que as reações de desidratação nas margens dos plútons seja um fator importante para o aumento da porosidade das rochas fonte de minério e facilite o fluxo de fluidos durante os estágios subsequentes de mineralização.

A segunda etapa de formação dos escarnitos envolve a saturação dos fluidos no magma (em função do *boiling* primário, secundário ou ambos) e há o escape desta fase fluida para as rochas encaixantes. Em porções profundas da crosta, o fluxo de fluido tende a ser canalizado em fraturas, falhas ou paralelo ao acamamento/foliação das encaixantes. Em níveis crustais mais rasos, o fluxo de fluidos tende a ser mais

pervasivo e menos canalizado, possivelmente devido ao hidrofraturamento, tanto nas encaixantes como na própria intrusão. As assembleias minerais metassomáticas formadas neste estágio são similares àquelas formadas na etapa anterior, entretanto, a alteração é mais pervasiva e com granulação mais grosseira. Além disso, é mais comum a mobilização de Si, Al, Fe e outros componentes da intrusão para a rocha carbonática, enquanto o Ca, Mg e CO_2 dos carbonatos tendem a serem incorporados na fase fluida. A cristalização de magnetita e scheelita tipicamente ocorre no final deste estágio. Entretanto, a deposição de sulfetos não é comum nesta etapa.

A última etapa contempla o resfriamento do plúton com possível acréscimo de fluidos meteóricos no sistema gerando substituição dos minerais formados em etapas anteriores por fases hidratadas. Os minerais mais comuns formados nesta etapa são epidoto, biotita, clorita, plagioclásio, calcita e quartzo (substituindo as granadas), tremolita-actinolita e talco (substituindo piroxênios) e serpentinas (substituindo as olivinas). A mineralização de sulfetos e óxidos ocorre nesta etapa de maneira disseminada ou em veios que cortam as assembleias formadas nas etapas iniciais. Assembleias do tipo pirita-calcopirita-magnetita geralmente caracterizam ambientes proximais enquanto bornita, esfalerita e galena são tipicamente distais. Os estágios de formação dos escarnitos estão exemplificados na Figura 6.

As mineralizações tardias na maior parte dos depósitos escarníticos indicam que a precipitação dos metais está relacionada com a redução da temperatura dos fluidos (reduzindo também a solubilidade), mistura de fluidos e neutralização dos fluidos pelas reações com litologias carbonáticas.

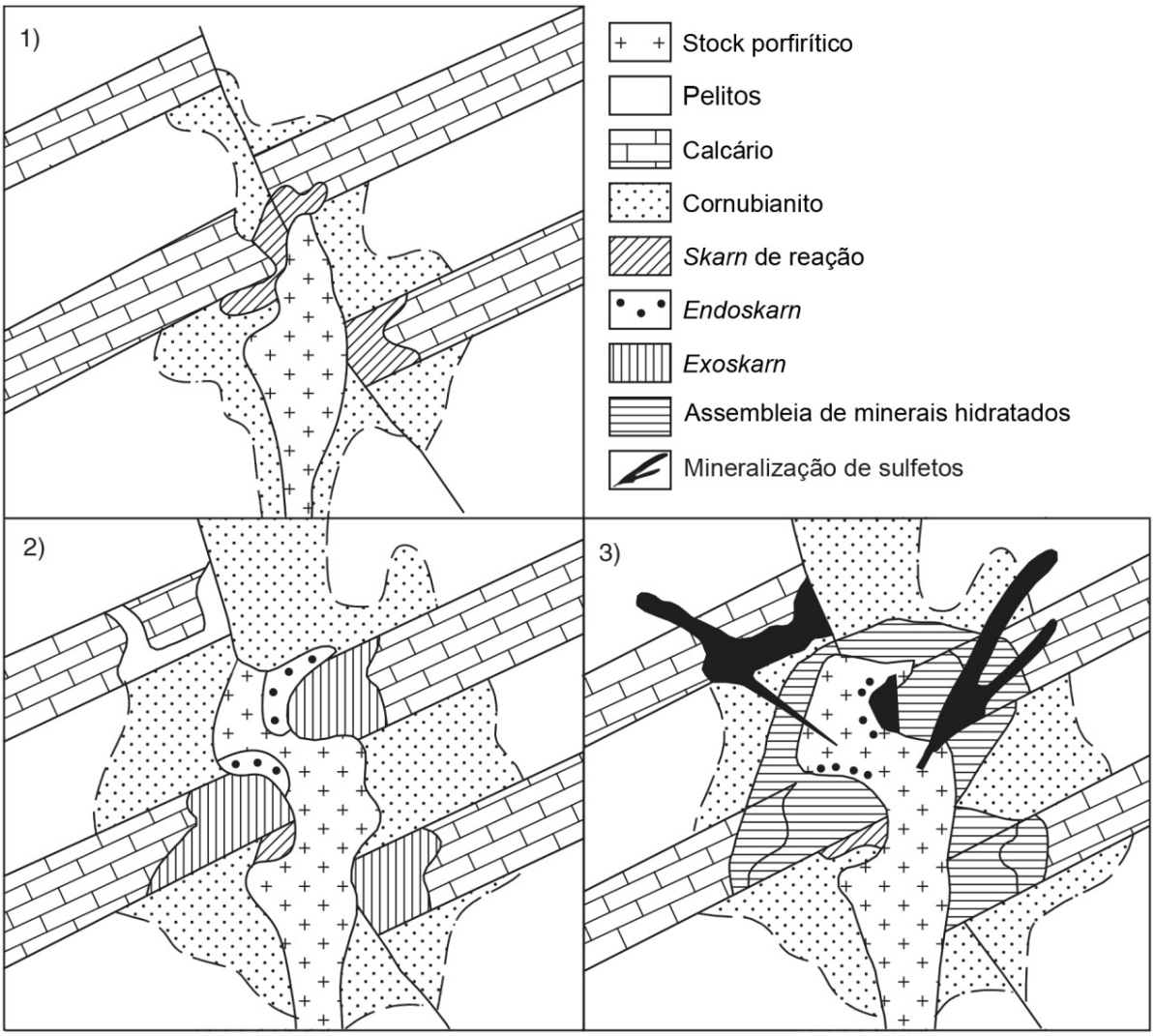

Figura 6: Exemplo de estágios de formação de escarnitos: (1) estágio isoquímico com desenvolvimento de cornubianitos em unidades não siliciclásticas e início da formação de escarnitos de reação; (2) estágio metassomático com amplo desenvolvimento de exoescarnitos e endoescarnitos; (3) estágio retrógrado com substituição de minerais dos escarnitos por minerais hidratados e sulfetos. Modificado de Einaudi *et al*. (1981) e Pirajno (2009).

5.3. ISÓTOPOS ESTÁVEIS APLICADOS AO ESTUDO DOS ESCARNITOS

Os isótopos estáveis de carbono, oxigênio, hidrogênio e enxofre são amplamente utilizados em estudos de escarnitos para identificar fontes e processos da formação desta litologia. A revisão apresentada nesta seção foi baseada principalmente no capítulo *Stable Isotopes Systematics of Skarns* de Bowman (1998) em função da completa abordagem do tema.

A utilização destes isótopos baseia-se no fato de que rochas e fluidos crustais ou do manto superior apresentam composições isotópicas distintas em relação a um ou mais isótopos. Deste modo, os fluidos em equilíbrio com um sistema isotópico passam por mudanças nas características isotópicas ao atravessar sistemas (rochosos ou fluidos) de composições distintas. Além disso, diversos processos geológicos e geoquímicos relacionados aos sistemas escarníticos, incluindo reações de descarbonatação, precipitação, oxirredução e interações fluido-rocha causam mudanças significativas nas razões isotópicas destes elementos. Portanto, as composições isotópicas destes elementos nos escarnitos e sua variação no espaço-tempo dentro do sistema podem fornecer informações sobre a fonte dos fluidos, os componentes dissolvidos e sobre os processos físico-químicos que resultaram em determinado sistema escarnítico.

Diversos reservatórios de rocha e água da terra apresentam valores distintos de δD (isótopo estável de deutério) e $\delta^{18}O$ (isótopo estável de oxigênio), ou ambos. O campo para água magmática, água em equilíbrio isotópico com rochas ígneas, não é alterado a altas temperaturas e é subdividido em campos Tipo I e Tipo S (enriquecido em ^{18}O). Os valores de δD para águas meteóricas e magmáticas coincidem no intervalo de -40 e -80 (por mil), mas mesmo as águas meteóricas relativamente ricas em D possuem valores de $\delta^{18}O$ (-7 ou menos) que são muito menores que aqueles de águas magmáticas. Já os fluidos magmáticos apresentam valores mais baixos de $\delta^{18}O$ que rochas carbonáticas marinhas, por exemplo. Sendo assim, qualquer interação entre rochas carbonáticas marinhas e fluidos magmáticos deve causar uma mudança nos valores de $\delta^{18}O$ de um ou outro ou ambos. Logo, os isótopos de oxigênio e hidrogênio são bons indicadores da origem de fluidos hidrotermais e de avaliação da interação entre fluidos magmáticos e rochas carbonáticas.

A tentativa da determinação do δD e $\delta^{18}O$ dos fluidos geradores de escarnitos pode ser feita de duas maneiras. A primeira delas é analisar diretamente os fluidos hidrotermais, que só é possível em sistemas geotermais modernos ou através de fluidos liberados de inclusões fluidas em minerais de sistemas paleo-hidrotermais. Esta opção tem a vantagem de indicar diretamente a composição isotópica dos fluidos hidrotermais, entretanto sabe-se que pode haver trocas de isótopos de oxigênio com minerais adjacentes (Ohmoto, 1986) e que há dificuldades na extração dos fluidos das inclusões. A segunda e mais comum opção para determinação isotópica dos

fluidos é analisar a composição isotópica dos minerais formados a partir do fluido hidrotermal e então estimar a composição isotópica do fluido levando em consideração fatores como fracionamento e temperatura. Para que esta técnica forneça dados válidos, duas premissas devem ser levadas em conta que (i) os minerais devem ter sido formados em equilíbrio isotópico com o fluido e (ii) que a composição isotópica do mineral no momento da sua formação foi mantida até o momento da análise. Estas premissas devem ser levadas em conta ao aplicar o estudo de isótopos estáveis em sistemas hidrotermais. Uma maneira comum de conferir a validade dos dados isotópicos é avaliar a composição isotópica de diferentes minerais formados pelo fluido em equilíbrio e verificar se há compatibilidade isotópica utilizando os devidos fatores de fracionamento. Além disso, para determinação do δD e $\delta^{18}O$ a partir do δ do mineral, é necessário conhecer a temperatura de formação daquele mineral. A princípio, esta temperatura pode ser estimada a partir de valores de δ de minerais em equilíbrio no sistema. Se não houver pares de minerais calibrados no sistema escarnítico, ou que não estiverem em equilíbrio isotópico, é fundamental que sejam feitos estudos de equilíbrio das fases minerais para determinação da temperatura e depois trabalhar em conjunto com os isótopos estáveis. A Figura 7 apresenta os principais campos de fontes de fluidos em relação às razões isotópicas de δD e $\delta^{18}O$.

Os intervalos de $\delta^{13}C$ e $\delta^{34}S$ nos principais reservatórios de C e S da crosta e do manto superior apresentam valores distintos entre si. O carbono derivado de fonte mantélica ou magmática, por exemplo, apresenta valores de $\delta^{13}C$ entre -5 e -10 por mil. Este carbono é empobrecido em ^{13}C se comparado ao carbono presente em rochas carbonáticas marinhas (entre -3 e +3 por mil) entretanto ambos são enriquecidos se comparados a matéria orgânica presente em rochas sedimentares. Os campos das razões isotópicas dos principais ambientes estão demonstrados na Figura 8 e na Figura 9. Rochas graníticas derivadas de fusão parcial de rochas crustais sedimentares podem apresentar intervalos maiores nos valores de $\delta^{13}C$ que as rochas mantélicas em função do carbono de origem sedimentar ser empobrecido em ^{13}C.

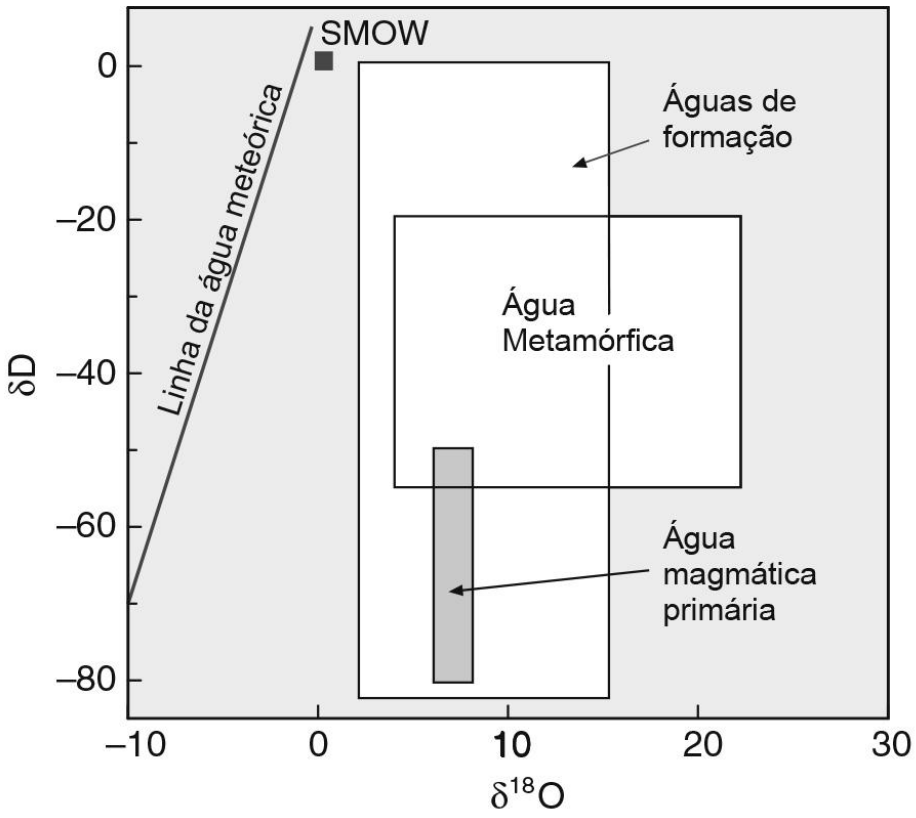

Figura 7: Diagrama δD x $\delta^{18}O$ demonstrando a linha para água meteórica e os principais campos das fontes de fluidos. Traduzido de Hoefs (2015).

Os valores de $\delta^{34}S$ no manto e em magmas derivados do manto (rochas basálticas) apresentam um intervalo estreito, entre 0 a +4 per mil. Hoefs (2015) descreve um intervalo maior de $\delta^{34}S$ para rochas graníticas (-1 a +8). Entretanto, por vezes as rochas granitoides apresentam valores fora desta faixa, tanto maiores como menores, e comumente este fenômeno está relacionado à fusão parcial ou assimilação de enxofre sedimentar da rocha encaixante. Qualquer destes ambientes magmáticos são depletados em ^{34}S em comparação com sulfatos formados a partir de água marinha, mesmo que haja uma variação nos valores de $\delta^{34}S$ durante o fanerozoico. Entretanto, os valores de $\delta^{34}S$ de enxofre sedimentar variam muito, desde -40 até valores enriquecidos como +50. Por causa dessa ampla variação, nem sempre é possível distinguir fontes sedimentares de enxofre de fontes magmáticas ou marinhas. Os valores de δ para minerais que contém C ou S precipitados a partir de um fluido hidrotermal dependem não só das condições de temperatura e dos elementos da fonte, mas também de fugacidade de O e de pH do fluido. Por essas razões que as interpretações dos valores de $\delta^{13}C$ e $\delta^{34}S$ para fonte de C e S num sistema escarnítico necessitam da estimativa de temperatura, $f(O_2)$ e pH do fluido.

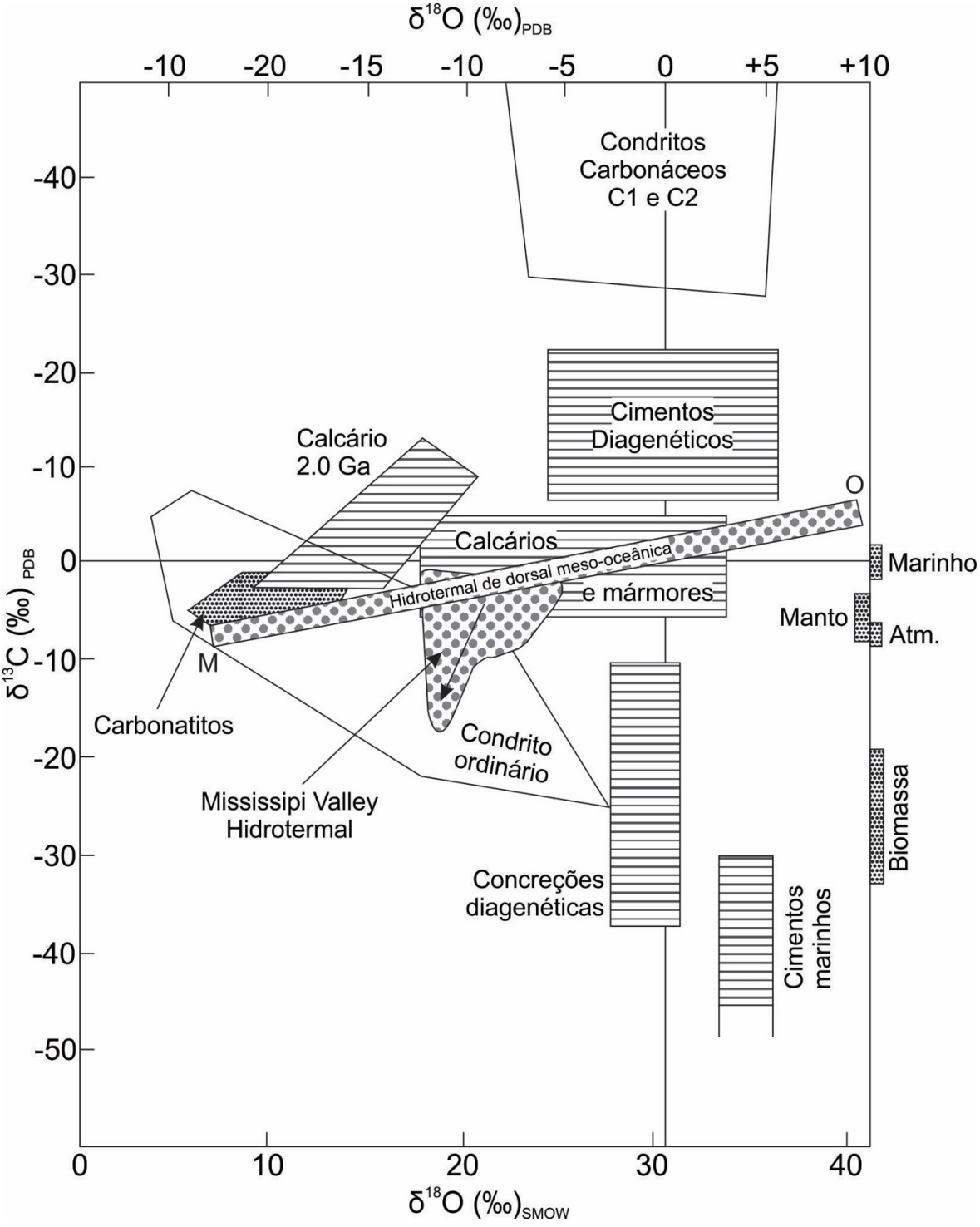

Figura 8: Diagrama δ18O-δ13C demonstrando as principais composições isotópicas dos carbonatos em diversos ambientes. M=manto, O=oceano. Atm.=atmosfera. Modificado de Rollinson (1993).

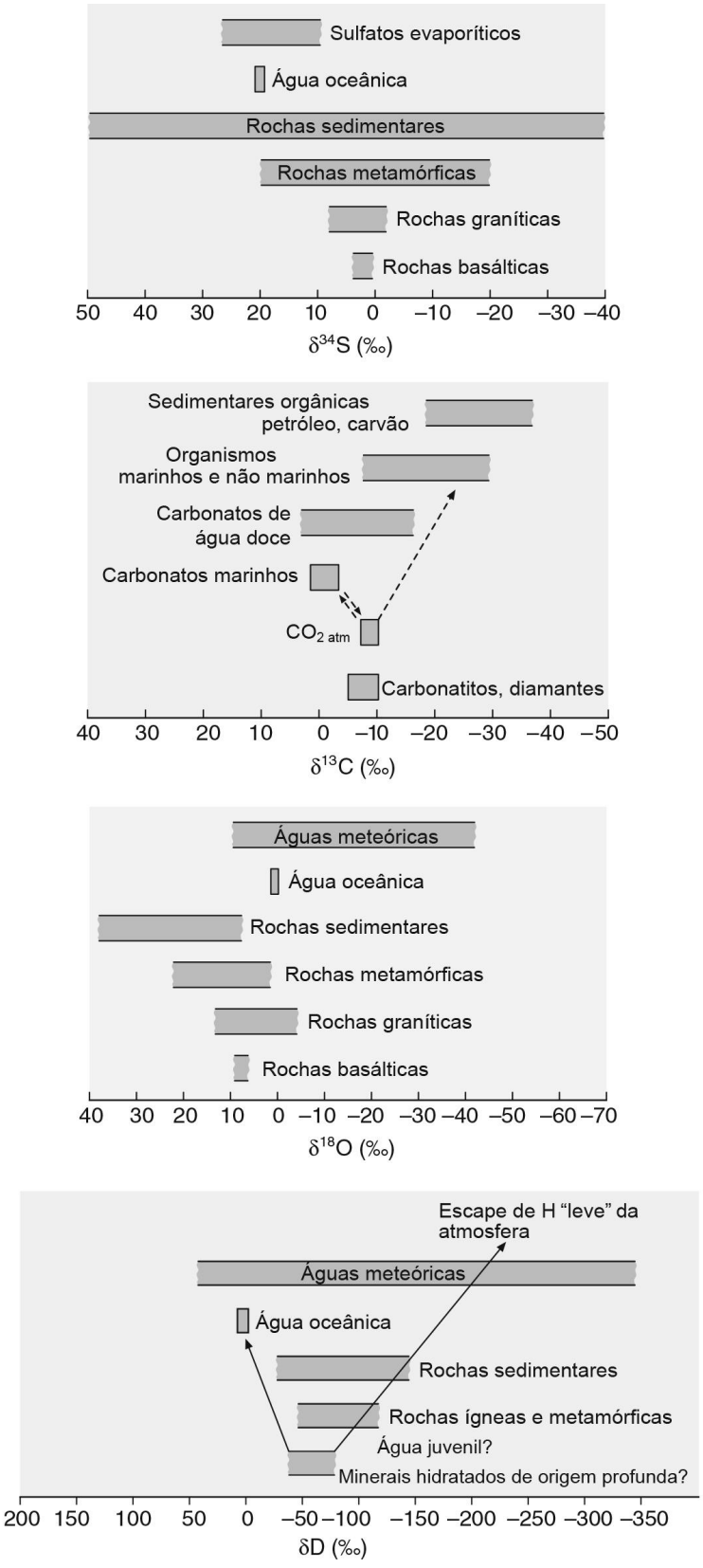

Figura 9: Valores de $\delta^{34}S$, $\delta^{13}C$, $\delta^{18}O$, δD de importantes reservatórios geológicos (Modificado de: Hoefs, 2015).

5.3.1. Processos de Fracionamento Isotópico

Reações de descarbonatação

As rochas carbonáticas que passam por reações de descarbonatação se tornam empobrecidas em ^{18}O e ^{13}C. A maneira que o CO_2 é liberado reflete no modo em como os isótopos serão modificados. Dois casos extremos podem ser observados: separação em estágio único ou separação contínua (destilação de Rayleigh). Uma discussão sobre as implicações das reações de descarbonatação em carbonatos hidrotermais e metamórficos pode ser encontrada em Valley (1986). Entretanto, os aspectos mais relevantes estão descritos a seguir:

1) Na separação em fase única, todo CO_2 fica em contato e em equilíbrio isotópico com a rocha carbonática até que a descarbonatação esteja completa. Então o CO_2 é liberado em uma única etapa. Para esta situação, a composição isotópica de um mineral residual (calcita, por exemplo) pode ser calculado por rearranjo de uma equação básica de balanço de massa (Valley, 1986);
2) Na separação contínua, o CO_2 é removido tão logo é formado e o valor final de δ pode ser calculado pela equação de Rayleigh (Rumble, 1982). A separação contínua gera os valores mais empobrecidos de ^{18}O e ^{13}C. Independentemente de como o CO_2 é separado, a maior depleção de ^{18}O pode resultar do equilíbrio de reações de descarbonatação. Isso ocorre por causa da fração significativa de oxigênio que fica na rocha no final da reação de descarbonatação (Rumble, 1982; Valley, 1986). O ponto crítico em relação à formação de escarnitos é que processos normais de descarbonatação, tanto de fase única como fase contínua podem produzir somente depleções limitadas (2 a 4 por mil) em rochas carbonáticas.

Misturas de H_2O e CO_2

A mistura de fluidos magmáticos com CO_2 produzido por reações de descarbonatação em rochas encaixantes carbonáticas ricas em ^{18}O podem causar enriquecimento de ^{18}O em fluidos formadores de escarnitos. A base para essa mistura e as equações apropriadas de balanço de massa estão descritos em Taylor & O'Neil (1977) e Taylor (1987).

Interação fluido-rocha

Em função das diferentes composições isotópicas de H e O de cada tipo de rocha e fluido, as misturas de fluidos e rochas distintas vão gerar diferenças nos valores de δD e $\delta^{18}O$ do fluido. Esses dois processos produzem diferentes padrões de evolução isotópica em termos de δD e $\delta^{18}O$. A mistura de dois fluidos isotopicamente diferentes vai produzir uma linha de mistura de tendências no diagrama de δD-$\delta^{18}O$, (Figura 10).

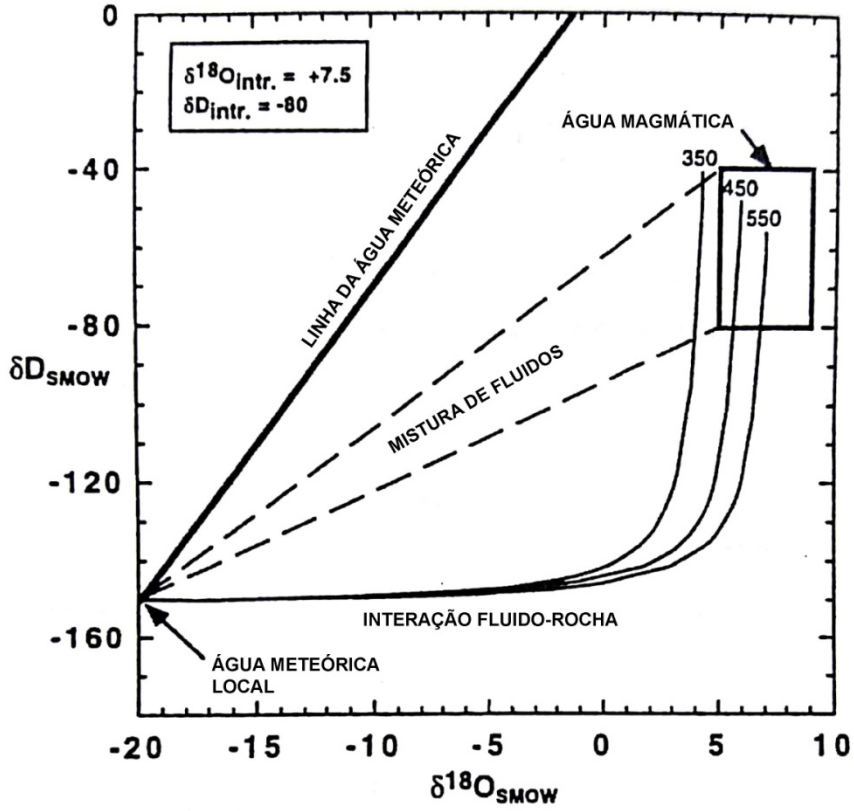

Figura 10: Diagrama δD-δ18O demonstrando a linha meteórica da água, campo da água magmática e linhas de mistura de fluidos e linhas de interação fluido rocha. Traduzido de Taylor (1974).

5.3.2. Fonte de fluidos

Uma característica comum a quase todos os escarnitos é a substituição de carbonatos enriquecidos em ^{18}O da rocha hospedeira por silicatos escarníticos acompanhados de redução significante nos valores de ^{18}O do escarnito até valores de ^{18}O próximos ao equilíbrio com as rochas ígneas intrusivas. Nabelek (1991) mostrou que os valores de $\delta^{18}O$ das calcitas escarníticas estavam correlacionadas com os valores de $\delta^{18}O$ da

intrusão adjacente em sete escarnitos onde informações de isótopos de O estavam disponíveis no momento. A exceção era o escarnito de Sn de Yukon no Canadá, onde os valores de $\delta^{18}O$ da calcita eram significantemente menores que os valores da intrusão adjacente. Em virtude da ocorrência da calcita em diferentes estágios do desenvolvimento destes escarnitos, apenas os valores de $\delta^{18}O$ do estágio inicial eram comparáveis aos valores de $\delta^{18}O$ da intrusão adjacente. A Figura 11 demonstra que há boa correlação entre os valores de $\delta^{18}O$ de silicatos de estágios iniciais dos escarnitos com valores de $\delta^{18}O$ da intrusão adjacente.

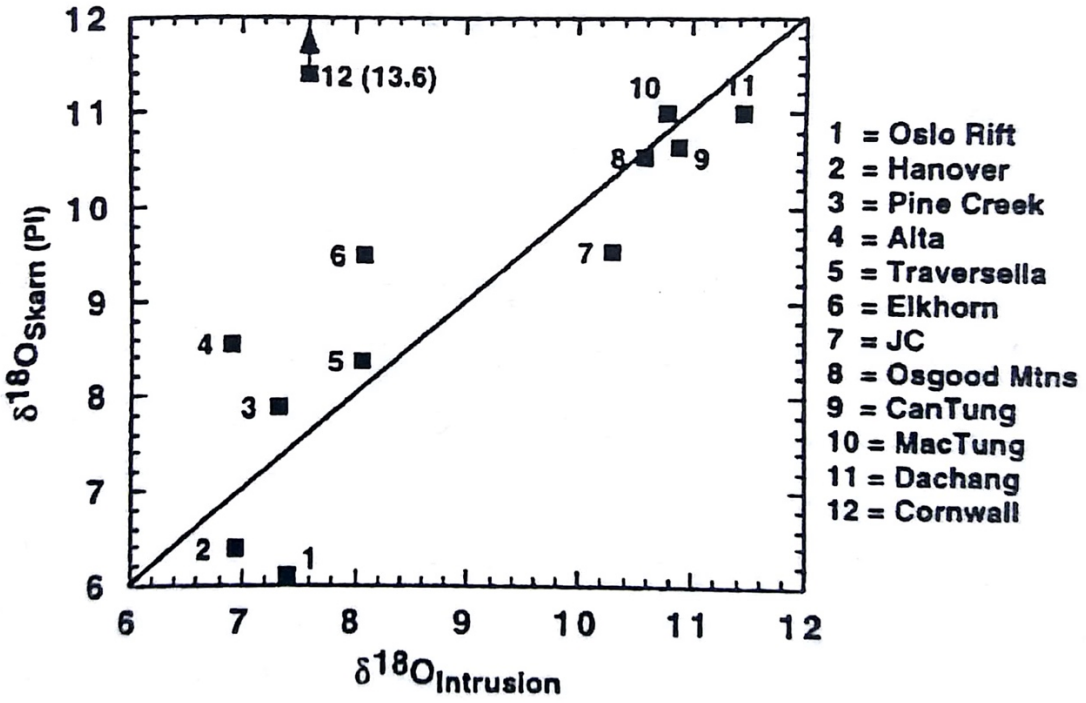

Figura 11: Comparação dos valores de $\delta^{18}O$ silicatos formados nas etapas iniciais de formação de escarnitos com $\delta^{18}O$ da intrusão adjacente (rocha total ou plagioclásio) Extraído de Bowman (1998).

Sistema Carbono-Oxigênio em calcitas de escarnitos

Uma característica comum a praticamente todos escarnitos é que os carbonatos dos escarnitos são significantemente empobrecidas em ^{18}O e ^{13}C quando comparadas as calcitas dos calcários ou dolomitos encaixantes. As reduções de ^{18}O e ^{13}C nos carbonatos são resultado da segregação contínua de CO_2 da rocha a partir de reações de descarbonatação em um intervalo de temperatura apropriado (300° e 550°C) para formação de calcita escarnítica, por exemplo. Reações de descarbonatação podem

resultar em reduções de ^{13}C significantes, mas limitadas de ^{18}O. Essas diminuições de ^{18}O nas calcitas dos escarnitos são grandes demais para serem resultado de processos de equilíbrio normais em reações de descarbonatação de rochas encaixantes carbonáticas. Os valores de $\delta^{13}C$ de muitas calcitas escarníticas coincidem com os valores de -5 a -8 por mil, geralmente característicos de C nos magmas. Além disso, os valores de $\delta^{18}O$ de amostras de calcitas escarníticas alcançam valores de equilíbrio a partir de trocas com a intrusão adjacente.

Padrões de depleção de ^{18}O em escarnitos

Se a maior parte dos padrões de fluxo do calor nos escarnitos pode ser determinado a partir de relações geológicas ou outras evidências então os padrões de distribuição dos valores de $\delta^{18}O$ podem ser utilizados para interpretar modelos de transporte para estimar gradientes termais integrando tempo e fluxo dos fluidos envolvidos na formação dos escarnitos. Se uma direção principal de fluxo pode ser estabelecida, então em qualquer local ao longo do eixo de fluxo o valor de $\delta^{18}O$ deverá ser constante. Por isso, o valor de $\delta^{18}O$ de qualquer mineral formado ao longo do caminho de fluxo depende somente da temperatura e do valor de $\delta^{18}O$ do fluido formador do escarnito. Para minerais comuns de formação de escarnitos, um padrão de diminuição de $\delta^{18}O$ em qualquer estágio de formação dos escarnitos em direção do fluxo do fluido indica um fluxo com aumento de temperatura, enquanto fluxos isotérmicos produzem um padrão constante de valores de $\delta^{18}O$ para os minerais escarníticos. Já o aumento de $\delta^{18}O$ na direção do fluido pode indicar tanto uma diminuição de temperatura ou fluxo isotérmico combinado com enriquecimento de ^{18}O nos fluidos escarníticos devidos a dispersão hidrodinâmica ou mistura. Os efeitos desta dispersão ou mistura com fluidos enriquecidos em ^{18}O dos mármores encaixantes serão não-lineares e maiores próximos às frentes de trocas (próximas ao contato). A Figura 12 ilustra esquematicamente as frentes de depleção de ^{18}O durante a formação de escarnitos.

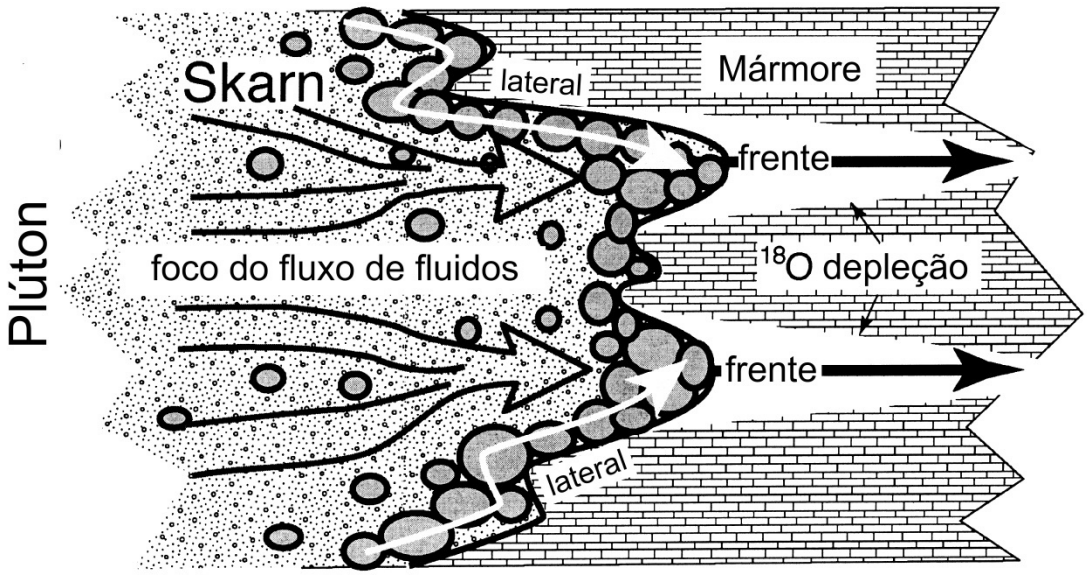

Figura 12: Ilustração esquemática dos limites dos escarnitos e o correspondente fluxo de fluidos ilustrando as frentes de depleção de ^{18}O. A reação de alteração nos isótopos de oxigênio se propaga mais rápido que a formação dos escarnitos em si. (Extraído e traduzido de Meinert *et al.,* 2005).

5.4. MINERALIZAÇÕES ASSOCIADAS AOS ESCARNITOS

Os escarnitos são tipicamente subdivididos em função dos metais associados a eles, discriminados principalmente nos trabalhos de Einaudi *et al.* (1981), Burt (1982) e Meinert (1992) citados anteriormente e revisados por Meinert *et al*. (2005). A subdivisão contempla: Escarnitos de Cu, W, Sn, Au, Zn-Pb, Mo e Fe.

5.4.1. Cu-Escarnitos

Os escarnitos de cobre são os mais comuns e estão tipicamente associados com granitos da série magnetita tipo I posicionados em ambientes rasos. Estas intrusões geralmente são acompanhadas por sistemas de *stockworks* e intensa alteração hidrotermal (Meinert *et al*., 2005). Os maiores depósitos estão associados a sistemas mineralizados do tipo cobre pórfiro e a fase retrogressiva dos escarnitos (descrita no Item 5.2.4) está temporalmente associada à fase de alteração sericítica do pórfiro. A mineralogia predominante dos escarnitos de cobre é composta por granada andradita, diopsídio, vesuvianita, wolastonita, actinolita e epidoto. Estes escarnitos apresentam zonação com granadas mais próximas ao corpo ígneo e clinopiroxênio e vesuvianita

e/ou wolastonita em porções distais. Os principais sulfetos são pirita, calcopirita e bornita e sua quantidade aumenta com a distância da intrusão (Meinert, 1992).

5.4.2. W-Escarnitos

Os escarnitos de tungstênio normalmente estão geneticamente associados a intrusões cálcico-alcalinas acompanhadas por pegmatitos e auréolas metamórficas de alta temperatura (Kwak, 1987; Newberry, 1998; Meinert *et al*., 2005). Os principais minerais de W são wolframita e scheelita. O segundo apresenta duas variedades principais: scheelita rica em Mo (powellita), encontrada em ambientes reduzidos e pobre em Mo, associada a ambientes oxidados. Além destes, os escarnitos de tungstênio de ambientes reduzidos comumente possuem hedenbergita, granadas espessartita e almandina associados a mineralizações de pirrotita, molibdenita, calcopirita, esfalerita e arsenopirita. Os minerais do estágio retrogressivo são epidoto, biotita e hornblenda. Nos W-escarnitos oxidados, predominam a granada andradita e o diopsídio (Meinert *et al.,* 2005).

5.4.3. Sn-Escarnitos

Os escarnitos de estanho estão ligados aos granitos de alta sílica e geralmente associados aos greisens e altas atividades de F (Meinert *et al*., 2005). São encontrados associados a plútons formados por fusão parcial de crosta continental em ambientes de riftes continentais. Os principais minerais de Sn nestas rochas são cassiterita e stannita. Estes escarnitos normalmente são zonados variando de cálcicos a magnesianos, rico em óxidos a rico em sulfetos.

5.4.4. Au-Escarnitos

São denominados Au-escarnitos aqueles que possuem o Au como principal minério, ainda que eles apresentem subprodutos como Cu, Pb e zinco. Além disso, outros tipos como os Cu-escarnitos também apresentam um pequeno teor de ouro que pode ser explorado como subproduto. A maior parte dos escarnitos de alta concentração de ouro estão associados a plútons e complexos de diques ou soleiras dioríticos a granodioríticos reduzidos. Estes escarnitos são dominados por piroxênios ricos em Fe e as zonas proximais podem conter granada grandita abundante. Além destes, normalmente possuem K-feldspato, escapolita, vesuvianita, apatita e anfibólios ricos

em Cl e Al. Os principais sulfetos são a pirita e a arsenopirita e a maior parte do ouro está presente como electrum ou associado com vários minerais de bismuto e telurídeos, incluindo bismuto nativo, hedleyita, wittchenita e maldonita (Meinert, 2000). Em geral, os Au-escarnitos mais reduzidos também apresentam uma associação metálica contendo Bi-Te-As ± Co e são relacionados aos complexos de plútons, diques e sills com ilmenita (Meinert *et al*., 2005). Os Au-escarnitos oxidados são caracterizados por altas razões de granada/piroxênio, baixo conteúdo de sulfetos e uma associação retrógrada com adulária e quartzo, sendo alguns deles transicionais para sistemas epitermais (Meinert *et al*., 2005). Os Au-escarnitos magnesianos associados a rochas dolomíticas apresentam paragêneses dominadas por forsterita, espinélio e serpentina, sendo a magnetita o principal espinélio, levando a exploração de Fe como subproduto (Meinert *et al*., 2005).

5.4.5. Zn-Escarnitos

Grande parte dos escarnitos de zinco ocorrem em ambientes continentais associados a subducção ou rifteamento e são de alta concentração de zinco. Apesar do Zn ser o principal metal, também são explorados pelo conteúdo de Pb e Ag. A composição da rocha intrusiva associada varia desde diorítica até granítica de alta sílica, assim como o ambiente tectônico que pode variar desde batólitos profundos a complexos rasos de diques, soleiras e rochas vulcânicas (Einaudi *et al*., 1981). Além das mineralizações de Zn, este tipo de escarnito apresenta características típicas como mineralogia distinta rica em Mn e Fe, ocorrência associada a contatos litológicos e superfícies estruturais e pela ausência de auréolas metamórficas. Praticamente todos os minerais neste tipo de escarnito são enriquecidos em Mn, incluindo granadas, piroxênios, olivina, ilvaita, piroxenoides, anfilbólios, clorita e serpentina. Esta característica faz que a ocorrência de Zn-escarnitos em porções distais de sistemas magmáticos hidrotermais sejam importantes guias exploratórios para descoberta de sistemas mineralizados.

5.4.6. Mo-Escarnitos

Os depósitos de escarnitos de molibdênio são geneticamente associados a granitoides leucocráticos e variam desde alta a baixas concentrações (Meinert *et al*., 2005). Estes depósitos normalmente apresentam, além do molibdênio, W, Cu, Zn, Pb,

Bi, Sn e U, sendo Mo-W-Cu a associação mais comum. A mineralogia indica um ambiente redutor com alta atividade de flúor e com predominância de hedenbergita, granada grandita, wolastonita, anfibólio e fluorita. Os minerais retrógrados mais comuns são epitodo, actinolita, serpentina, muscovita, clorita, fluorita e tremolita. Os principais minerais de minério são molibdenita, powellita, pirrotita, arsenopirita, calcopirita, pirita, esfalerita e magnetita (Einaudi *et al*., 1981).

5.4.7. Fe-Escarnitos

Os escarnitos de ferro representam os maiores depósitos de escarnitos em volume de minério. Estes podem ser subdivididos entre Fe-escarnitos cálcicos e magnesianos (Meinert *et al*., 2000). Os tipos cálcicos geralmente ocorrem em ambientes de arco de ilhas oceânico e são formados por plútons ricos em Fe intrusivos em calcários e rochas vulcânicas. A rocha intrusiva normalmente é diorítica, mas também ocorrem em gabros e sienitos. Alguns depósitos possuem volumes maiores de endoescarnitos em relação aos exoescarnitos, que não é o mais comum na maioria dos sistemas escarníticos. A mineralogia é composta predominantemente por ferrosalita, salita, magnetita, granada grandita, epidoto e actinolita, todos ricos em Fe. A assembleia retrógrada é predominantemente composta por anfibólio, clorita e ilvaita. A magnetita é o principal minério e pode ser acompanhada por calcopirita, cobaltita e pirrotita. Os Fe-escarnitos magnesianos ocorrem associados a diversos tipos de rochas ígneas, com predominânica de granodioritos formando stocks, diques e sills em diversos ambientes tectônicos com a rocha encaixante dolomítica em comum. Estes escarnitos também possuem a magnetita como principal minério e a mineralogia é composta por forsterita, diopsídio, periclásio, talco e serpentina sem altos conteúdos de Fe (incorporados pela magnetita).

5.5. AMBIENTES TECTÔNICOS E PRINCIPAIS MINERALIZAÇÕES ASSOCIADAS

De modo geral, quatro ambientes tectônicos principais levam a formação de escarnitos com mineralizações distintas (Meinert *et al*., 2005; Figura 13): (i) arco oceânico com mergulho acentuado da placa subductante; (ii) arco de ilhas oceânico com mergulho moderado; (iii) subducção sobre margem continental com carbonatos na margem; e (iv) rifte continental e intrusão associada à ascensão do manto.

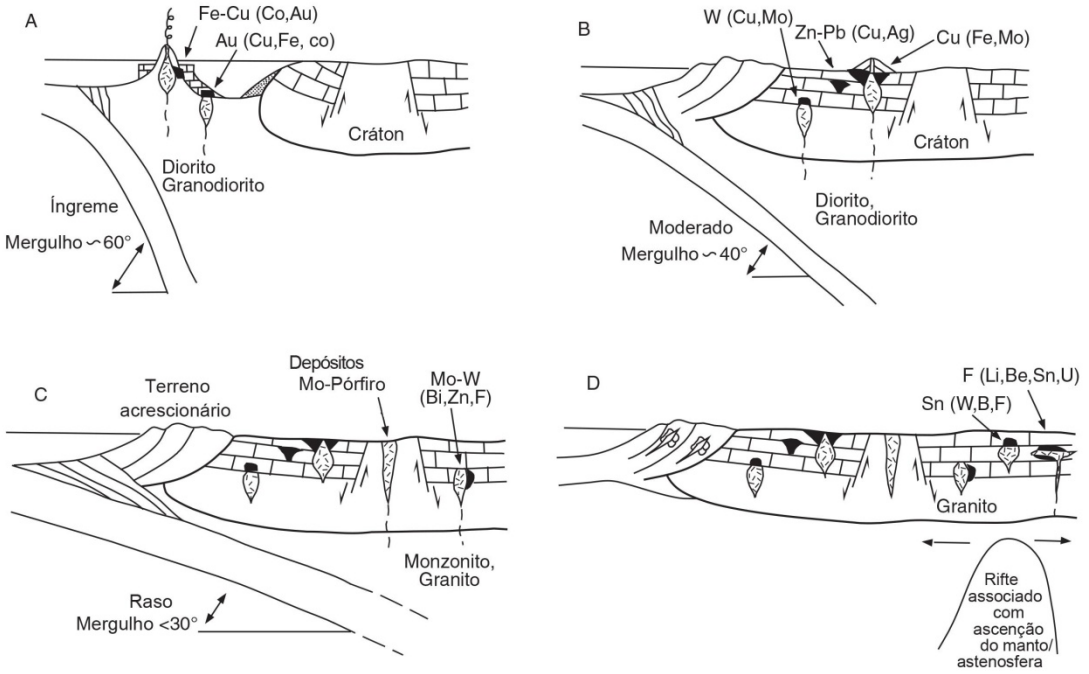

Figura 13: Principais ambientes tectônicos com desenvolvimento de escarnitos (A) arco oceânico com mergulho acentuado da placa subductante (B) arco de ilhas oceânico com mergulho moderado (C) subducção sobre margem continental com carbonatos na margem (D) rifte continental e intrusão associada à ascensão do manto. (traduzido de Meinert *et al*., 2005).

Os ambientes com subducção íngreme de placas oceânicas tendem a produzir escarnitos com mineralizações de Fe, Cu e Au associados a plútons dioríticos a granodioríticos (Figura 13a). Aqueles formados em arcos com subduções de mergulho moderado comumente estão associados a plútons monzoníticos e graníticos gerando escarnitos de Mo e W-Mo (Figura 13b). Já aqueles formados em ambientes relacionados a subducção com mergulho <30° geralmente geram mineralizações de Zn-Pb, Cu, Au, W e Mo, associados a granodioritos e granitos (Figura 13c). Por fim, os escarnitos formados em ambientes de rifteamento continental, associados a plumas mantélicas ou ascensão da astenosfera normalmente resultam em mineralizações de Sn e W, ligados a magmas graníticos anorogênicos (Figura 13d).

6. RESUMO E INTEGRAÇÃO DOS PRINCIPAIS RESULTADOS OBTIDOS

Os principais resultados obtidos estão apresentados e integrados nesta seção, resumidos e divididos nos principais grupos de dados: (i) aspectos e relações de campo; (ii) dados geocronológicos; (iii) composições químicas de rocha total; (iv) assembleias minerais e microestruturas e (v) isótopos estáveis. Demais resultados e detalhamentos estão apresentados nos artigos que compõe o corpo principal da tese (Capítulos 2 a 5).

Aspectos e relações de campo

Os mármores dolomíticos do PFMC ocorrem como corpos lenticulares espessos que são extensivamente intrudidos por apófises tabulares félsicas e máficas de espessura e composição variáveis. Os mármores ocorrem a leste do batólito granítico com contato mergulhando para leste em ângulos baixos a médios (~10-30°). O acamamento (S_0) e foliação metamórfica (S_1), desenvolvida durante o metamorfismo regional anterior a intrusão do CSGC, são tipicamente paralelos. Os mármores e algumas das apófises formam dobras inclinadas a recumbentes, cerradas a isoclinais com eixo N-S a NE-SW que mergulha em ângulos baixos (0-10°) principalmente para S-SW. A superfície axial média mergulha 20° para o leste, variando localmente para sub-horizontal ou raramente mergulhando para oeste em ângulos baixos (<15°). As superfícies axiais caracterizam a foliação S_2. Devido ao caráter isoclinal da maioria dos dobramentos, a foliação S_1 e S_2 são comumente subparalelas.

Intrusões tabulares félsicas e máficas estão bem expostas nas frentes de lavra e apresentam grande heterogeneidade de composição, espessura e grau de deformação. Um grupo de apófises máficas e félsicas com espessura pequena a moderada (~0,1 a 2 m) e granulação fina a média intrudiu paralelamente a foliação S_1 e foi dobrado juntamente com os mármores. Apófises félsicas mais espessas (> 2 m) de granulação média a grossa formam corpos tabulares que intrudem os mármores paralelos ou subparalelos às superfícies axiais (*i.e.*, S_2). Devido ao comum paralelismo das estruturas (S_1 e S_2) as relações de corte entre as gerações de apófises são escassas. Entretanto, relações de corte mútuo entre apófises máficas e félsicas são observadas localmente, indicando contemporaneidade.

As apófises máficas formam corpos tabulares predominantemente contínuos por dezenas a centenas de metros e concordantes com a foliação S_1. A espessura destas intrusões varia de poucos centímetros até aproximadamente meio metro. As apófises máficas apresentam aspectos de campo similares entre si. Eles possuem tamanho de grão médio e são compostas principalmente por minerais máficos hidratados (entre 40 e 80% de biotita e/ou anfibólio) em uma matriz composta por plagioclásio ± K-feldspato. Pirita e calcopirita disseminadas foram macroscopicamente identificadas em todas as apófises máficas em quantidades variáveis. A maior abundância de sulfetos foi observada junto a intrusões localizadas em até dezenas de metros de distância das falhas de sub-verticais que cortam as apófises máficas na pedreira mais ao norte. As apófises M1 apresentam foliação bem marcada pela orientação preferencial dos minerais máficos. A foliação observada é tipicamente paralela à orientação da intrusão e à foliação metamórfica (S_1) das encaixantes. Os contatos apófise máfica-mármore variam de nítidos a difusos. Escarnitos de contato são comuns nos limites entre as litologias ígneas e carbonáticas. Quando presentes, os escarnitos localizados nos contatos litológicos são assimétricos em relação às diferentes bordas das intrusões. Não há ocorrência preferencial de escarnitos nas bordas superior ou inferior das apófises. Ainda, estes escarnitos podem ser zonados ou não e são variáveis em espessura (variando tipicamente entre 5 - 100 cm). Os escarnitos de contato são mais frequentes nas dobras ou terminações das apófises máficas.

As apófises félsicas mais espessas e de granulação mais grossa são intrusões tipicamente subconcordantes ou concordantes com a foliação do plano axial S_2 das rochas hospedeiras e apófises máfico-félsicas dobradas. Menos comumente, elas cortam a foliação e ocorrem como corpos verticais irregulares. São rochas com quantidades variáveis de minerais máficos, principalmente biotita e anfibólio. A foliação nessas rochas é caracterizada pela orientação preferencial de fenocristais de biotita, anfibólio e estiramento dos feldspatos. Estas rochas correspondem à descrição dos principais litotipos do CSGC descritos por Nardi & Bitencourt (1989). Os contatos com os mármores são dominantemente nítidos e geralmente não apresentam endoescarnitos, embora fo escarnitos comumente ocorram nos limites entre os mármores e estas apófises félsicas. De modo semelhante às apófises máficas, a distribuição dos escarnitos no entorno das intrusões é normalmente assimétrica e

preferencial em uma das bordas da intrusão. Pegmatitos e aplitos ocorrem como pequenas porções dentro das apófises ou como corpos irregulares cortando predominantemente as apófises máficas e félsicas de pequenas espessuras e granulação fina. Em particular, é possível observar a formação de escarnitos de forsterita + calcita diretamente relacionados a porções pegmatíticas de apófises félsicas, evidenciando a origem ígnea dos fluidos formadores destes escarnitos.

Em geral, os mármores foram substituídos localmente por escarnitos que são encontrados nos contatos ou a poucos metros de distância das apófises máficas e félsicas. Menos comuns, e limitados à pedreira mais ao norte do distrito mineiro (CL), os mármores são cortados por veios de calcita-clorita-sulfeto e brechas e são geralmente encontrados a algumas dezenas de metros de falhas subverticais NW-SE.

Os escarnitos identificados foram classificados em função de seu posicionamento e assembleia mineral principal. Os escarnitos de veio são compostos de uma zona central dominantemente formada por diopsídio. Quando os escarnitos são zonados, os diopsídios são circundados por bandas ou lentes compostas por agregados de forsterita arredondados (ou pseudomorfos de antigorita) e calcita. Veios de diopsídio ou forsterita + calcita isolados também são comuns na área. Os escarnitos de veio formam estruturas tipo pinch-and-swell ou boudins. O tamanho destes escarnitos e das zonas mineralógicas variam de alguns centímetros, podendo alcançar um metro de espessura. Em geral, os escarnitos de veio mostram uma distribuição assimétrica das zonas mineralógicas em termos de espessura e texturas.

Os escarnitos de contato ocorrem nos limites entre apófises máficas e os mármores dolomíticos, embora nem todos os contatos desta natureza hospedem escarnitos. Os escarnitos de contato variam de alguns centímetros a aproximadamente 50 cm de espessura, sendo que os mais espessos são encontrados perto das charneiras de dobras. Em geral, os escarnitos de contato mostram uma sucessão de zonas mineralógicas da intrusão em direção ao protólito carbonático. No entanto, a presença e a espessura de tais zonas são variáveis entre os diferentes contatos. Em geral, uma sucessão completa de zonas mineralógicas inclui, desde a intrusão até o mármore inalterado: um endoescarnito, uma zona de diopsídio, uma zona de tremolita, uma zona de forsterita e uma zona de mármore alterada. Os escarnitos de veio e de contato

prógrados apresentam mineralizações de pirita, molibdenita, pirrotita e calcopirita disseminados e encontrados em maior abundância nas zonas de charneira.

Em particular, na pedreira localizada mais ao norte do distrito são encontrados escarnitos de veio retrógrados (*i.e.*, veios e brechas hidrotermais) compostos predominantemente por calcita de granulação grossa cimentada por clorita e calcopirita ± pirita. Estes veios são circundados por zonas de reação nos mármores com a formação de antigorita ± clorita e calcita substituindo a dolomita. A formação de calcopirita maciça é comum nestes veios e brechas.

Dados geocronológicos

Datações de U-Pb em zircão, titanita e apatita foram realizadas com a finalidade de obter idades dos eventos magmáticos e metassomáticos. As idades obtidas estão listadas na Tabela 2. Tentativas de recuperar zircões das apófises máficas foram no geral mal-sucedidas, devido a baixa quantidade e tamanho dos zircões. No entanto, apesar de conseguirmos datar os zircões extraídos de uma das apófises máficas, todas as idades obtidas (paleoproterozoicas) foram interpretadas como herdadas, considerando as idades disponíveis para o PFMC (*e.g.*, Remus *et al*., 2000; Lopes *et al*., 2015; Souza, 2020). Como alternativa para contornar este problema, selecionamos amostras de apófises félsicas cortadas por intrusões máficas ou com feições de intrusão mútua para obter uma idade indireta do magmatismo máfico. Neste caso, obtivemos idades de *ca.* 578 Ma para uma apófise granodiorítica localizada no distrito mineiro (área DB) e para a porção félsica de um dique composto localizado na área do Arroio das Pedras, na porção norte do PFMC. Ainda, a apófise granodiorítica datada apresenta uma porção pegmatítica que está diretamente associada a formação de forsterita escarnitos, possibilitando a definição indireta das idades destes escarnitos. Além disso, obtivemos idades U-Pb consistentes para apatitas e titanitas das apófises máficas que registram o resfriamento do CSGC há *ca.* 557 Ma. Esta idade foi associada ao evento de circulação hidrotermal tardio que levou ao retrometamorfismo das assembleias escarníticas de alta temperatura e resultou na formação dos veios de calcita-clorita-sulfeto mineralizados. Por fim, as idades obtidas, em combinação com trabalhos anteriores (*e.g.*, Leite *et al*., 1998; Remus *et al*., 2000) indicam que o magmatismo do CSGC ocorreu ao longo de aproximadamente 21 milhões de anos entre *ca.* 578 Ma e 557 Ma.

Litologia (amostra) – mineral	Idade magmática (Ma)	Idades herdadas (Ma)	Idade de metamorfismo ou resfriamento (Ma)
Granodiorito (DB-G2Z) – zircão	578.0±4.7	605 a 2045	-
Apófise máfica (DB-G1Z) – zircão	-	1787±14 2190±20	-
Dique composto, porção félsica (AP-01) – zircão	578.1±3.5	761 a 2500	-
Apófise máfica (AT-Z-01) – titanita	-	-	556.1±2.9
Apófise máfica (AT-Z-02) – apatita	-	-	557.8±3.4
Apófise máfica (AT-Z-03) – apatita	-	-	557.0±4.9

Tabela 2: Resumo das idades obtidas por U-Pb LA-ICP-MS em zircão, titanita e apatita.

Composições químicas de rocha total

Análises de rocha total foram obtidas para apófises máficas e diques compostos visando identificar o protólito e afinidade destas rochas que estão diretamente associadas aos escarnitos. As análises indicam composições atípicas para rochas básicas (*i.e.*, basaltos ou metabasaltos) com uma ampla variedade composicional incluindo termos ultrabásicos a intermediários. Além disso, as apófises máficas apresentam elevados teores de Mg, Cr, Ni e Co e padrões de elementos terras raras enriquecidos em LREE e empobrecidos em HREE. As composições das apófises máficas foram comparadas aos diques compostos localizados na porção norte do PFMC e às demais unidades magmáticas do Terreno São Gabriel. As composições químicas em combinação com observações de campo, microestruturas e química mineral sugerem um protólito lamprofírico para as apófises máficas.

Assembleias minerais e microestruturas

Os escarnitos de Caçapava do Sul são compostos por diversas associações minerais cálcio-magnesianas que compõe diferentes zonas mineralógicas. De modo geral, os escarnitos podem ser divididos em duas zonas principais: zona do diopsídio e zona da forsterita. A zona do diopsídio é composta por agregados de diopsídio com granulação grossa, com cristais que variam de poucos milímetros a alguns centímetros. O diopsídio comumente hospeda inclusões de sulfetos de Fe-Cu-Mo,

calcita e tremolita de tamanho micrométrico e raramente inclusões de flogopita. Nos limites das zonas do diopsídio, os grãos tendem a ser fraturados e divididos em subgrãos, sendo parcialmente substituídos por tremolita e calcita de tamanho milimétrico, que também cristalizam ao longo dos limites dos grãos e fraturas. Em amostras com efeito retrogressivo intenso, o diopsídio pode ser parcial ou totalmente substituído por antigorita.

A zona de forsterita consiste em olivinas arredondadas em uma matriz de calcita tipicamente anédrica, repleta de inclusões e aspecto túrbido ao ser observada em luz plano-polarizada. Deposição de pirita anédrica frequentemente disseminada na matriz calcítica ou em fraturas de olivina serpentinizada é comum nesta zona. A forsterita é comumente totalmente substituída por antigorita. A calcita da matriz mostra quantidades variáveis de exsolução de dolomita. Frequentemente, pequenas lamelas de flogopita ocorrem nesta zona. Localmente, a zona de forsterita contém espinélio verde e clorita. As variações texturais e composicionais das assembleias escarníticas são abordadas em detalhe nos artigos I, III e IV.

As apófises máficas mostram heterogeneidade em assembleias minerais e microestruturas, apesar de seus aspectos de campo serem aproximadamente homogêneos. Elas são compostas por quantidades variáveis de anfibólio cálcico + biotita + plagioclásio ± K-feldspato ± clinopiroxênio ± quartzo + titanita + apatita ± pirita ± clorita. Todas as amostras apresentam anfibólio, biotita e plagioclásio em proporções variáveis, enquanto a quantidade total de biotita + anfibólio nas amostras chega a 80%. Em geral, as apófises máficas apresentam texturas granoblásticas a lepidoblásticas que variam com as associações minerais e proporções minerais. Notamos que as amostras com maior conteúdo de biotita e anfibólio frequentemente mostram texturas lepidoblásticas e nematoblásticas com foliação bem espaçada marcada pela orientação preferencial desses minerais, enquanto as amostras com menores quantidades de minerais hidratados tendem a ser granoblásticas com uma orientação preferencial mais fraca das micas e anfibólios. A variação entre as amostras parece ser gradual e relacionada à composição e não controlada espacialmente. A biotita ocorre com granulação fina a grossa, frequentemente deformadas em agregados em forma sigmoidal a grãos anédricos menores que preenchem os espaços entre os anfibólios e os feldspatos. A biotita também ocorre substituindo a actinolita e o plagioclásio ou como inclusões em anfibólios e

clinopiroxênios. Os anfibólios ocorrem principalmente como cristais euédricos curtos a subédricos, comumente formando agregados ovais ou sigmoidais nas rochas máficas foliadas sem K-feldspato. Actinolita e hornblenda prismáticas sem orientação preferencial são mais comuns nas amostras menos deformadas, comumente associadas ao feldspato alcalino. O clinopiroxênio é raro e foi identificado principalmente nas apófises máficas da porção mais ao sul do distrito mineiro (área PI). O clinopiroxênio ocorre principalmente como porfiroblastos anédricos ou esqueletais, geralmente alongados paralelamente aos anfibólios e micas. Eles também ocorrem como grãos maiores (~ 2 mm) cheios de inclusões de biotita dentro de agregados de biotita.

As apófises félsicas apresentam assembleias compostas por quartzo, plagioclásio, K-feldspato e biotita e hornblenda como os principais minerais máficos. Bt-hbl-granodioritos representam o tipo mais comum dentro das apófises félsicas. O tamanho do grão e a quantidade e proporção de biotita e anfibólio variam entre diferentes apófises, mas são quase homogêneos dentro da mesma intrusão. Os fenocristais de K-feldspato são comuns e costumam ocorrer alongados ou com limites lobados. Quartzo geralmente possui extinção ondulosa e frequentemente dividido em subgrãos de 0,1 - 0,5 mm com limites suturados. A alanita, titanita e zircão ocorrem como principais acessórios, como inclusões em fenocristais de K-feldspato ou em contato com biotita e anfibólios cálcicos. Observações de campo mostram que a cloritização da biotita é comum e observada principalmente nas amostras com coloração vermelho-acastanhada. Esta alteração é mais frequentemente encontrada perto de zonas de falha, especialmente nas pedreiras centro e norte do distrito mineiro (áreas CL, FD e AT). As variações texturais e composicionais das assembleias ígneas são abordadas em detalhe nos artigos I, II e III. Estimativas de pressão e temperatura foram obtidas a partir da química mineral de fases ígneas e metassomáticas. Os geotermobarômetros utilizados e os valores obtidos para cada assembleia estão demonstrados na Tabela 3 e detalhados no artigo III.

Litologia	Geotermobarômetro utilizado	Intervalo de temperatura estimado	Intervalo de pressão estimado
Escarnitos prógrados	Teor de Mg na calcita	581° a 628°C	-
Apófises félsicas	Par anfibólio-plagioclásio	682° a 744°C	-
Apófises félsicas	Teor de Al na hornblenda	-	3.7 a 4.9 kbar
Escarnitos retrógrados	Al_{IV} na clorita	280° a 310°C	-

Tabela 3: Resumo das estimativas de geotermobarometria.

Isótopos estáveis

Composições isotópicas de carbonato-total foram obtidas para escarnitos prógrados e retrógrados e para uma amostra de mármore dolomíticos da porção mais distal do contato granítico (área IN). Além disso, composições de isótopos estáveis de oxigênio foram obtidas para diopsídio, olivina e tremolita de escarnitos prógrados. De maneira geral, os escarnitos prógrados demonstram um padrão de transição entre valores próximos ao protólito sedimentar em direção à valores tipicamente magmáticos próximo às principais superfícies de infiltração de fluidos. Estes padrões são apresentados e discutidos em detalhes no artigo IV. Os isótopos de $\delta^{18}O$ nos silicatos indicam desequilíbrio isotópico entre as zonas do diopsídio e forsterita. Calcitas dos escarnitos retrógrados apresentam valores tipicamente magmáticos para $\delta^{13}C$ e $\delta^{18}O$. O resumo das análises isotópicas está demonstrado na Figura 14.

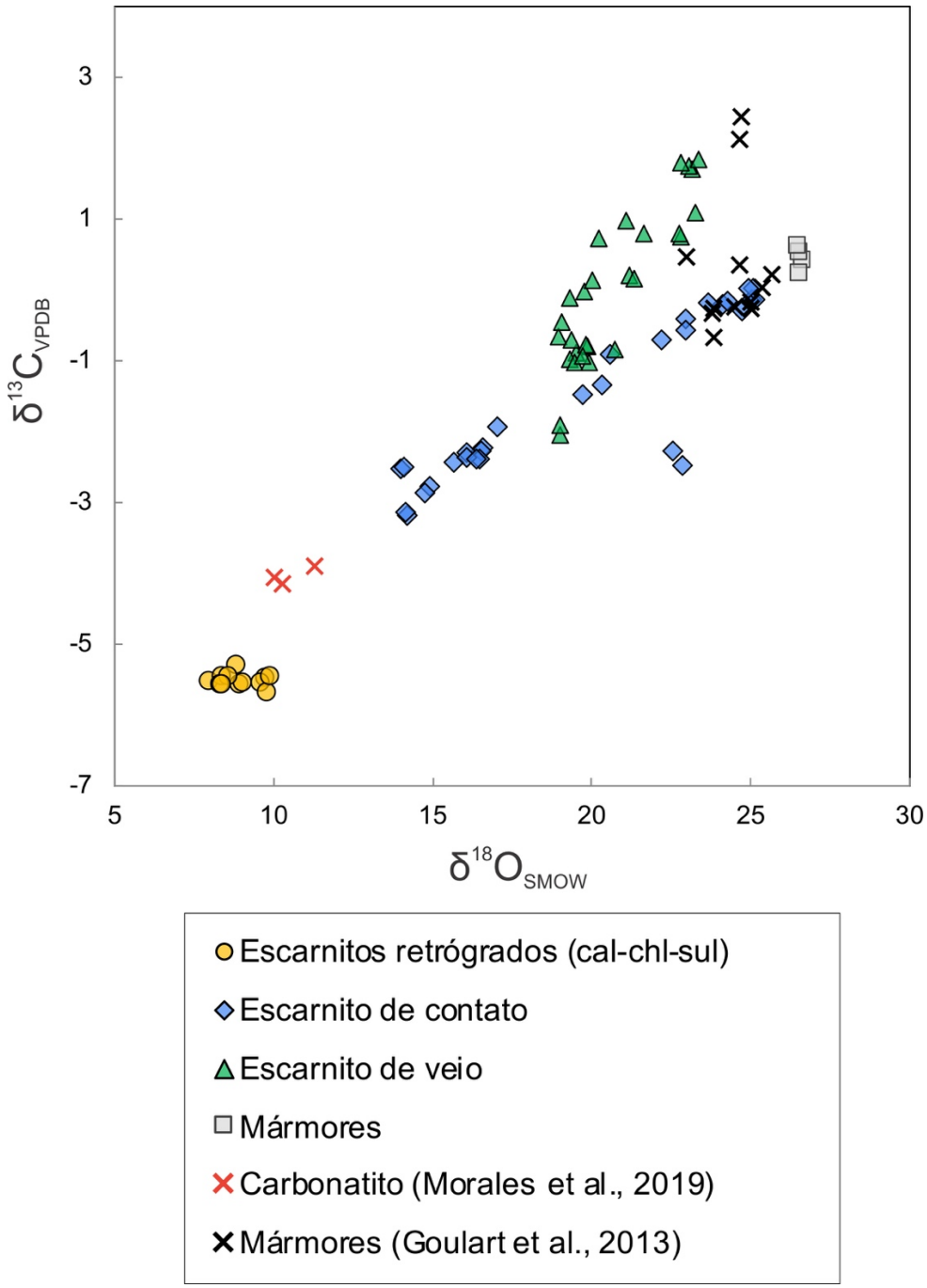

Figura 14: Resumo dos dados isotópicos obtidos e dados disponíveis dos mármores (Goulart *et al*., 2013) e do carbonatito Passo Feio (Morales *et al*., 2019).

7. CONCLUSÕES

Nesta tese são apresentadas evidências de campo, microestruturais, geocronológicas e geoquímicas para propor fluxo de fluidos episódico, associado a múltiplos estágios intrusivos do Complexo Granítico Caçapava do Sul nos mármores dolomíticos do Complexo Metamórfico Passo Feio. As principais conclusões obtidas estão listadas a seguir:

1) Idades U-Pb obtidas por LA-ICP-MS em zircão, apatita e titanita de apófises félsicas e máficas indicam que o magmatismo do Complexo Granítico Caçapava do Sul ocorreu entre *ca.* 578 Ma e 557 Ma. Idades magmáticas de 578.0 ± 4.7 Ma e 578.1 ± 3.5 Ma foram obtidas em uma apófise granodiorítica hospedada por mármores dolomíticos na porção leste do PFMC e em um dique composto localizado no norte do PFMC, respectivamente. Titanitas e apatitas de três apófises máficas que cortam os mármores do PFMC registram idades de 556.1± 2.9 Ma, 557.8 ± 3.4 Ma e 557.0±4.9, associadas ao efeito térmico das intrusões finais do CSGC.
2) A intrusão do Complexo Granítico Caçapava do Sul resultou na formação de rochas metassomáticas cálcio-silicáticas formadas em três estágios principais diretamente relacionados às diferentes etapas de evolução do complexo magmático.
3) O primeiro estágio resultou na formação de diopsídio-escarnitos. Eles foram formados a partir da infiltração canalizada de fluidos liberados de apófises máficas e félsicas ao longo de contatos litológicos ou planos de foliação pré-existentes. Neste estágio, os fluidos apresentavam altas atividades de CO_2.
4) A formação dos forsterita-escarnitos ocorreu em pulsos subsequentes nos quais os fluidos liberados pelo resfriamento de apófises félsicas infiltraram os mármores utilizando caminhos similares aos do estágio anterior. A porosidade gerada por reações de desvolatização foi reforçada por deformação dúctil-rúptil facilitou o fluxo de fluidos ao longo das interfaces entre os di-escarnitos e os mármores, resultando em escarnitos zonados. Os fluidos neste estágio eram ricos em H_2O e subsaturados em SiO_2, levando a substituição parcial do diopsídio por tremolita e calcita e dissolução da dolomita formando forsterita e calcita.

5) A serpentinização das assembleias escarníticas e cloritização de assembleias magmáticas em conjunto com os veios de calcita-clorita-sulfeto localizados em estruturas rúpteis registra o terceiro estágio metassomático, como resultado da exsolução de fluidos aquosos durante o resfriamento do batólito granítico a *ca.* 557 Ma.
6) Nos di- e fo escarnitos, o modo de ocorrência paralelo a sub-paralelo à foliação das encaixantes indica formação em maiores profundidades, coerentes com as pressões obtidas para o par anfibólio-plagioclásio em apófises monzoníticas e granodioríticas (~3.7 a 4.9 kbar). Além disso, estimativas de temperatura baseadas no teor de Mg na calcita indicam temperaturas entre 581 e 628°C para os estágios metassomáticos iniciais. No entanto, o padrão discordante dos veios e brechas de calcita-clorita-sulfeto e temperaturas obtidas a partir do geotermômetro da clorita indicam profundidades mais rasas e temperaturas entre 270 e 310°C.
7) As apófises máficas associadas aos escarnitos apresentam composições ultrabásicas a intermediárias com alto Mg#, Cr, Co, Ni, ricas em voláteis e com padrões de LREE elevados e HREE empobrecidos. A composição destas rochas em combinação com feições de campo indicando alto conteúdo de voláteis, acrescidos à presença de flogopitas ricas em Cr sugere uma origem lamprofírica para estas rochas. A proximidade espacial e temporal e as similaridades estruturais com os carbonatitos que intrudem o PFMC indicam uma possível correlação genética entre essas rochas. Ainda, propomos que as apófises máficas (metalamprófiros) representam marcadores tectônicos para a transição da tectônica extensional pós-colisional para a tectônica transpressiva na porção oriental do Terreno São Gabriel (Cinturão Dom Feliciano central).
8) Mineralizações de pirita, pirrotita, calcopirita e molibdenita disseminadas estão associada com os di- e fo escarnitos, formados a partir das intrusões iniciais e sin-cinemáticas de apófises máficas e félsicas. O alto teor de voláteis nas intrusões iniciais é interpretado como responsável pela mobilização e transporte de enxofre e metais do manto superior e níveis mais profundos da crosta para a crosta superior. Os fluidos liberados destas apófises no resfriamento resultaram na deposição dos sulfetos de Fe-Cu-Mo nos escarnitos prógrados.

9) As mineralizações maciças de calcopirita e pirita associada aos veios e brechas de calcita-clorita-sulfeto são associadas à remobilização a partir das soluções hidrotermais associadas à fase final de colocação e resfriamento do batólito granítico em *ca.* 557 Ma.
10) A partir das modificações isotópicas e na química mineral de dolomitas e flogopitas, concluímos que o alcance das frentes de reação transversais ao fluxo de fluido principal nas rochas carbonáticas extrapola as zonas de modificações nas assembleias minerais gerando dissolução e reprecipitação das assembleias pré-existentes.

8. REFERÊNCIAS

Ague J.J. 1994. Mass transfer during Barrovian metamorphism of pelites, south-central Connecticut. I: evidence for changes in composition and volume. *American Journal of Science*, 294: 989–1057.

Ague, J.J., 2003. Fluid Infiltration and Transport of Major, Minor, and Trace Elements During Regional Metamorphism of Carbonate Rocks, Wepawaug Schist, Connecticut, USA. *American Journal of Science,* 303: 753–816.

Ague, J.J., 2014. Fluid Flow in the Deep Crust, in: *Treatise on Geochemistry*. Elsevier, p. 203–247.

Anovitz, L.M., & Essene, E.J. 1990. Thermobarometry and Pressure-Temperature Paths in the Grenville Province of Ontario. *Journal of Petrology*, 31(1): 197–241.

Arena, K.R., Hartmann, L.A. & Lana, C. 2016. Evolution of Neoproterozoic ophiolites from the southern Brasiliano Orogen revealed by zircon U-Pb-Hf isotopes and geochemistry. *Precambrian Research*, 285: 299–314.

Atkinson, W.W., & Einaudi, M.T. 1978. Skarn formation and mineralization in the contact aureole at Carr Fork, Bingham, Utah. *Economic Geology*, 73(7): 1326–1365.

Babinski, M., Chemale, F., Hartmann, L.A., Van Schmus, W.R. & Da Silva, L.C. 1996. Juvenile accretion at 750-700 Ma in southern Brazil. *Geology*, 24: 439–442.

Bartley, J.M., Coleman, D.S. & Glazner, A.F., 2008. Incremental pluton emplacement by magmatic crack-seal. *Transactions of the Royal Society of Edinburgh: Earth Sciences* 97: 383–396.

Baumgartner, L.P. & Valley, J.W., 2001. Stable Isotope Transport and Contact Metamorphic Fluid Flow. *Reviews in Mineralogy and Geochemistry* 43: 415–467.

Bégué, F., Baumgartner, L.P., Bouvier, A.S. & Robyr, M., 2019. Reactive fluid infiltration along fractures: Textural observations coupled to in-situ isotopic analyses. *Earth and Planetary Science Letters*, 519: 264–273.

Bégué, F., Baumgartner, L.P., Müller, T., Putlitz, B. & Vennemann, T.W., 2020. Metasomatic Vein Formation by Stationary Fluids in Carbonate Xenoliths at the Eastern Margin of the Bergell Intrusion, Val Sissone, Italy. *Journal of Petrology,* 60: 2387–2412.

Bicalho, V., Remus, M.V.D., Rizzardo, R. & Dani, N. 2019. Geochemistry, metamorphic evolution and tectonic significance of metabasites from Caçapava do Sul, southern Brazil. *Brazilian Journal of Geology*, 49: 1–16.

Bitencourt, M.F. 1983. *Geologia petrologia e estrutura dos metamorfitos da região de Caçapava do Sul, RS*. Porto Alegre, 161p. Dissertação de Mestrado. Programa de Pós-Graduação em Geociências, Instituto de Geociências, Universidade Federal do Rio Grande do Sul.

Blackwell, D.D., Steele, J.L., Frohme, M.K., Murphey, C.F., Priest, G.R., & Black, G.L. 1990. Heat flow in the Oregon Cascade Range and its correlation with regional gravity, Curie point depths, and geology. *Journal of Geophysical Research*, 95(B12): 19475.

Bortolotto, O.J. 1988. Metamorfismo Termal dos Mármores de Caçapava do Sul, RS. *Ciência e Natura*, 10: 25–48.

Bowman, J.R. 1998. Stable-isotope systematics of skarns, Mineralized Intrusion-Related Skarn Systems. *Mineral. Assoc. Canada Short Course*, 26: 99-145.

Brown, P.E., Bowman, J.R. & Kelly, W.C., 1985. Petrologic and stable isotope constraints on the source and evolution of skarn-forming fluids at Pine Creek, California. *Economic Geology*, 80: 72–95.

Bucher-Nurminen, K., 1981. Petrology of chlorite-spinel marbles from NW Spitsbergen (Svalbard). *Lithos*, 1: 203–213.

Bucher-Nurminen, K., 1982. On the mechanism of contact aureole formation in dolomitic country rock by the Adamello intrusion (northern Italy). *American Mineralogist*, 67: 1101–1117.

Buddington, A.F. 1959. Granite emplacement with special reference to North America. *Geological Society of America Bulletin*, 70(6): 671-747.

Bulau, J.R., Waff, H.S. & Tyburczy, J.A., 1979. Mechanical and thermodynamic constraints on fluid distribution in partial melts. *Journal of Geophysical Research,* 84: 6102.

Burt, D.M. 1982. Skarn deposits - historical bibliography through 1970. *Economic Geology*, 77(4): 755-763.

Cerva-Alves, T., Hartmann, L.A., Remus M.V.D. & Lana, C. 2020. Integrated ophiolite and arc evolution, southern Brasiliano Orogen. *Precambrian Research*, 341: 105648.

Cerva-Alves, T., Remus, M.V.D., Dani, N. & Basei, M.A.S. 2017. Integrated field, mineralogical and geochemical characteristics of Caçapava do Sul alvikite and beforsite intrusions: A new Ediacaran carbonatite complex in southernmost Brazil. *Ore Geology Reviews*, 88: 352–369.

Chemale, F. 2000. Evolução Geológica do Escudo Sul-Riograndense, *In*: Holz, M., De Ros, L.F. (Eds.). *Geologia Do Rio Grande Do Sul*. Porto Alegre. Editora UFRGS. p. 13–52.

Chemale, F., J., Hartmann, L.A. & Da Silva, L.C. 1995. Stratigraphy and tectonism of the Brasiliano Cycle in southern Brazil. *Communications - Geological Survey of Namibia*, 10: 151–166.

Clarke, D.B., 1992, *Granitoid rocks*. London, Chapman and Hall, 283 p.

Clemens, J.D. & Mawer, C.K., 1992. Granitic magma transport by fracture propagation. *Tectonophysics,* 204: 339–360.

Cline, J.S. & Bodnar, R.J. 1991. Can economic porphyry copper mineralization be generated by a typical calc-alkaline melt? *Journal of Geophysical Research,* 96: 8113–8126.

Coleman, D.S., Gray, W. & Glazner, A.F., 2004. Rethinking the emplacement and evolution of zoned plutons: Geochronologic evidence for incremental assembly of the Tuolumne Intrusive Suite, California. *Geology* 32: 433–436.

Cook, S.J. & Bowman, J.R., 2000. Mineralogical Evidence for Fluid–Rock Interaction Accompanying Prograde Contact Metamorphism of Siliceous Dolomites: Alta Stock Aureole, Utah, USA. *Journal of Petrology,* 41: 739–757.

Cordani, U.G., Halpern, N. & Berenholc, M. 1974. Idades Radiométricas de Rochas do Escudo Sul-Riograndense e sua Significação Tectônica. X Carta do Brasil ao Milionésimo, Folha de Porto Alegre, DNPM

Costa, A.F.U., Fernandes, L.A.D., Shukowsky, W., Nardi, L.V.S. & Bitencourt, M.F. 1995. Teste dos modelos tectonicos e de posicionamento do complexo Granitico de Cacapava do Sul atraves de estudos de modelagem gravimetrica 3-D. Revista Brasileira de Geofisica, 13: 91–101.

Costa, E.O. 2021. *Evolução metamórfico-deformacional da porção sudeste do Complexo Metamórfico Passo Feio e interpretação do Lineamento de Caçapava, RS*. Porto Alegre, 88p. Dissertação de Mestrado. Programa de Pós-Graduação em Geociências. Universidade Federal do Rio Grande do Sul. 88p.

CPRM – SERVIÇO GEOLÓGICO DO BRASIL. 2010. Projeto Aerogeofísico Escudo do Rio Grande do Sul. LASA PROSPECÇÕES S.A., Relatório Técnico, 260 p.

Creach, M., Decarreau, A., Melfi, A. J., Nahon, D., Parisot, J. C., & Trescases, J. J. 2011. Estudo geoquímico do intemperismo do escarnito cuprífero de Santa Blandina (Itapeva, SP): acumulação supérgena do cobre em meio laterítico. *Geochimica Brasiliensis,* 6(1).

Ducoux, M., Branquet, Y., Jolivet, L., Arbaret, L., Grasemann, B., Rabillard, A., … Drufin, S. 2017. Synkinematic skarns and fluid drainage along detachments: The West Cycladic Detachment System on Serifos Island (Cyclades, Greece) and its related mineralization. *Tectonophysics*, 695: 1–26.

Einaudi, M.T., Meinert, L.D. & Newberry, R.J. 1981. Skarn deposits. *Economic Geology 75th Anniversary Vol*. pp 317–391

Engvik, A.K., Taubald, H., Solli, A., Grenne, T., & Austrheim, H. 2018. Dynamic Metasomatism: Stable Isotopes, Fluid Evolution, and Deformation of Albitite and Scapolite Metagabbro (Bamble Lithotectonic Domain, South Norway). *Geofluids*, 1–22.

Fernandes, L.A.D., Tommasi, A., Porcher, C.C. 1992. Deformation patterns in the southern Brazilian branch of the Dom Feliciano Belt: A reappraisal. Journal of South American Earth Sciences, 5: 77–96.

Ferry, J.M. & Dipple, G.M. 1991. Fluid flow, mineral reactions, and metasomatism. *Geology,* 19: 211–214.

Ferry, J.M. 1978. Fluid interaction between granite and sediment during metamorphism, South-central Maine. *American Journal of Science,* 278: 1025–1056.

Ferry, J.M. 1991. Dehydration and decarbonation reactions as a record of fluid infiltration. In: Kerrick D (ed) *Contact metamorphism* (Reviews in Mineralogy vol. 26). Mineralogical Society of America, Washington DC, pp. 351–393

Ferry, J.M. 1992. Regional metamorphism of the waits river formation, Eastern Vermont: Delineation of a new type of giant metamorphic hydrothermal system. *Journal of Petrology,* 33: 45–94.

Ferry, J.M. 1994. Overview of the petrologic record of fluid-flow during regional metamorphism in northern New England. *American Journal of Science,* 294: 905–988

Fragoso César, A.R.S., 1991. Tectônica de placas no Ciclo Brasiliano: as orogenias dos cinturões Dom Feliciano e Ribeira no Rio Grande do Sul. São Paulo, 387p. Programa de Pós-Graduação em Geociências. Universidade de São Paulo.

Goulart, R.V., Remus, M.V.D. & Reis, R.S. 2013. Composição isotópica de Sr, C e O e geoquímica de ETRs das rochas carbonáticas do Bloco São Gabriel, Rio Grande do Sul. Pesquisas em Geociencias, 40: 75–97.

Guo, S., Chu, X., Hermann, J., Chen, Y., Li, Q., Wu, F., Liu, C. & Sein, K. 2021. Multiple Episodes of Fluid Infiltration Along a Single Metasomatic Channel in Metacarbonates (Mogok Metamorphic Belt, Myanmar) and Implications for CO2 Release in Orogenic Belts. *Journal of Geophysical Research: Solid Earth*, 126: 1–23.

Guy, B., Fauré, N., Le Loc'h, G. & Varenne, J.L., (1988). Etude microthermométrique des inclusions fluides des skarns à tungstène de Costabonne (Pyrénées, France): *Quelques résultats: CR Acad. Sci. Paris*, 307: 33–38

Hames, W.E., Tracy, R.J. & Bodnar, R.J. 1989. Postmetamorphic unroofing history deduced from petrology, fluid inclusions, thermochronometry, and thermal modeling: an example from southwestern New England. *Geology*, 17(8): 727–730.

Harlov, D.E. & Austrheim, H.H., 2013. *Metasomatism and the Chemical Transformation of Rock*, Lecture Notes in Earth System Sciences, Lecture Notes in Earth System Sciences. Springer Berlin Heidelberg, Berlin, Heidelberg.

Hartmann, L.A., Chemale Jr, F. & Phillip, R.P. 2007. Evolução geotectônica do Rio Grande do Sul no Pré-Cambriano, *In*: Iannuzzi, R., Frantz, J.C. (Eds.), *50 Anos de Geologia No Rio Grande Do Sul*. Porto Alegre, p. 97–123.

Hartmann, L.A., Leite, J.A.D., Da Silva, L.C., Remus, M. V.D., McNaughton, N.J., Groves, D.I., Fletcher, I.R., Santos, J.O.S., Vasconcellos, M.A.Z. 2000. Advances in SHRIMP geochronology and their impact on understanding the tectonic and metallogenic evolution of southern Brazil. Australian Journal of Earth Sciences, 47: 829–844.

Hartmann, L.A., Philipp, R.P., Santos, J.O.S. & McNaughton, N.J. 2011. Time frame of 753-680 Ma juvenile accretion during the São Gabriel orogeny, southern Brazilian Shield. *Gondwana Research*, 19: 84–99.

Hartmann, L.A., Tindle, A. & Bitencourt, M. de F.A.S. 1990. O metamorfismo de facies anfibolito no complexo metamorfico Passo Feio, RS, com base em quimica dos minerais. *Pesquisas*, 17: 62–71.

He, C., Gong, S., Wang, L., Chen, N., Santosh, M. & Wang, Q., 2018. Protracted post-collisional magmatism during plate subduction shutdown in early Paleoproterozoic: Insights from post-collisional granitoid suite in NW China. *Gondwana Research*, 55: 92–111.

Hoefs, J. 2015. *Stable Isotope Geochemistry*. Springer International Publishing.

Holness, M.B., 1993. Temperature and pressure dependence of quartz-aqueous fluid dihedral angles: the control of adsorbed H2O on the permeability of quartzites. *Earth and Planetary Science Letters,* 117: 363–377.

Huang, W. & Rubenach, M. 1995. Structural controls on syntectonic metasomatic tremolite and tremolite-plagioclase pods in the Molanite Valley, Mt. Isa, Australia. *Journal of Structural Geology*, 17: 83–94

Jordt-Evangelista, H. & Viana, D.J. 2000. Mármores da região de Itaoca (ES) e escarnitos no contato com diques máficos e félsicos: mineralogia e petrogênese. *Geonomos*, 8(2): 61-67.

Kerrick, D.M. 1977. Genesis of zoned skarns in Sierra-Nevada, California. *Journal of Petrology,* 18: 144–181

Koehn, D., Piazolo, S., Beaudoin, N.E., Kelka, U., Spruženiece, L., Putnis, C. V. & Toussaint, R., 2021. Relative rates of fluid advection, elemental diffusion and replacement govern reaction front patterns. *Earth and Planetary Science Letters,* 565: 116950.

Kwak, T.A.P. 1987. W-Sn skarn deposits and related metamorphic skarns and granitoids. In: *Developments in economic geology 24*. Amsterdam Elsevier, 415p

Leinz, V., Barbosa, A.F. & Teixeira, E., 1941. Mapa Geológico Caçapava-Lavras. *Boletim da Secretaria de Agricultura, Indústria e Comércio*, 90: 39.

Leite, J.A.D., Hartman, L.O.A., McNaughton, N.J. & Chemale, F. 1998. Shrimp U/Pb zircon geochronology of Neoproterozoic juvenile and crustal-reworked terranes in southernmost Brazil. *International Geology Review*, 40: 688–705.

Lopes, C.G., Pimentel, M.M., Philipp, R.P., Gruber, L., Armstrong, R. & Junges, S. 2015. Provenance of the Passo Feio Complex, Dom Feliciano Belt: Implications for the age of supracrustal rocks of the São Gabriel Arc, southern Brazil. *Journal of South American Earth Sciences*, 58: 9–17.

McCaig, A.M., 1988. Deep fluid circulation in fault zones. *Geology,* 16: 867–870.

Meinert, L.D. 1992. Skarns and skarn deposits. *Geoscience Canada,* 19: 145–162

Meinert, L.D. 2000. Gold skarns related to epizonal plutons. *Reviews in Economic Geology,* 13: 347–375

Meinert, L.D., Dipple, G.M. & Nicolescu, S. 2005. World skarn deposits. *Economic Geology 100th Anniversary Volume*: 299–336

Mesquita, R.B. 2016. Petrogênese, geoquímica, balanço de massa e idade de escarnitos associados a diques metamáficos e félsicos do Complexo Paraíba do Sul, Sul do Espírito Santo. Dissertação de Mestrado, 123p. Escola de Minas, Universidade Federal de Ouro Preto.

Miller, R.B. & Paterson, S.R., 1999. In defense of magmatic diapirs. *Journal of Structural Geology*, 21: 1161–1173.

Morales, B.A. de A., Almeida, D.D.P.M. de, Koester, E., Rocha, A.M.R. da, Dorneles, N.T., Rosa, M.B. & Martins, A.A. 2019. Mineralogy, whole-rock geochemistry and C, O isotopes from Passo Feio Carbonatite, Sul-Riograndense Shield, Brazil. *Journal of South American Earth Sciences* 94, 102208.

Müller, T., Baumgartner, L.P., Foster, C.T. & Bowman, J.R. 2009. Crystal size distribution of periclase in contact metamorphic dolomite marbles from the Southern Adamello Massif, Italy. *Journal of Petrology,* 50: 451–465.

Müller, T., Baumgartner, L.P., Foster, C.T. & Vennemann, T.W. 2004. Metastable prograde mineral reactions in contact aureoles. *Geology,* 32: 821–824.

Nabelek, P.I. 1991. Stable isotope monitors. In: Kerrick DM (ed) *Contact metamorphism*, vol 26, Reviews in Mineralogy. Mineralogical Society of America, Washington, DC, pp 395–435

Nabelek, P.I., Bédard, J.H., Hryciuk, M., & Hayes, B. 2013. Short-duration contact metamorphism of calcareous sedimentary rocks by Neoproterozoic Franklin gabbro sills and dykes on Victoria Island, Canada. *Journal of Metamorphic Geology,* 31(2): 205–220.

Nardi, L.V.S. & Bitencourt, M. de F. 1989. Geologia, Petrologia e Geoquímica do Complexo Granítico de Caçapava do Sul, RS. *Revista Brasileira de Geociências*, 19: 153–169.

Naumann, K.F. 1826. *Lehrbuch der Mineralogie*. Leipzig, Engelman, 209p.

Neis, L.P. 2017. Aplicação de razão $^{87}Sr/^{86}Sr$ e geoquímica em mármores do Escudo Sul-Rio-Grandense. Porto Alegre, p. 80. Dissertação de Mestrado, Programa de Pós-Graduação em Geociências, Instituto de Geociências, Universidade Federal do Rio Grande do Sul.

Newberry, R.J. 1998. W- and Sn-skarn deposits: a 1998 status report. *Mineralogical Association Canada Short-Course Series,* 26: 289–335

Ohmoto, H. 1986. Stable isotope geochemistry of ore deposits. *Reviews in Mineralogy and Petrology*, 16: 491–559.

Parente, C.V., Veríssimo, C.U.V., Botelho, N.F., Santos, T.J.S., Oliveira, C.G., Lira Jr, J.A., & Martins, D.T. 2015. Depósitos de escarnitos mineralizados em ferro e cobre do Arco Magmático de Santa Quitéria, Ceará, Província Borborema do nordeste do Brasil. *Brazilian Journal of Geology*, 45(3): 359-382.

Pertille, J., Hartmann, L.A., Santos, J.O.S., McNaughton, N.J., Armstrong, R. 2017. Reconstructing the Cryogenian–Ediacaran evolution of the Porongos fold and thrust belt, Southern Brasiliano Orogen, based on Zircon U–Pb–Hf–O isotopes. *International Geology Review*, 59: 1532–1560.

Petford, N., Cruden, A.R., McCaffrey, K.J.W. & Vigneresse, J.L., 2000. Granite magma formation, transport and emplacement in the Earth's crust. *Nature*, 408: 669–673.

Philipp, R.P., Pimentel, M.M. & Basei, M.A.S. 2018. The Tectonic Evolution of the São Gabriel Terrane, Dom Feliciano Belt, Southern Brazil: The Closure of the Charrua Ocean, in: Siegesmund, S., Basei, Miguel A.S., Oyhantçabal, P., Oriolo, S. (Eds.), *Geology of Southwest Gondwana*. Springer International Publishing, Cham, p. 243–265.

Piccoli, F., Ague, J.J., Chu, X., Tian, M., Brovarone, A.V. 2021. Field-based evidence for intra-slab high-permeability channel formation at eclogite-facies conditions during subduction. *Geochemistry, Geophysics, Geosystems,* 1–17.

Pirajno, F. 2009. *Hydrothermal Processes and Mineral Systems*. Dordrecht, Springer Netherlands.

Pirajno, F. 2013. Effects of metasomatism on mineral systems and their host rocks: alkali metasomatism, skarns, greisens, tourmalinites, rodingites, black-wall alteration and listvenites. In: *Metasomatism and the Chemical Transformation of Rock*. Berlin, Springer Berlin Heidelberg. p. 203-251

Pivarunas, A.F. & Meert, J.G., 2019. Protracted magmatism and magnetization around the McClure Mountain alkaline igneous complex. *Lithosphere,* 11: 590–602.

Porcher, C.A. & Lopes, R.D.C., 2000. Programa Levantamentos Geológicos Básicos do Brasil–PLGB: Cachoeira do Sul (folha SH. 22-Y-A) CPRM/DNPM (CD-ROM).

Putnis, A., & Austrheim, H. 2010. Fluid-Induced Processes: Metasomatism and Metamorphism. *Frontiers in Geofluids*, 254–269.

Putnis, A., 2009. Mineral replacement reactions. *Reviews in Mineralogy and Geochemistry,* 70: 87–124.

Putnis, A., Putnis, C.V., 2007. The mechanism of reequilibration of solids in the presence of a fluid phase. *Journal of Solid State Chemistry,* 180: 1783–1786.

Putnis, C.V., Ruiz-Agudo, E., 2013. The Mineral-Water Interface: Where Minerals React with the Environment. *Elements*, 9: 177–182.

Remus, M. V. D., Dani, N., Gazzoni, C. P., Hoerlle, G. S. & Reis, R. S. 2011. Minério de Cu (Au) de alto teor em zonas de alteração clorítica em escarnitos magnesianos de Caçapava do Sul, RS. In: XIII CONGRESSO BRASILEIRO DE GEOQUÍMICA, 2011. Anais… Gramado: SBGq. CD-ROM

Remus, M.V.D., Hartmann, L.A., McNaughton, N.J., Groves, D.I. & Fletcher, I.R., 2000. The link between hydrothermal epigenetic copper mineralization and the Cacapava Granite of the Brasiliano cycle in southern Brazil. Journal of South American Earth Sciences 13, 191–216.

Remus, M.V.D., Massonne, H.J., Hartmann, L.A., Theye, T. & Braetz, H. 2010. Garnet zonation and monazite ages as monitors of contrasting metamorphic evolution in the Brasiliano schist belts of Southern Brazil, *In*: 45° Congresso Brasileiro de Geologia. Belém do Pará.

Ribeiro, M. 1970. *Geologia da folha de Bom Jardim: Rio Grande do Sul- Brasil*. In: Boletim: Divisão de Geologia e Mineralogia. Brasília, 247: p. 1-142.

Ribeiro, M., Fiqueiredo-Filho, P.M. & Tessari, R.I., 1966. *Geologia da quadrícula de Caçapava do Sul, RS, Brasil*. Boletim da Divisão de Geologia e Mineralogia DPM-DNPM p. 127–232.

Rollinson, H.R. 1993 Using Geochemical Data: Evaluation, Presentation and Interpretation. Longman, Harlow, 352 p.

Roselle, G.T., Baumgartner, L.P. & Valley, J.W., 1999. Stable isotope evidence of heterogeneous fluid infiltration at the Ubehebe Peak contact aureole, Death Valley National Park, California. *American Journal of Science*, 299: 93–138.

Rumble, D. 1982. Stable isotope fractionation during metamorphic devolatilization reactions. *Reviews in Mineralogy and Geochemistry*, 10(1): 327–353.

Saalmann, K., Gerdes, A., Lahaye, Y., Hartmann, L.A., Remus, M.V.D. & Läufer, A. 2011. Multiple accretion at the eastern margin of the Rio de la Plata craton: The prolonged Brasiliano orogeny in southernmost Brazil. *International Journal of Earth Sciences,* 100: 355–378.

Saalmann, K., Hartmann, L.A. & Remus, M.V.D. 2005. Tectonic evolution of two contrasting schist belts in southernmost Brazil: A plate tectonic model for the Brasiliano orogeny. *International Geology Review*, 47: 1234–1259.

Sartori, P.L.P. & Kawashita, K. 1985. Petrologia e geocronologia do Batólito Granítico de Caçapava do Sul-RS, *In*: II Simpósio Sul-Brasileiro de Geologia. SBG, Florianópolis, pp. 102–115.

Sartori, P.L.P.& Kawashita, K. 1989. Petrologia e geocronologia do Stock granítico Santos Ferreira e sua correlação com o Batólito de Cacapava do Sul, RS. *Estudos Tecnológicos*, 12: 131–141.

Silva-Filho, B.C., Matsdorf, M.C. 1987. Análise estrutural dos metamorfitos da borda oeste do granito Caçapava, Caçapava do Sul: Implicaçoes geológicas locais e regionais, in: Anais, III Simpósio Sul-Brasileiro de Geologia. Curitiba, p. 197–222.

Soliani, E. 1986. *Os dados geocronológicos do escudo sul-rio-grandense e suas implicações de ordem geotectônica*. São Paulo, 417p. Tese de Doutorado, Programa de Pós-Graduação em Geociências. Universidade de São Paulo.

Souza, T.L., 2020. *Gênese dos serpentinitos e esteatitos do Complexo Passo Feio (RS-Brasil): evidências mineralógicas, geoquímicas e isotópicas*. Porto Alegre, 204p. Tese de Doutorado. Universidade Federal do Rio Grande do Sul.

Taylor, B.E. 1987. Stable isotope geochemistry of ore-forming fluids. *In*: Kyser T(ed.) Stable Isotope Geochemistry of Low Temperature Processes, Short Course Notes, pp. 337–445. Ottawa, Mineralogical Association of Canada.

Taylor, B.E., & O'Neil, J.R. 1977. Stable isotope studies of metasomatic Ca-Fe-Al-Si skarns and associated metamorphic and igneous rocks, Osgood Mountains, Nevada. *Contributions To Mineralogy and Petrology*, 63(1): 1–49.

Taylor, H. P. 1974. The Application of Oxygen and Hydrogen Isotope Studies to Problems of Hydrothermal Alteration and Ore Deposition. Economic Geology, 69(6), 843–883.

Tennholm, T., 2019. Metamorphic evolution of the Passo Feio Complex (central part of the Dom Feliciano Belt, southern Brazil). Tromso, 97p. Dissertação de Mestrado. The Arctic University of Norway.

Tichomirowa, M., Käßner, A., Sperner, B., Lapp, M., Leonhardt, D., Linnemann, U., Münker, C., Ovtcharova, M., Pfänder, J.A., Schaltegger, U., Sergeev, S., von Quadt, A. & Whitehouse, M., 2019. Dating multiply overprinted granites: The effect of protracted magmatism and fluid flow on dating systems (zircon U-Pb: SHRIMP/SIMS, LA-ICP-MS, CA-ID-TIMS; and Rb–Sr, Ar–Ar) – Granites from the Western Erzgebirge (Bohemian Massif, Germany). *Chemical Geology,* 519: 11–38.

Törnebohm A.E. 1875. Geognostic beskrifning ofver Persbergets Grufvefält. Sverige Geol Undersökning, Norstedt and Sons, Stockholm

UFRGS. Universidade Federal do Rio Grande do Sul. 1998. *Projeto Caçapava do Sul: Mapeamento Geológico.* escala 1:25.000.

Valley, J.W. 1986. Stable isotope geochemistry of metamorphic rocks. *Reviews in Mineralogy and Geochemistry:* 16(1), 445–489.

Villa, I.M., Williams, M.L., 2013. Geochronology of Metasomatic Events, In: *Metasomatism and the Chemical Transformation of Rock: The Role of Fluids in Terrestrial and Extraterrestrial Processes*. pp. 171–202.

von Bargen, N. & Waff, H.S., 1986. Permeabilities, interfacial areas and curvatures of partially molten systems: Results of numerical computations of equilibrium microstructures. *Journal of Geophysical Research*, 91: 9261.

Winter, J.D., 2013. *Principles of Igneous and Metamorphic Petrology*: *Pearson New International Edition*. Pearson Education Limited.

Yardley, B.W.D. 2005. Metal concentrations in crustal fluids and their relationship to ore formation. *Economic Geology*, 100: 613–632

Yardley, B.W.D. 2009. The role of water in the evolution of the continental crust. *Journal of the Geological Society*, 166(4): 585–600.

Yardley, B.W.D. 2013. The Chemical Composition of Metasomatic Fluids in the Crust. In: *Metasomatism and the Chemical Transformation of Rock*. Lecture Notes in Earth System Sciences. Springer, Berlin, Heidelberg

Yardley, B.W.D., Bottrell, S.H. & Cliff, R.A. 1991. Evidence for a regional-scale fluid loss event during mid-crustal metamorphism. *Nature*, 490:151–154

Zharikov, V.A., Pertsev, N.N., Rusinov, V.L., Callegari, E. & Fettes, D.J., 2007. Metasomatism and metasomatic rocks. *Study Group on Metasomatic rocks*, 1–17.

CAPÍTULO 2 – ARTIGO I

Metasomatic reactions triggered by localized and episodic fluid flux record multistage intrusion history: An example from the syntectonic Caçapava do Sul Granitic Complex, Southern Brazil

RESEARCH PAPER

To: Journal of Metamorphic Geology

Metasomatic reactions triggered by localized and episodic fluid flux record multistage intrusion history: An example from the syntectonic Caçapava do Sul Granitic Complex, Southern Brazil

RUNNING TITLE:

Fluid flux record multistage intrusion

AUTHORS:

Guilherme S. Hoerlle[a]; Marcus V. D. Remus[a]; Thomas Müller[b,c]; Sandra Piazolo[b]; Cristiano C. Lana[d]; Dominik Sorger[c]

[a] Instituto de Geociências - Universidade Federal do Rio Grande do Sul, Porto Alegre, Brazil

[b] Institute of Geophysics and Tectonics, School of Earth and Environment - University of Leeds, United Kingdom

[c] Geoscience Center, Georg-August-Universität Göttingen, Göttingen, Germany

[d] Departamento de Geologia, Escola de Minas, Universidade Federal de Ouro Preto, Ouro Preto, Brazil

Corresponding author:
Guilherme Sonntag Hoerlle
guilherme.hoerlle@ufrgs.br
Av. Bento Gonçalves, 9500
43126/110
Porto Alegre, RS, Brazil
Zip code: 90650-001

ABSTRACT

In this study we report field, microstructural and geochronological evidence for multistage localized and episodic fluid flux associated with the syntectonic intrusion of the Caçapava do Sul Granitic Complex into the dolomitic marbles of the Passo Feio Metamorphic Complex (Dom Feliciano Belt, southern Brazil). The marbles were intruded by mafic and felsic intrusions from c. 578 to c. 557 Ma, which triggered a set of metasomatic reactions in the host and intrusive rocks at three stages. Calcsilicate rocks replacing the dolomites, *i.e.* skarns, and calcite-chlorite-sulphide veins were formed at different stages of the pluton assembly. These metasomatic lithologies were formed in response to fluid infiltration derived from igneous apophyses into the host rocks. Hence, they represent useful indicators of the pathways used by the magmatic fluids when infiltrating the dolomitic marbles. The first metasomatic stage resulted in the formation of diopside skarns. They were formed in restricted areas at lithological boundaries and along pre-existing foliation planes within the host rocks suggesting spatially-limited infiltration of fluids released from M1 mafic and felsic apophyses during an extensional regime. A second stage of metasomatism is recorded by the synkinematic formation of forsterite skarns during transpression triggered by H_2O-rich fluids derived from the cooling of M2 felsic apophyses. Zircon U-Pb age of c. 578 Ma obtained for a M2 felsic apophysis directly associated to forsterite skarns defines the age of the second metasomatic stage. Heat supply from repeated sheeted intrusions and transpression resulted in pinch-and-swell and boudin structures of the former diopside skarns together with deformation and metamorphism of the prior M1 mafic-felsic apophyses. The fluid pathways recorded by reaction textures were localized and characterized by heterogeneous flow along lithological boundaries, through diopside-skarn boudin and pinch-and-swell structures as well as structurally controlled focused flow in fold hinges and axial planes of the M1 apophyses. Fluid flux in the first two stages was highly localized and at high temperatures (~500 to 600°C) in which the changes of the skarn assemblages were controlled by either variable fluid fluxes or constant flux and variable physicochemical conditions of the fluid phase (*e.g.* silica activity, temperature). The third stage is mainly characterized by serpentinization of previous skarn silicate assemblages, chloritization of mafic and felsic apophyses and formation of calcite-chlorite-sulphide veins and breccias at c. 300°C. The fluid flow

regime at this stage was controlled by the porosity and permeability created due to brittle fracturing related to the cooling of the granitic complex. Apatite and titanite from different mafic apophyses record consistent U-Pb ages of c. 557 Ma that mark the thermal effect of the last igneous intrusions and subsequent cooling of the Caçapava do Sul Granitic Complex. Our study shows that the metasomatic reactions commonly observed in the host rocks and apophyses of a magmatic complex provide useful insights on timing of the pluton assembly, deformation and associated fluid activity.

Keywords: fluid-rock interaction, skarn, localized fluid flow, syntectonic magmatism, metasomatism

1. INTRODUCTION

Fluid flow is a fundamental process governing the distribution of elements in many geological settings. In hydrothermal systems, addition and removal of chemical components and modifications of mineral and bulk composition of rocks are directly linked to metasomatic processes. Here, fluids play a major role providing a much more efficient transport mechanism than solid state diffusion, recorded by the dissolution of pre-existing minerals and precipitation of new phases (*e.g.* Ducoux *et al*, 2017; Engvik, Taubald, Solli, Grenne, & Austrheim, 2018; Nabelek, Bédard, Hryciuk, & Hayes, 2013). However, fluid flow often occurs in heterogeneous and anisotropic media, in which case the fluid is structurally and/or lithologically controlled resulting in localized metasomatic domains that record the characteristics of fluid-rock interaction over time. Deciphering the spatial and temporal evolution of fluid-mediated rock alteration is crucial to understand complex processes in natural settings. Detailed studies of the zones of metasomatic reactions in terms of reaction textures and spatial distribution hold a wealth of information regarding the conditions at which fluid-rock interaction occurred.

Carbonate rocks and their metamorphic equivalents are well-known for being highly reactive when exposed to externally derived fluids or changing metamorphic conditions (*e.g.* Bégué, Baumgartner, Müller, Putlitz, & Vennemann, 2020; Bucher-Nurminen, 1981; Ferry, 1991; Müller, Baumgartner, Foster, & Bowman, 2009; Müller, Baumgartner, Foster, & Vennemann, 2004). Crystallizing plutons constitute important heat and fluid sources commonly associated with carbonate skarn systems that are characterized by coarse-grained calc-silicate rocks. Such skarn systems contain a variety of detailed information recording the metasomatic interaction as well as their metamorphic conditions. In general, there is a causal relationship between the sequence of emplacement, crystallization, alteration, and cooling of an intrusion and the corresponding spatial and temporal evolution during prograde and retrograde skarn formation (Brown, Bowman, & Kelly, 1985; Meinert, Dipple, & Nicolescu, 2005). Detailed knowledge on the mechanisms, rates and timing of the emplacement of plutonic bodies remains elusive but significantly impacts our understanding of the processes forming the associated metasomatic complexes. For example, several authors proposed that plutons ascend as large diapirs (*e.g.*, Buddington, 1959; Clarke,

1992; Miller & Paterson, 1999) whereas other authors consider this process as slow and inefficient. Other authors suggest that large igneous magmatic bodies are formed by the incremental supply of magma through dyke- and sill-like structures that can build up a magmatic body over millions of years (*e.g.*, Clemens & Mawer, 1992; Coleman, Gray, & Glazner, 2004; Petford, Cruden, McCaffrey, & Vigneresse, 2000). However, the recognition of incrementally assembled plutons recorded in the granitic rocks can be problematic because the setting prevails near the original magmatic temperatures for a long time potentially obscuring pristine contacts between individual increments (Bartley, Coleman, & Glazner, 2008). Yet, magmatic pulses with quiet intervals can last for tens of millions of years (*i.e.* protracted magmatism) and result in overprinted granitic batholiths (*e.g.* He *et al*., 2018; Pivarunas & Meert, 2019; Tichomirowa *et al*., 2019). While the diapir, incremental and protracted models are conceptually plausible, they are characterized by fundamentally different cooling and fluid infiltration histories. Therefore, studying in detail the metasomatic fingerprint of the interaction of magmatic fluids with host rocks offers the potential to reveal the detailed intrusion and infiltration history of a complex plutonic body.

In this contribution, we combine field relations, petrology of metasomatic rocks and LA-ICP-MS U-Pb dating of zircon, titanite and apatite of igneous apophyses of the Neoproterozoic Caçapava do Sul Granitic Complex (CSGC) to determine the intrusion, deformation and fluid infiltration history of the complex. The complex intruded into the dolomitic marbles of the Passo Feio Metamorphic Complex (PFMC) on the eastern border of the São Gabriel Terrane, southern Brazil. Emplacement of the CSGC resulted in a complex metasomatic system recorded by the formation of skarn and hydrothermal veins. The observations and geochronological data are successfully explained by a model of multistage localized metasomatic fluid-rock interaction events that provide a full record of the intrusion history of the granitic complex confirming a stage-wise growth of the magmatic body.

2. GEOLOGICAL BACKGROUND

The Passo Feio Metamorphic Complex (PFMC) and the Caçapava do Sul Granitic Complex (CSGC) are located at the eastern border of the São Gabriel Terrane (SGT), which itself belongs to the Dom Feliciano Belt (DFB) (Figures 1a-b).

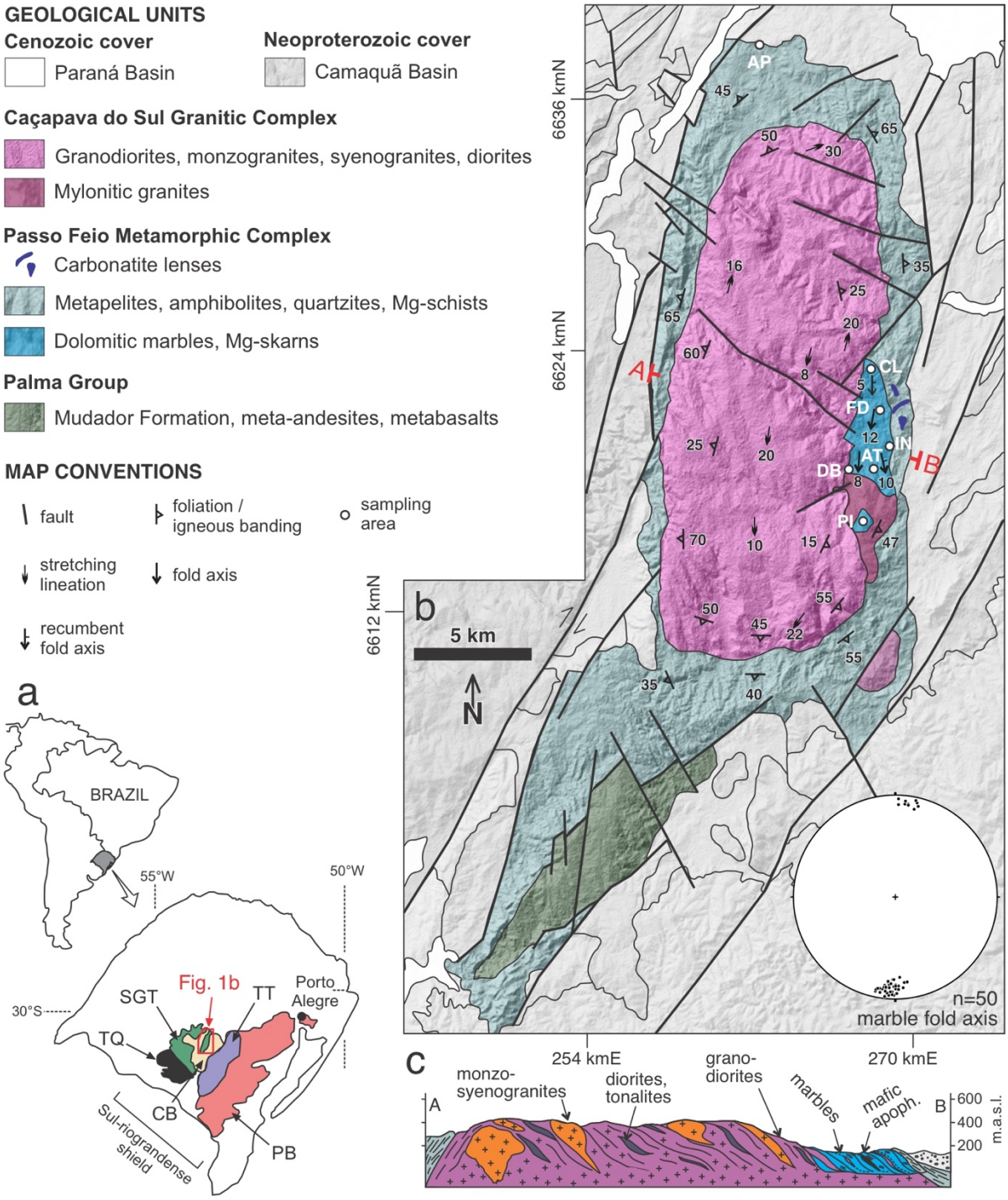

Figure 1: Location of the CSGC and PFMC in the Sul-riograndense shield, southern Brazil. (a) Tectonic domains of the Sul-riograndense Shield (TT: Tijucas Terrane; SGT: São Gabriel Terrane; PB: Pelotas Batholith; CB: Camaquã Basin; TQ: Taquarembó Terrane). (b and c) Geological map and cross-section of the PFMC and CSGC area showing main structural data and sampling locations (Modified from UFRGS, 1998 and Porcher & Lopes, 2000).

The DFB represents the southern portion of the Mantiqueira Province, *i.e.* the Neoproterozoic NE-SW orogenic system that extends from northeastern Brazil to the south of Uruguay. The SGT comprises a Neoproterozoic (920-680 Ma) juvenile magmatic arc association developed during the collision of the Kalahari and Rio de La Plata cratons (Chemale, 2000; Fernandes, Tomasi, & Porcher, 1992; Hartmann *et al*., 2000; Saalmann *et al*., 2010; Silva, McNaughton, Armstrong, Hartmann, & Fletcher, 2005). The terrane is composed of metavolcanic-sedimentary supracrustal sequences that were metamorphosed under amphibolite facies conditions and subsequently intruded by juvenile calc-alkaline magmas, now present as orthogneisses; ophiolites and mafic-ultramafic complexes (Babinski, Chemale, Hartmann, Van Schmus, & Da Silva, 1996; Hartmann *et al*., 2000; Hartmann, Philipp, Santos, & McNaughton, 2011; Philipp, Pimentel, & Basei, 2018; Remus, Hartmann, & Formoso, 1993; Saalmann, Hartmann, & Remus, 2005; Saalmann, Hartmann, Remus, Koester, & Conceição, 2005; Saalmann, Remus, & Hartmann, 2005). Additionally, the SGT hosts several Neoproterozoic granitic intrusions (*e.g.*, CSGC) and is partially covered by post collisional volcano-sedimentary sequences.

2.1. PASSO FEIO METAMORPHIC COMPLEX

The PFMC is located in the eastern border of the SGT and consists of a supracrustal association of metapelite, amphibolite, marble, calc-silicate and metavolcanic rocks that were intruded by the CSGC (Bitencourt, 1983; Leinz, Barbosa, & Teixeira, 1941; Remus, Hartmann, McNaughton, Groves, & Fletcher, 2000; Ribeiro, Bocchi, Figueiredo-Filho, & Tessari, 1966) in addition to some small sheet-like carbonatite intrusions (Cerva-Alves, Remus, Dani, & Basei, 2017; Morales *et al*., 2019).

The metamorphic events that formed the PFMC have been subject to controversial discussions. While there is a consensus that the complex records at least two metamorphic events displaying an increasing metamorphic grade towards the CSGC, contrasting ideas have been proposed regarding the thermal effect of the intrusion on the metamorphic record. Some authors described hornblende-hornfels and pyroxene-hornblende facies rocks surrounding the granite up to a few hundreds of meters from the contact, which were gradually followed by albite-epidote-hornfels and greenschist facies rocks further from the contact based on extensive field mapping of the area (Bortolotto, 1988; Leinz *et al*., 1941; Ribeiro *et al*., 1966; Ribeiro, 1970; Silva-Filho &

Matsdorf, 1987). These authors interpreted the observed distribution of mineral assemblages to be the result of a primary regional metamorphic event ranging from greenschist to amphibolite facies, followed by a second contact metamorphic event associated with the intrusion of the CSGC. In contrast, other authors interpret both metamorphic events as regional, with the first one reaching amphibolite facies (staurolite zone) conditions and the second, synchronous to the intrusion, as a greenschist facies (chlorite zone) with thermal and infiltration effects restricted to the border of some apophyses (Bitencourt, 1983; Hartmann, Tindle, & Bittencourt, 1990).

Zircon provenance studies in metapelites and schists revealed Archean, Paleoproterozoic and Neoproterozoic populations (3637 to 774 Ma) suggesting complex continental source areas (Lopes *et al*., 2015; Remus *et al*., 2000). C, O and Sr isotopic compositions of the dolomitic marbles reveal carbonate deposition between 770 and 730 Ma (Goulart, Remus, & Reis, 2013). LA-ICP-MS monazite dating yields a series of ages between 650 and 620 Ma, which were assigned to the first metamorphic event (Remus, Massonne, Hartmann, Theye, & Braetz, 2010). The second metamorphic event was then linked to the age of a granodiorite sill sample of the CSGC of 562±8 Ma based on SHRIMP U-Pb zircon dating (Remus *et al*., 2000).

2.2. CAÇAPAVA DO SUL GRANITIC COMPLEX

The CSGC exhibits a wide compositional range with mostly granodiorite, monzogranite, leucogranite, minor diorite, tonalite and quartz-diorite of metaluminous and calc-alkaline affinity (Leinz *et al*., 1941; Nardi & Bitencourt, 1989; Ribeiro *et al*., 1966; Sartori & Kawashita, 1985). Contrasting emplacement models were proposed: a diapir (Nardi & Bitencourt, 1989), a sheet-like intrusion (Fragoso César, 1991), a lens-shaped mega-porphyroblast (Fernandes *et al*., 1992) and an intrusion along a fault-bend-fold of a right lateral strike-slip shear zone (Costa, Fernandes, Shukowsky, Nardi, & Bitencourt, 1995).

First attempts to date the CSGC were made through K/Ar and Rb/Sr isochron dating, which resulted in ages ranging from 520 to 640 Ma (Cordani *et al*., 1974; Sartori & Kawashita, 1985; Sartori & Kawashita, 1989; Soliani, 1986). Two different U-Pb SHRIMP zircon studies were carried out on samples of a monzogranite and a granodiorite revealing a complex distribution of zircon ages indicating significant amounts of lead loss and reversely discordant ages (Leite, Hartmann, McNaughton, &

Chemale, 1998; Remus *et al*., 2000). Two magmatic ages were proposed based on SHRIMP zircon U-Pb analyses. The two studies reported concordant ages within the same error of 561±6 Ma (MSWD=1.04; n=4; Leite *et al*., 1998) and 562±8 Ma (MSWD=0.56; n=18; Remus *et al*., 2000) and one age of 540±11 Ma (MSWD=0.89; n=3; Leite *et al*., 1998). The younger age of c. 540 Ma was re-interpreted as the result of common Pb loss of older zircons (Remus *et al*., 2000). Inherited Paleoproterozoic zircon populations with ages ranging from 1.7 to 2.4 Ga were reported in both studies. Large variations in initial $^{87}Sr/^{86}Sr$ and εNd values, lead isotopes and zircon ages also suggest that the CSGC had a complex and heterogeneous crustal source of variable composition and age (Babinski *et al*., 1996; Sartori & Kawashita, 1989; Remus *et al*., 2000).

3. SAMPLING AND METHODS

Collection of field data and sampling focused on the Caçapava do Sul marble quarries due to the extensive exposure of marbles, igneous apophyses and metasomatic rocks (skarns and hydrothermal veins) providing the opportunity to sample the best sections for the study of igneous and carbonate rock interaction in the region (Figure 1b). Sample collection was made throughout the area aiming at obtaining representative samples of the different igneous components and skarns displaying their various degrees of deformation, spatial relationships and retrograde alteration. Petrographic analyses were made using a LEICA DM4500 optical microscope and a LEICA S6D Greenough stereo microscope in order to identify major constituent minerals and textures. Zircon, apatite and titanite grain concentrates were prepared at the Sample Preparation Laboratory at the Geosciences Institute of UFRGS (IGEO/UFRGS) using conventional jaw crusher, milling, manual panning, magnetic-Frantz isodynamic separator and heavy liquids separation. The grains were handpicked under a binocular microscope and mounted on epoxy disks. U-Pb laser-ablation inductively coupled plasma mass spectrometry (LA-ICP-MS) analyses of zircon, apatite and titanite samples were performed at the Isotopic Geochemistry Laboratory, Federal University of Ouro Preto (IGL-UFOP) except for sample AP-01 which was analyzed at the Center for Geochronological Research of the University of São Paulo (CPGeo-USP). Back-scattered electron (BSE) and cathodoluminescence (CL) images were obtained with a JEOL JSM-6610LV and a JEOL 6510 scanning electron microscopes at IGEO-UFRGS

and DEGEO-UFOP, respectively, to identify internal structures of the crystals. The LA-ICP-MS analyses were performed using a ThermoScientific Element 2 sector field ICP-MS coupled to a CETAC LSX-213 G2+ laser system. Zircon analyses calibration included GJ-1 (Jackson, Pearson, Griffin, & Belousova, 2004) with the additional Plešovice (Sláma *et al*., 2008) and Blue Berry (Santos *et al*., 2017) zircon standards. For titanite and apatite reference materials, BLR-1 (Aleinikoff *et al*., 2007) and KHAN (Kinny, McNaughton, Fanning, & Maas, 1994; Heaman, 2009) were used for the titanite while 401 (Thompson *et al*., 2016) and Madagascar (Thomson, Gehrels, Ruiz, & Buchwaldt, 2012) were used for the apatite. Glitter Data Reduction Software for laser ablation was used to reduce data (Van Achterberg, Ryan, Jackson, & Griffin, 2001). Calculated ages and concordia diagrams were done using Isoplot 3.0 (Ludwig, 2003) and errors are reported at the 2σ level. No common-Pb correction were applied to the titanite and apatite dataset. The calculated titanite and apatite ages are the lower intercept of anchored regressions through Pbc, using Stacey and Kramers (1975) on the Tera-Wasserburg diagram. The anchoring ratios are based on the samples intercept age and the zircon ages. T-XCO_2 and XCO_2-μSiO_2 phase diagrams were calculated using PerpleX (Connolly, 1990) using the dataset from Berman (1996) and equation of state for fluids from Holland and Powell (2011). Abbreviations for the mineral names and their end-members described in the text and figures are after Whitney and Evans (2010).

4. FIELD RELATIONSHIPS

4.1. GENERAL FIELD RELATIONSHIPS

Dolomitic marbles are located in the eastern portion of the PFMC and occur as lenticular bodies that are extensively intruded by tabular felsic and mafic apophyses of variable thickness and composition (Figures 2a-e). They occur to the east of the main granitic body of the CSGC (*i.e.* the granitic batholith; Figure 1b) with sharp and eastward dipping contact at low to medium angles (~10-30°). In this paper, we refer to the bedding of the marbles as S_0 and the metamorphic foliation developed during the first metamorphic event in the PFMC prior to the first magmatic intrusions as S_1. The marbles and some of the apophyses form overturned to recumbent isoclinal folds with N-S to NE-SW axis that plunges at low angles mostly to the S-SW (Figures 2a-e). The

average axial surface dips 20° to the east, locally varying to sub-horizontal or rarely dipping westward at low angles (<15°). The axial surfaces characterize the S_2 foliation.

Tabular felsic and mafic intrusions within the dolomitic marbles are well exposed in the quarries. A group of mafic and felsic apophyses with small to moderate thickness (~0.1 to 2 m) intruded parallel to S_1 foliation of the marbles and was folded accordingly (Figures 2a-d). For simplification, this group of thin and folded mafic-felsic apophyses are identified as M1. Thicker felsic apophyses (> 2 m) form tabular bodies that intrude the marbles parallel or sub-parallel to the S_2 foliation and will be referred to in the following as M2. Given that the orientation of M2 apophyses is parallel to the S_2 axial plane foliation and they are less deformed that M1 apophyses we consider M2 younger than M1 apophyses. However, distinguishing M2 and M1 felsic apophyses is difficult in some cases. Main criteria used for distinguishing M1 and M2 felsic apophyses are thickness, grain-size and emplacement-host geometry. M1 felsic apophyses are thin (20-200 cm), have fine to medium grain size and are commonly folded whereas M2 apophyses are thicker (~ 2 to >10 m), have medium to coarse grain size and emplaced parallel to the S_2 axial plane foliation (Section 4.4.2).

In general, the marbles were locally replaced by skarns that are found at the contacts or a few meters away from M1 and M2 apophyses (Figures 3a-d and 4a-c). Less commonly, and limited to the northernmost quarry (CL area in Figure 1b), the carbonates host calcite-chlorite-sulphide veins and breccias that cut S_1 and S_2 foliation and are generally found a few to tens of meters from NW-SE subvertical faults (Figures 5a-c).

The granitic batholith to the west of the dolomitic marbles outcrops over an area of c. 233 km² forming a N-S elongated asymmetrical domal structure dipping at high angles in the W and NW parts, at low angles in the E and SE parts, and sub-horizontally in the central parts of the granitic body (Figure 1b) (Leinz *et al*., 1941; Nardi & Bitencourt, 1989; Ribeiro *et al*., 1966; Sartori & Kawashita, 1985). The batholith comprises mainly granodiorite, monzogranite and syenogranite with minor diorite and tonalite. Pegmatite, aplitic dykes and quartz veins with pyrite and hematite occur in the eastern border of the body near the dolomitic marbles. Deformation is heterogeneous throughout the batholith from undeformed portions to highly foliated facies and contacts amongst lithotypes vary from sharp to diffuse.

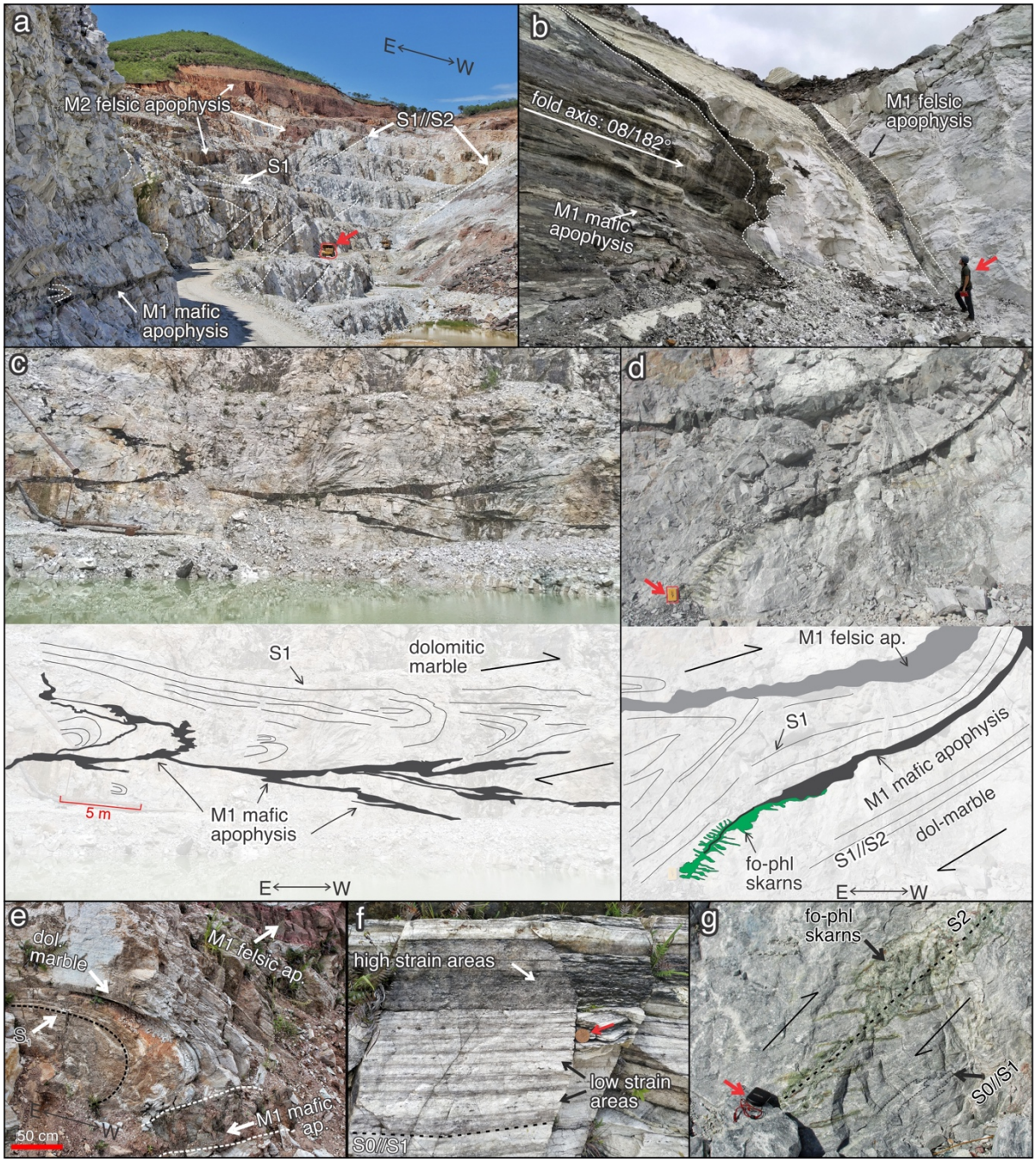

Figure 2: General field relations and structures of the dolomitic marbles of the PFMC and igneous apophyses of the CSGC. (a) General view of the marble quarry in the AT area showing folded marble (white dashed lines) forming major recumbent folds and concordant to subconcordant intrusions of M1 felsic and mafic apophyses; truck (approximate height 5 m) for scale. (b) Folded parallel intrusions of M1 apophyses with sub-horizontal N-S axis in the DB area; person (1.8 m) for scale. (c) Folded M1 mafic apophyses parallel to the subhorizontal N-S trending axial plane in the CL area. (d) Intrusion of M1 mafic and felsic apophyses parallel to the marble foliation and synkinematic fo-phl skarn formation at the termination of the mafic apophysis in the CL area; notepad (25 cm) for scale. (e) tight recumbent isoclinal fold in the dolomitic marble and intrusion of M1 mafic and felsic apophyses parallel to the axial plane in the AT area; (f) intercalation of high-strain “mylonites” and low-strain layers highlighting the foliation in the marbles; coin (diameter 3 cm) for scale. (g) tension

gashes filled with fo-phl skarns in a brittle-ductile shear zone parallel to the axial planes (S_2) of marble folding in the CL area; compass for scale.

Foliation and banding are common and mostly marked by the preferred orientation of biotite and amphibole, as well as elongate feldspar and quartz grains (Nardi & Bitencourt, 1989). A N-S to NE-SW sub-horizontal mineral grain and aggregate lineation is dominant in the granitic body and the foliation close to the boundary of the batholith is mostly concordant to S_2 foliation of the surrounding metamorphic rocks (Nardi & Bitencourt, 1989).

4.2. DOLOMITIC MARBLES

Marbles in the studied area vary from massive white to banded light gray layers and show variable degrees of brittle and ductile deformation. Bedding (S_0) is generally difficult to decipher except where there is compositional change characterized by fine to medium grained metamorphic layers with talc and tremolite resulting in gray tones (Figure 2f). Foliation (S_1) is well developed and defined by elongated crystals of dolomite, dominantly parallel to bedding. Marbles with a platy aspect caused by the foliation and highlighted by an intercalation of low and high strain areas (Figure 2f) prevail in the eastern portion of the metamorphic complex (*i.e.* IN area; Figure 1b). Low strain areas are characterized by a grain size of a few millimeters (~2 mm) and granular aspect with nearly equidimensional grains. In contrast, the high strain "mylonites" exhibit a range of grain sizes including 1-2 mm-sized porphyroclasts within a fine grained matrix, elongate crystal shapes seen for larger grains and a closely spaced foliation (Figure 2f). Towards the contact with the granitic batholith (*i.e.* DB area; Figure 1b), ductile deformation prevailed, *i.e.* tight recumbent folds with axial planes parallel to S_1 foliation and layering, generally N-S oriented dipping at 20° to the east (Figure 2e).

4.3. M1 MAFIC AND FELSIC APOPHYSES

4.3.1. M1 mafic apophyses

M1 mafic apophyses form tabular bodies predominantly continuous for tens to hundreds of meters and concordant to the S_1 foliation. Their thicknesses vary from a few to ~50 cm. There are no clear cross-cutting relationships between the M1 mafic

and felsic apophyses; instead if they occur in the same outcrop they are seen to form one intrusive body with interlayered mafic and felsic bands with parallel boundaries (Figures 2b-d). This suggests that these composite mafic-felsic sills (Figure 6a) formed contemporaneously from M1 mafic and felsic magmas.. Yet, the M1 mafic apophyses do not cut the M2 felsic apophyses and the main granitic body in the center of the complex. The M1 mafic apophyses show nearly homogeneous field aspects. They have medium grain size, 40 to 80% of modal abundance of biotite and amphibole and a groundmass with felsic minerals. Disseminated pyrite and chalcopyrite were macroscopically identified in all M1 mafic apophyses in variable amounts; higher contents were observed up to tens of meters away from sub-vertical NW-SE trending faults that cut the M1 mafic apophyses in the northernmost quarry (CL area in Figure 1b). In a few places, molybdenite was found disseminated in the M1 mafic apophyses. M1 apophyses are often strongly foliated and marked by the preferred orientation of mafic minerals. The observed foliation is parallel to sill orientation and to metamorphic foliation (S_1) of the country rocks. These igneous bodies are folded together with the marble sequence (Figures 2b-c). M1 mafic apophysis-marble contacts vary from sharp to diffuse. Skarns occur at the boundary between igneous and carbonate lithologies (Figures 3c-d). Skarns at the lithological contacts are asymmetrical (Figure 3c). There is no preferred occurrence of skarns in the upper or lower borders of the apophyses. When present, they are variable in thickness (5 - 100 cm) and texture (Figures 3c-d). No spatial relation between the contact type and thickness of the skarn was identified. Nevertheless, skarns are more frequent at fold hinges or terminations of the M1 mafic apophyses (Figures 2d and 3c).

4.3.2. M1 felsic apophyses

Fine to medium grained felsic apophyses form sills that vary from 0.2 to 2 m in thickness and are gray to reddish brown in color in outcrop. They were emplaced similarly to the M1 mafic apophyses, parallel to S_1 foliation and are commonly folded with the same axial plane as the mafic apophyses and the marbles (Figures 2b,d). They are less common than M1 mafic apophyses and M2 felsic apophyses.

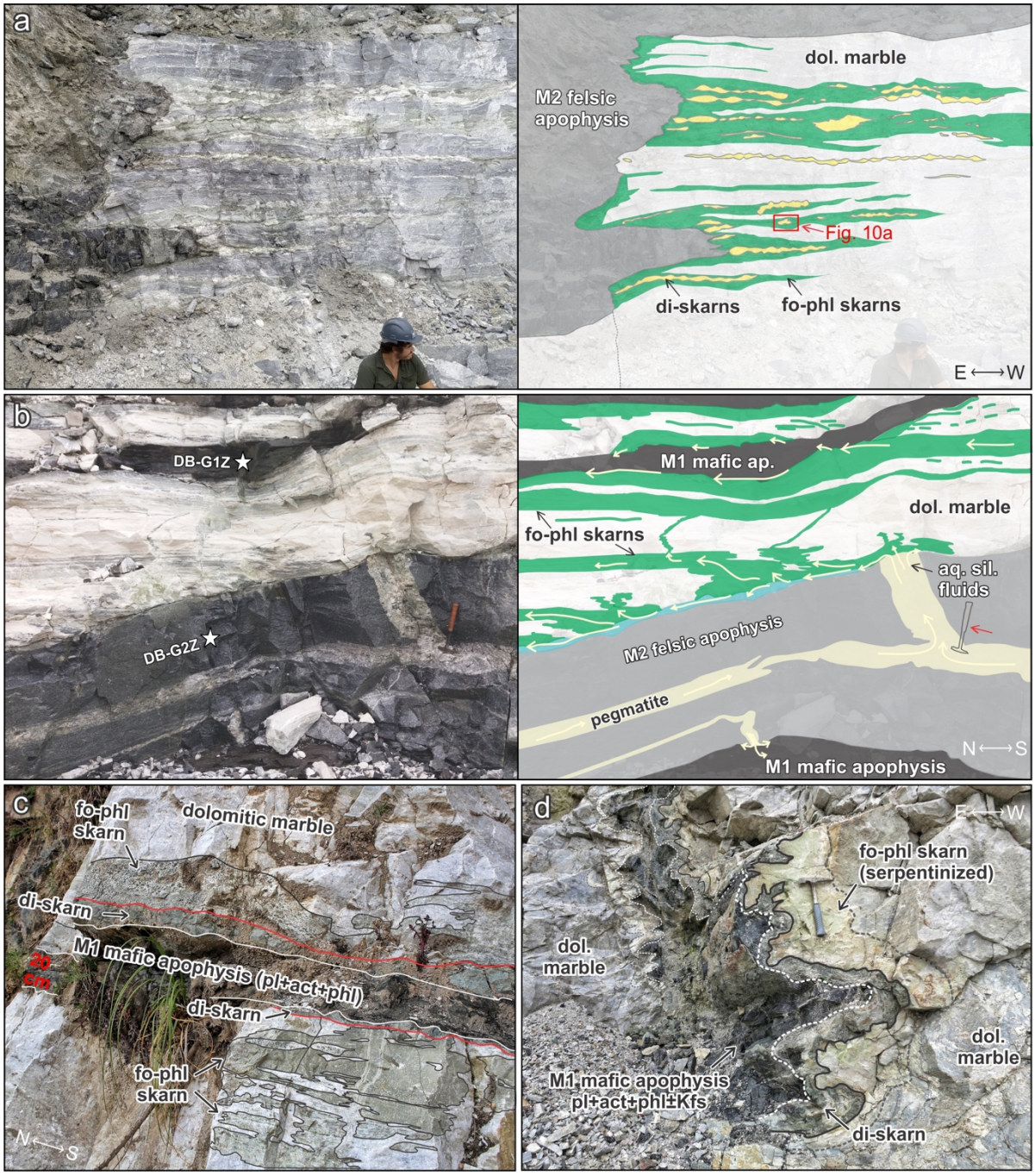

Figure 3: Outcrop scale relations of M1 and M2 apophyses and associated skarns. (a) di-skarns in pinch-and-swell structures bordered by fo-phl skarns formed perpendicular to irregular terminations of M2 felsic apophyses in the DB area. Location of the representative microstructures of the zoned skarns in Figure 10a marked by red rectangle. (b) Fo-phl skarns formed in lithological contacts and foliation parallel fractures of the marbles after infiltration of fluids released from pegmatitic portion of a M2 felsic apophysis. Yellow arrows indicate fluid pathways and possible flow direction. Stars in the left side image indicate the location of geochronological samples. Hammer (~40 cm) for scale. (c) Asymmetric skarn formation bordering mafic apophysis in the AT area. White lines indicate apophysis-skarn limit; red lines indicate the limit between di- and fo-phl skarns. Apophysis thickness of approximately 20 cm. (d) Folded mafic apophysis and associated zoned skarn formation at CL area; hammer (~35 cm) for scale.

4.3.3. M2 felsic apophyses

The M2 felsic apophyses are medium to thick (2 to >10 m) tabular intrusions mostly subconcordant or concordant with the axial plane S_2 foliation of the country rock and M1 mafic-felsic apophyses. Less commonly they cross-cut the foliation and occur as irregular vertical bodies (Figure 3a). They are coarse grained rocks with variable amounts of mafic minerals, *i.e.* biotite and amphibole. Foliation in these rocks is characterized by the preferred orientation of biotite, amphibole and K-feldspar phenocrysts (Figure 6b). Contacts with the marbles are generally sharp and unreacted, although forsterite-phlogopite skarns are developed in the dolomites at many of these contacts (Figures 3a-b). Similar to the M1 apophyses, when skarns are present, the distribution is asymmetric surrounding the M2 apophyses and the metasomatic rocks are most commonly restricted to one side of the intrusion. Pegmatites occur as small portions within sills (Figure 3b) or as irregular bodies predominantly cutting M1 mafic and felsic apophyses. Euhedral coarse garnet, titanite and biotite and disseminated pyrite and chalcopyrite are common in the pegmatitic bodies.

4.4. SKARNS

Skarns are divided into diopside and forsterite-phlogopite skarns. Diopside skarns consist of diopside with variable amounts of sulphides and tremolite + calcite whereas forsterite-phlogopite skarns consist of two zones corresponding to the silicate present, *i.e.* forsterite and phlogopite zones. The phlogopite zone, however, is difficult to recognize in the field due to its macroscopic similarity to the dolomitic marbles. The skarns are frequently associated with each other resulting in zoned skarns where the diopside zone typically occurs in the center, bordered or partly replaced by the forsterite and phlogopite zones (Figures 3c-d and 4b-c). These zones also occur separately, forming pinch-and-swell structures of diopside skarns (Figure 4a) or arrays and lenses of forsterite-phlogopite skarns (Figures 3b and 4a).

4.4.1. Diopside skarns

The diopside skarns consist of white to green aggregates of diopside (± calcite ± tremolite ± sulphides) forming irregular boudin/pinch-and-swell structures (Figures 4a-c) or bordering the M1 mafic apophyses (Figures 3c-d). The first are more common

and widespread. The diopside-skarn occur mostly parallel to the metamorphic foliation (S_1), are rarely folded with the marble layers and often replace marble mylonitic layers (Figure 4a). The thickness of diopside skarns varies from a few centimeters and rarely reaching 50 cm, with the majority ranging from 3 to 15 cm. They are commonly bordered by forsterite-phlogopite skarns (Figure 3a and 4b-c). Millimeter sized molybdenite aggregates and disseminated pyrite and pyrrhotite are common in the cores of diopside skarns.

Diopside skarns can be found bordering the M1 mafic apophyses with different thicknesses on each border of the apophysis (Figures 3c-d) and are often present at one border of the sill only. When bordering these intrusions, the coarse grained diopsides are partially or fully replaced by medium to fine grained tremolite. The thickness of these reaction zones vary from millimeters to a few centimeters and rarely exceeds 10 cm. Even though many M1 apophyses-marble contacts show no reaction zones, they are always found around the fold hinges (Figures 2b and 3c) and often found at terminations of M1 mafic apophyses (Figure 2d).

4.4.2. Forsterite-phlogopite skarns

The forsterite-phlogopite skarns comprise the most common and widespread skarn type that can border diopside skarns (Figures 3a,c,d and 4b,c), M1 and M2 apophyses (Figure 3b) or occur as isolated lenses (Figures 3b-c and 4a). This skarn type comprises a forsterite + calcite zone (forsterite zone) bordered by phlogopite + dolomite + calcite zone (phlogopite zone). The forsterite zone consists of μm to mm rounded fosterite clusters in a calcite matrix forming planar arrays. Coarser grained forsterite clusters are mostly located in low-strain zones whereas thin arrays with micrometric forsterite trails are located in higher strain zones (Figure 4c). Macroscopic black rounded grains are preserved olivines whereas green to light green rounded grains are olivines partially or fully replaced by serpentine. Most locations have portions of partially preserved to fully replaced forsterite. However, serpentinization is more intense near brittle structures and mainly fault zones. Bordering the forsterite zone, the phlogopite zone is composed of fine grained light brown to colorless phlogopite in a white dolomite + calcite matrix. This zone occurs between the forsterite zone and the dolomitic marble. Its thickness varies roughly proportionally to the width of the respective forsterite zone.

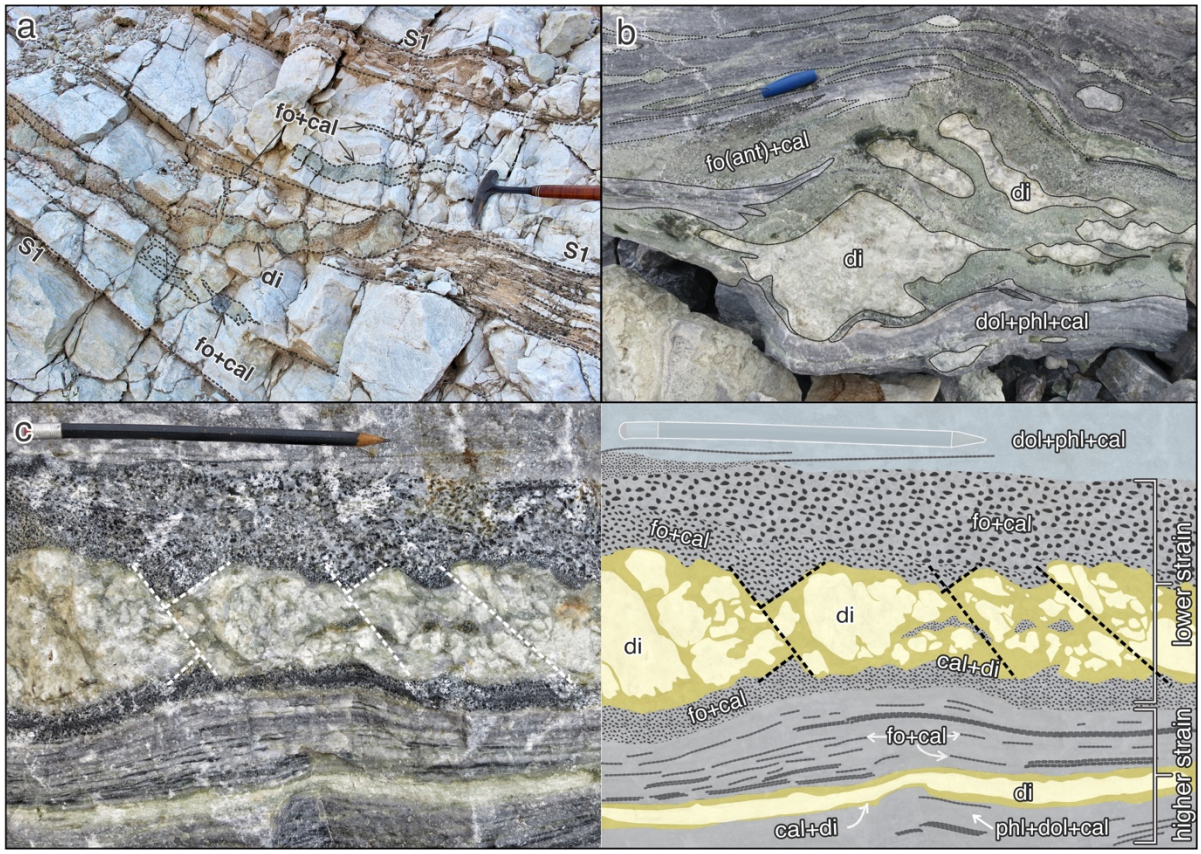

Figure 4: Field aspects of skarns. (a) Lenticular di- and fo-phl- skarns parallel to S_1 foliation of the marbles; diopside pinch-and-swell in high strain area; Brown colors indicate "crushed" unconsolidated fine grained carbonates; hammer (40 cm) for scale. (b) Zoned composite di- + fo-phl skarns with broken diopside boudin/pinch-and-swell structure bordered by forsterite and phlogopite zones; blue pen lid (4 cm) for scale. (c) Contrasting shapes and grain sizes in zoned skarns caused by strain contrast; broken diopside in pinch-and-swell structure bordered by coarser forsterite (lower strain areas) versus thin elongate diopside band bordered by fine grained forsterites in DB area. Note fo-cal skarn within diopside fragments and dashed lines indicating local fractures in the pinch-and-swell structure.

4.4.3. Hydrothermal veins and breccias

Within the area distinct fracture filling veins, stockworks and breccias are present. They are mostly found in the north of the marble quarry district (CL area; Figure 1b) where they occur a few to tens of meters away from subvertical NW trending fault zones and areas of brittle deformation, mainly crosscutting the metamorphic foliation and skarns (Figure 5a). They are not folded and commonly form stockworks (Figures 5b-c). They consist of centimeter sized veins with coarse euhedral calcite crystals and massive chalcopyrite and pyrite aggregates cemented by chlorite and calcite (Figures 5b-c). Locally, veins can reach more than 30 cm of thickness and coarser calcite crystals exceed 5 cm. Symmetrical rims around the veins are characterized by high abundance

of serpentine within a few centimeters into the host marble (Figure 5a-d). Breccias are composed of marble fragments and coarse subhedral calcites cemented by massive chlorite, pyrite and chalcopyrite (Figure 5d).

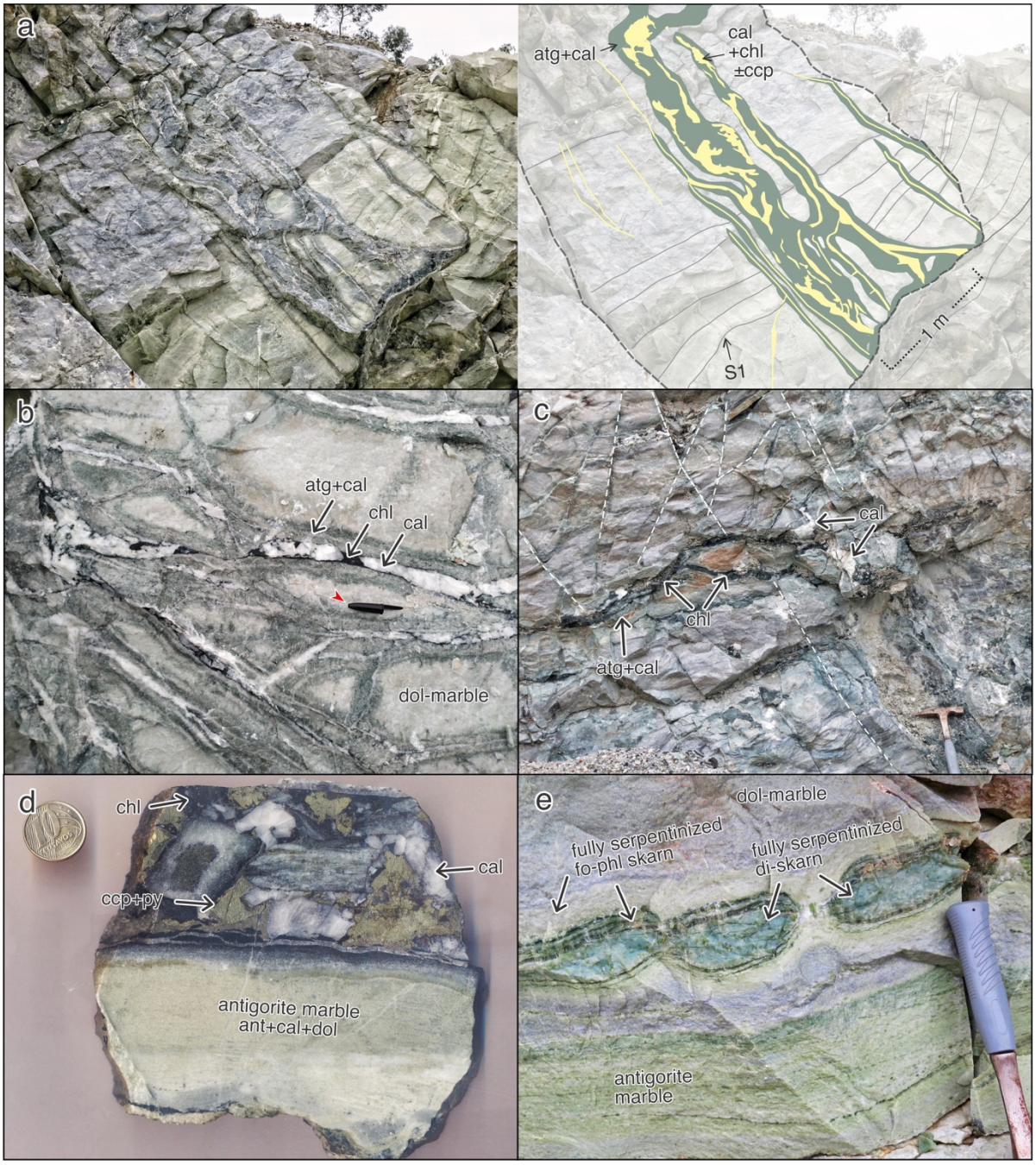

Figure 5: Macroscopic features of calcite-chlorite-sulphide veins and fully serpentinized skarns. (a) Calcite-chlorite-sulphide veins bordered by antigorite and calcite perpendicular to marble S_1 foliation; “green antigorite marbles” with primary antigorite in a calcite-dolomite matrix located near NW-SE subvertical fault zone in the CL area. (b-c) Calcite-chlorite stockworks bordered by antigorite + calcite reaction fronts towards the dolomitic marbles; 6 cm pen lid for scale. (d) Cal-chl-sulphide breccia with marble and coarse calcite fragments cemented by chlorite and

sulphides; CL area; coin for scale. (e) fully serpentinized diopside skarns and fo-phl skarns and antigorite-marbles.

5. PETROLOGY AND MICROSTRUCTURES

In this section, we describe the petrographic characteristics of igneous apophyses and skarns. Petrographic and geochemical characterization of the main facies of the granitic batholith can be found in previous studies by Nardi & Bitencourt (1989) and Sartori & Kawashita (1985). Petrography and geochemistry of the host dolomitic marbles is presented and discussed in Goulart *et al*. (2013).

5.1. M1 MAFIC AND FELSIC APOPHYSES

Even though the mafic rocks show similar aspects in the field, mineral assemblages and microstructures reveal heterogeneity among M1 mafic apophyses. Typical mineral assemblages consist of amphibole + biotite + plagioclase ± K-feldspar ± quartz (Figures 7a-d and 8d-f). Amphibole + biotite + plagioclase are present in all samples in variable proportions (Figures 7a-d) whereas K-feldspar and quartz occur in some of the samples (Figures 7a,c and 8d). Amphiboles vary from subhedral short hornblende grains (Figures 7c and 8d) to subhedral short to elongate actinolite (Figures 7c and 8e-f) and less commonly subhedral to euhedral tremolite. In general, biotite occurs as discontinuous lenticular and often anastomosing aggregates (Figures 7a-d and 8e-f). Biotite also occurs as inclusions in coarse grained and equidimensional hornblende crystals that resembles phenocrysts. The foliation in these rocks is well defined by the preferred orientation of the actinolite and biotite (Figures 7a-d). Some samples also show a subtle crenulation highlighted by shear bands defined by the biotite (Figure 7b). Local chloritization of biotite occurs near fractures or micro shear zones (Figure 7a). Titanite and apatite are common accessories. Titanite occur mostly within biotite aggregates and less commonly included in hornblende (Figures 8a-d) whereas apatite is frequently found in the grain boundaries of actinolite and generally with the same preferred orientation as that of the amphiboles (Figures 8b-c).

The M1 felsic apophyses comprise equigranular fine to medium grained (0.05 – 0.2 mm) rocks composed of K-feldspar, quartz, plagioclase and biotite (Figures 9a-b). Disseminated apatite and pyrite are common (Figure 9b). Biotite occurs along grain

boundaries and its preferred orientation characterizes a subtle foliation in the M1 felsic apophyses (Figures 9a-b).

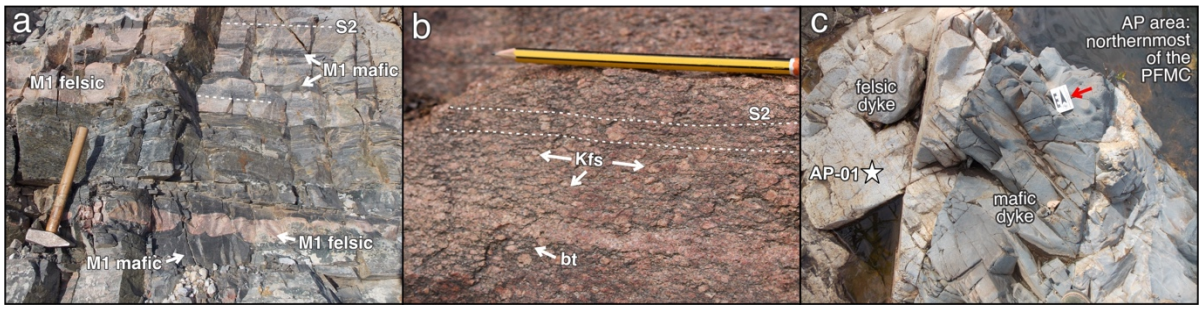

Figure 6: Macroscopic features of M1 and M2 apophyses. (a) Composite M1 mafic-felsic apophysis with pinch-and-swell felsic enclaves in M1 mafic apophysis (AT area); hammer (~45 cm) for scale; (b) Detail of the M2 felsic rock with elongate K-feldspar grains and thin biotite layers defining the foliation indicated by white dashed lines. (c) Composite mafic-felsic dykes (M1) from the northernmost portion of the metamorphic complex (AP area). Star symbol represent the location of the geochronological sample AP-01; 5 cm scale.

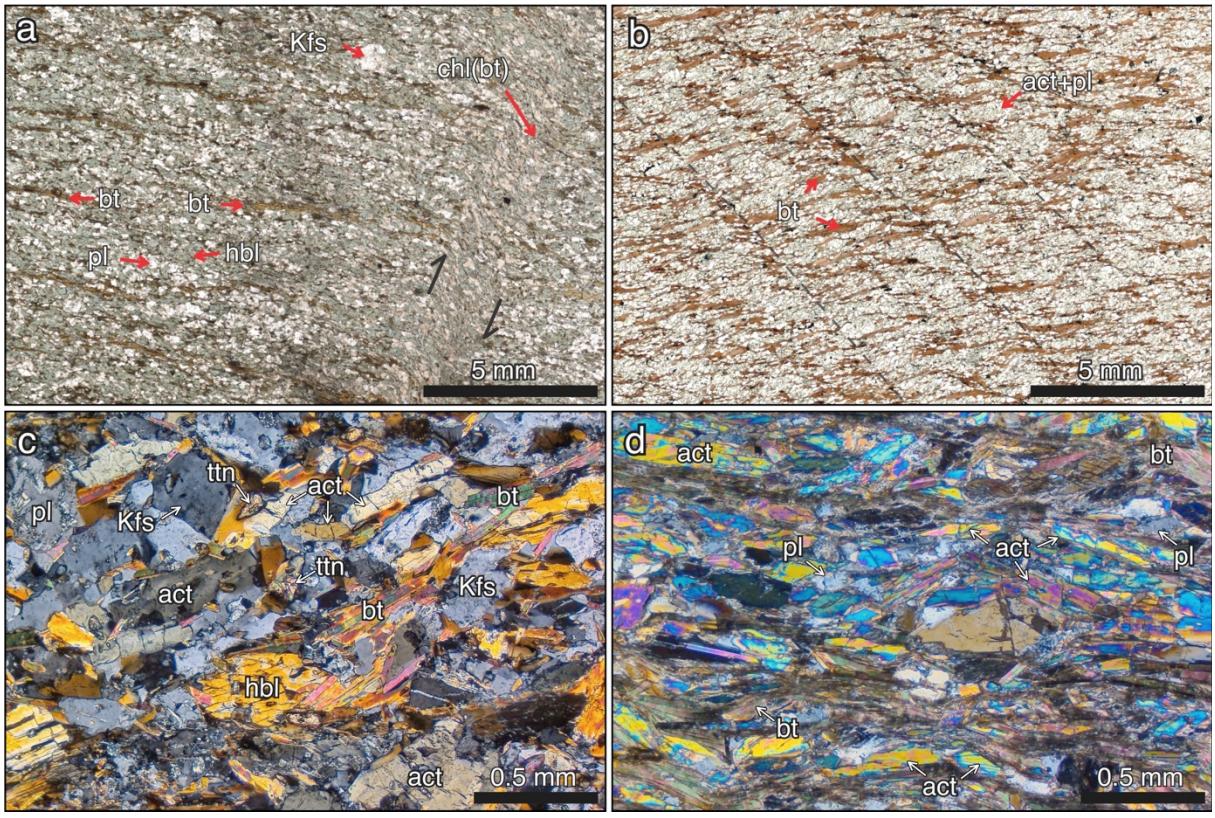

Figure 7: Microstructures of M1 mafic apophyses: (a) Wide photomicrograph of a bt-pl-hbl schist showing spaced foliation with intercalation of plagioclase and hornblende aggregates separated by discontinuous lenticular aggregates of biotite; chloritized biotite in a microshear zone in the right side of the image; scale bar: 5 mm; PPL. AT area (b) Wide photomicrograph of pl-act-bt schist showing sigmoidal biotites intercalated with aggregates of plagioclase and actinolite marking S_2 foliation of the mafic apophysis, subtle crenulation (black dashed lines); scale bar: 5 mm; PPL; CL area. (c) Photomicrograph of a pl-bt-kfs-amp schist showing preferred orientation of biotites and elongated actinolites marking the S_2 foliation; short prisms

of hornblende; subhedral titanites in grain boundaries of bt and act or Kfs; AT area; scale bar: 0.5 mm; XPL. (d) Photomicrograph of a pl-bt-act schist showing spaced foliation marked by intercalation of anastomosing biotites and elongate actinolites aggregates with small (<0.2 mm) grains of plagioclase in between the amphiboles. AT area; scale bar: 0.5 mm; XPL.

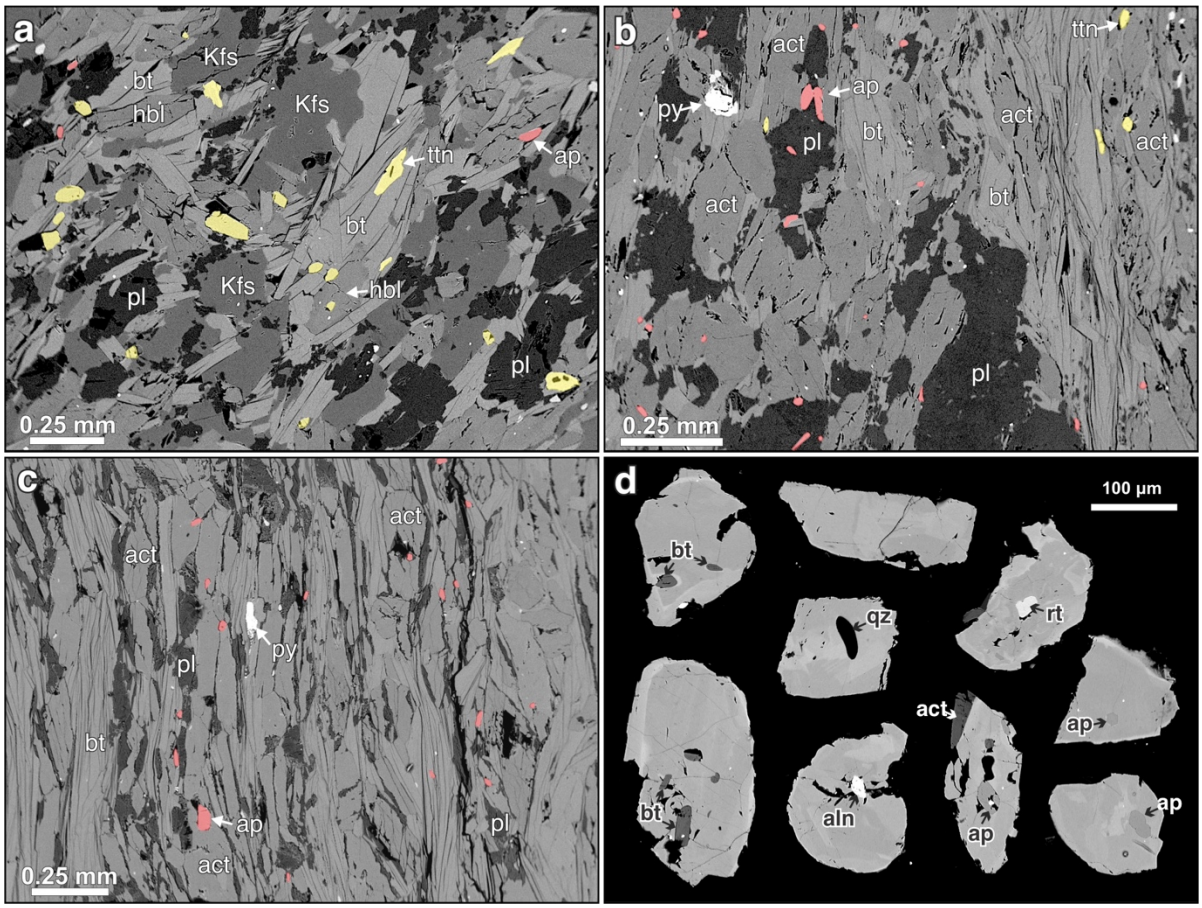

Figure 8: Backscattered electron (BSE) images of representative microstructures and highlighted accessory phases of M1 mafic apophyses; in yellow: titanites; in red: apatites. (a) Microstructures of pl-bt-kfs-hbl-act showing subhedral titanite included in biotite aggregates, small rounded grains of titanite included in hornblende and rounded and anhedral titanite in the grain boundaries of biotite and K-feldspar or plagioclase or amphibole; sample AT-Z-01; AT area; scale bar: 0.25 mm. (b-c) Microstructures of pl-bt-act schists showing apatite included in actinolites, next to plagioclases and included in plagioclase; samples AT-Z-02 and AT-Z-03, respectively; AT area; scale bar: 0.25 mm. (d) Internal structures and inclusions of titanite grains; sample AT-Z-01; AT area; scale bar: 100 µm.

5.2. M2 FELSIC APOPHYSES

The M2 felsic apophyses comprise mostly granodiorites, monzogranites and syenogranites. Biotite and hornblende are the main mafic minerals and biotite-hornblende granodiorites represent the most common type of M2 felsic apophyses (Figures 9c-d). The grain size and the amount and proportion of biotite and amphibole

is variable from one sill to another, but are nearly homogeneous within the same sill. K-feldspar phenocrysts are common and often occur elongate or with lobate boundaries (Figure 9d). Quartz grains generally shows undulose extinction and occur as recrystallized, c. 0.1 - 0.5 mm-sized grains with sutured boundaries (Figure 9c). Allanite and titanite occur as accessory phases, as inclusions in K-feldspar phenocrysts or in contact with biotite and calcic amphiboles. Prismatic elongated zircons to small rounded zircons are present. Biotite chloritization is common and mainly observed in the samples with a brownish-red color in the field. This alteration is more frequently found near fault zones, especially in the center and northern quarries of the marble district (CL, FD and AT areas; Figure 1b). Chloritites formed after intense hydrothermal alteration at c. 300°C of M2 felsic apophyses is found in the northernmost quarry (CL area) (Remus, Dani, Gazzoni, Hoerlle & Reis, 2011; Reis, Remus, Dani, & Anzolin, 2017).

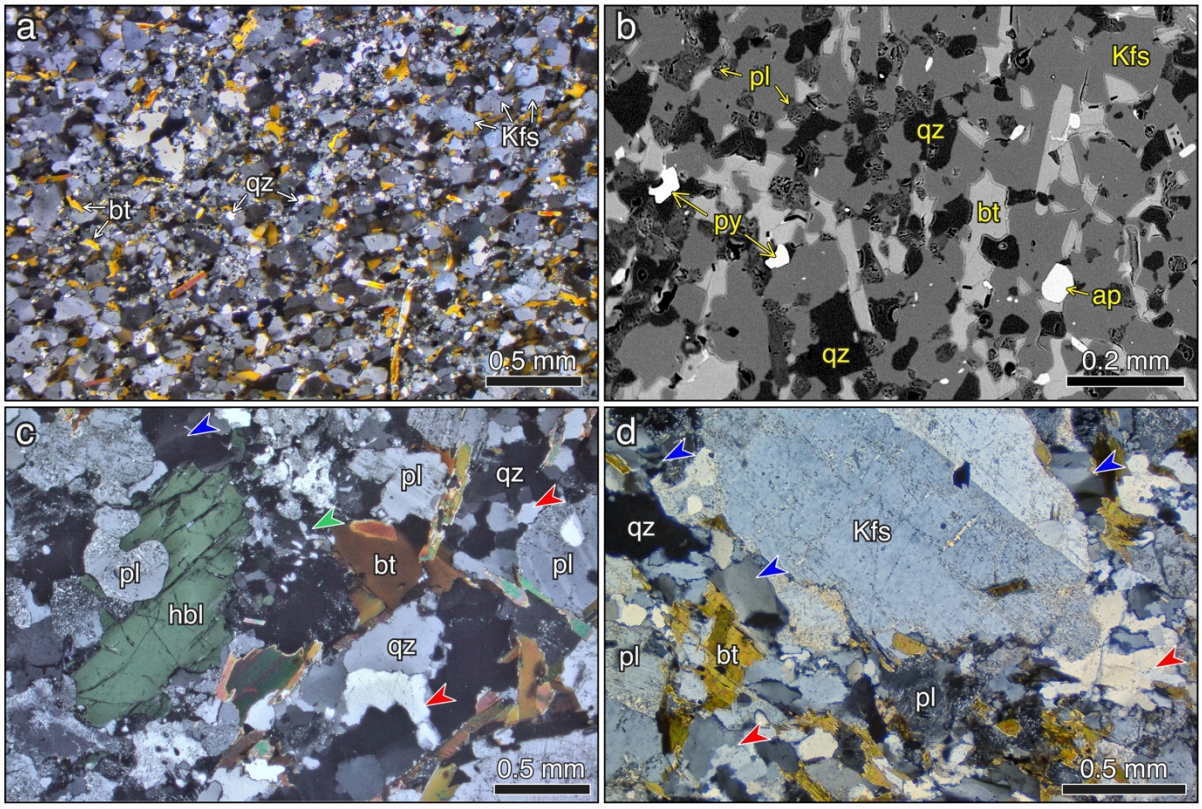

Figure 9: Microstructures of M1 and M2 felsic apophyses. (a) Photomicrograph of a M1 felsic apophysis showing a fine grained quartz-feldspatic matrix and abundant biotite. Scale bar: 0.5 mm. XPL. (b) BSE image of M1 felsic apophysis showing preferential orientation of biotites in a Kfs-qz-pl matrix. Scale bar: 0.2 mm. (c) Photomicrograph of a hbl-bt-granodiorite (M2) showing mirmekites (green arrow); quartz sutured grain boundaries (red arrows) and undulose extinction (blue arrows); cross-polarized light (XPL); scale bar: 0.5 mm; sample DB-G2Z from DB area shown in Figure 3b. (d) Photomicrograph of a bt-monzogranite (M2) showing K-feldspar

porphyrocrysts with lobate boundaries, quartz with undolose extinction (blue arrows) and sutured boundaries (red arrows) from AT area. Scale bar: 0.5 mm. XPL.

5.3. SKARNS

5.3.1. Diopside skarns

The diopside skarns have coarse diopside grains or aggregates that vary from millimeter to centimeter sized crystals. They host Fe-Cu-Mo sulphides, micrometer sized calcite and tremolite and rarely phlogopite inclusions. Where fracturing is more intense, diopside tend to be divided into sub-grains and partially replaced by millimeter sized tremolite and calcite, which also crystallize along the grain boundaries and fractures. Their boundaries are sharp when in contact with coarse grained forsterite-zone (Figures 10a-b) or irregular/corroded when bordered by fine grained trails of forsterite (Figures 10a,c).

5.3.2. Forsterite-phlogopite skarns

The forsterite-phlogopite skarns are divided into forsterite and phlogopite zones. The forsterite zone consists of round olivines in an irregularly shaped calcite matrix (Figure 10a). Anhedral pyrite often occurs disseminated in the calcite matrix of the forsterite zone. Forsterite is partially to fully replaced by antigorite. The degree of serpentinization is generally homogeneous within the same sample but variable in different samples (see Section 4.5.2). The calcite matrix shows variable amounts of dolomite exsolution. Commonly, small lamellae of phlogopite occurs within the forsterite zone. Rarely, the forsterite zone contains green spinel and chlorite.

The transition from the forsterite zone to the phlogopite zone is irregular and the main changes are the variation from a calcite to a mainly dolomitic matrix, the absence of forsterite and the increase in the abundance and grain size of phlogopite (Figure 10a). The carbonates in the phlogopite zone form a granoblastic texture with elongate subhedral to euhedral dolomites whereas irregular-shaped calcite occurs along dolomite or phlogopite grain boundaries (Figure 10d). The dolomites and phlogopites are generally oriented parallel with the same orientation of the boundaries of the diopside skarns. In the serpentinized samples phlogopite can be partially to fully replaced by antigorite.

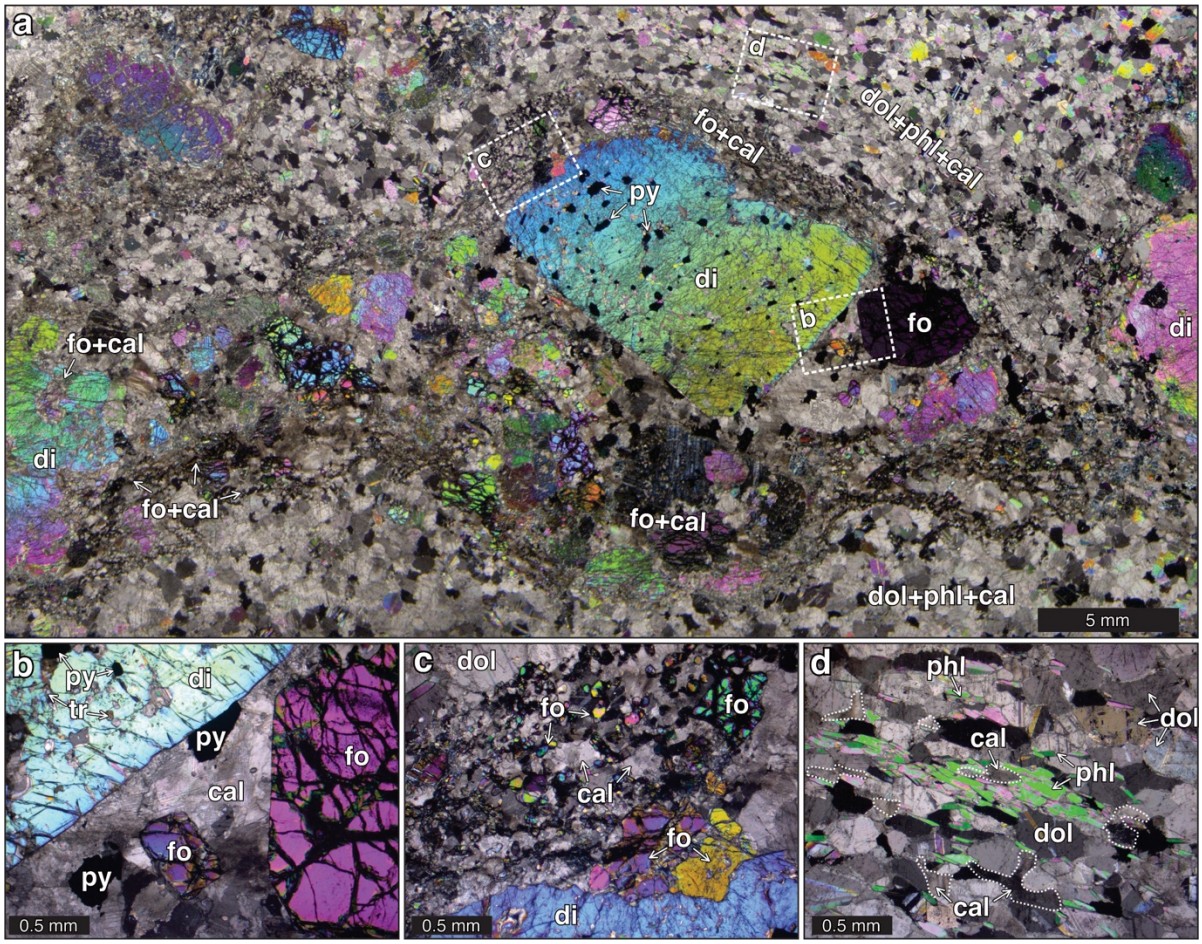

Figure 10: Microstructures of a zoned di- + fo-phl skarn, similar to the one indicated in Figure 3a in a smaller scale. (a) general view of the skarn zones in a thin section scale, dashed white lines indicate location of Figs. 10b-d; scale bar: 5 mm, XPL; (b) di and coarse euhedral fo (~4 mm) in equilibrium with a cal matrix in a strain shadow zone; rounded tr inclusions in di; subhedral py in the cal matrix; scale bar: 0.5 mm. (c) fo- zone with fine-grained rounded fo arrays (<0.2 mm) in cal matrix and coarser fo (~0.5 mm) partially replacing the di; scale bar: 0.5 mm, XPL; (d) phl- zone with oriented phl aggregates, recrystallized dol and anhedral interstitial cal. XPL.

6. LA-ICP-MS U-PB GEOCHRONOLOGY

6.1. ZIRCON U-PB AGES

6.1.1. M1 mafic apophyses

Zircons from a foliated fine grained mafic apophysis (DB area; DB-G1Z sample; location shown in Figure 3b) have an average length of c. 120 μm and a maximum of 170 μm. The aspect ratio varies from 2:1 to 3:1 and the zircon crystals are dominantly sub-rounded (Figure 11e). CL response varies from very bright to dark and grains exhibit zoning patterns from unzoned to irregular sector zoned. Twenty discordant

grains combined with five concordant zircons formed a Discordia line that yielded an upper intercept $^{207}Pb/^{206}Pb$ age of 1787±14 Ma (MSWD = 2.4; Figure 11b; Table S1). Three discordant analyses combined with three concordant grains formed another Discordia line that resulted in an upper intercept $^{207}Pb/^{206}Pb$ age of 2190±20 Ma (MSWD = 0.64; Figure 11b; Table S1). Both Paleoproterozoic ages are interpreted as inherited ages. The inherited ages are similar to those of the CSGC described in previous studies (Leite *et al*., 1998; Remus *et al*., 2000).

6.1.2. M2 felsic apophysis

A total of 28 zircons were separated and analyzed from a gray medium grained biotite-hornblende granodiorite (DB area; DB-G2Z sample; location shown Figure 3b). The grains are mostly prismatic and have an average length of c. 215 μm and aspect ratio of 4:1 reaching up to a maximum of 340 μm and 6:1, respectively (igneous zircons of Figure 12d). Twenty-two analyses on prismatic zircon grains with concentric or patchy CL zoning including cores and rims (Figure 11d) yielded a concordia $^{207}Pb/^{238}U$ age of 578.0±4.7 Ma (MSWD = 4.5; N = 22; Figure 11a; Table S3) interpreted as the magmatic age of the sill. Two spots on prismatic grains with concentric zoning are highly discordant (10 and 62% conc.); and four smaller subrounded grains (inherited zircons of d) yield inherited concordant ages of 611±18; 1231±16, 1733±45 and 2045±25 Ma.

6.1.3. Composite mafic-felsic dyke in the northernmost portion of the PFMC

For comparison, 26 zircons were separated from the felsic portion of a composite mafic-felsic dyke in a dyke swarm metamorphosed at low grade in the outermost portion of the PFMC (AP-01; Figure 1b and 6c). The felsic and mafic dykes are mutually crosscutting and were previously petrographically and geochemically described by Bicalho *et al*. (2019) (felsic dyke equivalent to the sample V11). These dykes show subgreenschist metamorphism and brittle deformation. Zircons from this sample vary from ~110 to ~230 μm and have aspect ratios from 1.5:1 to 3.5:1 (Figure 11f). Four spot analysis (spot number 3, 4, 7 and 22) yielded a concordia $^{238}U/^{206}Pb$ age of 578.1±3.5 Ma (MSWD = 0.021; N = 4; Figure 11c; Table S2) interpreted as the magmatic age of the sill, despite the few analyses. Thirteen grains (spots 2, 6, 8, 9, 11,

12, 14, 15, 18-21, 25) yielded a concordia $^{238}U/^{206}Pb$ age of 761.8±2.1 Ma (MSWD = 0.50; N = 13; Figure 11c; Table S2) interpreted as inherited from the host rocks. Three spots resulted in Paleoproterozoic ages (2.2 to 2.5 Ga) and 6 spots represent discordant grains (Table S2).

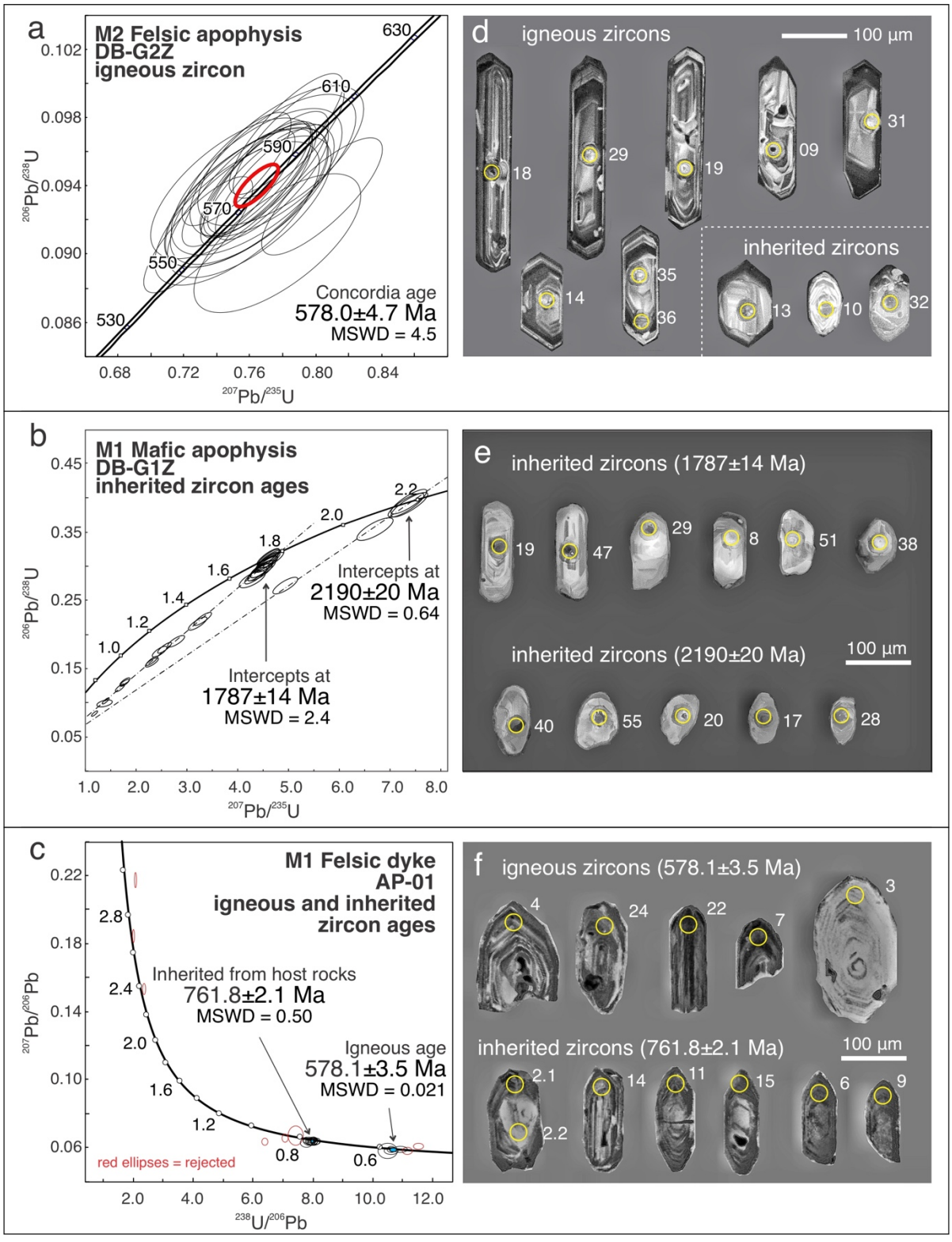

Figure 11: Concordia diagrams of felsic and mafic apophyses and respective CL images of representative zircon grains of each sample (a) M2 felsic apophysis magmatic age, hbl-bt granodiorite sample DB-G2Z, location in outcrop shown in Figure 3b. (b) M1 mafic apophysis inherited zircon ages, sample DB-G1Z, location in outcrop shown in Figure 3b; (c) Felsic dyke (M1) inherited and magmatic ages, sample AP-01 from the northermost portion of the metamorphic complex, location in outcrop shown in Figure 6c. (d) Magmatic and inherited zircon grains from M2 felsic apophysis, sample DB-G2Z. (e) Inherited zircon populations from M1 mafic apophysis, sample DB-G1Z. (f) Igneous and inherited zircon grains from M1 felsic dyke, sample AP-01.

6.2. APATITE AND TITANITE AGES

6.2.1. Mafic apophysis (M1)

Titanites were separated from a mafic apophysis sample (AT area; AT-Z-01 sample) in a quarry-scale fold hinge area. The rock is composed of actinolite (27%), biotite (23%), K-feldspar (24%) plagioclase (21%) and quartz (3%) with titanite, apatite, pyrite as common accessory phases and very fine grained zircon as traces. Titanite occurs included in biotite and amphiboles or along their grain boundaries (Figure 7c and 8a-b). Size of analyzed grains ranges from 100 to 200 μm. Biotite and apatite are commonly included in the titanite, which also host allanite, rutile and quartz inclusions (Figure 8d). BSE imaging shows simple or patchy zoning in the titanites. Twenty grains were analyzed aiming to cover different zones. A Tera-Wasserburg plot of titanite analytical results define a discordant array with a lower intercept on the concordia at 556.1±2.9 Ma (Pbc S/K = 0.869; MSWD = 1.2; N = 20; Figure 12a; Table S4).

Apatite samples were separated from two M1 mafic apophyses (AT area; AT-Z-02; AT-Z-03) that are mainly composed of phlogopite (40%), actinolite (40%), plagioclase (20%) and apatite as main accessory phase. The analyzed apatites are mainly prismatic, colorless, and have an average size of c. 150 μm reaching up to a maximum of 270 μm. They occur mainly in the grain boundaries with the same preferred orientation of the actinolite and phlogopite, but also included in the amphibole and plagioclase (Figures 8e-f). BSE and CL imaging revealed the absence of zoning and inclusions in the apatite crystals. The Tera-Wasserburg plots of apatite analytical results define discordant arrays with lower intercepts on the concordia at 557.8±3.4 Ma (Pbc S/K = 0.873; MSWD = 0.97; N = 20; Figure 12b; Table S5) and 557.0±4.9 Ma (Pbc S/K = 0.873; MSWD = 0.51; N = 18; Figure 12c; Table S6).

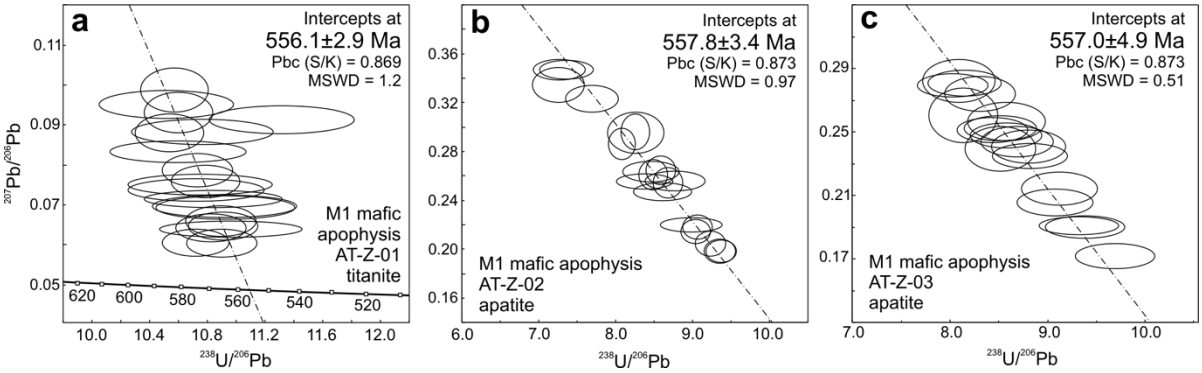

Figure 12: Tera-Wasserburg diagrams of (a) titanite and (b-c) apatite from M1 mafic apophyses.

7. DISCUSSION

7.1. IGNEOUS EMPLACEMENT SEQUENCE, GEOCHRONOLOGY AND RELATED TECTONICS

Crosscutting relationships and structural patterns of the igneous apophyses suggest that M1 mafic and felsic apophyses intruded the marbles and were subsequently deformed (Figures 2a-d). A different set of unfolded thicker felsic sills (> 2 m; M2) emplaced in the axial planes of M1 apophyses indicate that larger volumes of felsic magmatism succeeded the early intrusions. The orientation of the M2 apophyses and the preferred orientation of the minerals within these intrusions are parallel to the S_2 metamorphic foliation and the axial surfaces of the M1 folded intrusions. This indicates that M2 was synkinematic which is in agreement with Nardi & Bitencourt (1989) that describe an igneous foliation throughout the granitic batholith parallel to the S_2 foliation of the PFMC and suggests that most of the batholith was syntectonic. M1 mafic apophyses were not described in the inner portions of the granitic batholith which suggests that most of the body was assembled by the M2 felsic apophyses and subsequent intrusions and that M1 magmatism had restricted volume.

Field aspects and mineral assemblages of M1 mafic apophyses suggest that these rocks were metamorphosed after a basic protolith. These rocks are metabasites, but their composition and structural response are distinct from metabasalts. High amounts of biotite and amphibole (up to 80%), common co-existence of hydrous Mg-rich minerals with K-feldspar and quartz, highly incompetent structural behavior are atypical for metabasalts. Therefore, we consider two main alternatives for the M1 mafic

apophyses: metamorphism of (a) a lamprophyre protolith with limited and localized chemical change or (b) a basaltic protolith with significant metasomatic change. M1 mafic apophyses resemble lamprophyres in some aspects: emplacement as widespread thin and continuous sills; abundance of Mg-rich hydrous mineral assemblages in coexistence with plagioclase, K-felspar and quartz. In addition, the recent discovery of deformed tabular bodies of carbonatites (c. 603 Ma) in the PFMC located less than a kilometer from the CL area (Cerva-Alves *et al*., 2017) could be related to lamprophyre intrusions. However, the recognition and classification of metamorphic lamprophyres is problematic as many diagnostic features (*e.g.* mafic phenocrysts) are prone to destruction by metamorphism, deformation and metasomatism (Perring, Rock, Golding, & Roberts, 1989). Alternatively, if the M1 mafic apophyses were initially "typical" basic rocks (*i.e.* basalts) the actual mineral assemblages would require significant element exchange and hydration. Large amount of fluid is necessary to allow such changes and the closest source of fluids prior to the folding event are the cooling M1 felsic apophyses, which are thin and likely released limited amounts of fluids. Further studies including bulk-rock major and trace element, isotope and mineral geochemistry are needed to characterize and discuss in detail the protolith of the M1 mafic apophyses.

Composite mafic-felsic intrusive bodies suggest contemporaneous intrusion of the M1 felsic and mafic aphophyses (Figures 6a and 11a-e). A similar bimodal character with contemporaneous mafic and felsic volcanism at c. 600 to 580 Ma has been described in the region associated with an extensional regime in early stages of the development of the Camaquã Basin (Almeida, Chemale, & Machado, 2012; Almeida, Janikian, Fragoso-Cesar, & Fambrini, 2010; Chemale 2000; Janikian 2004; Janikian *et al*., 2012; Matté, Sommer, Lima, Philipp, & Basei, 2016; Oliveira, Chemale, Jelinek, Bicca, & Philipp, 2014; Wildner, Nardi, & Lima, 1999). We interpret the M1 mafic-felsic intrusions as correlated to this extensional magmatism. Bimodal magmatism typically occurs in extensional environments in various tectonic settings (*i.e.* Coulon, Maluski, Bollinger, & Wang, 1986; Duncan, Erlank, & Marsh, 1984; Frey, Gerlach, Hickey, Lopez-Escobar, & Munizaga-Villavicencio, 1984; Hochstaedter *et al*., 1990; Jolly, Lidiak & Dickin, 2008). We interpret the M1 intrusions in an overall extensional setting between c. 600 and 578 Ma and mafic apophyses limited to this time span. Attempts to obtain a magmatic age for the M1 mafic apophyses resulted in inherited ages only (sample DB-

G1Z; Figures 3c and 12b). However, we obtained an age of 578±3.5 Ma for a composite mafic-felsic dyke in a dyke swarm that intrudes the northernmost portion of the PFMC (AP-01; AP area; Figure 11c). These mafic-felsic dykes show evidence of limited brittle deformation and low grade metamorphism whilst the sills within the marbles exhibit evidence of ductile deformation and higher grade metamorphic effects. Such differences are explained by the depth of emplacement and distance to the granitic batholith that was subsequently emplaced. Therefore, we suggest that they are genetically and time-correlated with the M1 mafic-felsic sills. Nevertheless, the age of 578±4.7 Ma was obtained for a M2 felsic apophyses. If the composite dykes are in fact correlated to the M1 mafic-felsic apophyses, this age of c. 578 Ma marks the transition from the extensional related mafic-felsic magmatism (M1) to a compressional regime with felsic-dominated magmatism (M2). This shift is reflected in the skarn assemblage and texture modifications (Section 7.2).

The complexity of deciphering the magmatic source of the CSGC was highlighted in previous studies (Babinski *et al*., 1996; Nardi & Bitencourt 1989; Sartori & Kawashita, 1989; Remus *et al*., 2000). To the same end, the variable inherited zircon populations identified in the M2 felsic apophysis, M1 mafic apophysis, felsic dyke (AP-01) and in previous studies (Leite *et al*. 1998; Remus *et al*., 2000) equally point towards a heterogeneous magmatic source. Inherited zircon grains of c. 600 Ma were identified in the M2 felsic apophysis and in CSGC granodiorites from previous studies, which suggests that the M1 apophyses were part of the heterogeneous source of the M2 magmas.

The consistent ages obtained from titanite and apatite from three M1 mafic apophyses suggest that the U-Pb closure or resetting of these minerals occurred at c. 557 Ma. Titanite and apatite have different Pb closure temperatures typically 500-650°C (*e.g.* Cherniak, 1993) and 375-600°C (*e.g.* Cochrane *et al*., 2014; Schoene & Bowring, 2007) respectively. Since both minerals record the same age within the error, it is likely that the isotopic closure occurred below 500°C. Additionally, apatite is considered highly susceptible to metasomatic processes at variable pressures and temperatures (Harlov, 2015; Kirkland *et al*., 2018; Krenn & Finger, 2004; Spear & Pyle, 2002). Field relationships show that the M1 mafic apophyses crystallized before the folding event and the intrusion of M2 felsic apophyses. Therefore, the age recorded by titanite and apatite does not represent the age of the crystallization of the M1 mafic apophyses. If

we consider that M1 magmatism occurred from c. 600 up to 578 Ma and M2 at c. 578 Ma, another source of heat is needed at c. 557 Ma to reset the titanite and apatite. Two possible explanations are presented for the age recorded in titanite and apatite.

We interpret that previously dated intrusions of the CSGC (Leite *et al*., 1998; Remus *et al*., 2000) represent a different magmatic pulse at c. 557 Ma and heat from this episode reset the titanite and apatite in the M1 mafic apophyses. In this case, protracted magmatism was responsible for the assembly of the CSGC with a finite number of discrete pulses with cooling between pulses. Protracted assembly of plutons is recognized worldwide and commonly results in overprinted granites with heterogeneous textures and chemistry (*e.g.* He *et al*., 2018; Pivarunas & Meert, 2019; Tichomirowa *et al*., 2019). The last pulse that heated the wallrocks to sufficiently high temperature (<500°C) reset the titanite and apatites dates in the M1 mafic apophyses at c. 557 Ma.

Alternatively, the M2 apophysis and previously dated intrusions of Leite *et al*. (1998) and Remus *et al*. (2000) represent ages of the incremental intrusion of felsic magmas from c. 578 to 562 Ma resulting in the assembly of the CSGC. The heat from continuous intrusions maintains elevated temperatures (>500°) in the system, results in metamorphism of the M1 mafic apophyses and opens the isotopic system for titanite and apatite. The age of 557 Ma is recorded in apatite and titanite when magmatism ceased and temperature dropped below c. 500°C, defining the late magmatic stage of the system. However, if this alternative hypothesis is correct, temperatures within the batholith and inner aureole were maintained continuously at >500°C for c. 20 My. This implies that the thermal aureole surrounding the batholith would be very wide. The discussion of the width of the thermal aureole is out of the scope of this paper and future studies of the aureole may provide useful insights into the hypothesis of a continuously assembled batholith over 20 My. Nevertheless, either alternatives suggests that the CSGC was assembled from several intrusions from c. 578 to 557 Ma and that apatite and titanite record the age of late magmatism in the area (Figure 14).

7.2. MULTISTAGE FLUID INFLUX AND ASSOCIATED METASOMATISM REVEALS DETAILS OF INTRUSION HISTORY OF THE SYNTECTONIC CAÇAPAVA DO SUL GRANITIC COMPLEX

The development of three metasomatic stages can be directly to the crystallization history of the CSGC including the (i) early M1 mafic-felsic sheeted intrusions (ii) emplacement of M2 felsic sills and (iii) late voluminous felsic intrusions, cooling and uplift of the granitic complex.

7.2.1. Stage 1: diopside skarn formation associated with M1 mafic-felsic sheeted intrusions

The occurrence of diopside skarns, sometimes bordered and partially replaced by forsterite-phlogopite skarns suggests that the formation of diopside represents the first metasomatic interaction between the M1 apophyses and the dolomites. Fluid flow resulted in arrays of diopside skarns (Figure 14a) using preexisting weak surfaces in the marbles, mainly parallel to the metamorphic foliation or along the interface between a cooled sill and the marble. Based on the minor occurrence of silicate phases in the unreacted dolomite parts, we propose an igneous origin for the silica, in opposition to detrital silica (quartz) in the marbles, in agreement with the common presence of molybdenite aggregates and disseminated pyrite and pyrrhotite included in the diopsides (Figure 10a). The presence of sulphides indicates that other dissolved metals were in the magmatic fluid other than silica. Additionally, the diopside-skarns are spatially associated to the M1 apophyses and commonly found within a few meters of the intrusions. Tremolite is only found as minor phase along fracture diopside and texturally interpreted to be a product of retrogression. Hence, we interpret the prograde formation of diopside to proceeded via a reaction that is not involving tremolite. While we note that there are only weak pressure constraints available, a pressure of 0.45 GPa has been suggested based on the presence of igneous muscovite in the felsic apophyses by Nardi & Bitencourt (1989) for the emplacement of the CSGC. Assuming this pressure, diopside can be formed at via the reaction of the dolomite and silica according to the reaction:

$$2SiO_{2\,(aq)} + Dol = Di + 2CO_2 \quad (R1)$$

Furthermore, the formation of diopside from dolomite and silica depends on T, XCO_2 and $aSiO_2$ conditions. This reaction occurs at temperatures above 590°C, high Si-activities (>0.9) and high values for $X(CO_2) > 0.8$ (Figure 13a-c; arrows 1, 3 and 4) or at low values for $X(CO_2) < 0.2$ and low Si-activities (0.2-0.5) at c. 600°C (Figure 13c; arrow 6), for example.

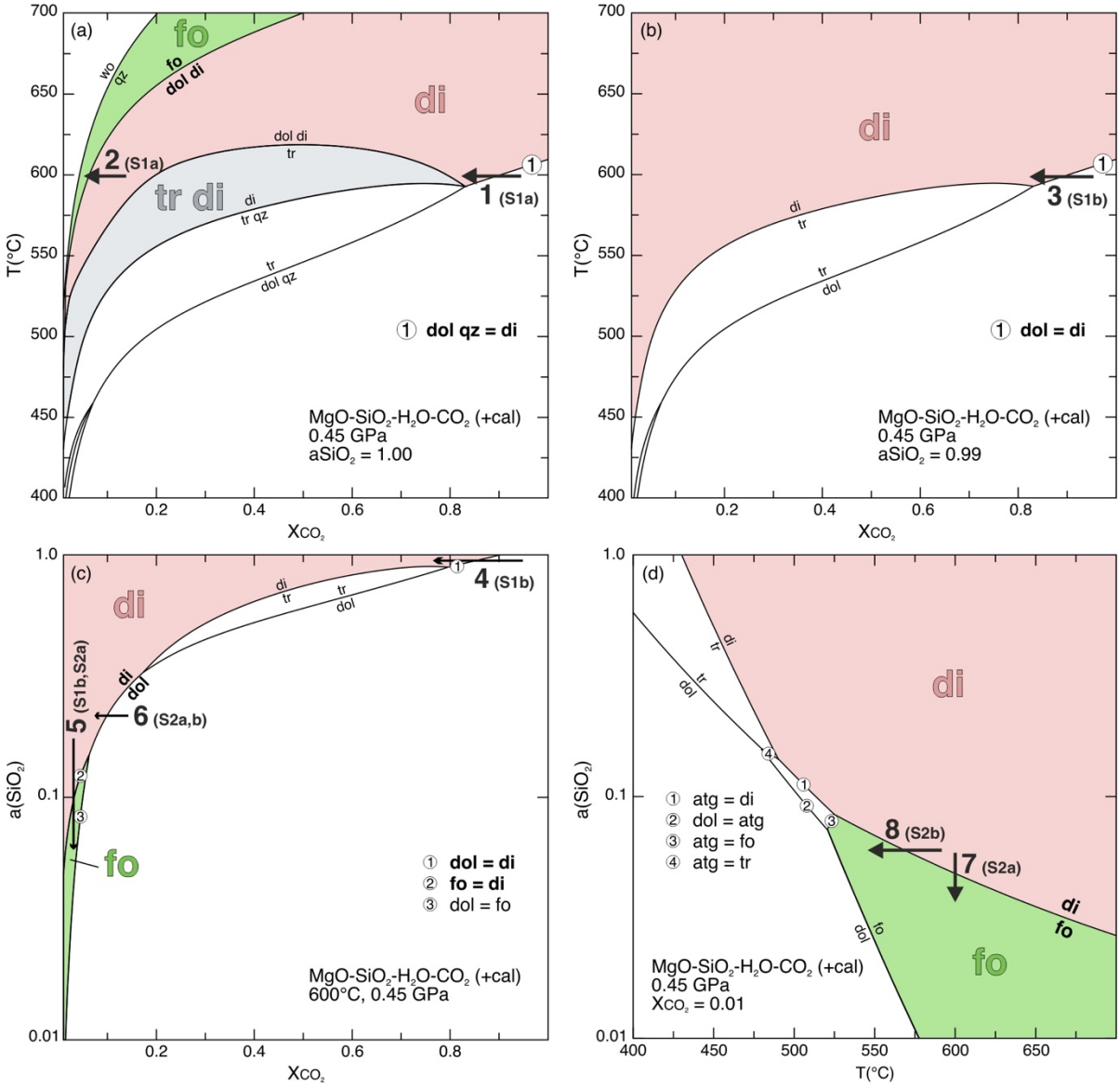

Figure 13: Calculated Schreinemarkers diagrams showing the effect of temperature, $X(CO_2)$ and SiO_2 activity on relevant diopside and forsterite forming reactions and stability fields and possible paths for the different interpretations described in the text. Arrows 1 to 5 represent the changes in effective fluid flux interpretation where 1 and 2 refer to variable XCO_2 at constant high $aSiO_2$ (S1a) and arrows 3 to 5 refer to the variable XCO_2 and $aSiO_2$ (S1b). Arrows 5 to 8 indicate possible paths (not in this order) for constant flux at low XCO_2 and variable $aSiO_2$ and/or temperatures.

The timespan between the formation of the diopside skarn and the subsequent forsterite-phlogopite skarn is unknown due to lack of geochronological data that can be directly related to diopside formation. However, diopside-skarns are deformed and occur in boudin and pinch-and-swell structures which suggests that they crystallized prior to a compressional event whereas the following forsterite-phlogopite skarns formed synkinematically (see Section 7.2.2). Therefore, we interpret that the diopside skarns are related to fluids released from cooling M1 mafic-felsic intrusions. The age

of c. 578±3.5 Ma obtained for a composite mafic-felsic dyke swarm in AP area and previous data for mafic-felsic intrusions in the region from c. 600 to 578 Ma (see Section 7.1) represent the approximate age interval for the M1 mafic-felsic apophyses in the marbles. Additional geochronological studies are required to detail the time span of the M1 magmatism and are beyond the scope of this paper. At present, we interpret the transition from M1 to M2 at c. 578 Ma, based on a concordant zircon U-Pb age of 578±4.7 Ma from a M2 felsic apophysis. The magmatic and deformation regime transition is reflected in the modification of the skarn assemblages from diopside-skarn to forsterite-phlogopite skarn. We note, however, that based on our observations we cannot unequivocally conclude whether the transition from M1 to M2 was related to continuous changes in fluid composition and/or flux or the consequence of episodic infiltration events (see Section 7.3 and Figure 15).

7.2.2. Stage 2: forsterite-phlogopite skarns associated with felsic intrusions at mid crustal level during syntectonic transpression

The subsequent formation of the forsterite-phlogopite skarn was consequence of changes in either fluid composition, fluid flux or temperature accompanying the cooling of the M2 felsic apophyses. The formation of metasomatic reaction veins during fluid infiltration is a well-established concept (*e.g.* Bégué, Baumgartner, Bouvier, & Robyr, 2019; Bucher-Nurminen, 1981; Yardley, Rochelle, Barnicoat, & Lloyd, 1991). Field relationships indicate that formation of the forsterite-phlogopite skarns is related to emplacement of the pegmatitic portions of the M2 felsic apophyses, and the spatial patterns of pegmatites and forsterite-phlogopite skarns highlight the source and pathways of the fluids (Figure 3b). The age of the forsterite-phlogopite skarn is inferred from the age of the adjacent M2 felsic apophysis of 578±4.7 Ma (sample DB-G2Z; Figure 3b). The flow paths are structurally controlled and comprise mainly contrasting lithological contacts such as mafic apophysis-marble (Figures 3b-d) and diopisde-skarn-marble (Figures 4b-c) or foliation planes within the carbonates (Figure 3b; Figure 14b). Lithological and structurally controlled fluid flow during metamorphism and deformation is a well-acknowledged phenomenon (*e.g.* Skelton, Graham, & Bickle, 1995; Pitcairn, Skelton, Broman, Arghe, & Boyce, 2010). Forsterite-calcite assemblage formed parallel to carbonate foliation has been previously reported as the result of fluid flow and metasomatism along foliation-parallel deformation enhanced permeability

(Holness, 1997). Asymmetrical occurrence and thickness of skarns bordering M1 and M2 apophyses from thick (<50 cm) to absent reaction zones indicate that fluid infiltration was heterogeneous and localized at preferred surfaces. Formation of pinch-and-swell structures, boudinage of diopside skarns and folding of the M1 apophyses enhanced the porosity at these interfaces and created a positive feedback of deformation and fluid influx. Brittle failure as part of the boudinage process was demonstrated by Gardner, Piazolo and Daczko, 2015. The occurrence of forsterite-phlogopite skarns in tension gashes (Figure 2g) and along the fold hinge zones (Figure 3a and 3d) suggests a synkinematic origin. Additionally, microstructures show that the forsterite and phlogopite zones are oriented parallel to the diopside-skarn pinch-and-swell boundaries and without solid state deformation (Figure 10a). Yet, recrystallization of dolomite "adjusting" its orientation parallel to the fluid pathways in the phlogopite zone suggests that the recrystallization was fluid-mediated as reported similarly by Holness (1997). Furthermore, coarse grained forsterite and calcite are found in strain shadows suggesting that they likely formed synchronous to the deformation event that resulted in boudinage and pinch-and-swell structures. Field observations and microstructures also suggest that as the diopside skarn bands broke brittle, fluid infiltration led to forsterite and calcite crystallization within the fractured diopside grains (Figures 4b-c and 10a).

Studies of calcite inclusions in forsterite in the same area reported temperatures of c. 590°C for the crystallization of forsterite and calcite (Hoerlle, Remus, & Gomes, 2019). Forsterite and calcite likely resulted from the reaction of aqueous silica and dolomite (R2) and locally after diopside + dolomite (R3). The metastable formation of forsterite directly from dolomite and silica was previously reported by Müller *et al*. (2004) and Ferry, Ushikubo and Valley (2011).

$$2Dol + SiO_{2(aq)} = 2\ Cal + Fo + 2CO_2 \quad (R2)$$

$$3Dol + Di = 4Cal + 2Fo + 2\ CO_2 \quad (R3)$$

At a Si-activity of 1, forsterite is formed at $X(CO_2) < 0.1$ for temperatures below 600°C at the assumed pressure of 0.45 GPa. Higher temperatures are required for forsterite formation at higher $X(CO_2)$ (Figure 13a). Remarkably, as soon as the Si-activity is below one, forsterite formation is limited to conditions of very low Si-activities of < 0.1 (Figure 13c).

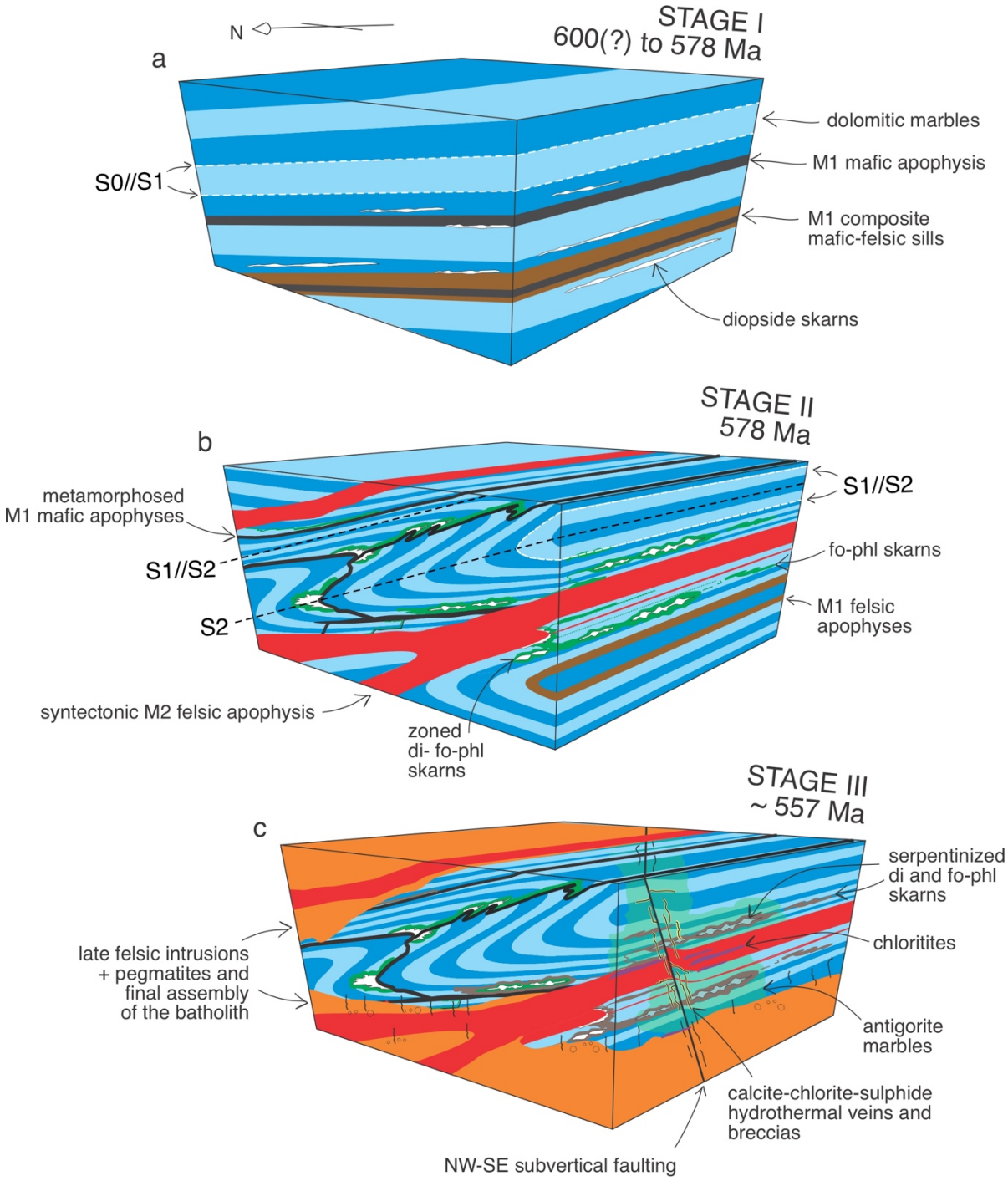

Figure 14: Schematic evolution model for metasomatic stages associated to the intrusion of the syntectonic CSGC. (a) Stage I: formation of di-skarns after the localized infiltration of siliceous fluids released from cooling M1 mafic and felsic apophyses into lithological contacts, cracks and fractures mostly parallel to marble foliation S_1; estimate age between 600(?) and 578 Ma, related to extensional regime (b) Stage II: change to a transpressional regime resulting in folding of the marbles and previously crystallized M1 apophyses; formation of pinch-and-swell structures in the di-skarns; intrusion of M2 felsic apophyses; metamorphism of prior mafic apophyses; formation of fo-phl skarns after aqueous siliceous fluid infiltration structurally controlled within dolomitic marbles released from cooling felsic apophyses at c. 578 Ma. (c) Stage III: final assembly and cooling of the magmatic complex after decrease in magmatic and tectonic activity, brittle fracturing and

aqueous fluid infiltration released from cooling of the final granitic bodies and pegmatites causing serpentinization of skarn assemblages, chloritization of biotite in felsic and mafic apophyses and formation of calcite-chlorite-sulphide hydrothermal veins and breccias near subvertical faults at c. 557 Ma.

The phlogopite zone comprises recrystallized dolomite and phlogopite with interstitial calcite (Figure 10d). The transition from the forsterite zone to the phlogopite zone can be explained by the propagating reaction front lowering silica activity that leads to the formation of dolomite + calcite (Figure 13b). The remaining amount of Si and other elements dissolved in the fluid (*e.g.* K, Fe, F) were incorporated in the phlogopite crystallized along grain boundaries of the carbonates.

7.2.3. Stage 3: Cooling of the granitic complex, late fluid circulation, serpentinization and chloritization

After the final magmatic intrusions crystallized at c. 557 Ma and temperature dropped, the host rocks, skarns and M1 and M2 apophyses started to deform in a brittle manner. Subvertical faults and fractures cross-cutting previous structures created new pathways for fluid flow. Fault zones are structures for fluid flow and commonly act as localized conduits (*e.g.* Caine, Evans, & Forster, 1996; Dipple & Ferry, 1992; Sibson, 2000). Calcite-chlorite-sulphide veins and breccias in the CSGC wallrocks (Figures 5a,c,e) indicate fluid flow associated with the brittle structures (Figure 14c). However, serpentinization of skarn assemblages suggest that the fluids also used pre-existing pathways (Figure 5e). Late-cooling granites and pegmatites are interpreted as the source for water-rich fluids that infiltrated brittle structures and previous pathways. Hydrothermal chloritization of biotite in granodiorites of the CSGC occurred at c. 300°C (Reis *et al*., 2017; Remus *et al*., 2011). We interpret that the serpentinization of skarns occurred at similar conditions because the calcite-chlorite-veins are bordered by antigorite and calcite in the host rock and temperature ranges for serpentinization and chloritization are similar. Silica and water-rich fluids use faults, fractures and marble-skarn interfaces as pathways leading to the serpentinization of forsterite and diopside (Figure 5e) according to reactions 4 and 5. Fully serpentinized skarns are symmetrically bordered by massive green antigorite marbles up to a few meters (*e.g.* Figure 5e).

$$3Fo + 2SiO_{2(aq)} + 4H_2O = 2Atg \quad (R4)$$

$$3Di + 6H^{+}_{(fluid)} = Atg + 3Ca^{+}_{(fluid)} + H_2O + 4SiO_{2(aq)} \quad (R5)$$

In both reactions, the volume change of the solids is positive. Additionally, at 300°C the serpentinization rate is highest (Martin & Fyfe, 1970). Fracturing occurs because the higher the reaction rate, the faster the volume of affected rock increases and there is little time to accommodate the stress resulting from volume increase (Jamtveit & Hammer, 2012). Serpentinization of the skarn assemblages is more intense near faults (<100 m) which indicates high fluid flux through the brittle structures. Serpentinization resulted in positive feedback between reaction-driven cracking and fluid infiltration that replaces all the silicate assemblages of the skarn. Remaining fluids infiltrate into the adjacent cracked dolomites leading to the formation of antigorite and calcite from dolomite and aqueous siliceous fluids (R6).

$$3Dol + 4SiO_{2(aq)} + H_2O = Atg + 3Cal + 3CO_2 \quad (R6)$$

In summary, fluid flow patterns throughout the metasomatic stages foresee: (i) fluid flow along foliation planes and lithological boundaries in the I, II and III stages (Figures 2d and 3a-c;); (ii) structurally controlled fluid flow focused through axial zones and localized fracturing associated with boudinage and pinch and swell structures in the II stage (Figures 2b and 3d); (iii) hydrofracturing associated to fluid flow through fractures and fault zones in the III stage (Figures 5a-c).

7.3. FLUID EVOLUTION AND SKARN ZONING CONTROLS

Despite the lack of geochronology data determining the exact age of the diopside and forsterite-phlogopite skarn formation, there is textural evidence documenting the sequential development of diopside + calcite, followed by forsterite + calcite and dolomite + phlogopite + calcite. The skarn formation itself is inherently linked to physicochemical conditions and the amount and composition of the infiltrating fluid and thus, the spatial and temporal field observations can be used to decipher the infiltration history recorded in the transition from diopside skarns to forsterite-phlogopite skarns. However, at least two main alternative interpretations can be used to explain the observed sequence.

The observed sequence could be explained by changes of the effective fluid flux (Figure 15; S1), *i.e.* the amount of fluid flux over time during the infiltration event governing the effective water-to-rock ratio (W/R). While the effect of locally changing

W/R-ratios have been successfully used to explain spatial variations (Bowman, Parry, Kropp, & Kruer, 1987), a similar concept could be envisaged for temporal changes within a propagating reaction front. Here, a very limited amount of fluid at the early stages resulting in a high molar fraction of CO_2 in the fluid ($X(CO_2)$) leads to formation of diopside by the breakdown of dolomite and aqueous silica (Figure 13a-c; arrows 1, 3 and 4; Figure 15). The system is initially internally buffered at high $X(CO_2)$ values (>0.8) requiring high Si-activities around 1 to form diopside. At this conditions, lower $X(CO_2)$ values would result in the formation of prograde tremolite (Figure 13a), which is not observed. The formation of forsterite could be facilitated by continued fluid infiltration or a second infiltration event caused by the intrusion of more felsic magma (M2) that increases the effective fluid flux lowering the $X(CO_2)$ and shifting the system into an externally buffered regime at low $X(CO_2)$ conditions. The formation of forsterite from diopside and dolomite can occur at approximately the same temperature (c. 600°) at $aSiO_2$ of 1 (Figure 13c; arrow 2) or by lowering the Si-activities below 0.1 (Figure 13c; arrow 5). A 'dry' heating stage with subsequent infiltration causing a shift in mineral reactions has previously been reported in contact aureoles involving impure dolomites (Müller *et al*., 2004).

In a second scenario, the observed sequence of diopside – forsterite – dolomite could be explained by constant fluid flux at low $X(CO_2)$ conditions and variable aSiO2 and/or temperatures (Figure 15; S2). In this context, diopside would be formed first at low XCO_2 ($0.1 < XCO_2 < 0.2$) and low silica activity (~0.2 $aSiO_2$; Figure 13c; arrow 6). The subsequent formation of forsterite can be explained by limited Si-mobility along the propagating reaction front (Figure 13b, arrows 5 and 7) as suggested by Bégué, Baumgartner, Müller, Putlitz and Vennemann (2020) and/or cooling (Figure 13d, arrow 8). The Si-concentration of the igneous fluid is indeed likely to be limited depending on its solubility and composition of the igneous rock it has equilibrated with before infiltration into the country rocks. We note, however, that the non-reacted dolomites have minor silicate phases, thus requiring either substantial Si-concentrations or large time integrated fluid fluxes (TIFF – see Baumgartner & Rumble, 1988).

In concluding this section, we note that the spatial and temporal succession of zoned skarn formation starting with diopside followed by forsterite + calcite can be explained in two ways regarding the effective fluid flux. While additional geochemical data such as isotope signatures, mass balance constraints, estimates of time integrated fluid

fluxes are needed to quantitatively answer some of the open questions regarding the infiltration history, such an analysis would be beyond the scope of this conceptual paper and will thus be addressed in follow-up contributions.

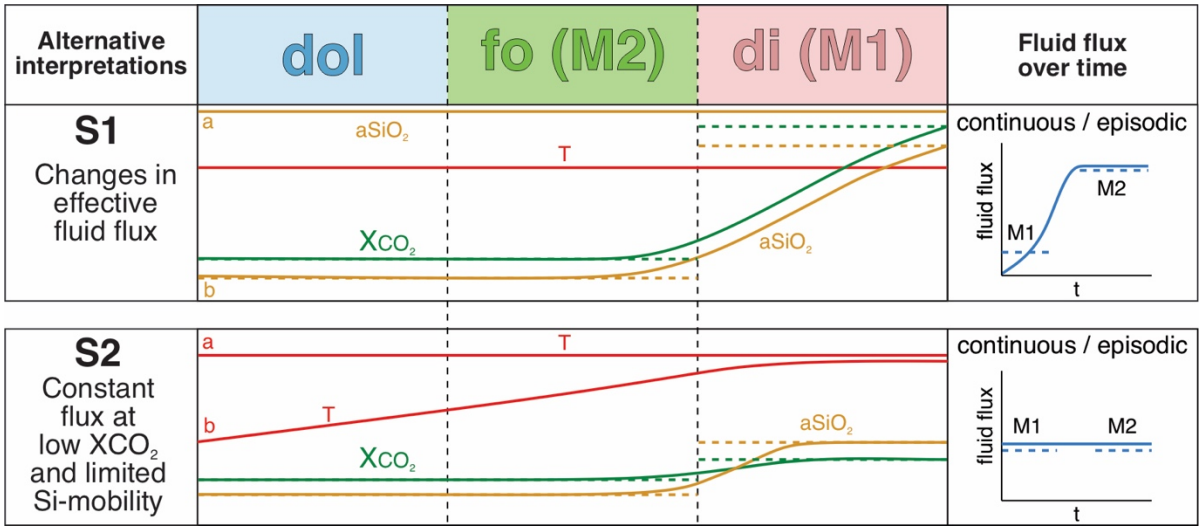

Figure 15: Schematic sketch showing the evolution of the decisive parameters temperature, $X(CO_2)$ and SiO_2 activity for the different interpretations of the diopiside-forsterite zoning. Dashed lines represent the variation of parameters for episodic fluid infiltration at M1 to M2 whereas continuous lines represent the possible continuous transition from M1 to M2. The right-side diagram illustrates the development of the fluid flux over time; a and b yellow lines relate to the two options for $aSiO_2$ at scenario 1 and a and b red lines relate to two options for T of scenario 2.

7.4. USING LOCALIZED METASOMATIC REACTIONS TO DECIPHER INTRUSION HISTORY: CHALLENGES AND OPPORTUNITIES

Magmatic systems where fluid source, deformation, geometry and timing constraints of the pluton are complex can be challenging to decipher and thus restrain the description of the sequence of events (*e.g.* CSGC; Remus *et al*., 2000). The different metasomatic rocks formed after the interaction of the CSGC and the marbles of the PFMC helped to reveal different stages of the history of the granitic complex. Contrasting emplacement models were proposed, including a diapir-like (Nardi & Bitencourt, 1989), a sheet-like intrusion (Fragoso César, 1991), a lens-shaped “mega-porphyroblast” (Fernandes *et al*., 1992) and an intrusion along a fault-bend-fold of a right lateral strike-slip shear zone (Costa *et al*., 1995). However, the study of the metasomatic rocks formed at different stages supported by field relationships, petrography and geochronological data suggests that the granitic complex was likely assembled by several pulses along c. 21 My. Additionally, skarns formed during

different deformational regimes suggest that the first intrusions were formed under an extensional regime before c. 578 Ma followed by folding and felsic magmatism until c. 557 Ma, marking the reduction of tectonic activity and the end of magmatism. Our findings are in agreement with the proposals that large igneous bodies can be formed by the protracted or incremental supply of magma build up over millions of years (*e.g.* Clemens & Mawer, 1992; Petford *et al*., 2000; Coleman *et al*., 2004; He *et al*., 2018; Pivarunas & Meert, 2019; Tichomirowa *et al*., 2019). Field and petrographical recognition of incrementally assembled plutons is difficult because conditions can prevail near the original magmatic temperatures for a long time, potentially obscuring pristine contacts between individual increments (Bartley *et al*., 2008). In this contribution, we have shown that studying the metasomatic reactions is a powerful tool to unveil different stages of the intrusion history of a complex magmatic body. This is particularly elucidative when carbonate rocks are present near the intrusion resulting in the formation of skarns. These rocks form distinct microstructures and mineral assemblages that can be related to the different stages of a pluton crystallization (Meinert *et al*., 2005). However, this is challenging because working with multistage fluid-rock interaction requires dealing with complicated overlapping of processes that can partially or totally erase previous features. In addition to the field relations and microstructures, dating minerals formed or reset during metamorphism and fluid infiltration (*e.g.* apatite and titanite) is a valuable tool in deciphering the timing constraints of fluid circulation during magmatic emplacement, even if they generally record the latest magmatic or fluid infiltration event in those rocks. Yet, precise dating of all metasomatic stages is impracticable, especially in magnesian skarn systems where the lack of datable phases is common. In calcic skarn systems, the direct dating of a metasomatic phase is achievable mainly when grossular-andradite garnet is present (*e.g.* Deng, Li, Luo, & Wang, 2017; Gevedon, Seman, Barnes, Lackey, & Stockli, 2018; Seman, Stockli, & McLean, 2017). Identifying precise intervals and duration of metasomatic processes in magnesian skarn systems remains challenging whereas integrated studies of magmatic zircon of the causative intrusion and metasomatic phases in metamorphic rocks provide a time-span for the pluton assembly. Finally, studying the metasomatic reactions commonly observed in the host rocks and apophyses of a magmatic complex provides useful insights on deformation and timing of pluton assembly and associated fluid activity.

ACKNOWLEDGEMENTS

This work was supported by CNPq-National Council for Scientific and Technological Development of Brazil (Proc. 141333/2017-0) and CAPES-PRINT (Proc. 88887.467220/2019-00). We thank Dagoberto Barcelos, Inducal, Ativa Minerais, Mônego, FIDA, Razzera, Vigor and Cruzeiro companies for access to the marble quarries. The careful and constructive reviews of two anonymous reviewers and editorial handling by Dr. Katy Evans are gratefully acknowledged.

REFERENCES

Aleinikoff, J.N., Wintsch, R., Tollo, R.P., Unruh, D.M., Fanning, C.M., Schmitz, M.D., (2007). Age and origins of rocks of the Killingworth dome, south-central Connecticut: implications for the tectonic evolution of southern New England. American Journal of Science 307, 63e118. https://doi.org/10.2475/01.2007.04.

Almeida, D. del P., Chemale, F., & Machado, A. (2012). Late to Post-Orogenic Brasiliano-Pan-African Volcano-Sedimentary Basins in the Dom Feliciano Belt, Southernmost Brazil. In Petrology - New Perspectives and Applications. https://doi.org/10.5772/25189

Almeida, R. P., Janikian, L., Fragoso-Cesar, A. R. S., & Fambrini, G. L. (2010). The Ediacaran to Cambrian rift system of Southeastern South America: Tectonic implications. Journal of Geology, 118(2), 145–161. https://doi.org/10.1086/649817

Babinski, M., Chemale, F., Hartmann, L. A., Van Schmus, W. R., & Da Silva, L. C. (1996). Juvenile accretion at 750-700 Ma in southern Brazil. Geology. https://doi.org/10.1130/0091-7613(1996)024<0439:JAAMIS>2.3.CO;2

Baumgartner, L. P., & Rumble, D. (1988). Transport of stable isotopes: I: Development of a kinetic continuum theory for stable isotope transport. Contributions to Mineralogy and Petrology. https://doi.org/10.1007/BF00372362

Bartley, J. M., Coleman, D. S., & Glazner, A. F. (2008). Incremental pluton emplacement by magmatic crack-seal. Transactions of the Royal Society of Edinburgh, Earth Sciences. 97(4). https://doi.org/10.1017/S0263593300001528

Bégué, F., Baumgartner, L. P., Bouvier, A. S., & Robyr, M. (2019). Reactive fluid infiltration along fractures: Textural observations coupled to in-situ isotopic analyses. Earth and Planetary Science Letters, 519, 264–273. https://doi.org/10.1016/j.epsl.2019.05.024

Bégué, F., Baumgartner, L. P., Müller, T., Putlitz, B., & Vennemann, T. (2020). Metasomatic Vein Formation By Stationary Fluids In Carbonate Xenoliths At The Eastern Margin Of The Bergell Intrusion, Val Sissone, Italy. Journal of Petrology, 41(0). https://doi.org/10.1093/petrology/egaa012

Bicalho, V., Remus, M. V. D., Rizzardo, R., & Dani, N. (2019). Geochemistry, metamorphic evolution and tectonic significance of metabasites from Caçapava do Sul, southern Brazil. Brazilian Journal of Geology. https://doi.org/10.1590/2317-4889201920180039

Bitencourt, M. de F. (1983). Geologia petrologia e estrutura dos metamorfitos da região de Caçapava do Sul RS. Universidade Federal do Rio Grande do Sul (unpublished MSc. thesis)

Bortolotto, O. J. (1988). Metamorfismo termal dos mármores de Caçapava do Sul, RS. Ciência e Natura. https://doi.org/10.5902/2179460x25479

Bowman, J. R., Parry, W. T., Kropp, W. P., & Kruer, S. A. (1987). Chemical and isotopic evolution of hydrothermal solutions at Bingham, Utah. Economic Geology, 82(2), 395–428. https://doi.org/10.2113/gsecongeo.82.2.395

Brown, P. E., Bowman, J. R., & Kelly, W. C. (1985). Petrologic and stable isotope constraints on the source and evolution of skarn-forming fluids at Pine Creek, California. Economic Geology. https://doi.org/10.2113/gsecongeo.80.1.72

Bucher-Nurminen, K. (1981). The formation of metasomatic reaction veins in dolomitic marble roof pendants in the Bergell intrusion (Province Sondrio, northern Italy). American Journal of Science. https://doi.org/10.2475/ajs.281.9.1197

Buddington, A. F. (1959). Granite emplacement with special reference to North America. Geological Society of America Bulletin. https://doi.org/10.1130/0016-7606(1959)70[671:gewsrt]2.0.co;2

Caine, J. S., Evans, J. P., & Forster, C. B. (1996). Fault zone architecture and permeability structure. Geology, 24(11), 1025–1028. https://doi.org/10.1130/0091-7613(1996)024<1025:FZAAPS>2.3.CO;2

Cerva-Alves, T., Remus, M. V. D., Dani, N., & Basei, M. A. S. (2017). Integrated field, mineralogical and geochemical characteristics of Caçapava do Sul alvikite and beforsite intrusions: A new Ediacaran carbonatite complex in southernmost Brazil. Ore Geology Reviews, 88, 352–369. https://doi.org/10.1016/j.oregeorev.2017.05.017

Chemale. F. (2000). Evolução Geológica do Escudo Sul-Riograndense. In: Holz M., De Ros L.F. (eds.). Geologia do Rio Grande do Sul. Editora UFRGS, Porto Alegre, p. 13-52.

Cherniak, D. J. (1993). Lead diffusion in titanite and preliminary results on the effects of radiation damage on Pb transport. Chemical Geology, 110(1–3), 177–194. https://doi.org/10.1016/0009-2541(93)90253-F

Clarke, D.B., 1992, Granitoid rocks: London, Chapman and Hall, 283 p.

Clemens, J. D., & Mawer, C. K. (1992). Granitic magma transport by fracture propagation. Tectonophysics. https://doi.org/10.1016/0040-1951(92)90316-X

Cochrane, R., Spikings, R. A., Chew, D., Wotzlaw, J. F., Chiaradia, M., Tyrrell, S., … Van der Lelij, R. (2014). High temperature (>350°C) thermochronology and mechanisms of Pb loss in apatite. Geochimica et Cosmochimica Acta, 127, 39–56. https://doi.org/10.1016/j.gca.2013.11.028

Coleman, D. S., Gray, W., & Glazner, A. F. (2004). Rethinking the emplacement and evolution of zoned plutons: Geochronologic evidence for incremental assembly of the Tuolumne Intrusive Suite, California. Geology. https://doi.org/10.1130/G20220.1

Connolly, J. A. D. (1990). Multivariable phase diagrams: an algorithm based on generalized thermodynamics. American Journal of Science. https://doi.org/10.2475/ajs.290.6.666

Cordani, U.G., Halpern, N. & Berenholc, M., (1974). Idades Radiométricas de Rochas do Escudo Sul-Riograndense e sua Significação Tectônica. X Carta do Brasil ao Milionésimo, Folha de Porto Alegre, DNPM

Costa, A. F. U., Fernandes, L. A. D., Shukowsky, W., Nardi, L. V. S., & Bitencourt, M. F. (1995). Teste dos modelos tectonicos e de posicionamento do complexo Granitico de Cacapava do Sul atraves de estudos de modelagem gravimetrica 3-D. Revista Brasileira de Geofisica. https://doi.org/10.22564/rbgf.v13i2.1185

Coulon, C., Maluski, H., Bollinger, C., & Wang, S. (1986). Mesozoic and cenozoic volcanic rocks from central and southern Tibet: 39Ar40Ar dating, petrological characteristics and geodynamical significance. Earth and Planetary Science Letters. https://doi.org/10.1016/0012-821X(86)90186-X

Deng, X. D., Li, J. W., Luo, T., & Wang, H. Q. (2017). Dating magmatic and hydrothermal processes using andradite-rich garnet U–Pb geochronometry. Contributions to Mineralogy and Petrology, 172(9), 1–11. https://doi.org/10.1007/s00410-017-1389-2

Dipple, G. M., & Ferry, J. M. (1992). Metasomatism and fluid flow in ductile fault zones. Contributions to Mineralogy and Petrology, 112(2–3), 149–164. https://doi.org/10.1007/BF00310451

Ducoux, M., Branquet, Y., Jolivet, L., Arbaret, L., Grasemann, B., Rabillard, A., … Drufin, S. (2017). Synkinematic skarns and fluid drainage along detachments: The West Cycladic Detachment System on Serifos Island (Cyclades, Greece) and its related mineralization. Tectonophysics. https://doi.org/10.1016/j.tecto.2016.12.008

Duncan, A. R., Erlank, A. J., & Marsh, J. S. (1984). Regional geochemistry of the Karoo igneous province. In Petrogenesis of the volcanic rocks of the Karoo Province (Vol. 13, pp. 355-388). Special Publication Geological Society South Africa.

Engvik, A. K., Taubald, H., Solli, A., Grenne, T., & Austrheim, H. (2018). Dynamic metasomatism: Stable isotopes, fluid evolution, and deformation of albitite and scapolite metagabbro (bamble lithotectonic domain, South Norway). Geofluids. https://doi.org/10.1155/2018/9325809

Fernandes, L. A. D., Tommasi, A., & Porcher, C. C. (1992). Deformation patterns in the southern Brazilian branch of the Dom Feliciano Belt: A reappraisal. Journal of South American Earth Sciences. https://doi.org/10.1016/0895-9811(92)90061-3

Ferry J. M. (1991) Dehydration and decarbonation reactions as a record of fluid infiltration. In: Kerrick D (ed) Contact metamorphism (Reviews in Mineralogy vol. 26). Mineralogical Society of America, Washington DC, pp 351–393

Ferry, J. M., Ushikubo, T., & Valley, A. W. (2011). Formation of forsterite by silicification of dolomite during contact metamorphism. Journal of Petrology, 52(9), 1619–1640. https://doi.org/10.1093/petrology/egr021

Fragoso-César, A.R.S. (1991). Tectônica de placas no Ciclo Brasiliano: As orogenias dos Cinturões Dom Feliciano e Ribeira no Rio Grande do Sul. Universidade de São Paulo (unpublished PhD thesis).

Frey, F. A., Gerlach, D. C., Hickey, R. L., Lopez-Escobar, L., & Munizaga-Villavicencio, F. (1984). Petrogenesis of the Laguna del Maule volcanic complex, Chile (36° S). Contributions to Mineralogy and Petrology. https://doi.org/10.1007/BF00371418

Gardner, R. L., Piazolo, S., & Daczko, N. R. (2015). Pinch and swell structures: Evidence for strain localisation by brittle-viscous behaviour in the middle crust. Solid Earth, 6(3), 1045–1061. https://doi.org/10.5194/se-6-1045-2015

Gevedon, M., Seman, S., Barnes, J. D., Lackey, J. S., & Stockli, D. F. (2018). Unraveling histories of hydrothermal systems via U–Pb laser ablation dating of skarn garnet. Earth and Planetary Science Letters, 498, 237–246. https://doi.org/10.1016/j.epsl.2018.06.036

Goulart, R. V., Remus, M. V. D., & Reis, R. S. dos. (2013). Composição isotópica de Sr, C e O e geoquímica de ETR das rochas carbonáticas do Bloco São Gabriel, Rio Grande do Sul. Pesquisas Em Geociências. https://doi.org/10.22456/1807-9806.40831

Harlov, D. E. (2015). Apatite: A fingerprint for metasomatic processes. Elements. https://doi.org/10.2113/gselements.11.3.171

Hartmann, L. A., Leite, J. A. D., Da Silva, L. C., Remus, M. V.D., McNaughton, N. J., Groves, D. I., … Vasconcellos, M. A. Z. (2000). Advances in SHRIMP geochronology and their impact on understanding the tectonic and metallogenic evolution of southern Brazil. Australian Journal of Earth Sciences. https://doi.org/10.1046/j.1440-0952.2000.00815.x

Hartmann, L. A., Philipp, R. P., Santos, J. O. S., & McNaughton, N. J. (2011). Time frame of 753-680 Ma juvenile accretion during the São Gabriel orogeny, southern Brazilian Shield. Gondwana Research. https://doi.org/10.1016/j.gr.2010.05.001

Hartmann, L. A., Tindle, A., & Bittencourt, M. D. F. (1990). O metamorfismo de fácies anfibolito no Complexo Metamórfico Passo Feio, RS, com base em química dos minerais. Pesquisas Em Geociências. https://doi.org/10.22456/1807-9806.21383

Heaman, L. M. (2009). The application of U-Pb geochronology to mafic, ultramafic and alkaline rocks: An evaluation of three mineral standards. Chemical Geology. https://doi.org/10.1016/j.chemgeo.2008.10.021

He, C., Gong, S., Wang, L., Chen, N., Santosh, M., & Wang, Q. (2018). Protracted post-collisional magmatism during plate subduction shutdown in early Paleoproterozoic: Insights from post-collisional granitoid suite in NW China. Gondwana Research, 55, 92–111. https://doi.org/10.1016/j.gr.2017.11.009

Hochstaedter, A. G., Gill, J. B., Kusakabe, M., Newman, S., Pringle, M., Taylor, B., & Fryer, P. (1990). Volcanism in the Sumisu Rift, I. Major element, volatile, and stable isotope geochemistry. Earth and Planetary Science Letters. https://doi.org/10.1016/0012-821X(90)90184-Y

Hoerlle, G.S., Remus, M.V.D., Gomes, M.E.B., (2019). Geothermometry of the Caçapava do Sul magnesian skarns: insights from calcite inclusions in forsterite. Presented at the IV Simpósio Brasileiro de Metalogenia. Gramado, Brazil.

Holland, T. J. B., & Powell, R. (2011). An improved and extended internally consistent thermodynamic dataset for phases of petrological interest, involving a new equation of state for solids. Journal of Metamorphic Geology, 29(3), 333–383. https://doi.org/10.1111/j.1525-1314.2010.00923.x

Holness, M. B. (1997). Fluid flow paths and mechanisms of fluid infiltration in carbonates during contact metamorphism: The Beinn an Dubhaich aureole, Skye. Journal of Metamorphic Geology, 15(1), 59–70. https://doi.org/10.1111/j.1525-1314.1997.00005.x

Jackson, S. E., Pearson, N. J., Griffin, W. L., & Belousova, E. A. (2004). The application of laser ablation-inductively coupled plasma-mass spectrometry to in situ U-Pb zircon geochronology. Chemical Geology. https://doi.org/10.1016/j.chemgeo.2004.06.017

Jamtveit, B., & Hammer, Ø. (2012). Sculpting of rocks by reactive fluids. Geochemical Perspectives, Vol. 1, pp. 341–491. https://doi.org/10.7185/geochempersp.1.3

Janikian L. (2004). Seqüências deposicionais e evolução paleoambiental do Grupo Bom Jardim e da Formação Acampamento Velho, Supergrupo Camaquã, Rio Grande do Sul. Universidade de São Paulo (unpublished PhD thesis).

Janikian, L., de Almeida, R. P., Fragoso-Cesar, A. R. S., Martins, V. T. de S., Dantas, E. L., Tohver, E., … D'Agrella-Filho, M. S. (2012). Ages (U-Pb SHRIMP and LA ICPMS) and stratigraphic evolution of the Neoproterozoic volcano-sedimentary successions from the extensional Camaquã Basin, Southern Brazil. Gondwana Research, 21(2–3), 466–482. https://doi.org/10.1016/j.gr.2011.04.010

Jolly, W. T., Lidiak, E. G., & Dickin, A. P. (2008). Bimodal volcanism in northeast Puerto Rico and the Virgin Islands (Greater Antilles Island Arc): Genetic links with Cretaceous subduction of the mid-Atlantic ridge Caribbean spur. Lithos. https://doi.org/10.1016/j.lithos.2007.10.008

Kinny, P.D., McNaughton, N.J., Fanning, C.M., Maas, R., (1994). 518 Ma Sphene (Titanite) from the Khan Pegmatite, Namibia, Southwest Africa: a potential ion-microprobe standard. In: Abstract Presented at the 8th International Conference on Geochronology, Cosmochronology and Isotope Geology, vol. 1107. USGS; Circular, p. 171.

Kirkland, C. L., Yakymchuk, C., Szilas, K., Evans, N., Hollis, J., McDonald, B., & Gardiner, N. J. (2018). Apatite: a U-Pb thermochronometer or geochronometer? Lithos, 318–319, 143–157. https://doi.org/10.1016/j.lithos.2018.08.007

Krenn, E., & Finger, F. (2004). Metamorphic formation of Sr-apatite and Sr-bearing monazite in a high-pressure rock from the Bohemian Massif. American Mineralogist. https://doi.org/10.2138/am-2004-8-921

Leinz, V., Barbosa, A.F. & Teixeira, E. (1941). Mapa geológico Caçapava-Lavras. Boletim 90, Secretaria da Agricultura, Indústria e Comércio - RS, 39p.

Leite, J. A. D., Hartmann, L. O. A., McNaughton, N. J., & Chemale, F. (1998). Shrimp u/pb zircon geochronology of neoproterozoic juvenile and crustal-reworked terranes in southernmost brazil. International Geology Review, 40(8), 688–705. https://doi.org/10.1080/00206819809465232

Lopes, C. G., Pimentel, M. M., Philipp, R. P., Gruber, L., Armstrong, R., & Junges, S. (2015). Provenance of the passo feio complex, dom feliciano belt: Implications for the age of supracrustal rocks of the são gabriel arc, southern brazil. Journal of South American Earth Sciences. https://doi.org/10.1016/j.jsames.2014.11.004

Ludwig, K. R. (2003). User's manual for Isoplot 3.00, a geochronological toolkit for Microsoft Excel. Berkeley Geochronology Center special publication no.4. Components.

Martin, B., & Fyfe, W. S. (1970). Some experimental and theoretical observations on the kinetics of hydration reactions with particular reference to serpentinization. Chemical Geology, 6(C), 185–202. https://doi.org/10.1016/0009-2541(70)90018-5

Matté, V., Sommer, C. A., Lima, E. F. de, Philipp, R. P., & Basei, M. A. S. (2016). Post-collisional Ediacaran volcanism in oriental Ramada Plateau, southern Brazil. Journal of South American Earth Sciences, 71, 201–222. https://doi.org/10.1016/j.jsames.2016.07.015

Meinert, L. D., Dipple, G. M., & Nicolescu, S. (2005). World Skarn Deposits. In One Hundredth Anniversary Volume (Vol. 100, pp. 299–336). https://doi.org/10.5382/AV100.11

Miller, R. B., & Paterson, S. R. (1999). In defense of magmatic diapirs. Journal of Structural Geology. https://doi.org/10.1016/S0191-8141(99)00033-4

Morales, B. A. de A., Almeida, D. D. P. M. de, Koester, E., Rocha, A. M. R. da, Dorneles, N. T., Rosa, M. B. da, & Martins, A. A. (2019). Mineralogy, whole-rock geochemistry and C, O isotopes from Passo Feio Carbonatite, Sul-Riograndense Shield, Brazil. Journal of South American Earth Sciences, 94(May), 102208. https://doi.org/10.1016/j.jsames.2019.05.024

Müller, T., Baumgartner, L. P., Foster, C. T., & Bowman, J. R. (2009). Crystal size distribution of periclase in contact metamorphic dolomite marbles from the Southern Adamello Massif, Italy. Journal of Petrology, 50(3), 451–465. https://doi.org/10.1093/petrology/egp007

Müller, T., Baumgartner, L. P., Foster, C. T., & Vennemann, T. W. (2004). Metastable prograde mineral reactions in contact aureoles. Geology, 32(9), 821–824. https://doi.org/10.1130/G20576.1

Nabelek, P. I., Bédard, J. H., Hryciuk, M., & Hayes, B. (2013). Short-duration contact metamorphism of calcareous sedimentary rocks by Neoproterozoic Franklin gabbro sills and dykes on Victoria Island, Canada. Journal of Metamorphic Geology. https://doi.org/10.1111/jmg.12015

Nardi, L. V. S., & Bitencourt, M. D. F. (1989). Geologia, petrologia e geoquímica do Complexo Granítico de Caçapava do Sul, RS. Revista Brasileira de Geociências. https://doi.org/10.25249/0375-7536.1989153169

Oliveira, C. H. E., Chemale, F., Jelinek, A. R., Bicca, M. M., & Philipp, R. P. (2014). U-Pb and Lu-Hf isotopes applied to the evolution of the late to post-orogenic transtensional basins of the Dom Feliciano Belt, Brazil. Precambrian Research, 246, 240–255. https://doi.org/10.1016/j.precamres.2014.03.008

Perring, C. S., Rock, N. M. S., Golding, S. D., & Roberts, D. E. (1989). Criteria for the recognition of metamorphosed or altered lamprophyres: A case study from the Archaean of Kambalda, Western Australia. Precambrian Research, 43(3). https://doi.org/10.1016/0301-9268(89)90057-0

Petford, N., Cruden, A. R., McCaffrey, K. J. W., & Vigneresse, J. L. (2000). Granite magma formation, transport and emplacement in the Earth's crust. Nature. https://doi.org/10.1038/35047000

Philipp, R.P., Pimentel, M.M. & Basei, M.A.S. (2018). The Tectonic Evolution of the São Gabriel Terrane, Dom Feliciano Belt, Southern Brazil: The Closure of the Charrua Ocean, in: Siegesmund, S., Basei, Miguel A S, Oyhantçabal, P., Oriolo, S. (Eds.), Geology of Southwest Gondwana. Springer International Publishing, Cham, pp. 243–265. https://doi.org/10.1007/978-3-319-68920-3_10

Pitcairn, I. K., Skelton, A. D. L., Broman, C., Arghe, F., & Boyce, A. (2010). Structurally focused fluid flow during orogenesis: The Islay Anticline, SW Highlands, Scotland. Journal of the Geological Society, 167(4), 659–674. https://doi.org/10.1144/0016-76492009-135

Pivarunas, A. F., & Meert, J. G. (2019). Protracted magmatism and magnetization around the McClure Mountain alkaline igneous complex. Lithosphere, 11(5), 590–602. https://doi.org/10.1130/L1062.1

Porcher, C. A. & Lopes, R. C. (2000). Carta Geológica: Cachoeira do Sul: folha SH.22-Y-A: estado do Rio Grande do Sul. Brasília: CPRM. Escala 1:250.000. Programa Levantamentos Geológicos Básicos do Brasil - PLGB.

Reis, R. S. dos, Remus, M. V. D., Dani, N., & Anzolin, H. D. M. (2017). Alteração clorítica no flanco leste do Granito Caçapava, Rio Grande do Sul: evolução do metassomatismo e sulfetos de Cu-Fe associados. Geologia USP. Série Científica. https://doi.org/10.11606/issn.2316-9095.v17-121013

Remus, M. V. D., Dani, N., Gazzoni, C. P., Hoerlle, G. S. & Reis, R. S. (2011). Minério de Cu (Au) de alto teor em zonas de alteração clorítica em escarnitos magnesianos de Caçapava do Sul, RS. XIII Congresso Brasileiro de Geoquímica, CD-ROM: CGQ07_T16. Gramado: SBGq.

Remus, M. V. D., Hartmann, L. A., & Formoso, M. L. L. (1993). Os padrões de elementos terras raras (ETR) e a afinidade geoquímica komatiítica dos xistos magnesianos e rochas associadas do Complexo Cambaizinho, São Gabriel/RS. Revista Brasileira de Geociências. https://doi.org/10.25249/0375-7536.1993234370387

Remus, M. V. D.; Massonne, H.; Hartmann, L. ; Theye, T. ; Braetz, H. (2010) Garnet zonation and monazite ages as monitors of contrasting metamorphic evolution in the Brasiliano schist belts of Southern Brazil. 45 Congresso Brasileiro de Geologia.

Remus, M. V.D., Hartmann, L. A., McNaughton, N. J., Groves, D. I., & Fletcher, I. R. (2000). The link between hydrothermal epigenetic copper mineralization and the Cacapava Granite of the Brasiliano cycle in southern Brazil. Journal of South American Earth Sciences. https://doi.org/10.1016/S0895-9811(00)00017-1

Ribeiro, M. (1970). Geologia da folha de Bom Jardim: Rio Grande do Sul- Brasil. In: Boletim: Divisão de Geologia e Mineralogia. Brasília, vol. 247, pp. 1e142.

Ribeiro, M., Bocchi, P.R., Figueiredo-Filho, P.M. & Tessari, R.I. (1966). Geologia da quadrícula de Caçapava do Sul, RS, Brasil. Boletim da Divisão de Geologia e Mineralogia, DPM-DNPM, pp. 127-232.

Rock, N. M. S. (1991). Lamprophyres. Boston: Springer US. 285 pp. https://doi.org/10.1007/978-1-4757-0929-2

Saalmann, K., Gerdes, A., Lahaye, Y., Hartmann, L. A., Remus, M. V.D., & Läufer, A. (2011). Multiple accretion at the eastern margin of the Rio de la Plata craton: The prolonged Brasiliano orogeny in southernmost Brazil. International Journal of Earth Sciences. https://doi.org/10.1007/s00531-010-0564-8

Saalmann, K., Hartmann, L. A., & Remus, M. (2005a). Tectonic evolution of two contrasting schist belts in southernmost Brazil: A plate tectonic model for the Brasiliano orogeny. International Geology Review. https://doi.org/10.2747/0020-6814.47.12.1234

Saalmann, K., Hartmann, L. A., Remus, M. V.D., Koester, E., & Conceição, R. V. (2005b). Sm-Nd isotope geochemistry of metamorphic volcano-sedimentary successions in the São Gabriel block, southernmost Brazil: Evidence for the existence of juvenile Neoproterozoic oceanic crust to the east of the Rio de la Plata craton. Precambrian Research. https://doi.org/10.1016/j.precamres.2004.10.006

Saalmann, K., Remus, M. V.D., & Hartmann, L. A. (2005). Geochemistry and crustal evolution of volcano-sedimentary successions and orthogneisses in the São Gabriel block, southernmost Brazil - Relics of Neoproterozoic magmatic arcs. Gondwana Research. https://doi.org/10.1016/S1342-937X(05)71114-X

Santos, M. M., Lana, C., Scholz, R., Buick, I., Schmitz, M. D., Kamo, S. L., … Wiedenbeck, M. (2017). A New Appraisal of Sri Lankan BB Zircon as a Reference Material for LA-ICP-MS U-Pb Geochronology and Lu-Hf Isotope Tracing. Geostandards and Geoanalytical Research. https://doi.org/10.1111/ggr.12167

Sartori, P. L. P., & Kawashita, K. (1985). Petrologia e geocronologia do Batólito Granítico de Caçapava do Sul-RS. In II Simpósio Sul-Brasileiro de Geologia (pp. 102–115). Florianópolis, Brazil

Sartori, P.L.P. & Kawashita, K. (1989). Petrologia e geocronologia do stock granítico Santos Ferreira e sua correlação com o batólito de Caçapava do Sul, RS. Acta Geologica Leopoldensia XII (29), 131±142 IV Simpósio Sul-Brasileiro de Geologia, Porto Alegre, Brazil

Schoene, B., & Bowring, S. A. (2007). Determining accurate temperature-time paths from U-Pb thermochronology: An example from the Kaapvaal craton, southern Africa. Geochimica et Cosmochimica Acta, 71(1), 165–185. https://doi.org/10.1016/j.gca.2006.08.029

Seman, S., Stockli, D. F., & McLean, N. M. (2017). U-Pb geochronology of grossular-andradite garnet. Chemical Geology, 460(April), 106–116. https://doi.org/10.1016/j.chemgeo.2017.04.020

Sibson, R. H. (2000). Fluid involvement in normal faulting. Journal of Geodynamics, 29(3–5), 469–499. https://doi.org/10.1016/S0264-3707(99)00042-3

Silva-Filho, B. C., & Matsdorf, M. (1987). Análise estrutural dos metamorfitos da borda oeste do Granito Caçapava, Caçapava do Sul: implicações geológicas locais e regionais. In Atas do III Simpósio Sul-Brasileiro de Geologia. Curitiba, Brazil.

Silva, L. C., McNaughton, N. J., Armstrong, R., Hartmann, L. A., & Fletcher, I. R. (2005). The neoproterozoic Mantiqueira Province and its African connections: A zircon-based U-Pb geochronologic subdivision for the Brasiliano/Pan-African systems of orogens. Precambrian Research. https://doi.org/10.1016/j.precamres.2004.10.004

Skelton, A. D. L., Graham, C. M., & Bickle, M. J. (1995). Lithological and structural controls on regional 3-D fluid flow patterns during greenschist facies metamorphism of the Dalradian of the SW Scottish Highlands. Journal of Petrology, 36(2), 563–586. https://doi.org/10.1093/petrology/36.2.563

Sláma, J., Košler, J., Condon, D. J., Crowley, J. L., Gerdes, A., Hanchar, J. M., … Whitehouse, M. J. (2008). Plešovice zircon - A new natural reference material for U-Pb and Hf isotopic microanalysis. Chemical Geology. https://doi.org/10.1016/j.chemgeo.2007.11.005

Soliani, E. (1986). Os dados geocronológicos do escudo sul-rio-grandense e suas implicações de ordem geotectônica (Universidade de São Paulo). https://doi.org/10.11606/T.44.1986.tde-15072015-153916

Spear, F. S., & Pyle, J. M. (2002). Apatite, Monazite, and Xenotime in Metamorphic Rocks. Reviews in Mineralogy and Geochemistry, 48(1), 293–335. https://doi.org/10.2138/rmg.2002.48.7

Stacey, J. S., & Kramers, J. D. (1975). Approximation of terrestrial lead isotope evolution by a two-stage model. Earth and Planetary Science Letters. https://doi.org/10.1016/0012-821X(75)90088-6

Thompson, J., Meffre, S., Maas, R., Kamenetsky, V., Kamenetsky, M., Goemann, K., … Danyushevsky, L. (2016). Matrix effects in Pb/U measurements during LA-ICP-MS analysis of the mineral apatite. Journal of Analytical Atomic Spectrometry, 31(6), 1206–1215. https://doi.org/10.1039/c6ja00048g

Thomson, S. N., Gehrels, G. E., Ruiz, J., & Buchwaldt, R. (2012). Routine low-damage apatite U-Pb dating using laser ablation-multicollector- ICPMS. Geochemistry, Geophysics, Geosystems. https://doi.org/10.1029/2011GC003928

Tichomirowa, M., Käßner, A., Sperner, B., Lapp, M., Leonhardt, D., Linnemann, U., … Whitehouse, M. (2019). Dating multiply overprinted granites: The effect of protracted magmatism and fluid flow on dating systems (zircon U-Pb: SHRIMP/SIMS, LA-ICP-MS, CA-ID-TIMS; and Rb–Sr, Ar–Ar) – Granites from the Western Erzgebirge (Bohemian Massif, Germany). Chemical Geology, 519(February), 11–38. https://doi.org/10.1016/j.chemgeo.2019.04.024

UFRGS, Universidade Federal do Rio Grande do Sul (1998). Projeto Caçapava do Sul: geological mapping 1:25.000

Van Achterbergh, E., Ryan, C.G., Jackson, S.E. & Griffin, W.L. (2001). Data reduction software for LA-ICP-MS. In: Laser-Ablation-ICPMS in the Earth Sciences: Principles and Applications (ed. Paul, J.S.), pp. 239–243. Mineralogical Association of Canada, Ottawa, ON, Canada.

Whitney, D. L., & Evans, B. W. (2010). Abbreviations for names of rock-forming minerals. American Mineralogist, 95(1), 185–187. https://doi.org/10.2138/am.2010.3371

Wildner, W., Nardi, L. V. S., & Lima, E. F. (1999). Post-collisional alkaline magmatism on the Taquarembó Plateau: A well-preserved neoproterozoic–cambrian plutono-volcanic association in southern Brazil. International Geology Review, 41(12), 1082–1098. https://doi.org/10.1080/00206819909465193

Yardley, B. W. D., Rochelle, C. A., Barnicoat, A. C., & Lloyd, G. E. (1991). Oscillatory zoning in metamorphic minerals: an indicator of infiltration metasomatism. Mineralogical Magazine, 55(380), 357–365. https://doi.org/10.1180/minmag.1991.055.380.06

SUPPORTING INFORMATION

Additional Supporting Information may be found online in the supporting information tab for this article.

Description:

Table S1. Results of LA-ICP-MS zircon U–Pb analysis for M1 mafic apophysis (DB-G1Z sample)

Table S2. Results of LA-ICP-MS zircon U–Pb analysis for M1 felsic dyke (AP-01 sample)

Table S3. Results of LA-ICP-MS zircon U–Pb analysis for M2 felsic apophysis (DB-G2Z sample)

Table S4. Results of LA-ICP-MS titanite U–Pb analysis for M1 mafic apophysis (AT-Z-01 sample)

Table S5. Results of LA-ICP-MS apatite U–Pb analysis for M1 mafic apophysis (AT-Z-02 sample)

Table S6. Results of LA-ICP-MS apatite U–Pb analysis for M1 mafic apophysis (AT-Z-03 sample)

CAPÍTULO 3 – ARTIGO II

Metalamprophyres in the Dom Feliciano Belt: insights for the development of strike-slip tectonics and localized metamorphism during the post-collisional stage

RESEARCH PAPER

To: Precambrian Research

Metalamprophyres in the Dom Feliciano Belt: insights for the development of strike-slip tectonics and localized metamorphism during the post-collisional stage

Guilherme S. Hoerlle[a]; Marcus V. D. Remus[a]; Norberto Dani[a]

[a] Instituto de Geociências - Universidade Federal do Rio Grande do Sul, Porto Alegre, Brazil

Corresponding author:
Guilherme Sonntag Hoerlle
guilherme.hoerlle@ufrgs.br
Av. Bento Gonçalves, 9500
43126/110
Porto Alegre, RS, Brazil
Zip code: 90650-001

ABSTRACT

The oblique collision of the Congo, Kalahari, and Rio de la Plata cratons resulted in the formation of the Dom Feliciano Belt that evolved from rifting, drifting, and amalgamation between *ca.* 1.0 and 0.5 Ga. The post-collisional stage of the orogenic event (ca. 600 – 530 Ma) is marked by lithospheric scale shear-zones, voluminous magmatism, and volcano-sedimentary sequences. However, metamorphism, tectonic regimes, and the development of space-forming structures are still debated. We present the first comprehensive petrographic, mineralogical and geochemical study of Neoproterozoic metalamprophyres from the easternmost portion of the São Gabriel Terrane (central Dom Feliciano Belt, southern Brazil). We aimed at deciphering the relationship of the metalamprophyres with the Neoproterozoic magmatism, metamorphism, and transitions in the tectonic regimes during the post-collisional stage of the Dom Feliciano Belt. Metamafic dyke and sill swarms from two key areas surrounding the Caçapava do Sul Granitic Complex (578 – 557 Ma) show indications of a lamprophyre protolith such as (i) sheeted emplacement mode; (ii) Ti-rich amphibole and clinopyroxene phenocrysts in a feldspathic groundmass; (iii) high Mg, Cr, Ni, Co contents; (iv) high LREE and lower HREE patterns and (v) Cr-rich biotite. The metalamprophyres from the different areas show distinct microstructures and whole-rock chemistry as a result of heterogeneous metamorphism, deformation, and metasomatism controlled by the distance to the granitic intrusion and high-strain domains. Low-grade metamorphism preserved Ti-rich amphibole and clinopyroxene phenocrysts in a feldspathic groundmass within metalamprophyre dykes located further away from the batholith. Medium to high-grade metamorphism, metasomatism, and deformation partially destroyed lamprophyre diagnostic features in the metalamprophyres adjacent to the main intrusion of the granitic complex. We propose that the lamprophyre intrusions represent markers of the development of a deep-rooted shear zone during the shift from an extensional to a transpressive regime influenced by K-rich metasomatism of the upper mantle. The shift in the tectonic regime marked by the lamprophyres may represent a missing link in the space-forming tectonics in the Camaquã Basin. Additionally, we interpret that the metamorphism and deformation during the post-collisional stage are controlled by the proximity to the granitic intrusions and shear-zones.

Keywords: Lamprophyre; Southwestern Gondwana; Dom Feliciano Belt; São Gabriel Terrane; Neoproterozoic; Post-collisional

1. INTRODUCTION

The Neoproterozoic Brasiliano-Pan-African orogenic cycle was responsible for the assembly of the Western Gondwana represented in southern Brazil by the Dom Feliciano Belt (DFB) (Fernandes *et al*., 1992; Basei *et al*., 2000; Chemale, 2000; Hartmann *et al*., 2000; Chemale *et al*., 2012; Philipp *et al*., 2016). The oblique collision of the Congo, Kalahari, and Rio de la Plata cratons resulted in the formation of the Dom Feliciano Belt that evolved from rifting, drifting, and amalgamation between 1.0 and 0.5 Ga (Fernandes *et al*., 1992; 1995; Basei *et al*., 2000; Chemale, 2000; Hartmann *et al*., 2007; Philipp *et al*., 2016). During the orogenic event, the mobile belt and associated Precambrian domains were affected by complex sets of shear zones formed during the collision and at post-collisional stages (Tommasi *et al*., 1994; Passarelli *et al*., 2011; Chemale *et al*., 2012; Hueck *et al*., 2018). In particular, the post-collisional stage of the Dom Feliciano Belt (~600 – 530 Ma) is marked by lithospheric scale shear-zones (*e.g.*, Fernandes *et al*., 1992; Tommasi *et al*., 1994; Chemale *et al*., 2012), voluminous magmatism (*e.g.* Philipp *et al*., 2002; Gastal *et al*., 2006; Nardi and Bitencourt, 2007) and volcano-sedimentary sequences of the Camaquã Basin (*e.g.*, Chemale, 2000; Paim *et al*., 2000; Oliveira *et al*., 2014). However, the tectonic regimes and transitions between extensional and transcurrent settings in the post-collisional stage of the DFB are widely debated (*e.g.*, Passarelli *et al*., 2011; Almeida R.P. *et al*., 2012; Oliveira *et al*., 2014; Hueck *et al*., 2019). In this contribution, we use field relationships, geochemical data, and petrographic observations to propose that lamprophyres and their metamorphic equivalents can be used as tectonic markers of the transition from extension to transpression in the easternmost portion of the São Gabriel Terrane, central Dom Feliciano Belt.

Lamprophyres are minor sheeted intrusions rich in volatiles with biotite, amphibole, or clinopyroxene phenocrysts in a feldspathic groundmass (Rock, 1991; Le Maitre *et al*., 2002). They are tabular hypabyssal rocks (*i.e.*, dykes and sills) typically interpreted to have formed from partial melting of the metasomatized mantle (*e.g.*, Bachinski and Scott, 1979; Schulze *et al*., 1985; Rock, 1991; Bédard, 1994, Soder and Romer, 2018). The emplacement of lamprophyres is commonly associated with extensional or strike-

slip movements (*e.g.*, Vaughan, 1996; Vaughan and Scarrow, 2003; Cao *et al*., 2011; Martina *et al*., 2018) and are often used as markers of changes in geodynamic regimes (*e.g.*, Scarrow *et al*., 2011; Casetta *et al*., 2019). In particular, lamprophyres associated with calc-alkaline plutons typically occur as enclaves, dyke swarms radiating from or cutting the plutons, or clusters of pipes immediately surrounding larger intrusive bodies (Rock, 1991). Despite their genetic and geodynamic implications, they are sometimes neglected in the studies of large igneous bodies (*i.e.*, granitic batholiths) mainly because of the relatively small volume of these intrusions (Perring and Rock, 1991). Furthermore, post-emplacement metamorphic, tectonic and metasomatic alteration effects may hinder the identification of a mafic dyke or sill as an original lamprophyre. Despite some proposals of criteria for recognizing metamorphosed lamprophyres (*e.g.*, Perring *et al*., 1989; Mathieu *et al*., 2018), the recognition of a metalamprophyre is not a simple task as many features diagnostic for lamprophyres are prone to destruction during metamorphism. The recognition is even more complicated if metamorphism is synchronous with deformation and associated with significant chemical changes. As a result, many metalamprophyres are more likely to be described in the literature as metadiabases, metadiorites, or amphibolites leading to misinterpretation of their tectonic significance (Perring *et al*., 1989; Rock, 1991).

Mafic dyke and sill swarms intrude the Passo Feio Complex (PFC) which itself is located in the easternmost portion of the São Gabriel Terrane (Fig. 1b-c). Notably, two areas in the PFC have extensive exposures of composite, mafic, and felsic sheeted swarms (AP and MD areas; Fig. 1c). Despite the distinct mineral assemblages and textures, these tabular intrusions were recently correlated based on field relationships and zircon, apatite, and titanite U-Pb geochronology (Hoerlle *et al*., 2021). In addition, the mafic intrusions are younger than the PFC amphibolite sequence and were considered atypical metabasic rocks (Bicalho *et al*., 2019; Hoerlle *et al*., 2021). Preliminary petrogenetic interpretations were proposed by Hoerlle *et al*. (2021) based on field relationships and petrographic observations: (i) metamorphism of a lamprophyre protolith with limited and localized chemical changes or (ii) a basaltic protolith with significant metasomatic changes. Moreover, recent findings of sheeted carbonatite intrusions intercalated with biotite- and amphibole-rich mafic rocks in the PFC indicated the presence of alkaline-rich magmas, rich in volatiles and probably with significant mantellic contribution (Cerva-Alves *et al*., 2017). However, the origin and

geodynamic significance of the sheeted mafic intrusions (and carbonatite bodies) in the PFC are still poorly understood. In this study, we provide bulk-rock and mineral chemistry data in combination with field and petrographic interpretations of metamafic dykes and sills emplaced in the easternmost portion of the São Gabriel Terrane (Fig. 1a-c) to propose a lamprophyre origin and an analysis of their tectonic significance for the post-collisional stage of the DFB.

2. GEOLOGICAL SETTING

The Dom Feliciano Belt (DFB) is the result of the Neoproterozoic collision between Congo, Kalahari, and Rio de la Plata cratons and it evolved from rifting to amalgamation and collapse from *ca.* 900 to *ca.* 540 Ma (Fernandes *et al*., 1995; Basei *et al*., 2000; Chemale, 2000; Philipp *et al*., 2016; Hueck *et al*., 2018). The evolution of the Rio Grande do Sul sector of the DFB (Fig. 1a-b) is represented by three main geotectonic events including the Passinho event (~879 Ma), the São Gabriel event (~767-675 Ma), and the Dom Feliciano event (~650-600 Ma) (Saalmann *et al*., 2011; Gubert *et al*., 2016; Hueck *et al*., 2018; Cerva-Alves *et al*., 2020). The studied metamafic dykes and sills intruded the Passo Feio Complex (PFC), located in the easternmost portion of the juvenile São Gabriel Terrane (Fig. 1b-c).

2.1. PASSO FEIO COMPLEX

The Passo Feio Complex (PFC) consists of a supracrustal association of Neoproterozoic metapelites, amphibolites, marbles, calc-silicate and metavolcanic rocks intruded by the Caçapava do Sul Granitic Complex (CSGC) (Leinz *et al*., 1942; Ribeiro *et al*., 1966; Bitencourt, 1983; Hartmann *et al*., 1990; Remus *et al*., 2000a). It has been considered to represent a passive margin sequence (Fragoso-César, 1991) or a back-arc sequence (Fernandes *et al*., 1992). There is a consensus that the PFC records at least two main metamorphic events. The first one varies from greenschist to amphibolite facies (staurolite zone) associated with regional metamorphism while the second is linked to the thermal effect of the intrusion of the CSGC reaching upper amphibolite facies near the contact with the granitic body (Leinz *et al*., 1941; Ribeiro *et al*., 1966; Ribeiro, 1970; Silva-Filho and Matsdorf, 1987; Bortolotto, 1988; Hoerlle *et al*., 2021). The second event has been also related to a second regional metamorphic event reaching greenschist facies (Bitencourt, 1983; Hartmann *et al*., 1990). Zircon

provenance studies in metapelites and schists revealed Archean, Paleoproterozoic, and Neoproterozoic populations with an estimated maximum depositional age of 774 Ma (Remus *et al*., 2000a; Lopes *et al*., 2015; Souza, 2020). In addition, chemostratigraphy dating of the dolomitic marbles was used to suggest that carbonate deposition occurred in the interval between 770 and 730 Ma (Goulart *et al*., 2013). The age of the first metamorphic event was inferred from monazites of pelitic schists that yielded U-Pb ages between 650 and 620 Ma (Remus *et al*., 2010). The age of the second metamorphic event was linked to the ages of the multi-stage intrusion of the CSGC which occurred between *ca.* 578 Ma and *ca.* 557 Ma (Remus *et al*., 2000a; Hoerlle *et al*., 2021).

2.2. THE CAMAQUÃ BASIN AND POST-COLLISIONAL MAGMATISM IN THE SÃO GABRIEL TERRANE

The Camaquã Basin (CB) corresponds to the late- to post-collisional basinal cycles of the Dom Feliciano Belt (*e.g.* Chemale, 2000; Paim *et al*., 2000). The CB is formed by the superposition of several basin cycles divided by distinct structural and lithological characteristics. It consists of four main units (from the base to the top): Maricá Formation, Bom Jardim Group, Santa Bárbara Group, and Guaritas Group. Three main cycles were proposed in different tectonic settings: a retroarc foreland setting (~601 – 593 Ma; Maricá Formation), a strike-slip setting (~593 – 580 Ma; Bom Jardim Group), and a transtensional rift setting (~574 – 473 Ma; Santa Bárbara and Guaritas groups) (Paim *et al*., 2000; Chemale, 2000; Bicca *et al*., 2013; Oliveira *et al*., 2014; Paim *et al*., 2014). Notably, the Camaquã Basin hosts several Cu-Pb-Zn (Au, Ag) base-metal deposits that have been explored since the 19th century, mainly in the Bom Jardim and Santa Bárbara Groups (*e.g.* Remus *et al*., 2000b; Laux *et al*., 2005; Fontana *et al*., 2017). Concomitant to the CB, the late to post-collisional stage of the DFB is marked by lithospheric scale shear-zones (*e.g.*, Fernandes *et al*., 1992; Tommasi *et al*., 1994; Chemale *et al*., 2012) and alkaline, shoshonitic, and calc-alkaline magmatism from *ca.* 610 to 540 Ma (*e.g.* Lima and Nardi, 1998; Sommer *et al*., 2005, 2006, 2017; Gastal *et al*., 2006; Nardi and Bitencourt, 2007; Janikian *et al*., 2012). The volcanic units of the CB are mainly represented by the andesitic shoshonitic rocks of the Hilário Formation (593- 580 Ma) (Nardi and Lima, 1985; Remus *et al*., 1999; Janikian *et al*., 2008) succeeded by the bimodal volcanism of the Acampamento Velho Formation

(579-549 Ma) (Ribeiro and Fantinel, 1978; Sommer *et al*., 2005, 2017; Janikian *et al*., 2012; Matté *et al*., 2016, 2021). Remarkably, the age of the studied mafic-felsic dyke swarms of *ca.* 578 Ma (Hoerlle *et al*., 2021) overlaps with the lower and upper age limits of the Hilário and Acampamento Velho formations.

At the easternmost portion of the SGT, the plutonic post-collisional magmatism is represented by the Caçapava do Sul Granitic Complex (CSGC; Fig. 1c). The CSGC consists of a granitic batholith and tabular apophyses that intruded the PFC between *ca.* 578 Ma and 562 Ma composed of granodiorites, monzogranites, leucogranites, minor diorites, tonalites, and quartz-diorites of metaluminous and calc-alkaline affinity (Leinz *et al*., 1941; Ribeiro *et al*., 1966; Sartori and Kawashita, 1985; Nardi and Bitencourt, 1989; Remus *et al*., 2000a; Hoerlle *et al*., 2021).

3. SAMPLE SELECTION AND METHODS

Sample collection was carried out at two key areas with extensive exposures of mafic dykes and sills that intrude the PFC, aiming at obtaining representative samples for petrographic and geochemical analyses. The two key areas comprise the marble mining district of Caçapava do Sul (MD area) in the eastern portion of the PFC and the Arroio das Pedras areas (AP area) located in the northernmost portion of the PFC (Fig. 1c). MD area is located near the contact of the granitic body and the PFC (ca. 100 to 1000 meters of the contact) whereas the AP area is situated approximately five kilometers away from the contact.

Petrographic analyses were made using a LEICA DM4500 optical microscope and a LEICA S6D Greenough stereo microscope to identify major constituent minerals and textures. Whole-rock major, minor, and selected trace elements were analyzed using a Rigaku RIX 2000 X-ray fluorescence spectrometer (XRF) at the X-ray fluorescence laboratory of the Rio Grande do Sul Federal University (UFRGS). Additional whole-rock geochemical analyses were carried out at SGS GEOSOL Lab using inductively coupled plasma optical emission spectroscopy (ICP-OES) for major, minor, and some trace elements (Ba, V, Zn, Sr, Zr), whereas other trace and rare-earth elements (REE) were measured using inductively coupled plasma mass spectrometry (ICP-MS) methods. Loss on ignition (LOI) was determined by weighting the difference after ignition at 450 °C and 1000 °C.

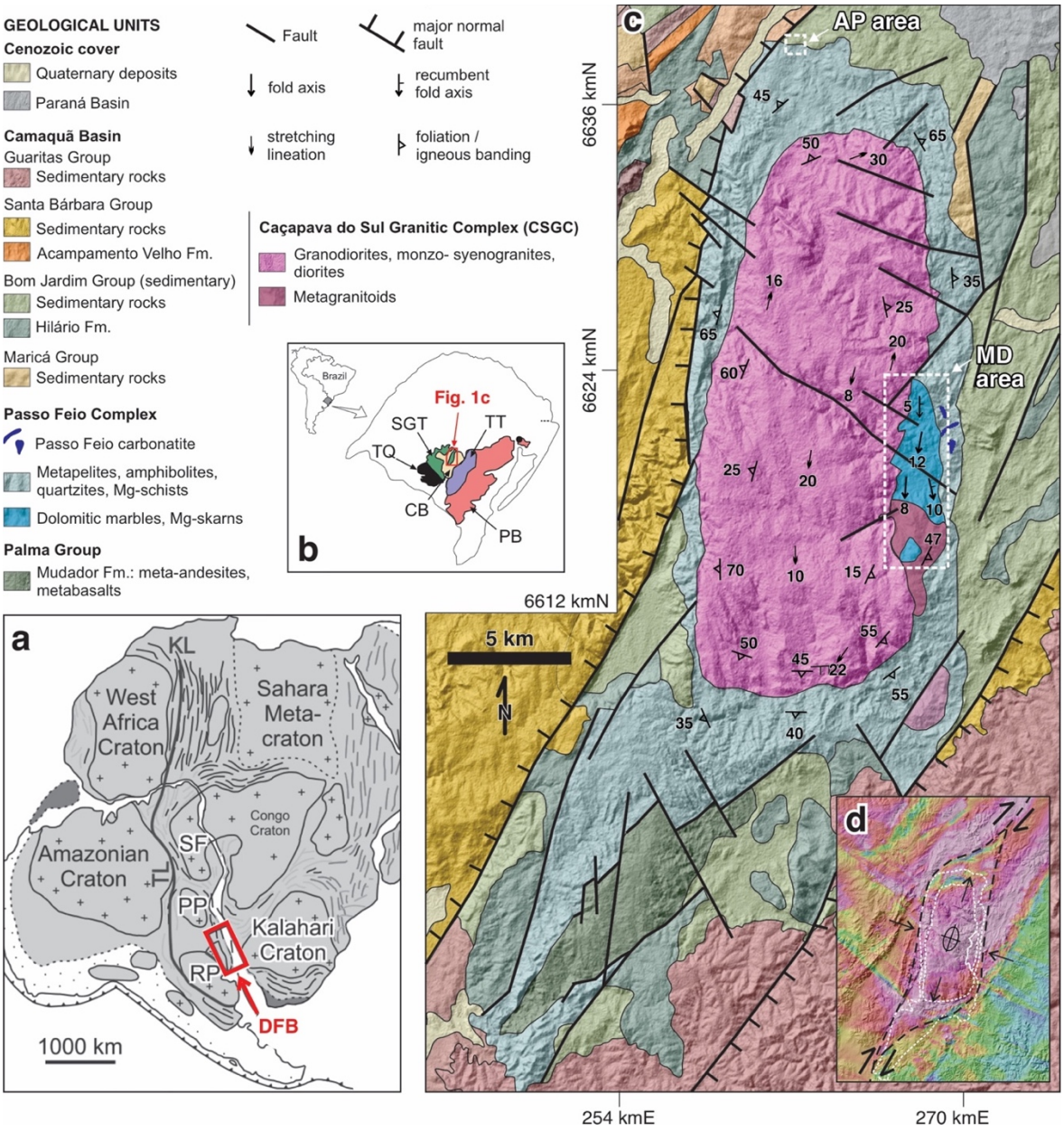

Figure 1: Location of the Caçapava do Sul Granitic Complex and Passo Feio Metamorphic Complex in the Sul-riograndense shield, southern Brazil. a) Location of the Dom Feliciano Belt (DFB) in the Western Gondwana map (RP: Rio de la Plata craton; PP: Paranapanema block, SF: São Francisco craton; KL: Kandi lineament; TL: Transbrasiliano lineament). b) Tectonic domains of the Sul-riograndense Shield (TT: Tijucas Terrane; SGT: São Gabriel Terran; PB: Pelotas Batholith; CB: Camaquã Basin; TQ: Taquarembó Craton). c) Geological map of the Passo Feio Metamorphic Complex and Caçapava do Sul Granitic Complex area showing AP and MD areas location (Modified from UFRGS, 1998 and Porcher and Lopes, 2000); d) Magnetometry and shaded relief map of the Caçapava do Sul region showing plane sigmoidal shape structure surrounding CSGC and PFC (CPRM, 2010).

The measurement of mineral compositions and backscattered electron imaging (BSE) were carried out on selected samples using a CAMECA SXFive electron microprobe

(EMPA) at the Electron Microprobe Laboratory at UFRGS and a JEOL JXA 8900 at the Electron Microprobe Laboratory at the Georg-August-Universität Göttingen. Analytical conditions were 15 nA beam current and 5 μm beam size at 15 kV accelerating voltage. Natural and synthetic materials were used as standards. Mineral chemistry analyses are presented in Table S2. Mineral abbreviations in the figures and text were follow Whitney and Evans (2010).

4. RESULTS

4.1. LOCAL GEOLOGY AND FIELD RELATIONSHIPS

4.1.1. Arroio das Pedras area

The Arroio das Pedras area (AP) is located in the northernmost portion of the PFC (Fig. 1) and comprises well-exposed dyke swarms along a creek. Two groups of dykes were defined for simplification purposes based on field aspects: mafic (APm) and felsic (APf) dykes. The mafic and felsic dykes show complex, often mutual cross-cutting relationships (Fig. 2a-c). The whole dyke swarm is sub-vertical with NE-SW orientation. The felsic dykes (APf) are holocrystalline porphyritic rocks and show light-gray altered surface in the field (Fig. 2a-b). Zircon U-Pb LA-ICP-MS dating yield an age of 578.1±3.5 Ma for an APf dyke cut by mafic dykes that was interpreted to represent the approximate age of the whole bimodal dyke swarm (Hoerlle *et al*., 2021). The mafic dykes (APm) generally form sharp contacts with the felsic dykes (Fig 2a-c). The APm dykes are porphyritic with amphibole and clinopyroxene phenocrysts in a felsic groundmass. The whole sequence of mafic and felsic dykes was affected by NW-SE vertical faulting and fracturing that are often filled by albite or carbonate veins (Fig 2a-b).

4.1.2. Marble district area

The marble district area (MD) comprises thick lenticular bodies of dolomitic marbles that were extensively intruded by mafic and felsic apophyses and less commonly by irregularly shaped bodies of granites, pegmatites, and aplites (Fig. 2d). The marbles are located to the east of the main granitic batholith, which itself outcrops as an N-S elongated asymmetrical domal structure dipping in high angles in the W and NW parts, in low angles in the E and SE parts, and sub-horizontally in the central parts of the

granitic body (Leinz *et al*., 1941; Ribeiro *et al*., 1966; Sartori and Kawashita, 1985; Nardi and Bitencourt, 1989). For simplification purposes, Hoerlle *et al*. (2021) grouped the apophyses that intrude the marbles based on field aspects such as thickness, emplacement mode (*i.e.*, concordant; discordant), cross-cutting relationships, and structures. In this study, the MD metamafic rocks are equivalent to the M1 mafic apophyses classified by Hoerlle *et al*. (2021). The M2 felsic intrusions will be addressed as thicker felsic apophyses and as the main facies of the CSGC. We note that the main facies of the CSGC has been extensively described previously by Sartori and Kawashita (1985) and Nardi and Bitencourt (1989) and we refer to these contributions for more details that are beyond the scope of this contribution.

The MD metamafic rocks comprise sheeted intrusions with very little to moderate thickness (~0.1 to 1 m) that intruded the marbles parallel to the metamorphic foliation (S1 described by Nardi and Bitencourt, 1989 and Hoerlle *et al*., 2021) and were folded accordingly (Fig. 2d-f). The host rocks and the MD metamafic rocks form overturned to recumbent isoclinal folds with N-S to NE-SW axis that plunges at low angles mostly to the S-SW. The average axial surface dips approximately 20° to the east, locally varying to sub-horizontal or rarely dipping westward at low angles and mark the S2 foliation detailed in previous works (*e.g.*, Nardi and Bitencourt, 1989; Remus *et al*., 2000a; Hoerlle *et al*., 2021).

In general, the metamafic rocks occur as medium-grained rocks, strongly foliated (Fig. 2f), and show high contents of hydrous mafic minerals (~ 40 to 80% of biotite + amphiboles). This is equally reflected in atypical whole-rock compositions with high contents of MgO, K_2O, and Cr_2O_3 (see Section 4.4.2). Even though these rocks are characterized as metabasic rocks (sensu lato), their composition and structural response are distinct from typical metabasalts. The behavior of the metamafic rocks during deformation is closer to a foliated pelitic schist than to a massive metabasalt. In addition, magnesian calc-silicate assemblages are common in the apophysis-marble interfaces (*i.e.*, endo- and exoskarns) or occurring as lenses near these bodies (Fig. 2f). These skarns record multiple fluid flux events associated with the emplacement and cooling of the mafic rocks and subsequent intrusions of the main facies of the CSGC (Hoerlle *et al*., 2021). Elongate and foliated metamafic enclaves are common in the porphyritic bt-granodiorite sills (Fig. 2g). The foliation of the metamafic enclaves is concordant with the foliation of the host bt-granodiorite sill.

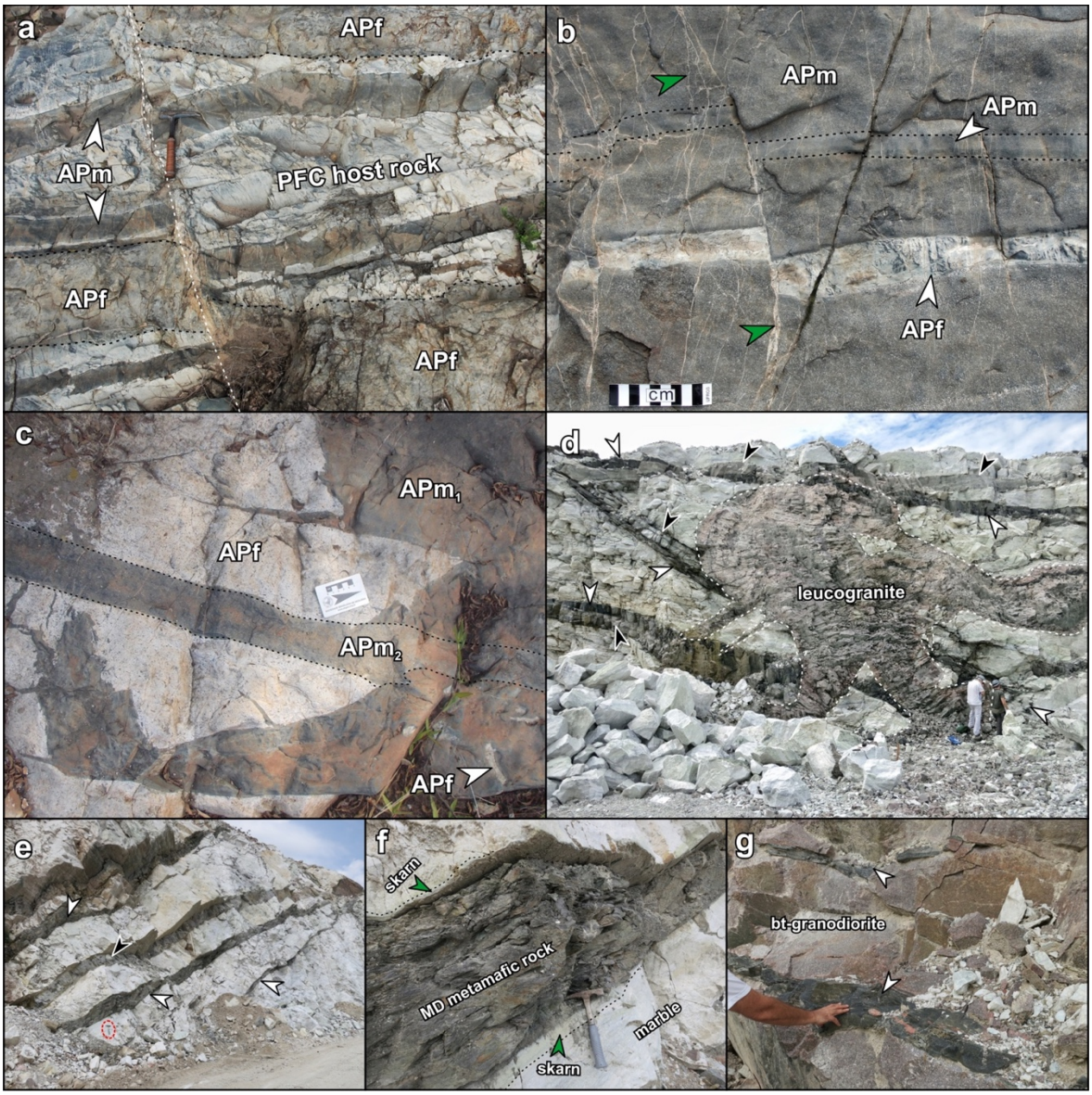

Figure 2: Field aspects of the AP (a-c) and MD areas (d-g). a) Field relationships of the AP dykes showing parallel APf and APm dykes cutting the PFC host rocks; outcrop top view; note vertical faulting; hammer for scale. b) Faulted APf dyke cutting APm; note abundant carbonate and albite veinlets. c) Composite mafic-felsic dyke (APf + APm1) cut by mafic dyke (APm2); top-view; 5 cm scale; d) Folded metamafic sills cut by a leucogranite apophysis of the CSGC (white arrows: basic to ultrabasic compositions; black arrows: intermediate compositions). e) metamafic rocks parallel to S1 marble foliation (white arrows: basic and ultrabasic compositions; black arrow: intermediate composition); note hammer as scale. f) MD metamafic sill bordered by thin contact skarns (di+fo+cal). g) MD metamafic enclaves (white arrows) in a bt-granodiorite sill of the CSGC.

4.2. WHOLE-ROCK GEOCHEMISTRY

Whole-rock geochemical analyses were performed on MD metamafic rocks and AP mafic and felsic dykes. The analyses are displayed in the Table S1 of the supplementary material. Published whole-rock geochemistry data of five dykes from the AP area from Bicalho *et al*. (2019) were added to the geochemical plots for comparison.

4.2.1. Arroio das Pedras dykes

The felsic dykes (APf) have an intermediate composition (~56-60 wt% SiO_2) while mafic dykes (APm) vary from basic to ultrabasic compositions (~43-47 wt% SiO_2). According to the TAS classification of Le Maitre *et al*. (2002), the APm dykes are chemically classified as picro-basalt and basalt whereas APf dykes plot in the basaltic-andesite and andesite fields. K/Na ratios for the APf dykes are below 0.5 whereas the APm show ratios near 1. Notably, the APm dykes show high Cr, Co, and Ni contents (~1000, 60, and 375 ppm, respectively). The bivariate plots for major and minor elements show mostly linear trends for the set of dykes (Fig. 3). Chondrite normalized REE patterns show fractionated La_N/Yb_N values (Fig. 5c).

4.2.2. Marble district metamafic rocks

The metamafic rocks of the MD area show a wide range of compositions from ultrabasic to intermediate compositions (37.01 to 61.39 wt% SiO_2) including large variations on K_2O 0.72 - 10.23 wt%; MgO 1.58 - 20.79 wt% and CaO 0.39 - 9.32 wt% (Figs. 3-4). The K/Na ratios for these samples vary widely from 0.4 to 24. The chromium contents range from 58 ppm in the intermediate compositions to 1538 ppm in the ultrabasic ones. Cobalt varies from ~30 to 50 ppm whereas nickel contents range from 90 to 590 ppm. Harker-type bivariant diagrams show poorly defined trends or no trend at all for most of the major elements (Figs. 3-4). In general, MgO, K_2O, and P_2O_5 in the MD metamafic rocks are much higher than the AP dykes whereas Fe_2O_3, MnO, CaO, and NaO are lower. Chondrite normalized multi-element patterns show negative Sr and Nd anomalies and negative Ti for the enriched samples (Fig. 5b). REE patterns show fractionated La_N/Yb_N, similar to the AP dykes and typical lamprophyre patterns (Fig. 5c).

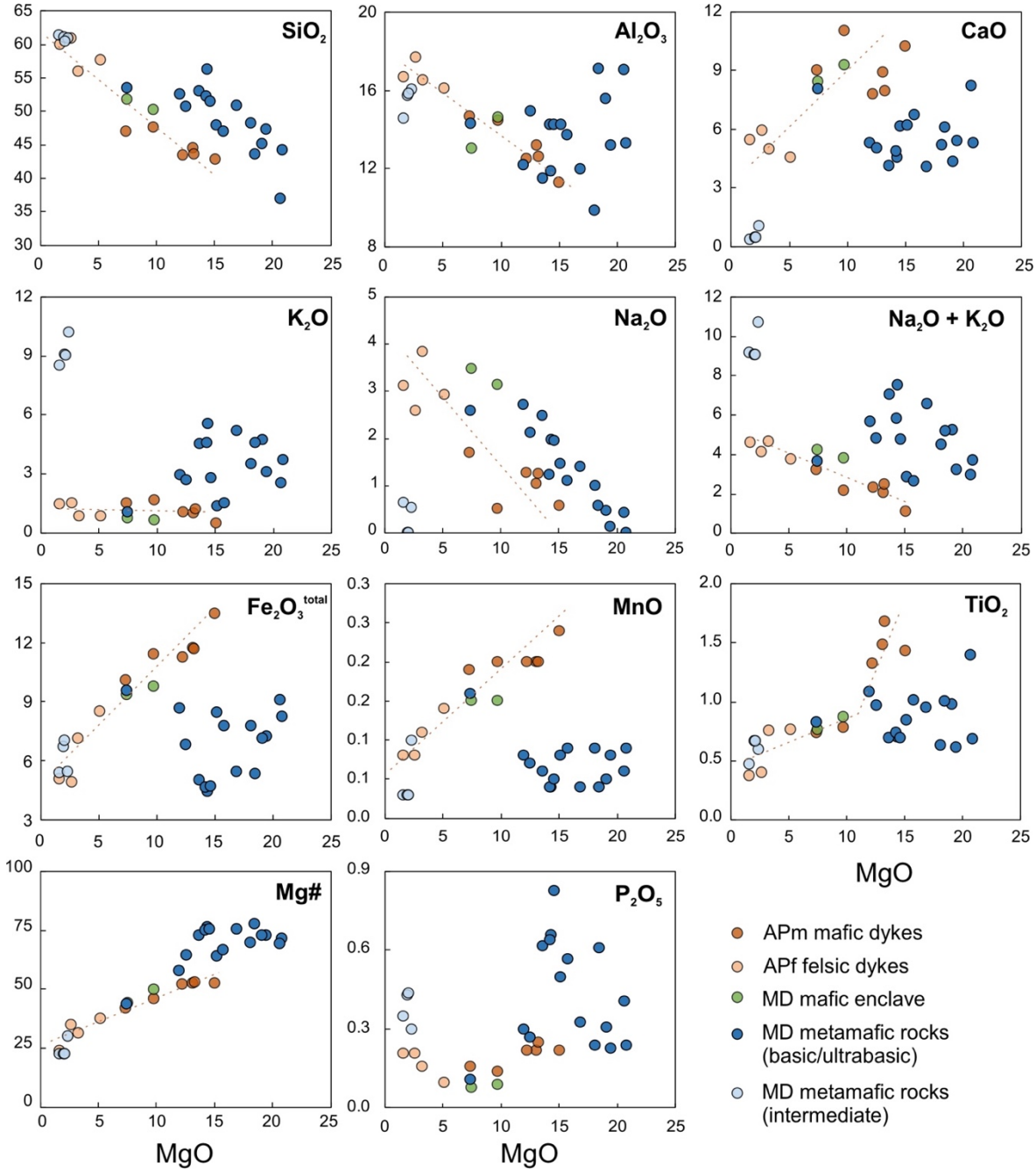

Figure 3: Bivariate plots of MgO versus major and minor components of AP dykes and MD metamafic rocks; Mg# = MgO/MgO+Fe_2O_{3tot}.

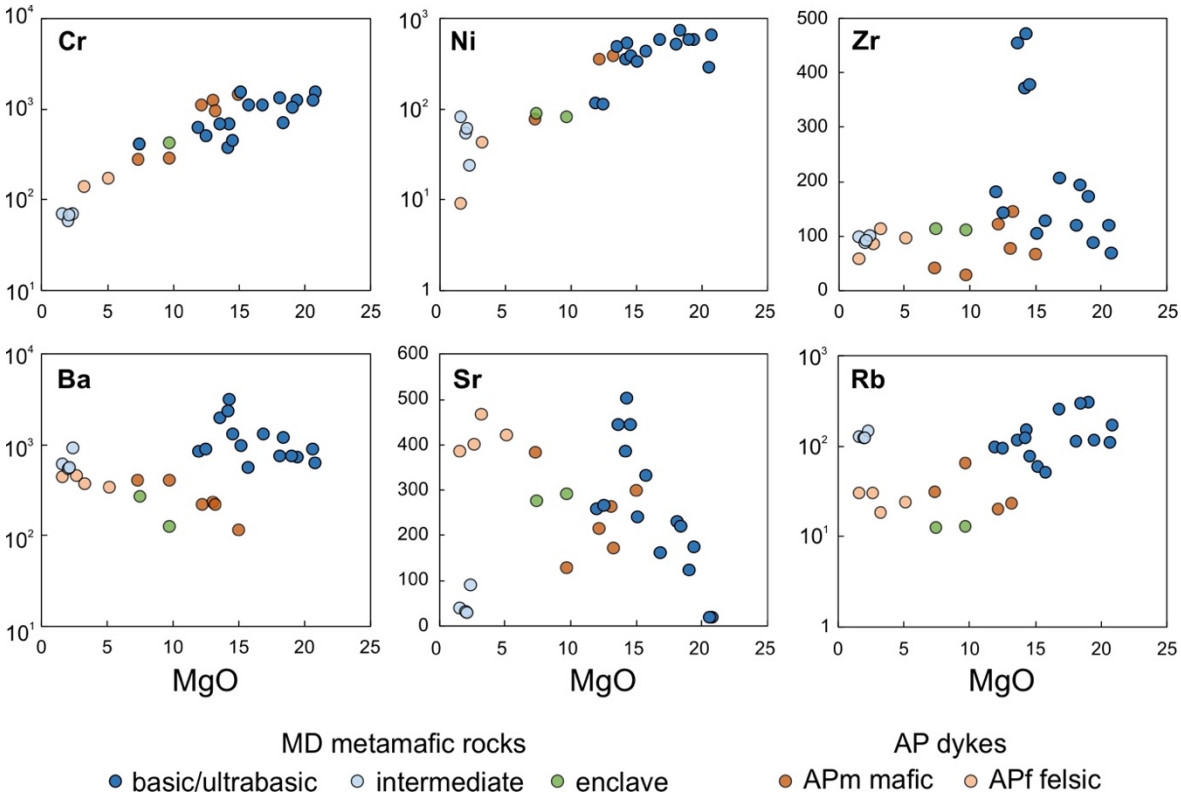

Figure 4: Bivariate plots of MgO versus selected trace elements of MD metamafic rocks and AP dykes.

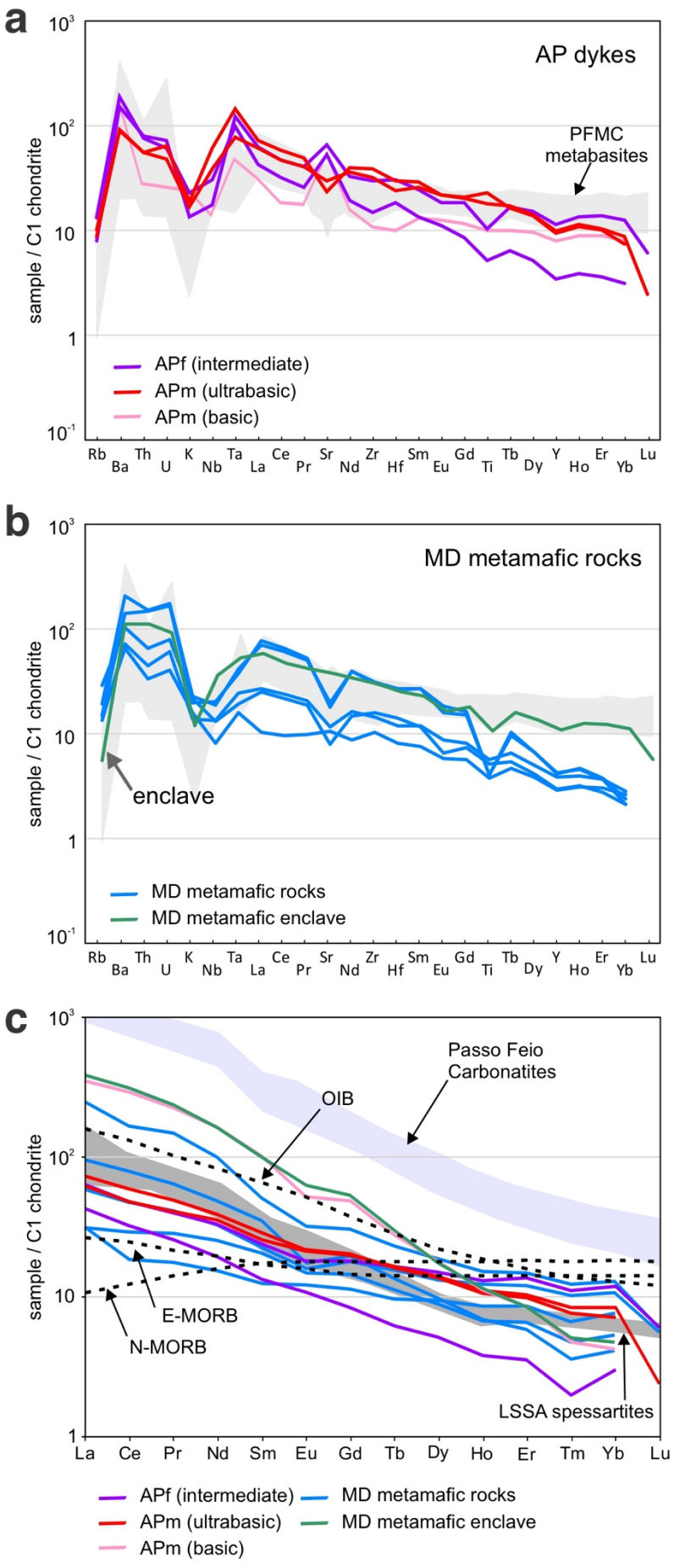
a
AP dykes
PFMC
metabasites
sample / C1 chondrite
APf (intermediate)
APm (ultrabasic)
APm (basic)
b
MD metamafic rocks
enclave
MD metamafic rocks
MD metamafic enclave
c
Passo Feio
Carbonatites
OIB
E-MORB
N-MORB
LSSA spessartites
APf (intermediate)
APm (ultrabasic)
APm (basic)
MD metamafic rocks
MD metamafic enclave

Figure 5: Chondrite normalized multi-element diagram for the (a) AP dykes and (b) MD metamafic rocks. Light-gray field for metabasites from Bicalho *et al*. (2019). c) REE chondrite normalized diagram for AP dykes and MD metamafic rocks (purple field: Passo Feio Carbonatites from Cerva-Alves *et al*., 2017; gray field: LSSA spessartites from Lima and Nardi (1998); N-MORB, E-MORB and OIB values from Sun and McDonough (1989).

4.3. MINERAL ASSEMBLAGES AND MICROSTRUCTURES

4.3.1. Arroio das Pedras dykes

The felsic dykes (APf) show two main petrographic facies where one is represented by phenocrysts of rounded quartz and subhedral hornblende partly or fully replaced by actinolite and chlorite (Fig. 6a). The matrix is composed of fine to medium-grained K-feldspar and plagioclase, being the latter almost fully sericitized. Embayment structures in the quartz phenocrysts and chlorite and actinolite marking the breaking down of hornblende are common (Fig. 6a). This facies is classified as a metadacite. The other facies is porphyritic with elongate prismatic actinolite (after hornblende phenocrysts) with no preferred orientation embedded in a groundmass composed of plagioclase and K-feldspar (Fig. 6b). The amphiboles are partially to fully replaced by chlorite and the feldspars are sericitized. This facies is classified as a meta-andesite.

The mafic dykes (APm) are fine- to medium-grained inequigranular rocks dominantly made of clinopyroxene, amphiboles, chlorite, and plagioclase. Despite being chemically classified as picro-basalts or basalts, these rocks have no olivine relics or pseudomorphs. The pyroxene content is composed of subhedral to euhedral augite and diopside, partly or fully replaced by randomly oriented actinolite ± chlorite (Fig. 6c-d). Subhedral to short prismatic brown to reddish-brown hornblende and kaersutite are common bordering clinopyroxene pseudomorphs or occurring as isolated crystals in a fine-grained plagioclase matrix (Fig. 6c-d). Hornblende and kaersutite are partially replaced by actinolite ± chlorite.

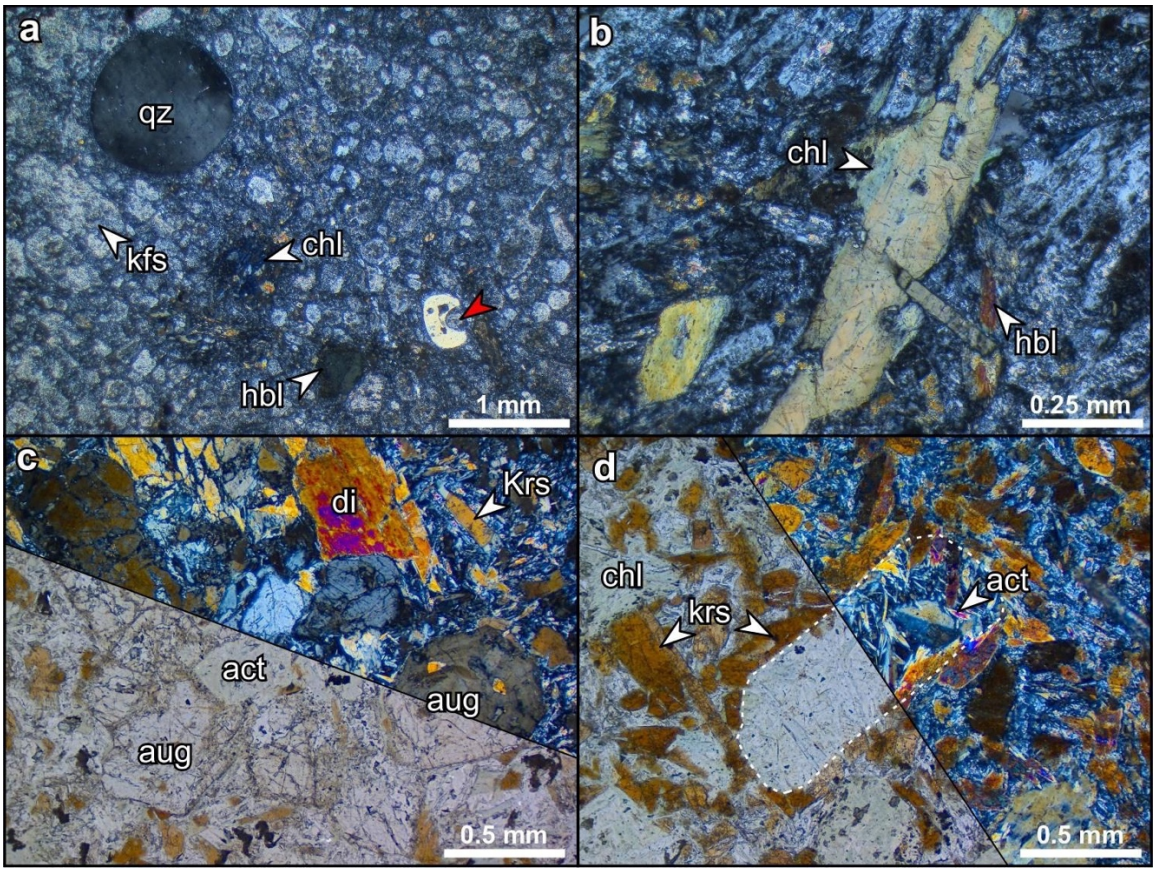

Figure 6: AP dykes microstructures. a) meta-dacite, note quartz embayment (red arrow), cross-polarized light (XPL); b) meta-andesite, chlorite partially replacing amphibole; XPL. c) metamafic dyke; XPL and PPL. d) Actinolite and chlorite replacing clinopyroxene (dashed white line) in metamafic dyke; note the kaersutite crystals surrounding the clinopyroxene pseudomorph; PPL and XPL.

4.3.2. Marble district metamafic rocks

The MD metamafic rocks show heterogeneity in mineral assemblages and microstructures despite that their field aspects are somewhat homogeneous. They are composed of variable amounts of calcic amphibole + biotite + plagioclase ± K-feldspar ± clinopyroxene ± quartz + titanite + apatite ± pyrite ± chlorite (Fig. 7a-i). All samples show amphibole, biotite, and plagioclase at variable proportions, whereas the total amount of biotite + amphibole in the samples reaches up to 80%. Most samples with well-developed foliation composed of amphibole, biotite, and plagioclase are not banded. However, some samples show compositional banding with biotite-rich bands and quartz-feldspathic ± amphibole layers. In such cases, bands are not continuous and show irregular endings (Fig. 7b). In general, the MD metamafic rocks show granoblastic (Fig. 7a-c) to lepidoblastic textures (Fig. 7f-h) that vary with the mineral

assemblages and mineral proportions. We note that samples with higher biotite and amphibole contents often show lepidoblastic and nematoblastic textures with closely spaced foliation marked by the preferred orientation of these minerals (Fig. 6g), whereas samples with lesser amounts of hydrous minerals tend to be granoblastic with a weaker preferred orientation of the micas and amphiboles (Fig. 7a).

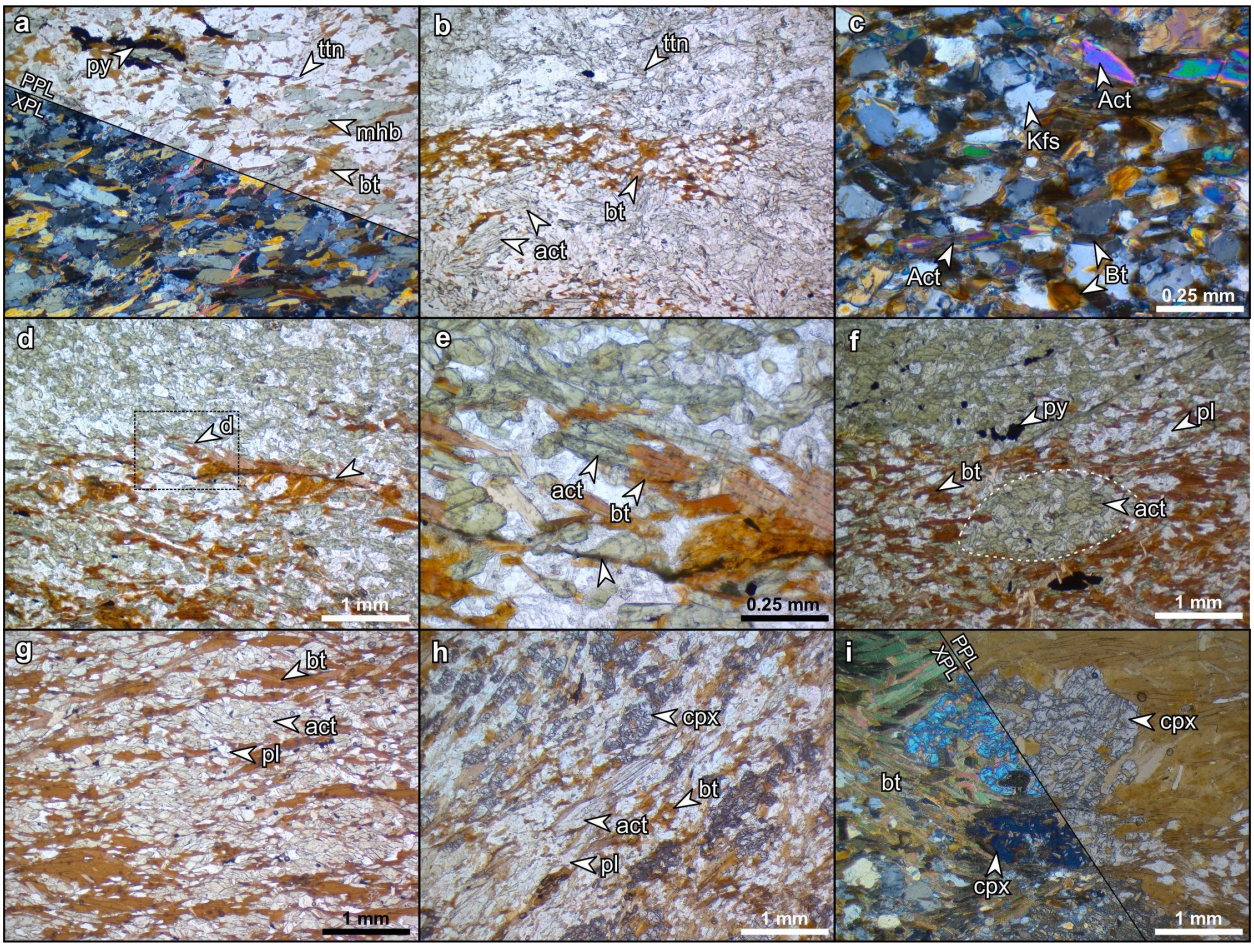

Figure 7: MD metamafic rocks' microstructures. a) mhb-kfs-pl-bt metamafic rock with granoblastic texture b) Irregular biotite rich band in act-pl-kfs metamafic rock; PPL. c) equigranular medium-grained band within act-kfs-pl-bt metamafic rock; d) bt surrounding opaque mineral trails in banded act-bt-pl metamafic rock; PPL. e) bt replacing act in act-phl-pl metamafic rock; PPL. f) Pseudomorphic act-pl aggregate in act-phl-bt MD metamafic rock g) sigmoidal shaped act-pl aggregates (pseudomorphs of igneous amphibole porphyrocrysts) surrounded by bt-pl; PPL. h-i) skeletal clinopyroxene porphyroblasts in a metamafic rock from the southernmost MD area.

The variation among samples appears to be gradual and composition-related and not spatially controlled. Biotite occurs from large euhedral plates or laths, often deformed to sigmoidal-shaped aggregates to smaller anhedral grains filling spaces between the amphiboles and feldspars (Fig. 7a-c). Biotite also occurs either replacing actinolite and

plagioclase (Fig. 7e) or as inclusions in amphiboles and clinopyroxenes (Fig. 7i). Amphiboles occur mostly as short euhedral to subhedral crystals commonly forming oval or sigmoidal aggregates (Fig. 7f-h) in the foliated mafic rocks without K-feldspar. Larger prismatic actinolite and hornblende without preferred orientation are more common in the less deformed samples, commonly associated with K-feldspar (Fig. 7a). Clinopyroxene is uncommon and was identified mainly in the metamafic rocks from the southernmost portion of the MD area. The clinopyroxene occurs mostly as anhedral or skeletal porphyroblasts, generally elongated parallel to amphiboles and micas (Fig. 7h). They also occur as bigger grains (~ 2 mm) full of biotite inclusions within biotite aggregates (Fig. 7i).

4.4. MINERAL CHEMISTRY

The mineral composition of amphiboles, biotites, and feldspars was analyzed using the electron microprobe for seven MD metamafic rocks and one MD metamafic enclave. Mineral chemistry data for amphiboles of an APm dyke were compiled from Bicalho *et al*. (2019) and plotted in the classification diagrams for comparison.

4.4.1. Amphiboles

The analyzed amphiboles in the MD metamafic rocks were classified according to the 2012 IMA report (Hawthorne *et al*., 2012) using the calculation spreadsheet of Li *et al*. (2020). All amphiboles are calcic, classified as magnesio-ferri-hornblende or actinolite, and rarely as tremolite or pargasite (Fig. 8a). The average X_{Mg} of the amphiboles varies directly proportional to the Mg# ($MgO/MgO+Fe_2O_{3tot}$) of the respective whole-rock composition (Fig. 8c). Therefore, actinolite ± tremolite occurs in the magnesium-rich samples (Mg# > 70) whereas hornblende ± actinolite is present in the samples with Mg# between 40 and 70. Chromium contents in the amphiboles vary from 205 to 2273 ppm (average: 856 ppm). The amphiboles do not show compositional zoning as verified by the observations using the polarizing microscope, BSE images, or by rim and core EMPA analyses for most of the samples, except for a few grains of the metamafic enclave sample and one sample located at the southernmost portion of the MD area. The amphiboles of the metamafic enclave are classified as magnesio-hornblende and some grains show a subtle chemical zonation characterized by the decrease of X_{Mg} and increase of Si (*apfu*) from the core to the rim (Fig. 8a). The

southernmost metamafic sample, which also holds the lowest silica content (37% wt% SiO_2), contains pargasites that mostly lack chemical zoning but show a few zoned grains with actinolite in the core and pargasite in the rims (Fig. 8a). Notably, zoned amphiboles in this sample show an increase of Cr content from the core (actinolite) to the rim (mg-hastingsite) from ~800 to ~2200 ppm. The unzoned pargasites show an average Cr content of 1600 ppm (min. 1028; max. 2268 ppm).

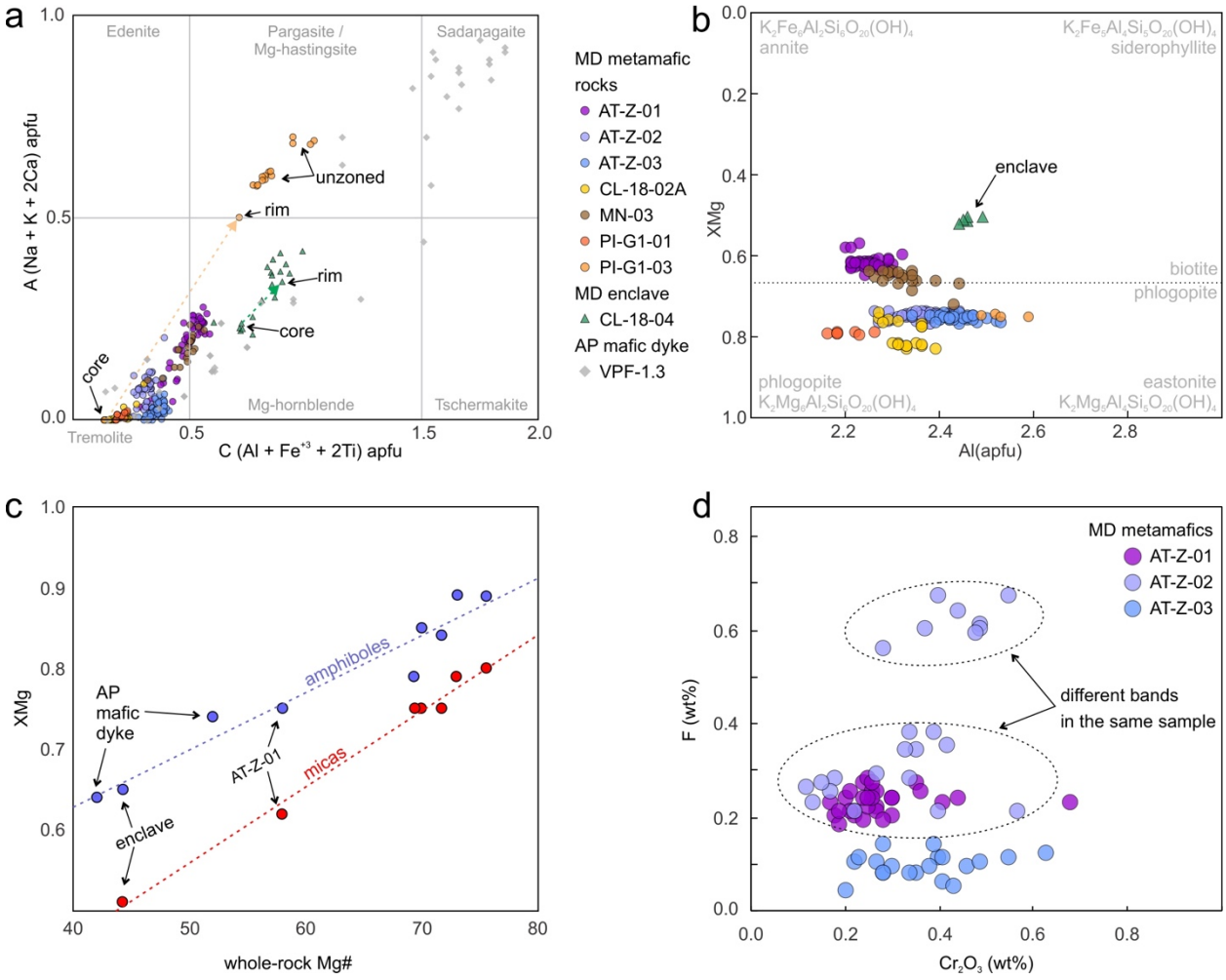

Figure 8: Amphiboles and micas mineral chemistry. a) amphibole classification diagram according to IMA 2012 recommendation (Hawthorne *et al.*, 2012). b) biotite classification after Rieder *et al.* (1998). c) direct relation of amphibole (blue) and biotite (red) XMg (average values) versus whole-rock mg# (without chloritized sample MN-03 and ultramafic pargasite bearing sample). d) fluorine versus chromium content in the biotites of md metamafic rocks.

4.4.2. Micas

A total of 180 biotite spot analyses were carried out in the MD metamafic rocks including the scarce biotite grains found in the metamafic enclave. Similar to the amphiboles, the composition of the biotite varies among the different samples proportionally to the whole rock Mg# (Fig. 8b-c). According to the recommendation of Rieder *et al*. (1998), the micas within the annite-siderophyllite-eastonite-phlogopite series are classified as biotites, and most of the analyzed micas plot within the range of 0.5 to 0.8 X_{Mg} and 2.2 to 2.5 Al apfu (Fig. 8b). The titanium content of the micas varies from 0.02 to 0.43 apfu (0.16 - 4.17 wt%) among samples and within the same samples. Yet, no spatial or microstructural controls were recognized. Similarly, Cr_2O_3 and F contents vary from not detectable to 0.72 wt% (4926 ppm) and 0.67 wt% (6700 ppm) respectively (Fig. 8d). No zoning pattern for Cr_2O_3 or F was identified. Wavelength-dispersive spectroscopy (WDS) compositional mapping highlights the concentration of chromium and titanium within the biotites despite the irregular distribution of these elements in the micas (Fig. 9).

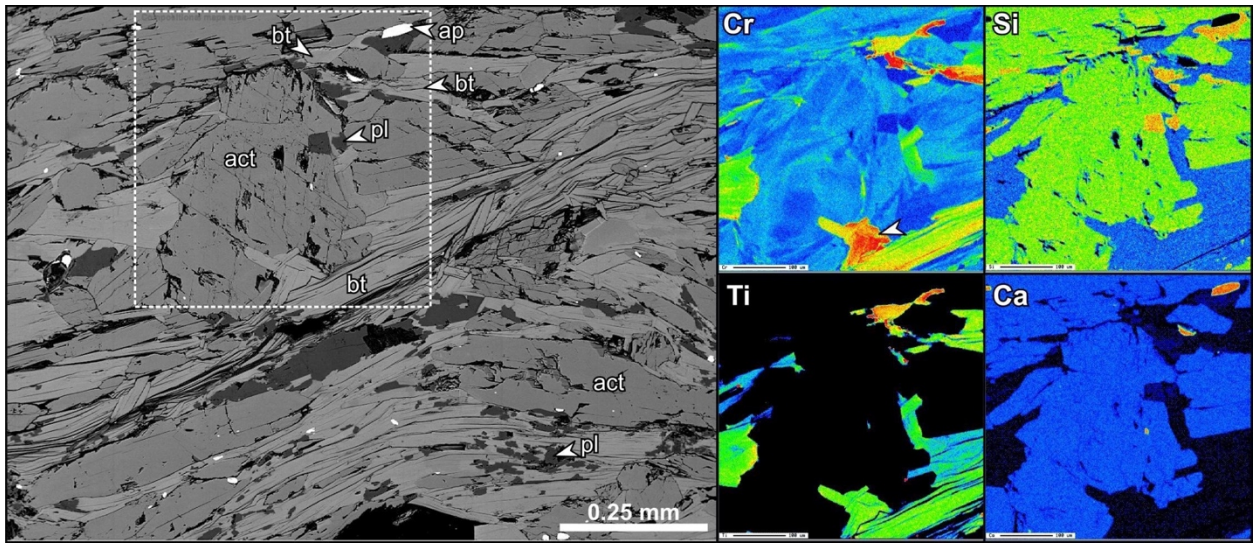

Figure 9: Microstructures and compositional maps of an MD metamafic rock. Left side: actinolite porphyroblast with high Cr biotite inclusions (BSE+SE image); Right side: WDS compositional maps of selected elements. Note the irregular distribution of Cr and Ti in the biotites.

4.4.3. Feldspars

The plagioclase composition in the MD metamafic rocks varies from albite to oligoclase whereas K-feldspar, when present, is represented by nearly end-member orthoclase. Nearly pure albite (An<5) is commonly found in veinlets or associated with late chloritization domains. The highest An-content (An ~ 28) was identified in the plagioclase associated with pargasite and biotite in the southernmost MD metamafic rock and in the MD enclave sample. The plagioclase and K-feldspar lack compositional zoning and are rarely twinned. Similarly, the plagioclase composition of the AP mafic dykes varies from oligoclase to albite (Bicalho *et al*., 2019).

5. DISCUSSIONS

5.1. CRITERIA FOR LAMPROPHYRE PROTOLITH DEFINITION

AP dykes and MD metamafic rocks show a series of characteristic features that suggest an origin as lamprophyres associated with fine to medium-grained felsic rocks (*i.e.* microdiorites, andesites, dacites) despite the metamorphic and metasomatic modifications. This interpretation is based on the integrated analysis of field, chemical (whole-rock and mineral), and petrological criteria as described in the following sections.

Field evidence that supports a lamprophyre origin for the metamafic rocks includes (i) emplacement mode as swarms of small-volume intrusions, including composite mafic and felsic dykes surrounding a calc-alkaline affinity pluton, such as the CSGC. The sheeted emplacement mode and igneous association are typical of many calc-alkaline lamprophyres worldwide (Rock, 1991); (ii) intrusions with little thickness (cm-sized) that are continuous for hundreds of meters suggesting very low viscosities of the magma; (iii) euhedral to subhedral amphiboles and clinopyroxene phenocrysts in a feldspathic groundmass (as observed in the AP dykes). In addition, the metadacite and meta-andesites from the AP area preserve subvolcanic characteristics such as the emplacement mode as dyke swarm, fine to medium grain size, and the porphyritic texture. Coeval sheeted felsic intrusions associated with lamprophyre bodies are common in calc-alkaline lamprophyre associations worldwide (*e.g.* Perring and Rock, 1991; Rezeau *et al*., 2018). Furthermore, the MD metamafic rocks are located close to the sheeted intrusions of carbonatites intercalated with metamafic rocks (<500 m; Fig. 1c). The genetic and spatial relationship of carbonatites and lamprophyres is well

acknowledged (*e.g.*, Beard *et al*., 1996; Vichi *et al*., 2005; Amores-Casals *et al*., 2019), even though the nature of this relationship is still poorly understood.

Using petrographic criteria to determine the origin as lamprophyres potentially serve as a powerful discriminator, especially concerning the biotite, amphibole, or clinopyroxene phenocryst *vs*. feldspathic groundmass relationship. However, the group of intrusions of the AP and MD areas was affected by different grades of metamorphism and deformation (see section 5.2). Moderate metamorphic and structural effects are commonly strong enough to modify and even erase lamprophyre diagnostic features (*e.g.*, Perring *et al*., 1989; Mathieu *et al*., 2018). The diagnostic petrographic characteristics are mainly preserved in the AP dykes characterized by amphibole ± clinopyroxene phenocrysts in a K-feldspar ± plagioclase groundmass. In addition, the presence of Ti-rich amphiboles and clinopyroxenes phenocrysts in a felsic matrix, as observed in the APm dykes, is characteristic of calc-alkaline lamprophyres (Rock, 1991). In agreement with previous studies, we interpret that the Ti-rich amphiboles and clinopyroxenes are igneous remnants (Bicalho *et al*. 2019). The MD metamafic rocks are mainly composed of biotite and amphibole grains (up to 80%) in a K-feldspar ± plagioclase matrix but lack the phenocryst *vs.* groundmass relationship. Notably, unusually high Cr contents in the biotite (bt and phl; up to 4926 ppm) from the MD metamafic rocks indicate that these micas probably retained Cr after the recrystallization from original biotite phenocrysts during metamorphism. Chromium-rich biotite is not common in typical metabasic rocks but it has been previously described in calc-alkaline lamprophyres from different locations (*e.g.* Jones and Smith, 1983; Meyer *et al*., 1994).

It is generally acknowledged that the major and minor element content of lamprophyres is far too variable to be used alone to classify these rocks (Rock, 1991). Nevertheless, the mafic rocks studied here show remarkably high Mg#, Cr, Co, and Ni contents indicative of significant contribution from mantle sources and compatible with a lamprophyre origin. Rare-earth element patterns display a high average of LREE and lower HREE, which is a typical feature for lamprophyres, even though it also applies to other alkaline rocks. The carbonatites are the most enriched rocks in the region and the intercalated mafic rocks reveal a similar REE pattern to the MD metamafic rocks (Fig. 5; Cerva-Alves *et al*., 2017). This is interpreted as a preliminary indication of a genetic relationship between the MD metamafic rocks and the Passo Feio carbonatite.

The lack of chemical trends for major and minor elements in the Harker-type diagrams (Fig. 3) shows that most MD metamafic rocks neither form evolutionary trends nor match the observed trend for the AP dykes. However, the mafic enclave and one of the MD metamafic rocks comprise exceptions that plot along with the same chemical trend of the AP dykes (Fig. 3). We interpret that most of the MD metamafic rocks experienced significant chemical changes driven by fluid-rock interaction during metamorphism (see section 5.2). In addition, despite the chemical changes caused by metasomatism, lamprophyre swarms typically show variable initial compositions in the same igneous association reflecting variable assimilation of the source and crustal materials (see section 5.3).

Given the set of characteristics described and discussed above, the mafic rocks are interpreted as lamprophyres with variable degrees of modification due to deformation, metamorphism, and metasomatism. Although it is difficult to classify metalamprophyres into sub-types, our closest attempt of classification based on Le Maitre *et al*. (2002) is that MD metamafic rocks were spessartites and kersantites and that AP dykes were camptonites.

5.2. METAMORPHISM AND METASOMATISM ASSOCIATED WITH THE CSGC INTRUSIONS

The metamorphic assemblage of actinolite ± chlorite ± albite observed in the AP dykes indicates that they were metamorphosed at greenschist facies conditions. As in many metamorphic terranes, the partial preservation of igneous minerals and microstructures is common at low metamorphic grades while they are commonly absent in higher grades (Bucher and Grapes, 2011). The AP dykes are located relatively far (> 4 km) from the main granitic body of the CSGC (Fig. 1c) therefore show a weak thermal effect from the intrusion.

The most common assemblage of the MD metamafic rocks consists of calcic amphibole + biotite + oligoclase ± K-feldspar that and was likely formed from the recrystallization of a similar igneous assemblage. Ti-rich amphibole phenocrysts recrystallized to aggregates of metamorphic amphiboles (*e.g.*, Mg-hornblende, actinolite, tremolite) and titanite (Fig. 7f). We interpret that the lack of amphibole zoning in most of the samples suggests that the amphibole phenocrysts were mostly fully recrystallized. The hornblende + plagioclase (An>17) + biotite assemblage is typical of

low-pressure amphibolite facies metamorphism of mafic rocks. Moreover, the presence of pargasite and diopside in the southernmost samples suggest localized higher metamorphic grade in that area. The southern portion of the MD area coincides with the highly deformed granitoids of the CSGC (Andrade, 2017; Fig. 1c). A few zoned grains with actinolite cores and pargasite rims suggest increasing metamorphic grade, similar to the zoning pattern observed in the mafic enclave (Fig. 8a). This amphibole core-rim compositional trend is also similar to that observed in the northern amphibolites of the PFC that records the low-T regional metamorphic event in the cores and higher temperatures resulting from the contact metamorphism recorded within the rims (Rizzardo *et al*, 2007; Bicalho *et al*., 2019). Given that the lamprophyres intruded the PFC after the regional metamorphic event, we interpret that the metamorphism of the mafic rocks is driven by the heat from repeated magma injections of the CSGC at the initial stages (ca. 578 Ma) but mainly from the post-kinematic pluton emplacement at *ca.* 557 Ma. The repeated mafic and felsic tabular intrusions maintained elevated temperatures in the system and resulted in the metamorphism of the lamprophyres whilst the felsic apophyses were mostly deformed but lack assemblage modification. This interpretation is in agreement with previous studies describing the metamorphism of contemporaneous intrusions of mafic and felsic rocks, often described as autometamorphism (*e.g.*, Bradshaw, 1989, 1990; Cook, 1988; Hollis *et al*., 2003, 2004; Vernon *et al*., 2012).

The presence of skarns at interfaces of MD metamafic rocks and marbles and the multi-stage fluid infiltration history described by Hoerlle *et al*. (2021) indicate that fluid-assisted element mobility acted at the bulk rock scale in the host rocks and apophyses in the MD area. We note that attempts to calculate element gains and losses in the MD metamafic rocks based on isocon methods (*e.g.* Grant, 1986) would be very speculative because of the variable compositions observed on less modified samples (samples from the AP area; Figs. 3-4). Lithological boundaries (*e.g.*, marble-apophysis) served as pathways for fluids released from cooling apophyses and variable amounts of fluids infiltrated the mafic rocks leading to localized chemical changes. Skarn reaction zones are thicker in the fold hinges of folded mafic rocks and indicate structural controls of fluid migration (Hoerlle *et al*., 2021). Fluid flow during metamorphism may result in significant changes in the mineralogical, bulk, and trace element composition (*e.g.*, Corey and Chatterjee, 1990; Ague, 2003). The

heterogeneity of apophyses' compositions and the occurrence of irregular biotite-rich bands in some samples (Fig. 7b, 7d) probably indicate channelized fluid flux and localized chemical changes in opposition to a pervasive flow. Extensive chemical alteration driven by fluid infiltration is localized and the presence or absence of metasomatism depends strongly on sample locations (Ague, 2011). Because of the medium grain size and dark colors in the field, the metasomatic effects in the mafic rocks are harder to be identified than in the marbles that show contrasting dark green calc-silicate assemblages (skarns) and white carbonates. Accordingly, the MD metamafic rocks were not only affected by heat and deformation but also by variable amounts of fluid infiltration leading to limited and localized chemical changes (Hoerlle *et al*., 2021). Detailed studies evaluating chemical changes in profiles transversal to the mafic rocks are beyond the scope of this paper but could provide useful insights regarding the extent of metasomatism and fluid infiltration localization.

Remarkably, the differences in metamorphism, deformation, and metasomatic alteration observed in the MD metamafic rocks and AP dykes suggest that the structural and metamorphic changes associated with granitic intrusions and strike-slip tectonics are very heterogeneous in the post-collisional stage of the DFB. Our study shows that the main factors that control the metamorphism at that time (ca. 578 to 557 Ma) are related to the proximity to intrusive bodies (heat and fluid supply) and shear zones development (oriented to isotropic fabrics).

5.3. SOURCES OF THE DYKE SWARMS AND RELATION TO NEOPROTEROZOIC POST-COLLISIONAL MAGMATISM OF THE SGT

Calc-alkaline lamprophyres are generally interpreted as products of progressive differentiation of basic, mantle-derived magmas with variable degrees of crustal assimilation (*e.g.*, Bachinski and Scott, 1979; Scott, 1979; Schulze *et al*, 1985). In the studied metalamprophyres, high Mg# (<76), Cr (<1538 ppm), Co (<63 ppm), and Ni (<593 ppm) suggests the influence of mantle-derived magmas. The variable Mg/Fe ratios of micas and amphiboles which are directly proportional to the Mg# suggest that individual apophyses were likely formed from batches of parental magma that had undergone different levels of fractional crystallization with apophyses exhibiting higher Fe-contents representing later stages of the evolutionary trend (Meyer *et al*., 1994). Melts in equilibrium with amphibole in the source typically show low Rb/Sr (<0.1) and

high Ba/Rb (>20), whereas melts in equilibrium with phlogopite may inherit low Ba and Ba/Rb ratios (*e.g.*, Furman and Graham, 1999; Ma *et al*., 2014). The AP dykes show low Rb/Sr ratios (0.04 - 0.14) and high Ba/Rb (9.4 - 19.8), whereas MD metamafic rocks and mafic enclaves show higher variability. Southernmost MD metamafic rocks and mafic enclaves yield similar ratios to the AP dykes (Rb/Sr: 0.05 - 0.3; Ba/Rb: 16.9 - 21.2). The ratios of all the other MD metamafic rocks vary from 0.38 - 1.60 for Rb/Sr and 5.1 to 8.7 for Ba/Rb. The large variation in Rb/Sr and Ba/Rb ratios probably suggests heterogeneous metasomatism of the mantle source resulting in amphibole and variable amounts of phlogopite in equilibrium with the melt. Variably focused fluid flow in the upper mantle produces geochemical heterogeneities which may lead to the spatial coexistence of various types of lamprophyres (Zack and John, 2007). Additionally, lamprophyres are often emplaced during or between two phases of the emplacement of a single granitic batholith (*e.g.* Camboly *et al*. 1967; Rock, 1991). This would explain the contemporaneity relationships of mafic and felsic rocks in the MD area, previously noted by Hoerlle *et al*. (2021). Several U-Pb zircon ages were obtained for the CSGC and indicated a wide age interval of *ca.* 578 - 540 Ma, despite that the younger ages (<550 Ma) were questioned because of the elevated Pb-loss in those samples (Leite *et al*., 1998; Remus *et al*., 2000a; Hoerlle *et al*., 2021). Composite plutons incrementally assembled over 30 My with different intrusive series including lamprophyre components have been reported in previous studies suggesting a geodynamic evolution from subduction to collision and post-collision (*e.g.*, Rezeau *et al*., 2018). This is likely the case for the CSGC which was assembled during *ca.* 20 My to 40 My.

Based on the age and geochemical constraints, the closest volcanic equivalent to the CSGC is represented by the Acampamento Velho Formation (579 – 549 Ma) (Sommer *et al*., 2005; Matté *et al*., 2011, 2016, 2021; Almeida D.D.P.M. *et al*., 2012; Vedana *et al*., 2017; Pereira *et al*., 2021). Therefore, based on the spatial distribution of the studied lamprophyres, they are likely related to the CSGC/Acampamento Velho magmatism. Alternatively, spessartite lamprophyres associated with Lavras do Sul Shoshonitic Association were described for the northern and southwestern portion of the São Gabriel Terrane (Roisenberg *et al*., 1983; Lima and Nardi, 1998; Buckowski, 2011; Almeida D.D.P.M. *et al*., 2012). Petrographic and geochemical similarities promote a comparison supporting the interpretation that the lamprophyres associated

with the LSSA and the studied metalamprophyres could be related, even though these occurrences are located further away (>50 km). The Hilário Fm. is found in the surrounding of the CSGC and it is considered cogenetic to the hypabyssal and plutonic rocks of the Lavras do Sul Shoshonitic Association (*e.g.*, Nardi and Lima, 2000). In addition, the high-K_2O basic to intermediate volcanic rocks of the Hilário Formation are associated to the Bom Jardim Group from the Camaquã basin formed from *ca.* 593 to 580 Ma (Ribeiro *et al*., 1966; Ribeiro and Fantinel, 1978; Chemale, 2000; Paim *et al*., 2000; Remus *et al*., 2000b; Janikian *et al*., 2008; Almeida D.D.P.M. *et al*., 2012). The Hilário Formation was described as calc-alkaline to alkaline magmatism (Roisenberg *et al*., 1983), reinterpreted as subduction-related shoshonitic magmatism (Nardi and Lima, 1985) and later considered as a product of lithospheric mantle partial melting modified by previous subduction (Nardi and Lima, 2000).

5.4. MELTING OF THE METASOMATIZED BASE OF THE LITHOSPHERE TRIGGERS POST-COLLISIONAL TRANSPRESSIVE TECTONICS

The identification of the lamprophyre bodies along with the recent discoveries of deformed carbonatite bodies in the Caçapava do Sul region (Cerva-Alves *et al*., 2017) provide insights for deep shear-zone development and magmatism in the easternmost portion of the SGT. Previous studies suggest that the variation in the degree of K-rich metasomatism of the upper mantle can control the location and origin of lithosphere-scale strike-slip shear zones and transtensional or transpressional tectonics (*e.g.*, Vaughan, 1996; Vaughan and Scarrow, 2003; Cao *et al*., 2011; Scarrow *et al*., 2011; Martina *et al*., 2018). A model of adiabatic decompression melting triggered by fault movements suggests that lamprophyre magmas would be preceded by deep seismic activity (>60 km) (Vaughan, 1996). The sigmoidal shape of the CSGC and surrounding rocks (Fig. 1d), synkinematic dyke and sill swarms, synmagmatic deformation, synkinematic skarns, and juxta-position of plutonic and hypabyssal suggests that a part of the magmas of the CSGC were emplaced during a transpressional regime (Fig. 10c). A similar geodynamic succession from extension at *ca.* 590 Ma followed by transpression at *ca.* 580-570 Ma was recognized in the Uruguay sector of the Dom Feliciano Belt (*e.g.* Oyhantçabal *et al*., 2009, 2010). In the MD area, folding of the mafic and felsic rocks and the boudinage of skarns indicate deformation at mid-crustal levels (Hoerlle *et al*., 2021). In opposition, normal and strike-slip faults developed to

accommodate stretching observed in the AP area are characteristics of upper-crust deformation. Oblique movements at shear zones produce complex structures like shear-wrench duplexes that will juxtapose coeval igneous rocks emplaced at different crustal levels (*e.g.*, Woodcock and Fischer, 1986; Vaughan, 1996). This mechanism can be used to explain the different crustal levels exposed in the CSGC and PFC area as well as the complexity and heterogeneity of the CSGC described in previous studies (*e.g.* Nardi and Bitencourt, 1989; Hoerlle *et al*., 2021). Nevertheless, detailed structural studies are beyond the scope of this paper and would be required to develop a precise model for the evolution of deformation in the Neoproterozoic igneous mafic rocks that intrude the PFC.

We suggest that a deep-rooted shear zone started to develop during the shift from an extensional to a transpressive regime at *ca.* 578 Ma influenced by K-rich metasomatism of the upper mantle (Fig. 10a-c). Notably, the age of *ca.* 578 Ma the Arroio das Pedras lamprophyres coincides with the younger ages of the Hilário Formation (593 – 580 Ma) and the older ages of Acampamento Velho (579 – 549 Ma) formations. This age-overlap with both units suggests that the lamprophyres were intruded during a transitional phase of the post-collisional stage. The shift from extension to transpression was followed by the intrusion of tabular bodies of the CSGC with synmagmatic deformation, which records the transpressive deformation (Nardi and Bitencourt, 2007; Saalmann *et al*., 2009). In particular, previous works suggested that the CSGC intruded along a fault-bend-fold of a right-lateral strike-slip shear zone (Costa *et al*, 1995). At the end of tectonic activity, acidic and more voluminous magmatism was emplaced finishing the assembly of the CSGC at *ca.* 557 Ma and resulting in contact metamorphism of the surrounding metasedimentary rocks and older mafic rocks (Fig. 10). The late-stage magmatism is interpreted to be associated with undeformed intrusions of *ca.* 550 Ma (*e.g.* São Sepé Granite; Remus *et al*., 1999) and late stages of the Acampamento Velho acidic volcanism (Sommer *et al*., 2005; Matté *et al*., 2011, 2016; Almeida D.D.P.M. *et al*., 2012; Pereira *et al*., 2021). Previous studies suggest that the Acampamento Velho volcanism occurred in a transtensional cycle of the Camaquã Basin (Oliveira *et al*., 2014). However, the Acampamento Velho volcanism occurred in a wide interval from *ca.* 579 and 549 Ma (Sommer *et al*., 2005; Matté *et al*., 2011, 2016, 2021; Almeida D.D.P.M. *et al*., 2012; Vedana *et al*., 2017; Pereira *et al*., 2021) that we consider to be formed in localized extensional domains

during the transpressive and transtensive regimes (Fig. 10c-d). At last, despite the geodynamic interpretations, we note that the transition from extension to strike-slip tectonics in the Camaquã Basin at *ca.* 578 Ma has significant implications for base metal prospecting as the Bom Jardim and Santa Bárbara groups host several Cu-Pb-Zn (Au-Ag) occurrences and deposits (*e.g.* Fontana *et al*., 2017; Laux *et al*., 2005; Remus *et al*., 2000b).

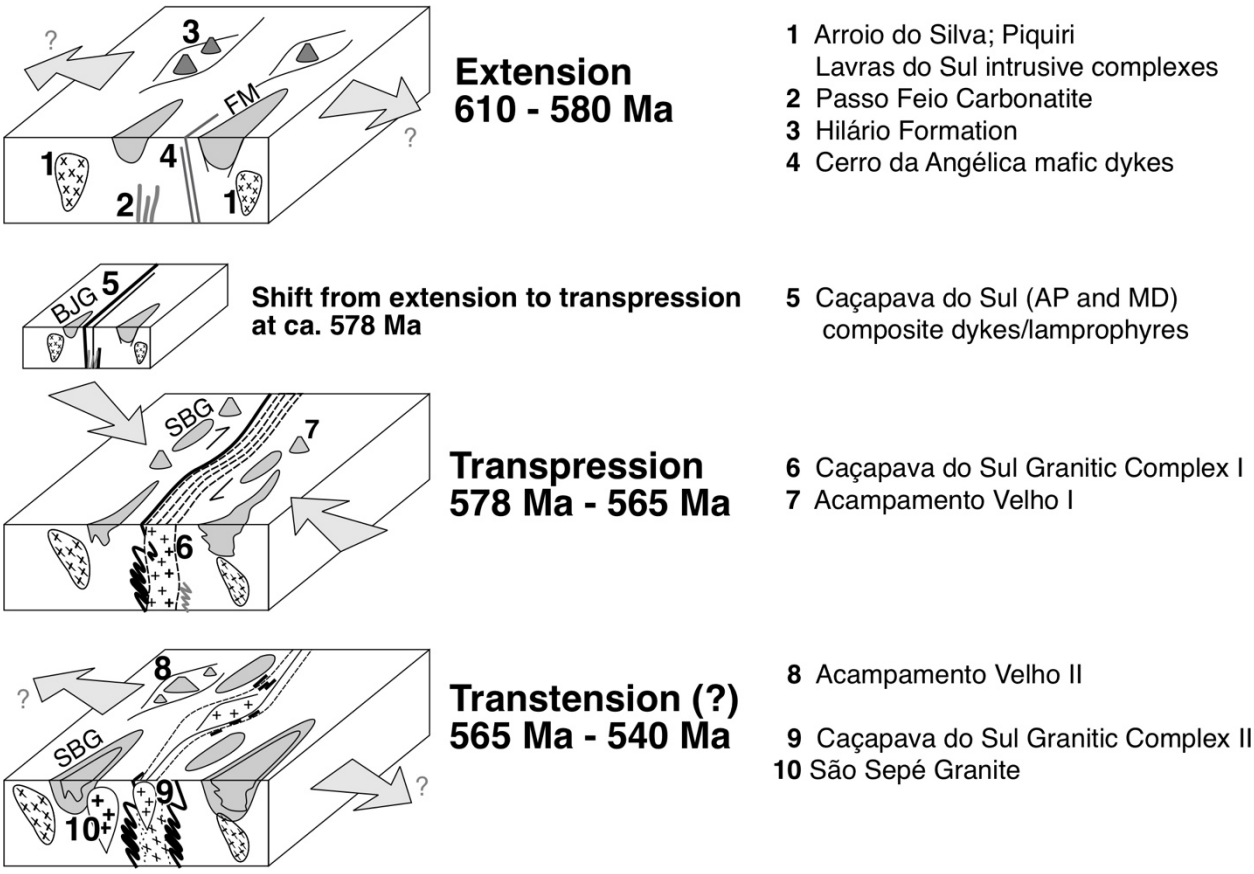

Figure 10: Schematic evolution and summary of representative units. (1: Remus *et al*., 1997, 2000b; Philipp *et al*., 2002; Gastal *et al*., 2006; Almeida D.D.P.M. *et al*., 2012; Bitencourt *et al*., 2015; Padilha *et al*., 2019. 2: Cerva-Alves *et al*., 2017; 3-4: Chemale, 2000; Janikian *et al*., 2008; 5-6: Chemale, 2000; Janikian *et al*., 2008; Sommer *et al*., 2017; Hoerlle *et al*., 2021; 8: Sommer *et al*., 2005; Matté *et al*., 2011, 2016; Almeida D.D.P.M. *et al*., 2012; Vedana *et al*., 2017; Pereira *et al*., 2021; 9: Leite *et al*., 1998; Remus *et al*., 2000a; 10: Remus *et al*., 1999)

6. CONCLUSIONS

1) Dyke and sill swarms in the eastern portion of the São Gabriel Terrane (central Dom Feliciano Belt) comprise metamafic rocks with high Mg#, Cr, Co, Ni, rich in volatiles and with high LREE and lower HREE patterns that are classified as metalamprophyres. Metamorphosed and deformed lamprophyres were described for the first time in the São Gabriel Terrane.

2) Localized medium to high-grade metamorphism, deformation, and metasomatism partially or fully destroyed lamprophyre diagnostic characteristics in the MD area whereas low-grade metamorphism preserved lamprophyre characteristics such as igneous Ti-rich amphibole and clinopyroxene phenocrysts in a feldspathic groundmass in the AP area.

3) Metamorphism and deformation of the lamprophyres occurred due to the subsequent syntectonic and post-tectonic acidic magmatism accompanied by localized fluid infiltration and metasomatism.

4) Metamorphism that occurred from *ca.* 578 to 557 Ma in the easternmost São Gabriel Terrane is controlled by the proximity of intrusive bodies that provide heat and fluid supply and by the distance to shear-zones that result in fabric heterogeneity (oriented *vs.* isotropic).

5) We propose that the Arroio das Pedras (AP) and Marble District (MD) lamprophyres represent tectonic markers for the transition from post-collisional extensional to transpressive tectonics in the eastern portion of the São Gabriel Terrane (central Dom Feliciano Belt).

6) The tectonic regime shift marked by the lamprophyres is reflected in the changes of space-forming tectonics of the Bom Jardim and Santa Bárbara groups of the Camaquã Basin. Despite the geodynamic implications, this is also significant for base metal exploration as the Bom Jardim and Santa Bárbara groups host several Cu-Pb-Zn (Au-Ag) deposits in the easternmost portion of the São Gabriel Terrane.

ACKNOWLEDGEMENTS

The authors acknowledge the National Council for Scientific and Technological Development of Brazil (CNPq) for funding through a Ph.D. scholarship to G.S. Hoerlle (141333/2017-0) and the Brazilian Federal Foundation for Support and Evaluation of Graduate Education for sandwich Ph.D. granted to G. S. Hoerlle (CAPES-PRINT 88887.467220/2019-00). Financial support from FAPERGS (Prog. Pesquisador Gaúcho 05/2019, proc. 19/2551-0001909-2) is acknowledged. A. Kronz, J. Gätjen, and S. Drago are acknowledged for EMPA assistance. Fruitful discussions and constructive comments on a preliminary version of the manuscript by T. Müller and S. Piazolo are gratefully acknowledged.

REFERENCES

Ague, J.J., 2003. Fluid Infiltration and Transport of Major, Minor, and Trace Elements During Regional Metamorphism of Carbonate Rocks, Wepawaug Schist, Connecticut, USA. Am. J. Sci. 303, 753–816. https://doi.org/10.2475/ajs.303.9.753

Ague, J.J., 2011. Extreme channelization of fluid and the problem of element mobility during Barrovian metamorphism. Am. Mineral. 96, 333–352. https://doi.org/10.2138/am.2011.3582

Almeida, D.D.P.M. de, Chemale, F., Machado, A., 2012. Late to Post-Orogenic Brasiliano-Pan-African Volcano-Sedimentary Basins in the Dom Feliciano Belt, Southernmost Brazil, in: Petrology - New Perspectives and Applications. InTech. https://doi.org/10.5772/25189

Almeida, R.P., Santos, M.G.M., Fragoso-Cesar, A.R.S., Janikian, L., Fambrini, G.L., 2012. Recurring extensional and strike-slip tectonics after the Neoproterozoic collisional events in the southern Mantiqueira province. An. Acad. Bras. Cienc. 84, 347–376. https://doi.org/10.1590/S0001-37652012005000034

Amores-Casals, Melgarejo, Bambi, Gonçalves, Morais, Manuel, Neto, Costanzo, Molist, 2019. Lamprophyre-Carbonatite Magma Mingling and Subsolidus Processes as Key Controls on Critical Element Concentration in Carbonatites—The Bonga Complex (Angola). Minerals 9, 601. https://doi.org/10.3390/min9100601

Andrade, B.V.R., 2017. Investigação estrutural do Gnaisse Neto Rodrigues e sua relação com Complexo Granítico Caçapava do Sul. UNIPAMPA. Retrieved from http://dspace.unipampa.edu.br:8080/jspui/handle/riu/2162

Bachinski, S.W., Scott, R.B., 1979. Rare-earth and other trace element contents and the origin of minettes (mica-lamprophyres). Geochim. Cosmochim. Acta 43, 93–100. https://doi.org/10.1016/0016-7037(79)90049-8

Basei, M., Siga, O., Masquelin, H., Harara, O., Reis Neto, J., & Preciozzi, F. (2000). The Dom Feliciano belt (Brazil-Uruguay)and its fore land (Rio de la Plata Craton): framework, tectonic evolution and correlations with similar terranes of southwestern Africa (INIS-UY-GEO--675). Uruguay

Beard, A.D., Downes, H., Vetrin, V., Kempton, P.D., Maluski, H., 1996. Petrogenesis of Devonian lamprophyre and carbonatite minor intrusions, Kandalaksha Gulf (Kola Peninsula, Russia). Lithos 39, 93–119. https://doi.org/10.1016/S0024-4937(96)00020-5

Bédard, J.H., 1994. Mesozoic east North American alkaline magmatism: Part 1. Evolution of Monteregian lamprophyres, Québec, Canada. Geochim. Cosmochim. Acta 58, 95–112. https://doi.org/10.1016/0016-7037(94)90449-9

Bicalho, V., Remus, M.V.D., Rizzardo, R., Dani, N., 2019. Geochemistry, metamorphic evolution and tectonic significance of metabasites from Caçapava do Sul, southern Brazil. Brazilian J. Geol. 49, 1–16. https://doi.org/10.1590/2317-4889201920180039

Bicca, M.M., Chemale, F., Jelinek, A.R., de Oliveira, C.H.E., Guadagnin, F., Armstrong, R., 2013. Tectonic evolution and provenance of the Santa Bárbara Group, Camaquã Mines region, Rio Grande do Sul, Brazil. J. South Am. Earth Sci. 48, 173–192. https://doi.org/10.1016/j.jsames.2013.09.006

Bitencourt, M.F., 1983. Geologia petrologia e estrutura dos metamorfitos da região de Caçapava do Sul RS. Universidade Federal do Rio Grande do Sul.

Bitencourt, M.F., Florisbal, L.M., Sbaraini, S., Rivera, C.B., 2015. Idades U-Pb e a duração do magmatismo ultrapotássico do Maciço Sienítico Piquiri. Sociedade Brasileira de Geociências (Ed.), Proceedings of IX Simpósio Sul-brasileiro de Geologia, Florianópolis, p. 143

Bortolotto, O.J., 1988. Metamorfismo Termal dos Mármores de Caçapava do Sul, RS. Ciência e Nat. 10, 25–48.

Bradshaw, J.Y., 1989. Origin and metamorphic history of an Early Cretaceous polybaric granulite terrain, Fiordland, southwest New Zealand. Contrib. to Mineral. Petrol. 103, 346–360. https://doi.org/10.1007/BF00402921

Bradshaw, J.Y., 1990. Geology of crystalline rocks of northern Fiordland: Details of the granulite facies Western Fiordland Orthogneiss and associated rock units. New Zeal. J. Geol. Geophys. 33, 465–484. https://doi.org/10.1080/00288306.1990.10425702

Bucher, K., Grapes, R., 2011. Petrogenesis of Metamorphic Rocks. Springer Berlin Heidelberg, Berlin, Heidelberg. https://doi.org/10.1007/978-3-540-74169-5

Buckowski, N., 2011. Caracterização dos Lamprófiros espessartíticos da região de Vila Nova do Sul, RS. Universidade Federal do Rio Grande do Sul. Retrieved from http://www.bibliotecadigital.ufrgs.br/da.php?nrb=000858639&loc=2012&l=b055ac7600cbb7a9

Camboly, J., Hameurt, J., & Rocci, G., 1967. Relations génétiques entre vaugnérite et kersantite et hypothèse originale sur la genèse des lamprophyres des Vosges. Comptes rendus de l'Académie des sciences. Série D, 264, 25-28.

Cao, S., Liu, J., Leiss, B., Neubauer, F., Genser, J., Zhao, C., 2011. Oligo-Miocene shearing along the Ailao Shan–Red River shear zone: Constraints from structural analysis and

zircon U/Pb geochronology of magmatic rocks in the Diancang Shan massif, SE Tibet, China. Gondwana Res. 19, 975–993. https://doi.org/10.1016/j.gr.2010.10.006

Casetta, F., Ickert, R.B., Mark, D.F., Bonadiman, C., Giacomoni, P.P., Ntaflos, T., Coltorti, M., 2019. The alkaline lamprophyres of the dolomitic area (Southern Alps, Italy): Markers of the late triassic change from orogenic-like to anorogenic magmatism. J. Petrol. 60, 1263–1298. https://doi.org/10.1093/petrology/egz031

Cerva-Alves, T., Hartmann, L.A., Remus, M.V.D., Lana, C., 2020. Integrated ophiolite and arc evolution, southern Brasiliano Orogen. Precambrian Res. 341, 105648. https://doi.org/10.1016/j.precamres.2020.105648

Cerva-Alves, T., Remus, M.V.D., Dani, N., Basei, M.A.S., 2017. Integrated field, mineralogical and geochemical characteristics of Caçapava do Sul alvikite and beforsite intrusions: A new Ediacaran carbonatite complex in southernmost Brazil. Ore Geol. Rev. 88, 352–369. https://doi.org/10.1016/j.oregeorev.2017.05.017

Chemale Jr, F., 2000. Evolução Geológica do Escudo Sul-Riograndense, in: Holz, M., De Ros, L.F. (Eds.), Geologia Do Rio Grande Do Sul. Editora UFRGS, Porto Alegre, pp. 13–52.

Chemale, F., Mallmann, G., Bitencourt, M. de F., Kawashita, K., 2012. Time constraints on magmatism along the Major Gercino Shear Zone, southern Brazil: Implications for West Gondwana reconstruction. Gondwana Res. 22, 184–199. https://doi.org/10.1016/j.gr.2011.08.018

Cook, N.D.J., 1988. Diorites and associated rocks in the Anglem Complex at The Neck, northeastern Stewart Island, New Zealand: an example of magma mingling. Lithos 21, 247–262. https://doi.org/10.1016/0024-4937(88)90031-X

Corey, M.C., Chatterjee, A.K., 1990. Characteristics of REE and other trace elements in response to successive and superimposed metasomatism within a portion of the South Mountain Batholith, Nova Scotia, Canada. Chem. Geol. 85, 265–285. https://doi.org/10.1016/0009-2541(90)90004-Q

Costa, A.F.U., Fernandes, L.A.D., Shukowsky, W., Nardi, L.V.S., Bitencourt, M.F., 1995. Teste dos modelos tectonicos e de posicionamento do complexo Granitico de Cacapava do Sul atraves de estudos de modelagem gravimetrica 3-D. Rev. Bras. Geofis. 13, 91–101.

CPRM – SERVIÇO GEOLÓGICO DO BRASIL. 2010. Projeto Aerogeofísico Escudo do Rio Grande do Sul. LASA PROSPECÇÕES S.A., Relatório Técnico, 260 p.

Fernandes, L.A.D., Menegat, R., Costa, A.F.U., Koester, E., Porcher, C.C., Tommasi, A., Kraemer, G., Ramgrab, G.E., Camozzato, E., 1995. Evolução tectônica do Cinturão Dom Feliciano no Escudo Sul-rio-grandense: Parte I - uma contribuição a partir do registro geológico. Rev. Bras. Geociências 25, 351–374. https://doi.org/10.25249/0375-7536.1995351374

Fernandes, L.A.D., Tommasi, A., Porcher, C.C., 1992. Deformation patterns in the southern Brazilian branch of the Dom Feliciano Belt: A reappraisal. J. South Am. Earth Sci. 5, 77–96. https://doi.org/10.1016/0895-9811(92)90061-3

Fontana, E., Mexias, A.S., Renac, C., Nardi, L.V.S., Lopes, R.W., Barats, A., Gomes, M.E.B., 2017. Hydrothermal alteration of volcanic rocks in Seival Mine Cu–mineralization – Camaquã Basin – Brazil (part I): Chloritization process and geochemical dispersion in

alteration halos. J. Geochemical Explor. 177, 45–60. https://doi.org/10.1016/j.gexplo.2017.02.004

Fragoso-Cesar, A.R.S., 1991. Tectônica de placas no ciclo brasiliano: as orogenias dos cinturões Dom Feliciano e Ribeira no Rio Grande do Sul. Universidade de São Paulo, São Paulo. https://doi.org/10.11606/T.44.1991.tde-23042013-162133

Furman, T., Graham, D., 1999. Erosion of lithospheric mantle beneath the East African Rift system: geochemical evidence from the Kivu volcanic province. Lithos 48, 237–262. https://doi.org/10.1016/S0024-4937(99)00031-6

Gastal, M.D.C., Lafon, J.M., Ferreira, F.J.F., Magro, F.U.S., Remus, M.V.D., Sommer, C.A., 2006. Reinterpretação do Complexo Intrusivo Lavras do Sul, RS, de acordo com os sistemas vulcano-plutônicos de subsidência. Parte 1: geologia, geofísica e geocronologia (207Pb/206Pb/238U). Rev. Bras. Geociências. https://doi.org/10.25249/0375-7536.2006361109124

Goulart, R.V., Remus, M.V.D., Reis, R.S., 2013. Composição isotópica de Sr, C e O e geoquímica de ETRs das rochas carbonáticas do Bloco São Gabriel, Rio Grande do Sul. Pesqui. em Geociencias 40, 75–97.

Grant, J.A., 1986. The isocon diagram; a simple solution to Gresens' equation for metasomatic alteration. Econ. Geol. 81, 1976–1982. https://doi.org/10.2113/gsecongeo.81.8.1976

Gubert, M.L., Philipp, R.P., Basei, M.A.S., 2016. The Bossoroca Complex, São Gabriel Terrane, Dom Feliciano Belt, southernmost Brazil: U Pb geochronology and tectonic implications for the neoproterozoic São Gabriel Arc. J. South Am. Earth Sci. 70, 1–17. https://doi.org/10.1016/j.jsames.2016.04.006

Hartmann, L.A., Chemale Jr, F., Phillip, R.P., 2007. Evolução geotectônica do Rio Grande do Sul no Pré-Cambriano, in: Iannuzzi, R., Frantz, J.C. (Eds.), 50 Anos de Geologia No Rio Grande Do Sul. Porto Alegre, pp. 97–123.

Hartmann, L.A., Leite, J.A.D., Da Silva, L.C., Remus, M. V.D., McNaughton, N.J., Groves, D.I., Fletcher, I.R., Santos, J.O.S., Vasconcellos, M.A.Z., 2000. Advances in SHRIMP geochronology and their impact on understanding the tectonic and metallogenic evolution of southern Brazil. Aust. J. Earth Sci. 47, 829–844. https://doi.org/10.1046/j.1440-0952.2000.00815.x

Hartmann, L.A., Tindle, A., Bitencourt, M. de F.A.S., 1990. O metamorfismo de facies anfibolito no complexo metamorfico Passo Feio, RS, com base em química dos minerais. Pesquisas 17, 62–71.

Hawthorne, F.C., Oberti, R., Harlow, G.E., Maresch, W. V., Martin, R.F., Schumacher, J.C., Welch, M.D., 2012. Nomenclature of the amphibole supergroup. Am. Mineral. 97, 2031–2048. https://doi.org/10.2138/am.2012.4276

Hoerlle, G. S., Remus, M. V. D., Dani, N., Lana, C., Müller, T., & Piazolo, S. (2021). Metasomatic reactions triggered by localized and episodic fluid flux record multistage intrusion history: An example from the syntectonic Caçapava do Sul Granitic Complex, Southern Brazil. Manuscript submitted to publication.

Hollis, J.A., Clarke, G.L., Klepeis, K.A., Daczko, N.R., Ireland, T.R., 2004. The regional significance of Cretaceous magmatism and metamorphism in Fiordland, New Zealand,

from U-Pb zircon geochronology. J. Metamorph. Geol. 22, 607–627. https://doi.org/10.1111/j.1525-1314.2004.00537.x

Hollis, J.A., Clarke, G.L., Klepeis, K.A., Daczko, N.R., Ireland, T.R., 2003. Geochronology and geochemistry of high-pressure granulites of the Arthur River Complex, Fiordland, New Zealand: Cretaceous magmatism and metamorphism on the palaeo-Pacific Margin. J. Metamorph. Geol. 21, 299–313. https://doi.org/10.1046/j.1525-1314.2003.00443.x

Hueck M., Oyhantçabal P., Philipp R.P., Basei M.A.S., Siegesmund S., 2018. The Dom Feliciano Belt in Southern Brazil and Uruguay. In: Siegesmund S., Basei M., Oyhantçabal P., Oriolo S. (eds) Geology of Southwest Gondwana. Regional Geology Reviews. Springer, Cham. https://doi.org/10.1007/978-3-319-68920-3_11

Hueck, M., Basei, M.A.S., Wemmer, K., Oriolo, S., Heidelbach, F., Siegesmund, S., 2019. Evolution of the Major Gercino Shear Zone in the Dom Feliciano Belt, South Brazil, and implications for the assembly of southwestern Gondwana. Int. J. Earth Sci. 108, 403–425. https://doi.org/10.1007/s00531-018-1660-4

Janikian, L., De Almeida, R.P., Da Trindade, R.I.F., Fragoso-cesar, A.R.S., D'Agrella-Filho, M.S., Dantas, E.L., Tohver, E., 2008. The continental record of Ediacaran volcano-sedimentary successions in southern Brazil and their global implications. Terra Nov. 20, 259–266. https://doi.org/10.1111/j.1365-3121.2008.00814.x

Janikian, L., de Almeida, R.P., Fragoso-Cesar, A.R.S., Martins, V.T. de S., Dantas, E.L., Tohver, E., McReath, I., D'Agrella-Filho, M.S., 2012. Ages (U-Pb SHRIMP and LA ICPMS) and stratigraphic evolution of the Neoproterozoic volcano-sedimentary successions from the extensional Camaquã Basin, Southern Brazil. Gondwana Res. 21, 466–482. https://doi.org/10.1016/j.gr.2011.04.010

Jones, A.P., Smith, J. V., 1983. Petrological Significance of Mineral Chemistry in the Agathla Peak and the Thumb Minettes, Navajo Volcanic Field. J. Geol. 91, 643–656. https://doi.org/10.1086/628817

Laux, J.H., Lindenmayer, Z.G., Guimarães Teixeira, J.B., Neto, A.B., 2005. Ore genesis at the Camaquã copper mine, a neoproterozoic sediment-hosted deposit in Southern Brazil. Ore Geol. Rev. https://doi.org/10.1016/j.oregeorev.2004.11.001

Le Maitre, R.., Streckeisen, A., Zanettin, B., Le Bas, M.J., Bonin, B., Bateman, P., 2002. Igneous Rocks: A Classification and Glossary of Terms (Recommendations of the IUGS Subcommission on the Systematics of Igneous Rocks), Cambridge University Press.

Leinz, V., Barbosa, A. F., 1942. Mapa Geológico Caçapava-Lavras. Secretaria de Estado dos Negócios da Agricultura, Indústria e Comércio. Secção de Informações e Propaganda Agrícola, Porto Alegre.

Leinz, V., Barbosa, A.F. Teixeira, E., 1941. Mapa geológico Caçapava-Lavras. Boletim 90, Secretaria da Agricultura, Indústria e Comércio, Porto Alegre.

Leite, J.A.D., Hartman, L.O.A., McNaughton, N.J., Chemale, F., 1998. Shrimp U/Pb zircon geochronology of Neoproterozoic juvenile and crustal-reworked terranes in southernmost Brazil. Int. Geol. Rev. 40, 688–705. https://doi.org/10.1080/00206819809465232

Li, X., Zhang, C., Behrens, H., Holtz, F., 2020. Calculating amphibole formula from electron microprobe analysis data using a machine learning method based on principal

components regression. Lithos 362–363, 105469. https://doi.org/10.1016/j.lithos.2020.105469

Lima, E.F., Nardi, L.V.S., 1998. The Lavras do Sul shoshonitic association: implications for the origin and evolution of Neoproterozoic shoshonitic magmatism in southernmost Brazil. J. South Am. Earth Sci. 11, 67–77. https://doi.org/10.1016/S0895-9811(97)00037-0

Lopes, C.G., Pimentel, M.M., Philipp, R.P., Gruber, L., Armstrong, R., Junges, S., 2015. Provenance of the Passo Feio Complex, Dom Feliciano Belt: Implications for the age of supracrustal rocks of the São Gabriel Arc, southern Brazil. J. South Am. Earth Sci. 58, 9–17. https://doi.org/10.1016/j.jsames.2014.11.004

Ma, L., Jiang, S.-Y., Hofmann, A.W., Dai, B.-Z., Hou, M.-L., Zhao, K.-D., Chen, L.-H., Li, J.-W., Jiang, Y.-H., 2014. Lithospheric and asthenospheric sources of lamprophyres in the Jiaodong Peninsula: A consequence of rapid lithospheric thinning beneath the North China Craton? Geochim. Cosmochim. Acta 124, 250–271. https://doi.org/10.1016/j.gca.2013.09.035

Martina, F., Canelo, H.N., Dávila, F.M., de Hollanda, M.H.M., Teixeira, W., 2018. Mississippian lamprophyre dikes in western Sierras Pampeanas, Argentina: Evidence of transtensional tectonics along the SW margin of Gondwana. J. South Am. Earth Sci. 83, 68–80. https://doi.org/10.1016/j.jsames.2018.02.006

Mathieu, L., Bouchard, É., Guay, F., Liénard, A., Pilote, P., Goutier, J., 2018. Criteria for the recognition of Archean calc-alkaline lamprophyres: examples from the Abitibi Subprovince. Can. J. Earth Sci. 55, 188–205. https://doi.org/10.1139/cjes-2017-0152

Matté, V., Sommer, C.A., Fernandes de Lima, E., Koester, E., 2021. Ediacaran Na-alkaline Acampamento Velho volcanism in the Ramada Plateau, southernmost Brazil: Sr–Nd–Pb isotopic data and petrogenetic evolution. Precambrian Res. 358, 106167. https://doi.org/10.1016/j.precamres.2021.106167

Matté, V., Sommer, C.A., Lima, E.F. de, Philipp, R.P., Basei, M.A.S., 2016. Post-collisional Ediacaran volcanism in oriental Ramada Plateau, southern Brazil. J. South Am. Earth Sci. 71, 201–222. https://doi.org/10.1016/j.jsames.2016.07.015

Matté, V., Sommer, C.A., Lima, E.F., Dantas, E.L., 2011. Relação das rochas dioríticas do Platô da Ramada (RS) com o vulcanismo alcalino da Formação Acampamento Velho (Neoproterozoico do Escudo Sul-Rio-Grandense). In: Anais do V Simpósio de vulcanismo e ambientes associados, Goiás.

Meyer, H.O.A., Mitchell, R.H., Jayaganapathy, S., 1994. Phlogopite in calc-alkaline lamprophyres of Northern England. Mineral. Petrol. 51, 227–237. https://doi.org/10.1007/BF01159728

Nardi, L. V. S., Lima, E. F., 2000. O magmatismo shoshonítico e alcalino da Bacia do Camaquã-RS. In: Holz, M., de Ros, L. F. (Eds.). Geologia do Rio Grande do Sul. Porto Alegre

Nardi, L.V.S., Bitencourt, M. de F., 1989. Geologia, Petrologia e Geoquímica do Complexo Granítico de Caçapava do Sul, RS. Rev. Bras. Geociências 19, 153–169.

Nardi, L.V.S., Bitencourt, M.F., 2007. Magmatismo granítico e evolução crustal do sul do Brasil. 50 Anos de Geologia. Instituto de Geociências. In: Iannuzzi, R., Frantz, J. C., Contribuições. Editora Comunicação e Identidade, Porto Alegre

Nardi, L.V.S., Lima, E.F., 1985. A Associação Shoshonítica de Lavras Do Sul, RS. Rev. Bras. Geociências 15, 139–146. https://doi.org/10.25249/0375-7536.1985139146

Oliveira, C.H.E., Chemale, F., Jelinek, A.R., Bicca, M.M., Philipp, R.P., 2014. U-Pb and Lu-Hf isotopes applied to the evolution of the late to post-orogenic transtensional basins of the dom feliciano belt, Brazil. Precambrian Res. 246, 240–255. https://doi.org/10.1016/j.precamres.2014.03.008

Oyhantçabal, P., Siegesmund, S., Wemmer, K., Layer, P., 2010. The Sierra Ballena Shear Zone in the southernmost Dom Feliciano Belt (Uruguay): Evolution, kinematics, and deformation conditions. Int. J. Earth Sci. 99, 1227–1246. https://doi.org/10.1007/s00531-009-0453-1

Oyhantçabal, P., Siegesmund, S., Wemmer, K., Presnyakov, S., Layer, P., 2009. Geochronological constraints on the evolution of the southern Dom Feliciano Belt (Uruguay). J. Geol. Soc. London. 166, 1075–1084. https://doi.org/10.1144/0016-76492008-122

Padilha, D.F., Bitencourt, M. de F., Nardi, L.V.S., Florisbal, L.M., Reis, C., Geraldes, M., Almeida, B.S., 2019. Sources and settings of Ediacaran post-collisional syenite-monzonite-diorite shoshonitic magmatism from southernmost Brazil. Lithos 344–345, 482–503. https://doi.org/10.1016/j.lithos.2019.06.004

Paim, P.S.G., Chemale Jr., F. & Lopes, R.C. (2000). A Bacia do Camaquã. In: Holz, M. & De Ros, L.F. (Eds.) Geologia do Rio Grande do Sul, Edições CIGO/UFRGS, pp. 231-274.

Paim, P.S.G., Chemale Junior, F., Wildner, W., 2014. Estágios evolutivos da Bacia do Camaquã (RS). Ciência e Nat. 36, 183–193. https://doi.org/10.5902/2179460X13748

Passarelli, C.R., Basei, M.A.S., Wemmer, K., Siga, O., Oyhantçabal, P., 2011. Major shear zones of southern Brazil and Uruguay: Escape tectonics in the eastern border of Rio de La plata and Paranapanema cratons during the Western Gondwana amalgamation. Int. J. Earth Sci. 100, 391–414. https://doi.org/10.1007/s00531-010-0594-2

Pereira, D.R., Macambira, M.J.B., Pires, K.C. de J., Lago, S.B. do, 2021. Isotopic study of the Pb-Zn (Cu-Ag) Santa Maria Deposit, Caçapava do Sul Region, Rio Grande do Sul, Brazil. Brazilian J. Geol. 51. https://doi.org/10.1590/2317-4889202120200091

Perring, C.S., Rock, N.M.S., 1991. Relationships between calc-alkaline acidic and basic (mantle-derived) magmas in Late Archaean composite dykes, Kambalda Goldfield, Western Australia. Precambrian Res. 52, 245–273. https://doi.org/10.1016/0301-9268(91)90083-M

Perring, C.S., Rock, N.M.S., Golding, S.D., Roberts, D.E., 1989. Criteria for the recognition of metamorphosed or altered lamprophyres: A case study from the Archaean of Kambalda, Western Australia. Precambrian Res. 43. https://doi.org/10.1016/0301-9268(89)90057-0

Philipp, R.P., Machado, R., Nardi, L.V.S., Lafon, J.M., 2002. O magmatismo granítico neoproterozóico do Batólito Pelotas no sul do Brasil: novos dados e revisão da geocronologia regional. Rev. Bras. Geociências 32, 277–290. https://doi.org/10.25249/0375-7536.2002322277290

Philipp, R.P., Pimentel, M.M., Chemale Jr, F., 2016. Tectonic evolution of the Dom Feliciano Belt in Southern Brazil: Geological relationships and U-Pb geochronology. Brazilian J. Geol. 46, 83–104. https://doi.org/10.1590/2317-4889201620150016

Porcher, C.A., Lopes, R.C., 2000. Carta Geológica: Cachoeira do Sul: folha SH.22-Y-A: estado do Rio Grande do Sul. Brasília: CPRM. Escala 1:250.000. Programa Levantamentos Geológicos Básicos do Brasil - PLGB. Porto Alegre.

Remus, M.V.D., Hartmann, L.A., McNaughton, N.J., Groves, D.I., Fletcher, I.R., 2000a. The link between hydrothermal epigenetic copper mineralization and the Cacapava Granite of the Brasiliano cycle in southern Brazil. J. South Am. Earth Sci. 13, 191–216. https://doi.org/10.1016/S0895-9811(00)00017-1

Remus, M.V.D., Hartmann, L.A., McNaughton, N.J., Groves, D.I., Reischl, J.L., 2000b. Distal Magmatic-Hydrothermal Origin for the Camaquã Cu (Au-Ag) and Santa Maria Pb, Zn (Cu-Ag) Deposits, Southern Brazil. Gondwana Res. 3, 155–174. https://doi.org/10.1016/S1342-937X(05)70094-0

Remus, M.V.D., Hartmann, L.F., Mcnaughton, N.J., Groves, D.I., Reischl, J.L., 1997. Pb-S isotope signature of sulphides and constrains on timing and sources of Cu (Au) Mineralization at the Camaquã and Santa Maria Mines, Caçapava do Sul, RS - Brazil. In: South American Symposium on Isotope Geology, 1997, Campos do Jordão, SP. Extended Abstracts, pp. 253-255

Remus, M.V.D., Massonne, H.J., Hartmann, L.A., Theye, T., Braetz, H., 2010. Garnet zonation and monazite ages as monitors of contrasting metamorphic evolution in the Brasiliano schist belts of Southern Brazil. In: 45° Congresso Brasileiro de Geologia. Belém.

Remus, M.V.D., McNaughton, N.J., Hartmann, L.A., Koppe, J.C., Fletcher, I.R., Groves, D.I., Pinto, V.M., 1999. Gold in the Neoproterozoic juvenile Bossoroca Volcanic Arc of southernmost Brazil: Isotopic constraints on timing and sources. J. South Am. Earth Sci. 12, 349–366. https://doi.org/10.1016/S0895-9811(99)00026-7

Rezeau, H., Leuthold, J., Tayan, R., Hovakimyan, S., Ulianov, A., Kouzmanov, K., Moritz, R., 2018. Incremental growth of mid- to upper-crustal magma bodies during Arabia-Eurasia convergence and collision: A petrological study of the calc-alkaline to shoshonitic Meghri-Ordubad pluton (southern Armenia and Nakhitchevan, Lesser Caucasus). J. Petrol. 59, 931–966. https://doi.org/10.1093/PETROLOGY/EGY050

Ribeiro, M., 1970. Geologia da fôlha de Bom Jardim, Rio Grande do Sul-Brasil. República Federativa do Brasil, Ministério das Minas e Energia, Departamento Nacional de Produção Mineral, Divisão de Geologia e Mineralogia. Porto Alegre.

Ribeiro, M., Bocchi, P.R., Figueiredo, F.P.M., Tessari, R.I., 1966. Geologia da Quadrícula de Caçapava do Sul, RS, DNPM/DFPM, Rio de Janeiro

Ribeiro, M., Fantinel, L.M., 1978. Associações petrotectônicas do Escudo Sul-Riograndense: I Tabulação e distribuição das associações petrotectônicas do Escudo do Rio Grande do Sul. Inheringia Serviço Geológico, 5: pp. 19–54.

Rieder, M., Cavazzini, G., D'Yakonov, Y.S., Frank-Kamenetskii, V.A., Gottardi, G., Guggenheim, S., Koval, P. V., Muller, G., Neiva, A.M.R., Radoslovich, E.W., Robert, J.L., Sassi, F.P., Takeda, H., Weiss, Z., Wones, D.R., 1998. Nomenclature of the micas. Clays Clay Miner. 46, 586–595. https://doi.org/10.1346/CCMN.1998.0460513

Rizzardo, R., Remus, M.V.D., Dani, N., Flores, R.P., 2007. Zonação Concêntrica nos Anfibólios dos Metabasitos do Complexo Metamórfico Passo Feio, Caçapava do Sul, Rs: Implicações para a Trajetória do Metamorfismo. In: V Congreso Uruguayo de Geología, 2007, Montevideo, Uruguay. Atas do Congresso Uruguayo de Geologia, 2007. v. CD-ROM.

Rock, N.M.S., 1991. Lamprophyres. Springer US, Boston. https://doi.org/10.1007/978-1-4757-0929-2

Roisenberg, A., Loss, E.L., Altamirano, J.A.F., Ferreira, A.C., 1983. Aspectos petrológicos e geoquímicos do vulcanismo Pré-cambriano — Eopaleozóico do Rio Grande do Sul com base nos elementos maiores. Atas do I Simpósio Sul-Brasileiro de Geologia Porto Alegre–RS, pp. 271–285.

Saalmann, K., Gerdes, A., Lahaye, Y., Hartmann, L.A., Remus, M.V.D.D., Läufer, A., 2011. Multiple accretion at the eastern margin of the Rio de la Plata craton: The prolonged Brasiliano orogeny in southernmost Brazil. Int. J. Earth Sci. 100, 355–378. https://doi.org/10.1007/s00531-010-0564-8

Saalmann, K., Remus, M.V.D., Hartmann, L.A., 2009. Neoproterozoic magmatic arc assembly in the southern Brazilian Shield – constraints for a plate tectonic model for the Brasiliano orogeny. Geotecton. Res. 95, 41–59. https://doi.org/10.1127/1864-5658/07/0095-0041

Sartori, P.L.P., Kawashita, K. 1985. Petrologia e geocronologia do Batólito Granítico de Caçapava do Sul-RS. In: II Simpósio Sul-Brasileiro de Geologia, Florianópolis, pp. 102–115.

Scarrow, J.H., Molina, J.F., Bea, F., Montero, P., Vaughan, A.P.M., 2011. Lamprophyre dikes as tectonic markers of late orogenic transtension timing and kinematics: A case study from the Central Iberian Zone. Tectonics 30. https://doi.org/10.1029/2010TC002755

Schulze, D.J., Smith, J.V., Nemec, D., 1985. Mica chemistry of lamprophyres from the Bohemian Massif, Czechoslovakia. Neues Jahrbuch Miner. Abh., 153(3), 321-334.

Scott, B.H., 1979. Petrogenesis of kimberlites and associated potassic lamprophyres from Central West Greenland, in: Kimberlites, Diatremes, and Diamonds: Their Geology, Petrology, and Geochemistry. American Geophysical Union, Washington, D. C., pp. 190–205. https://doi.org/10.1029/SP015p0190

Silva-Filho, B.C., Matsdorf, M., 1987. Análise Estrutural dos Metamorfitos da Borda Oeste do Granito Caçapava, Caçapava do Sul: Implicações Geológicas Locais e Regionais. Atas Do III Simpósio Sul-Brasileiro de Geologia, pp. 197–222. Curitiba.

Soder, C.G., Romer, R.L., 2018. Post-collisional potassic-ultrapotassic magmatism of the variscan orogen: Implications for mantle metasomatism during continental subduction. J. Petrol. 59, 1007–1034. https://doi.org/10.1093/petrology/egy053

Sommer, C.A., de Lima, E.F., Stoll Nardi, L.V., Graciano Figueiredo, A.M., Pierosan, R., 2005. Potassic and low- and high-Ti mildly alkaline volcanism in the Neoproterozoic Ramada Plateau, southernmost Brazil. J. South Am. Earth Sci. 18, 237–254. https://doi.org/10.1016/j.jsames.2004.11.003

Sommer, C.A., Leitzke, F.P., Lima, E.F. de, Barreto, C.J.S., Lafon, J.M., Matté, V., Philipp, R.P., Conceição, R.V., Basei, M.Â.S., 2017. Zircon U-Pb geochronology, Sm-Nd and Pb-Pb isotope systematics of Ediacaran post-collisional high-silica Acampamento Velho

volcanism at the Tupanci area, NW of the Sul-Rio-Grandense Shield, Brazil. Brazilian J. Geol. 47, 545–560. https://doi.org/10.1590/2317-4889201720170064

Sommer, C.A., Lima, E.F., Nardi, L.V.S., Liz, J.D., Waichel, B.L., 2006. The evolution of Neoproterozoic magmatism in Southernmost Brazil: Shoshonitic, high-K tholeiitic and silica-saturated, sodic alkaline volcanism in post-collisional basins. An. Acad. Bras. Cienc. 78, 573–589. https://doi.org/10.1590/s0001-37652006000300015

Souza, T.L., 2020. Gênese dos serpentinitos e esteatitos do Complexo Passo Feio (RS-Brasil) Evidências mineralógicas, geoquímicas e isotópicas. Unpublished PhD thesis. Universidade Federal do Rio Grande do Sul. Porto Alegre. Brasil

Sun, S., McDonough, W.F., 1989. Chemical and isotopic systematics of oceanic basalts: implications for mantle composition and processes. Geol. Soc. London, Spec. Publ. 42, 313–345. https://doi.org/10.1144/GSL.SP.1989.042.01.19

Tommasi, A., Vauchez, A., Femandes, L.A.D., Porcher, C.C., 1994. Magma-assisted strain localization in an orogen-parallel transcurrent shear zone of southern Brazil. Tectonics 13, 421–437. https://doi.org/10.1029/93TC03319

UFRGS, 1998. Projeto Caçapava do Sul: geological mapping. 1:25.000. Porto Alegre

Vaughan, A.P.M., 1996. A tectonomagmatic model for the genesis and emplacement of Caledonian calc-alkaline lamprophyres. J. Geol. Soc. London. 153, 613–623. https://doi.org/10.1144/gsjgs.153.4.0613

Vaughan, A.P.M., Scarrow, J.H., 2003. K-rich mantle metasomatism control of localization and initiation of lithospheric strike-slip faulting. Terra Nov. 15, 163–169. https://doi.org/10.1046/j.1365-3121.2003.00485.x

Vedana, L.A., Philipp, R.P., Sommer, C.A., 2017. Post-collisional basalts of the Acampamento Velho Formation, Camaquã Basin, São Gabriel Terrane, southernmost Brazil. Brazilian J. Geol. 47, 467–489. https://doi.org/10.1590/2317-4889201720170019

Vernon, R.H., Collins, W.J., Cook, N.D.J., 2012. Metamorphism and deformation of mafic and felsic rocks in a magma transfer zone, Stewart Island, New Zealand. J. Metamorph. Geol. 30, 473–488. https://doi.org/10.1111/j.1525-1314.2012.00977.x

Vichi, G., Stoppa, F., Wall, F., 2005. The carbonate fraction in carbonatitic Italian lamprophyres. Lithos 85, 154–170. https://doi.org/10.1016/j.lithos.2005.03.025

Whitney, D.L., Evans, B.W., 2010. Abbreviations for names of rock-forming minerals. Am. Mineral. 95, 185–187. https://doi.org/10.2138/am.2010.3371

Woodcock, N.H., Fischer, M., 1986. Strike-slip duplexes. J. Struct. Geol. 8, 725–735. https://doi.org/10.1016/0191-8141(86)90021-0

Zack, T., John, T., 2007. An evaluation of reactive fluid flow and trace element mobility in subducting slabs. Chem. Geol. 239, 199–216. https://doi.org/10.1016/j.chemgeo.2006.10.020

CAPÍTULO 4 – ARTIGO III

Post-collisional magmatic-hydrothermal mineralization in the São Gabriel Terrane (southern Brazil): insights from mineral chemistry, stable isotopes, and sulfide trace-elements of the Caçapava do Sul skarns

RESEARCH PAPER

To: **ORE GEOLOGY REVIEWS**

Post-collisional magmatic-hydrothermal mineralization in the São Gabriel Terrane (southern Brazil): insights from mineral chemistry, stable isotopes, and sulfide trace-elements of the Caçapava do Sul skarns

[1]HOERLLE, Guilherme Sonntag; [1]REMUS, Marcus Vinicius Dorneles; [2]SILVA, Marco; [2]LANA, Cristiano

[1] Departamento de Mineralogia e Petrologia, Instituto de Geociências, Universidade Federal do Rio Grande do Sul, Porto Alegre, Brazil

[2] Departamento de Geologia, Escola de Minas, Universidade Federal de Ouro Preto, Ouro Preto, Brazil

Corresponding author:
Guilherme Sonntag Hoerlle
guilherme.hoerlle@ufrgs.br
Av. Bento Gonçalves, 9500
43126/110
Porto Alegre, RS, Brazil
Zip code: 90650-001

ABSTRACT

Prograde and retrograde magnesian skarns associated with the Caçapava do Sul Granitic Complex intrusion (São Gabriel Terrane, southern Brazil) host Cu-Fe(Mo-Au) mineralization. Vein and contact prograde skarns contain disseminated pyrite, pyrrhotite, molybdenite, and chalcopyrite formed from the interaction of mafic and felsic intrusions and dolomitic marbles at *ca.* 578 Ma. The prograde skarn mineralization is mainly localized in fold hinges and pinch-and-swell structures. Retrograde skarns host massive chalcopyrite and pyrite associated with chlorite and calcite associated with brittle structures at *ca.* 557 Ma. In this contribution, we provide mineral chemistry analyses of magmatic and skarn assemblages, calcite stable isotope analyses, and trace-element characterization of Fe-Cu sulfides to assess ore-forming processes involved in the formation of the skarns. Amphibole-plagioclase geothermobarometry in granodiorite and monzonite apophyses related with the prograde stage yielded crystallization pressures between ~4 and 5 kbar and temperatures of ~680 and 750°C. Biotite and amphibole composition of granodiorite, monzonite, and Grt-leucogranite apophyses suggest a trend of decreasing oxygen fugacity from early to late intrusions. Calcite-dolomite thermometry indicates temperatures between 580 and 630°C for prograde skarn mineralization whereas chlorite thermometry shows that retrograde were formed at lower temperatures between 280 and 310°C. Calcite from the retrograde skarns yields values of approximately -5.5‰ for $\delta^{13}C_{VPDB}$ and ~9.0‰ for $\delta^{18}O_{SMOW}$, indicating a major contribution of magmatic fluids during the retrograde stage whereas previous studies indicate a mixed igneous-sedimentary character of the prograde skarns. Similarly, Co-Ni ratios in pyrite indicate a mixed origin for the prograde mineralization. In addition, variable Pb and Zn contents in chalcopyrite from retrograde skarns and alteration textures suggest that metals were probably remobilized from prograde pyrite and chalcopyrite to the retrograde skarn sulfides. Our findings are in agreement with a magmatic-hydrothermal origin for the Cu-Fe(Mo-Au) mineralization hosted by the Passo Feio Metamorphic Complex. The prograde and retrograde magnesian skarns of Caçapava do Sul occur in the same age interval (ca. 578-557 Ma) as many other magmatic-hydrothermal base and precious metals mineralization in the São Gabriel Terrane. We propose that the studied skarns belong

to a multi-intrusive copper-porphyry system in the São Gabriel Terrane formed during the post-collisional stage of the Dom Feliciano Belt.

Keywords: skarn; fluid-rock interaction; sulfide trace-element; post-collisional; São Gabriel Terrane

1. INTRODUCTION

Magmatic-hydrothermal Cu±Au mineralization associated with metalliferous, hydrous, and oxidized calc-alkaline magmas in collisional settings is widely recognized (*e.g.*, Richards, 2003; Sillitoe and Hedenquist, 2003; Hou *et al*., 2011). In these settings, the subduction processes are considered crucial to control the high fO_2, H_2O, metal, and sulfur enrichment in the magmatic arcs (*e.g.*, Candela and Holland, 1984; Richards, 2005; Kelley and Cottrell, 2009; Griffin *et al*., 2013). However, magmatic-hydrothermal Cu±Au mineralization associated with post-collisional magmatism has also been increasingly recognized worldwide (*e.g.*, Richards, 2009; Meng *et al*., 2016). In such cases, the causative intrusions tend to be mildly alkaline, relatively sulfur poor and emplaced as isolated complexes formed due to the remelting of previously subduction-modified arc lithosphere (Richards, 2009). In addition, post-collisional magmatic-hydrothermal Cu±Au deposits commonly take place in either extensional to transtensional settings (*e.g.*, Kelley and Ludington, 2002; Müller *et al*., 2002) or contractional environments (*e.g.*, Keskin *et al*., 2008). In both scenarios, the comprehension of physicochemical conditions of the magmatic and hydrothermal fluids is pivotal for understanding metal transport and ore concentration.

In this context, skarn systems formed in response to the reaction of igneous-derived fluids and carbonate rocks (or their metamorphic equivalents) provide a good opportunity to assess the physicochemical conditions of magmatic-hydrothermal fluids and ore-forming processes (*e.g.*, Meinert *et al*., 2005; Barker and Dipple, 2019). In general, there is a parallel relationship between the sequence of emplacement, crystallization, alteration, and cooling of a pluton that corresponds to prograde and retrograde stages of the associated skarns (*e.g.*, Meinert *et al*., 2005; Zhu *et al*., 2021).

The Caçapava do Sul Granitic Complex (CSGC) was emplaced in the easternmost portion of the São Gabriel Terrane (Fig. 1a-b) from *ca.* 578 to 557 Ma during the post-collisional stage of the Dom Feliciano Belt (Nardi and Bitencourt, 1989; 2007; Remus

et al., 2000a; Hoerlle *et al*., 2021a). The CSGC intrusion resulted in prograde and retrograde skarns and associated Fe, Cu (Au), and Mo mineralization hosted by the dolomitic marbles of the Passo Feio Metamorphic Complex (Fig. 1b) (Remus *et al*., 2000a; Remus *et al*., 2011a; Hoerlle *et al*., 2021a). The purpose of this contribution is to assess the ore-forming processes associated with the skarn mineralization based on mineral chemistry, sulfide trace-element contents, and stable isotope analyses. The definition of the physicochemical characteristics of the causative igneous intrusion and skarns can provide useful insights into the prospectivity and relationship of the magmatic rocks and skarn mineralization. In addition, we explore the ore genesis and discuss the relationship of the Caçapava do Sul skarns with other occurrences of post-collisional magmatic-hydrothermal Cu-Fe-(Au) mineralization in the eastern portion of the São Gabriel Terrane (*e.g.* Teixeira *et al*., 1978; Licht, 1980; Remus *et al*., 2000a; 2000b; Bongiolo *et al*., 2011; Camozzato *et al*., 2014; Renac *et al*., 2014; Fontana *et al*., 2017; Lopes *et al*., 2019).

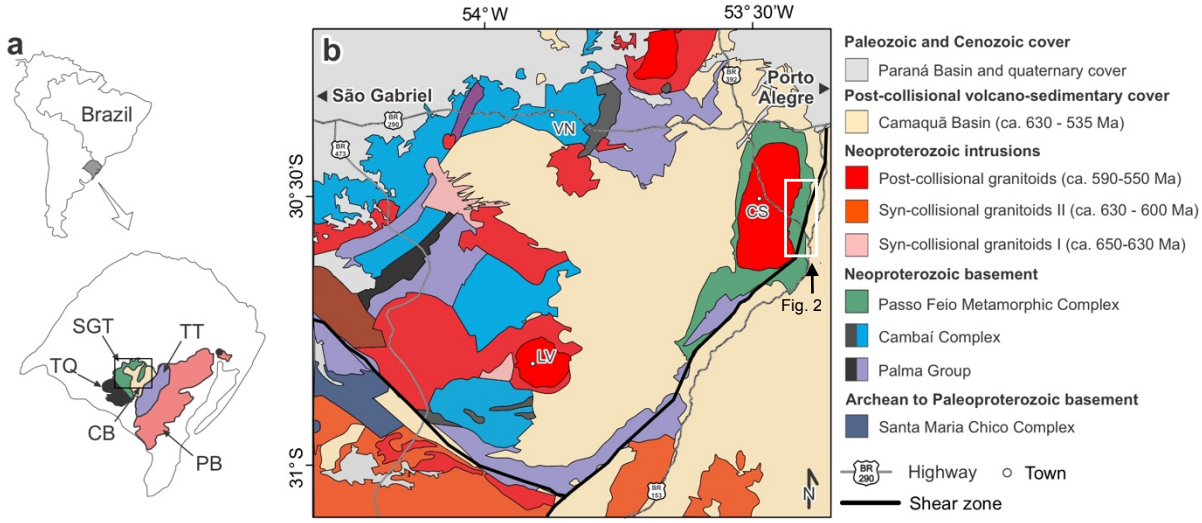

Figure 1: Location and lithotectonic associations of the (a) Sul-riograndense shield and (b) São Gabriel Terrane; IL: Ibaré Shear Zone; CSSZ: Caçapava do Sul shear zone; CSGC: Caçapava do Sul Granitic Complex; SSGC: São Sepé Granitic Complex; LSSA: Lavras do Sul Shoshonitic Association. (Adapted from Porcher and Lopes, 2000)

2. GEOLOGICAL AND METALLOGENIC BACKGROUND

The skarns are hosted by the dolomitic marbles of the Passo Feio Metamorphic Complex (PFMC), located at the easternmost portion of the São Gabriel Terrane (SGT) (Fig. 1b; 2a-b). The SGT represents the Neoproterozoic (920-680 Ma) juvenile magmatic arc association developed during the collision of the Kalahari and Rio de La

Plata cratons (Hartmann *et al*., 2000; Chemale Jr. *et al*., 2000; Fernandes *et al*., 1992, Silva *et al*., 2005; Saalmann *et al*., 2010). Significant base- and precious-metal (Cu, Pb, Zn, Au, Ag) deposits and prospects in the SGT are hosted by the Neoproterozoic volcano-sedimentary rocks of the Camaquã Basin (*e.g.*, Remus, 1999; Remus *et al*., 2000b; Toniolo *et al*., 2004; Laux *et al*., 2005; Remus *et al*., 2011b; Renac *et al*., 2014; Fontana *et al*., 2017; 2019; Lopes *et al*., 2018; 2019; Hoerlle *et al*., 2019), plutonic rocks (Mexias *et al*., 2005; Gastal *et al*., 2015) or metamorphic complexes (Remus *et al*., 2000a; Remus *et al*., 1999). Most of the recent metallogenic models indicate a magmatic-hydrothermal origin for the Cu-Pb-Zn(Au-Ag) mineralization in the São Gabriel Terrane (*e.g.*, Remus *et al*., 2000a; 2000b; Bongiolo *et al*., 2011; Renac *et al*., 2014; Fontana *et al*., 2017; Hoerlle *et al*., 2019; Lopes *et al*., 2019).

The Passo Feio Metamorphic Complex (PFMC) is located in the eastern border of the SGT and consists of a supracrustal association of metapelites, amphibolites, marbles, calc-silicate and metavolcanic rocks intruded by the Caçapava do Sul Granitic Complex (Fig. 1b) (Ribeiro *et al*., 1966; Bitencourt, 1983; Remus *et al*., 2000a). The PFMC hosts Cu-Pb-Zn-(Au) deposits and prospects represented mainly by the Andradas (Cu) and Santa Bárbara (Cu, Au) deposits and Faxinal (Pb, Cu) and Coronel Linhares (Cu, Fe, Au) prospects (Remus *et al*, 2000a). Gold is irregularly distributed in the lodes that reach up to 23 ppm in chip samples (Remus and Hartmann, 1997). The Coronel Linhares prospects are located in the dolomitic marbles area, represented by skarns and chloritites (Remus *et al*., 2000a; Remus *et al*., 2011a; Reis *et al*., 2017).

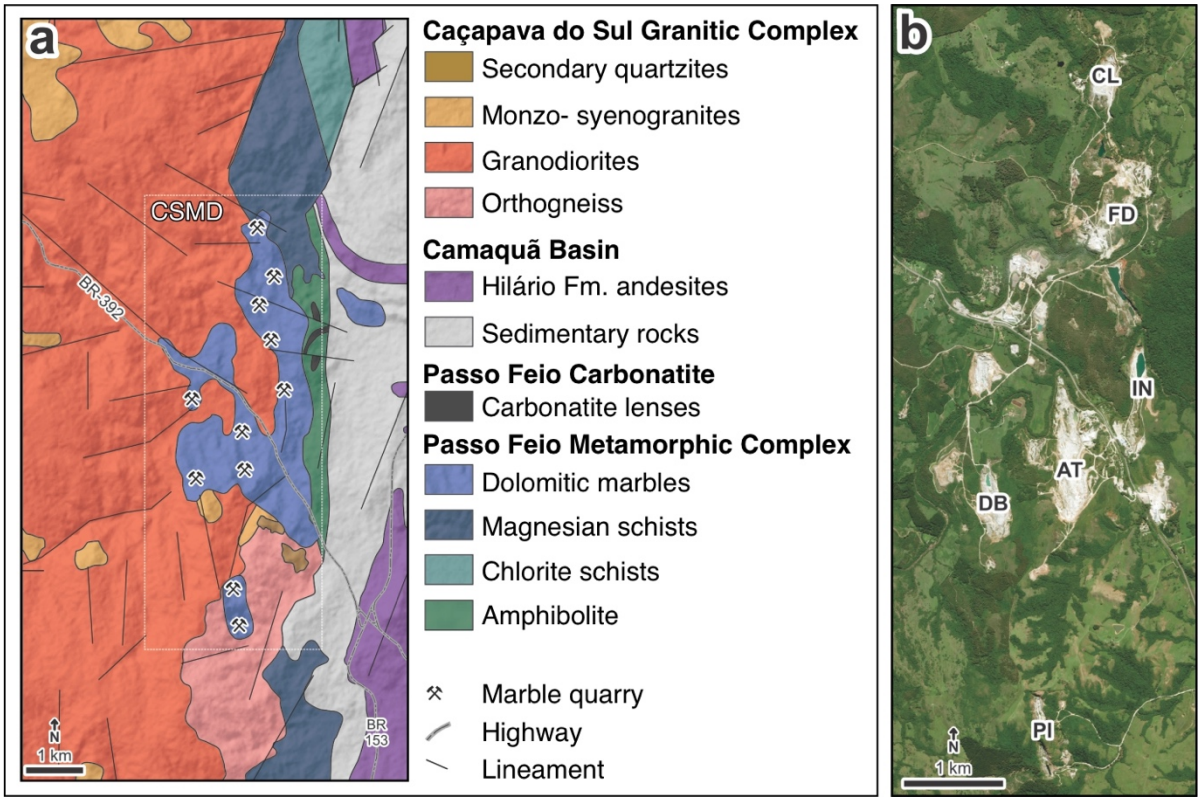

Figure 2: (a) Geological map of the Caçapava do Sul Marble Mining District (CSMD) with open-pit marble quarry locations and (b) location of the main sample collection areas (CL: Coronel Linhares; FD: Fida; IN: Inducal; AT: Ativa Minerais; DB: Dagoberto Barcelos; PI: Pinheiro) (Adapted from Cerva-Alves *et al*., 2017).

3. LOCAL GEOLOGY

The skarns are hosted by dolomitic marbles and mostly found at the contacts or a few meters away from mafic and felsic igneous apophyses. Previous characterization of the field aspects, structural relations and geochronological constraints of the skarns, host rocks, and igneous apophyses are described in Hoerlle *et al*. (2021a). For simplification purposes, we adopted descriptive terms to distinguish skarns based on their mineral assemblages and their spatial position in addition to the consolidated calcic vs. magnesian and endo- vs. exoskarn classifications (*e.g.*, Meinert *et al*., 2005; Winter, 2013). Skarns dominantly composed of carbonates and anhydrous high-temperature assemblages (*i.e.* diopside, forsterite, and spinel) are classified as prograde skarns whereas those with carbonates and hydrous low-temperature assemblages (*i.e.* chlorite, antigorite) are addressed to as retrograde skarns (*e.g.*, Meinert *et al*., 2005). In terms of spatial position, the skarns are divided into contact and vein skarns. Contact skarns occur in the interfaces between igneous apophyses and marbles due to diffusion and infiltration metasomatism along the lithological

boundaries (*e.g.*, Fig. 3i). Vein skarns refer to those formed by the infiltration of igneous derived fluids into cracks and discontinuities of the marbles leading to the replacement of carbonates by calc-silicate (± sulfides) assemblages (*e.g.*, Figs. 3e-h; 3k) (*e.g.*, Winter, 2013). Here, we use the term vein to refer either to the central open fracture-fill and the associated reaction zones into the host rock.

3.1. HOST ROCKS: DOLOMITIC MARBLES OF THE PFMC

The marbles form lenticular bodies that were extensively intruded by tabular felsic and mafic apophyses of variable composition and thickness. In this study, we refer to the sedimentary bedding of the dolomitic marbles as S_0 and the metamorphic foliation as S_1 and S_2. Metamorphic foliation S_1 was formed during the regional metamorphic event before the intrusion of the first apophyses of the CSGC whereas S_2 foliation was developed during the syntectonic intrusion of the apophyses (Nardi and Bitencourt, 1989; Hoerlle *et al*., 2021a). The marbles and the early tabular intrusions form overturned to recumbent isoclinal folds with N-S to NE-SW axis that plunges at low angles mostly to the S-SW (Hoerlle *et al*., 2021a). The dolomitic marbles vary from massive white pure dolomitic marbles to gray impure dolomitic marbles containing up to 15% of tremolite ± talc ± antigorite (Goulart *et al*., 2013).

3.2. MAGMATIC ROCKS: INTRUSIONS OF THE CSGC

The CSGC consists of a granitic batholith and tabular apophyses that intruded the PFMC from *ca.* 578 to 557 Ma (Leinz *et al*., 1941; Ribeiro *et al*., 1966; Sartori and Kawashita, 1985; Nardi and Bitencourt, 1989; Hoerlle *et al*., 2021a). The batholith outcrops an area of approximately 233 km² forming an N-S elongated asymmetrical domal structure dipping in high angles in the W and NW parts, in low angles in the E and SE parts, and sub-horizontally in the central parts (Nardi and Bitencourt, 1989). Mafic, felsic, and composite tabular intrusions within the PFMC are common in the eastern and northern portions of the main granitic body. Composition and deformation are very heterogeneous throughout the batholith. When present, foliation and banding are marked by the preferred orientation of biotite and amphibole, as well as elongate feldspar and quartz grains (Nardi and Bitencourt, 1989). The granitoids are classified as subalkaline medium- to high-K and were formed during the post-collisional stage of

the DFB mostly syntectonic to transcurrent movements (Nardi and Bitencourt, 1989; 2007; Costa *et al*., 1995).

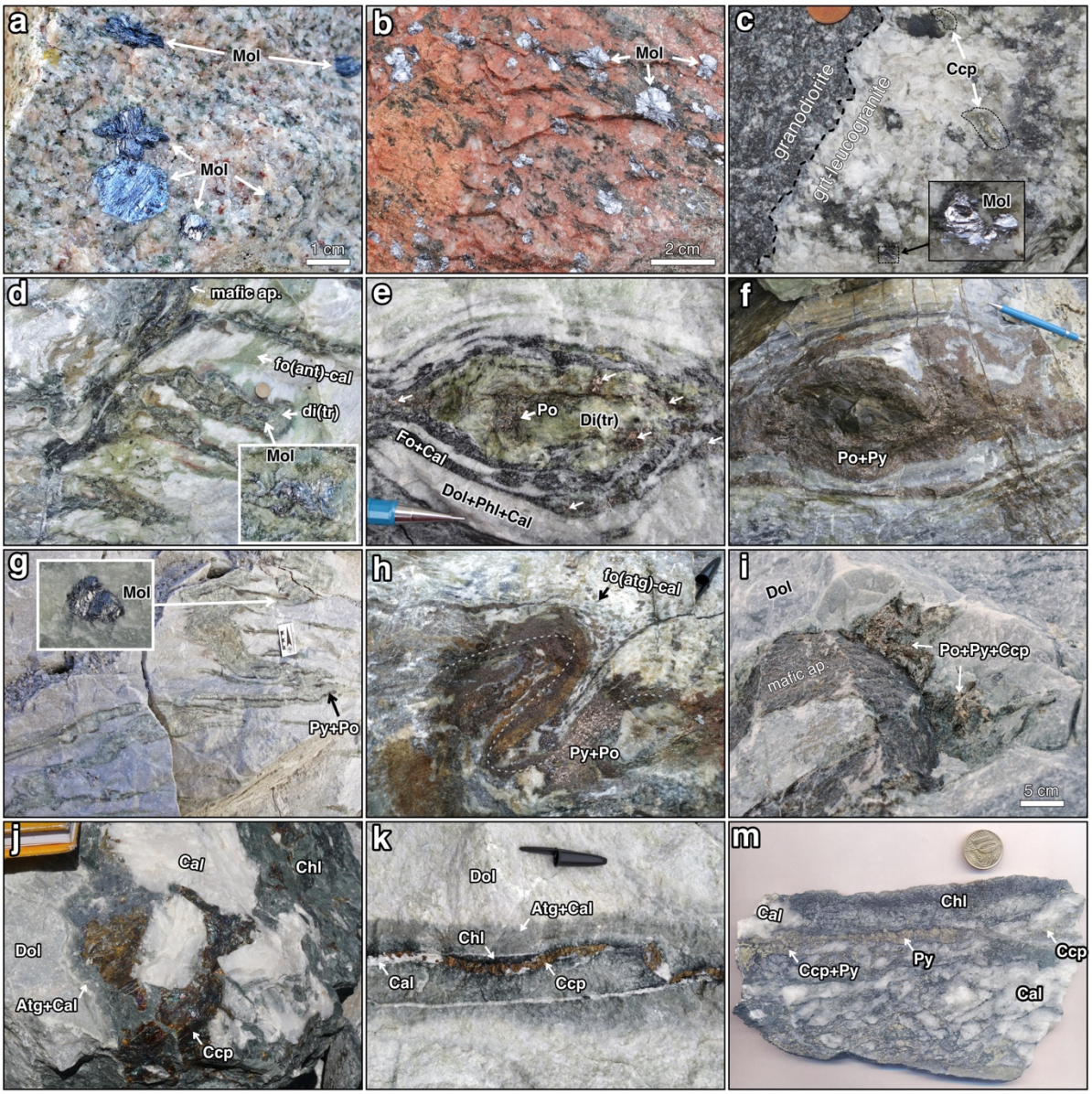

Figure 3: Macroscopic aspects of sulfide mineralization in apophyses, prograde skarns, and retrograde skarns. (a-b) molybdenite mineralization in (a) monzonite and (b) monzogranite apophyses; (c) Mol and Ccp mineralization in pegmatitic portions of syenogranite; (d) Mo in diopside skarns; (e-f) Po and Py in pinch-and-swell di-fo-phl skarns; (g-i) Mol, Po, Py and Ccp mineralization in folded prograde skarns; (j-m) Ccp and Py mineralization in calcite-chlorite±antigorite retrograde skarns.

The assembly of the igneous complex started with minor mafic and felsic tabular intrusions at *ca.* 578 Ma followed by voluminous felsic magmatism and cooling at 557 Ma (Remus *et al*., 2000a; Hoerlle *et al*., 2021a, 2021b). The CSGC is mainly composed of granodiorites, syeno- and monzogranites, monzonites, and quartz-diorites. Tonalites, aplites and pegmatites occur as minor intrusions mainly localized in the

eastern portion of the batholith. Biotite and hornblende comprise the main mafic minerals. However, the wide range of compositions includes variable amounts of biotite, amphibole, muscovite, and garnet. The granitoids are commonly porphyritic and vary from fine- to coarse-grained textures. Allanite, apatite, titanite, and zircon are common accessory phases while tourmaline, magnetite, and ilmenite are rare. Locally, alteration minerals include chlorite, sericite, epidote, and actinolite replacing biotite, feldspars, allanite, and hornblende, respectively. The CSGC apophyses (*i.e.* dykes and sills) are often mineralized with coarse molybdenite aggregates (Fig. 3a-b) or fine to medium grained disseminated pyrite, chalcopyrite, and molybdenite (Fig. 3c).

3.3. PROGRADE SKARNS: DIOPSIDE, FORSTERITE, AND SPINEL SKARNS

The prograde skarns are characterized by magnesian calc-silicate assemblages with diopside, forsterite, and locally spinel as the main prograde silicate phases forming contact and vein skarns. They were formed in response to metasomatic reactions after the infiltration of igneous fluids into lithological boundaries (contact skarns) and cracks, fractures, or discontinuities within the marbles (vein skarns) (Hoerlle *et al*., 2021a). In general, they are composed of three main zones (i) diopside zone (di), (ii) forsterite-calcite zone (fo-cal), and (iii) dolomite-phlogopite-calcite zone (dol-phl-cal). The latter shows the same assemblage as the host marbles but were affected by the igneous fluids causing the recrystallization of dolomite and phlogopite and isotopic modification (Hoerlle *et al*., 2021c). The diopside and forsterite-calcite zones are readly recognized in the field due to the medium to coarse grain sizes and the light to dark green colors in contrast with the white to gray marbles. Nevertheless, the dol-phl-cal zone is harder to be identified because its field aspect is very similar to the unaltered host marbles. The prograde skarns are commonly deformed into pinch-and-swell or boudins that are often folded as well (Fig. 3e-i). Field relations and microstructures suggest that the diopside crystallized before the subsequent fo-cal zone which itself was formed during transpressive deformation (Hoerlle *et al*., 2021a). The contact skarns were formed between metamafic apophyses and the dolomites and they are more abundant near fold hinges. The contact skarns typically show a tremolite-phlogopite-diopside rich layer (endoskarn) followed by di- ± fo-cal zones (exoskarns). Sulfide mineralization in the prograde skarns varies from disseminated molybdenite, pyrite, pyrrhotite, and

minor chalcopyrite (Fig. 3d-e; 3g) to localized massive pyrite and pyrrhotite crystallization in boudin structures and fold hinges (Fig. 3h-i).

3.4. RETROGRADE SKARNS: CALCITE-CHLORITE-SULFIDE VEINS

The retrograde skarns comprise open-fracture filling veins and associated reaction zones. They are typically formed by coarse calcite grains cemented by chlorite ± chalcopyrite ± pyrite bordered by a reaction zone composed of antigorite + calcite (*i.e.*, exoskarn) (Fig. 3j-m). They occur mostly in the northernmost portion of the studied area (CL area; Fig. 2b) adjacent to subvertical NW trending fault zones and areas of intense brittle deformation. The retrograde skarns crosscut S_0 bedding and previous S_1 and S_2 metamorphic foliations. Veins can reach more than 30 cm of thickness and calcite crystals commonly exceed several centimeters (Fig. 3j). Titanite and apatite are common accessory phases commonly disseminated within the chlorite aggregates. Locally, supergene alteration affects the prograde and retrograde skarns forming bornite, chalcocite, and covellite after chalcopyrite (Fig. 4m) (Madruga, 2018).

4. SAMPLING AND METHODS

Sampling aimed at obtaining representative samples of the prograde and retrograde skarns as well as the igneous apophyses located near the mineralized skarns. Sample collection was made out at six key areas of the Caçapava do Sul mining district: Coronel Linhares (CL), Fida (FD), Inducal (IN), Pinheiro (PI), Dagoberto Barcelos (DB) and Ativa (AT) (Fig. 2a; 2b). Mineral compositions and backscattered electron imaging (BSE) were carried out using a CAMECA SXFive electron microprobe at the Electron Microprobe Laboratory at UFRGS. Analytical conditions were set to 15 nA beam current and 5 µm beam size for silicates and 5 nA and 20 µm for carbonate at 15 kV accelerating voltage for both. Amphibole classification was made according to the 2012 IMA report (Hawthorne *et al*., 2012) using the calculation spreadsheet provided by Li *et al*. (2020).

Carbon and oxygen stable isotope analyses were conducted in calcite grains from the retrograde skarns. Coarse calcite grains were hand-picked and powdered with an agate mortar to <200 mesh size. The calcite powders were analyzed at the Laboratório de Geologia Isotópica (LGI) of the Centro de Estudos em Petrologia e Geoquímica (CPGq) of the Universidade Federal do Rio Grande do Sul (UFRGS) on a IRMS Delta

V Advantage mass spectrometer and gas bench using NBS 18, IAEA-CO8, IAEA-CO1 and REI standards. Published data of bulk carbonates stable isotopes for prograde skarns (Hoerlle *et al*., 2021a) and the host rocks (Goulart *et al*., 2013) were used for comparison.

Trace element composition of sulfide minerals was determined using a Thermo-Finnigan Element II sector field ICP-MS coupled to a laser ablation system CETAC Nd: YAG 213 nm UV in the laboratory of Isotope Geochemistry at the Universidade Federal de Ouro Preto. The trace element compositions were calibrated using USGS glass reference materials BHVO-2G and BCR-2 (Wilson, 1997a, 1997b) and STDGL3 (Belousov *et al*., 2015) for analysis of chalcophile and siderophile elements.

5. RESULTS AND DISCUSSIONS

5.1. MINERAL CHEMISTRY AND GEOTHERMOBAROMETRY

The main textural and chemical characteristics of the major constituents from igneous apophyses, prograde and retrograde skarns are presented in this section. In addition, geothermobarometry estimates based on mineral chemistry of amphibole-plagioclase, calcite-dolomite, and chlorite are presented and discussed below. All the electron microprobe analyses are displayed in the Table A.1.

5.1.1. Igneous apophyses and amphibole-plagioclase thermobarometry

Biotite is the main mafic mineral of the igneous apophyses and occurs in the granodiorites, monzonites, monzogranites, and Grt-leucogranites (Fig. 4a-c). Overall, X_{Mg} in unaltered biotite varies from 0.37 to 0.50 in the granodiorites, monzonites and monzogranites and from 0.22 to 0.31 in the Grt-leucogranites. Based on the oxygen fugacity estimative of Anderson *et al*. (2008), the biotite composition of the granitoids corresponds to the magnetite series whereas Grt-leucogranites show lower oxygen fugacity values at the limit between magnetite and ilmenite series (Fig. 5b). Partial chloritization of biotite is common and fully chloritized granodiorites (*i.e.* chloritites) occur mainly in the CL area. Previous chlorite thermometry studies on chloritites of the CL area indicated temperatures between 280°C and 300°C for chlorite alteration (Remus *et al*., 2011a; Reis *et al*., 2017).

The amphibole content of the granodiorites and monzonites is mainly composed of Mg-hastingsite, Mg-Fe-hastingsite, and hastingsite (Fig. 4d, 4f, 5e). Locally, actinolite occurs as a secondary amphibole replacing hastingsite (Fig. 4d). Oxygen fugacity estimates based on the amphibole composition indicate high fO_2 for monzonites and intermediate fO_2 for granodiorites (Fig. 5f). The feldspar content of the granodiorite, monzonite and Grt-leucogranites is composed of oligoclase, albite, and orthoclase (Fig. 5d).

To estimate the pressure conditions of magmatic rocks, the Al content in calcic amphibole in equilibrium with biotite, plagioclase, K-feldspar, quartz, and magnetite or ilmenite was empirically and experimentally developed as a useful geobarometer (Hammarstrom and Zen, 1986; Hollister *et al*., 1987; Schmidt, 1992; Mutch *et al*., 2016). Three granodiorite samples present calcic amphiboles in equilibrium with the above-mentioned assemblage and therefore are suitable for pressure estimates. Calculated pressures for the monzonites and granodiorites vary from 4.2 to 5.4 kbar using Ague (1997) calibration and 3.6 to 4.8 kbar after Mutch *et al*. (2016) calibration (Table 1). In addition, coexisting calcic amphibole and plagioclase in calc-alkaline magmatic rocks can be used to assess the crystallization temperatures of this mineral pair based on rocks crystallized in the range of 400-1100°C and 1-15 kbar (Blundy and Holland, 1990; Holland and Blundy, 1994). Temperatures for the amphibole-plagioclase pairs in the monzonite and granodiorite apophyses were calculated using the geothermometer of Holland and Blundy (1994) which resulted in a temperature range of 682 and 744±50°C (Table 1).

	Pressure (Ague, 1997 after Schmidt, 1992)	**Pressure (Mutch *et al*., 2016)**	**Temperature (Holland and Blundy, 1994)**
Monzonite (AT-MZ-01)	4.2 kbar	3.7 kbar	720±50 °C
Granodiorite (CL-GR-01)	4.9 kbar	4.2 kbar	682±50 °C
Granodiorite (DB-GR-01)	5.4 kbar	4.9 kbar	744±50 °C

Table 1: Geothermobarometry of hornblende and hornblende-plagioclase pairs in monzonite and granodiorite from DB, AT, and CL areas.

5.1.2. Prograde skarns and calcite-dolomite thermometry

Mineral compositions were obtained for clinopyroxene, olivine, amphibole, phlogopite, spinel, and carbonates for seven prograde skarn samples. The clinopyroxene content of the prograde skarns consists of near end-member diopside composition (X_{Mg} > 0.97). The diopsidic composition of clinopyroxene is common for Cu, Fe, and Au skarn deposits (Meinert, 1992). Locally, diopside shows sector zoning and the rims have higher Fe contents (X_{Mg} > 0.84) than the cores. Fe-rich rims in the diopside probably indicate fluid-induced re-equilibration when the rock was infiltrated by the second fluid pulse, responsible for the fo-cal zone. The infiltration of fluids out of equilibrium with the crystallized phases commonly leads to partial re-equilibration at mineral interfaces (*e.g.*, Putnis and Austrheim, 2013).

The amphibole content of the prograde vein skarns is limited to near end-member tremolite inclusions in the diopside (X_{Mg} > 0.97) or by Fe-richer secondary tremolite and actinolite formed along diopside fractures and grain boundaries (X_{Mg} > 0.89). The secondary tremolite generation is related to the fluid infiltration event related to the fo-cal zone formation. Amphibole from the contact skarns shows variable composition ranging from pargasite to actinolite compositions (Fig. 5e).

Olivine occurs as fine- to medium-grained rounded grains in a calcite matrix that are typically fractured and partially to fully replaced by serpentine ± pyrite (4g-i). The composition of the olivine in the prograde skarns is typically Mg-rich. Olivine in the vein skarns associated with diopside (Fig. 4g) is characterized as forsterite (Fo_{95-97}) whereas those in the assemblages with spinel (Fig. 4h) are classified as chrysolites (Fo_{83-84}). Green spinel grains occur locally in aluminum and iron-rich vein skarns associated with chlorite and calcite. The spinel is aluminum-rich (spinel-hercynite) classified as pleonaste with the X_{Mg} (MgO/(MgO+FeOt) ranging from 0.61 to 0.64. The occurrence of such spinel in magnesian skarn assemblages indicates skarn formation at high temperatures, typically above 600°C (*e.g.*, Ballivián-Justiniano *et al*., 2017; Mesquita *et al*., 2017).

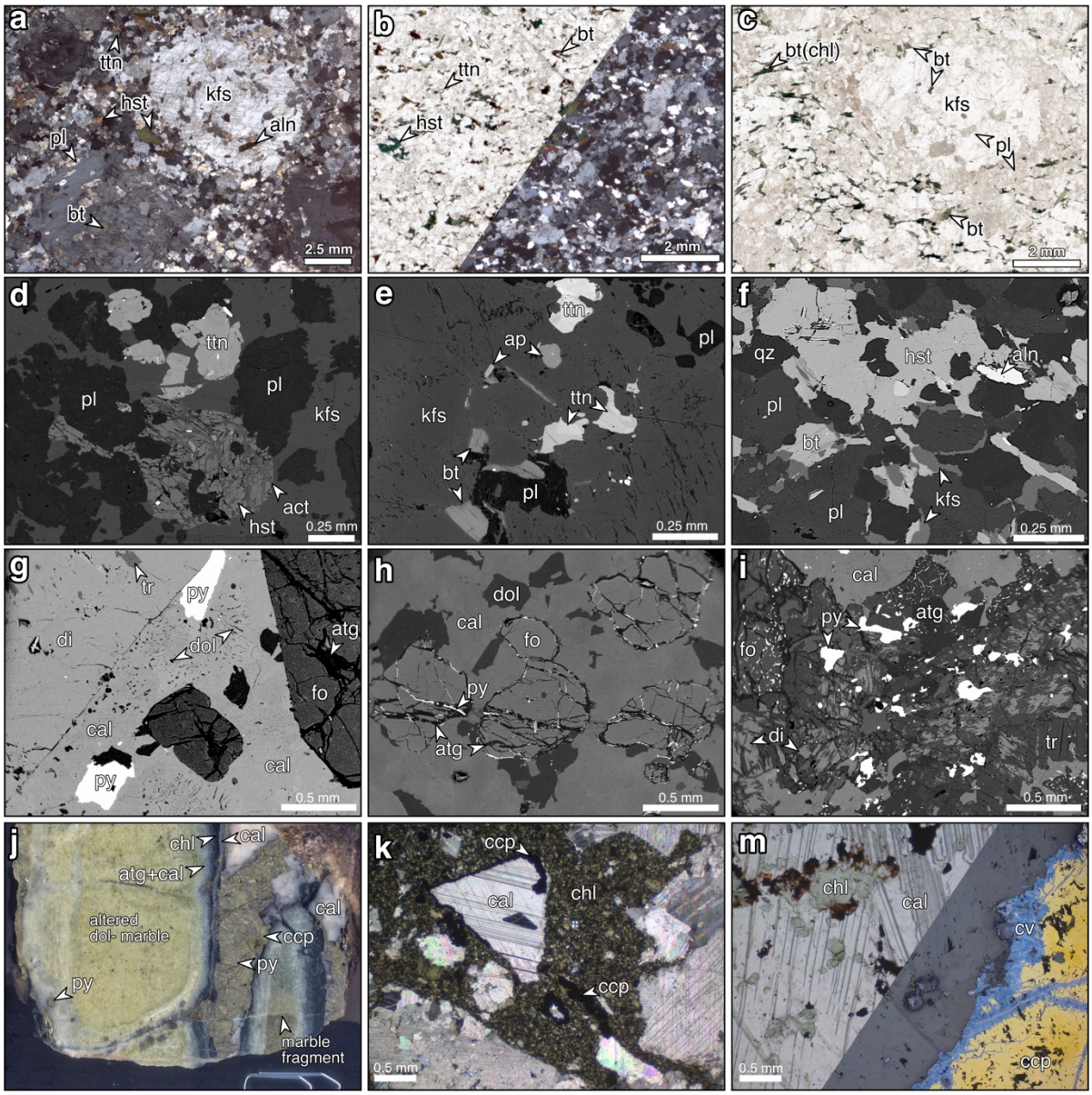

Figure 4: Representative microstructures of igneous apophyses, prograde and retrograde skarns; a) Kfs porphyrocryst with euhedral Pl, Aln and Bt inclusions surrounded by Kfs, Pl, Hst, Bt and Ttn in a porphyritic Bt-hst monzonite (AT-MZ-01, XPL); b) medium grained equigranular Bt-hst granodiorite (DB-GR-01; PPL/XPL); c) Kfs porphyrocryst with Bt and sericitized Pl inclusions in a porphyritic Bt monzogranite (AT-MG-01; PPL); d) Hst and secondary Act in a Bt-hst monzonite (AT-MZ-01; BSE); e) Bt, Ttn, Ap and Pl inclusions in Kfs porphyrocryst in a Bt monzogranite (AT-MG-01; BSE); f) Hst, Pl, Kfs, Qz and Aln in a Bt-hst granodiorite (DB-GR-01; BSE); g) Di with Tr inclusions, Cal with Dol exsolution blebs, Fo and Py in a prograde skarn (DB-PS-01; BSE); h) Py associated with serpentinization of Fo in a prograde skarn (CL-PS-02; BSE); i) Py mineralization associated with retrograde effects in di-fo prograde skarn (CL-PS-01; BSE); j) Ccp and Py mineralization in brecciated retrograde skarn (CL-RS-01; note paper clip for scale); k) Cal fragment in a Chl and Ccp cement in a brecciated retrograde skarn (CL-RS-01; XPL); Ccp mineralization and supergene cv replacement of Ccp in a Chl-cal-sul retrograde skarn (CL-RS-02; PPL/RL).

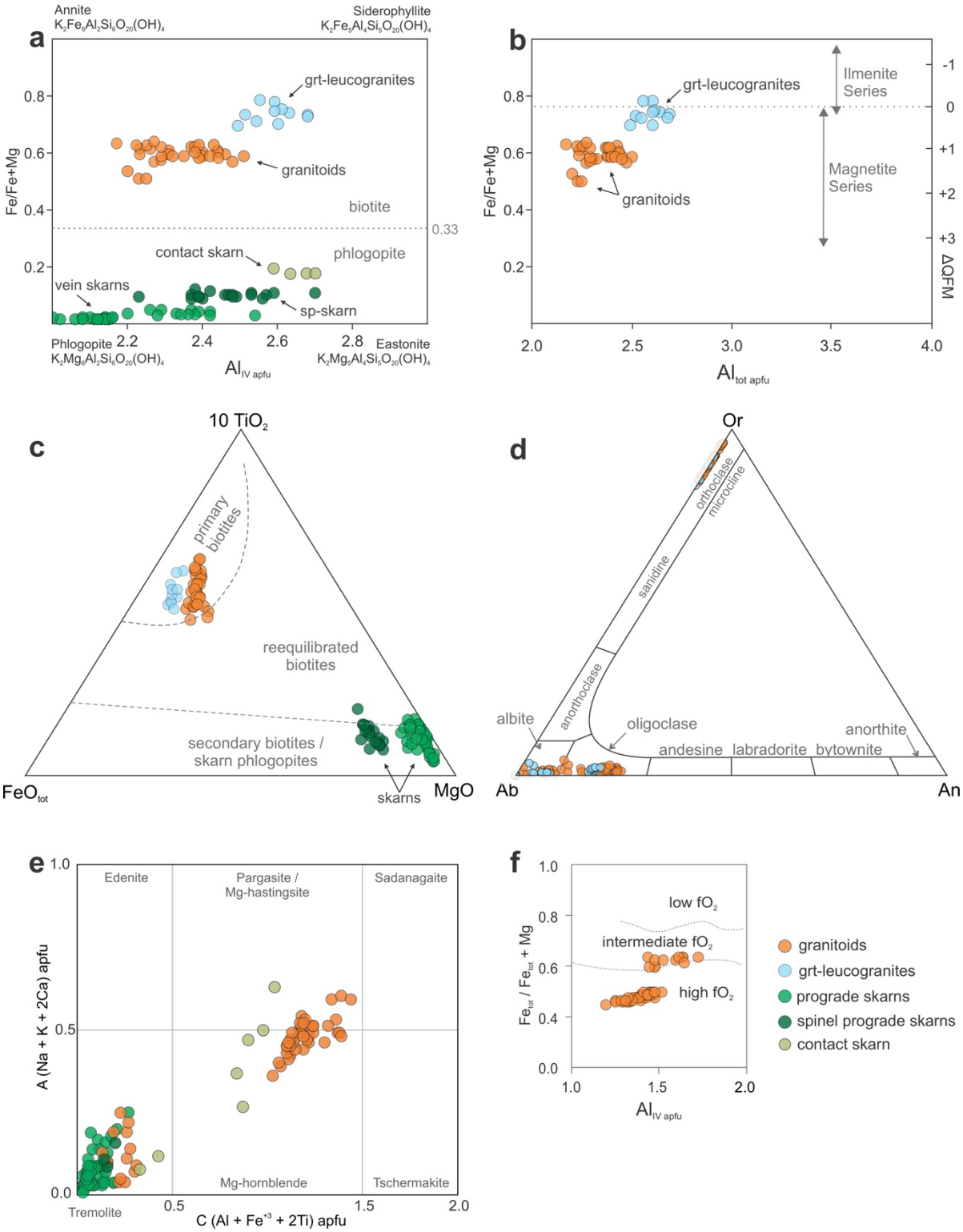

Figure 5: Classification diagrams for biotites (a-c), feldspars (d) and amphiboles (e-f). a) Biotite classification diagram after Deer *et al*. (1986); b) Oxygen fugacity estimative based on biotite chemistry after Anderson *et al*., (2008); c) Biotite FeOtot-MgO-10TiO_2 ternary diagram and classification suggested by Nachit *et al*. (2005); d) Feldspar classification diagram (Deer *et al*., 1992); e) Amphibole classification diagram according to IMA 2012 recommendation (Hawthorne *et al*., 2012); f) Oxygen fugacity classification based on amphibole composition (Anderson and Smith, 1995).

Phlogopite is common in the prograde skarns and occurs mostly along dolomite grain boundaries in the outer zones of vein and contact skarns. Phlogopites from vein skarns are Mg-rich (X_{Mg} ~ 0.98). Such phlogopites are closer to an end-member composition then those from the spinel-bearing vein skarns ($X_{Mg:}$ 0.90) and contact-skarns (X_{Mg} ~ 0.81) (Fig. 5a, 5c). Previous studies suggest that higher Al in metasomatic phlogopite indicate compositional modification of former phlogopite by the reaction with infiltrating fluid whereas low Al phlogopite is directly precipitated from the skarn-forming fluid (Bucher-Nurminen, 1988).

Calcite grains in coexistence with dolomite from four prograde skarns were analyzed to obtain crystallization temperatures using the calcite-dolomite thermometer (Goldsmith and Newton, 1969; Powell *et al*., 1984; Anovitz and Essene, 1987). The coexistence of calcite and dolomite allows the estimation of crystallization temperatures considering the range of immiscibility between both minerals in the $CaCO_3$-$CaMgCO_3$ system. However, large ranges in the X_{Mg} values and retrograde effects often complicate the interpretation of measured data. To work around this problem, we calculated the calcite crystallization temperatures using the mean X_{Mg} + 2σ approach proposed by Roselle (1997) and the calcite inclusions in forsterite approach described by Ferry (2001). A temperature of 581°C was calculated using the mean X_{Mg} + 2σ approach for the whole set of analyses (485 analyses in 4 samples). In addition, we used the calcite-in-forsterite approach on one prograde skarn. Even though the calcite inclusions in the forsterite were not fully isolated from retrograde effects, it showed less exsolved dolomite blebs than the matrix calcite, and yielded higher X_{Mg} values. Remarkably, the temperature estimate for the calcite inclusion using the X_{Mg} + 2σ approach resulted in the same value of 581°C. However, when the Mg content from the exsolved dolomite are reintegrated into the calcite inclusion (following the method of Mizuochi *et al*., 2010) to avoid the retrograde effects, we obtained a crystallization temperature of 628°C. Despite the variation of ~50°C from different approaches, calcite-dolomite thermometry indicates that the prograde skarns and the associated pyrite, pyrrhotite, and molybdenite mineralization were formed at high temperatures between ~580 and ~630°C (Table 2).

	X_{Mg} avg	X_{Mg} avg + 2σ	T °C (mean + 2σ)	T °C (reintegrated exsolved dolomite)
Calcite included in forsterite of prograde skarn (n=15)	0.044	0.065	581°C	628°C
Matrix and inclusion calcite of prograde skarns (n=485)	0.038	0.065	581°C	-

Table 2: X_{Mg} and calculated crystallization temperatures for calcite from prograde skarns.

5.1.3. Retrograde skarns and chlorite thermometry

The retrograde skarns are mainly composed of calcite, chlorite, and variable amounts of massive chalcopyrite and pyrite (Fig. 4j-m). Chlorites from all the analyzed retrograde vein skarns are Mg-rich and classified as clinochlore (Fig. 6a). To estimate the temperatures of the retrograde stage mineralization, we applied the empirical geothermometer proposed by Cathelineau (1988). The chlorite geothermometer considers that the Al_{IV} in chlorite is a function of temperature and it can be applied to diagenetic, hydrothermal, and metamorphic settings. A total of 306 analyses were performed in chlorites from retrograde skarns, as well as in retrograde chlorites from the spinel-bearing prograde skarn and igneous apophyses samples. Calculated temperatures for primary chlorites from the retrograde skarns indicate that the calcite-chlorite-sulfide veins were formed at ~300°C. Calculated values for secondary chlorites from Grt-leucogranites show slightly lower temperatures of ~275°C (Fig. 6b) whereas estimated temperatures for the spinel skarn vary from ~270 to ~370°C. The large range for the spinel skarn chlorites is attributed to variable degrees of re-equilibration of the chlorite during retrogression. Even the highest temperature estimates of ~ 370°C are far from the stability range for the observed assemblage of spinel + chlorite + dolomite + calcite + forsterite which is typically formed above 500°C at middle to upper crust depths (Bucher-Nurminen, 1981, 1982). Similar temperature ranges between 250 and 310°C were obtained in chlorites from chloritites and altered granite samples in the CL (Remus *et al*., 2011a; Reis *et al*., 2017). The same temperature range observed in the

chlorites from retrograde skarns and chloritites suggest that probably the same hydrothermal fluid event was responsible for the extensive chloritization in the area.

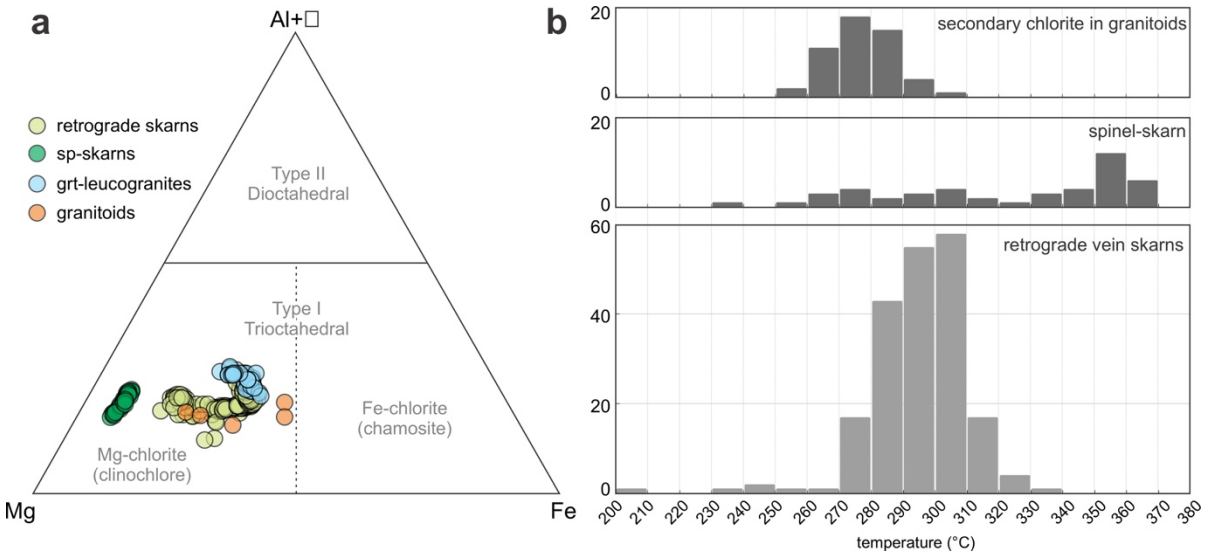

Figure 6: Chlorite classification diagram and crystallization temperature estimates; (a) Al+vacancy-Mg-Fe ternary diagram after Zane and Weiss (1998); (b) chlorite crystallization temperature histograms after Cathelineau (1988)

5.2. PYRITE AND CHALCOPYRITE TRACE-ELEMENT CONTENTS

LA-ICP-MS analyses were carried out in seven representative samples from prograde (5 samples) and retrograde (2 samples) skarns to characterize the trace element contents of pyrite and chalcopyrite in the different ore phases (Table A.2). Pyrite from the prograde skarns shows relatively high average amounts of Co, Ni, and Mn (~100 - 500 ppm), low As, Zn, and Se (~0.1 - 10 ppm), and Au, Ag, Te, Tl, and Bi values below detection limits. When present in the fluid phase, pyrite typically incorporates Co, Ni, As, and Se in the crystal lattice whereas Cu, Zn, Au, Te, Ag, Pb, and Bi are more commonly present as discrete nanoparticles or microinclusions in pyrite fractures (Steadman *et al.*, 2021). In general, pyrite formed from high-temperature fluids (*i.e.* Porphyry Cu, skarns, IOCG settings) contains higher amounts of Co, Ni, Te, and Se and lesser amounts of Tl, Sb, and Hg than pyrites formed from low-temperature fluids (*e.g.*, Fleet *et al.*, 1989; Maslennikov *et al.*, 2009; Keith *et al.*, 2018; Steadman *et al.*, 2021). Co-Ni ratios in the prograde skarn pyrite vary from 0.2 to 1.6 (Fig. 7a). High Co/Ni ratios (> 1) are commonly attributed to a magmatic origin for pyrite while low

ratios (Co/Ni < 1) are associated with sedimentary origins (Bralia *et al*., 1979). We consider that the variable Co/Ni ratios around 1 obtained for the prograde skarn pyrites indicate a mixed sedimentary-magmatic origin. Prograde skarn pyrites show variable Mn contents (~8 - 1700 ppm). Detailed characterization of isotopic and mineral chemistry profiles along a prograde contact skarn showed that Fe and Mn are incorporated into the host-rock phlogopite and dolomite in response to the infiltration of igneous derived fluids (Hoerlle *et al*., 2021c). In addition, the host-rock marbles of the PFMC are typically Mn poor (Goulart *et al*., 2013). Therefore, in our case, pyrite with higher Mn content could indicate an igneous origin whereas low Mn pyrite would have a sedimentary origin.

Chalcopyrite is typically a poor host for trace elements compared to other common Cu-Fe sulfides (*e.g.*, Cook *et al*., 2009; 2011; George *et al*., 2016; 2015). However, chalcopyrite tends to host more trace elements in the absence of other co-crystallizing sulfides, particularly sphalerite and galena (George *et al*., 2018). Among the analyzed chalcopyrites, only Zn, Mn, Cr, and Ti were present in significant amounts (>100 ppm). In particular, chalcopyrite from one retrograde skarn yields average Zn values of approximately 4000 ppm and maximum values up to 20,000 ppm whereas those from other retrograde skarn contains very low Zn values (~ 5 ppm) (Fig. 7b). On the other hand, the latter showed the highest Pb contents of 281 ppm and the first yielded lower values of ~42 ppm. In general, Zn concentrations above 2,000 ppm are attributed to microinclusions of sphalerite (*e.g.*, George *et al*., 2018; Moggi-Cecchi *et al*., 2002; Huston *et al*., 1995). In addition, the Zn and Pb ranges for chalcopyrite in the prograde skarns coincide with one of the retrograde skarn sample. Despite the macroscopic and mineralogical homogeneities in the retrograde skarn samples, we consider that distinct Pb and Zn ranges in the chalcopyrites could indicate variable physicochemical conditions of the mineralizing fluid. Alternatively, the coincidence of Pb and Zn ranges of prograde skarns and one of the retrograde skarn samples could indicate the remobilization of sulfides from the prograde skarn stage. However, our dataset only allows us to speculate on the controls of Pb and Zn distribution whereas further studies on larger datasets might unveil spatial, microstructural, or physicochemical controls of the distribution of these elements in the skarn system.

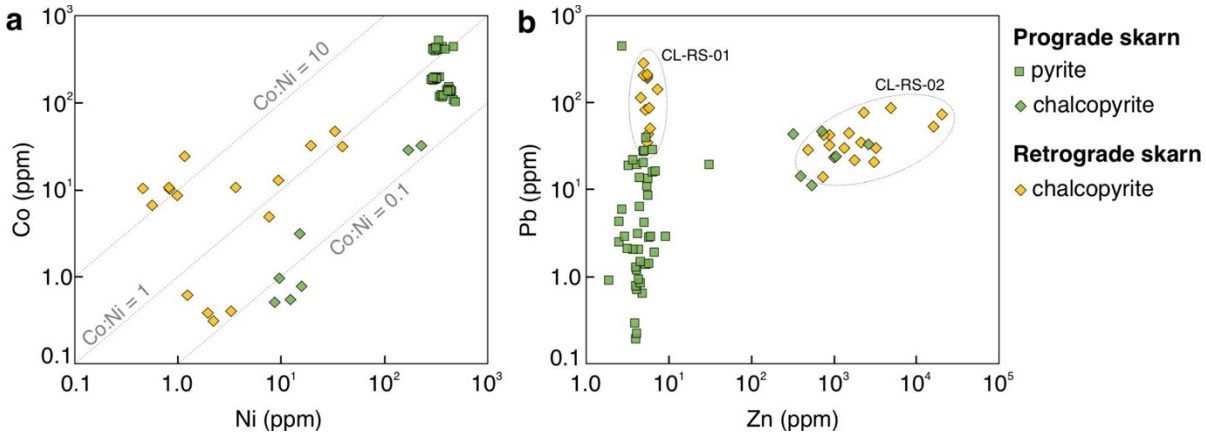

Figure 7: Trace element concentration biplots for pyrite and chalcopyrite from prograde and retrograde skarns. (a) Co vs. Ni biplot; (b) Pb vs. Zn biplot.

5.3. CARBON AND OXYGEN STABLE ISOTOPE COMPOSITION

$\delta^{13}C$ and $\delta^{18}O$ isotope analyses were performed on calcites from five retrograde vein skarn samples. Results are listed in Table 3 and plotted in Figure 7. Bulk carbonate $\delta^{13}C$ and $\delta^{18}O$ isotopic compositions of prograde skarns from Hoerlle *et al*. (2021c) and dolomitic marble from Goulart *et al*. (2013). The $\delta^{13}C_{VPDB}$ isotopic values of the retrograde calcites vary from −5.69 and -5.31‰, while the $\delta^{18}O_{SMOW}$ compositions range from 8.35 and 9.90‰ (Fig. 8). Both $\delta^{13}C$ and $\delta^{18}O$ isotope values overlap typical magmatic fields (Ohmoto, 1972; Hoefs, 2009) and show that the retrograde skarn calcites are largely depleted in respect to the carbonates from the host rocks and prograde skarns (Fig. 8). We interpret that the retrograde skarns were formed directly from water-rich magmatic fluids with little influence of metamorphic fluids (*i.e.*, CO_2 from devolatilization reactions).

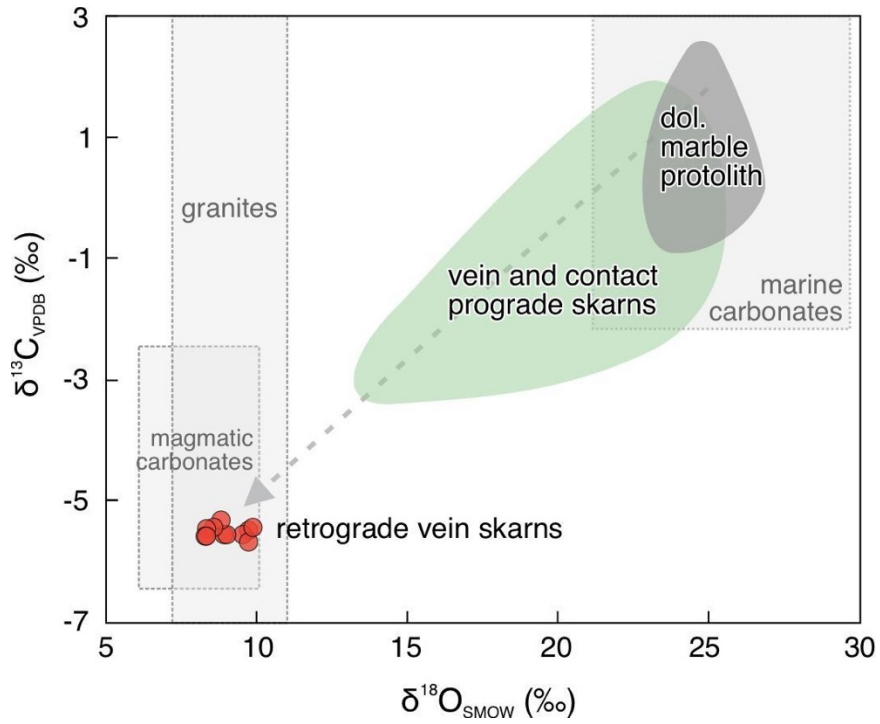

Figure 8: $\delta^{13}C_{VPDB}$ versus $\delta^{18}O_{SMOW}$ for the retrograde skarn calcite and comparison with the isotope composition of prograde skarns (Hoerlle *et al.*, 2021c), dolomitic marble protolith (Goulart *et al.*, 2013), and fields for marine carbonates, granites, and magmatic carbonates (Hoefs, 2009).

Sample	$\delta^{13}C_{VPDB}$ (‰)	$\delta^{18}O_{SMOW}$ (‰)	$\delta^{18}O_{VPDB}$(‰)
CL-RS-04a	-5.49	9.76	-20.47
CL-RS-04b	-5.56	9.58	-20.64
CL-RS-02a	-5.57	8.94	-21.26
CL-RS-02b	-5.56	9.04	-21.17
CL-RS-05a	-5.69	9.80	-20.43
CL-RS-05b	-5.45	9.90	-20.33
CL-RS-06a	-5.31	8.85	-21.35
CL-RS-06b	-5.45	8.60	-21.59
CL-RS-07a	-5.58	8.35	-21.84
CL-RS-07b	-5.58	8.40	-21.79

Table 3: δ13C and δ18O values for calcite in the retrograde skarns

5.4. SKARN EVOLUTION AND ORE-FORMING PROCESSES

Skarn ore mineralization commonly occurs in two stages associated with the emplacement and cooling phases of a pluton (Meinert *et al*., 2005). In the Caçapava do Sul skarn system, the prograde and retrograde stages led to different sulfide assemblages and mineralization styles (Fig. 9). Mineralization from the prograde stage occurred as lenticular or disseminated pyrite, pyrrhotite, molybdenite, and minor chalcopyrite. In general, the prograde mineralization exhibits low sulfide concentrations throughout the marble sequence with higher concentrations localized in contact skarns at mafic apophyses' fold hinges. At this stage, ore deposition is mainly associated with anhydrous skarn assemblages (*e.g.*, diopside, forsterite, spinel) formed at relatively high temperatures between 580°C and 630°C. The prograde skarns resulted from the infiltration and reaction of fluids released from mafic and felsic apophyses and the dolomitic marbles (Hoerlle *et al*., 2021a). The mafic apophyses were interpreted to be formed by metasomatized mantle-derived magmas with variable degrees of crustal assimilation (Hoerlle *et al*., 2021b). In addition, aluminum in amphibole barometry for porphyritic Bt-Hbl felsic apophyses indicated crystallization depths ranging from ~12 to 17 km (using 1 kbar for 3.3 km depth for continental crust). These pressure estimates suggest that felsic tabular apophyses originated at either two magma chambers at variable depths or one large magma chamber ranging from ~12 to 17 km. The volatile-rich mafic and felsic dykes are interpreted to be responsible for sulfur and metal mobilization and transport from the upper mantle and deeper levels of the crust to the upper crust. Furthermore, previous studies in a post-collisional porphyry-skarn system indicated that mixing between lower crust magmas and hydrous mantle-derived magmas plays a major role in providing sufficient metals, water, and sulfur to form a Cu±Mo±Au deposit (Yang *et al*., 2020). In our case, we consider that the intermediate and high oxidation state of the magmas controlled the behavior of the sulfur and metal partitioning into the fluid phases leading to further deposition of sulfides in the skarns or disseminated in the late Grt-leucogranites at a lower oxidation state. Such processes are critical for the development of magmatic-hydrothermal Cu±Au mineralization and porphyry Cu±Mo±Au, skarn, and epithermal deposit formation (*e.g.*, Candela and Holland, 1984; Sillitoe and Hedenquist, 2005; Richards, 2003, 2009; Cooke *et al*., 2013).

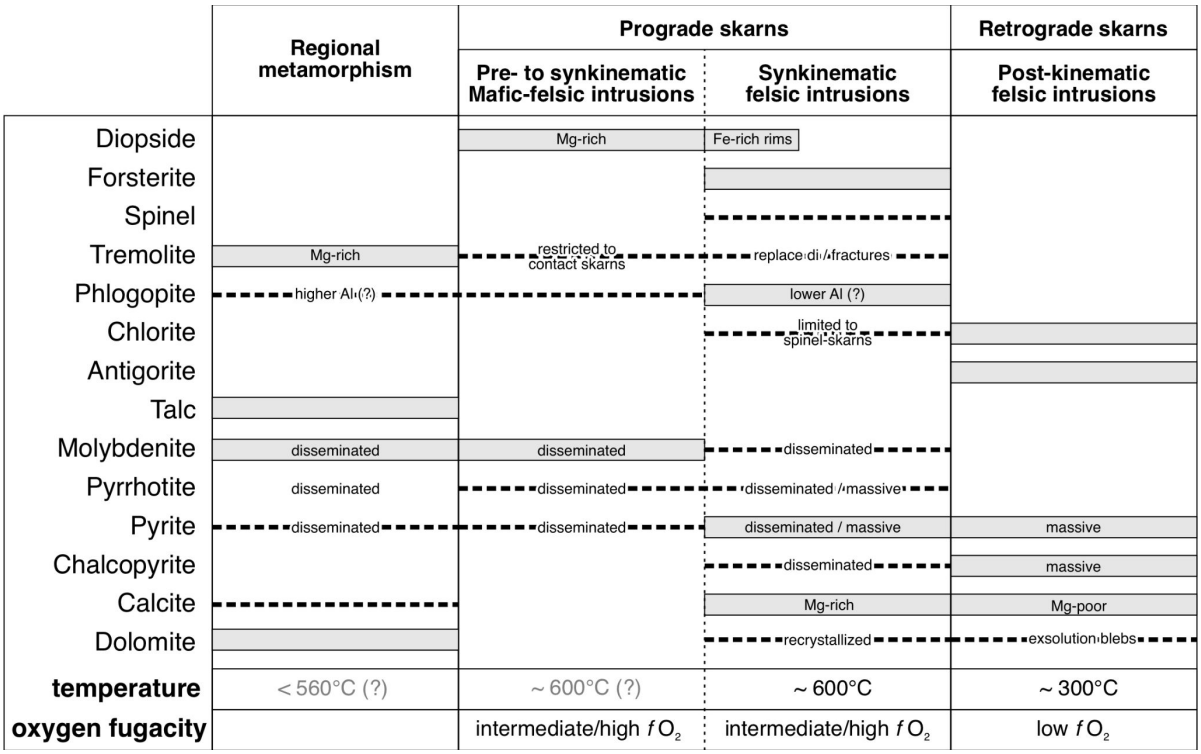

Figure 9: Schematic mineral evolution for the prograde and retrograde skarns of Caçapava do Sul.

In opposition to the prograde stage disseminated mineralization, the retrograde stage resulted in massive chalcopyrite and pyrite deposition highly localized at faults and fractures at lower temperatures between 270 and 310°C. However, retrograde effects are widespread along the marble district affecting the previous prograde skarns and mafic-felsic apophyses. The retrograde effects in the prograde assemblages are evidenced by diopside and forsterite replacement for hydrous assemblages (*e.g.*, tremolite and antigorite). Notably, the prograde skarns that were highly affected by retrograde effects show very little or no sulfide content at all. Therefore, we consider that late fluids associated with the retrograde stage were responsible for sulfide remobilization, transport and deposition at brittle structures. Similarly, previous studies indicated that the chloritization of biotite and plagioclase of felsic and mafic apophyses by magmatic-hydrothermal fluids resulted in the remobilization of major elements (*e.g.*, Fe, Mg, Si, Ca) and base metals Cu (Au) (Remus *et al.*, 2011a; Reis *et al.*, 2017). The carbon and oxygen stable isotope compositions of the retrograde skarn calcite indicate a strong magmatic character of the vein forming fluid, associated with high fluid inputs during the cooling of the granitic complex. Notably, the $\delta^{13}C$ composition indicates that

magmatic fluid had significant amounts of CO_2. In addition, we note that the lack of epidote and the abundance of calcite in these veins also suggest high CO_2 activity during the formation of calcite-chlorite-sulfide veins.

5.5. INSIGHTS INTO THE POST-COLLISIONAL MAGMATIC-HYDROTHERMAL CU±AU MINERALIZATION IN THE SÃO GABRIEL TERRANE

The occurrence and nature of the prograde and retrograde skarns associated with the CSGC are in agreement with a magmatic-hydrothermal origin for Cu±Au mineralization in the easternmost São Gabriel Terrane (Remus *et al*., 2000a). The mineralization is genetically associated with the CSGC intrusions with variable assimilation from the amphibolites, schists, and marbles of the PFMC (Remus *et al*., 2000a; Hoerlle *et al*., 2021a). Despite the geochemical, petrographic, and structural heterogeneities of the CSGC, its origin is attributed to either partial melting of the lower crust or from differentiation of mantle-derived basaltic magmas with variable crustal contamination (Nardi and Bitencourt, 1989). Recent findings indicate that lamprophyre dykes and coeval Bt-hbl-granodiorite apophyses were responsible for the formation of the prograde skarns at *ca.* 578 Ma whereas the retrograde skarns were formed at *ca.* 557 Ma (Hoerlle *et al*., 2021a). The wide age interval for the CSGC (ca. 578 - 557 Ma), the occurrence of hydrous mafic magmatism in the area and the multi-stage skarn system bring new perspectives to the understanding of the origins of the Cu±Au mineralization hosted by the PFCM. The prograde skarns were formed within the same age interval as the porphyry-epithermal Cu±Au mineralization associated with the Lavras do Sul Shoshonitic Association (LSSA) in the southwestern portion of the São Gabriel Terrane (Nardi and Lima, 1988; Mexias *et al*., 1994; Hartmann *et al*., 1999; Remus *et al*., 2000b; Bongiolo *et al*., 2011; Lopes *et al*., 2018). The age of the mineralization associated with the LSSA is estimated between *ca.* 573 and 588 Ma (Mexias, 2000; Bongiolo *et al*., 2003). For such mineralization, lamprophyre magmas were admitted as possible sources for metals and sulfur (Müller *et al*., 2012). In addition, shoshonitic magmatism commonly plays a major role in important porphyry gold-copper mineralization (*e.g.* Cadia district; Holliday *et al*., 2002). However, despite the age similarity and the presence of lamprophyre intrusions in the Caçapava do Sul skarn system and LSSA-related mineralization, further isotopic and geochemical studies on the causative dykes and mineralization are needed to test and establish a

genetic relationship between them. The age of the retrograde skarns, estimated at *ca.* 557 Ma (Hoerlle *et al*., 2021a), is closer to the age of the post-collisional and mostly undeformed alkaline granites such as the São Sepé Granitic Complex of *ca.* 550 Ma (Sartori, 1978; Remus *et al*., 1999).

Recent zircon geochronology and Pb isotopic studies in the Pb-Zn (Au-Ag) Santa Maria deposit hosted by the Santa Bárbara Group of the Camaquã Basin indicated an age of *ca.* 565 Ma for the mineralization (Pereira *et al*., 2021). The Santa Maria Pb-Zn (Au-Ag) and Camaquã Cu (Au-Ag) comprises the largest base metal deposits of the Sul-riograndense shield (Leinz and Almeida, 1941; Teixeira *et al*., 1978; Licht, 1980; Remus *et al*., 1999; Camozzato *et al*., 2014). These deposits are located in Caçapava do Sul to the south of the studied skarns (<40 km). Although the metallogenesis of the Santa Maria and Camaquã deposits has been widely debated, the most accepted hypotheses propose distal magmatic-hydrothermal or porphyry-epithermal models associated with the Neoproterozoic post-collisional magmatism of the DFB (Bettencourt, 1973, Beckel, 1992, Remus *et al*., 2000b, Ronchi *et al*., 2000, Laux *et al*., 2005, Renac *et al*., 2014). Therefore, we note that the Caçapava do Sul skarns were formed during this metallogenic significant age interval in the São Gabriel Terrane (ca. 590-560 Ma). Furthermore, previous studies indicated that the lead isotope composition of the least radiogenic Cu-Fe sulfides from the retrograde skarns and galena from other PFMC prospects (Faxinal) show values that are close to the initial ratio estimates of the Cu-Fe sulfides from the Camaquã and Santa Maria deposits (Remus *et al*., 2000a, 2000b). Hence, the retrograde skarn mineralization was interpreted to share the same Pb source and time of the Camaquã and Santa Maria deposits.

The Cu±Au magmatic-hydrothermal mineralization associated with the post-collisional magmatism of the Dom Feliciano Belt show an isolated distribution throughout the SGT. Such pattern of isolated occurrences over a large area and age interval is a common feature for porphyry-skarn Cu±Au and epithermal Au deposits in post-collisional settings (Richards, 2009). Therefore, we propose that the Caçapava do Sul skarns add supporting evidence to the hypothesis of the existence a multi-intrusive copper porphyry system in the São Gabriel Terrane formed during the post-collisional stage of the Dom Feliciano Belt.

6. CONCLUSIONS

1) Fe-Cu-Mo mineralization was formed in the contact of the Ediacaran post-collisional intrusion of the Caçapava do Sul Granitic Complex and the dolomitic marbles of the Passo Feio Metamorphic Complex.
2) Disseminated pyrite, pyrrhotite, chalcopyrite, and molybdenite mineralization associated with diopside-, forsterite-, and spinel-skarns was formed at high-temperatures (~600°C) during early and synkinematic emplacement of mafic and felsic apophyses.
3) Amphibole-plagioclase thermobarometry of tabular intrusions indicate crystallization pressures between 4 and 5 kbar (12 -17 km of depth) and temperatures from 680° to 750°C. Additionally, amphibole and biotite chemistry suggest decreasing oxygen fugacity of the magmas from early intrusions (*e.g.* Bt-hbl granodiorites) to the late felsic apophyses (Grt-leucogranites).
4) The early volatile-rich mafic and felsic intrusions are interpreted to be responsible for sulfur and metal mobilization and transport from the upper mantle and deeper levels of the crust to the upper crust. Fluids released from the cooling apophyses infiltrated the marbles and resulted in the deposition of the Fe-Cu-Mo sulfides in the prograde skarns.
5) Massive chalcopyrite and pyrite associated with chlorite and calcite were formed at brittle structures at approximately 300°C during final stage of granitic emplacement. $\delta^{13}C$ and $\delta^{18}O$ values of vein calcite indicate major magmatic contribution for retrograde stage fluids.
6) The prograde and retrograde magnesian skarns of Caçapava do Sul occur in the same age interval (ca. 578-557 Ma) as many other magmatic-hydrothermal base and precious metals mineralization in the São Gabriel Terrane, which itself may host a multi-intrusive copper porphyry system formed during the post-collisional stage of the Dom Feliciano Belt (ca. 590-550 Ma).

ACKNOWLEDGEMENTS

We acknowledge the National Council for Scientific and Technological Development of Brazil (CNPq) for funding through a Ph.D. scholarship to G.S. Hoerlle (141333/2017-0). We thank Gabriel Monaco for fieldwork and EMPA assistance. Denise M. Canarin, Susan Drago, and Rafael D. Hofmann are acknowledged sample preparation and EMPA assistance.

REFERENCES

Ague, J.J., 1997. Thermodynamic calculation of emplacement pressures for batholithic rocks, California: Implications for the aluminum-in-hornblende barometer. Geology 25, 563–566. https://doi.org/10.1130/0091-7613(1997)025<0563:TCOEPF>2.3.CO;2

Anderson, J.L., Barth, A.P., Wooden, J.L., Mazdab, F., 2008. Thermometers and Thermobarometers in Granitic Systems. Rev. Mineral. Geochemistry 69, 121–142. https://doi.org/10.2138/rmg.2008.69.4

Anderson, J.L., Smith, D.R., 1995. The effects of temperature and f O2 on the Al-in-hornblende barometer. Am. Mineral. 80, 549–559. https://doi.org/10.2138/am-1995-5-614

Anovitz, L.M., Essene, E.J., 1987. Phase equilibria in the system CaCO3-MgCO3-FeCO3. J. Petrol. 28, 389–414. https://doi.org/10.18372/2306-1472.30.1424

Ballivián Justiniano, C.A., Lanfranchini, M.E., Recio, C., de Barrio, R.E., Sato, A.M., Basei, M.A.S., Pimentel, M.M., Etcheverry, R.O., Tassinari, C.C.G., 2017. Geology and petrogenetic considerations of the Loma Marcelo skarn, Neoproterozoic basement of the Ventania System, Argentina. Precambrian Res. 302, 358–380. https://doi.org/10.1016/j.precamres.2017.09.021

Barker, S.L.L., Dipple, G.M., 2019. Exploring for Carbonate-Hosted Ore Deposits Using Carbon and Oxygen Isotopes, in: Ore Deposits: Origin, Exploration, and Exploitation. pp. 185–207. https://doi.org/10.1002/9781119290544.ch8

Beckel J., 1992. Características físico-químicas do fluido hidrotermal formador das mineralizações de cobre das minas do Camaquã, RS. in: Workshop sobre as Bacias Molássicas Brasilianas, Boletim de Resumos Expandidos, São Leopoldo, pp. 6-11.

Belousov, I.A., Danyushevsky, L.V., Olin, P.H., Gilbert, S.E., and Thompson, J., 2015. STDGL3-a new calibration standard for sulfide analysis by LA-ICP-MS. Goldschmidt 2015 Abstracts.

Bettencourt, J. S., 1973. Mina de Cobre de Camaquã, Rio Grande do Sul (Unpublished doctorate's thesis). Universidade de São Paulo, São Paulo. https://doi.org/10.11606/T.44.2015.tde-06072015-100922

Bitencourt, M. F., 1983. Geologia petrologia e estrutura dos metamorfitos da região de Caçapava do Sul RS (Unpublished master's thesis). Universidade Federal do Rio Grande do Sul. Porto Alegre

Blundy, J.D., Holland, T.J.B., 1990. Calcic amphibole equilibria and a new amphibole-plagioclase geothermometer. Contrib. to Mineral. Petrol. 104, 208–224. https://doi.org/10.1007/BF00306444

Bongiolo, E.M., Mexias, A.S., Santos, J.O.S., Hartmann, L.A., Conceição, R.V., Gomes, M.E.B., Formoso, M.L.L., 2003. Geocronologia do hidrotermalismo versus magmatismo no Distrito Aurífero de Lavras do Sul/RS, in: Encontro Sobre a Estratigrafia Do Rio Grande Do Sul. Porto Alegre.

Bongiolo, E.M., Renac, C., Mexias, A.S., Gomes, M.E.B., Ronchi, L.H., Patrier-Mas, P., 2011. Evidence of ediacaran glaciation in southernmost brazil through magmatic to meteoric fluid circulation in the porphyry-epithermal au-cu deposits of lavras do sul. Precambrian Res. 189, 404–419. https://doi.org/10.1016/j.precamres.2011.05.007

Bralia, A., Sabatini, G., Troja, F., 1979. A revaluation of the Co/Ni ratio in pyrite as geochemical tool in ore genesis problems. Miner. Depos. 14. https://doi.org/10.1007/BF00206365

Bucher-Nurminen, K., 1981. Petrology of chlorite-spinel marbles from NW Spitsbergen (Svalbard). Lithos 14, 203–213. https://doi.org/10.1016/0024-4937(81)90042-6

Bucher-Nurminen, K., 1982. On the mechanism of contact aureole formation in dolomitic country rock by the Adamello intrusion (northern Italy). Am. Mineral. 67, 1101–1117.

Bucher-Nurminen, K., 1988. Compositional variation of phlogopite in a marble sample: implications for geological thermobarometry. J. Metamorph. Geol. 6, 667–672. https://doi.org/10.1111/j.1525-1314.1988.tb00447.x

Camozzato, E.; Toniolo, J.A.; Laux, J.H. (2014). Metalogênese do Cinturão Dom Feliciano e Fragmentos Paleocontinentais associados (RS/SC) In: Silva, M. G., Rocha Neto, M. B., Jost, H., Kuyumjian, R. M. (Eds), Metalogênese das províncias tectônicas brasileiras, CPRM, Belo Horizonte, pp. 517-556; http://rigeo.cprm.gov.br/jspui/handle/doc/19389

Candela, P.A., Holland, H.D., 1984. The partitioning of copper and molybdenum between silicate melts and aqueous fluids. Geochim. Cosmochim. Acta 48, 373–380. https://doi.org/10.1016/0016-7037(84)90257-6

Cathelineau, M., 1988. Cation site occupancy in chlorites and illites as a function of temperature. Clay Miner. 23, 471–485. https://doi.org/10.1180/claymin.1988.023.4.13

Cerva-Alves, T., Remus, M.V.D., Dani, N., Basei, M.A.S., 2017. Integrated field, mineralogical and geochemical characteristics of Caçapava do Sul alvikite and beforsite intrusions: A new Ediacaran carbonatite complex in southernmost Brazil. Ore Geol. Rev. 88, 352–369. https://doi.org/10.1016/j.oregeorev.2017.05.017

Chemale Jr, F., 2000. Evolução Geológica do Escudo Sul-Riograndense, in: Holz, M., De Ros, L.F. (Eds.), Geologia Do Rio Grande Do Sul. Editora UFRGS, Porto Alegre, pp. 13–52.

Cook, N.J., Ciobanu, C.L., Danyushevsky, L. V., Gilbert, S., 2011. Minor and trace elements in bornite and associated Cu–(Fe)-sulfides: A LA-ICP-MS studyBornite mineral chemistry. Geochim. Cosmochim. Acta 75, 6473–6496. https://doi.org/10.1016/j.gca.2011.08.021

Cook, N.J., Ciobanu, C.L., Pring, A., Skinner, W., Shimizu, M., Danyushevsky, L., Saini-Eidukat, B., Melcher, F., 2009. Trace and minor elements in sphalerite: A LA-ICPMS

study. Geochim. Cosmochim. Acta 73, 4761–4791. https://doi.org/10.1016/j.gca.2009.05.045

Cooke, D.R., Hollings, P., Wilkinson, J.J., Tosdal, R.M., 2013. Geochemistry of Porphyry Deposits, 2nd ed, Treatise on Geochemistry: Second Edition. Elsevier Ltd. https://doi.org/10.1016/B978-0-08-095975-7.01116-5

Costa, A.F.U., Fernandes, L.A.D., Shukowsky, W., Nardi, L.V.S., Bitencourt, M.F., 1995. Teste dos modelos tectonicos e de posicionamento do complexo Granitico de Cacapava do Sul atraves de estudos de modelagem gravimetrica 3-D. Rev. Bras. Geofis. 13, 91–101.

Deer, W. A., Howie, R. A., and Zussman, J., 1992. An introduction to the rock-forming minerals, second ed. Mineralogical Society of Great Britain and Ireland. London

Deer, W. A., Howie, R. A., Zussman, J. (1986). Rock-forming minerals. 1B. Disilicates and ring silicates, second ed. Geological Society of London. London

Fernandes, L.A.D., Tommasi, A., Porcher, C.C., 1992. Deformation patterns in the southern Brazilian branch of the Dom Feliciano Belt: A reappraisal. J. South Am. Earth Sci. 5, 77–96. https://doi.org/10.1016/0895-9811(92)90061-3

Ferry, J.M., 2001. Calcite inclusions in forsterite. Am. Mineral. 86, 773–779. https://doi.org/10.2138/am-2001-0701

Fleet, M.E., MacLean, P.J., Barbier, J., 1989. Oscillatory-Zoned As-Bearing Pyrite from Strata-Bound and Stratiform Gold Deposits, in: The Geology of Gold Deposits. Society of Economic Geologists, pp. 356–362. https://doi.org/10.5382/Mono.06.27

Fontana, E., Mexias, A.S., Renac, C., Nardi, L.V.S., Lopes, R.W., Barats, A., Gomes, M.E.B., 2017. Hydrothermal alteration of volcanic rocks in Seival Mine Cu–mineralization – Camaquã Basin – Brazil (part I): Chloritization process and geochemical dispersion in alteration halos. J. Geochemical Explor. 177, 45–60. https://doi.org/10.1016/j.gexplo.2017.02.004

Fontana, E., Renac, C., Mexias, A.S., Barats, A., Gerbe, M.C., Lopes, R.W., Nardi, L.V.S., 2019. Mass balance and origin of fluids associated to smectite and chlorite/smectite alteration in Seival Mine Cu–Mineralization – Camaquã Basin – Brazil (Part II). J. Geochemical Explor. 196, 20–32. https://doi.org/10.1016/j.gexplo.2018.10.001

Gastal, M. do C., Ferreira, F.J.F., Cunha, J.U. da, Esmeris, C., Koester, E., Raposo, M.I.B., Rossetti, M. de M.M., 2015. Alojamento do granito Lavras e a mineralização aurífera durante evolução de centro vulcano-plutônico pós-colisional, oeste do Escudo Sul-riograndense: dados geofísicos e estruturais. Brazilian J. Geol. 45, 217–241. https://doi.org/10.1590/2317488920150002004

George, L., Cook, N.J., Ciobanu, C.L., Wade, B.P., 2015. Trace and minor elements in galena: A reconnaissance LA-ICP-MS study. Am. Mineral. 100, 548–569. https://doi.org/10.2138/am-2015-4862

George, L.L., Cook, N.J., Ciobanu, C.L., 2016. Partitioning of trace elements in co-crystallized sphalerite–galena–chalcopyrite hydrothermal ores. Ore Geol. Rev. 77, 97–116. https://doi.org/10.1016/j.oregeorev.2016.02.009

George, L.L., Cook, N.J., Crowe, B.B.P., Ciobanu, C.L., 2018. Trace elements in hydrothermal chalcopyrite. Mineral. Mag. 82, 59–88. https://doi.org/10.1180/minmag.2017.081.021

Goldsmith, J. R., Newton, R. C., 1969. P–T–X relations in the system CaCO,-MgCO, at high temperatures and pressures. Am. J. Sci, 160-190.

Goulart, R.V., Remus, M.V.D., Reis, R.S. dos, 2013. Composição isotópica de Sr, C e O e geoquímica de ETRs das rochas carbonáticas do Bloco São Gabriel, Rio Grande do Sul. Pesqui. em Geociencias 40, 75–97.

Griffin, W.L., Begg, G.C., O'Reilly, S.Y., 2013. Continental-root control on the genesis of magmatic ore deposits. Nat. Geosci. 6, 905–910. https://doi.org/10.1038/ngeo1954

Hammarstrom, J.M., Zen, E., 1986. Aluminum in hornblende: an empirical igneous geobarometer. Am. Mineral. 71, 1297–1313.

Hartmann, L., Nardi, L., Formoso, M., Remus, M., De Lima, E., Mexias, A., 1999. Magmatism and Metallogeny in the Crustal Evolution of Rio Grande do Sul Shield, Brazil. Pesqui. em Geociências 26, 45. https://doi.org/10.22456/1807-9806.21123

Hartmann, L.A., Leite, J.A.D., Da Silva, L.C., Remus, M. V.D., McNaughton, N.J., Groves, D.I., Fletcher, I.R., Santos, J.O.S., Vasconcellos, M.A.Z., 2000. Advances in SHRIMP geochronology and their impact on understanding the tectonic and metallogenic evolution of southern Brazil. Aust. J. Earth Sci. 47, 829–844. https://doi.org/10.1046/j.1440-0952.2000.00815.x

Hawthorne, F.C., Oberti, R., Harlow, G.E., Maresch, W. V., Martin, R.F., Schumacher, J.C., Welch, M.D., 2012. Nomenclature of the amphibole supergroup. Am. Mineral. 97, 2031–2048. https://doi.org/10.2138/am.2012.4276

Hoefs, J., 2009. Stable Isotope Geochemistry. Springer Berlin Heidelberg, Berlin, Heidelberg. https://doi.org/10.1007/978-3-540-70708-0

Hoerlle, G.S., Remus, M.V.D., Dani, N., 2021b. Metalamprophyres in the Dom Feliciano Belt: insights for the development of strike-slip tectonics and localized metamorphism during the post-collisional stage. Manuscript submitted to publication.

Hoerlle, G.S., Remus, M.V.D., Dani, N., Gomes, M.E.B., Ronchi, L.H., 2019. Evolution of fluorite-mica-feldspar veins: Evidences of a fossil geothermal system in the são Gabriel terrane and consequences for Pb-Zn-Cu metallogeny. J. South Am. Earth Sci. 92, 209–221. https://doi.org/10.1016/j.jsames.2019.03.006

Hoerlle, G. S., Remus, M. V. D., Dani, N., Lana, C., Müller, T., & Piazolo, S., 2021a. Metasomatic reactions triggered by localized and episodic fluid flux record multistage intrusion history: An example from the syntectonic Caçapava do Sul Granitic Complex, Southern Brazil. Manuscript submitted to publication.

Hoerlle, G.S., Remus, M.V.D., Müller, T., Piazolo, S., Sorger, D., Ramirez-Salazar, A., (2021c). Mechanisms of fluid infiltration and reaction front controls during synkinematic contact metamorphism: a stable isotope and mineral chemistry study of Mg-skarns of the Caçapava do Sul aureole (Dom Feliciano Belt, southern Brazil). Manuscript in preparation.

Holland, T., Blundy, J., 1994. Non-ideal interactions in calcic amphiboles and their bearing on amphibole-plagioclase thermometry. Contrib. to Mineral. Petrol. 116, 433–447. https://doi.org/10.1007/BF00310910

Holliday, J.R., Wilson, A.J., Blevin, P.L., Tedder, I.J., Dunham, P.D., Pfitzner, M., 2002. Porphyry gold-copper mineralisation in the Cadia district, Eastern Lachlan Fold Belt, New South Wales, and its relationship to shoshonitic magmatism. Miner. Depos. 37, 100–116. https://doi.org/10.1007/s00126-001-0233-8

Hollister, L.S., Grissom, G.C., Peters, E.K., Stowell, H.H., Sisson, V.B., 1987. Confirmation of the empirical correlation of Al in hornblende with pressure of solidification of calc-alkaline plutons. Am. Mineral.

Hou, Z., Zhang, H., Pan, X., Yang, Z., 2011. Porphyry Cu (-Mo-Au) deposits related to melting of thickened mafic lower crust: Examples from the eastern Tethyan metallogenic domain. Ore Geol. Rev. 39, 21–45. https://doi.org/10.1016/j.oregeorev.2010.09.002

Huston, D.L., Sie, S.H., Suter, G.F., Cooke, D.R., Both, R.A., 1995. Trace elements in sulfide minerals from eastern Australian volcanic-hosted massive sulfide deposits; Part I, Proton microprobe analyses of pyrite, chalcopyrite, and sphalerite, and Part II, Selenium levels in pyrite; comparison with delta 34 S values and. Econ. Geol. 90, 1167–1196. https://doi.org/10.2113/gsecongeo.90.5.1167

Keith, M., Smith, D.J., Jenkin, G.R.T., Holwell, D.A., Dye, M.D., 2018. A review of Te and Se systematics in hydrothermal pyrite from precious metal deposits: Insights into ore-forming processes. Ore Geol. Rev. 96, 269–282. https://doi.org/10.1016/j.oregeorev.2017.07.023

Kelley, K.A., Cottrell, E., 2009. Water and the oxidation state of subduction zone magmas. Science (80-.). 325, 605–607. https://doi.org/10.1126/science.1174156

Kelley, K.D., Ludington, S., 2002. Cripple Creek and other alkaline-related gold deposits in the southern Rocky Mountains, USA: influence of regional tectonics. Miner. Depos. 37, 38–60. https://doi.org/10.1007/s00126-001-0229-4

Keskin, M., Genç, Ş.C., Tüysüz, O., 2008. Petrology and geochemistry of post-collisional Middle Eocene volcanic units in North-Central Turkey: Evidence for magma generation by slab breakoff following the closure of the Northern Neotethys Ocean. Lithos 104, 267–305. https://doi.org/10.1016/j.lithos.2007.12.011

Laux, J.H., Lindenmayer, Z.G., Teixeira, J.B.G., Neto, A.B., 2005. Ore genesis at the Camaquã copper mine, a neoproterozoic sediment-hosted deposit in Southern Brazil. Ore Geol. Rev. 26, 71–89. https://doi.org/10.1016/j.oregeorev.2004.11.001

Leinz, V., Almeida, S.C., 1941. Gênese da Jazida de cobre “Camaquan”. Boletim - Divisão de Produção Mineral, DPM. Porto Alegre.

Leinz, V., Barbosa, A.F. and Teixeira, E., 1941. Mapa geológico Caçapava-Lavras. Boletim - Divisão de Produção Mineral, DPM. Porto Alegre.

Li, X., Zhang, C., Behrens, H., Holtz, F., 2020. Calculating amphibole formula from electron microprobe analysis data using a machine learning method based on principal components regression. Lithos 362–363, 105469. https://doi.org/10.1016/j.lithos.2020.105469

Licht, O., 1980. A descoberta da Jazida Santa Maria (Zn, Pb, Cu) Rio Grande Do Sul-Brasil: um caso histórico de prospecção geoquímica. In: Congresso Brasileiro de Geologia, 31, Camboriú. Anais, pp. 141-153.

Lopes, R.W., Mexias, A.S., Philipp, R.P., Bongiolo, E.M., Renac, C., Bicca, M.M., Fontana, E., 2018. Au–Cu–Ag mineralization controlled by brittle structures in Lavras do Sul Mining District and Seival Mine deposits, Camaquã Basin, southern Brazil. J. South Am. Earth Sci. 88, 197–215. https://doi.org/10.1016/j.jsames.2018.08.017

Lopes, R.W., Renac, C., Mexias, A.S., Nardi, L.V.S., Fontana, E., Gomes, M.E.B., Barats, A., 2019. Mineral assemblages and temperature associated with Cu enrichment in the Seival area (Neoproterozoic Camaquã Basin of Southern Brazil). J. Geochemical Explor. 201, 56–70. https://doi.org/10.1016/j.gexplo.2019.03.010

Madruga, D. da R., 2018. Caracterização da alteração supergênica nas mineralizações de sulfeto de cobre, região de Coronel Linhares, Caçapava do Sul. Universidade Federal do Rio Grande do Sul.

Maslennikov, V. V., Maslennikova, S.P., Large, R.R., Danyushevsky, L. V., 2009. Study of Trace Element Zonation in Vent Chimneys from the Silurian Yaman-Kasy Volcanic-Hosted Massive Sulfide Deposit (Southern Urals, Russia) Using Laser Ablation-Inductively Coupled Plasma Mass Spectrometry (LA-ICPMS). Econ. Geol. 104, 1111–1141. https://doi.org/10.2113/gsecongeo.104.8.1111

Meinert, L. D., 1992. Skarns and Skarn Deposits. Geoscience Canada, 19(4). Retrieved from https://journals.lib.unb.ca/index.php/GC/article/view/3773

Meinert, L.D., Dipple, G.M., Nicolescu, S., 2005. World Skarn Deposits, in: Hedenquist, J.W., Thompson, J.F.H., Goldfarb, R.J., Richards, J.P. (Eds.), One Hundredth Anniversary Volume. Society of Economic Geologists, pp. 299–336. https://doi.org/10.5382/AV100.11

Meng, X., Mao, J., Zhang, C., Zhang, D., Kong, Z., Jia, F., 2016. The timing, origin and T-fO2 crystallization conditions of long-lived magmatism at the Yangla copper deposit, Sanjiang Tethyan orogenic belt: Implications for post-collisional magmatic-hydrothermal ore formation. Gondwana Res. 40, 211–229. https://doi.org/10.1016/j.gr.2016.09.005

Mesquita, R.B. de, Jordt-Evangelista, H., Queiroga, G.N., Medeiros Júnior, E.B. de, Dussin, I.A., 2017. Petrogenesis and age of skarns associated with felsic and metamafic dykes from the Paraíba do Sul Complex, southern Espírito Santo State. Brazilian J. Geol. 47, 301–325. https://doi.org/10.1590/2317-4889201720160086

Mexias, A.S., 2000. Alteração Hidrotermal e Mineralização de Ouro Associada no Distrito Aurífero de Lavras do Sul/RS - A área do Bloco do Butiá (Unpublished doctorate's thesis). Universidade Federal do Rio Grande do Sul. Porto Alegre

Mexias, A. S.; Gomes, M. E.B. ; Formoso, Milton Ll ; Meunier, A., 1994. Considerações sobre a alteração hidrotermal da Área Bloco do Butiá (Complexo Granítico Lavras) Lavras do Sul - RS. In: XXXVIII Congresso Brasileiro de Geologia, 1994, Camburiú - SC. Boletim dos Resumos Expandidos, 1994. pp. 126-128

Mexias, A.S., Berger, G., Gomes, M.E.B., Formoso, M.L.L., Dani, N., Frantz, J.C., Bongiolo, E.M., 2005. Geochemical modeling of gold precipitation conditions in the Bloco do Butiá Mine, Lavras do Sul/Brazil. An. Acad. Bras. Cienc. 77, 717–728. https://doi.org/10.1590/S0001-37652005000400010

Mizuochi, H., Satish-Kumar, M., Motoyoshi, Y., Michibayashi, K., 2010. Exsolution of dolomite and application of calcite-dolomite solvus geothermometry in high-grade marbles: an

example from Skallevikshalsen, East Antarctica. J. Metamorph. Geol. 28, 509–526. https://doi.org/10.1111/j.1525-1314.2010.00877.x

Moggl-Cecchi, V., Cipriani, C., Rossi, P., Ceccato, D., Rudello, V., Somacal, H., 2002. Trace element contents and distribution maps of chalcopyrite: A micro-PIXE study. Period. di Mineral. 71, 101–109.

Müller, I.F., Nardi, L.V.S., Lima, E.F. De, Mexias, A.S., 2012. Os diques latíticos portadores de ouro e sulfetos da Associação Shoshonítica de Lavras do Sul – RS: petrogênese e geoquímica. Pesqui. em Geociências 39, 173. https://doi.org/10.22456/1807-9806.35911

Mutch, E.J.F., Blundy, J.D., Tattitch, B.C., Cooper, F.J., Brooker, R.A., 2016. An experimental study of amphibole stability in low-pressure granitic magmas and a revised Al-in-hornblende geobarometer. Contrib. to Mineral. Petrol. 171, 1–27. https://doi.org/10.1007/s00410-016-1298-9

Nachit, H., Ibhi, A., Abia, E.H., Ben Ohoud, M., 2005. Discrimation entre biotites magmatiques primaires, biotites rééquilibrées et biotites néoformées. Comptes Rendus - Geosci. 337, 1415–1420. https://doi.org/10.1016/j.crte.2005.09.002

Nardi, L.V.S., and Bitencourt, M.F., 2007. Magmatismo granítico e evolução crustal do sul do Brasil. In: Iannuzzi, R., Frantz, J. C. (Eds), 50 Anos de Geologia. Instituto de Geociências. Contribuições Editora Comunicação e Identidade, Porto Alegre, 2007, pp. 125-141.

Nardi, L.V.S., Bitencourt, M. de F., 1989. Geologia, Petrologia e Geoquímica do Complexo Granítico de Caçapava do Sul, RS. Rev. Bras. Geociências 19, 153–169.

Nardi, L.V.S., Lima, E.F. De, 1988. Hidrotermalismo no Complexo Granítico Lavras e vulcânicas associadas, RS. Rev. Bras. Geociências 18, 369–375. https://doi.org/10.25249/0375-7536.1988369375

Ohmoto, H., 1972. Systematics of Sulfur and Carbon Isotopes in Hydrothermal Ore Deposits. Econ. Geol. 67, 551–578. https://doi.org/10.2113/gsecongeo.67.5.551

Pereira, D.R., Macambira, M.J.B., Pires, K.C. de J., Lago, S.B. do, 2021. Isotopic study of the Pb-Zn (Cu-Ag) Santa Maria Deposit, Caçapava do Sul Region, Rio Grande do Sul, Brazil. Brazilian J. Geol. 51. https://doi.org/10.1590/2317-4889202120200091

Porcher, C.A., Lopes, R.C., 2000. Carta Geológica: Cachoeira do Sul: folha SH.22-Y-A: estado do Rio Grande do Sul. CPRM. Porto Alegre.

Powell, R., Condliffe, D.M., Condliffe, E., 1984. Calcite-dolomite geothermometry in the system CaCO3-MgCO3-FeCO 3 : an experimental study. J. Metamorph. Geol. 2, 33–41. https://doi.org/10.1111/j.1525-1314.1984.tb00283.x

Putnis, A., Austrheim, H., 2013. Mechanisms of Metasomatism and Metamorphism on the Local Mineral Scale: The Role of Dissolution-Reprecipitation During Mineral Re-equilibration. pp. 141–170. https://doi.org/10.1007/978-3-642-28394-9_5

Reis, R.S. dos, Remus, M.V.D., Dani, N., Anzolin, H.D.M., 2017. Alteração clorítica no flanco leste do Granito Caçapava, Rio Grande do Sul: evolução do metassomatismo e sulfetos de Cu-Fe associados. Geol. USP. Série Científica 17, 61. https://doi.org/10.11606/issn.2316-9095.v17-121013

Remus, M.V.D. 1999. Metalogênese dos depósitos hidrotermais de metais-base e Au do Ciclo Brasiliano no Bloco São Gabriel, RS (Unpublished PhD thesis). Universidade Federal do Rio Grande do Sul, Porto Alegre.

Remus, M.V.D., Dani, N., Gazzoni, C. P., Hoerlle, G. S., and Reis, R. S., 2011a. Minério de Cu (Au) de alto teor em zonas de alteração clorítica em escarnitos magnesianos de Caçapava do Sul, RS. In: XIII Congresso Brasileiro de Geoquímica; III Simpósio de Geoquímica Dos Países Do Mercosul. Gramado. pp. 1485–1488.

Remus, M.V.D., Hartmann, L.A., Toniolo, M.A., 2011b. Low-temperature, hydrothermal base and precious metal deposits hosted by volcanic-sedimentary sequences of the Camaquã basin, southernmost Brazil. In: EGU-2011 - European Geosciences Union General Assembly.

Remus, M.V.D., Hartmann, L.A., 1997. Caracterização do minério do Depósito Santa Bárbara-Rosso, Caçapava do Sul - RS. In: Caracterização de Minérios e Rejeitos de Depósitos Minerais Brasileiros, Resumos Expandidos, DNPM/DIREX, PADCT/GTM, Ministério das Minas e Energia, Brasília . pp. 91-98.

Remus, M.V.D., Hartmann, L.A., McNaughton, N.J., Groves, D.I., Fletcher, I.R., 2000a. The link between hydrothermal epigenetic copper mineralization and the Cacapava Granite of the Brasiliano cycle in southern Brazil. J. South Am. Earth Sci. 13, 191–216. https://doi.org/10.1016/S0895-9811(00)00017-1

Remus, M.V.D., Hartmann, L.A., McNaughton, N.J., Groves, D.I., Reischl, J.L., 2000b. Distal Magmatic-Hydrothermal Origin for the Camaquã Cu (Au-Ag) and Santa Maria Pb, Zn (Cu-Ag) Deposits, Southern Brazil. Gondwana Res. 3, 155–174. https://doi.org/10.1016/S1342-937X(05)70094-0

Remus, M.V.D., McNaughton, N.J., Hartmann, L.A., Koppe, J.C., Fletcher, I.R., Groves, D.I., Pinto, V.M., 1999. Gold in the Neoproterozoic juvenile Bossoroca Volcanic Arc of southernmost Brazil: Isotopic constraints on timing and sources. J. South Am. Earth Sci. 12, 349–366. https://doi.org/10.1016/S0895-9811(99)00026-7

Renac, C., Mexias, A.S., Gomes, M.E.B., Ronchi, L.H., Nardi, L.V.S., Laux, J.H., 2014. Isotopic fluid changes in a Neoproterozoic porphyry-epithermal system: The Uruguay mine, southern Brazil. Ore Geol. Rev. 60, 146–160. https://doi.org/10.1016/j.oregeorev.2013.12.016

Ribeiro, M., Bocchi, P.R., Figueiredo Filho, P.M., Tessari, R.I., 1966. Geologia da quadrícula de Caçapava do Sul, RS, Brasil. Boletim da Divisão de Geologia e Mineralogia, DPM-DNPM. Porto Alegre.

Richards, J.P., 2003. Tectono-magmatic precursors for porphyry Cu-(Mo-Au) deposit formation. Econ. Geol. 98, 1515–1533. https://doi.org/10.2113/gsecongeo.98.8.1515

Richards, J.P., 2005. Cumulative factors in the generation of giant calc-alkaline porphyry Cu deposits, in Porter, T.M. (Ed), Super porphyry copper and gold deposits: A global perspective: Volume 1: Linden Park, South Australia, Porter Geoscience Consulting Publishing, pp. 7–25.

Richards, J.P., 2009. Postsubduction porphyry Cu-Au and epithermal Au deposits: Products of remelting of subduction-modified lithosphere. Geology 37, 247–250. https://doi.org/10.1130/G25451A.1

Ronchi, L.H.; Lindenmayer, Z.G ; Bastos Neto, A. ; Murta, C.R., 2000. O stockwork e a zonação do minério sulfetado no arenito inferior da Mina Uruguai RS.. In: Ronchi, L.H., Lobato, A.O.C. (Eds.), Minas do Camaquã, um estudo multidisciplinar. 1ed.São Leopoldo: UNISINOS, pp. 163-188.

Roselle, G. T., 1997. Integrated petrologic, stable isotopic, and statistical study of fluid-flow in carbonates of the Ubehebe Peak contact aureole, Death Valley National Park, California. Ph.D. thesis, University of Wisconsin, Madison.

Saalmann, K., Gerdes, A., Lahaye, Y., Hartmann, L.A., Remus, M.V.D.D., Läufer, A., 2011. Multiple accretion at the eastern margin of the Rio de la Plata craton: The prolonged Brasiliano orogeny in southernmost Brazil. Int. J. Earth Sci. 100, 355–378. https://doi.org/10.1007/s00531-010-0564-8

Sartori P.L.P., 1978. Petrologia do Complexo Granítico São Sepé (Unpublished doctorate's thesis), Universidade de São Paulo. São Paulo. https://doi.org/10.11606/T.44.1978.tde-26082015-143549

Sartori, P.L.P., Kawashita, K., 1985. Petrologia e geocronologia do Batólito Granítico de Caçapava do Sul-RS. In: II Simpósio Sul-Brasileiro de Geologia. Florianópolis

Schmidt, M.W., 1992. Amphibole composition in tonalite as a function of pressure: an experimental calibration of the Al-in-hornblende barometer. Contrib. to Mineral. Petrol. 110, 304–310. https://doi.org/10.1007/BF00310745

Silva, L.C., McNaughton, N.J., Armstrong, R., Hartmann, L.A., Fletcher, I.R., 2005. The neoproterozoic Mantiqueira Province and its African connections: a zircon-based U–Pb geochronologic subdivision for the Brasiliano/Pan-African systems of orogens. Precambrian Res. 136, 203–240. https://doi.org/10.1016/j.precamres.2004.10.004

Steadman, J.A., Large, R.R., Olin, P.H., Danyushevsky, L. V., Meffre, S., Huston, D., Fabris, A., Lisitsin, V., Wells, T., 2021. Pyrite trace element behavior in magmatic-hydrothermal environments: An LA-ICPMS imaging study. Ore Geol. Rev. 128, 103878. https://doi.org/10.1016/j.oregeorev.2020.103878

Teixeira G., Gonzalez A.P., Gonzalez M.A., Licht O.A.B., 1978. Situação das Minas do Camaquã, Rio Grande do Sul. In: Congresso Brasileiro de Geologia, 30. Recife. pp. 1893-1905.

Toniolo, J.A., Remus, M.V.D., Macambira, M.J.B., Moura, C.A.V., 2004. Metalogênese do Depósito de Cobre Cerro dos Martins, RS -Revisão e Geoquímica Isotópica de Sr, S, O e C-. Pesqui. em Geociências 31, 41. https://doi.org/10.22456/1807-9806.19573

Wilson S. A., 1997b. The collection, preparation, and testing of USGS reference material BCR-2, Columbia River, Basalt. US Geological Survey Open-File Report.

Wilson, S. A., 1997a. Data compilation for USGS reference material BHVO-2, Hawaiian Basalt. US Geological Survey Open-File Report.

Winter, J. D., 2013. Principles of Igneous and Metamorphic Petrology: Pearson New International Edition. Pearson Education Limited.

Yang, M., Zhao, F., Liu, X., Qing, H., Chi, G., Li, X., Duan, W., Lai, C.K., 2020. Contribution of magma mixing to the formation of porphyry-skarn mineralization in a post-collisional

setting: The Machangqing Cu-Mo-(Au) deposit, Sanjiang tectonic belt, SW China. Ore Geol. Rev. 122, 103518. https://doi.org/10.1016/j.oregeorev.2020.103518

Zane, A., Weiss, Z., 1998. A procedure for classifying rock-forming chlorites based on microprobe data. Rend. Lincei 9, 51–56. https://doi.org/10.1007/BF02904455

CAPÍTULO 5 – ARTIGO IV

Mechanisms of fluid infiltration and reaction front controls during synkinematic contact metamorphism: a stable isotope and mineral chemistry study of Mg-skarns of the Caçapava do Sul aureole (Dom Feliciano Belt, southern Brazil)

RESEARCH PAPER

To: Chemical Geology

Mechanisms of fluid infiltration and reaction front controls during synkinematic contact metamorphism: a stable isotope and mineral chemistry study of Mg-skarns of the Caçapava do Sul aureole (Dom Feliciano Belt, southern Brazil)

Authors:

Guilherme S. Hoerlle[a]; Marcus V. D. Remus[a], Thomas Müller[b,c], Sandra Piazolo[b], Anthony Ramirez-Salazar[b], Dominik Sorger[c]

[a] Departamento de Mineralogia e Petrologia, Instituto de Geociências, Universidade Federal do Rio Grande do Sul, Avenida Bento Gonçalves, 9500, 91501-970 Porto Alegre, Rio Grande do Sul, Brazil

[b] Institute of Geophysics and Tectonics, School of Earth and Environment - University of Leeds, Leeds LS2 9JT, United Kingdom

[c] Geoscience Center, Georg-August-Universität Göttingen, Goldschmidtstraße 1, D-37077 Göttingen, Germany

Corresponding author:

Guilherme Sonntag Hoerlle

guilherme.hoerlle@ufrgs.br

Av. Bento Gonçalves, 9500

43126/110

Porto Alegre, RS, Brazil

Zip code: 90650-001

ABSTRACT

Fluid flow is a fundamental process that drive chemical reactions and is an efficient mechanism for heat and mass transfer through the crust. Fluid-assisted reactions influence crustal rheology, carbon oxide release or sequestration and are crucial for hydrothermal ore deposit formation. In particular, the study of skarns formed due to the infiltration of igneous-derived fluids into carbonates can provide key information in understanding fluid sources, compositions and element mobility. This study focuses on the chemical and isotopic footprints of igneous fluid infiltration along distinct pathways within dolomitic marbles. We use micro-XRF elemental maps, stable isotope compositions of bulk-carbonate and silicate phases in combination with mineral chemistry analyses along profiles of two types of skarns to understand the mechanisms, extent and history of fluid infiltration. Two main zoned skarn types from the Caçapava do Sul Granitic Complex (CSGC) contact aureole (southern Brazil) were selected for this study: a vein and a contact skarn. The first consist of a central zone composed mostly of diopside (di-zone) asymmetrically bordered by antigorite pseudomorphs after forsterite in a calcite matrix (fo-zone). The contact skarn is found in the interface between a mafic intrusion and the marble and show an analogue sequence of mineralogical zones. Based on the bulk-carbonate isotopic patterns and dolomite and phlogopite compositions of the wall-rocks, we were able to identify the effect of reactive fluid infiltration into the marbles without assemblage modifications. Notably, the extent of fluid infiltration without phase change is approximately the same size as that of the replacement zones. We interpret that a first fluid pulse was responsible for the dissolution of the dolomite and precipitation of diopside. Based on the textural, isotopic and chemical changes of both skarns, we propose that a subsequent water-rich fluid pulse reacted with the dolomite to form forsterite and calcite while diopside was partially replaced by tremolite and calcite (tr-zone). In both skarns, the second fluid pulse used the diopside-dolomite interface that had its permeability enhanced by deformation and devolatization reactions. The propagation of the reaction fronts was transversal to the main fluid pathway leading to two domains governed by replacement and dissolution-reprecipitation reactions. The di-, tr- and fo-zones characterize the replacement domains whereas isotopic and chemical modifications of dolomite and phlogopite mark the dissolution and reprecipitation of the

initial marble assemblage. In agreement with previous studies, we note that fluid-driven dissolution of the host rock assemblage can be achieved even by minor isotopic and chemical disequilibrium. In addition, fluid-rock reactions may occur much further than the observed extent of mineral replacement zones. We highlight the importance of understanding such processes as they have important implications for different studies involving fluid-rock interaction, such as radioactive storage, petrological and ore forming studies.

Keywords: fluid-rock interaction; skarn; reaction front; stable isotopes; dissolution-reprecipitation

1. INTRODUCTION

Crustal fluid flow and fluid-rock interaction are increasingly recognized as efficient mechanisms for heat and mass transfer as well as major driving forces metamorphic reactions (*e.g.*, Ferry, 1978; Bucher-Nurminen, 1982; Ferry and Dipple, 1991; Yardley *et al*., 1991; Baumgartner and Valley, 2001; Putnis and Austrheim, 2010; Ague, 2014; Koehn *et al*., 2021). Such processes influence rocks from the microscopic grain boundary scale (*e.g.*, Putnis, 2009; Bégué *et al*., 2019), to the kilometer-wide lithospheric scale (*e.g.*, McCaig, 1988; Ferry, 1992, Piccoli *et al*., 2021). Among the various geological settings, metamorphic contact aureoles are largely influenced by the infiltration of igneous fluids (*e.g.*, Roselle *et al*., 1999; Cook and Bowman, 2000). The igneous-derived fluid flux into the surrounding rocks typically influence the rheology of the surrounding rocks (*e.g.*, Ducoux *et al*., 2017) and may lead to the formation of ore deposits (*e.g.*, Meinert *et al*., 2005). In general, the channelized or pervasive nature of the fluid flow is scale dependent and the extent of fluid infiltration highly variable among different contact aureoles. In particular, channelized flow occurs through fractures, lithological contacts or structurally controlled surfaces that can be affected by several episodic pulses of fluid infiltration (*e.g.* Bucher-Nurminen, 1989; Putnis and Austrheim, 2010; Bégué *et al*., 2020). Different pulses may be separated in time by several million years and form distinct assemblages in response to different P-T-X conditions (Guo *et al*., 2021). However, the distinction between continuous flow or episodic fluid pulses remains relatively unknown, especially because many metasomatic reaction zones lack suitable geochronometers. This distinction can be particularly useful to decipher the intrusion history and metamorphic evolution of the

contact aureole. To address these questions, this study focused on the textural and chemical footprints of the igneous fluid infiltration into dolomitic marbles recorded in distinct reaction zones in skarns of the Caçapava do Sul Granitic Complex (CSGC) contact aureole (southern Brazil). The skarns were formed by channelized infiltration of aqueous-siliceous fluids into foliation parallel fractures and lithological contacts during the multi-stage intrusion of the CSGC from 578 and 557 Ma (Hoerlle *et al*., 2021a). In general, the skarns show two main mineralogical zones characterized by the dominant crystallization of diopside (di-zone) and forsterite and calcite (fo-zone). The silicate assemblages were locally altered to low-temperature hydrous assemblages (*e.g.*, serpentine, chlorite). The formation and alteration of the skarns were attributed to distinct episodes of igneous-derived fluid infiltration using the same pathways during the emplacement and cooling of the CSGC (Hoerlle *et al*., 2021a). However, the transition between the different mineralogical zones could be explained by different ways by varying thermodynamic conditions (*e.g.* T, XCO_2 or $aSiO_2$) either during a single continuous fluid influx or by discrete pulses with variable physicochemical parameters. In this contribution, we use stable isotopes and mineral chemistry profiles in combination with microstructural investigations of two representative skarn types to determine the fluid infiltration history and propose the mechanisms responsible for skarn zonation. With this, we aim at advancing the understanding of the formation mechanisms of zoned metasomatic lithologies and the implications for the continuous versus discrete fluid flux questions.

2. GEOLOGICAL BACKGROUND

The skarns are hosted by the dolomitic marbles of the Passo Feio Metamorphic Complex (PFMC), which itself belongs to the São Gabriel Terrane (Dom Feliciano Belt, southern Brazil; Fig. 1). The PFMC consists of a Neoproterozoic supracrustal metavolcano-sedimentary affected by regional (M_1) and contact (M_2) metamorphic events (Ribeiro *et al*., 1966; Bitencourt, 1983; Hartmann *et al*., 1990; Remus *et al*., 2000). The grade of the first metamorphic event varies from greenschist (chlorite-zone) to amphibolite (staurolite-zone) facies (Bitencourt, 1983) and the age was estimated between 620 and 650 Ma based on LA-ICP-MS monazite dating (Remus *et al*., 2010). The contact metamorphic event reached upper amphibolite facies associated with the intrusion of the CSGC from 578 and 557 Ma (Ribeiro *et al*., 1966; Silva-Filho &

Matsdorf, 1984; Bortolotto, 1988; Hoerlle *et al*., 2021a). At least two deformation events occur in the PFMC which are synchronous with M_1 and M_2 metamorphic events (Remus *et al*., 2000).

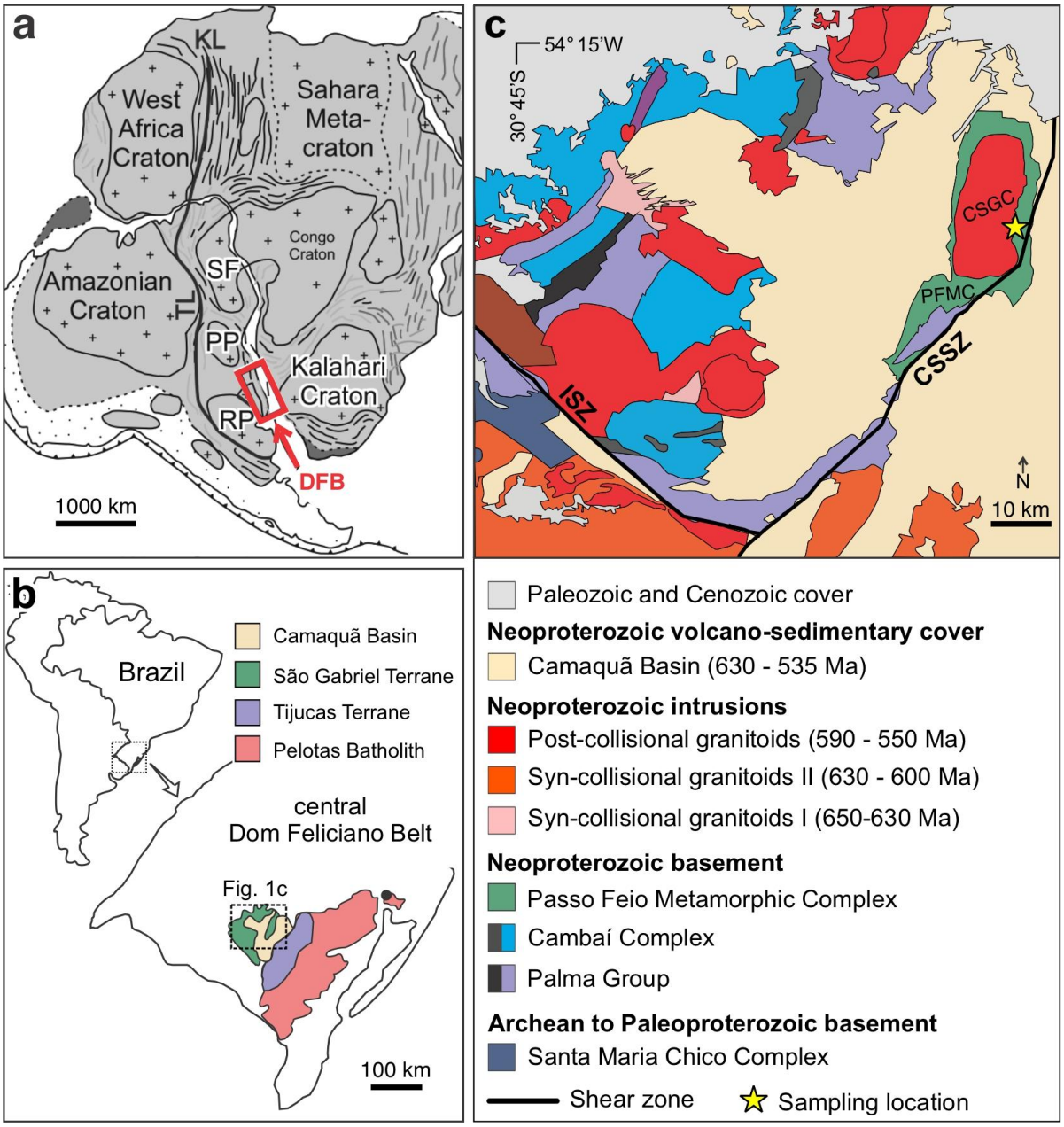

Figure 1: Regional setting and sampling location. (a) Location of the Dom Feliciano Belt (DFB) in the southwestern Gondwana; RP: Rio de la Plata craton; PP: Paranapanema Block; SF: São Francisco Craton; KL: Kandi Lineament; TL: Transbrasiliano lineament. Adapted from Cerva-Alves *et al*. (2020) (b) Distribution of the main geotectonic units of the central Dom Feliciano Belt. (c) Geological map of the São Gabriel Terrane; CSGC: Caçapava do Sul Granitic Complex; PFMC: Passo Feio Metamorphic Complex; CSSZ: Caçapava do Sul shear zone; ISZ: Ibaré shear zone; yellow star: sampling location. Modified from Porcher & Lopes (2000).

The Caçapava do Sul Granitic Complex (CSGC) is composed of a granitic batholith and several tabular intrusions of calc-alkaline affinity that intruded the PFMC during the post-collisional stage of the Dom Feliciano Belt orogeny (Fig. 1c; Leinz *et al*., 1941; Sartori & Kawashita, 1985; Nardi & Bitencourt, 1989). The granitic complex is compositionally and structurally heterogeneous composed of granodiorites, syeno- and monzogranites, monzonites, quartz-diorites and minor mafic intrusions that vary from underformed to strongly foliated (Nardi & Bitencourt, 1989).

3. ANALYTICAL METHODS

3.1. SAMPLING AND SAMPLE PREPARATION

The investigated samples were collected from marble quarries located in the eastern contact of the CSGC and the PFMC (sampling location on Fig. 1c). One representative sample of each of the two types of skarns (vein and contact skarn) was selected. Thick and thin sections cut perpendicular to the central fracture in the vein skarn and to the interface between the mafic apophysis and marble in the contact skarn were prepared. Micro-drill cores (<3 mm long, 2 mm in diameter, 4–35 mg in weight) were drilled from thick sections using a diamond-studded hollow drill and retrieved using a small chisel and tweezers. Carbonate samples were crushed and ground to powder using an agate mortar and pestle. Silicate samples were crushed and sieved keeping the grain size fraction between 0.05 and 0.25 mm then acidified in 10% HCl and dried.

3.2. PETROGRAPHY AND IMAGING

Mineral identification and microstructures were characterized with a petrographic microscope using plane-polarized light (PPL) and cross-polarized light (XPL). Major and minor element X-ray maps of thin and thick sections were conducted using a Bruker M4 TORNADO microX-ray fluorescence spectrometer at the Department of Mineralogy in the Centre of Geosciences of the University of Göttingen. Operating conditions were 50 kV accelerating voltage, probe current of 500 µA and 20 ms counting time. The spatial resolution was set to 20 µm in both x and y directions. Mapping data were processed using XMapTools 3.4.1 (Lanari *et al*. 2014; 2019). All mineral abbreviations are after Whitney and Evans (2010).

3.3. STABLE ISOTOPE COMPOSITIONS OF CARBONATES AND SILICATES

Bulk carbonate powders were reacted with 105% H_3PO_4 at 75 °C using a Finnigan Kiel IV Carbonate Device attached to a Finnigan DELTA V PLUS mass spectrometer in dual inlet mode to determine $\delta^{18}O$ and $\delta^{13}C$ values of each core. $\delta^{18}O$ results are expressed in ‰ VSMOW, after assigning a $\delta^{18}O$ VPDB value of −2.20‰ (VSMOW = 28.6419‰) to NBS19 and converting VPDB values to VSMOW by means of the equation of Wiedner (2004). The triple oxygen isotope compositions of olivine (n = 6), diopside (n = 3), tremolite (n = 3) and serpentine (n = 2) were determined from hand-picked mineral fractions using a setup of laser-assisted fluorination coupled to a MAT253 mass spectrometer (Pack *et al*., 2016). San Carlos olivine (Pack *et al*., 2016; Sharp *et al*., 2016; Wostbrock *et al*., 2020) and Gore Mountain garnet UWG-2 (Valley *et al*., 1995) were used as standards. Carbonate and silicate stable isotope measurements were carried out at the Geochemistry and Isotope Geology Department in the Centre of Geosciences of the University of Göttingen.

3.4. QUANTITATIVE ANALYSES OF PHLOGOPITE AND CARBONATES COMPOSITIONS

Major and minor element analyses of minerals were obtained with a JEOL JXA 8900 electron microprobe at the EPMA Laboratory in the Centre of Geosciences of the University of Göttingen. The concentration of the elements Si, Al, Ti, Fe, Mg, Mn, K, Na, Cr, Ca, F, Cl and Ni were measured. Counting times, standards and detection limits are displayed in Supplementary Table S1.

4. RESULTS

Two representative skarn types were selected for this study, one contact skarn and one vein skarn. The vein skarn was formed at a pre-existing discontinuity in the marble, such as a layer-parallel fracture or an internal contact. Here, we use the term vein to refer either to the central open fracture-fill and the associated reaction zones. The contact skarn was formed in the interface between a mafic apophysis and the dolomitic marble. A comprehensive characterization of the Caçapava do Sul skarns and causative intrusions, including field observations, structural description, geochronological constraints and a preliminary petrology discussion is presented in Hoerlle *et al*. (2021a). The authors indicate that both skarn types are contemporaneous and show similar succession of mineralogical zones. They were formed during the

emplacement of tabular mafic and felsic intrusions at *ca.* 578 Ma and locally altered at the final stages of the CSGC assembly at *ca.* 557 Ma (Hoerlle *et al*., 2021a).

4.1. FIELD RELATIONSHIPS

The dolomitic marbles occur as lenticular bodies that outcrop along the eastern contact with the CSGC batholith. The marbles vary from massive white to banded light gray layers and show variable degrees of brittle and ductile deformation (Fig. 2a). Dolomite grain size and shape are very heterogeneous throughout the marble sequence. The marbles that do not show evident modification caused by igneous fluid infiltration are dominantly made of dolomite (~90 - 97% dol) with variable amounts of talc, phlogopite, tremolite and calcite. Massive white to light gray layers composed of mostly pure dolomite (>97% dol) are commonly intercalated with beige layers with higher silicate contents (>90% dol) (Fig. 2a). The marbles were extensively intruded by different generations of mafic and felsic tabular intrusions of the CSGC.

Mafic and felsic apophyses with little to moderate thickness (~0.1 to 2 m) intruded the marbles parallel to the previous metamorphic foliation (S_1) and were folded accordingly. Subsequently, synkinematic thicker felsic intrusions (> 2 m) intruded the marbles parallel or sub-parallel to the axial planes and S_2 foliation.

The vein skarns are composed of a central zone made of diopside commonly surrounded by bands or lenses of rounded forsterite grains (or antigorite pseudomorphs after forsterite) in a calcite matrix. Despite being less abundant, isolated diopside or forsterite and calcite veins also occur in the area (*e.g.*, Fig. 2c; refer to Hoerlle *et al*., 2021a for more examples). The vein skarns are typically shaped as pinch-and-swell or boudin structures (Fig. 2c-d). The size of the vein skarn and mineralogical zones vary from a few centimeters reaching almost a meter in thickness. In general, the vein skarns show an asymmetrical distribution of the mineralogical zones in terms of thickness and textures (Fig. 2d; Fig. 3a-b).

The contact skarns occur in the boundaries between mafic apophyses and the dolomitic marbles, although not all contacts of this nature host skarns. The contact skarns vary from a few centimeters to approximately 50 cm in thickness being the thickest ones found near fold hinges (Fig. 2b). The mafic apophyses in contact with the skarns are mostly composed of calcic amphiboles (hornblende and actinolite), biotite

(or phlogopite) and plagioclase. The content of the amphibole and biotite varies from 40% up to 80% of the bulk composition. In addition, these mafic intrusions show a well-defined foliation marked by the preferred orientation of the amphiboles and biotite. In general, the contact skarns show a succession of mineralogical zones from the intrusion towards the marble protolith. However, the presence and thickness of such zones are variable among different contacts. In general, a complete succession of mineralogical zones includes, from the intrusion to the unaltered marble: an endoskarn, a diopside zone, a tremolite zone, a forsterite zone and an altered marble zone (dol-zone) (Fig. 5a; see Section 4.2.2 for detailed characterization of the mineralogical zones).

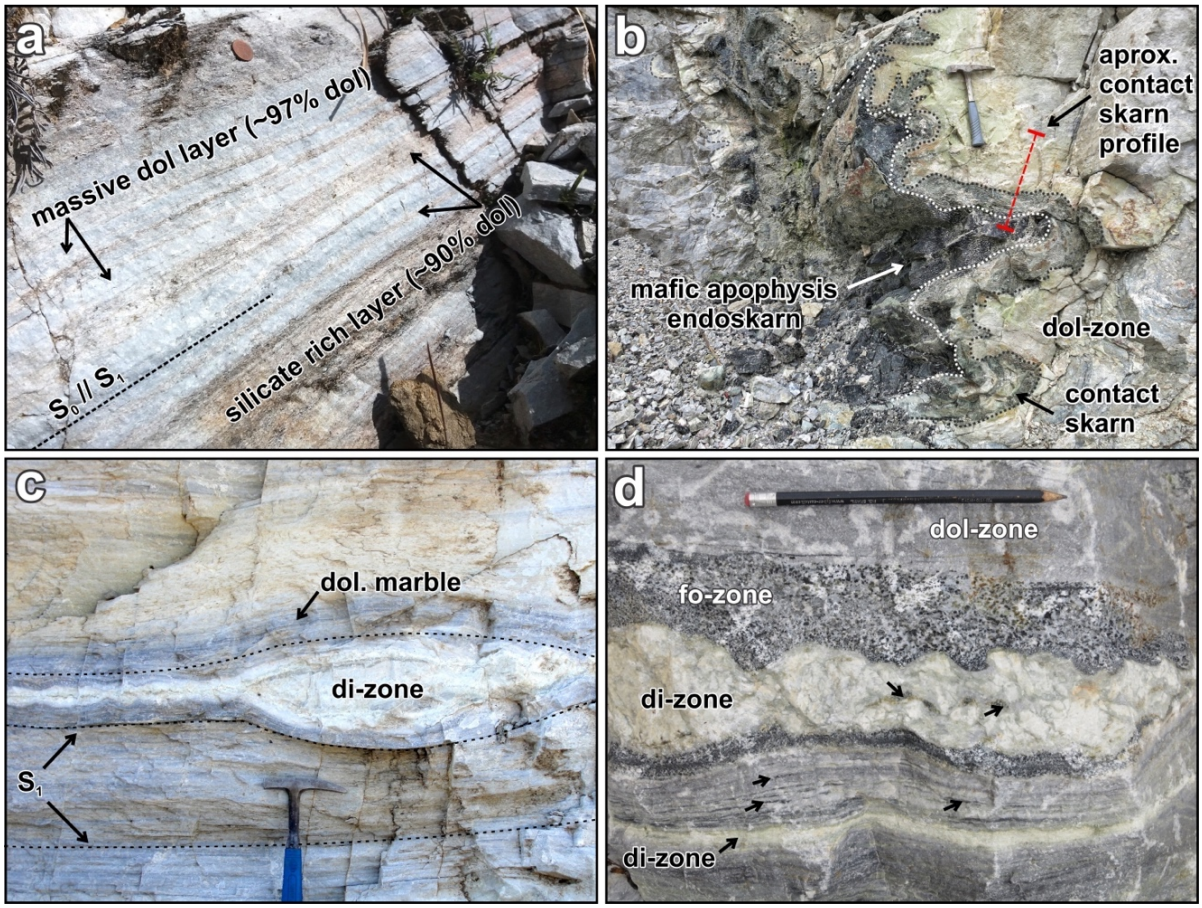

Figure 2: Field aspects of the marble and skarns. (a) Compositional layering of the dolomitic marble showing massive dolomite layers intercalated with higher silicate and calcite content; parallel bedding (S_0) and metamorphic foliation (S_1) indicated by dashed line. Note coin for scale (~ 2 cm). (b) Representative outcrop of contact skarn at a mafic apophysis fold hinge area; red dashed line shows the approximate profile location of the studied contact skarn profile. Note hammer for scale (~ 30 cm) (c) Isolated diopside skarn in pinch-and-swell structure without fo-zone border; note S_1 foliation following the pinch-and-swell shape of the diopside skarn (di-zone); note

hammer for scale (~ 30 cm); (d) representative outcrop of asymmetrical zoned vein skarn; black arrows indicate small fo+cal lenses; note pencil for scale.

4.2. MINERAL ASSEMBLAGES AND MICROSTRUCTURES

4.2.1. Vein skarn

For simplification purposes, we divided the vein skarn into three mineralogical zones namely the di-, fo-, and, dol-zones (Fig. 3a-b). The di-zone corresponds to the central zone which is surrounded by an asymmetric distribution of the fo- and dol-zone (Fig. 3a-b). Because of the asymmetry we address to the different sides of the central zone as the upper and lower sides, as indicated in Fig. 3a. The di-zone is composed of a granoblastic aggregate of coarse diopside grains (~0.25 – 1.5 mm) (Fig. 4a). The diopside grains are fractured and partially replaced by tremolite and antigorite. In addition, the diopside is cut by calcite veinlets with no preferred orientation and calcite veins fills the neck zone of the pinch-and-swell structure (Fig. 3c). The number of fractures and diopside replacement increase towards the contacts with the adjacent mineralogical zone (fo-zone) (Figs. 3c-g; 4a-b). The interface between the di-zone and the fo-zone in the upper side shows an irregular and thin (~1 – 3 mm) layer of massive antigorite (Figs. 3b; 4e). The fo-zone is composed of sub-rounded antigorite pseudomorphs after forsterite grains in a calcite matrix and minor dolomite and phlogopite (Figs. 4c, 4e). The average size of the antigorite pseudomorphs is 0.2 mm although they vary from less than 0.1 mm to more than 1 mm. The calcite of the fo-zone has lobate grain boundaries and no preferred orientation. These calcites are full of disseminated black inclusions (<0.1 μm) that gives the grains a hazy brown aspect when observed in plane-polarized light. Minor phlogopite occurs in the fo-zone (0 – 2%) typically oriented parallel to the mineralogical zone contacts. In the upper side, the fo-zone occurs as a thick layer of ~15 mm, bordering the di-zone with a sub-zone with only trace amounts of phlogopite (Fig. 3b, 3f). In the lower side, the fo-zone layer bordering the di-zone is thinner (~10 mm) and the average antigorite pseudomorphs are smaller than those on the upper side. In addition, fo-zone lenses occur along the lower side within the dol-zone (Fig. 3b). The dol-zone is dominantly composed of dolomite, ~90% in the upper side and 97% in the lower side, and variable amounts of phlogopite, calcite and antigorite (Fig. 4d, 4f-h). A rim of almost pure dolomite occurs in the contact between the dol- and fo-zone in the upper side (Fig. 3b-c). The dol-zone

on the upper side is formed by mostly polygonal granoblastic dolomite with an average size of 0.093 mm^2 (max: 0.426; min: 0.001). A poorly defined metamorphic foliation is observed in the dol-zone of the upper side, marked by the preferred orientation of the phlogopite. The dol-zone in the lower side have coarser dolomite with an average size of 0.165 mm^2 (max: 0.966; min: 0.002) and lobate boundaries (Fig. 4h).

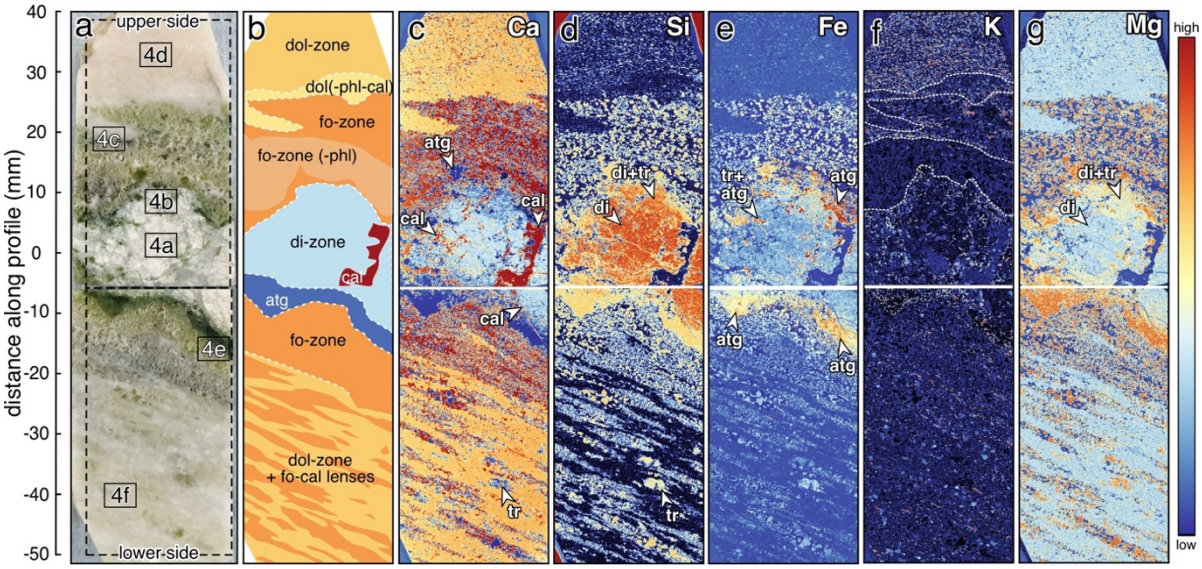

Figure 3: Vein skarn mineralogical zone distribution and compositional maps. (a) polished thick sections indicating the location of the microphotographs shown on figure 4. (b) Schematic distribution of the mineralogical zones. (c-g) Micro-XRF maps showing the distribution of Ca, Si, Fe, K and Mg through the mineralogical zones. Note zones of low phl contents marked by white dashed lines in (f). Note the partial replacement of diopside by antigorite and tremolite in the borders of di-zone.

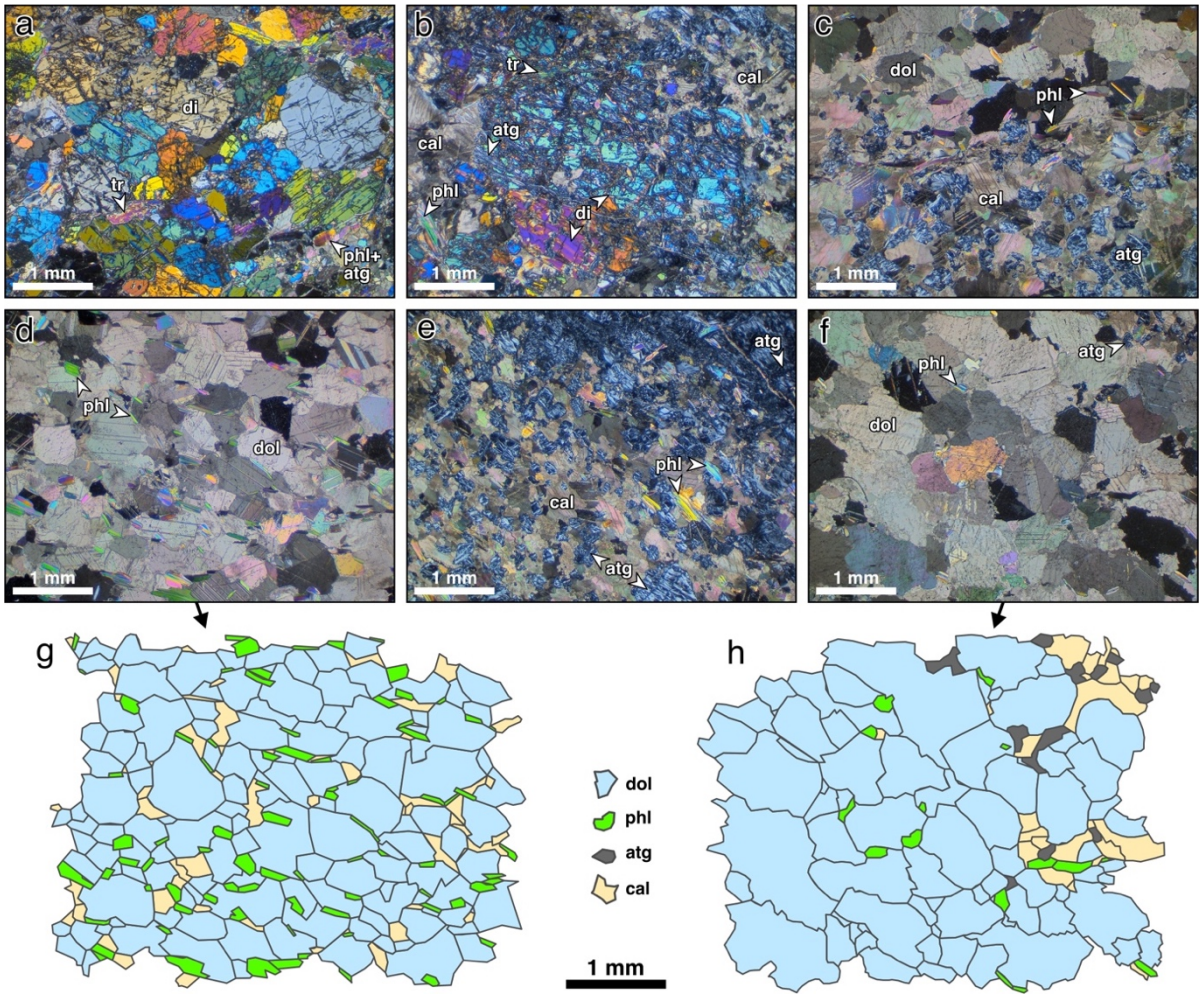

Figure 4: Vein skarn microstructures. Location of cross-polarized light microphotographs (a-f; XPL) indicated in Fig. 3a (a) Diopside aggregate in the center of the di-zone; note fracturing and the occurrence of tr and phl in the di grain boundaries (XPL); (b) Fractured diopside partially replaced by antigorite and tremolite in the border of the di-zone. (c) Interface between fo- and dol-zones; note phl concentration and preferred orientation parallel to the limit between the two zones. (d) dol-zone in side upper side; the preferred orientation of phl and elongate dolomite indicated a remnant metamorphic foliation; schematic mineral distribution shown in figure 4g. (e) fo-zone in the lower side; note massive atg deposition in the contact with di-zone (upper-right portion of the image); note the decreasing size of fo pseudomorphs outwards from the contact with the di-zone. (f) dol-zone in the side II; note coarse dolomite grains with lobate boundaries; schematic mineral distribution shown in figure 4h.

4.2.2. Contact skarn

Similar to the vein skarn, we divided the succession of different mineral assemblages from the mafic intrusion to the unaltered marble into mineralogical zones (Fig. 5a-b). The endoskarn is composed of inequigranular assemblage with diopside, phlogopite and calcite. The diopside form coarse porphyroblasts that range from ~1 to 5 mm,

extensively fractured and partially altered to an aggregate of carbonates and fine-grained brown phyllosilicates (Fig. 6a). Coarse phlogopite aggregates of a several millimeters to a few centimeters large. Disseminated fine- to medium-grained apatite is a common accessory in the endoskarn (Fig. 5i).

The di-zone is formed of diopside remnants that are mostly fully altered to fine-grained brown serpentine. The tr-zone consist of medium-grained tremolite aggregates with variable amounts of phlogopite, calcite and dolomite (Fig. 6b). Close to the contact with the di-zone, the tremolites show no preferred orientation (Fig. 6b). Tremolite gets progressively oriented through the tr-zone becoming mostly parallel with the contact with the subsequent fo-zone. In addition, phlogopite and carbonate content increase towards the limit with the fo-zone (Fig. 6b). The limit between the tr- and fo- zones is marked by coarse phlogopite aggregates which are oriented parallel to the contact. The fo-zone is composed of rounded olivine grains in a calcite matrix with minor amounts of phlogopite and apatite. The olivine is partially to fully altered to serpentine or iddingiste pseudomorphs. Coarse phlogopite aggregates, similar to those that occur in the endoskarn and in the interface between the tr- and fo- zones, are found within the fo-zone and at the contact with the dol-zone (Fig. 5f; 6d). The outer zone (dol-zone) is composed of dolomite (>90%), calcite, phlogopite and minor tremolite (Fig. 6f). This zone is cut by calcite veins (Fig. 5d) that coincide with tremolite-rich layers (Fig. 6e). Micro-XRF maps indicate that the dol-zone have higher Mn and Fe contents closer to the interface with the fo-zone (Fig. 5e; 5g).

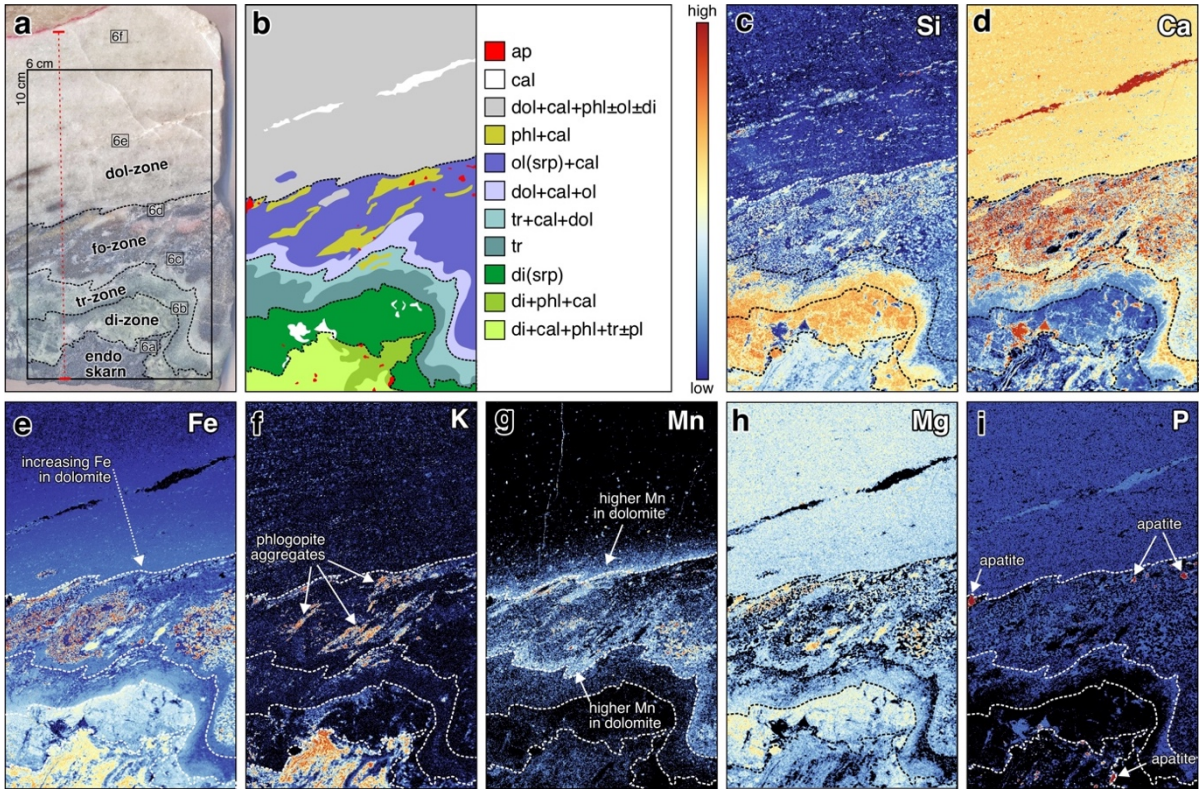

Figure 5: Contact skarn mineralogical zone distribution and compositional maps. (a) polished slab showing the mineralogical zones; black rectangle indicates the location of the microXRF maps. Red dashed line indicates the approximate location of the mineral chemistry profile of Figure 8 (b) schematic distribution of mineral assemblages; (c-i) Micro-XRF compositional maps.

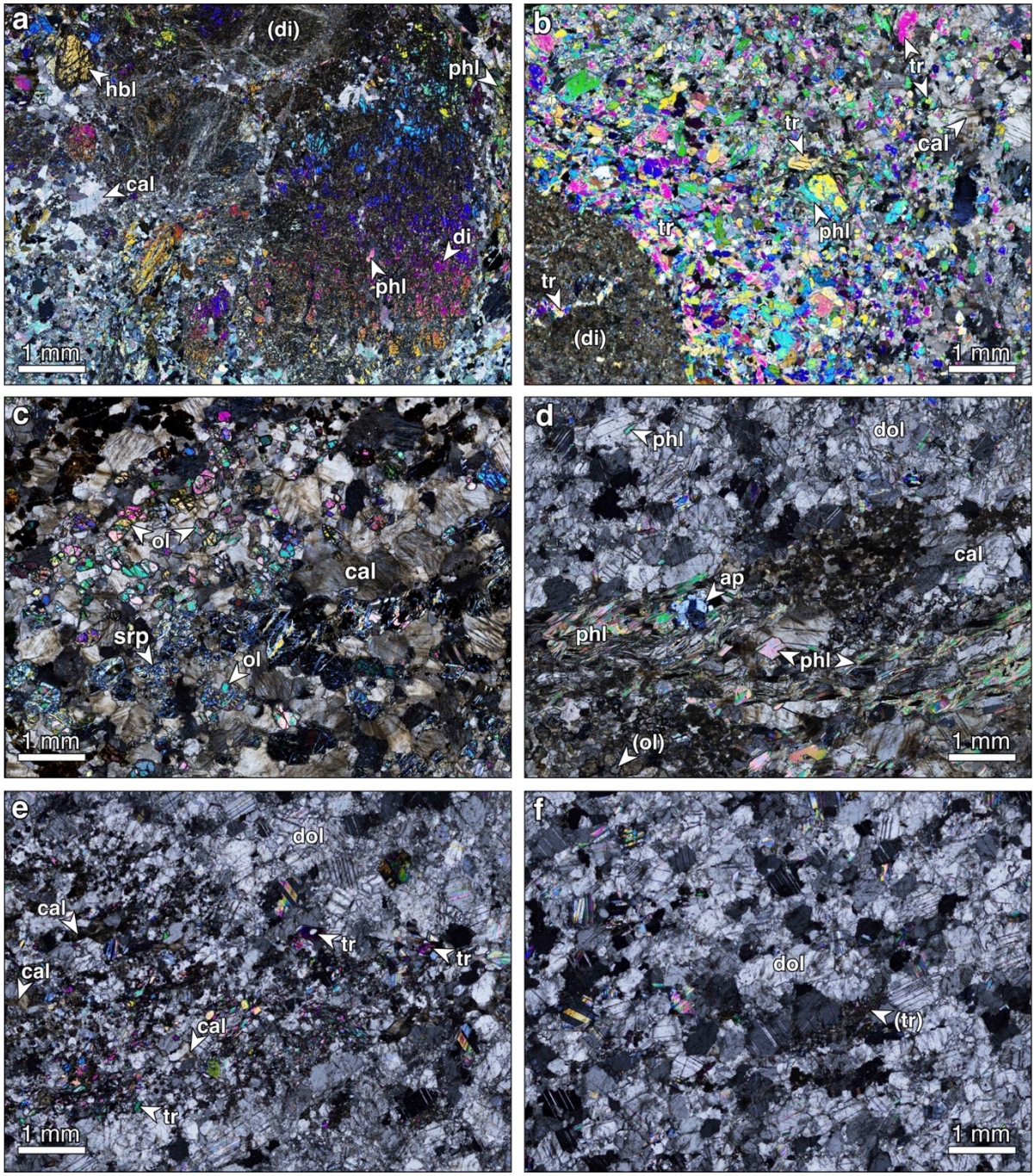

Figure 6: Contact skarn microstructures. The location of each photo is indicated in figure 5a (a) Endoskarn; note diopside porphyroblast fractured and partially replaced by fine grained serpentine and carbonates (b) interface between di- and tr-zones; note the increasing amount of calcite across the tr-zone. (c) fo-zone; note olivine grains partially replaced by serpentine and hazy calcite grains in the matrix; (d) fo- and dol-zone interface with coarse phl aggregates and apatite; (e) silicate-rich portion within altered-marlbe dol-zone; (f) unaltered-marble dol-zone. All microphotographs in XPM; 1 mm scale for all.

4.3. MINERAL CHEMISTRY

4.3.1. Vein skarn

Phlogopite compositions were obtained along a profile transversal to the main central zone orientation. The composition of the phlogopite is variable along the profile. Fluorine content decreases from ~0.8 to 0.4 wt% from the dol-zone towards the di-zone in the upper side whereas in the lower side it is approximately constant at ~0.4 wt% (Fig. 7a). Sodium shows a similar behavior to fluorine with higher contents in the upper-side dol-zone and lower values in the di-zone (Fig. 7b). However, a sharp change in the sodium content of the phlogopites is observed within the fo-zone in the upper side (Fig. 7b). This decrease from ~0.5 to ~0.2 NaO wt% coincides with the transition to the phlogopite-poor within the fo-zone (Fig. 3b, 3f). TiO_2 and X_{Mg} show similar patterns of higher values in the dol- and fo-zones and lower values in the di-zone (Fig. 7c-d). Notably, the average XMg values are slightly different on each side of the di-zone (Fig. 7d). The iron content is low on the dol-zones with an average of 0.35 FeO wt% on the upper side and 0.21 FeO wt% on the lower side (Fig. 7e). In general, the iron content increases along the fo-zones towards the di-zone, which itself shows the highest values with an average of 1.08 FeO wt%. The Fe rich phlogopites are found in the diopside fractures or as inclusions in the calcite veins that cut the diopside. The aluminum content in the phlogopites along the profile showed no defined trends or significant changes (Fig. 7f), as similarly observed for other major and minor elements (*e.g.* Si, K, Ca). The chlorine and manganese content of the analyzed phlogopites is very low (<0.02 Cl wt% and <0.03 MnO wt%) along the profile. In addition to the phlogopite profile, a few diopside and tremolite grains from the di-zone were analyzed. The diopside has an end-member composition with very low iron (from <0.007 to 0.39 FeO wt%) and fluorine (from <0.024 to 0.026 F wt%) contents. Manganese was not detected in the diopside (<0.025 MnO wt%). The tremolites also have a near end-member composition but show higher iron contents (from 0.45 to 0.72 FeO wt%). Minor contents of sodium in these amphiboles vary from 0.05 to 0.28 NaO wt%. Fluorine was detected in all the analyzed tremolites (n=14) reaching 0.18 F wt%. Mn is typically low and mostly below detection limits in the analyzed amphiboles.

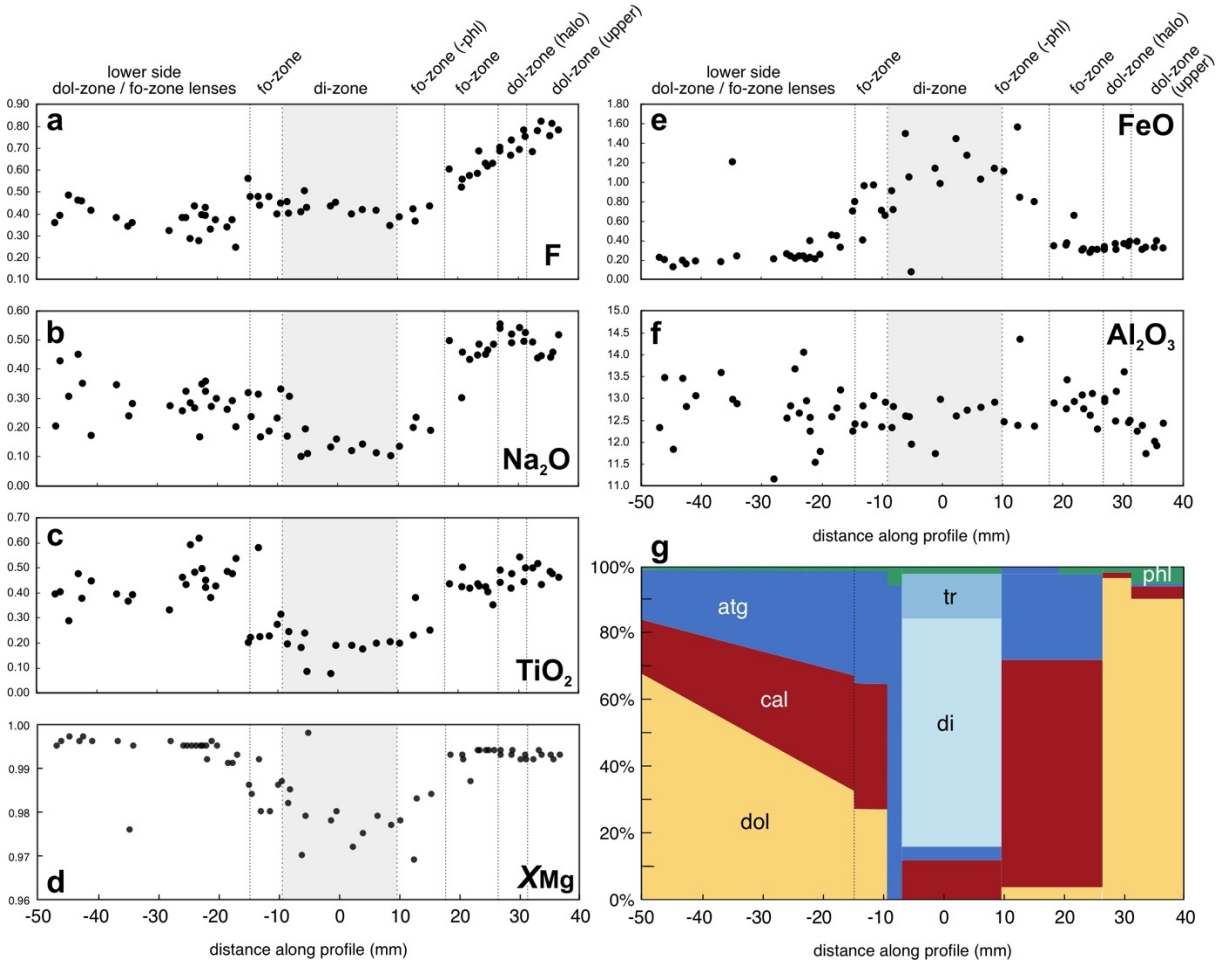

Figure 7: (a-f) Major and minor element composition of phlogopites (all values in wt%, except X_{Mg} = MgO/MgO+FeO$_{tot}$) and (g) modal abundance along the vein skarn profile.

4.3.2. Contact skarn

Phlogopite and dolomite were analyzed along a profile transversal to the mineralogical zones from the endoskarn to the unaltered marble. The composition of the micas and dolomites along the outer portion of the dol-zone (unaltered marble; ~80 – 120 mm) is nearly constant. In the unaltered marble portion of the dol-zone, the micas are near end-member phlogopites (X_{Mg} = 0.99; Al_{apfu} = 2.4; Fig. 8d) and show the highest fluorine and sodium contents with averages of 0.65 F wt% and 0.73 Na_2O wt% (Fig. 8a-b). In the same portion, the dolomites have the lowest iron and manganese contents along the profile (Fig. 8e-f). However, phlogopite and dolomite show a gradual variation in composition through the altered-marble dol- and fo-zones (~25 – 80 mm). Both phlogopite and dolomite show a gradual increase in Fe along this interval (Fig. 8e).

Similarly, the manganese content in the dolomites increases from mostly below detection level in the unaltered marble to ~0.24 MnO wt% in the tr-zone (Fig. 8f). The phlogopites show a gradual decrease in the fluorine, sodium and titanium contents as well as the XMg along the altered marble dol- and fo-zones (Fig. 8a-d). Despite that some elements show trends that are nearly continuous from the fo-zone into the tr-zone (*e.g.*, F, Ti, Fe), sodium and aluminum indicate an abrupt compositional change at this zone boundary (Fig. 8b, 8g). Likewise, the transition from the tr- to the di-zone is marked by sharp increase of Ti, Fe, and Al and decrease of F and Mg contents in the phlogopite (Fig. 8a-g). Along the di-zone, most elements in phlogopite are fairly constant, except for Fe and Mn, which are higher at the zone boundaries (Fig. 8e-f). At last, compositional variations in the phlogopites along the endoskarn are nearly continuous for F, Fe, and Al. Fluorine decreases whereas Fe and Al increase from the di-zone boundary towards the intrusion. In addition, the endoskarn phlogopites show the highest titanium (~1.1 TiO_2 wt%) contents of the whole contact skarn profile (Fig. 8c).

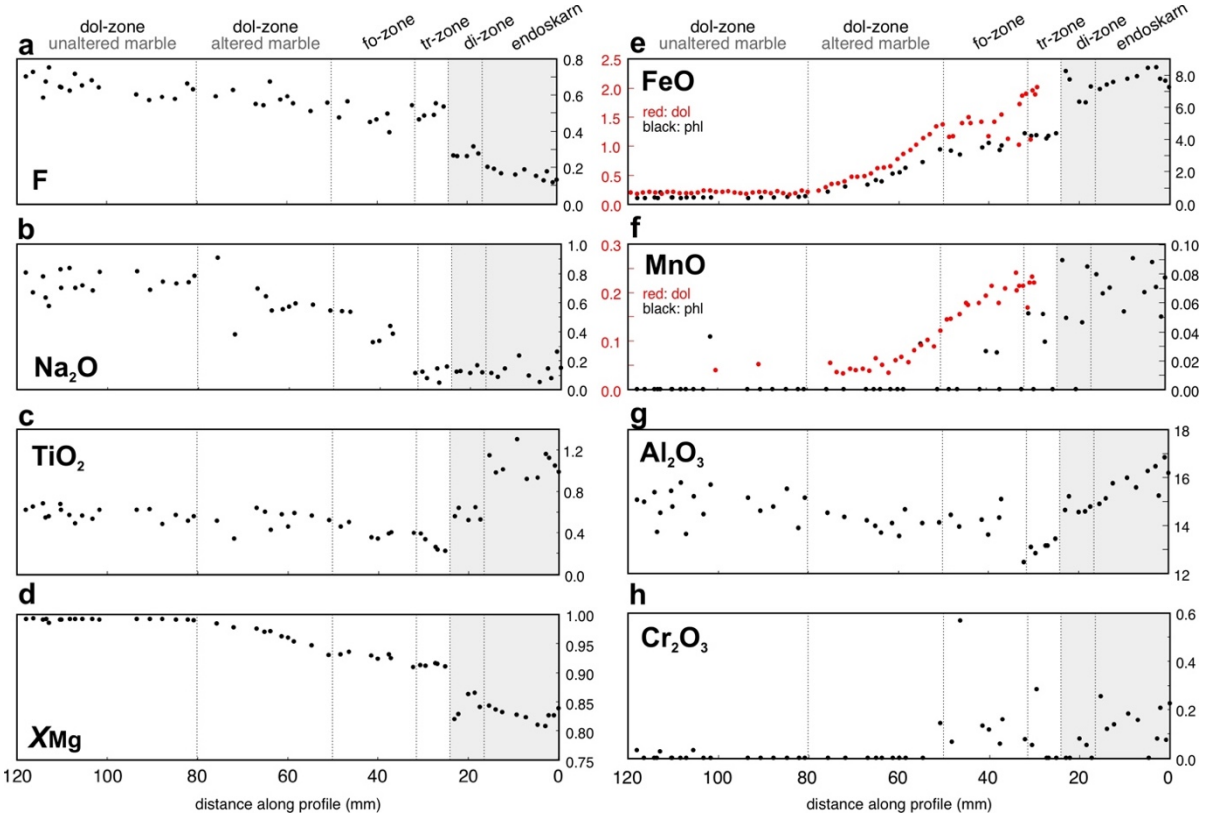

Figure 8: Phlogopite and dolomite composition along profile; black circles = phlogopite; red circles = dolomite; profile indicated in Figure 5a.

4.4. CARBON AND OXYGEN STABLE ISOTOPE COMPOSITION OF CARBONATES

Microdrilled bulk-carbonate powders were analyzed for carbon and oxygen stable isotopes along profiles in both vein and contact skarns. In addition, one dolomitic marble sample from the outermost portion of the metamorphic aureole was analyzed aiming at obtaining initial isotopic values for the marble (sample from the outcrop shown on Fig. 2a). The $\delta^{13}C_{VPDB}$ and $\delta^{18}O_{SMOW}$ values obtained are listed on Table 1 and plotted in Figures 9-11.

4.4.1. Vein skarn

All isotopic compositions of the vein skarn are plotted in Figure 9. The carbon and oxygen stable isotope values resulted in an asymmetrical distribution in both sides of the central di-zone (Fig. 9a-b). In addition, the patterns of isotopic variation along the profile are distinct for carbon and oxygen isotopes, except for the di-zone and the upper-side dol-zone where both isotopes show similar distributions. The carbonates from the dol-zone of the upper side show nearly constant $\delta^{13}C$ and $\delta^{18}O$ values of ~1.8‰ and ~23.1‰, respectively. These values are the highest for both carbon and oxygen isotopes along the vein skarn profile. A sharp decrease in the $\delta^{13}C$ and $\delta^{18}O$ values on the upper side corresponds to the transition between the dol- and fo-zones. The oxygen isotopes decrease continuously through the fo-zone (including the analyses of the fo-cal lenses on the lower side) from the dol-zones toward the di-zone (Fig. 9b). Furthermore, $\delta^{18}O$ values of the lower-side dol-zone show a similar gradual decrease towards the di-zone (Fig. 9b). The transition between the fo-zones and the central di-zone is marked by a sharp increase in the $\delta^{18}O$ values (Fig. 9b). However, a similar abrupt change is only observed for the $\delta^{13}C$ values on the upper side (Fig. 9a). It is important to note that the carbonates in the di-zone correspond to calcite veins and veinlets that cut the diopside and fill its fractures along with tremolite, antigorite and phlogopite (see Fig. 3a-c). The calcite from the di-zone show average values of -0.9‰ for $\delta^{18}O$ and 19.9‰ $\delta^{13}C$. The $\delta^{13}C$ values form flat distributions for the dol-zone and intercalated fo-zone lenses of the lower side (Fig. 9a).

Lithology	zone	Lab number	$\delta^{13}C_{VPDB}$ ‰	$\delta^{18}O_{SMOW}$ ‰
dol-marble	dol-marble	M1	0.41	26.65
dol-marble	dol-marble	M2	0.22	26.59
dol-marble	dol-marble	M3	0.52	26.55
dol-marble	dol-marble	M4	0.61	26.49
vein skarn	dol-zone (upper side)	V5	1.72	23.15
vein skarn	dol-zone (upper side)	V6	1.75	23.07
vein skarn	dol-zone (upper side)	V7	1.85	23.40
vein skarn	dol-zone (upper side)	V8	1.80	22.82
vein skarn	fo-zone (upper side)	V9	-0.89	19.52
vein skarn	fo-zone (upper side)	V10	-0.98	19.30
vein skarn	fo-zone (upper side)	V11	-2.04	19.04
vein skarn	fo-zone (upper side)	V12	-1.90	19.03
vein skarn	di-zone	V13	-0.79	19.89
vein skarn	di-zone	V14	-0.78	19.81
vein skarn	di-zone	V15	-0.85	20.73
vein skarn	di-zone	V16	-1.01	19.46
vein skarn	di-zone	V17	-1.03	19.93
vein skarn	di-zone	V18	-0.92	19.75
vein skarn	fo-zone (lower side)	V19	-0.66	18.95
vein skarn	fo-zone (lower side)	V20	-0.46	19.08
vein skarn	fo-zone (lower side)	V21	-0.12	19.31
vein skarn	dol-zone (lower side)	V22	0.73	20.24
vein skarn	dol-zone (lower side)	V23	0.99	21.09
vein skarn	dol-zone (lower side)	V24	0.81	21.66
vein skarn	dol-zone (lower side)	V25	0.76	22.82
vein skarn	dol-zone (lower side)	V26	0.80	22.76
vein skarn	dol-zone (lower side)	V27	1.10	23.27
vein skarn	fo-zone lens	V28	-0.01	19.79
vein skarn	fo-zone lens	V29	0.21	21.22
vein skarn	fo-zone lens	V30	0.17	21.35
vein skarn	fo-zone (lower side)	V31	0.15	20.01
vein skarn	fo-zone (lower side)	V32	-0.70	19.37
contact skarn	dol-zone	C1	-0.29	24.75
contact skarn	dol-zone	C2	-0.13	25.05
contact skarn	dol-zone	C3	-0.16	24.98
contact skarn	dol-zone	C4	-0.14	25.15
contact skarn	dol-zone	C5	0.03	25.11
contact skarn	dol-zone	C6	0.01	24.96
contact skarn	dol-zone	C7	-0.20	24.16
contact skarn	dol-zone	C8	-0.16	24.31
contact skarn	dol-zone	C9	-0.19	23.70
contact skarn	dol-zone	C10	-0.40	22.96
contact skarn	dol-zone (cal+silicate lens)	C11	-2.28	22.59
contact skarn	dol-zone (cal+silicate lens)	C12	-2.47	22.85
contact skarn	dol-zone	C13	-0.56	22.96
contact skarn	dol-zone	C14	-0.70	22.19
contact skarn	dol-zone (cal+silicate lens)	C15	-1.47	19.75
contact skarn	dol-zone (cal+silicate lens)	C16	-1.35	20.32
contact skarn	dol-zone	C17	-0.91	20.61
contact skarn	fo-zone	C18	-1.94	17.03

Lithology	zone	Lab number	$\delta^{13}C_{VPDB}$ ‰	$\delta^{18}O_{SMOW}$ ‰
contact skarn	fo-zone	C19	-2.23	16.61
contact skarn	fo-zone	C20	-2.27	16.54
contact skarn	fo-zone	C21	-2.31	16.08
contact skarn	fo-zone	C22	-2.44	15.70
contact skarn	fo-zone	C25	-2.37	16.11
contact skarn	fo-zone	C26	-2.40	16.49
contact skarn	tr-zone	C27	-2.53	14.02
contact skarn	di-zone	C28	-2.39	16.37
contact skarn	di-zone	C29	-3.19	14.22
contact skarn	di-zone	C30	-3.14	14.15
contact skarn	di-zone	C31	-2.86	14.75
contact skarn	di-zone	C32	-2.78	14.92
contact skarn	di-zone	C33	-2.50	14.13

Table 1: Isotopic composition of dolomitic marble, vein skarn and contact skarn.

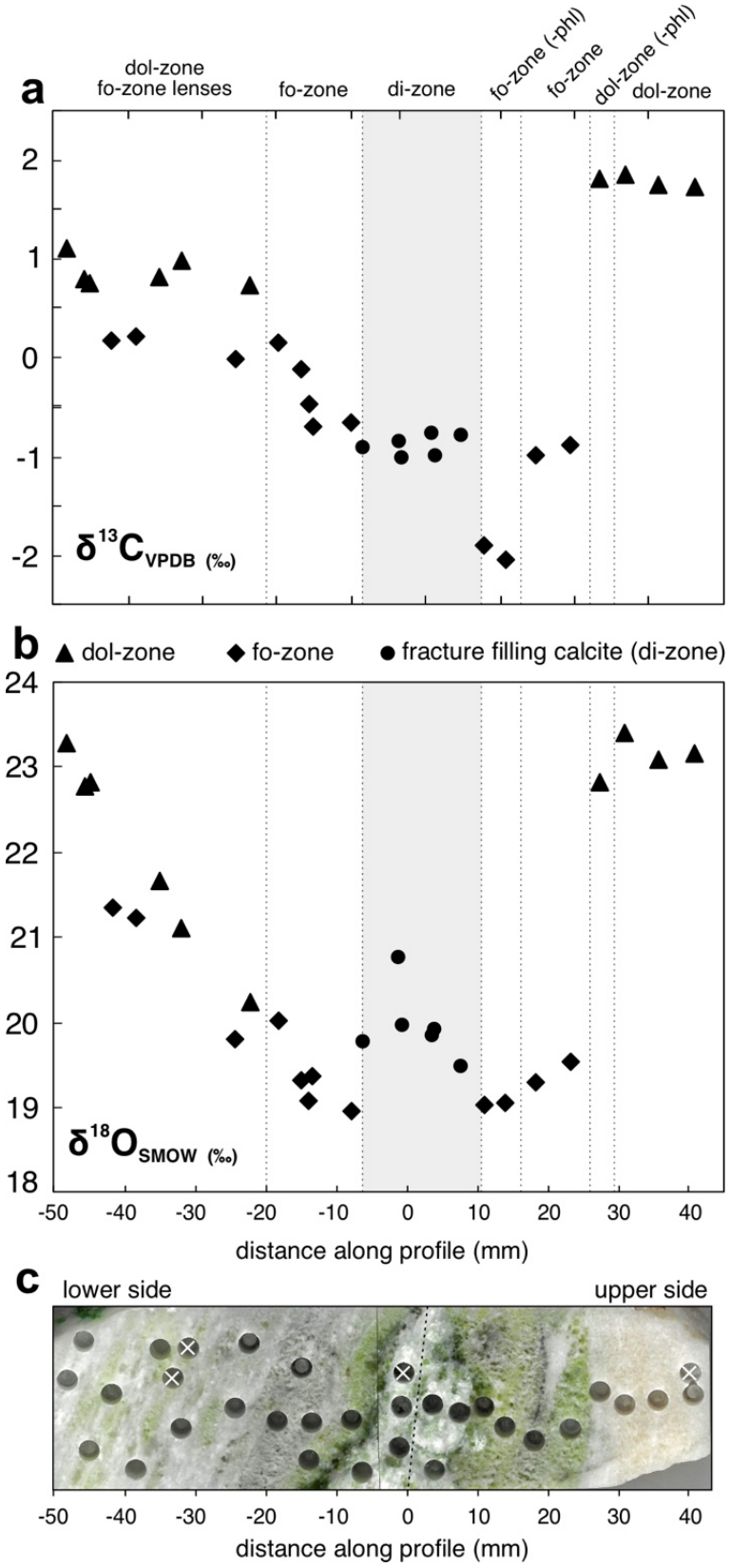

Figure 9: Isotopic profile along the vein skarn showing the bulk carbonate (a) $\delta^{13}C$ and (b) $\delta^{18}O$ values. (c) Thick section and location of the microdrilled areas; white cross indicate drills that were not analyzed.

4.4.2. Contact skarn

The $\delta^{13}C$ and $\delta^{18}O$ values along the contact skarn are plotted in Figure 10. Both carbon and oxygen isotopes show a similar behavior through the profile varying from lower values closer to the intrusion to higher values at the unaltered marble. The isotopic profiles across the contact skarn can be described by: (i) a flat profile of high $\delta^{13}C$ and $\delta^{18}O$ values at the unaltered-marble dol-zone; (ii) a gradual decrease of both $\delta^{13}C$ and $\delta^{18}O$ values across the altered-marble dol-zone with localized alterations at silicate-rich lenses; (iii) a sharp decrease in $\delta^{13}C$ and $\delta^{18}O$ values coinciding with the fo-zone boundary followed by gently decrease in both isotopes across the fo-zone; (iv) low $\delta^{13}C$ and $\delta^{18}O$ values along the tr-, di- and endoskarn zones (Fig. 10). Small amounts of carbonates in the tr-zone (<10% cal) complicated the obtainment of more bulk-carbonate isotopic compositions across this zone. We note that the highest $\delta^{13}C$ and $\delta^{18}O$ values obtained for the di-zone corresponds to a coarse calcite aggregate formed at the di- and endoskarn zone interface. Therefore, considering the remaining analyses of the di-zone we observe a trend of increasing $\delta^{13}C$ from the tr- and di-zone boundary towards the endoskarn. In this same area, the $\delta^{18}O$ values form a flat pattern at low values.

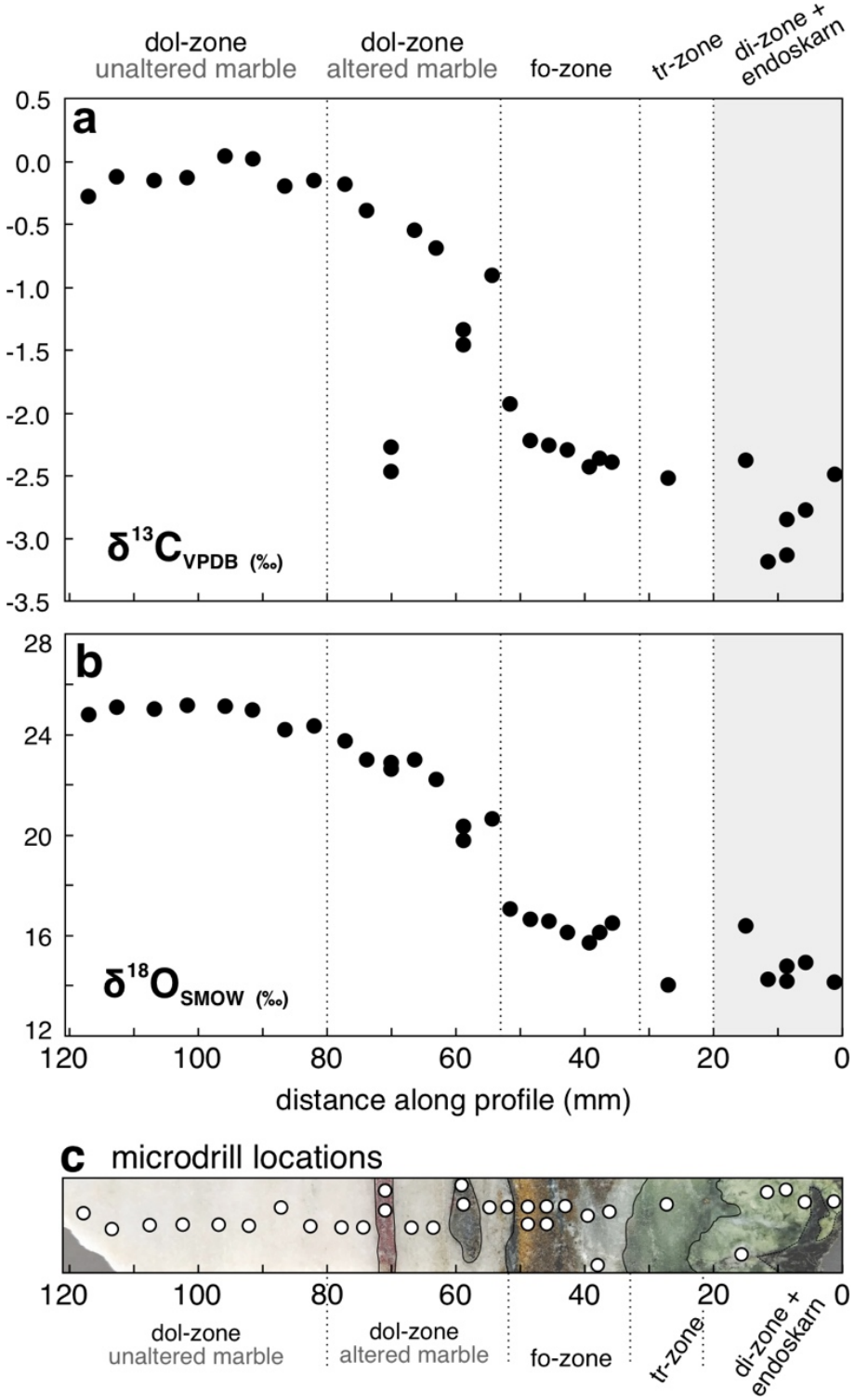

Figure 10: Isotopic profile along the contact skarn showing the bulk carbonate (a) $\delta^{13}C$ and (b) $\delta^{18}O$ values. (c) Polished slab and location of the microdrills.

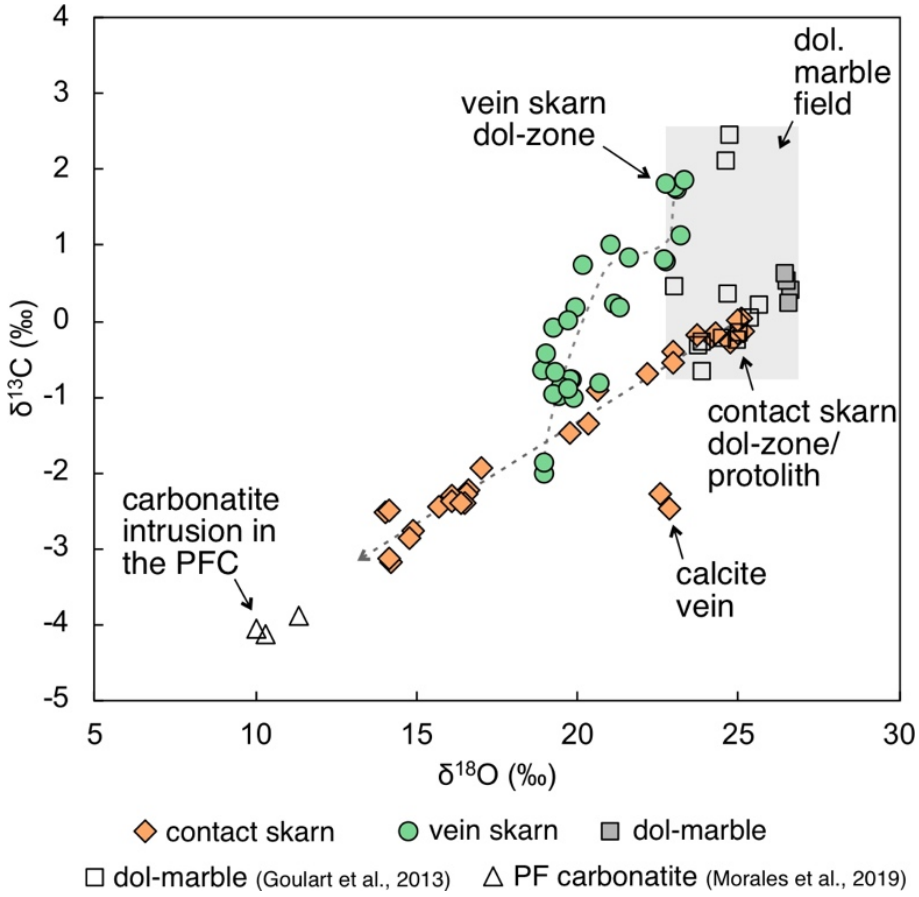

Figure 11: $\delta^{13}C$ vs. $\delta^{18}O$ for dolomitic marble, vein and contact skarns. Dolomitic marble values from Goulart *et al*. (2013) and carbonatite values from Morales *et al*. 2019.

4.5. TRIPLE OXYGEN ISOTOPE COMPOSITIONS OF SKARN SILICATES

The triple O isotope compositions of diopside, olivine, tremolite and serpentine from the vein and contact skarns are given in Table 2. Because of the intense retrograde effects on the vein skarn, obtaining pure diopside grains from the vein skarn and contact skarns was complicated. Therefore, we analyzed diopside and olivine grains from similar skarns and used for comparison. Olivine $\delta^{18}O$ values for the contact skarn range between 13.17 and 17.04‰. This fairly wide range for the olivines may be a result of mixing with other phases (*e.g.*, serpentine, iddingsite and iron oxides). Tremolite and serpentine have lower values between 13.15 – 15.19‰ and 8.43 – 9.13‰, respectively. Diopside grains from the vein skarn and from similar vein skarns have a range of $\delta^{18}O$ values between 12.97 and 20.79‰. Similar to the olivine, this wide range may be related to the contamination of tremolite inclusions as well as serpentine and tremolite replacements. Late and lower temperature phases or

aggregates such as serpentine, iddingsite and iron oxides have significant differences in the isotopic composition from high temperature anhydrous phases.

Lab#	Sample	Mineral	$\delta^{17}O_{VSMOW}$ (‰)	$\delta^{18}O_{VSMOW}$ (‰)	$\Delta'^{17}O_{0.528}$ (‰)
8676	Vein skarn	diopside (±tremolite)	8.13	15.61	-0.080
9148	Contact skarn	olivine (±serpentine)	6.86	13.17	-0.070
9151	Contact skarn	olivine (±serpentine)	8.89	17.04	-0.073
9152	Contact skarn	olivine (±serpentine)	8.76	16.78	-0.063
9155	Contact skarn	serpentine	4.38	8.43	-0.057
9154	Contact skarn	serpentine	4.76	9.13	-0.054
9146	Contact skarn	tremolite	7.30	13.98	-0.063
9147	Contact skarn	tremolite	6.85	13.15	-0.072
9150	Contact skarn	tremolite	7.92	15.19	-0.069
8665	Vein skarn (other; a)	diopside (±tremolite)	8.40	16.13	-0.079
8674	Vein skarn (other; a)	diopside (±tremolite)	8.40	16.13	-0.083
8664	Vein skarn (other; b)	diopside (±tremolite)	8.05	15.45	-0.079
8675	Vein skarn (other; c)	diopside (±pyrite)	10.84	20.79	-0.084
8678	Vein skarn (other; c)	olivine (±serpentine)	7.21	13.87	-0.092
8679	Vein skarn (other; c)	olivine (±serpentine)	7.73	14.86	-0.091
8684	Vein skarn (other; c)	olivine (±serpentine)	6.73	12.97	-0.094

Table 2: Triple O isotope composition of skarn silicates.

5. DISCUSSION

5.1. FLUID SOURCES AND ISOTOPIC EXCHANGE

For both vein and contact skarns, the areas with flat and high $\delta^{13}C$ and $\delta^{18}O$ values are interpreted as the unaltered dolomitic marble. In particular, the contact skarn sample has wider unaltered marble zone which provide us a well-constrained version of the dolomitic marble prior to the metasomatic effects. The vein skarn appears to have the initial isotopic compositions preserved only in the dol-zone of the upper side due to the high and flat distribution of $\delta^{13}C$ and $\delta^{18}O$ values. Note that hereafter we will refer to the initial isotopic composition as the $\delta^{13}C$ and $\delta^{18}O$ values of the dolomitic marbles that were not infiltrated by igneous fluids. Bulk-carbonate isotopic compositions of the dolomitic marbles obtained in a previous study in combination with the marble sample analyzed here indicate that the marbles have variable initial isotopic composition (Fig. 11) (Goulart *et al.*, 2013). $\delta^{13}C$ values of the unaltered marble range from -0.67 to 2.44‰ whereas $\delta^{18}O$ varies from 23.01 to 26.65‰ (Fig. 11). The

observed variations in the initial isotopic composition is reflected in the different values obtained in the unaltered dol-zones of the studied skarns. We note that isotopic profiles for each skarn derive from distinct initial values (Fig. 11).

The general trend from higher to lower $\delta^{13}C$ and $\delta^{18}O$ values towards the intrusion in the contact skarn or the central zone in the vein skarn suggests that isotopic exchange occurred due to the infiltration of a fluid with lower $\delta^{13}C$ and $\delta^{18}O$ values. The only $\delta^{13}C$ and $\delta^{18}O$ isotopic data available for the igneous or metamorphic rocks (except the marbles) located nearby the skarns correspond to calcites from a carbonatite intrusion that outcrop near the contact skarn site (<500 m). The carbonatite calcites yield values of ~-4‰ for $\delta^{13}C$ and 10.5‰ for $\delta^{18}O$, respectively (Morales *et al*., 2019). These carbonatite intrusions are intercalated with mafic intrusions rich in biotite and amphiboles that share many structural and chemical similarities with the mafic apophyses that intruded the marbles, suggesting a genetic correlation (Hoerlle *et al*., 2021b). In addition, typical magmatic fluids have $\delta^{18}O$ values ranging from 6 to 10‰ and $\delta^{13}C$ of -6 and -8‰ (*e.g.*, Taylor, 1968, 1974; Sheppard, 1986). Therefore, we interpret that both skarns were formed from the infiltration of igneous-derived fluids. The infiltration of igneous fluids is the main skarn forming process (*e.g.* Einaudi *et al*., 1981; Meinert *et al*., 2003).

The serpentinization of skarn silicates (mainly olivine and diopside) is greater on the vein skarn, hence the effects of this retrograde phase in the stable isotopes are better recorded in this skarn. Serpentinization occurred during the late stages of the CSGC emplacement because of the infiltration of water-rich fluids at ~300°C (Hoerlle *et al*., 2021a). The effect of the water-rich fluids in the isotopic composition is mainly observed in the modifications of the $\delta^{18}O$ values where $\delta^{13}C$ is much less affected. Massive antigorite rims and calcite veinlets along the di- and fo-zone boundary in the vein skarn (Fig. 3) mark the main fluid pathway for the late water-rich fluids. Along this interface, the $\delta^{18}O$ values are lower and closer to magmatic values than the surrounding indicating that calcite was, at least partially, re-equilibrated by the water-rich fluids (Fig. 9). Remarkably, the general isotopic trends observed for the contact and vein skarns show similarities and some differences that are associated with variations in the fluid infiltration mechanisms and reaction front development (see further discussions for particularities on sections 5.3 and 5.4).

5.2. MINERAL CHEMISTRY MODIFICATION

The observed modifications in the phlogopite and dolomite chemistry across the skarn profiles provide information on the chemistry and extent of the fluids. In general, both vein and contact skarns show well-defined trends of increasing Fe and decreasing F and Na in phlogopites across fo- and dol-zones. In addition, the dolomites from the contact skarn indicate a similar behavior for Fe and Mn. In particular, the relatively large range of the unaltered-marble dol-zone in the contact skarn (~40 mm) allowed us to obtain a well-constrained composition of the host-rock phlogopite and dolomite. In addition, the contrasting composition of the phlogopites from the contact skarn at different zones suggest formation or recrystallization from different origins (*e.g.*, igneous, metamorphic or metasomatic). The gradual changes on composition across the dol- and fo-zones suggest the recrystallization of pre-existing metamorphic micas. On the other hand, the high Ti, Fe, Mn contents of endoskarn phlogopites indicate the recrystallization from igneous micas. The micas from the di-zone share more similarities with the endoskarn phlogopites. The chemical profiles indicate that the fluids that formed the fo-zone and infiltrated the dol-zones had some amount of Fe and Mn but were undersaturated in F and Na. Fluids with such compositions are more likely to be expelled from mafic magmas than felsic ones.

Recent studies at the grain scale on forsterite-calcite veins hosted by dolomitic marbles demonstrated that Fe-Mn-rich dolomite was formed under a fluid-assisted dissolution-reprecipitation regime from pre-existing dolomites (Bégué *et al*., 2019). The authors indicated that dolomite recrystallization is driven by minor element disequilibrium. Recrystallization is an efficient and well-acknowledge process to achieve isotopic and chemical equilibration (*e.g.* Niedemeyer *et al*., 2009; Putnis, 2009) We consider that the same process was responsible for the recrystallization of the dolomites and phlogopites in this study. Previous studies indicated that solid-state diffusion of halogens and H_2O in biotite is very slow and therefore that F and Cl are good monitors of the halogen composition of the fluids present during the formation or recrystallization of biotite (Siron *et al*., 2018). In concluding this section, we emphasize that mineral chemistry profiles along metasomatic rocks can be useful to trace the extent, sources and mechanisms associated with fluid infiltration.

5.3. VEIN SKARN FORMATION REACTIONS AND MECHANISMS

The origin of the vein skarns and controls of the mineralogical zoning were discussed on Hoerlle *et al*. (2021a) based on field observations, microstructures and phase-diagram models. However, the authors indicated that the changes of the assemblages across the skarn zones could be explained by one or more fluid pulses with either variable fluid fluxes or constant flux and variable physicochemical conditions of the fluid phase (*e.g.* silica activity, temperature). In this study, use the isotopic and phlogopite chemistry data in combination with the microstructure observations aiming at constraining the mechanisms responsible for the vein skarn formation and asymmetric zonation.

The differences in grain size, mineral assemblages, phlogopite chemistry, and isotopic distribution in both sides of the central di-zone suggest that different mechanisms acted on each side of the central di-zone. Given that the PFMC marbles show heterogeneities in terms of grain size, silicate content (Fig. 2a), and isotopic composition (Fig. 11) we interpret that the central zone of the vein was formed along the contact between two slightly different marble layers (Fig. 12a). Previous studies in different metamorphic complexes indicated that the contact between different layers or lithologies is typically a preferred pathway for localized fluid infiltration (*i.e.*, layer-parallel fluid flow (*e.g.*, Bickle and Backer, 1990; Yardley and Lloyd, 1995; Oliver, 1996; Ague, 2003). Dolomitic marbles are very reactive under amphibolite facies where dolomite is only stable at very low water and silica activities (Slaughter *et al*., 1975; Cliff *et al*., 1993). Thus, even relatively small amounts of fluids can trigger the reaction and form the diopside. Fluids with variable amount of dissolved silica released from mafic and felsic intrusions infiltrated the contact of two marble layers and reacted with dolomite forming diopside according to the reaction:

$$2SiO_2\ (aq) + Dol = Di + 2CO_2 \quad (1)$$

Calcite-dolomite thermometry of the skarns and amphibole-plagioclase barometry of monzonite and granodiorite apophyses indicated that the skarns were formed between 580°C and 630°C and 4 to 5 kbar (Hoerlle *et al*., 2021c). At these conditions, diopside is typically formed at high XCO_2 (~0.8 to 1) if $aSiO_2$ is near 1 (Hoerlle *et al*., 2021a). However, if the fluid is undersaturated in silica ($aSiO_2$ between ~0.1 and 1) diopside can be formed at lower XCO_2 conditions (Hoerlle *et al*., 2021a). If the fluids were water-

rich ($XCO_2 < 0.1$) with low silica activities ($aSiO_2 < 0.1$) the reaction with dolomite would have resulted in the formation of forsterite and calcite (*e.g.*, Bucher-Nurminen, 1981; Ferry *et al*., 2011; Bégué *et al*., 2019). Field relations indicate that the diopside formation was related to the early mafic and felsic intrusions of the CSGC. Gases exsolved from basic magmas (and lamprophyres) have relatively high CO_2 concentrations that can even exceed water concentrations (*e.g.*, Gerlach, 1980; Rock, 1991). Thus, early exsolution of fluids from mafic rocks will likely have XCO_2 values greater that 0.1. In addition, previous studies showed that the presence of CO_2 in magmas and the relatively low solubility results in early exsolution of CO_2-rich fluids (Holloway, 1976; Lowenstern, 2001). Therefore, we interpret that the diopside was formed from the early, relatively CO_2-rich fluids exsolved from the mafic intrusions.

$\delta^{18}O$ isotopic thermometry estimates based on the curves of Zheng *et al*. (1993) indicates that diopside and calcite of the di-zone are in isotopic disequilibrium. Temperature estimates based on this isotopic pair (~280 and 380°C) are far below the diopside stability range. Such isotopic disequilibrium in combination with the replacement textures of tremolite and calcite over the diopside indicate that the calcite in the di-zone crystallized during a subsequent phase.

The mechanisms responsible for the transition from the di-zone to the fo-zone remained unclear in the previous study of Hoerlle *et al*., (2021a). However, new evidence including mineral chemistry, isotopic composition, and microstructures point out to the hypothesis of different fluid pulses with different CO_2-H_2O proportions. A high-permeability surface was developed along the pre-existing diopside-dolomite interface during the pinch-and-swell structure formation. Therefore, these surfaces became favorable pathways for channelized fluid flow. In addition, fracturing of the diopside grains and grain boundaries also turned into preferred pathways (Fig. 12b). The di-dol surface was infiltrated by water-rich fluids loaded with low amounts of silica and iron and possibly trace amounts of other elements. Disequilibrium with the diopside and the dolomite resulted in the fluid-assisted bi-metasomatic reactions transversal to the main fluid pathway (see schematic model fluid infiltration and reaction front directions in Fig. 12b). The reaction front that migrated towards the marble side promoted the dissolution of the dolomite enhancing the permeability along the pathway. While dolomite was dissolved, forsterite and calcite were formed through SiO_2 metasomatism according to Reaction 2.

$$2Dol + SiO_{2(aq)} = 2\ Cal + Fo + 2CO_2 \quad (2)$$

The isotopic signature of the calcite that was formed during this process represents the mixture between the CO_2 released from the dolomite and the H_2O-CO_2 from the igneous derived fluids. As the reaction front moved further towards the wall-rocks, silica availability was drastically reduced after it was consumed in reaction 2. The small amount of fluids that remained infiltrated the dol-zone, most likely along the dolomite grain boundaries and recrystallized the phlogopite to equilibrate with the chemistry of the fluids. Fluorine and iron trends for the phlogopite highlight the extent of the fluid infiltration. However, the isotopic composition of the bulk carbonates were not modified at this scale of study. Previous studies show that the fluid infiltration along the reaction fronts in dolomitic marbles occur along the grain boundaries towards the center of the dolomites (Bégué *et al*., 2019). The authors showed that isotopic changes are limited to recrystallized portions of the dolomite. Here, we interpret that the isotopic modification of the dolomite was localized at the grain boundaries and the scale of our study could not detect such changes. Nevertheless, we were able to identify such process along the contact skarn (see section 5.4).

The reaction front that moved into the di-zone resulted in the dissolution of diopside and crystallization of tremolite and calcite according to Reaction 3.

$$5Di + 3CO_2 + H_2O = 3Cal + Tr + 2SiO_{2(aq)} \quad (3)$$

In opposition to the virtual lack of silica in the dolomite zones, the fluid was undersaturated in silica in relation to the diopside zone. Hence, silica was mobilized into the fluid phase, likely using some of the silica released from reaction 3 to form the forsterite via reaction 2. Similarly, the excess of CO_2 released from reaction 2 was likely used in reaction 3 to form calcite. The resulting texture between the diopside and the dolomite can be described as a fluid-assisted corona texture (*e.g.*, Putnis and Austrheim, 2013). The tremolites show higher Fe contents, which were dissolved in minor amounts in the incoming fluid as the pre-existing diopside was virtually Fe-free.

The lower side of the vein skarn have forsterite and calcite lenses across the dol-zone. The abundance and size of these lenses reduce with the distance from the di-zone. These lenses are interpreted as localized flux in high permeability domains, most likely along pre-existing foliation planes in the dolomitic marbles. This mechanism was previously recognized in the thin section scale (Cartwright and Buick, 2000) and

aureole scale (Roselle *et al*., 1999). The presence of a tremolite grains and less phlogopite on the lower side indicate that this layer of the protolith likely had more quartz whereas the upper side was likely clay richer (Fig. 2a; 3c-d). Furthermore, as previously noted in the outcrop scale by Hoerlle *et al*. (2021a), the occurrence of isolated forsterite or diopside veins (Fig. 2a) point to the hypothesis of individual fluid flux events responsible for the formation of each of the di- and fo-zones.

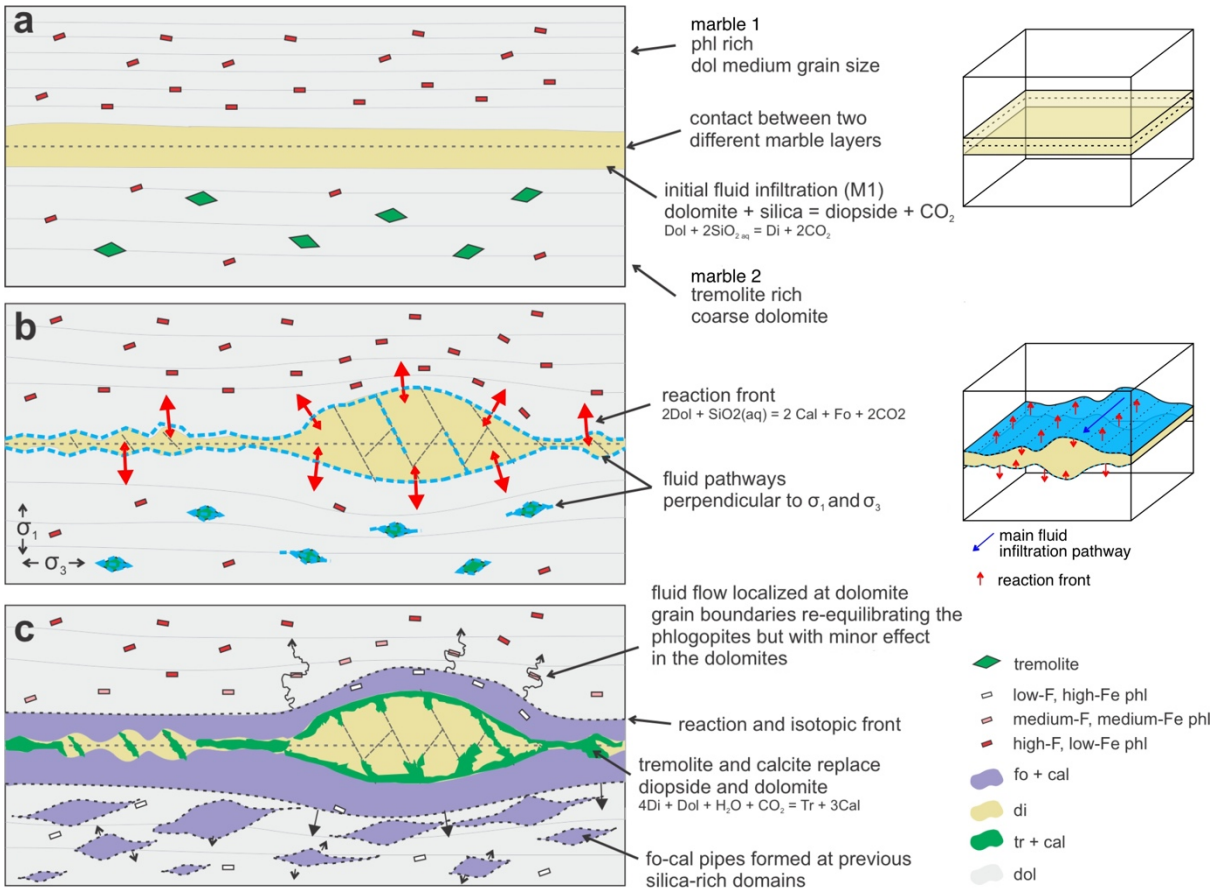

Figure 12: Schematic evolution of the prograde stage of the vein skarn.

5.4. CONTACT SKARN FORMATION REACTIONS AND MECHANISMS

The mechanisms responsible for the formation of the contact skarn are considered similar to those characterized for the vein skarn. In particular, the processes described for the development of the fo-zone and modification of the dol-zone in both skarns can be directly compared as isotopic and mineral composition distributions are alike and can be even better recognized in the contact skarn. However, the contact of two

chemically contrasting lithologies and the formation of the endoskarn are unique to the contact skarn.

The intrusion of a hot mafic magma into the dolomitic marbles generate a chemical disequilibrium along the contact that leads to bi-metasomatic reactions (*e.g.* Kerrick, 1977; Holness, 2000). Such reactions developed in the interface between two chemically incompatible rocks typically generates a layer that is much more permeable than each of the lithologies and therefore fluids tend to be channelized along the reacting interface (Yardley and Lloyd, 1995). Unlike the relatively limited components involved in the first stage of the vein skarn formation (CaO-MgO-SiO_2-CO_2-H_2O), the contact skarn has extra components derived from the intrusion (*e.g.*, Al_2O3, K_2O, FeO, TiO_2, PO_4) resulting in reactions with reactants and products. Thus, a series of simultaneous reactions likely occurred involving the dolomites from the marbles and the mafic apophysis phases (*e.g.*, hbl, phl, pl, ap, ttn).

Diopside is the main phase observed either in the endoskarn and di-zone that was not present in the mafic apophysis or the dolomitic marble. In addition, calcite is common in the endoskarn while it was not described for the intrusions in previous studies (*e.g.*, Hoerlle *et al*., 2021a; 2021b). The remaining major phases observed in the endoskarn such as hornblende, biotite and plagioclase are also present in the intrusion. We interpret that the formation of diopside resulted from the dissolution of dolomite that reacted with the siliceous fluids and possibly melt to form diopside and calcite. The CO_2 released from the diopside forming reaction probably reacted with the hornblende and plagioclase leading to the dehydration of the amphibole and replacement by clinopyroxene (Fig. 13a). We interpret that the formation of the diopside in the contact skarn is contemporaneous to the diopside formation in the vein skarns. The subsequent folding of the intrusions and di-skarn created favorable pathways along the interface between the skarn and marbles, mainly focused around fold hinge areas. Structural fluid channeling through axial regions is well acknowledge along metamorphic terranes (*e.g.*, Pitcairn *et al*., 2010; Skelton *et al*., 2015). At this stage, the processes that led to the formation of the fo-zone and diopside replacement by tremolite and calcite are considered basically the same that acted during the second stage of fluid infiltration on the vein skarns (Fig. 13b). The fo-zone of the contact skarn was formed from the dissolution of the marble dolomite and precipitation of forsterite, phlogopite and calcite as well as minor phases such as apatite, indicating a higher

variety of dissolved components in the fluids in comparison to the vein skarn. The reaction front propagated from the interface between the tr- and fo-zone towards the marble. Along the fo-zone, dissolution-precipitation reactions dominated resulting in replacement and recrystallization of phases. The subsequent zone (altered-marble dol-zone) shows a gradual transition from lighter to heavier isotopes, with exceptions of the sharp fronts at calcite veins, which are interpreted as channeled fluid infiltration along higher permeability domains close to the main fluid pathway. These are considered to be formed from a similar process described for the fo-cal lenses on the lower side of the vein skarn. In addition, the gradual modification of dolomite and phlogopite chemistry towards the unaltered marble indicates a coupled isotopic and chemical re-equilibration through dissolution and re-precipitation reactions. For as long as the infiltrating fluid was in disequilibrium with the host dolomite and phlogopite, the reactions occurred consuming the dissolved elements such as Fe and Mn. The transition from the altered- to unaltered-marble is marked by the flattening of isotopic and mineral compositions and therefore the extent of fluid infiltration. Despite that the fluid infiltration was channelized in the outcrop and aureole scale, it was pervasive in the thin section scale as highlighted by Fe and Mn compositional maps of the polished slab (Fig. 5). The grain scale analysis is beyond the scope of this investigation, however we speculate that fluid flow occurred through a grain-boundary permeability network in a positive feedback process where deformation leads to fluid infiltration and devolatization reactions that both elevate fluid pressure and create porosity (Hanson, 1995).

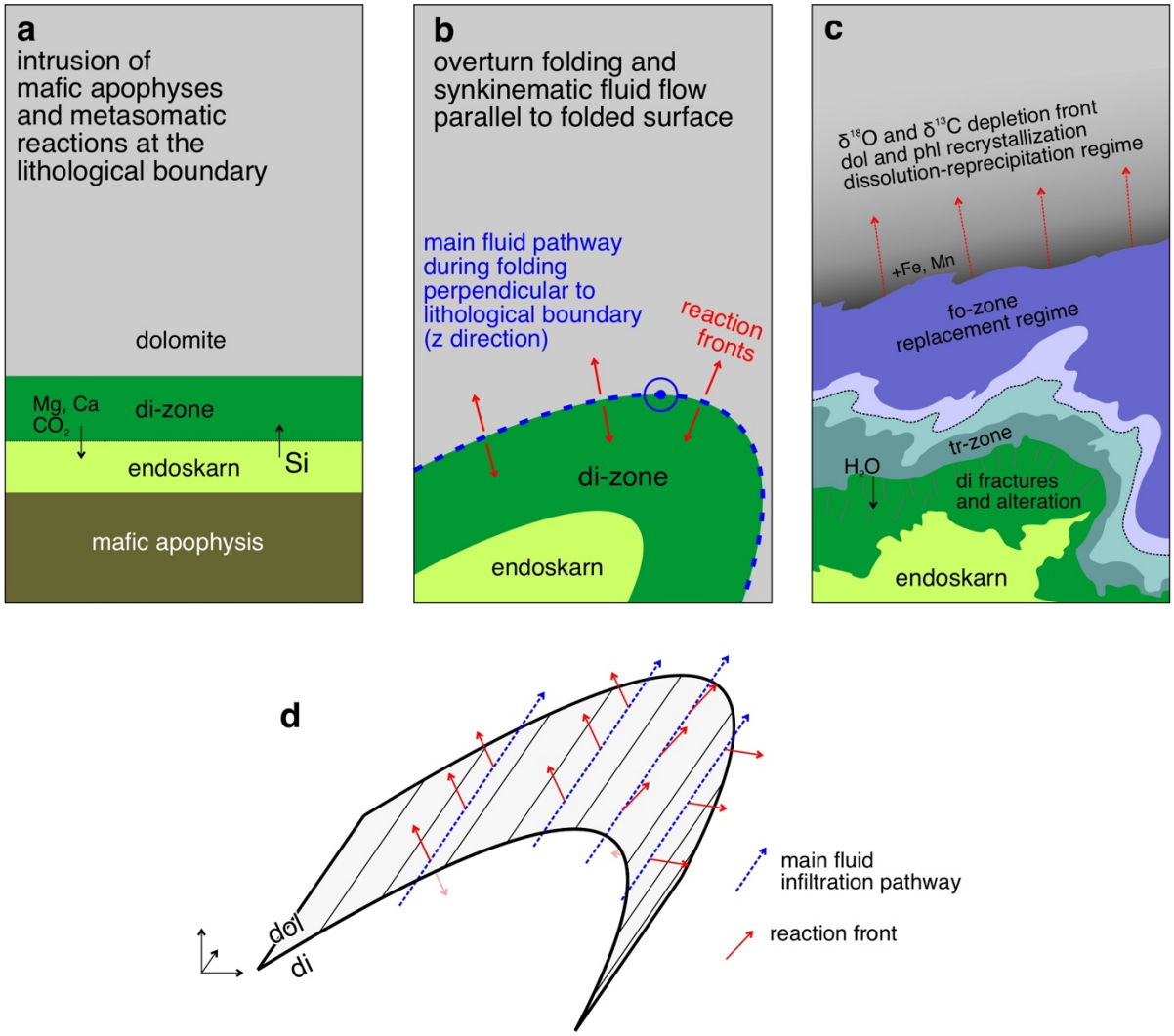

Figure 13: Schematic evolution of the prograde stage of the contact skarn. (a) intrusion of the mafic apophysis causing metamorphism and localized metasomatism at the interface between the intrusion and the dolomitic marble; (b) folding and synkinematic fluid flow along the di-zone and the marble; red arrows indicate the propagation of reaction fronts transversal to the main fluid pathway; (c) actual configuration of the mineralogical zones along the contact skarn; red dashed arrows indicate the propagating reaction front causing dissolution and reprecipitation of dolomite and phlogopite. (d) 3D schematic model showing the direction of the direction of the main fluid pathway (surface and blue dashed lines) and direction of the propagating reaction fronts (red arrows).

5.5. CONCLUSIONS: USING SKARN REACTION CHARACTERISTICS TO DECIPHER FLUID PULSE HISTORY OF A METAMORPHIC TERRANE

Based on the provided bulk-carbonate isotopic compositions, mineral chemistry and microstructure observations, we were able to characterize two main fluid pulses during the early stage of the CSGC emplacement. The distinct fluid infiltration events led to (i) the dissolution of dolomite and precipitation of diopside from relatively CO_2-rich and

SiO_{2aq} fluids exsolved from the early mafic intrusions and (ii) replacement of dolomite and diopside by forsterite+calcite and tremolite from water-rich fluids released from felsic intrusions during synkinematic emplacement. In both skarns, the second fluid pulse used the diopside-dolomite interface that had its permeability enhanced by deformation and devolatization reactions. Furthermore, the propagation of the reaction fronts was transversal to the main fluid pathways (Fig. 12b; 13b) leading to two domains governed by replacement and dissolution-reprecipitation reactions. The di-, tr- and fo-zones characterize the replacement domains whereas isotopic and chemical modifications of dolomite and phlogopite mark the dissolution and reprecipitation of the initial marble assemblage. In this study, we were able to successfully trace the fluid infiltration into the host rock by isotopic modifications of the bulk-carbonates and Fe-Mn contents of the dolomites. Here, fluid-driven dissolution of the host rock assemblage is achieved by isotopic and chemical disequilibrium resulting in dissolution and reprecipitation, as similarly described for the grain size scale (*e.g.*, Bégué *et al*., 2019). In addition, we show that phlogopites are useful tracers of fluid flow as they chemically re-equilibrate with the infiltrating fluid via recrystallization. Notably, these findings indicate that fluid-rock reactions may affect the host-rocks much further than the observed extent of mineral replacement zones.

REFERENCES

Ague, J.J., 2003. Fluid Infiltration and Transport of Major, Minor, and Trace Elements During Regional Metamorphism of Carbonate Rocks, Wepawaug Schist, Connecticut, USA. Am. J. Sci. 303, 753–816. https://doi.org/10.2475/ajs.303.9.753

Ague, J.J., 2014. Fluid Flow in the Deep Crust, in: Treatise on Geochemistry. Elsevier, pp. 203–247. https://doi.org/10.1016/B978-0-08-095975-7.00306-5

Baumgartner, L.P., Valley, J.W., 2001. Stable Isotope Transport and Contact Metamorphic Fluid Flow. Rev. Mineral. Geochemistry 43, 415–467. https://doi.org/10.2138/gsrmg.43.1.415

Bégué, F., Baumgartner, L.P., Bouvier, A.S., Robyr, M., 2019. Reactive fluid infiltration along fractures: Textural observations coupled to in-situ isotopic analyses. Earth Planet. Sci. Lett. 519, 264–273. https://doi.org/10.1016/j.epsl.2019.05.024

Bégué, F., Baumgartner, L.P., Müller, T., Putlitz, B., Vennemann, T.W., 2020. Metasomatic Vein Formation by Stationary Fluids in Carbonate Xenoliths at the Eastern Margin of the Bergell Intrusion, Val Sissone, Italy. J. Petrol. 60, 2387–2412. https://doi.org/10.1093/petrology/egaa012

Bickle, M.J., Baker, J., 1990. Advective-diffusive transport of isotopic fronts: an example from Naxos, Greece. Earth Planet. Sci. Lett. 97, 78–93. https://doi.org/10.1016/0012-821X(90)90100-C

Bitencourt, M.F., 1983. Geologia petrologia e estrutura dos metamorfitos da região de Caçapava do Sul, RS. Universidade Federal do Rio Grande do Sul.

Bortolotto, O.J., 1988. Metamorfismo Termal dos Mármores de Caçapava do Sul, RS. Ciência e Nat. 10, 25–48.

Bucher-Nurminen, K., 1981. The Formation of Metasomatic Reaction Veins in Dolomitic Marble Roof Pendants in the Bergell Intrusion (Province Sondrio , Northern Italy). Am. J. Sci. 281.

Bucher-Nurminen, K., 1982. On the mechanism of contact aureole formation in dolomitic country rock by the Adamello intrusion (northern Italy). Am. Mineral. 67, 1101–1117.

Bucher-Nurminen, K., 1989. Reaction veins in marbles formed by a fracture-reaction-seal mechanism. Eur. J. Mineral. 1, 701–714. https://doi.org/10.1127/ejm/1/5/0701

Cartwright, I., Buick, I.S., 2000. Millimetre-scale variation in metamorphic permeability of marbles during transient fluid flow: An example from the Reynolds Range, central Australia. Contrib. to Mineral. Petrol. 140, 163–179. https://doi.org/10.1007/s004100000180

Cerva-Alves, T., Hartmann, L.A., Remus, M.V.D., Lana, C., 2020. Integrated ophiolite and arc evolution, southern Brasiliano Orogen. Precambrian Res. 341, 105648. https://doi.org/10.1016/j.precamres.2020.105648

Cliff, R.A., Yardley, B.W.D., Bussy, F., 1993. U–Pb isotopic dating of fluid infiltration and metasomatism during Dalradian regional metamorphism in Connemara, western Ireland. J. Metamorph. Geol. 11, 185–191. https://doi.org/10.1111/j.1525-1314.1993.tb00141.x

Cook, S.J., Bowman, J.R., 2000. Mineralogical Evidence for Fluid–Rock Interaction Accompanying Prograde Contact Metamorphism of Siliceous Dolomites: Alta Stock Aureole, Utah, USA. J. Petrol. 41, 739–757. https://doi.org/10.1093/petrology/41.6.739

Ducoux, M., Branquet, Y., Jolivet, L., Arbaret, L., Grasemann, B., Rabillard, A., Gumiaux, C., Drufin, S., 2017. Synkinematic skarns and fluid drainage along detachments: The West Cycladic Detachment System on Serifos Island (Cyclades, Greece) and its related mineralization. Tectonophysics 695, 1–26. https://doi.org/10.1016/j.tecto.2016.12.008

Einaudi, M.T., Meinert, L.D., Newberry, R.J., 1981. Skarn Deposits, in: Seventy-Fifth Anniversary Volume. Society of Economic Geologists. https://doi.org/10.5382/AV75.11

Ferry, J.M., 1978. Fluid interaction between granite and sediment during metamorphism, South-central Maine. Am. J. Sci. 278, 1025–1056. https://doi.org/10.2475/ajs.278.8.1025

Ferry, J.M., 1992. Regional metamorphism of the waits river formation, Eastern Vermont: Delineation of a new type of giant metamorphic hydrothermal system. J. Petrol. 33, 45–94. https://doi.org/10.1093/petrology/33.1.45

Ferry, J.M., Dipple, G.M., 1991. Fluid flow, mineral reactions, and metasomatism. Geology 19, 211–214. https://doi.org/10.1130/0091-7613(1991)019<0211:FFMRAM>2.3.CO;2

Ferry, J.M., Ushikubo, T., Valley, A.W., Valley, J.W., 2011. Formation of forsterite by silicification of dolomite during contact metamorphism. J. Petrol. 52, 1619–1640. https://doi.org/10.1093/petrology/egr021

Gerlach, T.M., Graeber, E.J., 1985. Volatile budget of Kilauea volcano. Nature 313, 273–277. https://doi.org/10.1038/313273a0

Goulart, R.V., Remus, M.V.D., Reis, R.S. dos, 2013. Composição isotópica de Sr, C e O e geoquímica de ETRs das rochas carbonáticas do Bloco São Gabriel, Rio Grande do Sul. Pesqui. em Geociencias 40, 75–97.

Guo, S., Chu, X., Hermann, J., Chen, Y., Li, Q., Wu, F., Liu, C., Sein, K., 2021. Multiple Episodes of Fluid Infiltration Along a Single Metasomatic Channel in Metacarbonates (Mogok Metamorphic Belt, Myanmar) and Implications for CO2 Release in Orogenic Belts. J. Geophys. Res. Solid Earth 126, 1–23. https://doi.org/10.1029/2020JB020988

Hanson, R.B., 1995. The hydrodynamics of contact metamorphism. Geol. Soc. Am. Bull. 107, 595–611. https://doi.org/10.1130/0016-7606(1995)107<0595:THOCM>2.3.CO

Hartmann, L.A., Tindle, A., Bitencourt, M. de F.A.S., 1990. O metamorfismo de facies anfibolito no complexo metamorfico Passo Feio, RS, com base em quimica dos minerais. Pesquisas 17, 62–71.

Hoerlle, G.S., Remus, M.V.D., Dani, N., 2021b. Metalamprophyres in the Dom Feliciano Belt: insights for the development of strike-slip tectonics and localized metamorphism during the post-collisional stage. Manuscript submitted to publication.

Hoerlle, G.S., Remus, M.V.D., Müller, T., Piazolo, S., Lana., C.C., Sorger, D. 2021a. Metasomatic reactions triggered by localized and episodic fluid flux record multistage intrusion history: An example from the syntectonic Caçapava do Sul Granitic Complex, Southern Brazil. Manuscript submitted to publication.

Hoerlle, G.S., Remus, M.V.D., Silva, M., Lana, C., 2021c. Post-collisional magmatic-hydrothermal mineralization in the São Gabriel Terrane (southern Brazil): insights from mineral chemistry, stable isotopes, and sulfide trace-elements of the Caçapava do Sul skarns. Manuscript submitted to publication.

Holloway, J.R., 1976. Fluids in the evolution of granitic magmas: Consequences of finite CO2 solubility. Bull. Geol. Soc. Am. 87, 1513–1518. https://doi.org/10.1130/0016-7606(1976)87<1513:FITEOG>2.0.CO;2

Holness, M.B., 2000. Metasomatism and self-organization of dolerite dyke-marble contacts: Beinn an Dubhaich, Skye. J. Metamorph. Geol. 18, 103–118. https://doi.org/10.1046/j.1525-1314.2000.00244.x

Kerrick, D.M., 1977. The Genesis of Zoned Skarns in the Sierra Nevada, California. J. Petrol. 18, 144–181. https://doi.org/10.1093/petrology/18.1.144

Koehn, D., Piazolo, S., Beaudoin, N.E., Kelka, U., Spruženiece, L., Putnis, C. V., Toussaint, R., 2021. Relative rates of fluid advection, elemental diffusion and replacement govern reaction front patterns. Earth Planet. Sci. Lett. 565, 116950. https://doi.org/10.1016/j.epsl.2021.116950

Lanari, P., Vho, A., Bovay, T., Airaghi, L., Centrella, S., 2019. Quantitative compositional mapping of mineral phases by electron probe micro-analyser. Geol. Soc. Spec. Publ. 478, 39–63. https://doi.org/10.1144/SP478.4

Lanari, P., Vidal, O., De Andrade, V., Dubacq, B., Lewin, E., Grosch, *E.G.*, Schwartz, S., 2014. XMapTools: A MATLAB©-based program for electron microprobe X-ray image processing and geothermobarometry. Comput. Geosci. 62, 227–240. https://doi.org/10.1016/j.cageo.2013.08.010

Leinz, V., Barbosa, A.F., Teixeira, E., 1941. Mapa Geológico Caçapava-Lavras. Bol. da Secr. Agric. Indústria e Comércio 90, 39.

Lowenstern, J.B., 2001. Carbon dioxide in magmas and implications for hydrothermal systems. Miner. Depos. 36, 490–502. https://doi.org/10.1007/s001260100185

McCaig, A.M., 1988. Deep fluid circulation in fault zones. Geology 16, 867–870. https://doi.org/10.1130/0091-7613(1988)016<0867:DFCIFZ>2.3.CO;2

Meinert, L.D., Dipple, G.M., Nicolescu, S., 2005. World Skarn Deposits, in: Hedenquist, J.W., Thompson, J.F.H., Goldfarb, R.J., Richards, J.P. (Eds.), One Hundredth Anniversary Volume. Society of Economic Geologists, pp. 299–336. https://doi.org/10.5382/AV100.11

Meinert, L.D., Hedenquist, J.W., Satoh, H., Matsuhisa, Y., 2003. Formation of anhydrous and hydrous skarn in Cu-Au ore deposits by magmatic fluids. Econ. Geol. 98, 147–156. https://doi.org/10.2113/gsecongeo.98.1.147

Morales, B.A. de A., Almeida, D.D.P.M. de, Koester, E., Rocha, A.M.R. da, Dorneles, N.T., Rosa, M.B. da, Martins, A.A., 2019. Mineralogy, whole-rock geochemistry and C, O isotopes from Passo Feio Carbonatite, Sul-Riograndense Shield, Brazil. J. South Am. Earth Sci. 94, 102208. https://doi.org/10.1016/j.jsames.2019.05.024

Nardi, L.V.S., Bitencourt, M. de F., 1989. Geologia, Petrologia e Geoquímica do Complexo Granítico de Caçapava do Sul, RS. Rev. Bras. Geociências 19, 153–169.

Niedermeier, D.R.D., Putnis, A., Geisler, T., Golla-Schindler, U., Putnis, C. V., 2009. The mechanism of cation and oxygen isotope exchange in alkali feldspars under hydrothermal conditions. Contrib. to Mineral. Petrol. 157, 65–76. https://doi.org/10.1007/s00410-008-0320-2

Oliver, N.H.S., 1996. Review and classification of structural controls on fluid flow during regional metamorphism. J. Metamorph. Geol. 14, 477–492. https://doi.org/10.1046/j.1525-1314.1996.00347.x

Pack, A., Tanaka, R., Hering, M., Sengupta, S., Peters, S., Nakamura, E., 2016. The oxygen isotope composition of San Carlos olivine on the VSMOW2-SLAP2 scale. Rapid Commun. Mass Spectrom. 1495–1504. https://doi.org/10.1002/rcm.7582

Piccoli, F., Ague, J.J., Chu, X., Tian, M., Brovarone, A.V., 2021. Field-based evidence for intra-slab high-permeability channel formation at eclogite-facies conditions during subduction. Geochemistry, Geophys. Geosystems 1–17. https://doi.org/10.1029/2020gc009520

Pitcairn, I.K., Skelton, A.D.L., Broman, C., Arghe, F., Boyce, A., 2010. Structurally focused fluid flow during orogenesis: The Islay Anticline, SW Highlands, Scotland. J. Geol. Soc. London. 167, 659–674. https://doi.org/10.1144/0016-76492009-135

Porcher, C.A., Lopes, R.D.C., 2000. Programa Levantamentos Geológicos Básicos do Brasil–PLGB: Cachoeira do Sul (folha SH. 22-Y-A) CPRM/DNPM (CD-ROM).

Putnis, A., 2009. Mineral replacement reactions. Rev. Mineral. Geochemistry 70, 87–124. https://doi.org/10.2138/rmg.2009.70.3

Putnis, A., Austrheim, H., 2010. Fluid-Induced Processes: Metasomatism and Metamorphism. Front. Geofluids 10, 254–269. https://doi.org/10.1002/9781444394900.ch18

Putnis, A., Austrheim, H., 2013. Mechanisms of Metasomatism and Metamorphism on the Local Mineral Scale: The Role of Dissolution-Reprecipitation During Mineral Re-equilibration. pp. 141–170. https://doi.org/10.1007/978-3-642-28394-9_5

Remus, M.V.D., Hartmann, L.A., McNaughton, N.J., Groves, D.I., Fletcher, I.R., 2000. The link between hydrothermal epigenetic copper mineralization and the Cacapava Granite of the Brasiliano cycle in southern Brazil. J. South Am. Earth Sci. 13, 191–216. https://doi.org/10.1016/S0895-9811(00)00017-1

Ribeiro, M., Bocchi, P.R., Figueiredo Filho, P.M., Tessari, R.I., 1966. Geologia da quadrícula de Caçapava do Sul, RS, Brasil. Boletim da Divisão de Geologia e Mineralogia, DPM-DNPM, pp. 127-232.

Rock, N.M.S., 1991. Lamprophyres. Springer US, Boston, MA. https://doi.org/10.1007/978-1-4757-0929-2

Roselle, G.T., Baumgartner, L.P., Valley, J.W., 1999. Stable isotope evidence of heterogeneous fluid infiltration at the Ubehebe Peak contact aureole, Death Valley National Park, California. Am. J. Sci. 299, 93–138. https://doi.org/10.2475/ajs.299.2.93

Roselle, G.T., Baumgartner, L.P., Valley, J.W., 1999. Stable isotope evidence of heterogeneous fluid infiltration at the Ubehebe Peak contact aureole, Death Valley National Park, California. Am. J. Sci. 299, 93–138. https://doi.org/10.2475/ajs.299.2.93

Sartori, P.L.P., Kawashita, K., 1985. Petrologia e geocronologia do batólito granítico de Caçapava do Sul - RS. In: Atas do II Simpósio Sul-Brasileiro de Geologia (Florianópolis, Brasil), pp. 102 -115.

Sharp, Z.D., Gibbons, J.A., Maltsev, O., Atudorei, V., Pack, A., Sengupta, S., Shock, E.L., Knauth, L.P., 2016. A calibration of the triple oxygen isotope fractionation in the SiO2–H2O system and applications to natural samples. Geochim. Cosmochim. Acta 186, 105–119. https://doi.org/10.1016/j.gca.2016.04.047

Sheppard, S.M.F., 1986. Characterization and Isotopic Variations in Natural Waters, in: Valley, J.W., Taylor, H.P., O'Neil, J.R. (Eds.), Stable Isotopes in High Temperature Geological Processes. De Gruyter, Berlin, Boston, pp. 165–184. https://doi.org/10.1515/9781501508936-011

Silva-Filho, B.C., Matsdorf, M.C., 1987. Análise estrutural dos metamorfitos da borda oeste do granito Caçapava, Caçapava do Sul: Implicaçoes geológicas locais e regionais, in: Anais, III Simpósio Sul-Brasileiro de Geologia. Curitiba, pp. 197–222.

Siron, G., Baumgartner, L., Bouvier, A.S., 2018. Significance of OH, F and Cl content in biotite during metamorphism of the Western Adamello contact aureole. Contrib. to Mineral. Petrol. 173, 1–19. https://doi.org/10.1007/s00410-018-1491-0

Skelton, A., Lewerentz, A., Kleine, B., Webster, D., Pitcairn, I., 2015. Structural Channelling of Metamorphic Fluids on Islay, Scotland: Implications for Paleoclimatic Reconstruction. J. Petrol. 56, 2145–2172. https://doi.org/10.1093/petrology/egv067

Slaughter, J., Kerrick, D.M., Wall, V.J., 1975. Experimental and thermodynamic study of equilibria in the system CaO-MgO-SiO2-H2O-CO2. Am. J. Sci. 275, 143–162. https://doi.org/10.2475/ajs.275.2.143

Taylor, H.P., 1968. The oxygen isotope geochemistry of igneous rocks. Contrib. to Mineral. Petrol. 19, 1–71. https://doi.org/10.1007/BF00371729

Taylor, H.P., 1974. The Application of Oxygen and Hydrogen Isotope Studies to Problems of Hydrothermal Alteration and Ore Deposition. Econ. Geol. 69, 843–883. https://doi.org/10.2113/gsecongeo.69.6.843

Valley, J.W., Kitchen, N., Kohn, M.J., Niendorf, C.R., Spicuzza, M.J., 1995. UWG-2, a garnet standard for oxygen isotope ratios: Strategies for high precision and accuracy with laser heating. Geochim. Cosmochim. Acta 59, 5223–5231. https://doi.org/10.1016/0016-7037(95)00386-X

Whitney, D.L., Evans, B.W., 2010. Abbreviations for names of rock-forming minerals. Am. Mineral. 95, 185–187. https://doi.org/10.2138/am.2010.3371

Wiedner, E.A., 2004. Kinetic fractionation of stable isotopes during speleothem formation in laboratory experiments. Ruprecht-Karls-Universität Heidelberg. https://doi.org/https://doi.org/10.11588/heidok.00004824

Wostbrock, J.A.G., Cano, E.J., Sharp, Z.D., 2020. An internally consistent triple oxygen isotope calibration of standards for silicates, carbonates and air relative to VSMOW2 and SLAP2. Chem. Geol. 533, 119432. https://doi.org/10.1016/j.chemgeo.2019.119432

Yardley, B., Bottrell, S.H., Cliff, R.A., 1991. Evidence for a regional-scale fluid loss event during mid-crustal metamorphism. Nature 349, 151–154. https://doi.org/10.1038/349151a0

Yardley, B.W.D., Lloyd, G.E., 1995. Why metasomatic fronts are really metasomatic sides. Geology 23, 53–56. https://doi.org/10.1130/0091-7613(1995)023<0053:WMFARM>2.3.CO;2

Zheng, Y.F., 1993. Calculation of oxygen isotope fractionation in anhydrous silicate minerals. Geochim. Cosmochim. Acta 57, 1079-1091.

ANEXOS

ANEXO A: RELAÇÃO DE AMOSTRAS ANALISADAS, COORDENADAS E TÉCNICAS UTILIZADAS.

ANEXO B: COMPROVANTES DE SUBMISSÃO DOS ARTIGOS CIENTÍFICOS

ANEXO C: MATERIAL SUPLEMENTAR DO ARTIGO I

ANEXO D: MATERIAL SUPLEMENTAR DO ARTIGO II

ANEXO E: MATERIAL SUPLEMENTAR DO ARTIGO III

ANEXO A - Relação de amostras analisadas, coordenadas e técnicas utilizadas

Cód. amostra	Litologia	Artigo	Área	UTM E SIRGAS 2000 zona 22S	UTM N SIRGAS 2000 zona 22S	EMPA UFRGS	EMPA GAU-Gött	FRX UFRGS	FRX GEOSOL	Geocron. UFOP	Geocron. CPGeo-USP	Elem. traço sulf. UFOP	µXRF	Isótopos est. UFRGS	Isótopos est. GAU-Gött
APF-01 (AP-01)	dique félsico	I, II	AP	262476	6638705				X		U-Pb - zircão				
APF-02	dique félsico	II	AP	262476	6638705				X						
APM-01	dique máfico	II	AP	262476	6638705				X						
APM-02	dique máfico	II	AP	262476	6638705				X						
APM-03	dique máfico	II	AP	262476	6638705				X						
A-RAZ	apófise metamáfica	II	AT	268396	6617483			X							
AT-G1-01	apófise metamáfica	II	AT	267561	6616660			X							
AT-MD-01	apófise metamáfica	II	AT	268434	6616677				X						
AT-MD-03	apófise metamáfica	II	AT	268414	6616680				X						
AT-MG-01	monzogranito	III	AT	268403	6616559	X									
AT-MZ-01	monzonito	III	AT	268473	6616943	X									
AT-MZ-02	monzonito	III	AT	268451	6616957	X									
AT-PS-01 (AT-01A)	escarnito de veio/prógrado	III, IV	AT	268416	6616687	X	X						X		X
AT-PS-02	escarnito (prógrado)	III	AT	268473	6616943	X									
AT-PS-03	escarnito (prógrado)	III	AT	268447	6616605	X									
AT-Z-01	apófise metamáfica	I, II	AT	268434	6616677	X	X	X		U-Pb - titanita					
AT-Z-02	apófise metamáfica	I, II	AT	268426	6616668	X	X	X		U-Pb - apatita					
AT-Z-03	apófise metamáfica	I, II	AT	268414	6616680	X	X	X		U-Pb - apatita					
MN-03	apófise metamáfica	II	AT	268403	6616559	X		X							
CL-18-02A	apófise metamáfica	II	CL	268639	6620955	X		X							
CL-18-02B	apófise metamáfica	II	CL	268639	6620955			X							
CL-18-04	enclave máfico	II	CL	268694	6621008	X		X							
CL-GR-01	granodiorito	III	CL	268716	6621071	X									
CL-MD-02A	apófise metamáfica	II	CL	268639	6620955	X			X						
CL-MDE-04	enclave máfico	II	CL	268694	6621008	X			X						
CL-PS-01	escarnito (prógrado)	III	CL	268583	6621125	X						X			
CL-PS-02	escarnito (prógrado)	III	CL	268596	6621088	X									
CL-PS-03	escarnito (prógrado)	III	CL	268635	6621032	X									
CL-PS-04	escarnito (prógrado)	III	CL	268635	6621032	X						X			
CL-PS-05	escarnito (prógrado)	III	CL	268635	6621032							X			
CL-RS-01	escarnito (retrógrado)	III	CL	268635	6621032	X						X			
CL-RS-02	escarnito (retrógrado)	III	CL	268635	6621032	X						X		X	
CL-RS-03	escarnito (retrógrado)	III	CL	268635	6621032										
CL-RS-04	escarnito (retrógrado)	III	CL	268635	6621032									X	
CL-RS-05	escarnito (retrógrado)	III	CL	268635	6621032									X	
CL-RS-06	escarnito (retrógrado)	III	CL	268635	6621032									X	
CL-RS-07	escarnito (retrógrado)	III	CL	268635	6621032									X	
CS-1	escarnito de contato	IV	CL	268602	6620932		X						X		X
CS-2	escarnito de contato	IV	CL	268602	6620932		X						X		X
CS-3	escarnito de contato	IV	CL	268602	6620932		X						X		X
DB-G1Z	apófise metamáfica	I	DB	267561	6616660			X		U-Pb - zircão					
DB-G2Z	granodiorito	I, II	DB	267561	6616660	X				U-Pb - zircão					
DB-GR-01	granodiorito	III	DB	267561	6616660	X									
DB-MD-01Z	apófise metamáfica	II	DB	267561	6616660				X						
DB-PG-01	leucogranito	III	DB	267542	6616554	X									

Cód. amostra	Litologia	Artigo	Área	UTM E SIRGAS 2000 zona 22S	UTM N SIRGAS 2000 zona 22S	EMPA UFRGS	EMPA GAU-Gött	FRX UFRGS	FRX GEOSOL	Geocron. UFOP	Geocron. CPGeo-USP	Elem. traço sulf. UFOP	µXRF	Isótopos est. UFRGS	Isótopos est. GAU-Gött
DB-PG-02	grt-leucogranito	III	DB	267570	6616462	X									
DB-PS-01	escarnito (prógrado)	III	DB	267592	6616450	X						X			
DR-GR-MG	apófise metamáfica	II	DB	267592	6616450			X							
FD-SI-01	grt-leucogranito	III	FD	268772	6619667	X									
PI-G1-01	apófise metamáfica	II	PI	268091	6614496	X		X							
PI-G1-02	apófise metamáfica	II	PI	268051	6614489			X							
PI-G1-03	apófise metamáfica	II	PI	268012	6614633	X		X							
PI-MD-01	apófise metamáfica	II	PI	268091	6614496	X			X						
PI-MD-02	apófise metamáfica	II	PI	268051	6614489				X						

Gmail Guilherme Sonntag Hoerlle <gui.ois@gmail.com>

Manuscript submitted - JMG-20-0095

1 mensagem

Vibha Nim <onbehalfof@manuscriptcentral.com> 25 de setembro de 2020 10:24
Responder a: JMGoffice@wiley.com
Para: guilherme.hoerlle@ufrgs.br, gui.ois@gmail.com, marcus.remus@ufrgs.br, norberto.dani@ufrgs.br, cristiano.lana@ufop.edu.br, thomas.mueller@geo.uni-goettingen.de, s.piazolo@leeds.ac.uk

25-Sep-2020

Dear Mr. Guilherme Hoerlle

Thank you for submitting your manuscript on Metasomatic reactions triggered by localized and episodic fluid flux record multistage intrusion history: An example from the syntectonic Caçapava do Sul Granitic Complex, Southern Brazil to the Journal of Metamorphic Geology. Receipt of your paper is acknowledged, and it has been given the reference No: JMG-20-0095.

Please note that the JMG has a Publication Pack that provides details of the manner in which manuscripts should be submitted to the JMG, how they will be processed by the Journal, and what is expected of authors, editors and reviewers. There is also information provided on how the review process has operated over recent years. You are asked to review this information, and follow the guidelines provided. Any comments you have on these matters would be welcomed by the Editor-in-Chief.

Your manuscript will now be assigned to a handling editor by the EIC. Please note that the review process can take anywhere from three weeks to three months, depending on the availability of reviewers and timeliness for returning reviews. The handling editor will contact you as soon as a decision has been made about the paper.

If you notice a problem with the technical aspect of your paper (files did not upload or convert correctly, something is missing etc), please contact me.

Regards,

Ms. Vibha Nim
JMGoffice@wiley.com

Gmail Guilherme Sonntag Hoerlle <gui.ois@gmail.com>

Journal of Metamorphic Geology - JMG-20-0095.R1

1 mensagem

Vibha Nim <onbehalfof@manuscriptcentral.com> 29 de março de 2021 09:36
Responder a: JMGoffice@wiley.com
Para: guilherme.hoerlle@ufrgs.br, gui.ois@gmail.com
Cc: guilherme.hoerlle@ufrgs.br, gui.ois@gmail.com, marcus.remus@ufrgs.br, thomas.mueller@geo.uni-goettingen.de, s.piazolo@leeds.ac.uk, cristiano.lana@ufop.edu.br, dominik.sorger@uni-goettingen.de

29-Mar-2021

Dear Mr. Guilherme Hoerlle,

Thank you for submitting the revised version of your manuscript "Metasomatic reactions triggered by localized and episodic fluid flux record multistage intrusion history: An example from the syntectonic Caçapava do Sul Granitic Complex, Southern Brazil" to the JMG. The handling editor has been informed of the re-submission and will be contacting you with a decision in due course.

This journal offers a number of license options, information about this is available here: https://authorservices.wiley.com/author-resources/Journal-Authors/licensing/index.html. All co-authors are required to confirm that they have the necessary rights to grant in the submission, including in light of each co-author's funder policies. For example, if you or one of your co-authors received funding from a member of Coalition S, you may need to check which licenses you are able to sign.

Should you have questions, please get back to me.

Yours sincerely,

Miss Vibha Nim

Gmail

Guilherme Sonntag Hoerlle <gui.ois@gmail.com>

Confirming handling editor for submission to Precambrian Research

1 mensagem

Precambrian Research <em@editorialmanager.com> 8 de maio de 2021 10:10
Responder a: Precambrian Research <precam-eo@elsevier.com>
Para: Guilherme Sonntag Hoerlle <guilherme.hoerlle@ufrgs.br>

This is an automated message.

Manuscript Number: PRECAM-D-21-00179

Metalamprophyres in the Dom Feliciano Belt: insights for the development of strike-slip tectonics and localized metamorphism during the post-collisional stage

Dear Mr. Sonntag Hoerlle,

The above referenced manuscript will be handled by Editor Professor Wilson Teixeira .

To track the status of your manuscript, please log into Editorial Manager at https://www.editorialmanager.com/precam/.

Thank you for submitting your work to this journal.

Kind regards,

Precambrian Research

More information and support

You will find information relevant for you as an author on Elsevier's Author Hub: https://www.elsevier.com/authors

FAQ: How can I reset a forgotten password?
https://service.elsevier.com/app/answers/detail/a_id/28452/supporthub/publishing/kw/editorial+manager/

For further assistance, please visit our customer service site: https://service.elsevier.com/app/home/supporthub/publishing/. Here you can search for solutions on a range of topics, find answers to frequently asked questions, and learn more about Editorial Manager via interactive tutorials. You can also talk 24/7 to our customer support team by phone and 24/7 by live chat and email.

In compliance with data protection regulations, you may request that we remove your personal registration details at any time. (Use the following URL: https://www.editorialmanager.com/precam/login.asp?a=r). Please contact the publication office if you have any questions.

Gmail Guilherme Sonntag Hoerlle <gui.ois@gmail.com>

Confirming handling editor for submission to Ore Geology Reviews

Ore Geology Reviews <em@editorialmanager.com> 25 de maio de 2021 23:31
Responder a: Ore Geology Reviews <support@elsevier.com>
Para: Guilherme Sonntag Hoerlle <guilherme.hoerlle@ufrgs.br>

This is an automated message.

Manuscript Number: ORGEO-D-21-00409

Post-collisional magmatic-hydrothermal mineralization in the São Gabriel Terrane (southern Brazil): insights from mineral chemistry, stable isotopes, and sulfide trace-elements of the Caçapava do Sul skarns

Dear Mr. Sonntag Hoerlle,

The above referenced manuscript will be handled by Editor-in-Chief Professor Franco Pirajno .

To track the status of your manuscript, please log into Editorial Manager at https://www.editorialmanager.com/orgeo/.

Thank you for submitting your work to this journal.

Kind regards,

Ore Geology Reviews

More information and support

You will find information relevant for you as an author on Elsevier's Author Hub: https://www.elsevier.com/authors

FAQ: How can I reset a forgotten password?
https://service.elsevier.com/app/answers/detail/a_id/28452/supporthub/publishing/kw/editorial+manager/

For further assistance, please visit our customer service site: https://service.elsevier.com/app/home/supporthub/publishing/. Here you can search for solutions on a range of topics, find answers to frequently asked questions, and learn more about Editorial Manager via interactive tutorials. You can also talk 24/7 to our customer support team by phone and 24/7 by live chat and email.

#AU_ORGEO#

ANEXO C - Material suplementar do Artigo I

Supplementary table S1

			Ages						Isotopic ratios						
Sample	U (µg g-1)	Th/U	207Pb/206Pb	2s (%)	207Pb/235U	2s (%)	206Pb/238U	2s (%)	207Pb/206Pb	2s (%)	207Pb/235U	2s (%)	206Pb/238U	2s (%)	Rho
DB-G1Z															
28	9.604587	0.595472	2110.963	41.1879	1840.099	35.28779	1610.271	47.75748	0.130966	2.348168	5.124036	4.082211	0.28376	3.339244	0.817999
40	46.20919	0.136182	2198.752	34.90346	2182.641	36.47713	2165.539	63.80706	0.137722	2.009324	7.581199	3.99414	0.39924	3.451923	0.864247
20	33.72255	0.15754	2177.601	34.8347	2179.739	36.13467	2182.011	63.54578	0.136057	2.000721	7.556713	3.958799	0.40282	3.416022	0.862893
~~18~~	~~168.0817~~	~~0.113015~~	~~2185.439~~	~~35.13799~~	~~2173.526~~	~~35.66698~~	~~2160.93~~	~~61.79827~~	~~0.136671~~	~~2.019878~~	7.504515	3.911632	0.39824	3.349769	0.856361
55	23.00502	0.008131	2192.685	43.58094	2099.465	39.21493	2005.689	61.28849	0.137242	2.507204	6.906286	4.337007	0.36497	3.538863	0.815969
17	263.6767	0.07013	2081.528	35.25526	1623.227	32.88662	1293.647	40.63454	0.12879	2.003286	3.946279	3.994534	0.22223	3.455885	0.865154
38	18.77244	0.170815	1781.349	51.03021	1759.818	37.41919	1741.74	51.92915	0.108915	2.798464	4.65849	4.39483	0.31021	3.388676	0.77106
8	21.45826	0.233833	1745.883	40.40911	1749.968	33.22456	1753.39	49.90485	0.106822	2.206271	4.603862	3.918397	0.31258	3.238241	0.82642
29	21.80668	0.157106	1775.892	37.64088	1749.586	33.99003	1727.653	52.28176	0.10859	2.062809	4.601755	4.0075	0.30735	3.435822	0.857348
37	56.98602	0.114606	1738.805	38.58959	1748.825	33.17846	1757.22	50.95305	0.10641	2.105065	4.597559	3.914006	0.31336	3.299719	0.843054
39	30.90688	0.092775	1765.971	37.34369	1743.102	34.01904	1724.102	52.51745	0.108001	2.044008	4.566097	4.016455	0.30663	3.457447	0.860821
47	19.75941	0.762658	1786.508	39.37859	1741.622	33.56102	1704.486	49.97691	0.109224	2.160873	4.557991	3.964533	0.30266	3.323876	0.838403
53	19.92346	0.276501	1796.988	50.99846	1727.767	38.58659	1671.194	53.19236	0.109854	2.802121	4.482663	4.560748	0.29595	3.598408	0.788995
27	16.26047	0.444231	1797.83	40.20534	1726.325	34.0546	1667.96	49.81847	0.109905	2.209319	4.474886	4.035306	0.2953	3.376775	0.836808
52	17.72757	0.313104	1807.257	50.39774	1719.2	38.29215	1647.823	52.39792	0.110476	2.772609	4.436602	4.535171	0.29126	3.588929	0.791355
19	39.38868	0.184807	1792.785	37.03178	1712.557	33.92643	1647.723	50.83281	0.109601	2.033666	4.401147	4.032674	0.29124	3.482336	0.86353
51	17.11464	0.191342	1802.296	41.25387	1703.227	34.87762	1623.865	50.1251	0.110175	2.268181	4.351748	4.152517	0.28647	3.478326	0.837643
14	2.436663	0.311754	1812.238	62.99676	1691.166	41.31395	1595.239	49.44711	0.110779	3.467854	4.288553	4.916856	0.28077	3.485608	0.70891
54	11.62677	0.264078	1755.8	42.97499	1481.111	33.99685	1296.969	42.31654	0.107402	2.349265	3.300246	4.290476	0.22286	3.590145	0.836771
30	10.78747	0.214586	1759.846	49.25943	1459.336	36.06473	1261.871	42.54302	0.10764	2.694166	3.209008	4.576904	0.21622	3.699935	0.808393
31	16.74937	0.247597	1736.788	53.62869	1350.582	35.93825	1120.237	38.30941	0.106293	2.924711	2.7815	4.727691	0.18979	3.714449	0.785679
56	11.40724	0.128427	1669.157	41.15342	1287.636	30.62618	1071.344	34.48606	0.10246	2.225259	2.554195	4.134442	0.1808	3.484513	0.842801
10	33.50115	0.133627	1661.681	56.39334	1261.158	35.09073	1039.766	35.41988	0.102047	3.046406	2.462711	4.7762	0.17503	3.678517	0.770177
35	53.4845	0.016423	1717.266	52.48522	1212.942	33.21494	949.8821	32.1154	0.105169	2.855347	2.302125	4.616196	0.15876	3.627155	0.785746
33	112.407	0.168972	1687.922	39.61427	1212.898	29.85886	963.9972	31.94719	0.103506	2.147153	2.301981	4.156677	0.1613	3.559171	0.856254
11	272.0151	0.061083	1602.754	53.36501	1037.908	30.22338	790.8883	26.68373	0.098861	2.861001	1.779257	4.580952	0.13053	3.577681	0.780991
9	77.14176	0.151978	1606.931	47.67618	1032.413	27.29908	782.9575	24.2015	0.099083	2.557399	1.764257	4.156326	0.12914	3.276394	0.788291
12	171.219	0.0822	1618.971	53.05607	998.5808	30.22468	740.4559	26.06241	0.099726	2.850425	1.673671	4.685133	0.12172	3.718272	0.793632
13	73.45481	0.051582	1605.886	41.55647	887.8693	25.10308	628.1661	21.26659	0.099028	2.228828	1.39748	4.189374	0.10235	3.547278	0.846732
36	2.16925	0.134129	1608.376	146.6154	876.8462	53.55141	616.2839	24.30065	0.09916	7.866075	1.371593	8.882881	0.10032	4.126794	0.464578
~~48~~	~~51.1368~~	~~0.103579~~	~~1636.421~~	~~41.77533~~	~~786.4827~~	~~23.06037~~	~~521.5597~~	~~17.58813~~	~~0.100666~~	~~2.24943~~	1.169653	4.165309	0.08427	3.50569	0.84164

Supplementary table S2

	SPOT	RATIOS															AGES				conc.
		207/235	1sigma	206/238	1 sigma	coef. corr	238/206	1 sigma	207/206	1 sigma	208/206	1 sigma	Pb total comum %	Pb rad ppm	Th ppm	U ppm	Th/U	T206/238	1 sigma	T207/206	1 sigma	206/238 207/206 %
AP-01																					
SPL 1008,5mJ,6Hz, 32um																					
AP-01	7.1	0.7504	0.0157	0.0917	0.0013	0.98	10.9104	0.1522	0.0594	0.0012	0.1482	0.0068	0.65	136.5	689.2	1383.5	0.498	0.565	0.008	0.581	0.043	97
AP-01	4.1	0.7617	0.0182	0.0942	0.0014	0.79	10.6141	0.1527	0.0586	0.0013	0.1669	0.0059	1.44	65.7	359.6	646.1	0.557	0.580	0.008	0.554	0.049	104
AP-01	22.1	0.7745	0.0155	0.0943	0.0008	0.30	10.6083	0.0940	0.0596	0.0012	0.2229	0.0243	0.30	110.5	876.1	997.5	0.878	0.581	0.005	0.589	0.043	98
AP-01	3.1	0.7708	0.0396	0.0954	0.0020	0.67	10.4854	0.2160	0.0586	0.0031	0.3540	0.0189	0.71	17.5	164.6	145.4	1.132	0.587	0.012	0.553	0.122	106
AP-01	21.1	1.0898	0.0211	0.1232	0.0011	0.70	8.1192	0.0724	0.0642	0.0012	0.1242	0.0084	0.34	96.6	366.0	707.4	0.517	0.749	0.006	0.747	0.040	100
AP-01	11.1	1.0947	0.0237	0.1245	0.0018	0.50	8.0294	0.1148	0.0638	0.0013	0.1167	0.0092	0.28	68.2	225.2	536.5	0.4200	0.757	0.010	0.733	0.044	103
AP-01	15.1	1.1183	0.0198	0.1246	0.0011	0.85	8.0248	0.0682	0.0651	0.0011	0.1606	0.0093	3.92	58.3	241.7	432.4	0.559	0.757	0.006	0.777	0.036	97
AP-01	18.1	1.1057	0.0242	0.1246	0.0012	0.98	8.0284	0.0759	0.0644	0.0015	0.1160	0.0092	0.06	79.9	262.7	589.3	0.446	0.757	0.007	0.754	0.048	100
AP-01	20.1	1.1052	0.0226	0.1248	0.0011	0.98	8.0159	0.0731	0.0643	0.0013	0.1407	0.0162	0.37	105.0	429.7	745.9	0.5760	0.758	0.007	0.750	0.043	101
AP-01	25.1	1.1127	0.0204	0.1250	0.0011	0.85	8.0009	0.0696	0.0646	0.0012	0.1179	0.0077	0.35	84.8	252.2	643.2	0.392	0.759	0.006	0.760	0.038	99
AP-01	12.1	1.1097	0.0258	0.1256	0.0018	0.26	7.9638	0.1168	0.0641	0.0014	0.0995	0.0051	0.27	66.6	169.6	523.3	0.324	0.763	0.011	0.745	0.045	102
AP-01	19.1	1.1243	0.0211	0.1257	0.0011	0.93	7.9578	0.0699	0.0649	0.0012	0.1275	0.0054	0.18	85.6	287.8	635.0	0.453	0.763	0.006	0.771	0.040	99
AP-01	8.1	1.1076	0.0251	0.1258	0.0018	0.01	7.9484	0.1160	0.0639	0.0013	0.1487	0.0093	0.33	69.5	252.1	517.6	0.487	0.764	0.011	0.737	0.045	103
AP-01	6.1	1.1116	0.0251	0.1265	0.0018	0.58	7.9060	0.1154	0.0637	0.0014	0.0989	0.0044	0.42	71.9	180.0	548.3	0.328	0.768	0.011	0.733	0.045	104
AP-01	2.1	1.1307	0.0273	0.1274	0.0019	0.78	7.8468	0.1179	0.0643	0.0015	0.1062	0.0078	0.73	55.7	170.1	415.0	0.410	0.773	0.011	0.753	0.049	102
AP-01	9.1	1.1213	0.0350	0.1285	0.0023	0.91	7.7797	0.1376	0.0633	0.0018	0.1026	0.0137	2.21	66.3	244.5	528.4	0.463	0.780	0.013	0.717	0.063	108
AP-01	14.1	1.1520	0.0220	0.1288	0.0011	0.97	7.7629	0.0686	0.0649	0.0012	0.1126	0.0067	0.00	68.7	178.9	503.9	0.355	0.781	0.007	0.770	0.040	101
AP-01	23.1	0.7249	0.0153	0.0868	0.0008	0.97	11.5242	0.1058	0.0606	0.0013	0.1438	0.0079	5.52	71.3	496.3	806.9	0.615	0.536	0.005	0.625	0.044	85
AP-01	24.1	0.7175	0.0181	0.0895	0.0009	0.38	11.1714	0.1113	0.0581	0.0015	0.1909	0.0145	0.76	41.1	208.1	415.2	0.501	0.553	0.005	0.535	0.055	103
AP-01	2.2	1.2384	0.0651	0.1345	0.0029	0.48	7.4325	0.1628	0.0668	0.0038	0.0958	0.0232	2.56	15.3	42.4	116.1	0.365	0.814	0.017	0.830	0.114	98
AP-01	13.1	1.2767	0.0328	0.1415	0.0015	0.61	7.0695	0.0740	0.0655	0.0017	0.1289	0.0153	0.28	54.0	192.6	361.3	0.533	0.853	0.008	0.789	0.055	108
AP-01	17.1	1.3640	0.0291	0.1563	0.0014	0.89	6.3977	0.0569	0.0633	0.0015	0.2764	0.0916	1.87	84.0	636.3	593.5	1.072	0.936	0.008	0.718	0.047	130
AP-01	16.1	12.5910	0.1875	0.4960	0.0043	0.99	2.0162	0.0174	0.1841	0.0026	0.1158	0.0070	0.55	106.1	78.3	183.4	0.427	2.596	0.019	2.690	0.024	96
AP-01	5.1	8.9756	0.1387	0.4252	0.0056	1.00	2.3516	0.0312	0.1531	0.0021	0.1460	0.0137	0.29	150.4	207.6	293.2	0.708	2.284	0.026	2.381	0.024	95
AP-01	1.1	14.4496	0.2358	0.4826	0.0067	0.75	2.0720	0.0287	0.2171	0.0029	0.0560	0.0035	0.57	221.4	97.3	400.8	0.243	2.539	0.029	2.960	0.020	85
AP-01	10.1	0.6808	0.0162	0.0825	0.0012	0.94	12.1190	0.1782	0.0598	0.0014	0.1127	0.0086	9.37	104.3	798.9	1248.6	0.640	0.511	0.007	0.598	0.050	85

Supplementary table S3

			Ages						Isotopic ratios						
Sample	U (µg g-1)	Th/U	207Pb/206Pb	2s (%)	207Pb/235U	2s (%)	206Pb/238U	2s (%)	207Pb/206Pb	2s (%)	207Pb/235U	2s (%)	206Pb/238U	2s (%)	Rho
DB-G2Z															
7	131.4337	1.607555	529.565	46.85694	555.8866	16.1739	562.3348	16.42585	0.057995	2.146605	0.728865	3.726708	0.09115	3.046382	0.817446
8	137.6489	0.641762	525.2698	87.14324	567.5893	23.71656	578.2075	19.83258	0.057881	3.9893	0.748906	5.360541	0.09384	3.580626	0.66796
9	95.7463	1.134971	507.7008	46.84063	569.3629	15.78653	584.9225	16.03323	0.05742	2.137931	0.751963	3.573776	0.09498	2.863761	0.801326
10	118.0956	1.356746	570.5188	85.46598	569.6876	24.0684	569.4794	20.33823	0.059093	3.942403	0.752524	5.424238	0.09236	3.725563	0.686836
11	120.9705	1.334825	536.4984	47.49509	570.0537	16.32556	578.5022	16.51089	0.058179	2.178386	0.753156	3.6915	0.09389	2.980236	0.807324
12	202.9947	0.651807	563.7669	85.44629	572.8504	23.71501	575.1422	19.7471	0.05891	3.937041	0.757991	5.323617	0.09332	3.583379	0.67311
13	222.4413	1.751104	565.5163	86.90612	572.9674	23.90195	574.8474	19.65334	0.058957	4.005479	0.758194	5.364277	0.09327	3.568138	0.665167
14	121.9694	1.777276	581.155	85.28021	573.8573	23.98026	572.0165	20.04236	0.059383	3.940833	0.759735	5.375461	0.09279	3.655874	0.680104
15	180.1373	1.158686	568.8512	85.17445	574.8594	23.82697	576.3803	19.93337	0.059048	3.927859	0.761473	5.334604	0.09353	3.609699	0.676657
16	118.7677	1.550472	552.7551	46.31947	575.9148	16.10742	581.8015	16.26898	0.058613	2.130286	0.763305	3.61506	0.09445	2.920709	0.807928
17	233.1599	1.376597	568.0203	43.71073	576.3328	15.97054	578.4432	16.40804	0.059025	2.01546	0.764031	3.582656	0.09388	2.961983	0.826756
18	78.06447	1.25835	560.4999	89.64534	576.4042	24.88713	580.4466	20.69017	0.058822	4.128256	0.764155	5.55802	0.09422	3.721436	0.669562
19	174.8605	1.156032	559.5376	47.70178	576.5367	16.20678	580.859	16.10346	0.058796	2.19636	0.764385	3.63428	0.09429	2.895513	0.796723
20	89.45419	1.401503	562.2565	48.87146	577.6457	16.43851	581.5659	16.21309	0.058869	2.251242	0.766313	3.680591	0.09441	2.911814	0.791127
27	62.77475	1.122177	567.3998	50.85398	580.4607	17.39158	583.8038	17.2657	0.059008	2.344585	0.771217	3.878212	0.09479	3.089248	0.796565
28	118.4175	1.205389	586.9039	46.41488	581.7157	16.242	580.3877	16.18457	0.05954	2.146908	0.773407	3.618137	0.09421	2.912336	0.804927
29	172.9132	0.870972	566.7111	85.28878	582.1379	24.02937	586.0998	20.1898	0.05899	3.931722	0.774145	5.329615	0.09518	3.598104	0.675115
30	157.4446	2.00796	679.7108	82.77959	583.6502	24.10463	559.262	19.60634	0.062163	3.88802	0.776789	5.335896	0.09063	3.654462	0.684882
31	397.5986	0.907012	566.2536	84.93624	584.7872	23.77929	589.5717	19.7976	0.058977	3.91517	0.77878	5.257177	0.09577	3.508468	0.667367
32	627.6422	0.490843	546.6556	44.23905	586.6053	16.24869	596.98	16.94583	0.05845	2.03252	0.781968	3.597371	0.09703	2.968154	0.82509
33	164.1493	0.709277	559.914	44.87777	587.4262	15.87506	594.5703	16.14674	0.058806	2.066463	0.783409	3.511683	0.09662	2.839305	0.808531
34	83.57822	0.881031	689.1893	47.18771	598.9409	17.11978	575.3781	16.52988	0.062439	2.219756	0.803748	3.731243	0.09336	2.999143	0.803792
35	101.7774	1.636032	630.7481	50.63495	615.4518	18.25239	611.3021	18.12262	0.06076	2.359202	0.833319	3.898016	0.09947	3.103014	0.796049
36	160.9833	1.278439	910.3768	41.86635	642.2882	17.24116	568.7122	15.98564	0.069391	2.039795	0.882419	3.572588	0.09223	2.933023	0.82098
37	1793.712	0.540887	3079.48	77.6637	953.6334	145.1783	304.0146	63.37753	0.233981	4.870191	1.557898	21.78899	0.04829	21.23774	0.9747
38	94.40696	1.084627	1194.99	39.9643	1218.252	25.16424	1231.428	31.9252	0.079919	2.031589	2.319439	3.492649	0.21049	2.840993	0.813421
39	102.8626	1.245449	1742.989	37.03874	1737.572	30.32424	1733.075	45.09265	0.106653	2.026162	4.535863	3.584522	0.30845	2.956936	0.824918
40	72.97645	1.83195	2020.77	35.52487	2033.06	31.05889	2045.191	49.95379	0.124435	2.008751	6.405767	3.478106	0.37336	2.839391	0.816361

Supplementary table S4

Identifier	207Pb CPS	206Pb CPS	U (µg g-1) a	Th/U	Ratios b 207Pb/206Pb	2s%	207Pb/235U	2s%	206Pb/238U	2s%	RHO	Ages b 207Pb/206Pb	2s%	207Pb/235U	2s%	206Pb/238U	2s%
							Data for Tera Was plot c										
AT-Z-01 TITANITES		**Single Stage S/K = Pb composition 0.869**															
11	158,746	11,477	104	0.61	0.0728	4.2	0.9074	4.2	0.0933	1.8	0.42	1,008	86	656	21	575	10
12	85,777	7,555	57	0.41	0.0885	4.3	1.0964	4.3	0.0927	1.8	0.42	1,394	82	752	23	572	10
13	122,661	9,415	82	0.97	0.0771	4.2	0.9447	4.2	0.0917	1.8	0.43	1,125	84	675	21	565	10
14	45,575	4,776	30	2.63	0.1063	4.4	1.3402	4.4	0.0943	1.8	0.41	1,737	81	863	26	581	10
15	82,507	7,535	54	1.02	0.0916	4.3	1.1398	4.3	0.0932	1.8	0.43	1,458	81	772	23	574	10
16	59,493	5,963	38	3.2	0.1012	4.3	1.2833	4.3	0.0949	1.8	0.42	1,646	80	838	25	584	10
17	107,579	8,212	71	0.84	0.0766	4.3	0.9457	4.3	0.0924	1.8	0.43	1,111	85	676	21	570	10
18	112,757	8,214	75	0.79	0.0727	4.5	0.8908	4.5	0.0917	1.8	0.41	1,005	90	647	22	566	10
19	38,778	4,315	25	0.62	0.1122	4.5	1.4183	4.5	0.0946	1.8	0.4	1,836	82	897	27	583	10
20	82,845	6,426	55	1.27	0.0783	4.4	0.9607	4.4	0.0918	1.8	0.41	1,155	88	684	22	566	10
31	43,216	4,639	28	1.31	0.1085	4.5	1.3788	4.5	0.0951	3.6	0.8	1,775	83	880	27	586	20
32	160,277	12,164	108	0.98	0.0762	4.3	0.9288	4.3	0.0912	3.7	0.86	1,100	86	667	21	563	20
33	51,963	4,420	34	1.2	0.0864	4.5	1.0767	4.5	0.0933	3.6	0.8	1,347	87	742	24	575	20
34	81,799	7,186	54	1.4	0.0877	4.6	1.0903	4.6	0.093	3.8	0.83	1,376	88	749	24	574	21
35	64,339	5,279	43	0.93	0.0822	4.8	1.0064	4.8	0.0916	3.7	0.78	1,251	93	707	25	565	20
36	134,615	11,254	89	1.71	0.084	4.2	1.0353	4.2	0.0923	3.6	0.86	1,292	82	722	22	569	20
37	70,491	6,691	46	3.97	0.0963	4.4	1.2145	4.4	0.0944	3.6	0.83	1,554	82	807	25	581	20
38	52,309	5,273	35	5.54	0.1014	4.5	1.258	4.5	0.0929	3.7	0.82	1,650	84	827	26	573	20
39	54,146	4,446	36	1.2	0.0818	4.7	1.0006	4.7	0.0915	3.6	0.77	1,241	92	704	24	565	20
40	37,049	3,909	26	0.87	0.1045	4.6	1.2335	4.6	0.0884	3.6	0.79	1,705	85	816	26	546	19

Supplementary table S5

Identifier	207Pb	206Pb	U (µg g-1) a	Th/U	Ratios b					Ages b					
	CPS	CPS			207Pb/206Pb	2s%	207Pb/235U	2s%	206Pb/238U	2s%	RHO	207Pb/206Pb	2s%	207Pb/235U	2s%	206Pb/238U	2s%
					Data for Tera Was plot c												
AT-Z-02 APATITE SAMPLE	**Single Stage S/K = Pb composition 0.873**																
11	237,204	54,656	19	0.7	0.238	4	4.247	4	0.117	1.8	0.5	3,106	64	1683	34	710	12
12	255,880	48,198	21	0.6	0.193	4.1	3.271	4.1	0.111	1.8	0.4	2,768	67	1474	32	677	11
13	276,761	53,073	23	0.8	0.196	4.1	3.317	4.1	0.11	1.8	0.4	2,794	66	1485	32	675	11
14	293,752	51,347	25	0.8	0.179	4.1	2.919	4.1	0.107	1.8	0.4	2,639	68	1387	31	654	11
15	162,355	29,199	14	1.2	0.184	4.4	3.056	4.4	0.108	1.7	0.4	2,690	72	1422	34	663	11
16	134,269	29,929	11	1.2	0.229	4.5	4.039	4.5	0.115	1.8	0.4	3,044	71	1642	37	703	12
17	82,552	21,227	6	1.1	0.267	4.4	4.951	4.4	0.121	1.8	0.4	3,287	69	1811	38	737	13
18	92,633	16,132	8	0.8	0.179	4.5	2.929	4.5	0.107	1.8	0.4	2,641	74	1389	34	655	11
19	116,244	26,519	9	1	0.235	4.3	4.245	4.3	0.118	1.8	0.4	3,087	68	1683	36	718	12
20	175,058	45,114	13	0.9	0.258	4.1	4.886	4.1	0.124	1.8	0.4	3,233	65	1800	35	752	13
31	138,226	41,277	9	0.7	0.312	4.3	6.582	4.3	0.138	3.8	0.9	3,531	66	2057	38	832	29
32	239,519	53,284	18	1.7	0.23	4.1	4.2	4.1	0.119	3.6	0.9	3,050	66	1674	34	727	25
33	93,127	20,842	8	0.8	0.23	4.4	4.024	4.4	0.114	3.6	0.8	3,055	71	1639	37	696	24
34	134,479	40,141	9	1.2	0.312	4.3	6.504	4.3	0.136	3.9	0.9	3,533	67	2046	39	821	30
35	148,106	28,602	12	0.7	0.198	4.2	3.372	4.2	0.111	3.6	0.9	2,807	69	1498	34	681	24
36	162,838	47,020	11	0.9	0.301	5.1	6.357	5.1	0.138	3.8	0.7	3,475	79	2026	46	833	30
37	43,276	11,022	3	1.6	0.266	5.9	4.941	5.9	0.121	3.6	0.6	3,283	93	1809	51	737	25
38	129,899	27,935	10	0.7	0.222	4.3	3.958	4.3	0.116	3.6	0.8	2,998	69	1626	35	708	24
39	76,017	21,292	5	1	0.291	4.5	5.796	4.5	0.13	3.6	0.8	3,422	70	1946	40	788	27
40	102,672	23,485	8	0.8	0.237	4.4	4.294	4.4	0.118	3.6	0.8	3,100	70	1692	37	721	24

Supplementary table S6

Identifier	207Pb	206Pb	U (µg g-1) a	Th/U	Ratios b					Ages b					
	CPS	CPS			207Pb/206Pb	2s%	207Pb/235U	2s%	206Pb/238U	2s%	RHO	207Pb/206Pb	2s%	207Pb/235U	2s%	206Pb/238U	2s%
							Data for Tera Was plot c										
AT-Z-03 APATITE SAMPLE		**Single Stage S/K = Pb composition 0.873**															
51	196,150	44,233	15	0.9	0.232	4.3	4.148	4.3	0.1166	3.5	0.8	3,067	69	1664	36	711	24
52	263,364	46,620	23	1.7	0.181	4.2	2.973	4.2	0.1073	3.5	0.8	2,661	70	1401	33	657	22
53	167,456	38,157	13	0.6	0.235	4.3	4.269	4.3	0.1186	3.5	0.8	3,086	69	1687	36	722	24
54	119,122	22,556	10	0.7	0.194	4.8	3.273	4.8	0.1101	3.5	0.7	2,776	78	1475	38	674	23
55	127,698	32,100	9	0.3	0.26	4.2	4.97	4.2	0.1245	3.7	0.9	3,250	66	1814	36	757	26
56	111,459	23,893	9	0.3	0.22	4.4	3.827	4.4	0.1134	3.5	0.8	2,983	71	1598	36	692	23
58	176,175	40,283	14	1.1	0.236	4.3	4.245	4.3	0.1174	3.6	0.8	3,093	68	1683	36	716	24
60	75,061	14,799	6	0.7	0.202	5.1	3.393	5.1	0.1096	3.5	0.7	2,843	84	1503	41	671	22
71	75,213	16,546	6	0.5	0.224	5.8	4.038	5.8	0.1174	3.5	0.6	3,013	94	1642	49	716	24
72	136,542	30,374	11	0.6	0.229	4.6	4.031	4.6	0.1151	3.5	0.8	3,042	74	1640	38	702	23
73	69,028	16,242	5	0.8	0.244	6.3	4.586	6.3	0.1229	3.5	0.6	3,144	100	1747	54	747	25
74	111,034	17,912	10	0.7	0.163	4.9	2.584	4.9	0.1032	3.5	0.7	2,492	83	1296	37	633	21
75	127,996	32,275	10	0.8	0.262	4.4	4.915	4.4	0.1227	3.8	0.9	3,256	69	1805	38	746	27
76	76,216	18,716	6	0.6	0.256	4.8	4.715	4.8	0.1204	3.6	0.7	3,220	76	1770	41	733	25
77	159,221	28,657	14	0.5	0.18	4.5	2.939	4.5	0.1066	3.5	0.8	2,653	75	1392	35	653	22
78	60,011	15,208	4	0.6	0.263	5.3	4.975	5.3	0.1236	3.7	0.7	3,264	83	1815	46	751	27
79	147,209	34,372	12	0.4	0.24	5.4	4.284	5.4	0.1166	3.8	0.7	3,120	85	1690	45	711	26
80	89,560	19,348	7	0.6	0.226	4.9	3.926	4.9	0.1136	3.5	0.7	3,022	79	1619	41	693	23

ANEXO D - Material suplementar do artigo II
Supplementary Table S1 (XRF analyses)

		Sample	Area	Group	SiO_2	TiO_2	Al_2O_3	Fe_2O_{3tot}	MnO	MgO	CaO	Na_2O	K_2O	P_2O5	Cr_2O3	LOI	TOTAL
GEOSOL	ICP-OES/MS	APF-01	AP	APF felsic dyke	60.05	0.38	16.72	5.09	0.08	1.59	5.51	3.12	1.52	0.21	<0.01	1.79	96.06
		APF-02	AP	APF felsic dyke	56.03	0.76	16.53	7.13	0.11	3.23	5.03	3.84	0.89	0.16	0.02	2.02	95.73
		APM-01	AP	APM mafic dyke	47.11	0.74	14.69	10.12	0.19	7.32	9.03	1.70	1.57	0.16	0.04	2.48	95.11
		APM-02	AP	APM mafic dyke	43.66	1.68	12.61	11.71	0.20	13.22	7.99	1.26	1.25	0.25	0.14	3.36	97.19
		APM-03	AP	APM mafic dyke	43.42	1.33	12.53	11.28	0.20	12.19	7.83	1.27	1.10	0.22	0.16	3.49	94.86
		CL-MDE-04	MD	MD mafic enclave	51.87	0.77	13.05	9.38	0.15	7.43	8.46	3.48	0.80	0.08	0.06	0.98	96.45
		DB-MD-01Z	MD	MD mafic apophysis	61.39	0.48	14.57	5.38	0.03	1.58	0.39	0.64	8.55	0.35	0.01	3.27	96.63
		PI-MD-02	MD	MD mafic apophysis	56.35	0.71	11.86	4.42	0.04	14.30	4.58	1.98	5.60	0.66	0.10	1.91	102.41
		PI-MD-01	MD	MD mafic apophysis	53.14	0.70	11.53	5.03	0.06	13.58	4.15	2.50	4.59	0.62	0.10	2.06	97.96
		AT-MD-01	MD	MD mafic apophysis	52.64	1.09	12.19	8.66	0.08	11.93	5.32	2.72	2.98	0.30	0.09	2.26	100.17
		CL-MD-02A	MD	MD mafic apophysis	50.84	0.96	11.96	5.45	0.04	16.82	4.09	1.40	5.21	0.33	0.16	2.27	99.37
		AT-MD-03	MD	MD mafic apophysis	48.25	0.64	9.89	7.77	0.09	18.07	5.21	1.00	3.55	0.24	0.19	2.59	97.30
FRX-UFRGS	XRF	CL-18-04	MD	MD mafic enclave	50.27	0.88	14.61	9.80	0.15	9.70	9.32	3.15	0.72	0.09		1.31	100.00
		DB-G1ZB	MD	MD mafic apophysis	61.04	0.67	15.73	6.72	0.03	1.98	0.49	0.00	9.13	0.43		3.72	99.94
		DR-GR-MG	MD	MD mafic apophysis	61.01	0.60	16.08	5.45	0.10	2.33	1.09	0.54	10.23	0.30		0.27	98.00
		DB-G1ZA	MD	MD mafic apophysis	60.48	0.67	15.86	7.05	0.03	2.06	0.48	0.00	9.08	0.44		3.84	99.99
		A-RAZ	MD	MD mafic apophysis	53.60	0.83	14.30	9.60	0.16	7.40	8.10	2.60	1.10	0.11		1.01	98.81
		PI-G1-02	MD	MD mafic apophysis	52.24	0.74	14.28	4.65	0.04	14.19	4.93	1.24	4.64	0.64		2.41	100.00
		PI-G1-01	MD	MD mafic apophysis	51.48	0.70	14.29	4.72	0.05	14.56	6.19	1.96	2.83	0.83		2.39	100.00
		AT-Z-01	MD	MD mafic apophysis	50.82	0.97	14.96	6.82	0.07	12.49	5.06	2.14	2.73	0.27		3.63	99.96
		CL-18-02B	MD	MD mafic apophysis	47.95	0.85	14.28	8.49	0.08	15.12	6.25	1.48	1.41	0.50		3.52	99.93
		AT-Z-03	MD	MD mafic apophysis	47.36	0.62	13.18	7.27	0.08	19.41	5.43	0.13	3.14	0.23		3.20	100.05
		AT-G1-01	MD	MD mafic apophysis	47.07	1.02	13.76	7.78	0.09	15.72	6.78	1.11	1.59	0.57		4.52	100.01
		CL-18-02A	MD	MD mafic apophysis	45.17	0.98	15.57	7.13	0.05	19.04	4.36	0.47	4.80	0.31		2.14	100.02
		AT-Z-02	MD	MD mafic apophysis	44.25	0.69	13.29	8.23	0.09	20.79	5.33	0.00	3.77	0.24		3.23	99.91
		MN-03	MD	MD mafic apophysis	43.64	1.01	17.13	5.32	0.04	18.40	6.10	0.58	4.63	0.61		2.56	100.02
		PI-G1-03	MD	MD mafic apophysis	37.01	1.40	17.07	9.12	0.06	20.61	8.25	0.43	2.56	0.41		3.07	99.99

* All values in wt%

	Sample	Area	Group	Cr	Ni	Ba	Sr	Zr	Rb	Zn	V	Ce	Co	Cs	Cu	Dy	Er	Eu	Ga	Gd	Hf	Ho
GEOSOL / ICP-OES/MS	APF-01	AP	APF felsic dyke	<68.4	9	446	385	57	31	72	119	53.6	36.1	8.6	29	3.1	1.4	1.4	18.4	4.6	3.9	0.5
	APF-02	AP	APF felsic dyke	136.8	43	367	468	114	19	53	83	17.5	49.8	13.2	44	2.3	1.1	0.9	12.7	3.0	2.4	0.4
	APM-01	AP	APM mafic dyke	273.7	77	412	384	41	31	95	81	48.5	42.5	23.0	50	2.5	1.0	1.0	18.2	4.0	4.7	0.4
	APM-02	AP	APM mafic dyke	957.9	393	217	171	146	23	68	227	28.9	41.7	0.1	44	3.4	2.0	0.9	18.0	3.6	2.6	0.7
	APM-03	AP	APM mafic dyke	1094.7	354	221	214	121	20	76	198	101.1	30.1	2.5	160	4.8	2.4	1.9	21.2	6.3	2.5	0.9
	CL-MDE-04	MD	MD mafic enclave	410.5	90	269	276	113	13	81	254	11.2	38.6	1.0	55	2.4	1.4	0.7	15.5	2.3	1.0	0.5
	DB-MD-01Z	MD	MD mafic apophysis	68.4	82	605	39	99	128	76	198	101.1	30.1	2.5	160	4.8	2.4	1.9	21.2	6.3	2.5	0.9
	PI-MD-02	MD	MD mafic apophysis	684.2	534	3162	503	473	153	55	48	174.2	32.6	12.0	28	4.4	1.4	3.0	19.1	9.8	10.5	0.6
	PI-MD-01	MD	MD mafic apophysis	684.2	496	1954	443	456	115	40	54	19.3	20.8	0.8	42	1.3	0.6	0.6	17.6	1.7	1.9	0.2
	AT-MD-01	MD	MD mafic apophysis	615.8	118	848	259	181	98	93	180	28.7	19.2	0.6	89	3.8	2.2	1.0	17.7	3.6	3.1	0.7
	CL-MD-02A	MD	MD mafic apophysis	1094.7	593	1318	161	206	257	145	229	28.8	58.6	0.7	51	3.5	1.7	1.2	17.2	4.0	2.5	0.6
	AT-MD-03	MD	MD mafic apophysis	1300.0	517	752	229	119	113	153	215	35.7	63.3	0.7	91	3.4	1.6	1.2	18.9	4.1	3.1	0.6
FRX-UFRGS / XRF	CL-18-04	MD	MD mafic enclave	421	82	127	290	111	13	72	n/a	n/a	n/a	n/a	n/a	n/a	n/a	n/a	n/a	n/a	n/a	n/a
	DB-G1ZB	MD	MD mafic apophysis	58	55	547	31	87	124	76	n/a	n/a	n/a	n/a	n/a	n/a	n/a	n/a	n/a	n/a	n/a	n/a
	DR-GR-MG	MD	MD mafic apophysis	69	24	934	89	100	147	48	n/a	n/a	n/a	n/a	n/a	n/a	n/a	n/a	n/a	n/a	n/a	n/a
	DB-G1ZA	MD	MD mafic apophysis	68	61	556	30	91	124	80	n/a	n/a	n/a	n/a	n/a	n/a	n/a	n/a	n/a	n/a	n/a	n/a
	A-RAZ	MD	MD mafic apophysis	413	n/a	n/a	n/a	n/a	n/a	n/a	n/a	n/a	n/a	n/a	n/a	n/a	n/a	n/a	n/a	n/a	n/a	n/a
	PI-G1-02	MD	MD mafic apophysis	373	360	2392	385	373	124	47	n/a	n/a	n/a	n/a	n/a	n/a	n/a	n/a	n/a	n/a	n/a	n/a
	PI-G1-01	MD	MD mafic apophysis	446	388	1320	444	379	78	65	n/a	n/a	n/a	n/a	n/a	n/a	n/a	n/a	n/a	n/a	n/a	n/a
	AT-Z-01	MD	MD mafic apophysis	495	114	908	265	142	96	62	n/a	n/a	n/a	n/a	n/a	n/a	n/a	n/a	n/a	n/a	n/a	n/a
	CL-18-02B	MD	MD mafic apophysis	1526	335	987	239	105	59	8	n/a	n/a	n/a	n/a	n/a	n/a	n/a	n/a	n/a	n/a	n/a	n/a
	AT-Z-03	MD	MD mafic apophysis	1226	578	739	173	88	116	59	n/a	n/a	n/a	n/a	n/a	n/a	n/a	n/a	n/a	n/a	n/a	n/a
	AT-G1-01	MD	MD mafic apophysis	1089	436	569	333	129	52	82	n/a	n/a	n/a	n/a	n/a	n/a	n/a	n/a	n/a	n/a	n/a	n/a
	CL-18-02A	MD	MD mafic apophysis	1040	584	746	122	173	311	0	n/a	n/a	n/a	n/a	n/a	n/a	n/a	n/a	n/a	n/a	n/a	n/a
	AT-Z-02	MD	MD mafic apophysis	1538	659	637	18	69	171	74	n/a	n/a	n/a	n/a	n/a	n/a	n/a	n/a	n/a	n/a	n/a	n/a
	MN-03	MD	MD mafic apophysis	698	744	1200	220	193	295	82	n/a	n/a	n/a	n/a	n/a	n/a	n/a	n/a	n/a	n/a	n/a	n/a
	PI-G1-03	MD	MD mafic apophysis	1232	289	886	19	119	110	52	n/a	n/a	n/a	n/a	n/a	n/a	n/a	n/a	n/a	n/a	n/a	n/a

*All values in ppm

	Sample	Area	Group	La	Lu	Mo	Nb	Nd	Ni	Pr	Sm	Sn	Ta	Tb	Th	Tl	Tm	U	W	Y	Yb
GEOSOL / ICP-OES/MS	APF-01	AP	APF felsic dyke	24.6	<0,05	2.0	10.5	25.4	118.0	6.9	5.5	0.5	1.2	0.6	5.6	<0,5	0.2	2.1	1.3	14.4	1.0
	APF-02	AP	APF felsic dyke	7.4	<0,05	<2	5.6	11.6	517.0	2.7	3.1	<0,3	0.7	0.4	3.9	0.6	0.1	1.3	1.8	10.1	0.9
	APM-01	AP	APM mafic dyke	22.2	<0,05	<2	10.0	22.5	593.0	6.0	5.3	0.5	0.9	0.5	9.0	0.8	0.1	3.0	3.6	10.3	0.7
	APM-02	AP	APM mafic dyke	13.6	0.1	<2	8.6	15.2	90.0	3.9	3.4	<0,3	0.7	0.6	3.2	<0,5	0.3	0.7	2.2	17.1	1.8
	APM-03	AP	APM mafic dyke	58.0	0.2	7.0	8.6	46.4	82.0	13.8	7.7	0.5	1.5	0.9	7.2	<0,5	0.3	2.3	5.5	23.0	2.2
	CL-MDE-04	MD	MD mafic enclave	7.5	<0,05	<2	3.4	7.2	77.0	1.7	1.9	<0,3	0.6	0.4	0.8	<0,5	0.2	0.2	1.5	12.3	1.3
	DB-MD-01Z	MD	MD mafic apophysis	58.0	0.2	7.0	8.6	46.4		13.8	7.7	0.5	1.5	0.9	7.2	<0,5	0.3	2.3	5.5	23.0	2.2
	PI-MD-02	MD	MD mafic apophysis	81.8	<0,05	<2	15.9	75.3	534.0	21.0	15.2	0.3	2.4	1.0	25.9	0.6	0.1	7.8	2.0	16.0	0.7
	PI-MD-01	MD	MD mafic apophysis	10.0	<0,05	<2	7.3	8.8	9.0	2.4	2.0	<0,3	1.3	0.2	2.2	<0,5	0.1	0.5	7.0	5.5	0.5
	AT-MD-01	MD	MD mafic apophysis	14.8	0.2	<2	4.2	15.0	43.0	3.8	3.6	<0,3	1.7	0.6	2.3	<0,5	0.3	0.5	2.3	18.0	2.0
	CL-MD-02A	MD	MD mafic apophysis	14.5	0.1	<2	9.3	16.4	354.0	3.8	3.8	<0,3	1.0	0.6	1.6	<0,5	0.2	0.4	1.5	15.6	1.4
	AT-MD-03	MD	MD mafic apophysis	17.0	<0,05	<2	14.7	17.9	393.0	4.6	4.3	0.5	2.0	0.6	1.6	<0,5	0.2	0.5	3.1	14.7	1.2
FRX-UFRGS / XRF	CL-18-04	MD	MD mafic enclave	n/a	n/a	n/a	n/a	n/a	n/a	n/a	n/a	n/a	n/a	n/a	n/a	n/a	n/a	n/a	n/a	n/a	n/a
	DB-G1ZB	MD	MD mafic apophysis	n/a	n/a	n/a	n/a	n/a	n/a	n/a	n/a	n/a	n/a	n/a	n/a	n/a	n/a	n/a	n/a	n/a	n/a
	DR-GR-MG	MD	MD mafic apophysis	n/a	n/a	n/a	n/a	n/a	n/a	n/a	n/a	n/a	n/a	n/a	n/a	n/a	n/a	n/a	n/a	n/a	n/a
	DB-G1ZA	MD	MD mafic apophysis	n/a	n/a	n/a	n/a	n/a	n/a	n/a	n/a	n/a	n/a	n/a	n/a	n/a	n/a	n/a	n/a	n/a	n/a
	A-RAZ	MD	MD mafic apophysis	n/a	n/a	n/a	n/a	n/a	n/a	n/a	n/a	n/a	n/a	n/a	n/a	n/a	n/a	n/a	n/a	n/a	n/a
	PI-G1-02	MD	MD mafic apophysis	n/a	n/a	n/a	n/a	n/a	n/a	n/a	n/a	n/a	n/a	n/a	n/a	n/a	n/a	n/a	n/a	n/a	n/a
	PI-G1-01	MD	MD mafic apophysis	n/a	n/a	n/a	n/a	n/a	n/a	n/a	n/a	n/a	n/a	n/a	n/a	n/a	n/a	n/a	n/a	n/a	n/a
	AT-Z-01	MD	MD mafic apophysis	n/a	n/a	n/a	n/a	n/a	n/a	n/a	n/a	n/a	n/a	n/a	n/a	n/a	n/a	n/a	n/a	n/a	n/a
	CL-18-02B	MD	MD mafic apophysis	n/a	n/a	n/a	n/a	n/a	n/a	n/a	n/a	n/a	n/a	n/a	n/a	n/a	n/a	n/a	n/a	n/a	n/a
	AT-Z-03	MD	MD mafic apophysis	n/a	n/a	n/a	n/a	n/a	n/a	n/a	n/a	n/a	n/a	n/a	n/a	n/a	n/a	n/a	n/a	n/a	n/a
	AT-G1-01	MD	MD mafic apophysis	n/a	n/a	n/a	n/a	n/a	n/a	n/a	n/a	n/a	n/a	n/a	n/a	n/a	n/a	n/a	n/a	n/a	n/a
	CL-18-02A	MD	MD mafic apophysis	n/a	n/a	n/a	n/a	n/a	n/a	n/a	n/a	n/a	n/a	n/a	n/a	n/a	n/a	n/a	n/a	n/a	n/a
	AT-Z-02	MD	MD mafic apophysis	n/a	n/a	n/a	n/a	n/a	n/a	n/a	n/a	n/a	n/a	n/a	n/a	n/a	n/a	n/a	n/a	n/a	n/a
	MN-03	MD	MD mafic apophysis	n/a	n/a	n/a	n/a	n/a	n/a	n/a	n/a	n/a	n/a	n/a	n/a	n/a	n/a	n/a	n/a	n/a	n/a
	PI-G1-03	MD	MD mafic apophysis	n/a	n/a	n/a	n/a	n/a	n/a	n/a	n/a	n/a	n/a	n/a	n/a	n/a	n/a	n/a	n/a	n/a	n/a

*All values in ppm

Supplementary Table S2 (EMPA analyses - University of Göttingen)

Sample	spot #	mineral	SiO2	TiO2	Al2O3	Cr2O3	FeO	NiO	MnO	MgO	CaO	Na2O	K2O	F	Cl	wt% total
AT-Z-01	14	bt	37.53	2.60	13.70	0.68	15.06	<0.035	0.08	15.65	<0.029	0.04	9.01	0.23	<0.008	94.60
AT-Z-01	15	bt	37.91	3.20	13.76	0.24	15.60	<0.035	0.09	14.38	<0.028	0.07	9.82	0.27	0.02	95.38
AT-Z-01	16	bt	37.73	3.02	13.74	0.30	15.91	<0.036	0.09	14.53	<0.030	0.05	9.92	0.20	0.01	95.52
AT-Z-01	17	bt	37.90	2.73	13.85	0.20	16.07	<0.035	0.09	14.48	<0.032	0.08	9.89	0.24	<0.008	95.53
AT-Z-01	18	bt	38.01	3.33	14.12	0.22	15.28	<0.035	0.08	14.08	0.18	0.30	9.60	0.20	0.04	95.46
AT-Z-01	19	amph	50.68	0.45	5.27	0.15	11.54	0.04	0.15	15.38	11.82	1.06	0.48	0.12	<0.008	97.16
AT-Z-01	20	amph	50.66	0.46	4.86	0.08	11.26	<0.034	0.13	16.03	11.86	0.97	0.45	0.11	0.01	96.89
AT-Z-01	21	amph	51.18	0.43	4.77	0.05	11.10	<0.035	0.13	15.84	11.97	0.91	0.42	0.08	<0.008	96.87
AT-Z-01	22	amph	51.12	0.39	5.21	0.15	11.42	<0.035	0.13	15.61	11.87	1.07	0.45	0.06	<0.008	97.48
AT-Z-01	23	amph	50.65	0.49	5.33	0.06	11.63	<0.035	0.17	15.50	11.72	1.13	0.53	0.06	0.01	97.29
AT-Z-01	24	bt	37.62	2.77	14.08	0.27	15.24	<0.035	0.10	15.35	<0.031	0.07	9.55	0.22	0.02	95.33
AT-Z-01	25	bt	37.67	2.99	14.06	0.41	15.21	0.05	0.07	14.64	<0.030	0.07	9.83	0.23	0.02	95.24
AT-Z-01	26	bt	37.72	2.73	13.68	0.26	15.93	<0.035	0.05	14.45	<0.029	0.04	9.81	0.25	0.01	94.93
AT-Z-01	27	bt	37.54	2.65	13.75	0.35	16.26	<0.035	0.09	14.51	0.05	0.06	9.68	0.27	0.02	95.22
AT-Z-01	28	bt	37.02	3.45	13.82	0.22	15.63	<0.036	0.06	14.35	<0.029	0.09	9.55	0.21	0.01	94.39
AT-Z-01	29	amph	51.36	0.47	4.63	0.11	11.46	<0.035	0.16	15.71	11.97	0.97	0.45	0.07	<0.008	97.35
AT-Z-01	30	amph	51.39	0.41	4.69	0.15	11.71	<0.035	0.15	15.72	12.25	0.86	0.40	0.07	<0.007	97.81
AT-Z-01	31	amph	50.56	0.52	5.23	0.13	11.95	<0.034	0.12	15.09	12.03	0.97	0.53	0.13	0.01	97.28
AT-Z-01	32	amph	50.58	0.44	5.32	<0.029	12.06	<0.034	0.18	15.33	11.70	1.07	0.48	0.10	0.01	97.28
AT-Z-01	33	amph	49.79	0.54	5.58	0.08	11.95	<0.035	0.13	15.06	11.86	1.04	0.54	0.10	0.01	96.68
AT-Z-01	34	bt	37.87	3.32	13.77	0.21	15.72	<0.036	0.11	14.36	<0.030	0.07	9.87	0.21	0.01	95.51
AT-Z-01	35	bt	37.44	3.16	13.86	0.30	15.99	<0.036	0.10	13.95	<0.030	0.08	9.81	0.24	0.01	94.97
AT-Z-01	36	bt	37.98	2.82	13.64	0.36	15.98	<0.035	0.07	14.19	<0.030	0.05	9.87	0.25	<0.008	95.23
AT-Z-01	37	bt	37.71	2.62	13.66	0.18	16.12	<0.036	0.12	14.65	<0.031	0.05	9.74	0.20	0.01	95.08
AT-Z-01	38	bt	37.80	3.30	13.79	0.25	15.68	<0.034	0.08	14.46	<0.028	0.07	10.00	0.28	0.02	95.75
AT-Z-01	39	amph	52.10	0.30	4.19	<0.028	10.72	<0.034	0.16	16.26	11.84	0.84	0.36	0.12	0.01	96.95
AT-Z-01	40	amph	50.28	0.45	5.70	0.12	11.74	<0.035	0.11	15.49	11.57	1.08	0.57	0.14	<0.008	97.27
AT-Z-01	41	amph	51.66	0.36	4.28	0.07	11.04	<0.036	0.14	16.18	12.19	0.83	0.34	0.11	<0.008	97.19
AT-Z-01	42	amph	50.30	0.53	5.65	0.07	11.86	<0.035	0.13	15.24	11.93	1.16	0.59	0.11	<0.008	97.59
AT-Z-01	43	amph	50.50	0.42	5.34	0.07	11.75	<0.034	0.17	15.33	11.76	1.07	0.52	0.08	<0.008	97.02
AT-Z-01	44	bt	37.82	3.43	13.89	0.17	14.94	<0.036	0.10	14.50	<0.029	0.04	9.72	0.23	0.02	94.86
AT-Z-01	45	bt	37.61	3.29	13.88	0.27	15.46	0.04	0.06	14.55	<0.030	0.07	9.87	0.25	0.02	95.37
AT-Z-01	46	bt	37.62	3.08	14.00	0.21	15.56	<0.036	0.05	14.68	<0.031	0.04	9.67	0.25	<0.008	95.16
AT-Z-01	47	bt	37.90	3.37	13.76	0.30	15.41	<0.036	0.07	14.41	<0.032	0.08	9.80	0.24	<0.008	95.35
AT-Z-01	48	bt	37.64	3.35	13.84	0.27	15.92	<0.035	0.10	14.44	<0.031	0.06	9.69	0.21	0.01	95.53

Sample	spot #	mineral	SiO2	TiO2	Al2O3	Cr2O3	FeO	NiO	MnO	MgO	CaO	Na2O	K2O	F	Cl	wt% total
AT-Z-01	49	amph	50.97	0.42	4.97	0.23	11.53	<0.035	0.10	15.59	11.77	1.00	0.45	0.13	<0.008	97.16
AT-Z-01	50	amph	53.83	0.23	2.82	0.04	9.92	<0.034	0.15	17.09	11.96	0.60	0.21	0.09	<0.008	96.96
AT-Z-01	51	amph	50.42	0.56	5.56	0.10	11.97	<0.035	0.15	15.36	11.88	1.06	0.51	0.12	0.01	97.69
AT-Z-01	52	amph	50.57	0.54	5.50	0.07	11.92	<0.034	0.14	15.37	12.05	1.03	0.53	0.07	<0.008	97.82
AT-Z-01	53	amph	49.72	0.54	5.85	0.16	11.95	<0.035	0.15	15.16	11.71	1.14	0.55	0.12	<0.008	97.05
AT-Z-01	54	bt	37.35	3.07	13.66	0.44	15.32	<0.034	0.10	14.31	<0.027	0.06	9.72	0.24	<0.008	94.30
AT-Z-01	55	bt	37.27	3.76	13.79	0.24	15.56	<0.034	0.09	14.04	<0.029	0.04	9.65	0.19	0.01	94.66
AT-Z-01	56	bt	37.73	3.43	13.76	0.25	15.76	<0.036	0.08	14.05	<0.030	0.08	9.98	0.22	<0.008	95.37
AT-Z-01	57	bt	37.63	3.26	13.62	0.28	15.39	<0.035	0.08	14.51	<0.032	0.09	9.71	0.19	0.01	94.77
AT-Z-01	58	bt	38.01	3.03	13.72	0.26	15.57	<0.036	0.10	14.59	<0.032	<0.033	10.00	0.24	0.01	95.56
AT-Z-01	59	amph	50.68	0.49	5.58	0.11	11.71	<0.035	0.18	15.41	11.76	1.20	0.55	0.09	<0.008	97.75
AT-Z-01	60	amph	50.68	0.45	5.40	0.14	11.68	0.04	0.14	15.52	11.92	1.07	0.53	0.11	0.01	97.70
AT-Z-01	61	amph	50.70	0.47	5.12	0.10	11.67	<0.035	0.14	15.28	11.94	1.03	0.46	0.09	<0.008	97.00
AT-Z-01	62	amph	49.94	0.50	5.33	0.14	11.55	<0.035	0.14	15.98	11.38	0.84	0.45	0.12	0.01	96.38
AT-Z-01	63	amph	50.09	0.52	5.41	0.06	11.89	<0.035	0.14	15.37	11.67	1.11	0.53	0.09	<0.008	96.88
AT-Z-01	64	bt	37.70	2.67	14.02	0.19	16.29	<0.036	0.10	14.05	<0.030	0.10	9.47	0.18	0.01	94.81
AT-Z-01	65	bt	37.78	2.50	14.04	0.24	16.32	0.05	0.09	14.26	<0.031	0.09	9.82	0.24	0.02	95.44
AT-Z-01	66	bt	37.31	2.93	13.83	0.26	15.78	<0.035	0.11	14.24	<0.031	0.08	9.74	0.27	0.02	94.57
AT-Z-01	67	bt	37.84	2.44	13.76	0.25	16.01	<0.036	0.09	14.40	<0.029	0.07	9.78	0.24	0.01	94.91
AT-Z-01	68	bt	37.50	2.27	14.20	0.19	16.71	<0.036	0.08	13.86	0.06	0.05	9.71	0.21	0.02	94.85
AT-Z-01	69	amph	53.68	0.16	3.13	0.08	10.28	<0.034	0.15	17.01	11.85	0.72	0.21	0.09	0.03	97.40
AT-Z-01	70	amph	53.78	0.23	2.94	0.12	10.74	<0.034	0.13	16.69	12.10	0.53	0.21	0.05	0.01	97.55
AT-Z-01	71	amph	51.76	0.37	4.09	0.08	11.40	<0.035	0.16	15.96	11.92	0.69	0.32	0.08	0.01	96.85
AT-Z-01	72	amph	52.64	0.33	3.72	<0.029	11.06	<0.035	0.17	16.20	12.00	0.59	0.29	0.08	<0.008	97.11
AT-Z-01	73	amph	53.95	0.18	2.86	<0.028	9.98	<0.035	0.16	17.24	12.10	0.58	0.21	0.08	<0.008	97.36
AT-Z-02	74	bt	38.77	1.55	14.06	0.44	10.57	0.17	0.09	18.85	<0.029	0.04	9.92	0.64	0.02	95.11
AT-Z-02	75	amph	53.42	0.14	3.56	0.09	7.04	0.07	0.14	18.90	12.18	0.76	0.30	0.23	<0.008	96.84
AT-Z-02	76	bt	38.77	1.68	13.90	0.49	10.21	0.18	0.09	18.68	<0.030	0.09	10.04	0.61	0.02	94.78
AT-Z-02	77	bt	38.72	1.31	14.26	0.49	10.87	0.08	0.10	18.50	<0.030	0.05	10.11	0.60	0.02	95.11
AT-Z-02	78	bt	38.93	1.39	14.12	0.40	10.75	0.08	0.09	18.53	<0.028	0.08	10.18	0.67	0.02	95.23
AT-Z-02	79	amph	54.00	0.16	3.34	0.18	7.26	<0.034	0.14	18.82	12.37	0.79	0.27	0.23	<0.008	97.57
AT-Z-02	80	amph	53.47	0.12	3.53	0.05	7.57	0.08	0.13	18.63	12.41	0.84	0.31	0.19	<0.008	97.35
AT-Z-02	81	amph	53.72	0.16	3.45	0.13	7.26	<0.034	0.16	18.49	12.45	0.79	0.26	0.23	<0.008	97.13
AT-Z-02	82	amph	53.91	0.16	3.57	0.10	6.97	0.05	0.14	18.99	12.42	0.82	0.28	0.24	<0.008	97.64

Sample	spot #	mineral	SiO2	TiO2	Al2O3	Cr2O3	FeO	NiO	MnO	MgO	CaO	Na2O	K2O	F	Cl	wt% total
AT-Z-02	83	amph	54.10	0.16	3.43	0.12	6.93	0.07	0.15	18.88	12.31	0.84	0.33	0.23	<0.007	97.56
AT-Z-02	84	bt	39.22	1.52	14.10	0.48	10.55	0.10	0.11	18.51	<0.028	0.06	9.90	0.59	0.01	95.15
AT-Z-02	85	bt	39.16	1.54	14.37	0.55	10.38	0.09	0.07	18.68	<0.031	0.07	9.82	0.67	0.02	95.44
AT-Z-02	86	bt	39.45	1.53	14.10	0.37	10.82	0.11	0.09	18.64	0.04	0.06	9.85	0.60	0.02	95.67
AT-Z-02	87	pl	63.87	<0.024	22.68	<0.026	0.13	<0.031	<0.023	<0.024	3.78	9.69	0.12	<0.024	<0.007	100.30
AT-Z-02	88	bt	38.91	1.71	13.86	0.28	11.61	0.13	0.09	18.18	<0.029	0.05	10.09	0.56	0.02	95.49
AT-Z-02	89	amph	51.88	0.24	5.26	0.03	7.57	<0.035	0.13	17.89	12.48	1.13	0.45	0.25	<0.007	97.33
AT-Z-02	90	amph	54.11	0.09	3.35	0.16	7.12	0.08	0.13	18.82	12.28	0.72	0.24	0.25	0.01	97.37
AT-Z-02	91	amph	53.72	0.15	3.56	0.18	6.90	<0.034	0.12	18.94	12.24	0.80	0.26	0.22	<0.008	97.13
AT-Z-02	92	amph	53.89	0.16	3.87	0.26	6.96	<0.034	0.13	18.71	12.32	0.85	0.34	0.23	<0.008	97.74
AT-Z-02	93	amph	54.37	0.12	3.24	0.19	7.07	<0.035	0.11	19.00	12.54	0.78	0.27	0.27	<0.008	97.99
AT-Z-02	94	bt	38.91	2.13	14.36	0.35	10.73	0.10	0.10	18.09	<0.029	0.09	9.92	0.34	0.01	95.13
AT-Z-02	95	bt	38.98	2.14	14.26	0.33	11.01	0.09	0.08	17.88	<0.028	0.05	9.89	0.34	0.01	95.07
AT-Z-02	96	bt	39.00	2.16	14.28	0.42	10.84	0.09	0.09	18.05	<0.027	0.07	9.87	0.35	0.01	95.23
AT-Z-02	97	bt	38.64	2.09	14.13	0.34	10.90	0.10	0.09	18.26	<0.028	0.10	9.87	0.38	0.02	94.93
AT-Z-02	98	bt	39.07	1.84	14.32	0.39	10.91	0.07	0.09	18.28	<0.030	0.06	9.86	0.38	0.01	95.28
AT-Z-02	99	amph	54.60	0.20	3.30	0.06	7.05	0.05	0.12	18.58	12.46	0.76	0.25	0.14	<0.007	97.58
AT-Z-02	100	amph	54.36	0.19	3.50	0.06	7.16	<0.035	0.13	18.65	12.35	0.75	0.27	0.13	<0.008	97.57
AT-Z-02	101	amph	54.39	0.23	3.38	0.09	7.01	0.04	0.13	18.71	12.37	0.80	0.26	0.13	0.01	97.55
AT-Z-02	102	amph	54.20	0.22	3.52	0.12	7.28	0.05	0.13	18.72	12.45	0.81	0.34	0.15	<0.008	97.99
AT-Z-02	103	amph	54.07	0.22	3.62	0.07	7.28	0.06	0.15	18.64	12.40	0.77	0.31	0.13	0.01	97.73
AT-Z-02	104	bt	38.37	1.70	14.58	0.18	11.08	0.07	0.09	18.65	<0.029	0.04	9.32	0.28	0.02	94.39
AT-Z-02	105	bt	38.57	1.69	14.19	0.17	11.12	0.06	0.12	18.44	<0.029	0.10	9.71	0.25	0.01	94.44
AT-Z-02	106	bt	38.53	1.75	14.04	0.15	11.69	0.07	0.12	18.27	0.04	0.06	9.70	0.27	0.02	94.72
AT-Z-02	107	bt	38.73	1.78	14.58	0.34	10.85	0.04	0.07	18.43	<0.030	0.08	10.08	0.28	0.02	95.30
AT-Z-02	108	bt	38.79	1.74	14.58	0.27	10.21	0.09	0.07	18.95	0.09	0.06	9.39	0.29	0.02	94.54
AT-Z-02	109	amph	54.42	0.19	3.43	0.08	7.21	0.05	0.16	18.95	12.24	0.74	0.28	0.09	<0.008	97.84
AT-Z-02	110	amph	54.85	0.12	3.06	0.04	7.15	0.07	0.16	18.85	12.25	0.68	0.24	0.08	<0.007	97.55
AT-Z-02	111	amph	54.79	0.14	2.74	0.11	7.08	<0.033	0.15	18.70	12.54	0.56	0.22	0.10	<0.008	97.15
AT-Z-02	112	amph	54.35	0.21	3.48	0.07	7.43	0.04	0.16	18.80	12.43	0.87	0.32	0.08	<0.008	98.23
AT-Z-02	113	amph	54.41	0.14	3.17	0.08	7.22	<0.034	0.16	19.11	12.70	0.69	0.23	0.13	0.01	98.08
AT-Z-02	114	bt	38.49	1.61	14.43	0.22	11.36	0.08	0.09	18.75	0.04	0.06	9.37	0.21	0.02	94.72
AT-Z-02	115	bt	38.53	1.92	14.55	0.57	11.45	0.08	0.10	17.97	<0.029	0.03	9.52	0.21	0.01	94.95
AT-Z-02	116	bt	38.45	1.66	14.55	0.13	11.42	0.07	0.10	18.25	<0.027	0.08	9.79	0.23	0.03	94.76

Sample	spot #	mineral	SiO2	TiO2	Al2O3	Cr2O3	FeO	NiO	MnO	MgO	CaO	Na2O	K2O	F	Cl	wt% total
AT-Z-02	117	bt	38.50	1.37	14.63	0.40	11.30	0.13	0.07	18.41	<0.029	0.06	9.74	0.21	0.03	94.88
AT-Z-02	118	bt	39.14	2.04	14.61	0.12	10.71	0.12	0.09	18.31	<0.029	<0.034	10.15	0.26	0.01	95.57
AT-Z-02	119	amph	54.08	0.14	3.59	0.07	7.50	<0.035	0.14	18.62	12.42	0.82	0.29	0.08	<0.008	97.79
AT-Z-02	120	amph	53.80	0.12	3.64	0.11	7.51	0.06	0.14	18.54	12.39	0.79	0.30	0.11	<0.008	97.51
AT-Z-02	121	amph	54.71	0.12	2.97	0.11	7.25	<0.035	0.14	18.76	12.41	0.59	0.21	0.05	0.01	97.33
AT-Z-02	122	amph	55.89	0.08	1.96	0.10	6.58	<0.035	0.13	19.36	12.49	0.44	0.13	0.05	0.01	97.22
AT-Z-02	123	amph	54.22	0.17	3.34	0.14	7.18	0.04	0.12	18.77	12.39	0.65	0.26	0.06	<0.008	97.34
AT-Z-03	124	bt	38.87	1.63	15.04	0.28	10.89	0.09	0.08	18.21	<0.030	0.09	9.72	0.08	0.02	95.00
AT-Z-03	125	bt	38.67	1.64	14.78	0.41	11.14	0.06	0.06	17.97	<0.027	0.15	9.84	0.06	0.03	94.83
AT-Z-03	126	bt	38.95	1.62	15.06	0.27	11.01	0.09	0.09	18.25	0.07	0.10	9.53	0.10	0.03	95.16
AT-Z-03	127	bt	38.80	1.62	14.83	0.35	10.52	0.06	0.08	17.86	0.05	0.03	10.04	0.08	0.02	94.36
AT-Z-03	128	bt	38.96	1.95	14.88	0.43	10.87	0.07	0.07	17.81	<0.031	0.09	9.99	0.05	0.02	95.20
AT-Z-03	129	amph	55.44	0.07	2.57	0.11	6.87	0.06	0.17	19.26	12.40	0.42	0.11	<0.027	<0.008	97.51
AT-Z-03	130	amph	54.67	0.12	3.27	0.17	6.69	0.06	0.15	18.77	12.39	0.54	0.16	<0.028	<0.007	97.01
AT-Z-03	131	amph	55.85	0.08	2.62	0.05	6.91	0.05	0.15	19.00	12.48	0.45	0.09	<0.028	0.01	97.73
AT-Z-03	132	amph	54.37	0.14	3.60	0.21	7.14	0.05	0.12	18.51	12.29	0.55	0.17	<0.027	<0.008	97.15
AT-Z-03	133	amph	54.85	0.10	3.43	0.04	7.55	<0.034	0.19	18.66	12.47	0.59	0.10	0.03	<0.007	98.04
AT-Z-03	134	bt	38.66	1.68	15.13	0.30	10.76	0.10	0.08	18.23	<0.029	0.16	9.63	0.09	0.03	94.87
AT-Z-03	135	bt	38.68	1.70	15.11	0.40	10.52	0.08	0.08	17.96	<0.029	0.13	9.69	0.11	0.03	94.52
AT-Z-03	136	bt	39.24	1.63	14.63	0.22	10.78	0.05	0.08	17.89	0.05	0.10	9.75	0.10	0.03	94.55
AT-Z-03	137	bt	38.13	1.53	15.32	0.20	10.81	0.12	0.09	18.56	<0.029	<0.033	9.40	0.04	0.02	94.25
AT-Z-03	138	bt	38.48	1.70	14.82	0.41	10.58	0.08	0.09	18.13	<0.030	0.13	9.71	0.11	0.02	94.24
AT-Z-03	139	amph	54.41	0.12	3.54	0.11	7.39	<0.034	0.16	18.55	12.38	0.61	0.19	<0.028	<0.008	97.49
AT-Z-03	140	amph	54.17	0.18	3.89	0.10	7.11	0.05	0.16	18.94	12.44	0.62	0.19	0.03	<0.008	97.89
AT-Z-03	141	amph	54.93	0.12	3.47	0.08	7.40	<0.034	0.18	18.61	12.37	0.50	0.17	<0.028	<0.008	97.87
AT-Z-03	142	amph	54.97	0.10	2.95	0.11	7.05	<0.036	0.16	19.01	12.55	0.47	0.15	0.03	<0.008	97.57
AT-Z-03	143	amph	53.93	0.14	3.59	0.07	7.25	<0.034	0.17	18.83	12.45	0.56	0.18	0.03	<0.008	97.21
AT-Z-03	144	amph	54.94	0.13	3.12	0.07	7.16	0.05	0.13	18.81	12.29	0.50	0.14	0.05	<0.007	97.39
AT-Z-03	145	bt	38.74	1.27	15.10	0.63	10.48	0.10	0.08	18.33	<0.030	0.10	9.74	0.12	0.03	94.71
AT-Z-03	146	bt	38.68	1.30	15.15	0.28	10.93	0.08	0.06	18.33	<0.029	0.10	9.75	0.14	0.03	94.85
AT-Z-03	147	bt	38.70	1.41	15.07	0.23	10.65	0.07	0.07	18.20	0.04	0.14	9.61	0.11	0.03	94.33
AT-Z-03	148	bt	38.69	1.41	14.80	0.55	10.67	0.07	0.10	18.02	<0.031	0.12	9.62	0.11	0.02	94.18
AT-Z-03	149	bt	38.89	1.32	15.16	0.38	10.95	0.10	0.07	18.09	<0.030	0.05	9.75	0.09	0.02	94.88
AT-Z-03	150	amph	53.89	0.11	3.71	0.22	7.25	<0.034	0.16	18.61	12.38	0.60	0.21	0.03	<0.008	97.20

Sample	spot #	mineral	SiO2	TiO2	Al2O3	Cr2O3	FeO	NiO	MnO	MgO	CaO	Na2O	K2O	F	Cl	wt% total
AT-Z-03	151	amph	54.38	0.10	3.46	0.08	7.08	0.08	0.13	18.74	12.48	0.60	0.16	0.04	<0.007	97.34
AT-Z-03	152	amph	54.06	0.12	3.94	0.17	7.18	0.04	0.14	18.53	12.24	0.61	0.21	0.06	<0.008	97.30
AT-Z-03	153	amph	54.06	0.11	3.86	0.17	7.31	0.04	0.14	18.45	12.29	0.64	0.18	0.03	<0.008	97.30
AT-Z-03	154	amph	54.70	0.13	3.54	0.06	7.29	<0.034	0.14	18.61	12.21	0.59	0.19	<0.028	<0.007	97.51
AT-Z-03	155	bt	38.94	1.15	15.18	0.28	10.16	0.11	0.08	18.62	<0.028	0.14	9.85	0.08	0.03	94.61
AT-Z-03	156	bt	38.75	1.16	15.46	0.46	10.32	0.12	0.10	18.47	0.03	0.13	9.66	0.09	0.01	94.77
AT-Z-03	157	bt	38.43	1.08	15.14	0.39	10.48	0.09	0.07	18.48	<0.031	0.07	9.83	0.14	0.02	94.25
AT-Z-03	158	bt	38.71	1.15	14.98	0.34	10.37	0.11	0.05	18.64	0.05	0.08	9.68	0.08	0.03	94.27
AT-Z-03	159	bt	38.75	1.29	15.49	0.49	9.96	0.12	0.08	18.24	<0.026	0.08	9.99	0.10	0.02	94.62
AT-Z-03	160	amph	53.99	0.10	3.92	0.08	7.09	0.04	0.15	18.40	12.54	0.59	0.22	0.03	<0.007	97.17
AT-Z-03	161	amph	52.32	0.13	3.99	0.12	7.08	0.06	0.16	17.85	12.02	0.62	0.15	<0.027	0.05	94.56
AT-Z-03	162	amph	53.36	0.13	4.22	0.13	7.33	<0.035	0.16	18.35	12.20	0.68	0.22	0.04	<0.008	96.84
AT-Z-03	163	amph	54.00	0.11	3.84	0.11	7.08	0.06	0.15	18.51	12.43	0.66	0.21	0.03	<0.008	97.19
AT-Z-03	164	amph	53.63	0.11	4.21	0.13	7.10	0.05	0.18	18.63	12.43	0.65	0.21	<0.027	<0.008	97.36
AT-Z-03	165	amph	53.49	0.14	4.15	0.13	7.07	<0.034	0.14	18.75	12.32	0.66	0.24	<0.027	<0.008	97.15

Supplementary Table S3 (EMPA analyses - Universidade Federal do Rio Grande do Sul)

Sample	spot #	mineral	SiO2	TiO2	Al2O3	Cr2O3	FeO	MnO	MgO	CaO	Na2O	K2O	wt% total
AT-Z-01	54	amph	52.99	0.27	3.52	0.08	10.75	0.17	16.95	12.05	0.70	0.26	97.74
AT-Z-01	55	amph	53.29	0.18	2.62	0.08	10.43	0.14	17.22	12.17	0.52	0.18	96.84
AT-Z-01	56	amph	49.64	0.53	5.72	0.20	12.10	0.15	15.32	11.69	1.12	0.55	97.01
AT-Z-01	57	amph	50.17	0.48	5.45	0.10	11.80	0.12	15.31	11.58	1.05	0.54	96.60
AT-Z-01	58	amph	50.14	0.46	5.32	0.11	12.19	0.10	15.67	11.91	0.99	0.47	97.37
AT-Z-01	59	bt	38.28	4.17	13.53	0.19	15.17	0.08	14.30	0.01	0.05	9.49	95.26
AT-Z-01	60	bt	38.15	3.44	13.56	0.24	15.50	0.06	14.70	0.01	0.05	9.49	95.20
AT-Z-01	61	bt	37.14	3.21	13.53	0.33	15.89	0.08	14.24	0.03	0.08	9.45	93.98
AT-Z-01	62	bt	37.30	3.70	13.62	0.24	15.43	0.05	14.03	0.00	0.07	9.51	93.97
AT-Z-01	63	bt	37.45	3.83	13.89	0.30	15.65	0.05	13.61	0.00	0.08	9.69	94.56
AT-Z-01	64	pl	63.64	0.01	22.43	0.02	0.22	0.00	0.01	3.67	9.40	0.14	99.55
AT-Z-01	65	pl	62.77	0.00	22.53	0.00	0.12	0.00	0.00	3.64	9.48	0.20	98.73
AT-Z-01	66	pl	63.71	0.00	22.56	0.01	0.09	0.00	0.00	4.00	9.25	0.33	99.96
AT-Z-01	67	pl	63.36	0.00	22.53	0.04	0.06	0.00	0.02	3.73	9.43	0.34	99.50
AT-Z-01	68	kfs	63.08	0.00	18.32	0.04	0.11	0.03	0.00	0.00	0.97	14.96	97.51
AT-Z-01	69	kfs	63.96	0.00	18.38	0.00	0.08	0.01	0.01	0.00	1.18	14.63	98.25
AT-Z-01	70	kfs	63.93	0.00	18.42	0.00	0.08	0.00	0.00	0.02	1.51	14.24	98.19
AT-Z-01	71	kfs	64.06	0.00	18.23	0.00	0.13	0.00	0.00	0.01	1.26	14.63	98.33
AT-Z-01	72	amph	52.85	0.13	3.10	0.06	10.41	0.18	17.01	12.11	0.61	0.19	96.65
AT-Z-01	73	amph	49.80	0.46	5.43	0.16	11.91	0.09	15.25	11.72	1.01	0.51	96.34
AT-Z-01	74	amph	50.69	0.41	5.04	0.21	11.46	0.13	15.80	11.86	0.96	0.42	96.99
AT-Z-01	75	amph	53.19	0.21	3.31	0.05	10.83	0.16	17.15	12.02	0.72	0.15	97.78
AT-Z-01	76	amph	51.92	0.35	3.96	0.09	11.05	0.15	16.53	12.06	0.73	0.31	97.15
AT-Z-01	77	bt	37.10	2.75	13.47	0.37	17.42	0.07	13.51	0.00	0.07	9.34	94.10
AT-Z-01	78	bt	37.28	2.85	13.64	0.21	18.06	0.06	13.49	0.04	0.06	9.20	94.88
AT-Z-01	79	bt	37.72	2.98	13.55	0.27	15.30	0.08	14.66	0.00	0.04	9.46	94.07
AT-Z-01	80	bt	37.16	3.10	13.54	0.21	15.69	0.06	14.18	0.00	0.10	9.51	93.55
AT-Z-01	81	bt	37.67	2.93	13.73	0.17	15.69	0.05	14.31	0.00	0.09	9.43	94.08
AT-Z-01	82	bt	37.50	2.68	13.52	0.27	17.86	0.09	13.76	0.00	0.06	9.26	95.00
AT-Z-01	83	kfs	64.11	0.00	18.29	0.00	0.05	0.00	0.00	0.00	1.32	14.66	98.43

Sample	spot #	mineral	SiO2	TiO2	Al2O3	Cr2O3	FeO	MnO	MgO	CaO	Na2O	K2O	wt% total
AT-Z-01	84	pl	63.06	0.00	22.45	0.01	0.21	0.00	0.68	3.59	8.95	0.21	99.16
AT-Z-01	85	pl	64.03	0.00	22.17	0.01	0.21	0.00	0.00	3.44	9.45	0.30	99.61
AT-Z-01	86	amph	49.81	0.46	5.58	0.21	11.90	0.13	15.25	11.80	1.14	0.54	96.82
AT-Z-01	87	amph	50.30	0.42	5.39	0.09	11.71	0.13	15.68	11.67	1.01	0.50	96.89
AT-Z-01	88	amph	50.82	0.47	4.94	0.14	11.66	0.13	15.79	11.87	0.94	0.46	97.22
AT-Z-01	89	amph	50.46	0.36	5.48	0.08	11.81	0.12	15.69	11.87	1.06	0.52	97.45
AT-Z-01	90	amph	49.88	0.47	5.60	0.11	12.03	0.14	15.25	11.78	1.12	0.50	96.88
AT-Z-01	91	bt	37.16	2.91	13.90	0.31	15.33	0.07	14.38	0.02	0.04	9.48	93.60
AT-Z-01	92	bt	37.90	3.26	13.82	0.25	15.36	0.08	14.48	0.00	0.09	9.51	94.76
AT-Z-01	93	bt	37.69	3.32	13.86	0.27	15.86	0.08	14.57	0.02	0.08	9.43	95.19
AT-Z-01	94	bt	37.43	3.27	13.63	0.28	15.96	0.07	14.39	0.00	0.07	9.61	94.70
AT-Z-01	95	bt	37.72	3.08	13.93	0.26	15.82	0.05	14.65	0.01	0.05	9.57	95.15
AT-Z-01	96	pl	64.08	0.00	22.29	0.00	0.09	0.00	0.00	3.64	9.51	0.22	99.82
AT-Z-01	97	pl	63.67	0.00	22.68	0.04	0.09	0.00	0.00	3.76	9.36	0.36	99.95
AT-Z-01	98	pl	64.28	0.00	22.47	0.00	0.12	0.00	0.00	3.76	9.19	0.33	100.14
AT-Z-01	99	amph	50.30	0.36	5.05	0.19	11.59	0.13	15.96	11.78	1.02	0.47	96.86
AT-Z-01	100	amph	50.58	0.43	5.30	0.07	11.89	0.17	15.77	11.84	1.08	0.47	97.61
AT-Z-01	101	bt	37.26	3.24	13.81	0.23	15.67	0.07	14.35	0.00	0.05	9.48	94.16
AT-Z-01	102	bt	37.80	2.32	13.86	0.28	16.31	0.07	15.04	0.00	0.03	9.39	95.10
AT-Z-02	1	amph	53.06	0.21	3.28		7.10	0.09	19.27	11.84	0.61	0.19	95.65
AT-Z-02	2	amph	53.32	0.18	3.53		7.38	0.14	19.05	12.31	0.70	0.26	96.87
AT-Z-02	3	amph	55.39	0.11	1.71		6.56	0.12	20.01	12.72	0.40	0.12	97.15
AT-Z-02	4	amph	53.61	0.14	3.68		7.57	0.13	18.83	12.21	0.83	0.25	97.25
AT-Z-02	5	amph	53.72	0.13	3.60		7.57	0.12	19.03	12.47	0.80	0.28	97.71
AT-Z-02	6	pl	61.99	0.00	23.67		0.10	0.00	0.00	4.98	8.61	0.33	99.67
AT-Z-02	7	pl	63.48	0.04	23.08		0.10	0.00	0.03	3.47	9.60	0.19	99.99
AT-Z-02	8	pl	63.30	0.00	23.24		0.16	0.01	0.01	3.99	9.52	0.27	100.48
AT-Z-02	9	pl	63.38	0.00	23.23		0.14	0.05	0.01	3.98	9.46	0.24	100.50
AT-Z-02	10	pl	63.40	0.00	23.10		0.16	0.00	0.00	3.96	9.44	0.33	100.39
AT-Z-02	11	bt	38.37	1.52	14.84		11.52	0.10	18.45	0.00	0.06	9.80	94.65

Sample	spot #	mineral	SiO2	TiO2	Al2O3	Cr2O3	FeO	MnO	MgO	CaO	Na2O	K2O	wt% total
AT-Z-02	12	bt	38.80	1.70	14.70		11.23	0.11	18.58	0.00	0.06	9.71	94.90
AT-Z-02	13	bt	38.57	1.58	14.45		11.59	0.13	18.33	0.00	0.08	9.97	94.69
AT-Z-02	14	bt	38.51	1.73	14.70		11.31	0.11	18.46	0.00	0.03	9.66	94.51
AT-Z-02	15	bt	38.12	1.66	14.65		11.61	0.10	18.41	0.00	0.06	9.92	94.53
AT-Z-02	16	amph	53.93	0.16	3.20		7.13	0.10	18.97	12.61	0.72	0.20	97.02
AT-Z-02	17	amph	53.50	0.18	3.27		7.34	0.14	18.81	12.43	0.76	0.25	96.68
AT-Z-02	18	amph	53.53	0.19	3.59		7.30	0.11	18.93	12.49	0.74	0.27	97.14
AT-Z-02	19	amph	53.17	0.26	3.63		7.61	0.18	18.89	12.42	0.74	0.26	97.15
AT-Z-02	20	amph	53.54	0.14	3.32		7.23	0.11	19.03	12.60	0.66	0.22	96.85
AT-Z-02	21	pl	63.47	0.00	22.94		0.08	0.00	0.00	3.93	9.37	0.25	100.05
AT-Z-02	22	pl	64.48	0.00	22.91		0.12	0.02	0.15	2.31	9.63	0.29	99.90
AT-Z-02	23	pl	63.82	0.00	23.11		0.19	0.00	0.03	3.87	9.36	0.09	100.47
AT-Z-02	24	pl	63.42	0.01	23.20		0.20	0.00	0.01	3.93	9.75	0.10	100.62
AT-Z-02	25	pl	62.87	0.03	23.35		0.10	0.01	0.01	4.39	8.85	0.31	99.92
AT-Z-02	26	bt	38.18	1.77	14.83		11.27	0.06	18.30	0.00	0.06	9.70	94.18
AT-Z-02	27	bt	38.57	2.00	14.92		11.41	0.08	18.01	0.00	0.07	9.69	94.76
AT-Z-02	28	bt	38.50	1.95	14.61		11.14	0.05	18.41	0.00	0.10	9.85	94.60
AT-Z-02	29	bt	38.92	1.71	14.58		11.10	0.08	18.59	0.00	0.08	9.85	94.91
AT-Z-02	30	bt	38.42	1.66	14.57		11.59	0.08	18.37	0.00	0.06	9.95	94.69
AT-Z-02	31	amph	53.77	0.21	3.50		7.27	0.14	18.97	12.37	0.75	0.25	97.22
AT-Z-02	32	amph	54.04	0.15	2.99		7.05	0.15	19.29	12.81	0.64	0.17	97.30
AT-Z-02	33	amph	53.51	0.17	3.59		7.36	0.11	19.03	12.36	0.78	0.29	97.20
AT-Z-02	34	amph	53.19	0.24	3.91		7.44	0.13	18.67	12.40	0.82	0.33	97.13
AT-Z-02	35	amph	55.23	0.13	2.30		6.71	0.14	19.69	12.57	0.51	0.14	97.40
AT-Z-02	36	pl	63.77	0.03	22.92		0.12	0.00	0.00	3.82	9.45	0.22	100.33
AT-Z-02	37	pl	64.41	0.01	22.78		0.19	0.00	0.00	3.49	9.74	0.17	100.80
AT-Z-02	38	pl	63.57	0.01	23.35		0.17	0.00	0.02	3.93	9.46	0.15	100.66
AT-Z-02	39	pl	60.95	0.10	21.99		0.88	0.01	1.80	3.01	8.55	0.40	97.69
AT-Z-02	40	pl	64.02	0.01	22.62		0.18	0.00	0.00	3.75	9.56	0.29	100.43
AT-Z-02	41	bt	38.06	2.39	14.63		11.19	0.13	18.16	0.00	0.08	9.82	94.47

Sample	spot #	mineral	SiO2	TiO2	Al2O3	Cr2O3	FeO	MnO	MgO	CaO	Na2O	K2O	wt% total
AT-Z-02	42	bt	38.61	2.28	14.49		11.04	0.07	18.37	0.00	0.12	9.73	94.71
AT-Z-02	43	bt	38.15	2.06	14.86		11.20	0.09	18.04	0.01	0.01	9.09	93.50
AT-Z-02	44	bt	38.43	2.39	14.35		11.28	0.11	17.97	0.00	0.06	9.83	94.43
AT-Z-02	45	bt	38.39	2.36	14.37		11.55	0.11	18.14	0.00	0.04	9.91	94.87
AT-Z-02	46	cal	0.06	0.00	0.00		0.29	0.20	0.33	59.30	0.00	0.00	60.17
AT-Z-02	47	cal	0.03	0.00	0.00		0.25	0.21	0.23	59.24	0.02	0.00	59.98
AT-Z-02	48	amph	52.94	0.16	3.24		7.75	0.11	18.78	12.56	0.69	0.27	96.50
AT-Z-02	49	cal	0.06	0.00	0.00		0.27	0.21	0.30	59.43	0.03	0.00	60.30
AT-Z-02	50	cal	0.01	0.00	0.00		0.30	0.24	0.28	59.22	0.01	0.03	60.09
AT-Z-02	51	chl	45.20	0.00	5.54	0.06	5.12	0.04	23.03	0.43	0.02	0.00	79.45
AT-Z-02	52	chl	36.39	0.00	10.82	0.04	7.59	0.07	29.38	0.33	0.02	0.00	84.64
AT-Z-02	53	chl	34.79	0.00	7.62	0.06	5.84	0.06	24.09	0.46	0.00	0.02	72.95
AT-Z-02	54	chl	47.03	0.01	7.34	0.00	5.54	0.02	24.19	0.53	0.01	0.01	84.68
AT-Z-02	55	chl	46.85	0.00	6.16	0.04	4.88	0.01	24.43	0.63	0.02	0.02	83.04
AT-Z-03	65	amph	54.45	0.21	3.53		7.34	0.17	19.00	12.55	0.55	0.21	98.01
AT-Z-03	66	amph	54.49	0.18	3.49		7.23	0.14	18.89	12.35	0.53	0.17	97.46
AT-Z-03	67	amph	55.04	0.16	2.78		7.23	0.13	19.35	12.24	0.46	0.13	97.50
AT-Z-03	68	amph	54.68	0.10	3.43		7.25	0.16	19.07	12.18	0.56	0.17	97.61
AT-Z-03	69	amph	55.11	0.09	3.52		7.16	0.17	19.22	12.48	0.58	0.18	98.51
AT-Z-03	70	pl	62.39	0.00	23.55		0.13	0.00	0.00	5.27	8.53	0.09	99.96
AT-Z-03	71	pl	62.37	0.00	23.26		0.16	0.02	0.01	4.91	8.63	0.16	99.52
AT-Z-03	72	pl	62.04	0.00	23.48		0.16	0.00	0.01	4.95	8.72	0.19	99.55
AT-Z-03	73	pl	62.48	0.00	23.65		0.14	0.01	0.00	4.49	8.75	0.43	99.94
AT-Z-03	74	pl	62.86	0.00	23.46		0.17	0.00	0.01	4.92	8.87	0.13	100.42
AT-Z-03	75	bt	38.94	1.92	14.61		10.63	0.15	18.40	0.00	0.14	9.43	94.23
AT-Z-03	76	bt	38.61	1.95	14.65		11.47	0.07	17.80	0.00	0.12	9.75	94.42
AT-Z-03	77	bt	39.10	1.95	14.53		10.90	0.00	18.23	0.00	0.09	9.78	94.57
AT-Z-03	78	bt	38.45	2.30	14.41		11.11	0.05	17.83	0.00	0.12	9.57	93.85
AT-Z-03	79	bt	38.88	1.87	14.70		10.82	0.06	18.10	0.00	0.14	9.57	94.12
AT-Z-03	80	amph	55.47	0.11	2.69		7.01	0.14	19.51	12.71	0.44	0.07	98.16

Sample	spot #	mineral	SiO2	TiO2	Al2O3	Cr2O3	FeO	MnO	MgO	CaO	Na2O	K2O	wt% total
AT-Z-03	81	amph	54.97	0.08	3.25		7.35	0.18	19.52	12.73	0.50	0.16	98.74
AT-Z-03	82	amph	54.05	0.18	3.87		7.32	0.18	18.75	12.42	0.60	0.19	97.56
AT-Z-03	83	amph	54.38	0.19	3.55		7.29	0.16	18.96	12.50	0.50	0.19	97.72
AT-Z-03	84	amph	54.36	0.17	3.71		7.49	0.10	18.88	12.41	0.62	0.17	97.91
AT-Z-03	85	pl	62.34	0.01	23.52		0.16	0.00	0.00	5.39	8.52	0.14	100.10
AT-Z-03	86	pl	61.63	0.03	24.06		0.12	0.00	0.00	5.51	8.82	0.19	100.34
AT-Z-03	87	pl	62.18	0.05	23.75		0.27	0.02	0.01	5.19	8.68	0.13	100.28
AT-Z-03	88	bt	39.25	1.72	14.81		10.79	0.05	18.58	0.00	0.19	9.31	94.70
AT-Z-03	89	bt	39.61	1.81	14.55		11.11	0.06	18.82	0.00	0.12	9.54	95.62
AT-Z-03	90	bt	38.52	1.82	15.00		10.81	0.08	17.99	0.00	0.09	9.62	93.94
AT-Z-03	91	bt	38.75	1.63	14.84		10.95	0.05	18.07	0.01	0.15	9.30	93.76
AT-Z-03	92	bt	38.36	1.50	15.19		10.79	0.10	18.23	0.00	0.13	9.76	94.07
AT-Z-03	93	amph	54.21	0.12	3.95		7.31	0.14	18.96	12.48	0.59	0.16	97.92
AT-Z-03	94	amph	53.98	0.09	3.91		7.59	0.18	18.74	12.44	0.69	0.19	97.81
AT-Z-03	95	amph	54.27	0.18	3.80		7.21	0.17	18.91	12.34	0.60	0.19	97.67
AT-Z-03	96	amph	52.95	0.18	4.37		7.73	0.13	18.47	12.36	0.73	0.24	97.16
AT-Z-03	97	amph	54.21	0.14	3.78		7.37	0.14	18.66	12.30	0.56	0.19	97.35
AT-Z-03	98	bt	38.82	1.40	15.06		11.15	0.05	18.28	0.00	0.11	9.52	94.38
AT-Z-03	99	bt	38.07	1.51	15.30		10.58	0.14	18.09	0.00	0.07	9.61	93.38
AT-Z-03	100	bt	38.65	1.26	14.83		10.70	0.12	19.63	0.00	0.05	8.56	93.80
AT-Z-03	101	amph	54.50	0.09	3.27		7.23	0.17	19.06	12.21	0.57	0.16	97.26
AT-Z-03	102	amph	54.34	0.14	3.56		7.26	0.14	19.23	11.88	0.56	0.17	97.28
AT-Z-03	103	amph	54.78	0.15	3.20		7.30	0.08	19.26	12.20	0.55	0.14	97.66
AT-Z-03	104	amph	54.34	0.10	3.66		7.16	0.18	19.06	12.21	0.59	0.20	97.50
AT-Z-03	105	amph	56.17	0.06	2.24		6.88	0.16	19.74	12.20	0.38	0.07	97.89
AT-Z-03	106	pl	62.99	0.00	23.23		0.16	0.01	0.01	4.77	8.81	0.09	100.07
AT-Z-03	107	pl	62.66	0.01	23.12		0.14	0.00	0.00	4.78	8.91	0.19	99.81
AT-Z-03	108	pl	62.86	0.00	23.28		0.27	0.02	0.00	4.71	8.75	0.26	100.16
AT-Z-03	109	pl	62.69	0.00	23.61		0.14	0.01	0.02	5.03	8.89	0.15	100.54
AT-Z-03	110	pl	62.58	0.01	23.11		0.12	0.00	0.03	4.57	8.94	0.25	99.61

Sample	spot #	mineral	SiO2	TiO2	Al2O3	Cr2O3	FeO	MnO	MgO	CaO	Na2O	K2O	wt% total
AT-Z-03	111	bt	39.00	1.74	14.79		10.63	0.03	18.57	0.00	0.23	9.18	94.16
AT-Z-03	112	bt	38.90	1.63	15.04		10.96	0.08	18.40	0.00	0.13	9.38	94.54
AT-Z-03	113	bt	39.02	1.66	14.86		10.66	0.09	18.66	0.00	0.14	9.42	94.50
AT-Z-03	114	bt	38.84	1.49	14.59		10.69	0.09	18.52	0.00	0.05	9.58	93.85
AT-Z-03	115	amph	55.34	0.11	2.81		6.89	0.19	19.35	12.27	0.42	0.13	97.51
AT-Z-03	116	amph	54.88	0.14	3.12		7.23	0.17	19.27	12.52	0.55	0.14	98.02
AT-Z-03	117	amph	54.85	0.13	2.47		6.83	0.20	19.65	12.56	0.49	0.10	97.27
AT-Z-03	118	amph	55.29	0.15	2.82		7.16	0.11	19.51	12.47	0.46	0.11	98.08
AT-Z-03	119	amph	54.71	0.11	3.43		7.37	0.15	18.93	12.48	0.55	0.16	97.89
AT-Z-03	120	pl	62.30	0.05	23.86		0.12	0.00	0.00	5.16	8.83	0.11	100.43
AT-Z-03	121	pl	62.52	0.00	23.69		0.15	0.00	0.01	4.98	8.64	0.44	100.43
AT-Z-03	122	pl	62.33	0.02	23.63		0.17	0.00	0.01	5.17	8.81	0.10	100.24
AT-Z-03	123	pl	63.04	0.00	23.10		0.12	0.01	0.02	4.79	8.92	0.17	100.17
AT-Z-03	124	pl	61.81	0.00	23.62		0.17	0.01	0.00	5.14	8.74	0.16	99.64
AT-Z-03	125	bt	39.07	1.78	14.49		11.50	0.08	18.21	0.00	0.14	9.16	94.43
AT-Z-03	126	bt	38.97	1.55	15.14		10.82	0.12	18.45	0.00	0.07	9.57	94.70
AT-Z-03	127	bt	38.79	1.61	14.74		11.07	0.07	18.06	0.00	0.08	9.59	94.00
CL-18-02A	1	amph	56.48	0.11	1.71		5.78	0.07	20.70	12.55	0.44	0.13	97.96
CL-18-02A	2	amph	56.98	0.13	1.51		5.65	0.09	20.99	12.55	0.31	0.13	98.34
CL-18-02A	3	amph	56.25	0.14	1.54		5.66	0.05	20.64	12.61	0.35	0.14	97.38
CL-18-02A	4	amph	56.66	0.02	0.95		5.29	0.09	21.25	12.76	0.21	0.05	97.27
CL-18-02A	5	amph	56.23	0.09	1.83		5.69	0.04	20.87	12.47	0.43	0.11	97.75
CL-18-02A	8	kfs	64.42	0.00	18.40		0.02	0.00	0.00	0.00	1.10	15.12	99.07
CL-18-02A	9	kfs	62.79	0.00	18.43		0.02	0.03	0.00	0.00	0.75	15.07	97.08
CL-18-02A	10	amph	56.36	0.11	1.34		5.83	0.06	20.90	12.98	0.24	0.08	97.90
CL-18-02A	11	amph	55.53	0.09	1.71		6.13	0.04	20.33	12.63	0.40	0.10	96.97
CL-18-02A	12	amph	54.73	0.09	2.52		6.38	0.05	19.97	12.81	0.45	0.19	97.18
CL-18-02A	13	kfs	64.19	0.00	18.28		0.10	0.00	0.00	0.00	1.43	14.66	98.66
CL-18-02A	14	kfs	63.97	0.01	18.35		0.20	0.01	0.00	0.00	1.35	14.74	98.64
CL-18-02A	15	kfs	63.71	0.01	18.35		0.11	0.00	0.00	0.00	1.58	14.36	98.11

Sample	spot #	mineral	SiO2	TiO2	Al2O3	Cr2O3	FeO	MnO	MgO	CaO	Na2O	K2O	wt% total
CL-18-02A	16	bt	39.13	1.96	14.43		9.95	0.02	19.04	0.00	0.04	9.72	94.30
CL-18-02A	17	bt	38.91	2.07	14.49		10.18	0.03	19.00	0.00	0.08	9.74	94.48
CL-18-02A	18	bt	39.28	2.04	14.48		9.91	0.05	19.13	0.00	0.07	9.96	94.91
CL-18-02A	19	amph	56.26	0.09	1.36		6.04	0.05	20.44	12.51	0.34	0.13	97.23
CL-18-02A	20	amph	57.03	0.02	1.02		5.84	0.02	20.69	12.61	0.24	0.11	97.59
CL-18-02A	21	amph	54.33	0.23	3.66		6.94	0.00	19.36	12.62	0.75	0.18	98.07
CL-18-02A	22	amph	56.87	0.13	1.24		4.74	0.08	21.37	13.18	0.32	0.09	98.02
CL-18-02A	23	amph	55.86	0.19	2.00		6.47	0.08	20.20	12.70	0.42	0.13	98.05
CL-18-02A	24	amph	56.68	0.08	1.21		5.91	0.07	20.55	12.67	0.29	0.09	97.54
CL-18-02A	25	amph	56.82	0.01	0.71		6.09	0.08	20.82	13.01	0.19	0.06	97.79
CL-18-02A	26	kfs	63.95	0.01	18.33		0.15	0.00	0.02	0.00	1.60	13.95	98.00
CL-18-02A	27	kfs	64.32	0.00	18.28		0.19	0.01	0.00	0.00	1.12	14.84	98.76
CL-18-02A	28	kfs	64.09	0.00	18.25		0.08	0.00	0.01	0.00	1.33	14.60	98.36
CL-18-02A	29	kfs	63.17	0.00	18.41		0.12	0.00	0.00	0.00	1.81	13.32	96.83
CL-18-02A	30	bt	38.82	3.32	13.88	0.38	10.21	0.08	17.68	0.00	0.04	9.85	94.26
CL-18-02A	31	bt	38.54	3.43	13.92	0.43	10.91	0.04	17.58	0.00	0.06	9.93	94.84
CL-18-02A	32	bt	39.16	3.18	14.02	0.72	10.30	0.06	18.13	0.00	0.03	9.65	95.25
CL-18-02A	33	bt	39.16	3.06	14.00	0.55	10.13	0.00	18.39	0.02	0.06	9.92	95.31
CL-18-02A	34	bt	39.34	2.93	14.17	0.34	10.36	0.07	18.48	0.00	0.05	10.03	95.77
CL-18-02A	35	pl	67.91	0.02	19.87		0.09	0.00	0.01	0.47	11.48	0.15	100.00
CL-18-02A	36	pl	65.65	0.00	19.57		0.09	0.01	0.60	0.87	6.96	5.73	99.48
CL-18-02A	37	pl	64.82	0.03	21.67		0.09	0.00	0.01	2.99	9.87	0.19	99.66
CL-18-02A	38	pl	68.04	0.00	19.37		0.14	0.00	0.01	0.56	11.23	0.18	99.53
CL-18-02A	39	kfs	64.65	0.00	18.34		0.01	0.00	0.00	0.00	1.74	14.19	98.93
CL-18-02A	40	kfs	64.11	0.02	18.20		0.07	0.00	0.00	0.00	1.15	14.79	98.34
CL-18-02A	41	kfs	64.12	0.00	18.13		0.08	0.03	0.01	0.00	1.31	14.54	98.22
CL-18-02A	42	amph	54.72	0.21	3.56		3.97	0.05	20.69	12.68	0.66	0.25	96.79
CL-18-02A	43	amph	55.71	0.20	2.52		4.15	0.01	21.02	12.87	0.52	0.14	97.14
CL-18-02A	44	amph	57.02	0.09	1.34		4.51	0.07	21.32	12.90	0.32	0.07	97.65
CL-18-02A	45	amph	56.39	0.13	1.49		4.40	0.07	21.42	12.87	0.30	0.12	97.19

Sample	spot #	mineral	SiO2	TiO2	Al2O3	Cr2O3	FeO	MnO	MgO	CaO	Na2O	K2O	wt% total
CL-18-02A	46	amph	56.60	0.06	1.49		4.48	0.02	21.56	13.19	0.32	0.08	97.79
CL-18-02A	47	amph	56.54	0.07	1.68		4.49	0.04	21.24	12.90	0.35	0.13	97.44
CL-18-02A	48	bt	39.72	2.55	14.18	0.27	8.07	0.03	20.17	0.00	0.07	9.87	94.94
CL-18-02A	49	bt	40.03	2.14	14.45	0.37	7.81	0.01	20.47	0.00	0.08	9.93	95.27
CL-18-02A	50	bt	39.92	2.55	14.13	0.38	7.90	0.01	19.87	0.00	0.04	9.89	94.70
CL-18-02A	51	bt	39.65	1.93	14.65	0.33	7.64	0.03	20.64	0.00	0.06	9.98	94.92
CL-18-02A	52	bt	40.01	2.03	14.25		7.54	0.03	20.69	0.00	0.08	9.99	94.62
CL-18-02A	53	bt	39.89	2.39	14.27		7.76	0.03	20.32	0.00	0.07	10.08	94.81
CL-18-02A	54	bt	39.67	2.60	14.42		7.96	0.01	19.80	0.00	0.09	9.89	94.45
CL-18-02A	55	amph	56.02	0.12	2.21		4.99	0.06	20.94	12.79	0.41	0.13	97.66
CL-18-02A	56	amph	56.67	0.09	1.16		4.46	0.03	21.54	12.84	0.31	0.04	97.14
CL-18-02A	57	amph	56.68	0.01	1.59		4.75	0.06	20.93	12.96	0.32	0.11	97.41
CL-18-02A	58	amph	55.59	0.11	2.40		4.99	0.06	20.90	12.68	0.51	0.19	97.43
CL-18-02A	59	amph	56.47	0.07	1.40		4.51	0.07	21.19	12.96	0.27	0.09	97.04
CL-18-02A	60	kfs	63.98	0.00	18.24		0.11	0.01	0.00	0.07	0.81	14.99	98.23
CL-18-02A	61	pl	66.79	0.01	20.79		0.08	0.01	0.01	1.07	11.13	0.17	100.05
CL-18-02A	62	pl	66.73	0.00	20.57		0.11	0.01	0.01	0.81	11.34	0.12	99.70
CL-18-02A	63	pl	67.98	0.03	19.59		0.15	0.00	0.00	0.79	11.21	0.19	99.94
CL-18-02A	64	kfs	64.19	0.00	18.35		0.07	0.01	0.01	0.00	0.98	15.05	98.65
CL-18-02A	65	kfs	63.95	0.01	18.13		0.12	0.00	0.01	0.00	1.16	14.81	98.18
CL-18-02A	66	kfs	63.95	0.00	18.33		0.04	0.02	0.00	0.00	1.18	15.14	98.66
CL-18-02A	67	kfs	64.55	0.03	18.30		0.05	0.00	0.00	0.00	1.50	14.47	98.91
CL-18-02A	68	bt	40.22	2.49	14.11		8.14	0.03	20.24	0.00	0.07	10.07	95.37
CL-18-02A	69	bt	39.60	2.24	14.43		7.95	0.00	20.08	0.00	0.07	9.90	94.27
CL-18-02A	70	bt	39.86	2.25	14.28		7.89	0.04	20.38	0.00	0.06	9.99	94.74
CL-18-02A	71	bt	39.94	2.54	14.17		7.92	0.05	20.15	0.00	0.06	9.84	94.66
CL-18-04	56	amph	47.25	0.72	8.40	0.12	14.48	0.27	12.50	11.84	0.98	0.73	97.29
CL-18-04	57	amph	47.76	0.43	7.36	0.06	13.86	0.15	16.29	7.47	0.66	0.50	94.53
CL-18-04	58	amph	46.85	0.56	8.41	0.08	15.49	0.26	12.26	11.93	1.15	0.79	97.79
CL-18-04	59	amph	48.53	0.47	6.86	0.03	14.13	0.31	13.55	11.69	0.72	0.54	96.83

Sample	spot #	mineral	SiO2	TiO2	Al2O3	Cr2O3	FeO	MnO	MgO	CaO	Na2O	K2O	wt% total
CL-18-04	60	amph	48.33	0.52	6.75	0.06	15.34	0.31	12.62	12.23	0.73	0.56	97.44
CL-18-04	61	pl	61.34	0.00	24.60		0.18	0.01	0.01	5.64	8.51	0.13	100.41
CL-18-04	62	pl	61.16	0.00	24.44		0.17	0.00	0.00	5.64	8.49	0.29	100.20
CL-18-04	63	pl	61.37	0.01	24.40		0.12	0.01	0.00	5.73	8.32	0.25	100.22
CL-18-04	64	pl	61.22	0.01	24.41		0.18	0.06	0.00	5.60	8.44	0.21	100.12
CL-18-04	65	pl	61.23	0.00	24.42		0.13	0.05	0.00	5.76	8.31	0.24	100.13
CL-18-04	66	bt	36.35	3.30	15.06		19.20	0.14	11.36	0.00	0.08	9.81	95.28
CL-18-04	67	bt	36.15	2.51	15.07		20.21	0.10	11.54	0.00	0.05	9.32	94.95
CL-18-04	68	bt	36.15	2.57	15.26		19.94	0.18	11.33	0.00	0.08	9.44	94.94
CL-18-04	69	bt	36.52	3.40	15.02		18.89	0.15	11.13	0.00	0.08	9.80	94.99
CL-18-04	70	bt	36.63	2.53	14.94		19.28	0.17	11.85	0.00	0.06	9.61	95.07
CL-18-04	71	kfs	62.58	0.00	18.65		0.21	0.00	0.00	0.00	1.03	14.83	97.29
CL-18-04	72	kfs	62.76	0.01	18.68		0.09	0.02	0.00	0.00	0.80	15.14	97.49
CL-18-04	73	amph	46.43	0.63	8.85		15.41	0.28	12.32	11.99	1.17	0.83	97.89
CL-18-04	74	amph	45.68	0.46	9.89		15.64	0.31	11.60	11.69	1.30	0.86	97.44
CL-18-04	75	amph	46.57	0.51	9.04		15.27	0.27	12.15	11.55	1.17	0.79	97.32
CL-18-04	76	amph	46.42	0.68	8.68		15.32	0.23	12.08	11.78	1.12	0.81	97.11
CL-18-04	77	amph	45.82	0.74	8.81		16.41	0.24	11.37	11.89	1.05	0.87	97.21
CL-18-04	78	amph	46.85	0.64	8.28		15.16	0.26	12.52	11.93	1.05	0.80	97.48
CL-18-04	79	pl	61.15	0.02	24.50		0.17	0.02	0.02	5.71	8.44	0.16	100.19
CL-18-04	80	pl	62.02	0.03	27.41		0.35	0.00	0.47	1.43	8.18	2.24	102.13
CL-18-04	81	pl	61.48	0.00	24.21		0.18	0.00	0.00	5.60	8.50	0.20	100.17
CL-18-04	82	pl	61.27	0.01	24.80		0.13	0.00	0.02	6.03	8.22	0.17	100.65
CL-18-04	83	pl	61.13	0.01	24.39		0.15	0.00	0.01	5.89	8.38	0.21	100.17
CL-18-04	84	chl	26.83	0.01	18.32	0.15	25.00	0.38	16.47	0.08	0.01	0.00	87.25
CL-18-04	85	cal	0.01	0.00	0.00	0.00	1.35	0.26	0.52	57.97	0.03	0.02	60.15
CL-18-04	86	amph	49.54	0.39	5.54		14.73	0.27	14.04	12.13	0.79	0.48	97.91
CL-18-04	87	amph	48.99	0.41	6.79		15.07	0.27	12.90	11.87	0.91	0.54	97.75
CL-18-04	88	amph	46.78	0.58	8.31		15.75	0.23	12.31	11.89	0.99	0.75	97.59
CL-18-04	89	amph	48.17	0.55	7.16		14.93	0.28	12.82	11.90	0.89	0.60	97.28

Sample	spot #	mineral	SiO2	TiO2	Al2O3	Cr2O3	FeO	MnO	MgO	CaO	Na2O	K2O	wt% total
CL-18-04	90	amph	47.07	0.72	7.85		15.28	0.27	12.50	11.72	0.98	0.68	97.09
CL-18-04	91	pl	66.69	0.00	20.28		0.56	0.00	0.19	0.53	11.09	0.19	99.54
CL-18-04	92	pl	67.49	0.04	20.45		0.40	0.00	0.40	0.49	11.00	0.14	100.41
CL-18-04	93	pl	65.16	0.03	21.11		0.48	0.00	0.68	1.31	10.11	0.57	99.44
CL-18-04	94	pl	61.73	0.00	24.57		0.22	0.02	0.00	5.49	8.75	0.21	100.98
CL-18-04	95	pl	61.31	0.01	24.98		0.13	0.00	0.02	5.85	8.36	0.20	100.86
CL-18-04	96	pl	60.97	0.00	24.97		0.12	0.00	0.11	5.69	8.19	0.25	100.31
CL-18-04	97	kfs	62.38	0.03	19.04		0.17	0.03	0.01	0.00	1.09	14.51	97.26
CL-18-04	98	amph	49.31	0.38	6.90		14.22	0.30	13.45	11.95	1.01	0.53	98.06
CL-18-04	99	amph	46.70	0.67	8.58		15.18	0.25	12.15	11.70	1.08	0.79	97.12
CL-18-04	100	amph	47.37	0.66	8.01		14.97	0.27	12.72	11.76	1.08	0.70	97.55
CL-18-04	101	amph	47.85	0.61	7.77		14.68	0.21	12.88	11.79	1.01	0.66	97.47
CL-18-04	102	amph	48.89	0.34	6.97		14.25	0.23	13.31	11.83	0.97	0.45	97.25
CL-18-04	103	amph	46.57	0.63	8.59		15.26	0.25	12.34	11.94	1.19	0.82	97.58
CL-18-04	104	pl	60.88	0.02	24.91		0.14	0.03	0.00	6.06	8.31	0.22	100.57
CL-18-04	105	pl	61.36	0.02	24.57		0.14	0.00	0.00	5.71	8.46	0.23	100.48
CL-18-04	106	pl	64.03	0.04	22.83		0.19	0.00	0.00	3.46	9.71	0.16	100.42
CL-18-04	107	pl	67.65	0.02	20.64		0.21	0.00	0.00	0.90	11.59	0.10	101.11
CL-18-04	108	pl	61.41	0.02	24.33		0.15	0.03	0.00	5.68	8.52	0.19	100.34
CL-18-04	109	chl	27.15	0.02	18.20	0.00	25.01	0.37	16.37	0.07	0.00	0.00	87.19
CL-18-04	110	chl	26.91	0.01	18.14	0.02	25.46	0.36	16.20	0.06	0.01	0.00	87.18
DB-GR-MG	29	kfs	65.33	0.00	18.25	0.05	0.09	0.00	0.00	0.04	1.09	15.47	100.32
DB-GR-MG	30	kfs	65.07	0.00	18.48	0.00	0.12	0.00	0.01	0.00	0.90	15.58	100.16
DB-GR-MG	31	kfs	64.47	0.00	18.29	0.00	0.10	0.01	0.00	0.00	0.90	15.70	99.47
DB-GR-MG	32	bt	36.47	2.83	17.39	0.06	15.75	0.43	12.34	0.00	0.12	9.41	94.80
DB-GR-MG	33	bt	37.00	3.00	17.37	0.10	15.94	0.46	12.22	0.00	0.10	9.88	96.06
DB-GR-MG	34	bt	36.45	2.95	17.83	0.08	15.01	0.43	12.25	0.06	0.16	9.46	94.67
MN-03	1	amph	50.44	0.51	5.25		11.06	0.11	16.03	12.05	1.05	0.45	96.95
MN-03	2	amph	51.00	0.40	4.80		10.50	0.17	16.33	11.98	0.82	0.39	96.39
MN-03	3	amph	51.17	0.36	4.75		10.57	0.12	16.53	12.16	0.85	0.36	96.87

Sample	spot #	mineral	SiO2	TiO2	Al2O3	Cr2O3	FeO	MnO	MgO	CaO	Na2O	K2O	wt% total
MN-03	4	kfs	61.43	0.02	18.36		0.07	0.00	0.01	0.00	0.62	14.65	95.16
MN-03	5	amph	52.03	0.37	4.31		10.53	0.20	16.75	12.17	0.75	0.30	97.41
MN-03	6	pl	63.37	0.00	22.77		0.24	0.00	0.01	4.03	9.37	0.31	100.10
MN-03	7	pl	63.42	0.00	22.55		0.34	0.02	0.07	2.31	9.16	0.68	98.54
MN-03	8	pl	63.82	0.00	22.33		0.15	0.00	0.01	3.48	9.68	0.20	99.68
MN-03	9	pl	64.71	0.00	22.51		0.45	0.02	0.12	0.76	9.50	1.84	99.91
MN-03	10	pl	64.45	0.03	22.26		0.17	0.00	0.02	3.30	9.83	0.23	100.29
MN-03	11	bt	37.11	2.81	14.01		14.73	0.09	15.17	0.03	0.05	8.69	92.69
MN-03	12	bt	37.69	3.09	14.65		13.79	0.11	15.23	0.00	0.04	9.44	94.05
MN-03	13	bt	37.80	3.09	13.86		14.64	0.07	15.38	0.03	0.07	9.04	93.99
MN-03	14	chl	28.90	0.04	17.30	0.69	19.11	0.18	21.33	0.09	0.00	0.03	87.68
MN-03	15	chl	29.18	0.07	17.82	0.46	16.05	0.15	23.07	0.00	0.00	0.00	86.80
MN-03	16	chl	29.47	0.02	17.35	0.21	17.96	0.21	22.06	0.11	0.00	0.00	87.39
MN-03	17	amph	50.64	0.33	7.34	0.21	12.38	0.15	18.66	8.82	0.61	0.28	99.42
MN-03	18	chl	29.76	0.04	16.69	0.38	15.90	0.16	22.87	0.14	0.04	0.08	86.07
MN-03	19	chl	30.45	0.12	15.07	0.30	18.00	0.22	22.17	0.14	0.01	0.01	86.47
MN-03	20	chl	29.29	0.05	18.34	0.39	16.82	0.11	23.00	0.04	0.01	0.02	88.06
MN-03	21	amph	50.97	0.43	5.13		10.83	0.16	16.34	11.98	0.99	0.42	97.25
MN-03	22	amph	51.40	0.49	5.00		10.89	0.16	16.46	12.10	0.94	0.40	97.85
MN-03	23	amph	50.50	0.40	5.48		11.19	0.16	16.06	11.74	1.04	0.41	96.96
MN-03	24	amph	51.57	0.44	4.63		10.48	0.13	16.78	12.27	0.80	0.34	97.43
MN-03	25	kfs	62.21	0.01	18.63		0.10	0.00	0.01	0.00	1.35	13.79	96.10
MN-03	26	pl	63.45	0.00	22.98		0.20	0.00	0.00	4.21	9.04	0.36	100.24
MN-03	27	pl	63.88	0.00	22.46		0.09	0.00	0.00	3.77	9.36	0.35	99.91
MN-03	28	pl	64.12	0.00	23.03		0.13	0.00	0.00	3.49	9.35	0.19	100.32
MN-03	29	pl	63.72	0.00	22.59		0.17	0.00	0.04	3.81	9.04	0.34	99.71
MN-03	30	pl	63.29	0.01	22.63		0.06	0.00	0.03	3.99	9.18	0.31	99.50
MN-03	31	bt	37.63	3.46	13.81		15.15	0.04	14.97	0.00	0.08	9.47	94.60
MN-03	32	bt	36.55	2.94	14.38		15.06	0.11	16.39	0.02	0.01	7.87	93.33
MN-03	33	bt	36.61	2.69	14.10		15.29	0.07	15.20	0.03	0.03	8.47	92.50

Sample	spot #	mineral	SiO2	TiO2	Al2O3	Cr2O3	FeO	MnO	MgO	CaO	Na2O	K2O	wt% total
MN-03	34	bt	37.26	3.07	14.03		15.06	0.03	15.12	0.02	0.05	8.99	93.62
MN-03	35	amph	51.38	0.40	5.06		10.80	0.15	16.28	11.79	0.96	0.43	97.25
MN-03	36	kfs	60.46	0.00	18.53		0.14	0.00	0.01	0.00	1.03	13.31	93.48
MN-03	37	amph	51.72	0.36	4.82		10.74	0.12	16.31	11.83	0.90	0.38	97.18
MN-03	38	kfs	60.86	0.00	17.92		0.12	0.00	0.00	0.00	0.63	14.44	93.97
MN-03	39	amph	51.13	0.41	4.87		10.90	0.16	16.22	12.13	0.85	0.32	96.98
MN-03	40	pl	66.74	0.00	21.27		0.31	0.00	0.06	1.37	10.72	0.32	100.80
MN-03	41	pl	65.24	0.01	21.12		0.39	0.04	0.19	1.45	10.32	0.71	99.47
MN-03	42	pl	62.99	0.00	23.31		0.17	0.00	0.00	4.07	9.30	0.14	99.98
MN-03	43	pl	63.09	0.02	22.58		0.53	0.00	0.23	1.17	9.29	1.84	98.75
MN-03	45	chl	30.71	0.13	14.90	0.51	15.64	0.21	20.71	0.12	0.00	0.11	83.03
MN-03	46	chl	28.76	0.11	18.21	0.33	16.92	0.23	22.24	0.07	0.00	0.00	86.88
MN-03	47	chl	29.55	0.04	16.67	0.68	17.83	0.17	21.80	0.06	0.00	0.00	86.80
MN-03	48	bt	37.44	3.05	13.95		15.25	0.11	15.14	0.02	0.05	8.99	94.00
MN-03	49	bt	37.06	2.71	14.23		15.63	0.10	16.14	0.05	0.01	8.69	94.62
MN-03	50	bt	34.00	2.22	14.86		13.78	0.09	19.92	0.16	0.02	5.19	90.24
MN-03	51	chl	29.10	0.04	18.90	0.37	16.19	0.14	22.36	0.07	0.01	0.00	87.19
MN-03	52	amph	51.97	0.31	4.23		10.34	0.14	16.89	11.97	0.78	0.32	96.94
MN-03	53	amph	52.72	0.27	3.54		9.93	0.14	17.19	12.61	0.68	0.25	97.34
MN-03	54	amph	52.45	0.26	3.62		10.02	0.14	17.43	12.09	0.68	0.20	96.88
MN-03	55	amph	51.35	0.44	4.81		10.57	0.21	16.43	12.09	0.94	0.39	97.24
MN-03	56	amph	51.70	0.41	4.89		10.83	0.17	16.69	12.08	0.76	0.35	97.87
MN-03	57	pl	63.97	0.01	22.65		0.12	0.01	0.00	3.93	9.12	0.34	100.14
MN-03	58	pl	63.27	0.03	22.61		0.38	0.01	0.43	2.14	9.22	0.75	98.84
MN-03	59	pl	65.59	0.00	22.78		0.83	0.02	0.18	0.51	10.34	0.89	101.14
MN-03	60	pl	63.68	0.00	22.12		0.72	0.01	0.35	2.19	9.85	0.52	99.44
MN-03	61	pl	63.48	0.01	22.32		0.55	0.04	0.21	1.87	9.73	0.62	98.81
MN-03	62	bt	36.72	3.00	14.31		15.24	0.09	15.07	0.01	0.04	8.60	93.07
MN-03	63	bt	36.55	1.44	14.36		15.33	0.21	18.57	0.10	0.05	7.84	94.45
MN-03	64	bt	36.45	2.97	14.31		15.22	0.13	16.61	0.09	0.06	7.70	93.54

Sample	spot #	mineral	SiO2	TiO2	Al2O3	Cr2O3	FeO	MnO	MgO	CaO	Na2O	K2O	wt% total
MN-03	65	bt	37.58	2.92	14.31		15.50	0.12	16.03	0.00	0.03	8.38	94.88
MN-03	66	chl	28.92	0.02	17.10	0.43	17.57	0.18	21.95	0.07	0.03	0.00	86.26
MN-03	67	chl	29.76	0.05	16.02	0.67	18.85	0.19	21.15	0.08	0.00	0.01	86.79
MN-03	68	chl	28.96	0.07	15.99	0.23	14.67	0.14	22.20	0.74	0.01	0.00	83.01
MN-03	69	chl	29.97	0.06	16.93	0.52	17.76	0.16	22.63	0.11	0.04	0.02	88.20
MN-03	70	chl	29.57	0.06	17.44	0.24	16.80	0.19	22.88	0.08	0.01	0.00	87.28
MN-03	71	amph	50.37	0.42	5.33		10.82	0.14	15.95	12.09	0.95	0.38	96.45
MN-03	72	amph	49.76	0.35	5.35		10.94	0.12	15.71	11.83	0.91	0.43	95.41
MN-03	73	kfs	61.89	0.02	18.50		0.03	0.00	0.00	0.00	1.02	14.30	95.76
MN-03	74	amph	50.84	0.46	5.14		10.72	0.17	16.21	12.16	0.92	0.41	97.03
MN-03	75	amph	50.21	0.39	5.62		10.91	0.14	16.20	12.00	0.93	0.45	96.85
MN-03	76	pl	63.30	0.00	22.98		0.15	0.02	0.00	4.12	8.97	0.41	99.96
MN-03	77	pl	62.81	0.02	22.81		0.16	0.00	0.00	4.11	9.15	0.31	99.37
MN-03	78	pl	63.16	0.03	23.06		0.17	0.00	0.00	4.07	9.37	0.13	99.99
MN-03	79	pl	63.38	0.02	22.66		0.11	0.01	0.00	3.92	9.02	0.34	99.47
MN-03	80	pl	62.50	0.00	22.74		0.52	0.00	0.15	4.12	9.09	0.39	99.52
MN-03	81	bt	36.69	2.70	13.99		14.87	0.12	16.17	0.09	0.07	8.45	93.16
MN-03	82	bt	37.56	2.85	14.22		14.73	0.05	15.62	0.03	0.07	9.11	94.26
MN-03	83	bt	36.17	2.66	14.92		14.62	0.09	16.55	0.00	0.04	8.01	93.07
MN-03	84	bt	37.04	3.91	14.14		14.69	0.12	14.65	0.00	0.07	9.52	94.13
MN-03	85	bt	37.25	2.60	14.14		14.22	0.06	15.97	0.12	0.07	6.98	91.41
PI-G1-01	159	amph	56.01	0.10	1.40	0.20	5.76	0.17	20.65	12.37	0.54	0.14	97.34
PI-G1-01	160	amph	56.51	0.07	1.00	0.07	5.55	0.17	20.96	12.52	0.45	0.10	97.40
PI-G1-01	161	amph	56.12	0.08	1.13	0.04	5.66	0.18	20.72	12.31	0.47	0.11	96.83
PI-G1-01	162	amph	56.16	0.08	1.27	0.09	5.68	0.16	20.79	12.37	0.50	0.13	97.22
PI-G1-01	163	amph	56.18	0.08	1.19	0.06	5.62	0.17	20.73	12.34	0.50	0.13	96.98
PI-G1-01	164	amph	55.30	0.13	1.84	0.09	6.02	0.16	20.31	12.23	0.60	0.18	96.87
PI-G1-01	165	amph	55.51	0.13	1.74	0.09	6.02	0.14	20.49	12.28	0.54	0.18	97.11
PI-G1-01	166	kfs	62.96	0.04	18.92	0.00	0.10	0.00	0.00	0.00	1.51	14.43	97.96
PI-G1-01	167	pl	65.54	0.02	21.40	0.00	0.12	0.00	0.00	1.93	10.46	0.25	99.73

Sample	spot #	mineral	SiO2	TiO2	Al2O3	Cr2O3	FeO	MnO	MgO	CaO	Na2O	K2O	wt% total
PI-G1-01	168	pl	65.91	0.01	21.42	0.00	0.09	0.00	0.00	1.88	10.56	0.22	100.09
PI-G1-01	169	pl	65.85	0.01	21.66	0.00	0.10	0.03	0.00	1.87	10.67	0.11	100.30
PI-G1-01	170	pl	66.18	0.01	21.46	0.00	0.12	0.02	0.01	1.67	10.75	0.23	100.45
PI-G1-01	171	pl	65.22	0.01	21.73	0.01	0.13	0.00	0.00	1.98	10.75	0.12	99.95
PI-G1-01	172	pl	65.55	0.00	21.40	0.01	0.21	0.00	0.01	1.71	10.81	0.15	99.86
PI-G1-01	173	bt	39.24	2.44	13.35	0.24	9.18	0.09	19.46	0.00	0.07	9.90	93.97
PI-G1-01	174	bt	39.76	2.19	13.35	0.32	9.28	0.09	19.94	0.00	0.05	9.90	94.89
PI-G1-01	175	bt	39.82	2.39	13.37	0.28	9.35	0.08	19.63	0.00	0.07	9.92	94.91
PI-G1-01	176	bt	39.81	2.38	13.25	0.30	9.30	0.06	19.87	0.00	0.06	9.92	94.95
PI-G1-01	179	amph	55.36	0.14	1.83	0.06	6.00	0.13	20.47	12.14	0.63	0.20	96.97
PI-G1-01	180	amph	56.56	0.10	1.23	0.09	5.56	0.17	21.13	12.32	0.47	0.12	97.76
PI-G1-01	181	amph	56.88	0.06	1.00	0.06	5.41	0.10	21.17	12.48	0.41	0.10	97.66
PI-G1-01	182	amph	55.80	0.10	1.39	0.07	5.71	0.17	20.60	12.25	0.51	0.14	96.74
PI-G1-01	183	amph	55.77	0.11	1.45	0.06	5.78	0.15	20.60	12.28	0.52	0.13	96.86
PI-G1-01	184	amph	55.45	0.14	1.77	0.15	5.90	0.15	20.44	12.19	0.60	0.18	96.95
PI-G1-01	185	amph	55.65	0.11	1.45	0.08	5.74	0.12	20.48	12.29	0.54	0.16	96.62
PI-G1-01	186	amph	56.00	0.07	1.30	0.10	5.86	0.14	20.84	12.41	0.53	0.16	97.40
PI-G1-01	187	pl	65.50	0.01	21.63	0.00	0.15	0.00	0.00	2.00	10.55	0.28	100.13
PI-G1-01	188	pl	66.92	0.01	20.45	0.00	0.10	0.02	0.00	1.08	11.02	0.15	99.74
PI-G1-01	189	pl	66.49	0.01	21.32	0.00	0.09	0.00	0.00	1.65	10.78	0.18	100.53
PI-G1-01	190	pl	65.39	0.01	21.28	0.00	0.24	0.02	0.00	1.49	10.98	0.25	99.66
PI-G1-01	191	bt	39.45	2.16	13.61	0.25	9.28	0.08	19.39	0.00	0.08	10.03	94.34
PI-G1-01	192	bt	39.36	2.21	13.82	0.37	9.24	0.06	19.38	0.00	0.07	10.03	94.55
PI-G1-01	193	bt	39.66	2.17	13.68	0.27	9.09	0.09	19.94	0.00	0.07	9.89	94.85
PI-G1-01	194	bt	39.25	2.45	13.39	0.33	9.11	0.08	19.33	0.00	0.08	9.95	93.97
PI-G1-03	40	amph	44.25	0.87	11.26	0.33	10.22	0.07	16.68	10.70	1.59	1.29	97.27
PI-G1-03	41	amph	56.04	0.07	1.30	0.12	6.24	0.04	20.57	12.92	0.39	0.05	97.75
PI-G1-03	42	amph	45.33	0.70	10.95	0.16	9.92	0.02	15.06	12.06	2.00	0.88	97.07
PI-G1-03	43	amph	45.29	0.76	10.75	0.15	10.06	0.05	15.03	12.02	1.92	0.91	96.93
PI-G1-03	44	amph	44.11	0.71	11.93	0.27	10.48	0.13	14.62	12.00	2.00	1.03	97.30

Sample	spot #	mineral	SiO2	TiO2	Al2O3	Cr2O3	FeO	MnO	MgO	CaO	Na2O	K2O	wt% total
PI-G1-03	45	amph	44.06	0.59	12.38	0.25	10.24	0.09	15.28	11.53	2.02	0.78	97.21
PI-G1-03	46	amph	43.41	0.77	12.13	0.24	10.61	0.07	14.24	12.15	2.04	1.01	96.67
PI-G1-03	47	pl	60.63	0.01	24.18	0.04	0.19	0.03	0.01	5.25	8.54	0.14	99.03
PI-G1-03	48	pl	60.40	0.02	24.62	0.03	0.35	0.00	0.03	5.93	8.26	0.10	99.73
PI-G1-03	49	pl	59.22	0.03	23.84	0.00	0.33	0.03	3.93	6.06	7.81	0.09	101.33
PI-G1-03	50	bt	37.72	2.16	15.44	0.25	10.78	0.12	17.68	0.00	0.34	9.45	93.94
PI-G1-03	51	bt	38.14	2.36	15.50	0.26	10.80	0.06	18.35	0.00	0.34	9.57	95.38
PI-G1-03	52	bt	38.02	2.24	15.24	0.26	10.73	0.05	17.88	0.00	0.30	9.56	94.29
PI-G1-03	53	chl	37.22	0.04	14.07	0.01	1.11	0.08	33.12	0.28	0.03	0.03	85.99
PI-G1-03	54	chl	38.02	0.02	12.75	0.00	0.99	0.08	33.96	0.25	0.03	0.03	86.14
PI-G1-03	55	bt	38.07	1.65	15.85	0.10	10.79	0.02	18.38	0.00	0.38	9.32	94.55
PI-G1-03	56	amph	47.38	0.59	9.12	0.16	9.23	0.07	16.56	12.21	1.61	0.63	97.56
PI-G1-03	57	amph	45.12	0.77	10.77	0.25	10.35	0.05	14.96	12.00	1.88	0.92	97.07
PI-G1-03	58	amph	45.15	0.69	10.76	0.22	10.29	0.06	14.97	12.25	1.86	0.82	97.08
PI-G1-03	59	amph	45.37	0.76	10.23	0.24	10.04	0.06	15.06	12.25	1.95	0.65	96.62
PI-G1-03	60	amph	45.63	0.82	10.51	0.32	10.04	0.08	15.17	12.06	1.90	0.83	97.36
PI-G1-03	61	amph	45.24	0.78	10.24	0.33	9.94	0.07	15.08	12.30	1.81	0.79	96.58
PI-G1-03	62	pl	61.52	0.00	24.32	0.00	0.18	0.00	0.02	5.39	8.44	0.16	100.04
PI-G1-03	63	pl	61.39	0.02	24.07	0.00	0.16	0.00	0.00	5.50	8.20	0.16	99.50
PI-G1-03	64	pl	60.42	0.02	24.79	0.06	0.17	0.00	0.00	6.09	8.16	0.11	99.82
PI-G1-03	65	amph	45.33	0.69	10.61	0.33	10.31	0.07	15.10	12.12	1.80	0.87	97.22
PI-G1-03	66	amph	46.13	0.76	10.17	0.31	10.00	0.10	15.52	12.19	1.80	0.81	97.78
PI-G1-03	67	amph	45.13	0.73	10.53	0.2	9.93	0.04	15.13	12.14	1.84	0.85	96.53

ANEXO E - MATERIAL SUPLEMENTAR DO ARTIGO III
Supplementary Table A.1 - EMPA data

AMPHIBOLES

Sample	Rock group	obs	anal. #	SiO2	TiO2	Al2O3	Cr2O3	FeO	MnO	MgO	CaO	Na2O	K2O	Total	Cr ppm	XMg
AT-MZ-01	igneous apophysis	monzonite	46	43.69	0.8	9.45	0.06	18.59	0.2	10.23	11.59	1.41	1.19	97.21	410.52	0.5
AT-MZ-01	igneous apophysis	monzonite	48	44.2	0.79	9.28	0.06	18.63	0.22	10.51	11.48	1.35	1.14	97.67	410.52	0.5
AT-MZ-01	igneous apophysis	monzonite	52	43.97	0.85	9.5	0.03	18.85	0.18	10.42	11.48	1.55	1.16	97.99	205.26	0.5
AT-MZ-01	igneous apophysis	monzonite	58	43.4	0.98	9.67	0.04	18.4	0.23	10.48	11.63	1.34	1.12	97.29	273.68	0.5
AT-MZ-01	igneous apophysis	monzonite	64	43.58	0.85	9.67	0.02	18.28	0.24	10.31	11.42	1.53	1.2	97.09	136.84	0.5
AT-MZ-01	igneous apophysis	monzonite	26	44.01	0.83	9.38	0.03	18.18	0.24	10.8	11.45	1.45	1.18	97.53	205.26	0.51
AT-MZ-01	igneous apophysis	monzonite	50	44.2	0.78	9.29	0.07	18.16	0.22	10.74	11.56	1.5	1.11	97.63	478.94	0.51
AT-MZ-01	igneous apophysis	monzonite	60	43.98	0.79	9.41	0.04	18.28	0.24	10.57	11.39	1.45	1.2	97.34	273.68	0.51
AT-MZ-01	igneous apophysis	monzonite	54	44.8	0.67	8.75	0.06	17.81	0.22	10.97	11.52	1.39	0.97	97.17	410.52	0.52
AT-MZ-01	igneous apophysis	monzonite	56	45.25	0.73	8.28	0.03	17.79	0.23	11.27	11.58	1.4	0.91	97.47	205.26	0.53
AT-MZ-01	igneous apophysis	monzonite	66	45.21	0.62	8.81	0.06	17.62	0.24	11.17	11.38	1.47	1.04	97.61	410.52	0.53
AT-MZ-01	igneous apophysis	monzonite	44	45.89	0.64	7.77	0.04	16.96	0.19	11.79	11.79	1.15	0.83	97.07	273.68	0.55
AT-MZ-01	igneous apophysis	monzonite	57	43.8	0.9	9.51		18.34	0.2	10.39	11.36	1.51	1.35	97.36		0.5
AT-MZ-01	igneous apophysis	monzonite	2	44.13	0.93	9.27		17.82	0.21	10.49	11.48	1.55	1.12	96.99		0.51
AT-MZ-01	igneous apophysis	monzonite	14	43.93	0.78	9.65		18.12	0.24	10.74	11.38	1.58	1.25	97.68		0.51
AT-MZ-01	igneous apophysis	monzonite	43	44.09	0.88	9.18		18.26	0.18	10.58	11.68	1.51	1.23	97.61		0.51
AT-MZ-01	igneous apophysis	monzonite	44	44.41	0.85	9.3		18.03	0.17	10.62	11.61	1.58	1.16	97.73		0.51
AT-MZ-01	igneous apophysis	monzonite	3	44.67	0.98	8.87		17.96	0.18	10.78	11.62	1.34	1.06	97.45		0.52
AT-MZ-01	igneous apophysis	monzonite	4	44.26	0.84	9.3		17.56	0.18	10.83	11.64	1.6	1.15	97.37		0.52
AT-MZ-01	igneous apophysis	monzonite	16	44.57	0.87	9.17		17.74	0.2	10.81	11.62	1.51	1.14	97.64		0.52
AT-MZ-01	igneous apophysis	monzonite	27	43.75	0.75	9.61		17.86	0.18	10.81	11.56	1.52	1.22	97.26		0.52
AT-MZ-01	igneous apophysis	monzonite	42	44	0.84	9.37		17.64	0.17	10.82	11.55	1.51	1.21	97.1		0.52
AT-MZ-01	igneous apophysis	monzonite	52	44.76	0.81	8.88		17.94	0.15	10.91	11.52	1.51	1.15	97.61		0.52
AT-MZ-01	igneous apophysis	monzonite	53	44.59	0.69	9.22		17.9	0.18	10.95	11.56	1.51	1.11	97.69		0.52
AT-MZ-01	igneous apophysis	monzonite	1	45.36	0.58	8.2		17.75	0.18	11.26	11.64	1.25	0.94	97.16		0.53
AT-MZ-01	igneous apophysis	monzonite	12	44.84	0.8	8.62		17.75	0.18	11.04	11.64	1.43	1.02	97.32		0.53
AT-MZ-01	igneous apophysis	monzonite	15	44.58	0.75	8.75		17.6	0.16	11.13	11.38	1.5	1.13	96.97		0.53
AT-MZ-01	igneous apophysis	monzonite	26	44.89	0.84	8.97		17.3	0.13	11.16	11.53	1.45	1.07	97.34		0.53
AT-MZ-01	igneous apophysis	monzonite	28	44.51	0.65	9.3		17.48	0.18	11.25	11.32	1.59	1.19	97.46		0.53
AT-MZ-01	igneous apophysis	monzonite	55	44.77	0.58	9.18		17.55	0.23	11.03	11.25	1.6	1.12	97.3		0.53
AT-MZ-01	igneous apophysis	monzonite	13	44.81	0.78	8.85		17.17	0.18	11.18	11.68	1.43	1.03	97.11		0.54
AT-MZ-01	igneous apophysis	monzonite	25	45.24	0.71	8.87		17.21	0.19	11.28	11.51	1.49	1.05	97.55		0.54
AT-MZ-01	igneous apophysis	monzonite	54	44.92	0.67	8.9		17.25	0.21	11.2	11.44	1.5	1.08	97.18		0.54
AT-MZ-01	igneous apophysis	monzonite	56	45.41	0.66	8.67		17.17	0.19	11.36	11.3	1.42	1.01	97.19		0.54
AT-MZ-02	igneous apophysis	monzonite	24	42.05	0.88	10.66	0.05	18.53	0.11	9.98	11.53	1.61	1.43	96.83	342.1	0.49
AT-MZ-02	igneous apophysis	monzonite	22	42.62	0.93	10.52	0.02	17.29	0.15	10.66	11.69	1.58	1.35	96.81	136.84	0.52
AT-MZ-02	igneous apophysis	monzonite	32	53.18	0.08	2.21	0	13.42	0.16	14.88	12.28	0.3	0.14	96.66		0.66

AMPHIBOLES

Sample	Rock group	obs	anal. #	SiO2	TiO2	Al2O3	Cr2O3	FeO	MnO	MgO	CaO	Na2O	K2O	Total	Cr ppm	XMg
AT-MZ-02	igneous apophysis	monzonite	38	52.85	0.11	2.54	0	13.86	0.22	14.89	12.21	0.33	0.11	97.11		0.66
AT-MZ-02	igneous apophysis	monzonite	42	52.93	0.13	2.36	0.04	13.67	0.21	14.93	12.72	0.34	0.11	97.43	273.68	0.66
AT-MZ-02	igneous apophysis	monzonite	40	53.74	0.01	1.91	0.01	13.51	0.17	15.38	12.51	0.24	0.09	97.56	68.42	0.67
AT-MZ-02	igneous apophysis	monzonite	1	54.41	0	1.9	0.04	13.17	0.16	16.09	12.29	0.2	0.07	98.33	273.68	0.69
AT-MZ-02	igneous apophysis	monzonite	34	53.93	0.06	1.89	0	12.52	0.18	16.03	12.54	0.25	0.07	97.47		0.7
AT-MZ-02	igneous apophysis	monzonite	36	53.56	0.17	2.18	0	12	0.19	15.69	12.4	0.35	0.1	96.64		0.7
DB-GR-01	igneous apophysis	granodiorite	1	41.8	1.04	10.58	0.08	22.64	0.57	7.19	11.15	1.5	1.37	97.92	537.62	0.36
DB-GR-01	igneous apophysis	granodiorite	2	41.91	1.03	10.78	0.05	22.75	0.46	7.23	11.13	1.43	1.36	98.13	319.1	0.36
DB-GR-01	igneous apophysis	granodiorite	3	41.28	0.89	11.29	0	22.72	0.52	7.05	11.29	1.59	1.49	98.12	0.1	0.36
DB-GR-01	igneous apophysis	granodiorite	11	42	0.61	10.56	0	22.87	0.53	7.27	11.32	1.38	1.25	97.79	0.1	0.36
DB-GR-01	igneous apophysis	granodiorite	4	42.08	1.32	10.62	0.03	21.96	0.5	7.26	11.18	1.43	1.37	97.76	210.42	0.37
DB-GR-01	igneous apophysis	granodiorite	12	41.98	1.06	10.63	0.02	22.29	0.48	7.7	11.2	1.43	1.32	98.12	118.33	0.38
CL-GR-01-mafic	igneous apophysis - mafic	granodiorite	44	43.07	1.37	9.67	0	22.17	0.63	7.16	11.01	1.55	1.19	97.82		0.37
CL-GR-01-mafic	igneous apophysis - mafic	granodiorite	45	42.59	1.38	9.87	0.01	21.69	0.58	7.28	10.97	1.49	1.23	97.11	68.42	0.37
CL-GR-01-mafic	igneous apophysis - mafic	granodiorite	46	42.42	1.38	10.06	0.01	22.19	0.61	7.28	10.95	1.42	1.24	97.56	68.42	0.37
CL-GR-01-mafic	igneous apophysis - mafic	granodiorite	31	42.73	1.23	9.79	0	21.08	0.55	7.82	11.2	1.4	1.15	96.95		0.4
CL-GR-01-mafic	igneous apophysis - mafic	granodiorite	32	43.06	1.29	9.93	0.01	21.17	0.58	7.89	11.11	1.54	1.2	97.79	68.42	0.4
CL-GR-01-mafic	igneous apophysis - mafic	granodiorite	33	43.17	1.23	9.51	0.02	21.23	0.57	8.01	11.13	1.43	1.12	97.41	136.84	0.4
DB-GRT-3B	igneous apophysis - pegmatite	pegmatite	111	51.24	0.05	0.66	0.04	14.82	0.33	9.4	22.59	0.53	0	99.66	280.72	0.53
DB-GRT-3B	igneous apophysis - pegmatite	pegmatite	132	51.22	0.04	0.33	0.01	15	0.32	9.47	22.77	0.3	0	99.46	76.97	0.53
DB-GRT-3B	igneous apophysis - pegmatite	pegmatite	109	51.23	0.05	0.77	0.05	14.39	0.38	9.53	22.13	0.67	0	99.19	326.38	0.54
DB-GRT-3B	igneous apophysis - pegmatite	pegmatite	110	51.22	0.04	0.59	0.06	14.33	0.36	9.46	22.63	0.46	0	99.16	376.34	0.54
DB-GRT-3B	igneous apophysis - pegmatite	pegmatite	112	51.32	0.04	0.67	0	14.51	0.37	9.63	22.34	0.44	0	99.33	31.72	0.54
DB-GRT-3B	igneous apophysis - pegmatite	pegmatite	114	51.3	0.03	0.73	0.02	14.55	0.39	9.44	22.42	0.54	0	99.41	108.74	0.54
DB-GRT-3B	igneous apophysis - pegmatite	pegmatite	115	51.2	0.03	0.37	0.05	14.6	0.35	9.68	22.65	0.37	0.01	99.34	348.85	0.54
DB-GRT-3B	igneous apophysis - pegmatite	pegmatite	117	50.83	0.08	0.71	0.02	14.28	0.37	9.36	22.51	0.57	0	98.74	167.78	0.54
DB-GRT-3B	igneous apophysis - pegmatite	pegmatite	130	50.34	0.03	0.47	0	14.37	0.35	9.62	22.9	0.37	0	98.46	0.1	0.54
DB-GRT-3B	igneous apophysis - pegmatite	pegmatite	131	51.21	0.06	0.62	0.04	14.63	0.35	9.47	22.38	0.48	0.01	99.25	280.85	0.54
DB-GRT-3B	igneous apophysis - pegmatite	pegmatite	134	51.27	0.05	0.59	0.04	14.33	0.31	9.48	22.52	0.5	0.01	99.11	253.98	0.54
DB-GRT-3B	igneous apophysis - pegmatite	pegmatite	113	50.84	0.06	0.76	0.01	14.35	0.38	9.69	22.14	0.59	0.01	98.84	45.32	0.55
DB-GRT-3B	igneous apophysis - pegmatite	pegmatite	135	51.4	0.05	0.51	0.03	14.16	0.41	9.81	22.71	0.38	0.04	99.48	186.1	0.55
DB-GRT-3B	igneous apophysis - pegmatite	pegmatite	116	51.68	0.03	0.44	0.01	14.19	0.36	9.93	22.66	0.33	0	99.64	99.82	0.56
DB-GRT-3B	igneous apophysis - pegmatite	pegmatite	133	51.43	0	0.4	0	13.98	0.36	10.1	22.55	0.33	0	99.14	0.1	0.56
DB-GRT-3B	igneous apophysis - pegmatite	pegmatite	129	50.73	0.03	0.55	0	13.19	0.36	10.38	22.55	0.51	0	98.29	0.1	0.58
AT-PS-01	prograde skarn		10	58.03	0.08	1.03		0.47	0.01	24.71	13.4	0.33	0.14	98.22		0.99
AT-PS-01	prograde skarn		11	58.92	0	0.18		0.55	0.01	24.66	13.56	0.08	0.02	97.98		0.99
AT-PS-01	prograde skarn		37	59.16	0.03	0.26		0.58	0	25.01	13.63	0.1	0.05	98.81		0.99

AMPHIBOLES

Sample	Rock group	obs	anal. #	SiO2	TiO2	Al2O3	Cr2O3	FeO	MnO	MgO	CaO	Na2O	K2O	Total	Cr ppm	XMg
AT-PS-01	prograde skarn		49	58.87	0.09	0.24		0.56	0.05	24.66	13.46	0.11	0.04	98.08		0.99
AT-PS-01	prograde skarn		50	58.59	0.02	0.34		0.52	0	24.63	13.65	0.09	0.06	97.9		0.99
AT-PS-01	prograde skarn		61	58.39	0.05	0.64		0.5	0	24.68	13.42	0.19	0.07	97.94		0.99
AT-PS-01	prograde skarn		62	58.6	0.02	0.36		0.58	0	24.7	13.55	0.11	0.04	97.96		0.99
AT-PS-01	prograde skarn		71	58.47	0.02	0.39		0.54	0	24.68	13.61	0.12	0.04	97.88		0.99
AT-PS-01	prograde skarn		75	58.56	0.02	0.71		0.49	0.03	25.11	13.41	0.15	0.06	98.55		0.99
AT-PS-01	prograde skarn		76	58.14	0.06	1.09		0.62	0	24.77	13.53	0.32	0.09	98.62		0.99
AT-PS-01	prograde skarn		77	58.38	0.08	0.58		0.5	0.01	24.88	13.58	0.19	0.06	98.27		0.99
AT-PS-01	prograde skarn		78	57.96	0.04	0.69		0.51	0.07	24.46	13.54	0.21	0.1	97.58		0.99
AT-PS-01	prograde skarn		90	58.76	0.03	0.33		0.51	0.03	24.63	13.55	0.12	0.06	98.03		0.99
AT-PS-01	prograde skarn		91	58.87	0.06	0.29		0.52	0.01	25.12	13.59	0.09	0.04	98.6		0.99
AT-PS-02	prograde skarn		35	57.72	0.08	1.2		4.64	0.07	21.61	13.22	0.23	0.07	98.85		0.89
AT-PS-02	prograde skarn		38	57.22	0.05	0.98		4.55	0.05	21.48	13.23	0.17	0.08	97.82		0.89
AT-PS-02	prograde skarn		33	56.87	0.03	1.08		4.45	0.08	21.84	13.1	0.22	0.09	97.74		0.9
AT-PS-02	prograde skarn		43	56.91	0.05	1.45		4.41	0.07	21.94	13.18	0.22	0.07	98.32		0.9
AT-PS-02	prograde skarn		44	57.37	0.06	0.94		4.21	0.03	21.98	13.29	0.2	0.05	98.13		0.9
AT-PS-02	prograde skarn		53	56.66	0.13	1.51		4.42	0.07	21.64	13.24	0.23	0.07	97.99		0.9
AT-PS-02	prograde skarn		54	57.24	0.05	0.72		4.42	0.04	21.67	13.68	0.14	0.06	98.03		0.9
AT-PS-02	prograde skarn		55	57.42	0.06	0.58		4.23	0.08	22.34	13.31	0.15	0.03	98.2		0.9
AT-PS-02	prograde skarn		42	58.87	0.01	0.24		1.75	0	23.97	13.66	0.16	0.04	98.7		0.96
AT-PS-02	prograde skarn		41	59.25	0	0.02		0.64	0.01	24.96	13.65	0.04	0.01	98.57		0.99
CL-PS-01A	prograde skarn		200	56.9	0.05	1.01	0	3.67	0.06	22.07	13.27	0.14	0.06	97.22	26.91	0.91
CL-PS-01A	prograde skarn		211	58.36	0.04	0.46	0.02	1.17	0.01	24.15	13.48	0.15	0.07	97.93	169.75	0.97
CL-PS-01A	prograde skarn		214	57.36	0.05	0.58	0	1.25	0	23.76	13.51	0.19	0.06	96.76	0.1	0.97
CL-PS-01A	prograde skarn		199	58.32	0.05	0.39	0	1.07	0	24.05	13.46	0.13	0.04	97.51	0.1	0.98
CL-PS-01A	prograde skarn		201	55.46	0.1	2.47	0	1.03	0.02	23.44	13.25	0.7	0.16	96.62	0.1	0.98
CL-PS-01A	prograde skarn		202	58.09	0.03	0.26	0	0.81	0.01	24.12	13.66	0.11	0.03	97.13	0.1	0.98
CL-PS-01A	prograde skarn		212	58.72	0.04	0.32	0.01	1.11	0.01	24.29	13.37	0.1	0.04	98.02	88.27	0.98
CL-PS-01A	prograde skarn		213	58.36	0.05	0.52	0.02	1	0	24.26	13.41	0.14	0.06	97.83	142.75	0.98
CL-PS-01B	prograde skarn		228	55.69	0.08	2.1	0.04	1.56	0.03	23.3	13.13	0.48	0.15	96.55	262.27	0.96
CL-PS-01B	prograde skarn		226	55.38	0.09	1.57	0	1.11	0.01	23.32	13.41	0.45	0.13	95.48	23.45	0.97
CL-PS-01B	prograde skarn		229	56.34	0.06	0.66	0.04	1.35	0.02	23.19	13.53	0.15	0.04	95.37	271.96	0.97
CL-PS-01B	prograde skarn		230	57.37	0.06	0.37	0.04	1.4	0.01	23.52	13.39	0.09	0.05	96.3	281.36	0.97
CL-PS-01B	prograde skarn		232	56.28	0.04	1	0	1.37	0.04	23.33	13.36	0.3	0.09	95.82	0.1	0.97
CL-PS-01B	prograde skarn		231	57.02	0.06	1.37	0	0.99	0.04	23.68	13.54	0.15	0.05	96.9	0.1	0.98
CL-PS-01C	prograde skarn		264	55.04	0.21	4.11	0.01	0.95	0.01	23.25	13.42	0.85	0.2	98.04	65.74	0.98
CL-PS-01C	prograde skarn		265	53.78	0.42	4.83	0	1	0	22.9	13.5	0.92	0.22	97.56	0.1	0.98

AMPHIBOLES

Sample	Rock group	obs	anal. #	SiO2	TiO2	Al2O3	Cr2O3	FeO	MnO	MgO	CaO	Na2O	K2O	Total	Cr ppm	XMg
CL-PS-01C	prograde skarn		266	55.62	0.14	2.93	0	0.91	0.01	23.68	13.42	0.54	0.19	97.44	0.1	0.98
CL-PS-01C	prograde skarn		267	55.82	0.16	2.81	0.04	0.91	0	23.86	13.55	0.62	0.18	97.96	272.48	0.98
DB-PS-01	prograde skarn		19	55.85	0	3.66	0.01	1.19	0.05	23.46	13.34	0.85	0.15	98.57	68.42	0.97
DB-PS-01	prograde skarn		20	58.53	0	0.4	0	1.13	0.08	24.21	13.58	0.11	0.03	98.06		0.97
DB-PS-01	prograde skarn		7	57.66	0	0.49	0.02	1.05	0.09	23.87	13.5	0.11	0.01	96.81	136.84	0.98
DB-PS-01	prograde skarn		8	57.86	0	0.91	0.01	0.83	0.08	24.12	13.59	0.2	0.03	97.63	68.42	0.98
DB-PS-01	prograde skarn		9	58.09	0	0.6	0	0.86	0.06	24.33	13.42	0.14	0.03	97.52		0.98
DB-PS-01	prograde skarn		17	58.57	0.01	0.72	0.03	0.83	0.01	24.54	13.55	0.23	0.08	98.55	205.26	0.98
DB-PS-01	prograde skarn		18	57.17	0	1.67	0.01	0.99	0.06	24.07	13.4	0.43	0.13	97.93	68.42	0.98
AT-PS-03	prograde skarn		158	58.69	0.05	0.47		0.76	0.03	24.74	13.49	0.12	0.03	98.38		0.98
AT-PS-03	prograde skarn		161	58.95	0	0.1		0.7	0.05	25.17	13.43	0.09	0.01	98.51		0.98
AT-PS-03	prograde skarn		181	58.78	0	0.21		0.72	0.05	24.52	13.45	0.1	0	97.83		0.98
AT-PS-03	prograde skarn		184	58.64	0	0.64		0.68	0.02	24.77	13.47	0.17	0.02	98.42		0.98
AT-PS-03	prograde skarn		199	59.45	0.05	0.07		0.69	0	24.89	13.54	0.05	0	98.74		0.98
AT-PS-03	prograde skarn		138	59.36	0	0.27		0.61	0.01	24.77	13.55	0.12	0	98.69		0.99
AT-PS-03	prograde skarn		139	58.86	0.01	0.22		0.63	0	24.7	13.64	0.06	0	98.11		0.99
AT-PS-03	prograde skarn		159	59.07	0.04	0.14		0.6	0.04	25.07	13.56	0.05	0.01	98.58		0.99
AT-PS-03	prograde skarn		160	59.23	0	0.13		0.55	0.07	25.02	13.54	0.05	0.01	98.6		0.99
AT-PS-03	prograde skarn		182	59.07	0.04	0.12		0.56	0	25.16	13.38	0.03	0	98.35		0.99
AT-PS-03	prograde skarn		183	58.9	0.02	0.12		0.65	0.01	24.91	13.54	0.05	0.01	98.22		0.99
AT-PS-03	prograde skarn		198	58.99	0	0.12		0.55	0.03	25.06	13.56	0.04	0	98.36		0.99
AT-PS-03	prograde skarn		200	59.13	0.02	0.07		0.58	0.01	24.84	13.61	0.05	0	98.31		0.99
AT-PS-03	prograde skarn		201	59.05	0	0.11		0.54	0.03	24.95	13.52	0.06	0.01	98.28		0.99
AT-PS-03	prograde skarn		202	57.96	0	0.13		0.6	0.02	25.07	13.24	0.03	0.01	97.06		0.99
CL-PS-03	prograde skarn - contact skarn		151	44.83	0.57	12.66	0.04	7.08	0.07	16	12.47	2.05	0.88	96.65	295.31	0.8
CL-PS-03	prograde skarn - contact skarn		157	46.53	0.51	10.98	0.07	7.34	0.11	16.38	12.42	1.76	0.68	96.79	502.78	0.8
CL-PS-03	prograde skarn - contact skarn		152	46.79	0.38	10.41	0.15	7.13	0.13	17.01	12.4	1.75	0.59	96.73	1029.26	0.81
CL-PS-03	prograde skarn - contact skarn		154	46.4	0.32	8.56	0.1	6.57	0.13	17.04	11.41	1.24	0.48	92.25	711.6	0.82
CL-PS-03	prograde skarn - contact skarn		156	48.27	0.37	9.47	0.15	6.24	0.12	17.56	12.47	1.44	0.51	96.61	1051.4	0.83
CL-PS-03	prograde skarn - contact skarn		155	53.8	0.08	3.43	0.02	5.66	0.11	20.06	12.97	0.53	0.15	96.8	106.91	0.86
CL-PS-03	prograde skarn - contact skarn		158	53.6	0.07	2.76	0.01	5.06	0.1	20.91	11.4	0.42	0.1	94.43	65.18	0.88
CL-PS-02A	prograde skarn - sp skarn		345	57.91	0.05	0.29	0.05	2.54	0.03	23.7	13.18	0.09	0.03	97.86	360.33	0.94
CL-PS-02A	prograde skarn - sp skarn		316	57.35	0.04	0.65	0.05	2.16	0.14	23.63	13.05	0.21	0.05	97.32	308.98	0.95
CL-PS-02A	prograde skarn - sp skarn		317	57.25	0.06	0.38	0	2.17	0.1	23.62	13.35	0.12	0.03	97.06	14.04	0.95

BIOTITE-PHLOGOPITE

Sample	Rock group	anal. #	SiO2	TiO2	Al2O3	Cr2O3	FeO	MnO	MgO	CaO	Na2O	K2O	Total	Cr ppm	XMg
AT-PS-01	prograde skarn	1	42.27	0.49	13.45		0.47	0	28.11	0.04	0.45	9.63	94.9		0.99
AT-PS-01	prograde skarn	2	42.38	0.5	13.3		0.47	0.04	28.6	0	0.48	9.66	95.43		0.99
AT-PS-01	prograde skarn	3	41.9	0.47	12.93		0.49	0	29.23	0	0.41	8.73	94.16		0.99
AT-PS-01	prograde skarn	4	42.27	0.56	13.62		0.5	0.01	28.07	0.02	0.47	9.69	95.21		0.99
AT-PS-01	prograde skarn	8	43.17	0.47	12.73		0.49	0.01	28.78	0	0.41	9.72	95.78		0.99
AT-PS-01	prograde skarn	9	43.09	0.24	7.17		0.66	0.03	35.37	0.11	0.17	5.07	91.92		0.99
AT-PS-01	prograde skarn	100	42.79	0.12	11.99		1	0.02	28.91	0	0.1	10.07	95		0.98
AT-PS-01	prograde skarn	101	43.31	0.26	12.36		0.83	0.03	28.54	0	0.26	10.33	95.91		0.98
AT-PS-01	prograde skarn	102	43.33	0.13	12.47		0.89	0	27.97	0.02	0.23	10.18	95.22		0.98
AT-PS-01	prograde skarn	103	42.32	0.2	13.37		0.85	0.04	28.15	0	0.2	10.27	95.4		0.98
AT-PS-01	prograde skarn	104	42.19	0.2	13.23		0.92	0	28.12	0	0.15	10.44	95.23		0.98
AT-PS-01	prograde skarn	107	42.63	0.16	13.02		0.79	0	28.36	0.02	0.21	10.01	95.2		0.98
AT-PS-01	prograde skarn	118	42.34	0.31	13.29		0.76	0.01	28.36	0.11	0.23	10.01	95.42		0.99
AT-PS-01	prograde skarn	119	42.34	0.34	13.33		0.78	0.01	28.21	0.1	0.25	9.97	95.34		0.98
AT-PS-01	prograde skarn	21	42.25	0.52	13.09		0.5	0	29.19	0.03	0.39	9.3	95.26		0.99
AT-PS-01	prograde skarn	23	42.93	0.43	12.89		0.63	0.04	28.68	0.03	0.34	9.85	95.83		0.99
AT-PS-01	prograde skarn	30	42.28	0.32	13.67		0.58	0	28.16	0	0.23	10.21	95.45		0.99
AT-PS-01	prograde skarn	64	42.77	0.17	12.81		1.04	0	28.6	0	0.12	10.23	95.73		0.98
AT-PS-01	prograde skarn	99	42.17	0.25	13.87		0.8	0	27.8	0.04	0.19	10.27	95.38		0.98
AT-MZ-01	igneous apophysis	33	36.2	3.08	13.5		21.34	0.16	10.85	0	0.02	9.02	94.17		0.48
AT-MZ-01	igneous apophysis	34	36.42	2.87	13.67		20.35	0.17	11.44	0	0.07	8.65	93.65		0.5
AT-MZ-01	igneous apophysis	35	36.38	2.72	13.79		20.82	0.09	11.73	0	0.06	9.1	94.68		0.5
AT-MZ-02	igneous apophysis	30	35.69	3.48	13.88	0.02	22.96	0.16	10.12	0.03	0.08	8.5	94.91	136.84	0.44
AT-MZ-02	igneous apophysis	31	34.79	3.26	14.04	0	23.44	0.13	10.01	0	0.04	7.99	93.71		0.43
CL-PS-01A	prograde skarn	203	40.85	0.36	14.3	0	1.48	0	26.45	0	0.12	10.17	93.75	0.1	0.97
CL-PS-01A	prograde skarn	204	38.79	0.27	13.86	0.01	2.47	0.01	29.07	0.06	0.02	6.13	90.7	35.24	0.95
CL-PS-01A	prograde skarn	205	39.91	0.32	14.01	0.01	2.09	0	27.55	0.07	0.05	9.01	93.03	48.72	0.96
CL-PS-01A	prograde skarn	206	39.04	0.42	14.49	0	2.19	0	27.55	0.09	0.02	7.7	91.51	0.1	0.96
CL-PS-01A	prograde skarn	210	39.88	0.47	14.83	0.01	1.72	0.02	27.3	0.08	0.25	8.74	93.29	48.8	0.97
CL-PS-01A	prograde skarn	220	41.4	0.23	13.5	0.04	1.66	0	27.26	0.04	0.27	9.07	93.47	266.13	0.97
CL-PS-01A	prograde skarn	221	40.32	0.27	14.65	0.01	1.78	0.01	26.76	0.02	0.24	9.04	93.1	47.14	0.96
CL-PS-01C	prograde skarn	242	40.19	0.44	14.86	0.02	1.26	0.03	27.7	0.13	0.35	8.79	93.77	163.16	0.98
CL-PS-01C	prograde skarn	243	41.28	0.49	14.37	0	1.11	0.01	27.02	0.05	0.41	9.34	94.07	0.1	0.98
CL-PS-01C	prograde skarn	244	39.45	0.34	15.87	0	1.24	0	27.39	0.07	0.4	8.63	93.39	13.99	0.98
CL-PS-03	prograde skarn - contact skarn	148	38.42	0.78	16.94	0.06	7.81	0.09	20.42	0	0.26	9.99	94.77	444.06	0.82
CL-PS-03	prograde skarn - contact skarn	149	38.73	0.81	16.66	0.1	7.93	0	20.78	0.01	0.18	10.06	95.26	686.61	0.82

BIOTITE-PHLOGOPITE

Sample	Rock group	anal. #	SiO2	TiO2	Al2O3	Cr2O3	FeO	MnO	MgO	CaO	Na2O	K2O	Total	Cr ppm	XMg
CL-PS-03	prograde skarn - contact skarn	150	38.23	0.77	16.56	0.11	7.87	0.07	20.4	0.11	0.15	10.24	94.5	750.68	0.82
CL-PS-03	prograde skarn - contact skarn	153	38.26	0.96	15.88	0.07	8.66	0.07	20.21	0.02	0.11	10.11	94.34	474.68	0.81
DB-GR-01	igneous apophysis	13	36.19	3.76	14.16	0	23.64	0.34	8.85	0	0.04	9.51	96.48	0.1	0.4
DB-GR-01	igneous apophysis	19	35.23	3.29	14.62	0.04	23.39	0.33	9.68	0.69	0.04	8.33	95.65	286.29	0.42
DB-GR-01	igneous apophysis	20	36.11	3.34	14.16	0.09	22.41	0.34	8.97	0	0.05	9.33	94.79	622.27	0.42
DB-GR-01	igneous apophysis	8	36.44	3.06	14.24	0.02	22.69	0.33	9.27	0.04	0.05	9.46	95.59	121.72	0.42
DB-GR-01	igneous apophysis	9	35.94	2.66	14.41	0.03	23.26	0.32	9.5	0	0.05	8.8	94.97	212.36	0.42
DB-GR-02	igneous apophysis	21	35.18	3.76	14.61	0.01	22.82	0.41	8.82	0.13	0.07	9.24	95.05	43.45	0.41
DB-GR-02	igneous apophysis	28	35.25	3.01	14.87	0	24.09	0.48	8.32	0	0.06	9.46	95.52	0.1	0.38
DB-PS-01	prograde skarn	13	40.35	0.44	14.33	0	1.3	0.03	26.23	0	0.27	10.33	93.28	0	0.97
DB-PS-01	prograde skarn	12	40.6	0.52	14.67	0.05	1.17	0.03	26.28	0.01	0.21	10.34	93.89	342.1	0.98
DB-PS-01	prograde skarn	14	40.71	0.47	14.5	0.02	1.2	0.04	26.29	0	0.21	10.38	93.83	136.84	0.98
AT-MG-01	igneous apophysis	110	35.66	3.84	14.53		23.07	0.4	8.16	0	0.07	9.38	95.11		0.39
AT-MG-01	igneous apophysis	111	35.69	2.99	15.05		22.68	0.31	9.06	0	0.08	9.58	95.43		0.42
AT-MG-01	igneous apophysis	112	35.67	3.85	14.69		22.71	0.4	8.67	0	0.11	9.51	95.62		0.4
AT-MG-01	igneous apophysis	113	35.8	3.15	14.58		23.57	0.39	8.35	0	0.05	9.54	95.45		0.39
AT-MG-01	igneous apophysis	93	35.52	3.91	14.95		22.85	0.36	8.58	0	0.05	9.3	95.51		0.4
AT-MG-01	igneous apophysis	94	35.18	3.66	14.94		22.84	0.41	8.81	0	0.06	9.21	95.11		0.41
AT-MG-01	igneous apophysis	95	35.65	3.39	15.37		21.89	0.38	8.83	0	0.05	9.69	95.26		0.42
AT-MG-01	igneous apophysis	96	35.32	3.57	14.67		23.52	0.37	8.23	0	0.09	9.42	95.21		0.38
AT-MG-01	igneous apophysis	97	35.33	3.33	15.17		21.94	0.37	9.59	0	0.05	9.04	94.82		0.44
AT-MG-01	igneous apophysis	98	35.67	4.09	14.72		22.31	0.37	9.05	0	0.04	9.62	95.87		0.42
AT-MG-01	igneous apophysis	99	35.79	3.85	14.85		22.24	0.42	9.04	0	0.08	9.61	95.86		0.42
CL-PS-02A	prograde skarn - sp skarn	273	41.68	0.43	14.21	0.26	4.22	0.04	25.01	0	0.61	9.21	95.67	1762.26	0.91
CL-PS-02A	prograde skarn - sp skarn	274	39.2	0.49	15.77	0.23	4.7	0	24.21	0	0.68	8.97	94.25	1551.19	0.9
CL-PS-02A	prograde skarn - sp skarn	275	40.53	0.47	15.24	0.26	4.36	0	24.41	0.01	0.63	9.43	95.34	1793.64	0.91
CL-PS-02A	prograde skarn - sp skarn	287	39.41	0.5	15.53	0.14	4.8	0	24.14	0.04	0.73	8.85	94.14	980.54	0.9
CL-PS-02A	prograde skarn - sp skarn	288	40	0.68	15.66	0.19	4.65	0.06	24.06	0.04	0.75	9.08	95.16	1321.86	0.9
CL-PS-02A	prograde skarn - sp skarn	289	39.93	0.44	15.11	0.12	4.56	0.04	24.29	0	0.5	9.15	94.13	787.94	0.9
CL-PS-02A	prograde skarn - sp skarn	318	39.34	0.36	14.56	0	5.7	0.02	24.86	0.02	0.12	8.96	93.94	0.1	0.89
CL-PS-02A	prograde skarn - sp skarn	319	40.69	0.4	14.82	0.02	4.74	0.06	24.65	0.11	0.27	9.26	95.01	105.98	0.9
CL-PS-02A	prograde skarn - sp skarn	320	39.48	0.45	15.9	0.02	4.62	0.06	23.97	0.05	0.46	9.69	94.69	147.48	0.9
CL-PS-02B	prograde skarn - sp skarn	348	39.09	0.42	15.91	0.07	4.72	0.04	23.63	0	0.72	9.04	93.65	511.23	0.9
CL-PS-02B	prograde skarn - sp skarn	349	38.27	0.47	16.93	0.1	4.57	0.01	23.06	0	0.81	9.28	93.5	709.8	0.9
CL-PS-02B	prograde skarn - sp skarn	350	39.77	0.36	15.18	0.02	4.45	0.03	23.93	0	0.79	9.27	93.8	119.91	0.91
CL-PS-02B	prograde skarn - sp skarn	355	40.25	0.31	14.7	0.13	3.78	0.01	24.47	0.01	0.61	9.22	93.49	897.03	0.92

BIOTITE-PHLOGOPITE

Sample	Rock group	anal. #	SiO2	TiO2	Al2O3	Cr2O3	FeO	MnO	MgO	CaO	Na2O	K2O	Total	Cr ppm	XMg
CL-PS-02B	prograde skarn - sp skarn	356	38.59	0.23	15.68	0.44	4.01	0.02	24.42	0	0.58	8.52	92.48	3005.44	0.92
CL-PS-02B	prograde skarn - sp skarn	357	39.59	0.35	14.5	0.14	3.96	0.07	24.39	0.07	0.66	8.94	92.67	974.8	0.92
CL-PS-02B	prograde skarn - sp skarn	358	40.2	0.26	14.67	0.01	4.1	0.02	23.96	0.06	0.34	9.74	93.35	46.19	0.91
CL-PS-02B	prograde skarn - sp skarn	359	39.54	0.2	14.85	0	4.18	0	19.65	0.01	0.83	9.26	88.51	0.1	0.89
CL-PS-02B	prograde skarn - sp skarn	360	40.54	0.3	14.95	0.04	4.24	0.02	24.43	0.05	0.77	9.17	94.52	286.27	0.91
CL-PS-02B	prograde skarn - sp skarn	361	39.8	0.27	15.28	0.06	4.13	0	23.95	0	0.48	9.67	93.64	420.17	0.91
CL-PS-02B	prograde skarn - sp skarn	362	39.5	0.3	15.21	0.14	4.31	0.01	23.82	0.01	0.68	9.41	93.38	936.59	0.91
CL-GR-01-mafic	igneous apophysis - mafic	24	28.04	0.17	17.28	0.06	29.7	0.3	12.66	0.11	0	0.06	88.37	410.52	0.43
CL-GR-01-mafic	igneous apophysis - mafic	27	31.74	2.37	15.47	0.02	25.6	0.28	11.11	0.01	0.04	4.08	90.72	136.84	0.44
CL-GR-01-mafic	igneous apophysis - mafic	21	31.51	2.41	15.52	0.02	25.86	0.25	11.85	0.07	0.05	3.51	91.06	136.84	0.45
CL-GR-01-mafic	igneous apophysis - mafic	23	28.16	1.09	16.52	0.02	27.3	0.3	12.39	0.07	0.03	0.87	86.76	136.84	0.45
CL-GR-01-mafic	igneous apophysis - mafic	22	29.77	1.48	15.46	0.02	27.68	0.3	13.12	0.07	0.01	1.13	89.03	136.84	0.46
CL-GR-01-mafic	igneous apophysis - mafic	25	35.28	3.78	14.97	0	22.94	0.19	9.53	0.01	0.03	8.24	94.97		0.43
CL-GR-01-mafic	igneous apophysis - mafic	26	35.98	3.86	14.04	0	23	0.27	9.26	0	0.02	8.79	95.22		0.42
CL-GR-01-mafic	igneous apophysis - mafic	34	35.67	4.04	13.82	0.01	23.99	0.28	8.65	0	0.05	9.32	95.84	68.42	0.39
CL-GR-01-mafic	igneous apophysis - mafic	35	35.54	4.15	13.27	0.03	24.74	0.34	8.27	0.04	0.02	9.2	95.58	205.26	0.37
CL-GR-01-mafic	igneous apophysis - mafic	36	35.58	3.89	13.65	0.02	24.29	0.29	8.73	0.02	0.07	9.18	95.71	136.84	0.39
CL-GR-01-mafic	igneous apophysis - mafic	39	36.01	4.03	13.69	0.01	23.17	0.36	9.16	0	0.07	9.28	95.79	68.42	0.41
CL-GR-01-mafic	igneous apophysis - mafic	47	35.79	4.09	13.59	0	24.31	0.37	8.38	0.04	0.03	9.2	95.79		0.38
CL-GR-01-mafic	igneous apophysis - mafic	48	35.6	4.56	13.81	0.05	23.98	0.26	8.23	0.01	0.06	9.34	95.89	342.1	0.38
CL-GR-01-mafic	igneous apophysis - mafic	49	35.88	4.53	14.04	0.01	23.48	0.25	8.27	0	0.03	9.29	95.79	68.42	0.39
CL-GR-01-mafic	igneous apophysis - mafic	50	35.46	4.18	13.9	0.01	24.51	0.35	7.99	0	0.04	9.32	95.76	68.42	0.37
DB-PG-02	igneous apophysis - grt-leucogranite	73	31.67	3.5	16.27		27.46	0.69	6.33	0	0.03	6.68	93.08		0.29
DB-PG-02	igneous apophysis - grt-leucogranite	24	32.24	3.42	16.69		27.54	0.73	6.67	0.01	0.04	6.43	94.19		0.3
DB-PG-02	igneous apophysis - grt-leucogranite	84	30.86	2.93	16.32		27.62	0.66	7.35	0.07	0.06	5.29	91.44		0.32
DB-PG-02	igneous apophysis - grt-leucogranite	75	31.72	3.23	16.2		27.5	0.68	7.7	0	0.08	6.02	93.29		0.33
DB-PG-02	igneous apophysis - grt-leucogranite	11	30.88	3.41	15.89		27.1	0.54	7.53	0	0.07	5.4	91.2		0.33
DB-PG-02	igneous apophysis - grt-leucogranite	143	32.49	4	15.49		25.92	0.73	7.09	0	0.03	6.58	92.69		0.33
DB-PG-02	igneous apophysis - grt-leucogranite	25	32.09	2.83	16.31		26.92	0.61	7.83	0.06	0.09	4.74	91.58		0.34
DB-PG-02	igneous apophysis - grt-leucogranite	26	30.69	2.88	16.74		27.96	0.67	8.32	0.07	0.09	4.8	92.33		0.35
DB-PG-02	igneous apophysis - grt-leucogranite	23	30.98	2.87	16.77		26.22	0.5	8.02	0.13	0.09	4.18	90.06		0.35
DB-PG-02	igneous apophysis - grt-leucogranite	96	32.88	3.02	15.89		25.45	0.62	7.93	0.07	0.05	5.74	91.68		0.36
DB-PG-02	igneous apophysis - grt-leucogranite	100	30.64	2.14	17.09		27.61	0.52	9.54	0.08	0.01	3.37	91.27		0.38
DB-PG-02	igneous apophysis - grt-leucogranite	139	32.73	0.92	18.74		23.68	0.46	8.06	0.17	0.08	3.99	89.01		0.38
DB-PG-02	igneous apophysis - grt-leucogranite	82	30.87	4.03	16.62		25.06	0.63	9.27	0.16	0.02	4.07	91.06		0.4
DB-PG-02	igneous apophysis - grt-leucogranite	22	31.17	3.73	16.71		23.97	0.43	9.34	0.25	0.08	3.89	89.85		0.41

BIOTITE-PHLOGOPITE

Sample	Rock group	anal. #	SiO2	TiO2	Al2O3	Cr2O3	FeO	MnO	MgO	CaO	Na2O	K2O	Total	Cr ppm	XMg
DB-PG-02	igneous apophysis - grt-leucogranite	117	31.58	1.89	16.42		26.95	0.7	10.87	0.14	0.06	3.97	92.71		0.42
DB-PG-02	igneous apophysis - grt-leucogranite	88	29.83	2.54	16.87		26.19	0.63	11.18	0.05	0.05	2.51	90.06		0.43
DB-PG-02	igneous apophysis - grt-leucogranite	65	30.35	2.67	15.51		26.05	0.53	11.04	0.17	0.08	1.93	88.57		0.43
DB-PG-02	igneous apophysis - grt-leucogranite	13	32.47	2.45	15.58		25.19	0.46	12.11	0.07	0.04	4.35	93.23		0.46
DB-PG-02	igneous apophysis - grt-leucogranite	98	31.14	2.13	16.26		24.87	0.42	11.74	0.07	0.04	2.74	89.63		0.46
DB-PG-02	igneous apophysis - grt-leucogranite	21	30.04	2.64	16.6		25.31	0.43	12.63	0.27	0.07	1.98	90.09		0.47
DB-PG-02	igneous apophysis - grt-leucogranite	66	29.6	1.61	16.27		24.21	0.63	15.77	0.03	0.06	1.08	89.41		0.54
DB-PG-02	igneous apophysis - grt-leucogranite	12	32.97	3.48	15.97		26.3	0.66	6.43	0	0.05	7.11	93.28		0.3
DB-PG-02	igneous apophysis - grt-leucogranite	120	32.3	4.57	15.44		26.07	0.85	5.5	0.08	0.03	8.06	93.3		0.27
DB-PG-02	igneous apophysis - grt-leucogranite	137	32.94	3.86	15.95		27.06	0.96	4.37	0	0.01	8.84	94.3		0.22
DB-PG-02	igneous apophysis - grt-leucogranite	140	33.96	4.38	15.7		26.67	0.92	4.2	0	0.07	9.15	95.22		0.22
DB-PG-02	igneous apophysis - grt-leucogranite	144	31.41	3.72	15.63		26.31	0.82	5.73	0.02	0.04	7.01	91.15		0.28
DB-PG-02	igneous apophysis - grt-leucogranite	162	32.97	3.52	16.18		26.71	0.97	5.35	0	0.05	7.94	93.68		0.26
DB-PG-02	igneous apophysis - grt-leucogranite	163	33.56	3.68	16.05		26.73	0.9	5.02	0	0.01	8.97	95.13		0.25
DB-PG-02	igneous apophysis - grt-leucogranite	164	33.09	3.2	15.29		27.57	0.91	6.9	0.21	0.06	7.06	94.5		0.31
DB-PG-02	igneous apophysis - grt-leucogranite	51	33	3.3	16.49		27.1	0.93	5.56	0	0.05	8.11	94.89		0.27
DB-PG-02	igneous apophysis - grt-leucogranite	86	33.29	3.18	15.95		27.32	0.74	5.39	0.01	0.07	7.36	93.65		0.26
DB-PG-02	igneous apophysis - grt-leucogranite	99	32.43	3.32	16.46		27.23	0.61	5.85	0	0.03	7.12	93.33		0.28

FELDSPARS

Sample	Rock group	anal. #	SiO2	TiO2	Al2O3	Cr2O3	FeO	MnO	MgO	CaO	Na2O	K2O	Total	Cr ppm	XMg	mineral
AT-MZ-01	igneous apophysis	63	64.35	0	18.48	0	0.09	0.04	0	0	1.34	14.48	98.78	0	0	k-feldspar
AT-MZ-01	igneous apophysis	62	64.12	0	18.26	0	0.05	0.02	0	0	0.67	15.35	98.48	0	0	k-feldspar
AT-MZ-01	igneous apophysis	27	68.24	0	19.85	0	0.08	0	0	0.56	11.31	0.04	100.08	0	0	plagioclase
AT-MZ-01	igneous apophysis	67	65.08	0	22.26	0.05	0.32	0.02	0.02	2.26	9.8	0.48	100.29	342.1	0.1	plagioclase
AT-MZ-01	igneous apophysis	47	63.92	0	22.44	0.03	0.21	0	0.01	4.06	9.22	0.21	100.09	205.26	0.08	plagioclase
AT-MZ-01	igneous apophysis	61	64.14	0	22.6	0	0.11	0	0	4.12	9.3	0.16	100.44	0	0	plagioclase
AT-MZ-01	igneous apophysis	65	63.53	0	22.92	0	0.17	0	0	4.22	9.02	0.3	100.16	0	0	plagioclase
AT-MZ-01	igneous apophysis	59	63.1	0	22.92	0	0.2	0.02	0	4.29	9.22	0.2	99.96	0	0	plagioclase
AT-MZ-01	igneous apophysis	51	63.27	0	22.85	0	0.21	0	0.02	4.31	9.11	0.35	100.12	0	0.15	plagioclase
AT-MZ-01	igneous apophysis	57	63.36	0	23.12	0.03	0.18	0	0	4.32	9.1	0.26	100.36	205.26	0	plagioclase
AT-MZ-01	igneous apophysis	49	63.6	0	22.84	0	0.15	0	0	4.41	9.22	0.27	100.49	0	0	plagioclase
AT-MZ-01	igneous apophysis	53	63.08	0	23	0.02	0.24	0	0.01	4.48	8.93	0.23	99.99	136.84	0.07	plagioclase
AT-MZ-01	igneous apophysis	55	63.31	0	23.25	0.06	0.1	0	0	4.6	8.79	0.18	100.29	410.52	0	plagioclase
AT-MZ-01	igneous apophysis	51	64.62	0	18.39		0.01	0	0	0	1.67	14.11	98.8		0	k-feldspar
AT-MZ-01	igneous apophysis	39	64.45	0.02	18.16		0.04	0	0.01	0	1.63	14.22	98.54		0.31	k-feldspar
AT-MZ-01	igneous apophysis	41	64.59	0.02	18.41		0.04	0	0.01	0	1.58	14.3	98.95		0.31	k-feldspar
AT-MZ-01	igneous apophysis	40	65.09	0	18.15		0.04	0.03	0.01	0	1.55	14.43	99.29		0.31	k-feldspar
AT-MZ-01	igneous apophysis	64	64.44	0.03	18.2		0.05	0	0.01	0	1.5	14.44	98.67		0.26	k-feldspar
AT-MZ-01	igneous apophysis	62	64.74	0.04	18.05		0.17	0	0	0	1.32	14.45	98.77		0	k-feldspar
AT-MZ-01	igneous apophysis	22	64.52	0.02	18.43		0.08	0	0	0	1.46	14.62	99.13		0	k-feldspar
AT-MZ-01	igneous apophysis	23	64.62	0	18.04		0.07	0.01	0	0	1.23	14.76	98.73		0	k-feldspar
AT-MZ-01	igneous apophysis	9	64.48	0.01	18.5		0.06	0	0	0	1.2	14.87	99.12		0	k-feldspar
AT-MZ-01	igneous apophysis	24	64.32	0.02	18.33		0.08	0	0	0	1.08	14.93	98.77		0	k-feldspar
AT-MZ-01	igneous apophysis	63	64.44	0.02	18.07		0.07	0	0	0	1.13	14.99	98.72		0	k-feldspar
AT-MZ-01	igneous apophysis	49	64.76	0	18.3		0.21	0.01	0	0	0.98	15.13	99.41		0	k-feldspar
AT-MZ-01	igneous apophysis	11	63.92	0	18.17		0.03	0	0	0	0.98	15.14	98.25		0	k-feldspar
AT-MZ-01	igneous apophysis	10	64.62	0.02	18.25		0.05	0	0	0	0.88	15.24	99.05		0	k-feldspar
AT-MZ-01	igneous apophysis	21	66.9	0	20.62		0	0.03	0.02	1.43	10.85	0.05	99.91		1	plagioclase
AT-MZ-01	igneous apophysis	29	66.92	0	21.06		0.18	0	0.03	1.97	10.79	0.04	100.99		0.23	plagioclase
AT-MZ-01	igneous apophysis	47	64.4	0.02	21.7		0.25	0.01	0.01	2.96	9.67	0.34	99.36		0.07	plagioclase
AT-MZ-01	igneous apophysis	6	65.92	0	22.42		0.19	0	0.02	3.59	10.36	0.1	102.61		0.16	plagioclase
AT-MZ-01	igneous apophysis	48	64.01	0.01	22.9		0.4	0.01	0.01	3.65	9.23	0.32	100.55		0.04	plagioclase
AT-MZ-01	igneous apophysis	7	64.83	0	22.2		0.4	0.03	0.02	3.71	9.37	0.17	100.73		0.08	plagioclase
AT-MZ-01	igneous apophysis	20	64.34	0	22.45		0.24	0	0	3.87	9.38	0.27	100.56		0	plagioclase
AT-MZ-01	igneous apophysis	17	62.97	0.02	22.66		0.22	0	0	4.15	9.04	0.29	99.35		0	plagioclase
AT-MZ-01	igneous apophysis	58	64.18	0.02	22.29		0.16	0	0	4.18	9.04	0.31	100.19		0	plagioclase
AT-MZ-01	igneous apophysis	8	63.86	0.04	22.79		0.17	0	0	4.25	8.92	0.3	100.32		0	plagioclase
AT-MZ-01	igneous apophysis	45	63.94	0	22.4		0.25	0	0.02	4.27	9.01	0.27	100.15		0.12	plagioclase
AT-MZ-01	igneous apophysis	61	64.04	0	22.44		0.11	0	0	4.28	9.22	0.36	100.47		0	plagioclase
AT-MZ-01	igneous apophysis	18	63.56	0	22.9		0.19	0.02	0.02	4.29	9.33	0.12	100.42		0.16	plagioclase
AT-MZ-01	igneous apophysis	60	64	0.02	22.65		0.08	0.02	0	4.29	9.06	0.24	100.34		0	plagioclase

FELDSPARS

Sample	Rock group	anal. #	SiO2	TiO2	Al2O3	Cr2O3	FeO	MnO	MgO	CaO	Na2O	K2O	Total	Cr ppm	XMg	mineral
AT-MZ-01	igneous apophysis	30	64.24	0.04	22.41		0.16	0	0	4.3	9.12	0.22	100.48		0	plagioclase
AT-MZ-01	igneous apophysis	19	63.68	0.01	22.86		0.2	0	0	4.33	8.98	0.18	100.22		0	plagioclase
AT-MZ-01	igneous apophysis	46	63.25	0.02	22.73		0.24	0	0.01	4.35	9.04	0.31	99.94		0.07	plagioclase
AT-MZ-01	igneous apophysis	5	63.78	0.01	22.72		0.22	0.02	0	4.36	9.05	0.19	100.35		0	plagioclase
AT-MZ-01	igneous apophysis	38	63.45	0	22.83		0.04	0	0	4.38	9.07	0.29	100.07		0	plagioclase
AT-MZ-01	igneous apophysis	32	63.76	0.01	22.83		0.23	0	0	4.39	9.17	0.16	100.55		0	plagioclase
AT-MZ-01	igneous apophysis	31	63.66	0	23.09		0.12	0	0	4.47	9.16	0.25	100.75		0	plagioclase
AT-MZ-01	igneous apophysis	36	63.38	0	23.03		0.09	0	0	4.48	9.14	0.26	100.38		0	plagioclase
AT-MZ-01	igneous apophysis	59	63.16	0	22.71		0.15	0.01	0.01	4.49	8.97	0.2	99.7		0.11	plagioclase
AT-MZ-01	igneous apophysis	37	63.2	0.05	22.93		0.1	0.03	0.01	4.6	8.96	0.3	100.17		0.15	plagioclase
AT-MZ-02	igneous apophysis	23	64.21	0	18.19	0	0.1	0	0	0	1.23	14.65	98.37	0	0	k-feldspar
AT-MZ-02	igneous apophysis	8	64.09	0	18.1	0.01	0.14	0	0.01	0	0.89	14.97	98.23	68.42	0.11	k-feldspar
AT-MZ-02	igneous apophysis	25	64.18	0	18.32	0	0.31	0	0	0.01	0.98	14.87	98.68	0	0	k-feldspar
AT-MZ-02	igneous apophysis	21	63.46	0	18.5	0	0.09	0	0	0.02	1.76	13.38	97.21	0	0	k-feldspar
AT-MZ-02	igneous apophysis	20	63.79	0	18.25	0	0.07	0	0.01	0.03	1.16	14.35	97.67	0	0.2	k-feldspar
AT-MZ-02	igneous apophysis	41	66.78	0	20.17	0.04	0.15	0	0	1.63	10.63	0.12	99.51	273.68	0	plagioclase
AT-MZ-02	igneous apophysis	13	65.47	0	21.27	0.02	0.04	0	0	2.43	10.15	0.15	99.52	136.84	0	plagioclase
AT-MZ-02	igneous apophysis	16	62.83	0.02	23.44	0	0.15	0	0.01	3.84	9.02	0.36	99.67	0	0.11	plagioclase
AT-MZ-02	igneous apophysis	4	63.37	0	22.67	0	0.09	0	0.02	4.08	9.36	0.1	99.69	0	0.28	plagioclase
AT-MZ-02	igneous apophysis	37	62.68	0	22.98	0	0.17	0	0.02	4.33	8.83	0.16	99.18	0	0.17	plagioclase
AT-MZ-02	igneous apophysis	43	63.24	0	22.75	0	0.14	0	0	4.36	9.05	0.16	99.69	0	0	plagioclase
AT-MZ-02	igneous apophysis	35	63.16	0	22.94	0	0.19	0	0	4.51	8.92	0.3	100.02	0	0	plagioclase
AT-MZ-02	igneous apophysis	39	63.14	0	23.12	0	0.13	0.01	0	4.52	8.8	0.2	99.92	0	0	plagioclase
AT-MZ-02	igneous apophysis	18	62.89	0	23.17	0.01	0.17	0.03	0.01	4.52	8.76	0.23	99.79	68.42	0.09	plagioclase
AT-MZ-02	igneous apophysis	10	62.64	0	23.13	0.03	0.14	0	0.01	4.63	8.92	0.26	99.75	205.26	0.11	plagioclase
AT-MZ-02	igneous apophysis	33	62.38	0	23.22	0	0.2	0	0	4.72	8.76	0.2	99.48	0	0	plagioclase
AT-MZ-02	igneous apophysis	6	62.74	0	23.25	0	0.15	0	0	4.74	8.57	0.24	99.69	0	0	plagioclase
AT-MZ-02	igneous apophysis	2	62.77	0	23.06	0	0.16	0	0.01	4.9	8.53	0.22	99.66	0	0.1	plagioclase
DB-GR-01	igneous apophysis	10	64.35	0.03	18.72	0	0.19	0.01	0.01	0	0.98	15.41	99.69	0.1	0.07	k-feldspar
DB-GR-01	igneous apophysis	14	63.28	0.03	23.66	0.04	0.19	0	0	3.97	9.11	0.43	100.7	245.09	0	plagioclase
DB-GR-01	igneous apophysis	5	63.1	0.01	23.49	0	0.15	0	0.02	4.26	9.22	0.28	100.52	0.1	0.22	plagioclase
DB-GR-01	igneous apophysis	6	63.69	0.02	23.38	0.02	0.16	0.02	0	4.28	9.06	0.32	100.96	155.49	0	plagioclase
DB-GR-01	igneous apophysis	7	63.53	0	23.24	0.01	0.13	0.01	0.01	4.33	9.03	0.36	100.63	56.56	0.07	plagioclase
DB-GR-01	igneous apophysis	15	64.04	0.02	23.23	0.01	0.14	0	0	4.35	8.94	0.38	101.11	56.59	0.05	plagioclase
DB-GR-02	igneous apophysis	24	62.24	0.02	19.14	0	0.1	0	0	0	1.16	15.01	97.68	0.1	0	k-feldspar
DB-GR-02	igneous apophysis	25	63.5	0.03	19	0	0.16	0	0.01	0	1.12	15.17	98.99	0.1	0.1	k-feldspar
DB-GR-02	igneous apophysis	27	62.13	0.01	23.63	0	0.12	0.01	0	4.31	9.28	0.43	99.92	0.1	0	plagioclase
DB-GR-02	igneous apophysis	26	61.67	0.02	23.73	0.03	0.11	0	0	4.38	9.06	0.37	99.39	235.8	0	plagioclase
DB-GR-02	igneous apophysis	23	61.83	0.04	23.35	0	0.39	0.01	0	4.43	8.96	0.32	99.33	0.1	0	plagioclase
DB-GR-02	igneous apophysis	22	62.74	0.04	23.71	0.03	0.24	0.04	0	4.47	9.23	0.28	100.78	216.8	0	plagioclase
FD-SI-01	igneous apophysis	84	64.85	0	17.86		0.02	0.02	0	0	1.41	14.75	98.92		0	k-feldspar

FELDSPARS

Sample	Rock group	anal. #	SiO2	TiO2	Al2O3	Cr2O3	FeO	MnO	MgO	CaO	Na2O	K2O	Total	Cr ppm	XMg	mineral
FD-SI-01	igneous apophysis	138	65.02	0.02	17.77		0.04	0.02	0	0	1.38	14.85	99.11		0	k-feldspar
FD-SI-01	igneous apophysis	83	64.2	0.05	18.05		0.05	0.02	0	0	1.31	15.07	98.74		0	k-feldspar
FD-SI-01	igneous apophysis	116	64.9	0.02	17.49		0.09	0.04	0.01	0	0.96	15.38	98.9		0.17	k-feldspar
FD-SI-01	igneous apophysis	136	64.72	0	17.68		0.35	0.3	0.01	0	0.81	15.51	99.38		0.05	k-feldspar
FD-SI-01	igneous apophysis	137	64.79	0.02	17.6		0.33	0.25	0	0	0.94	15.51	99.43		0	k-feldspar
FD-SI-01	igneous apophysis	114	64.65	0.01	17.54		0.1	0.06	0	0	0.84	15.67	98.87		0	k-feldspar
FD-SI-01	igneous apophysis	115	64.8	0	17.65		0.07	0	0.01	0	0.64	15.9	99.06		0.2	k-feldspar
FD-SI-01	igneous apophysis	85	64.37	0	17.68		0.09	0.03	0	0	0.55	15.94	98.66		0	k-feldspar
FD-SI-01	igneous apophysis	139	64.44	0.02	17.32		0.03	0	0	0	0.43	16.08	98.32		0	k-feldspar
FD-SI-01	igneous apophysis	86	64.18	0	17.98		0.15	0.09	0.02	0	0.51	16.11	99.02		0.19	k-feldspar
FD-SI-01	igneous apophysis	140	68.74	0	18.69		0.08	0.02	0	0.28	11.44	0.13	99.38		0	plagioclase
FD-SI-01	igneous apophysis	141	67.82	0	19.71		0.06	0	0.03	1.09	11.11	0.2	100.01		0.47	plagioclase
FD-SI-01	igneous apophysis	119	67.18	0	19.99		0.07	0.02	0	1.21	10.72	0.24	99.42		0	plagioclase
FD-SI-01	igneous apophysis	88	66.55	0	20.08		0.08	0	0	1.4	10.74	0.2	99.05		0	plagioclase
FD-SI-01	igneous apophysis	118	67.08	0.04	20.07		0.04	0	0	1.49	10.67	0.29	99.69		0	plagioclase
FD-SI-01	igneous apophysis	117	66.9	0	19.94		0.01	0	0	1.5	10.66	0.27	99.28		0	plagioclase
FD-SI-01	igneous apophysis	87	66.57	0	20.43		0.04	0.01	0	1.71	10.71	0.24	99.72		0	plagioclase
FD-SI-01	igneous apophysis	89	65.89	0	20.8		0.04	0	0	2.08	10.36	0.29	99.45		0	plagioclase
AT-MG-01	igneous apophysis	106	63.69	0	18.29		0.08	0	0	0	1.2	14.78	98.03		0	k-feldspar
AT-MG-01	igneous apophysis	103	63.8	0.02	18.42		0.08	0.02	0	0	1.22	14.81	98.36		0	k-feldspar
AT-MG-01	igneous apophysis	90	63.66	0.03	18.52		0.03	0.03	0.01	0	1.06	15.05	98.4		0.37	k-feldspar
AT-MG-01	igneous apophysis	105	63.29	0.01	18.52		0.09	0	0.01	0	0.95	15.07	97.95		0.17	k-feldspar
AT-MG-01	igneous apophysis	91	64.01	0.02	18.33		0.02	0	0.01	0	0.99	15.12	98.5		0.47	k-feldspar
AT-MG-01	igneous apophysis	104	63.84	0.01	18.53		0.11	0	0	0	1.01	15.15	98.66		0	k-feldspar
AT-MG-01	igneous apophysis	92	63.62	0.04	18.42		0.22	0.04	0	0	0.87	15.31	98.52		0	k-feldspar
AT-MG-01	igneous apophysis	89	63.25	0.01	18.29		0	0	0	0	0.45	15.9	97.9			k-feldspar
AT-MG-01	igneous apophysis	100	62.78	0	23.36		0.1	0.02	0	4.55	8.9	0.33	100.05		0	plagioclase
AT-MG-01	igneous apophysis	101	63.02	0	22.94		0.13	0.01	0	4.55	9.06	0.35	100.07		0	plagioclase
AT-MG-01	igneous apophysis	87	62.96	0.02	23.12		0.13	0	0	4.59	8.63	0.36	99.82		0	plagioclase
AT-MG-01	igneous apophysis	88	62.29	0	23.38		0.13	0.01	0.01	4.61	9.01	0.28	99.72		0.12	plagioclase
AT-MG-01	igneous apophysis	102	62.52	0.04	23.36		0.11	0	0.01	4.62	8.73	0.2	99.61		0.14	plagioclase
AT-MG-01	igneous apophysis	107	62.61	0.01	23.25		0.13	0.01	0	4.67	8.73	0.39	99.8		0	plagioclase
AT-MG-01	igneous apophysis	86	62.32	0	23.35		0.1	0	0	4.68	8.77	0.26	99.48		0	plagioclase
AT-MG-01	igneous apophysis	109	62.4	0	23.51		0.11	0	0.01	4.72	8.98	0.18	99.91		0.14	plagioclase
AT-MG-01	igneous apophysis	108	62.41	0	23.38		0.16	0.04	0	4.72	8.66	0.29	99.67		0	plagioclase
CL-GR-01-felsic	igneous apophysis - mafic	13	63.86	0	18.4	0.01	0.05	0.03	0.01	0	1.17	14.85	98.38	68.42	0.26	k-feldspar
CL-GR-01-felsic	igneous apophysis - mafic	16	64.06	0	18.45	0.02	0.12	0	0	0	1.01	15.13	98.8	136.84	0	k-feldspar
CL-GR-01-felsic	igneous apophysis - mafic	11	62.9	0	18.44	0	0.08	0	0.01	0	0.88	15.32	97.62	0	0.18	k-feldspar
CL-GR-01-felsic	igneous apophysis - mafic	12	64.34	0	18.34	0	0.04	0	0.01	0	0.84	15.45	99.03	0	0.31	k-feldspar
CL-GR-01-felsic	igneous apophysis - mafic	14	63.84	0	18.35	0	0.04	0	0	0.01	1.1	14.93	98.27	0	0	k-feldspar
CL-GR-01-felsic	igneous apophysis - mafic	10	63.99	0	18.26	0	0.09	0.04	0.01	0.02	0.91	15.06	98.39	0	0.17	k-feldspar

FELDSPARS

Sample	Rock group	anal. #	SiO2	TiO2	Al2O3	Cr2O3	FeO	MnO	MgO	CaO	Na2O	K2O	Total	Cr ppm	XMg	mineral
CL-GR-01-felsic	igneous apophysis - mafic	15	64.19	0	18.4	0	0.11	0.06	0	0.02	0.78	15.29	98.85	0	0	k-feldspar
CL-GR-01-felsic	igneous apophysis - mafic	20	68.25	0	19.96	0	0.03	0	0	0.16	11.43	0.44	100.28	0	0	plagioclase
CL-GR-01-felsic	igneous apophysis - mafic	19	64.77	0	22.5	0	0.08	0	0.05	3.14	9.77	0.16	100.49	0	0.53	plagioclase
CL-GR-01-felsic	igneous apophysis - mafic	18	63.7	0	22.52	0.05	0.09	0.02	0.07	3.59	9.53	0.26	99.82	342.1	0.58	plagioclase
CL-GR-01-felsic	igneous apophysis - mafic	3	64.04	0	22.48	0.04	0.1	0	0	3.71	9.67	0.23	100.27	273.68	0	plagioclase
CL-GR-01-felsic	igneous apophysis - mafic	8	64.06	0	22.56	0	0.04	0.01	0	3.91	9.17	0.34	100.09	0	0	plagioclase
CL-GR-01-felsic	igneous apophysis - mafic	9	63.16	0	22.9	0.01	0.13	0	0.46	4.24	8.8	0.51	100.21	68.42	0.86	plagioclase
CL-GR-01-mafic	igneous apophysis - mafic	37	63.47	0	18.27	0	0.16	0.02	0.01	0	1.26	14.54	97.73	0	0.1	k-feldspar
CL-GR-01-mafic	igneous apophysis - mafic	38	64.46	0	18.37	0	0.23	0.02	0	0	1.12	14.94	99.14	0	0	k-feldspar
CL-GR-01-mafic	igneous apophysis - mafic	28	64.6	0	22.13	0.01	0.3	0	0.02	1.89	9.78	0.73	99.46	68.42	0.11	plagioclase
CL-GR-01-mafic	igneous apophysis - mafic	53	63.31	0	22.92	0	0.17	0	0	4.17	8.97	0.31	99.84	0	0	plagioclase
CL-GR-01-mafic	igneous apophysis - mafic	30	63.33	0	22.88	0.04	0.09	0.02	0	4.25	9.01	0.22	99.84	273.68	0	plagioclase
CL-GR-01-mafic	igneous apophysis - mafic	29	63.86	0	22.92	0	0.15	0.03	0	4.27	9.15	0.23	100.61	0	0	plagioclase
CL-GR-01-mafic	igneous apophysis - mafic	52	63.52	0	22.93	0	0.2	0.05	0	4.3	9.12	0.19	100.31	0	0	plagioclase
CL-GR-01-mafic	igneous apophysis - mafic	40	62.68	0	23.39	0.03	0.3	0	0	4.4	9.17	0.2	100.18	205.26	0	plagioclase
CL-GR-01-mafic	igneous apophysis - mafic	51	63.05	0	22.91	0.05	0.19	0	0	4.42	9.05	0.18	99.86	342.1	0	plagioclase
CL-GR-01-mafic	igneous apophysis - mafic	42	62.1	0.02	23.57	0.01	0.45	0	0	4.84	8.83	0.18	100	68.42	0	plagioclase
DB-PG-02	igneous apophysis - grt-leucogranite	104	66.01		19.14		0.24		0.01	0	4.67	11.2	101.27		0.07	plagioclase
DB-PG-02	igneous apophysis - grt-leucogranite	61	65.16		18.61		0.01		0.02	0	1.27	15.06	100.16		0.78	k-feldspar
DB-PG-02	igneous apophysis - grt-leucogranite	60	64.85		18.75		0.08		0.03	0	1.22	15.12	100.1		0.4	k-feldspar
DB-PG-02	igneous apophysis - grt-leucogranite	118	62.96	0.03	18.57		0.89	0.02	0.12	0	0.37	15.18	98.19		0.19	k-feldspar
DB-PG-02	igneous apophysis - grt-leucogranite	123	64.18		18.52		0.05		0.01	0	1	15.27	99.04		0.26	k-feldspar
DB-PG-02	igneous apophysis - grt-leucogranite	3	65.08		18.52		0.03		0.01	0	1.08	15.27	100		0.37	k-feldspar
DB-PG-02	igneous apophysis - grt-leucogranite	62	64.87		18.67		0.06		0.01	0	1.13	15.3	100.06		0.23	k-feldspar
DB-PG-02	igneous apophysis - grt-leucogranite	103	64.89		18.52		0.07		0	0	1.19	15.37	100.05		0	k-feldspar
DB-PG-02	igneous apophysis - grt-leucogranite	14	64.41		18.72		0		0.01	0	1.07	15.39	99.6		1	k-feldspar
DB-PG-02	igneous apophysis - grt-leucogranite	16	64.69		18.53		0.13		0	0	1.01	15.47	99.84		0	k-feldspar
DB-PG-02	igneous apophysis - grt-leucogranite	124	64.28		18.44		0.01		0	0	0.91	15.51	99.16		0	k-feldspar
DB-PG-02	igneous apophysis - grt-leucogranite	102	64.91		18.75		0		0.01	0	1.07	15.53	100.29		1	k-feldspar
DB-PG-02	igneous apophysis - grt-leucogranite	42	64.77		18.62		0.03		0	0	0.84	15.7	99.96		0	k-feldspar
DB-PG-02	igneous apophysis - grt-leucogranite	30	64.67		18.62		0.11		0	0	0.79	15.81	100		0	k-feldspar
DB-PG-02	igneous apophysis - grt-leucogranite	177	64.06		18.76		0.01		0	0	0.76	15.82	99.47		0	k-feldspar
DB-PG-02	igneous apophysis - grt-leucogranite	31	64.69		18.54		0.09		0.01	0	0.72	15.85	99.93		0.17	k-feldspar
DB-PG-02	igneous apophysis - grt-leucogranite	49	64.91		18.5		0.06		0	0	0.84	15.88	100.25		0	k-feldspar
DB-PG-02	igneous apophysis - grt-leucogranite	32	64.7		18.65		0.08		0	0	0.66	16.09	100.21		0	k-feldspar
DB-PG-02	igneous apophysis - grt-leucogranite	41	65.13		18.56		0.14		0	0	0.49	16.19	100.53		0	k-feldspar
DB-PG-02	igneous apophysis - grt-leucogranite	125	63.98		18.36		0.04		0	0	0.45	16.21	99.09		0	k-feldspar
DB-PG-02	igneous apophysis - grt-leucogranite	15	64		18.67		0.3		0.01	0	0.39	16.48	99.88		0.06	k-feldspar
DB-PG-02	igneous apophysis - grt-leucogranite	138	63.65	0.57	18.85		6.56	0.3	0.5	0.03	7.38	1.46	99.32		0.12	plagioclase
DB-PG-02	igneous apophysis - grt-leucogranite	130	66.68		20.25		0.04		0.01	0.85	10.6	0.19	98.62		0.31	plagioclase
DB-PG-02	igneous apophysis - grt-leucogranite	107	67.62		20.46		0.05		0	0.86	11.11	0.08	100.17		0	plagioclase

FELDSPARS

Sample	Rock group	anal. #	SiO2	TiO2	Al2O3	Cr2O3	FeO	MnO	MgO	CaO	Na2O	K2O	Total	Cr ppm	XMg	mineral
DB-PG-02	igneous apophysis - grt-leucogranite	185	65.91		20.07		0.04		0	0.88	10.82	0.15	97.9		0	plagioclase
DB-PG-02	igneous apophysis - grt-leucogranite	109	67.29		20.38		0.08		0	0.88	10.74	0.23	99.61		0	plagioclase
DB-PG-02	igneous apophysis - grt-leucogranite	128	67.36		20.43		0.04		0.02	1	10.7	0.13	99.69		0.47	plagioclase
DB-PG-02	igneous apophysis - grt-leucogranite	148	65.19		20.53		0.06		0.02	1.06	10.41	0.16	97.45		0.37	plagioclase
DB-PG-02	igneous apophysis - grt-leucogranite	150	65.45		20.51		0.03		0	1.17	10.39	0.12	97.68		0	plagioclase
DB-PG-02	igneous apophysis - grt-leucogranite	180	66.72		20.91		0.03		0	1.17	10.58	0.15	99.6		0	plagioclase
DB-PG-02	igneous apophysis - grt-leucogranite	121	62.21	0.25	20.16		3.28	0.13	0.35	1.19	8.21	0.92	96.79		0.16	plagioclase
DB-PG-02	igneous apophysis - grt-leucogranite	151	65.46		20.43		0		0	1.21	10.4	0.09	97.59			plagioclase
DB-PG-02	igneous apophysis - grt-leucogranite	149	65.28		20.63		0.06		0	1.21	10.39	0.17	97.73		0	plagioclase
DB-PG-02	igneous apophysis - grt-leucogranite	155	66.75		20.92		0		0	1.24	10.82	0.1	99.84			plagioclase
DB-PG-02	igneous apophysis - grt-leucogranite	152	65.6		20.64		0.07		0.02	1.25	10.54	0.11	98.27		0.34	plagioclase
DB-PG-02	igneous apophysis - grt-leucogranite	167	66.1		20.65		0.05		0	1.26	10.51	0.25	98.81		0	plagioclase
DB-PG-02	igneous apophysis - grt-leucogranite	147	64.95		20.78		0.04		0.02	1.28	10.24	0.2	97.5		0.47	plagioclase
DB-PG-02	igneous apophysis - grt-leucogranite	108	66.73		20.85		0.04		0	1.29	10.46	0.35	99.73		0	plagioclase
DB-PG-02	igneous apophysis - grt-leucogranite	170	65.37		20.87		0		0	1.31	10.19	0.35	98.08			plagioclase
DB-PG-02	igneous apophysis - grt-leucogranite	111	66.63		20.86		0.01		0	1.32	10.68	0.22	99.74		0	plagioclase
DB-PG-02	igneous apophysis - grt-leucogranite	129	65.39		20.71		0		0	1.34	10.28	0.09	97.84			plagioclase
DB-PG-02	igneous apophysis - grt-leucogranite	166	65.94		21.44		0.06		0.02	1.35	9.19	0.21	98.2		0.37	plagioclase
DB-PG-02	igneous apophysis - grt-leucogranite	184	65.62		20.7		0.06		0	1.36	10.34	0.23	98.31		0	plagioclase
DB-PG-02	igneous apophysis - grt-leucogranite	153	65.33		20.56		0.05		0	1.36	10.32	0.28	97.9		0	plagioclase
DB-PG-02	igneous apophysis - grt-leucogranite	105	67.14		20.88		0.02		0	1.37	10.34	0.18	99.93		0	plagioclase
DB-PG-02	igneous apophysis - grt-leucogranite	168	65.7		20.82		0.04		0	1.37	10.38	0.21	98.53		0	plagioclase
DB-PG-02	igneous apophysis - grt-leucogranite	182	65.51		20.73		0.04		0	1.37	10.18	0.25	98.09		0	plagioclase
DB-PG-02	igneous apophysis - grt-leucogranite	179	66.21		21.03		0.03		0.01	1.38	10.62	0.21	99.52		0.37	plagioclase
DB-PG-02	igneous apophysis - grt-leucogranite	178	66.18		20.88		0.03		0	1.38	10.44	0.22	99.17		0	plagioclase
DB-PG-02	igneous apophysis - grt-leucogranite	169	65.69		20.7		0.04		0	1.39	10.26	0.15	98.22		0	plagioclase
DB-PG-02	igneous apophysis - grt-leucogranite	110	66.25		20.96		0.04		0	1.39	10.64	0.24	99.53		0	plagioclase
DB-PG-02	igneous apophysis - grt-leucogranite	173	66.56		21.03		0.07		0	1.39	10.42	0.25	99.71		0	plagioclase
DB-PG-02	igneous apophysis - grt-leucogranite	146	65.66		20.87		0.01		0.01	1.4	10.24	0.2	98.42		0.64	plagioclase
DB-PG-02	igneous apophysis - grt-leucogranite	171	64.86		20.67		0.06		0	1.4	10.15	0.38	97.52		0	plagioclase
DB-PG-02	igneous apophysis - grt-leucogranite	154	66.65		20.88		0.05		0.04	1.41	10.64	0.18	99.89		0.59	plagioclase
DB-PG-02	igneous apophysis - grt-leucogranite	159	66.67		20.92		0.09		0	1.41	10.59	0.3	99.98		0	plagioclase
DB-PG-02	igneous apophysis - grt-leucogranite	172	65.41		20.47		0.01		0	1.42	10.3	0.25	97.88		0	plagioclase
DB-PG-02	igneous apophysis - grt-leucogranite	158	66.7		20.95		0		0	1.42	10.63	0.26	99.98			plagioclase
DB-PG-02	igneous apophysis - grt-leucogranite	127	66.41		20.81		0.03		0.01	1.43	10.48	0.19	99.36		0.37	plagioclase
DB-PG-02	igneous apophysis - grt-leucogranite	174	66.62		20.86		0		0.01	1.43	10.67	0.21	99.82		1	plagioclase
DB-PG-02	igneous apophysis - grt-leucogranite	106	66.81		20.95		0.09		0	1.44	10.56	0.13	99.99		0	plagioclase
DB-PG-02	igneous apophysis - grt-leucogranite	156	66.56		20.95		0.03		0	1.44	10.57	0.2	99.76		0	plagioclase
DB-PG-02	igneous apophysis - grt-leucogranite	165	65.73		20.71		0.08		0.02	1.44	10.23	0.22	98.42		0.31	plagioclase
DB-PG-02	igneous apophysis - grt-leucogranite	157	66.39		21.21		0.07		0	1.44	10.41	0.23	99.78		0	plagioclase
DB-PG-02	igneous apophysis - grt-leucogranite	43	67.33		21.09		0.06		0	1.46	10.69	0.11	100.76		0	plagioclase

FELDSPARS

Sample	Rock group	anal. #	SiO2	TiO2	Al2O3	Cr2O3	FeO	MnO	MgO	CaO	Na2O	K2O	Total	Cr ppm	XMg	mineral
DB-PG-02	igneous apophysis - grt-leucogranite	175	66.66		20.92		0		0	1.46	10.72	0.12	99.91			plagioclase
DB-PG-02	igneous apophysis - grt-leucogranite	63	66.84		20.78		0.04		0	1.48	10.35	0.34	99.89		0	plagioclase
DB-PG-02	igneous apophysis - grt-leucogranite	64	66.71		20.95		0.06		0.01	1.49	10.68	0.12	100.02		0.23	plagioclase
DB-PG-02	igneous apophysis - grt-leucogranite	39	67	0.04	21.32		0.25	0	0.12	1.49	10.62	0.2	101.03		0.46	plagioclase
DB-PG-02	igneous apophysis - grt-leucogranite	44	67.2		21.04		0.08		0	1.5	10.62	0.17	100.65		0	plagioclase
DB-PG-02	igneous apophysis - grt-leucogranite	181	65.36		20.75		0.05		0	1.51	10.37	0.15	98.19		0	plagioclase
DB-PG-02	igneous apophysis - grt-leucogranite	28	66.93		21.27		0.07		0.01	1.53	10.49	0.17	100.47		0.2	plagioclase
DB-PG-02	igneous apophysis - grt-leucogranite	145	65.07		20.77		0.04		0	1.57	10.28	0.13	97.86		0	plagioclase
DB-PG-02	igneous apophysis - grt-leucogranite	183	65.33		21.05		0.05		0	1.57	10.27	0.19	98.46		0	plagioclase
DB-PG-02	igneous apophysis - grt-leucogranite	176	66.47		21.31		0.05		0.01	1.64	10.56	0.09	100.14		0.26	plagioclase
DB-PG-02	igneous apophysis - grt-leucogranite	131	65.16		21.21		0		0.01	1.66	10.01	0.28	98.35		1	plagioclase
DB-PG-02	igneous apophysis - grt-leucogranite	132	65.12		20.87		0.03		0.01	1.69	10.28	0.15	98.19		0.37	plagioclase
DB-PG-02	igneous apophysis - grt-leucogranite	27	66.59		20.97		0.12		0	1.7	10.46	0.32	100.16		0	plagioclase
DB-PG-02	igneous apophysis - grt-leucogranite	29	67.13		21.32		0.07		0.02	1.71	10.41	0.35	101.01		0.34	plagioclase

PYROXENE

Sample	Rock group	anal. #	SiO2	TiO2	Al2O3	Cr2O3	FeO	MnO	MgO	CaO	Na2O	K2O	Total	Cr ppm	XMg
AT-PS-02	prograde skarn	30	55.83	0	0.02		0.1	0	18.98	26.08	0.01	0	101.02		1.00
AT-PS-02	prograde skarn	36	55.84	0	0.03		0.08	0.04	18.93	26.15	0.03	0	101.09		1.00
AT-PS-01	prograde skarn	55	55.57	0.04	0.04		0.49	0	19.19	25.44	0.02	0	100.79		0.99
AT-PS-01	prograde skarn	36	55.44	0.02	0.06		0.48	0.02	18.72	25.36	0	0	100.1		0.99
AT-PS-01	prograde skarn	34	55.65	0.01	0.07		0.45	0.02	18.78	25.62	0.04	0	100.62		0.99
AT-PS-01	prograde skarn	38	55.33	0.01	0.01		0.44	0.04	18.72	25.49	0.02	0	100.04		0.99
AT-PS-01	prograde skarn	45	55.68	0.04	0.01		0.42	0.01	18.68	25.6	0.01	0	100.44		0.99
AT-PS-01	prograde skarn	44	55.64	0.02	0.02		0.41	0	19.1	25.63	0	0	100.81		0.99
AT-PS-01	prograde skarn	33	55.98	0.03	0.02		0.4	0.02	18.89	25.67	0.02	0	101.04		0.99
AT-PS-01	prograde skarn	82	56.39	0.03	0.02		0.39	0.08	19.29	25.67	0.03	0	101.89		0.99
AT-PS-01	prograde skarn	57	55.66	0	0.01		0.39	0	18.97	25.77	0	0	100.82		0.99
AT-PS-01	prograde skarn	47	55.57	0.05	0.06		0.38	0	18.81	25.5	0.02	0	100.38		0.99
AT-PS-01	prograde skarn	35	55.39	0.05	0.02		0.38	0.03	18.55	25.56	0.01	0	99.98		0.99
AT-PS-01	prograde skarn	46	55.77	0.01	0.03		0.36	0.01	18.79	25.65	0	0	100.62		0.99
AT-PS-01	prograde skarn	67	55.52	0.07	0.02		0.34	0	18.81	25.67	0.02	0	100.44		0.99
AT-PS-02	prograde skarn	52	55.7	0.02	0		0.48	0	18.79	26.1	0.01	0	101.09		0.99
AT-PS-02	prograde skarn	46	55.71	0.02	0		0.45	0	18.65	25.93	0.01	0	100.76		0.99
AT-PS-02	prograde skarn	50	55.58	0	0.02		0.38	0	18.89	26.06	0.01	0	100.93		0.99
AT-PS-02	prograde skarn	45	55.61	0	0.01		0.36	0.01	18.79	26.11	0.06	0	100.96		0.99
AT-PS-02	prograde skarn	31	55.55	0	0.07		0.23	0	18.74	26.15	0.02	0	100.76		0.99
AT-PS-02	prograde skarn	39	55.47	0	0		0.21	0	18.88	26.19	0	0	100.75		0.99
AT-PS-02	prograde skarn	49	55.47	0.01	0.03		0.2	0	18.88	26.01	0.03	0	100.64		0.99
CL-PS-01C	prograde skarn	259	54.54	0.06	0.07	0	0.49	0	18.36	25.74	0	0	99.25	9.41	0.99
AT-PS-03	prograde skarn	136	55.8	0	0.1		0.46	0.01	18.98	25.42	0.03	0	100.79		0.99
AT-PS-03	prograde skarn	175	55.17	0.03	0.08		0.45	0.05	18.82	25.47	0.01	0	100.08		0.99
AT-PS-03	prograde skarn	137	56.01	0	0.14		0.43	0.01	19.13	25.48	0.03	0	101.23		0.99
AT-PS-03	prograde skarn	179	55.68	0	0.1		0.43	0.01	18.96	25.38	0.01	0	100.57		0.99
AT-PS-03	prograde skarn	185	55.43	0.02	0.13		0.42	0.04	18.62	25.53	0	0	100.18		0.99
AT-PS-03	prograde skarn	178	55.56	0	0.13		0.41	0.02	18.84	25.13	0.06	0	100.16		0.99
AT-PS-03	prograde skarn	177	55.86	0.02	0.04		0.4	0	18.97	25.38	0	0	100.68		0.99
AT-PS-03	prograde skarn	154	55.37	0	0.08		0.39	0.06	19.24	25.42	0.03	0	100.6		0.99
AT-PS-03	prograde skarn	156	55.37	0	0.09		0.37	0.02	19.09	25.49	0.02	0	100.44		0.99

PYROXENE

Sample	Rock group	anal. #	SiO2	TiO2	Al2O3	Cr2O3	FeO	MnO	MgO	CaO	Na2O	K2O	Total	Cr ppm	XMg
AT-PS-03	prograde skarn	196	55.39	0	0.12		0.37	0.05	18.8	25.49	0	0	100.22		0.99
AT-PS-03	prograde skarn	130	55.01	0.05	0.1		0.36	0.07	18.64	25.57	0.02	0	99.81		0.99
AT-PS-03	prograde skarn	153	55.41	0.01	0.03		0.34	0.04	19.06	25.28	0.01	0	100.18		0.99
AT-PS-03	prograde skarn	152	55.47	0.05	0.02		0.33	0	19.02	25.54	0.03	0	100.46		0.99
AT-PS-03	prograde skarn	134	56.01	0	0.06		0.33	0	19.24	25.35	0.02	0	101.02		0.99
AT-PS-03	prograde skarn	173	55.73	0.04	0.04		0.32	0.01	18.98	25.51	0.02	0.01	100.66		0.99
AT-PS-03	prograde skarn	174	55.39	0	0.04		0.32	0.02	18.77	25.46	0.03	0	100.02		0.99
AT-PS-03	prograde skarn	133	55.53	0	0.05		0.31	0	19.17	25.32	0.02	0	100.42		0.99
AT-PS-03	prograde skarn	131	55.96	0	0.04		0.31	0	19.27	25.43	0	0	101		0.99
AT-PS-03	prograde skarn	176	55.62	0.01	0.02		0.29	0.05	18.87	25.54	0.02	0.01	100.41		0.99
AT-PS-03	prograde skarn	180	55.73	0.03	0.01		0.28	0.02	19.12	25.55	0.01	0	100.76		0.99
AT-PS-03	prograde skarn	132	55.7	0	0.05		0.25	0.01	18.98	25.27	0.01	0	100.27		0.99
AT-PS-03	prograde skarn	197	55.61	0.02	0.08		0.22	0	18.84	25.61	0.02	0	100.4		0.99
AT-PS-03	prograde skarn	172	55.36	0	0.02		0.22	0.01	18.92	25.47	0.03	0	100.03		0.99
AT-PS-01	prograde skarn	68	55.33	0	0.45		0.84	0.03	18.58	25.27	0.03	0	100.53		0.98
AT-PS-01	prograde skarn	58	55.31	0.02	0.22		0.78	0.03	18.84	24.96	0.08	0.01	100.23		0.98
AT-PS-01	prograde skarn	59	55.31	0.04	0.24		0.76	0.01	18.69	25.13	0.07	0	100.24		0.98
AT-PS-01	prograde skarn	66	55.52	0.01	0.5		0.73	0.03	18.55	25.19	0.06	0	100.59		0.98
AT-PS-01	prograde skarn	89	55.59	0	0.14		0.72	0	18.82	25.34	0.02	0	100.64		0.98
AT-PS-01	prograde skarn	65	55.58	0.03	0.46		0.72	0.01	18.63	25.37	0.07	0	100.87		0.98
AT-PS-01	prograde skarn	56	55.4	0.01	0.21		0.69	0	18.57	25.4	0.04	0	100.33		0.98
AT-PS-01	prograde skarn	12	55.67	0.06	0.41		0.69	0	18.59	25.12	0.09	0	100.64		0.98
AT-PS-01	prograde skarn	80	55.79	0.01	0.1		0.67	0.04	18.84	25.56	0.01	0	101.01		0.98
AT-PS-01	prograde skarn	70	55.59	0.06	0.07		0.67	0	18.68	25.43	0.04	0	100.55		0.98
AT-PS-01	prograde skarn	13	55.54	0.02	0.24		0.65	0.01	18.69	25.29	0.05	0	100.49		0.98
AT-PS-01	prograde skarn	42	55.33	0.01	0.33		0.65	0	18.66	25.27	0.02	0	100.28		0.98
AT-PS-01	prograde skarn	48	55.81	0.02	0.08		0.61	0.01	18.8	25.41	0.01	0	100.75		0.98
AT-PS-01	prograde skarn	69	55.83	0.04	0.23		0.61	0	18.7	25.51	0.05	0	100.96		0.98
AT-PS-01	prograde skarn	81	55.67	0	0.18		0.6	0.01	18.71	25.49	0.03	0	100.69		0.98
AT-PS-01	prograde skarn	60	55.58	0.06	0.04		0.57	0.05	18.86	25.39	0.04	0	100.59		0.98
AT-PS-01	prograde skarn	79	55.62	0.04	0.31		0.55	0	18.76	25.38	0.05	0.01	100.73		0.98
CL-PS-01A	prograde skarn	196	55.14	0.03	0.33	0.03	0.63	0.01	18.48	25.24	0.02	0	99.91	171.63	0.98

PYROXENE

Sample	Rock group	anal. #	SiO2	TiO2	Al2O3	Cr2O3	FeO	MnO	MgO	CaO	Na2O	K2O	Total	Cr ppm	XMg
CL-PS-01A	prograde skarn	217	55.02	0.05	0.2	0.02	0.8	0	18.23	25.25	0.01	0	99.59	139.48	0.98
CL-PS-01A	prograde skarn	195	54.63	0.02	0.3	0.02	0.67	0	18.37	25.39	0.04	0	99.43	127.47	0.98
CL-PS-01A	prograde skarn	218	54.62	0.04	0.1	0	0.71	0	18.43	25.41	0.01	0	99.32	25.54	0.98
CL-PS-01A	prograde skarn	219	55.06	0.04	0.12	0	0.78	0.03	18.44	25.46	0.02	0	99.95	0.1	0.98
CL-PS-01A	prograde skarn	216	55.35	0.02	0.29	0	0.76	0.01	18.59	25.32	0.03	0.01	100.37	0.1	0.98
CL-PS-01B	prograde skarn	233	54.05	0.06	0.06	0	0.77	0	18.24	25.82	0.02	0	99.02	0.1	0.98
CL-PS-01B	prograde skarn	236	53.91	0.04	0.03	0	0.74	0.02	17.87	25.72	0.01	0	98.35	0.1	0.98
CL-PS-01B	prograde skarn	234	54.56	0.05	0.01	0	0.56	0	18.17	25.71	0.01	0.01	99.08	0.1	0.98
CL-PS-01C	prograde skarn	268	54.51	0.08	0.05	0.01	0.62	0.03	18.46	25.54	0.01	0	99.31	42.37	0.98
CL-PS-01C	prograde skarn	258	54.9	0.09	0.01	0	0.53	0	18.98	25.82	0	0	100.33	0.1	0.98
DB-PS-01	prograde skarn	3	55.09	0	0.2	0.04	0.79	0.04	18.51	25.3	0.04	0	100.01	273.68	0.98
DB-PS-01	prograde skarn	15	55.69	0	0.12	0	0.84	0.08	18.84	25.35	0	0	100.92		0.98
DB-PS-01	prograde skarn	1	54.13	0	0.17	0	0.77	0.1	18.16	25.8	0.05	0	99.17		0.98
DB-PS-01	prograde skarn	2	54.51	0	0.15	0	0.68	0.09	18.39	25.23	0.06	0	99.11		0.98
AT-PS-03	prograde skarn	157	55.68	0	0.13		0.65	0.01	19.22	25.66	0.04	0	101.39		0.98
AT-PS-03	prograde skarn	155	55.71	0	0.01		0.55	0.04	18.88	25.47	0.03	0	100.68		0.98
AT-PS-03	prograde skarn	135	55.43	0	0.09		0.51	0.01	18.52	25.46	0	0	100.02		0.98
CL-PS-01A	prograde skarn	215	55.85	0.04	0.28	0.01	1.12	0	18.87	25.16	0.03	0	101.35	90.1	0.97
CL-PS-01A	prograde skarn	198	54.93	0.05	0.38	0.01	1.1	0.03	18.11	25.38	0.07	0	100.05	59.43	0.97
CL-PS-01B	prograde skarn	235	54.62	0.04	0.29	0.02	0.99	0.01	18.28	25.22	0.02	0	99.49	141.03	0.97
DB-PS-01	prograde skarn	16	55.12	0	0.06	0	0.85	0.1	18.55	25.44	0.01	0	100.14		0.97
CL-PS-01A	prograde skarn	197	54.32	0.03	0.33	0	2.34	0.05	17.17	25.33	0.11	0	99.67	0.1	0.93
AT-PS-02	prograde skarn	34	55	0.03	0.54		2.69	0.07	17.1	25.26	0.29	0	100.98		0.92
AT-PS-02	prograde skarn	37	54.84	0.03	0.37		2.69	0.05	17.12	25.51	0.19	0	100.8		0.92
AT-PS-02	prograde skarn	32	54.37	0.02	0.37		2.68	0.06	17.02	25.49	0.16	0	100.18		0.92
AT-PS-02	prograde skarn	48	55.15	0.02	0.5		2.51	0.02	17.39	25.25	0.26	0	101.1		0.92
AT-PS-02	prograde skarn	47	54.65	0.02	0.43		3.3	0.04	16.75	25.22	0.23	0	100.64		0.90
AT-PS-02	prograde skarn	51	55.13	0.04	0.45		3.26	0.08	16.85	25.17	0.26	0	101.24		0.90
AT-PS-02	prograde skarn	40	54.4	0.01	0.52		5.18	0.07	15.58	24.84	0.32	0	100.91		0.84
AT-MZ-02	igneous apophysis	14	53.88	0	0.48	0	7.37	0.17	13.96	23.8	0.37	0	100.04	0	0.77
AT-MZ-02	igneous apophysis	15	53.66	0.08	0.95	0.03	7.84	0.19	13.79	23.24	0.71	0	100.48	205.26	0.76
AT-MZ-02	igneous apophysis	5	53.51	0	0.18	0.01	7.87	0.12	13.87	24.27	0.16	0	100	68.42	0.76

PYROXENE

Sample	Rock group	anal. #	SiO2	TiO2	Al2O3	Cr2O3	FeO	MnO	MgO	CaO	Na2O	K2O	Total	Cr ppm	XMg
AT-MZ-02	igneous apophysis	3	53.02	0	0.25	0.03	8.13	0.12	13.34	24.45	0.26	0	99.59	205.26	0.75
AT-MZ-02	igneous apophysis	19	53.32	0.02	0.79	0.06	8.4	0.15	13.14	23.29	0.65	0	99.84	410.52	0.74
AT-MZ-02	igneous apophysis	17	52.96	0.02	1.02	0.05	8.5	0.23	13.09	23.15	0.74	0.01	99.78	342.1	0.73
AT-MZ-02	igneous apophysis	11	52.79	0	0.61	0.01	9.51	0.25	12.57	22.86	0.52	0	99.12	68.42	0.70
AT-MZ-02	igneous apophysis	9	52.47	0.01	1.03	0.01	10.35	0.24	11.82	22.77	0.68	0	99.4	68.42	0.67
AT-MZ-02	igneous apophysis	7	52.83	0.02	1.05	0.04	10.77	0.21	11.55	22.81	0.71	0.03	100.02	273.68	0.66
AT-MZ-02	igneous apophysis	12	51.56	0.11	1.87	0.06	11.63	0.17	11.06	22.16	0.98	0	99.59	410.52	0.63

OLIVINE

Sample	Rock group	anal. #	SiO2	TiO2	Al2O3	Cr2O3	FeO	MnO	MgO	CaO	Na2O	K2O	Total	Cr ppm	XMg
CL-PS-02A	prograde skarn - sp skarn	313	38.81	0.01	0	0.04	15.85	0.38	44.84	0.01	0	0	99.95	256.23	0.83
CL-PS-02A	prograde skarn - sp skarn	315	39.09	0	0	0	15.8	0.35	44.74	0.02	0	0	99.99	0.1	0.83
CL-PS-02A	prograde skarn - sp skarn	344	39.14	0	0.01	0.02	15.14	0.33	45.42	0.06	0	0.01	100.12	163.99	0.84
CL-PS-02A	prograde skarn - sp skarn	314	39.47	0.02	0	0	15.47	0.32	45.62	0.02	0.04	0	100.95	0.1	0.84
CL-PS-02A	prograde skarn - sp skarn	343	39.82	0.01	0	0.01	14.62	0.32	46.28	0.03	0	0.01	101.11	88.88	0.85
CL-PS-02A	prograde skarn - sp skarn	312	39.55	0.01	0.03	0	14.93	0.35	46.16	0.03	0	0	101.07	0.1	0.85
CL-PS-01C	prograde skarn	269	40.96	0.01	0	0.02	4.79	0.08	53.33	0.05	0	0	99.24	138.45	0.95
CL-PS-01C	prograde skarn	270	41.44	0	0	0	4.86	0.04	53.61	0.07	0.01	0	100.04	0.1	0.95
DB-PS-01	prograde skarn	5	40.81	0	0.01	0.03	4.61	0.28	53.57	0.06	0	0	99.36	205.26	0.95
DB-PS-01	prograde skarn	4	40.57	0	0	0	4.6	0.2	53.83	0.02	0	0	99.22	0	0.95
DB-PS-01	prograde skarn	6	41.18	0	0	0	4.58	0.24	53.9	0.04	0.01	0	99.96	0	0.95
AT-PS-03	prograde skarn	167	42.32	0	0.02		4.53	0.12	53.26	0.02	0.01	0	100.26		0.95
CL-PS-01C	prograde skarn	245	42.15	0	0.02	0.03	3.76	0.06	55.31	0.04	0.02	0	101.38	176.08	0.96
CL-PS-01C	prograde skarn	247	41.54	0.02	0.04	0.01	3.84	0.06	55.22	0	0	0	100.73	37.04	0.96
CL-PS-01C	prograde skarn	246	41.75	0.02	0.01	0	3.8	0.05	55.12	0.04	0	0	100.79	0.1	0.96
AT-PS-03	prograde skarn	193	42.07	0	0		4.05	0.06	53.06	0.02	0.01	0.01	99.27		0.96
AT-PS-03	prograde skarn	165	42.17	0.02	0		4.01	0.12	53.04	0	0	0	99.37		0.96
AT-PS-03	prograde skarn	195	42.24	0.01	0		3.99	0.14	53.51	0.01	0	0	99.89		0.96
AT-PS-03	prograde skarn	194	42.26	0	0		3.91	0.07	53.72	0.02	0.02	0	100		0.96
AT-PS-03	prograde skarn	166	42.34	0	0		3.88	0.1	53.74	0	0.01	0	100.08		0.96
AT-PS-03	prograde skarn	140	42.54	0	0		3.85	0.1	53.49	0.01	0	0	99.99		0.96
AT-PS-03	prograde skarn	192	42.15	0	0		3.79	0.06	53.61	0.01	0	0	99.62		0.96
AT-PS-03	prograde skarn	164	42.02	0	0		3.62	0.09	53.54	0	0	0	99.27		0.96
AT-PS-03	prograde skarn	141	42.74	0	0		3.6	0.06	54.03	0	0	0	100.42		0.96
AT-PS-03	prograde skarn	162	42.4	0	0		3.4	0.11	53.7	0	0	0	99.61		0.97
AT-PS-03	prograde skarn	142	42.96	0.01	0		3.31	0.14	54.42	0.01	0.03	0	100.87		0.97
AT-PS-03	prograde skarn	163	42.7	0	0		3.28	0.09	53.94	0.01	0.01	0	100.03		0.97
AT-PS-03	prograde skarn	191	42.44	0	0		3.18	0.04	54.63	0	0.02	0	100.3		0.97
AT-PS-03	prograde skarn	120	42.17	0	0		3.16	0.07	53.68	0	0.01	0	99.08		0.97
AT-PS-03	prograde skarn	144	42.94	0.03	0.02		3.13	0.09	54.24	0	0	0	100.47		0.97
AT-PS-03	prograde skarn	15	42.33	0	0		3.13	0.11	53.99	0.02	0.02	0	99.6		0.97
AT-PS-03	prograde skarn	143	42.88	0.01	0		3.12	0.1	54.42	0	0.02	0	100.56		0.97

OLIVINE

Sample	Rock group	anal. #	SiO2	TiO2	Al2O3	Cr2O3	FeO	MnO	MgO	CaO	Na2O	K2O	Total	Cr ppm	XMg
AT-PS-03	prograde skarn	123	42.44	0.01	0		3.06	0.09	53.66	0	0	0	99.26		0.97
AT-PS-03	prograde skarn	124	42.37	0	0		3.03	0.07	53.79	0	0.01	0.01	99.29		0.97
AT-PS-03	prograde skarn	122	42.5	0	0		3	0.13	53.85	0	0.01	0.01	99.5		0.97
AT-PS-03	prograde skarn	121	42.59	0	0		3	0.03	53.91	0.02	0.02	0	99.55		0.97

CARBONATES

Sample	Rock group	anal. #	FeO	MnO	MgO	CaO	Total	XMg	mineral
AT-PS-01	prograde skarn	150	0.19	0.04	2.1	52.33	54.66	0.95	calcite
AT-PS-01	prograde skarn	152	0.16	0	2.8	51.45	54.41	0.97	calcite
AT-PS-01	prograde skarn	160	0.14	0.01	1.89	52.44	54.48	0.96	calcite
AT-PS-01	prograde skarn	175	0.13	0.05	1.85	52.65	54.68	0.96	calcite
AT-PS-01	prograde skarn	169	0.12	0.08	1.46	52.99	54.65	0.96	calcite
AT-PS-01	prograde skarn	174	0.12	0.03	1.31	53.29	54.75	0.95	calcite
AT-PS-01	prograde skarn	148	0.11	0.03	1.84	54.92	56.9	0.97	calcite
AT-PS-01	prograde skarn	138	0.11	0.02	1.8	52.91	54.84	0.97	calcite
AT-PS-01	prograde skarn	135	0.11	0	2.68	52.22	55.01	0.98	calcite
AT-PS-01	prograde skarn	167	0.11	0.01	1.9	52.56	54.58	0.97	calcite
AT-PS-01	prograde skarn	158	0.11	0	1.83	52.87	54.81	0.97	calcite
AT-PS-01	prograde skarn	149	0.11	0	2.19	52.32	54.62	0.97	calcite
AT-PS-01	prograde skarn	172	0.11	0.02	1.46	53.52	55.11	0.96	calcite
AT-PS-01	prograde skarn	153	0.1	0.04	2.43	52.27	54.84	0.98	calcite
AT-PS-01	prograde skarn	120	0.1	0.05	2.9	51.43	54.48	0.98	calcite
AT-PS-01	prograde skarn	151	0.1	0.01	2.14	51.74	53.99	0.97	calcite
AT-PS-01	prograde skarn	182	0.1	0.03	2.51	51.82	54.46	0.98	calcite
AT-PS-01	prograde skarn	163	0.1	0.08	2.07	52.58	54.83	0.97	calcite
AT-PS-01	prograde skarn	159	0.1	0.01	2.05	52.06	54.22	0.97	calcite
AT-PS-01	prograde skarn	145	0.09	0.03	1.21	52.95	54.28	0.96	calcite
AT-PS-01	prograde skarn	137	0.09	0.01	1.84	52.95	54.89	0.97	calcite
AT-PS-01	prograde skarn	162	0.09	0	2.08	52.39	54.56	0.98	calcite
AT-PS-01	prograde skarn	166	0.08	0.09	1.34	53.03	54.54	0.97	calcite
AT-PS-01	prograde skarn	165	0.08	0.02	2.23	52.29	54.62	0.98	calcite
AT-PS-01	prograde skarn	122	0.08	0.01	2.72	51.41	54.22	0.98	calcite
AT-PS-01	prograde skarn	126	0.08	0.02	2.73	53.28	56.11	0.98	calcite
AT-PS-01	prograde skarn	131	0.08	0.02	0.09	54.92	55.11	0.67	calcite
AT-PS-01	prograde skarn	181	0.08	0.08	1.79	53.07	55.02	0.98	calcite
AT-PS-01	prograde skarn	177	0.07	0	0.86	53.86	54.79	0.95	calcite
AT-PS-01	prograde skarn	180	0.07	0	2.02	52.77	54.86	0.98	calcite

CARBONATES

Sample	Rock group	anal. #	FeO	MnO	MgO	CaO	Total	XMg	mineral
AT-PS-01	prograde skarn	139	0.07	0	1.19	53.3	54.56	0.97	calcite
AT-PS-01	prograde skarn	157	0.07	0	1.2	53.37	54.64	0.97	calcite
AT-PS-01	prograde skarn	183	0.07	0.05	2.12	52.15	54.39	0.98	calcite
AT-PS-01	prograde skarn	187	0.06	0.02	2.51	51.87	54.46	0.99	calcite
AT-PS-01	prograde skarn	146	0.06	0	1.15	52.96	54.17	0.97	calcite
AT-PS-01	prograde skarn	121	0.06	0.03	2.42	51.91	54.42	0.99	calcite
AT-PS-01	prograde skarn	130	0.06	0.06	0.06	54.95	55.13	0.64	calcite
AT-PS-01	prograde skarn	142	0.06	0.07	1.27	53.28	54.68	0.98	calcite
AT-PS-01	prograde skarn	123	0.05	0.06	2.19	52.32	54.62	0.99	calcite
AT-PS-01	prograde skarn	147	0.05	0.04	1.72	52.63	54.44	0.99	calcite
AT-PS-01	prograde skarn	161	0.05	0	1.9	52.62	54.57	0.99	calcite
AT-PS-01	prograde skarn	171	0.04	0	1.79	52.36	54.19	0.99	calcite
AT-PS-01	prograde skarn	186	0.04	0.03	2.89	51.59	54.55	0.99	calcite
AT-PS-01	prograde skarn	136	0.04	0	2.35	52.28	54.67	0.99	calcite
AT-PS-01	prograde skarn	119	0.04	0.03	2.57	51.83	54.47	0.99	calcite
AT-PS-01	prograde skarn	133	0.04	0	0.05	55.74	55.83	0.69	calcite
AT-PS-01	prograde skarn	141	0.04	0.05	0.73	53.9	54.72	0.97	calcite
AT-PS-01	prograde skarn	168	0.03	0.06	1.08	53.05	54.22	0.98	calcite
AT-PS-01	prograde skarn	189	0.03	0	1.18	53.25	54.46	0.98	calcite
AT-PS-01	prograde skarn	188	0.03	0.03	1.72	52.89	54.67	0.99	calcite
AT-PS-01	prograde skarn	173	0.03	0	1.31	53.32	54.66	0.99	calcite
AT-PS-01	prograde skarn	132	0.03	0.04	0.05	55.12	55.24	0.75	calcite
AT-PS-01	prograde skarn	155	0.02	0.02	1.37	53.22	54.63	0.99	calcite
AT-PS-01	prograde skarn	144	0.02	0.08	1.17	53.16	54.43	0.99	calcite
AT-PS-01	prograde skarn	154	0.02	0.01	0.8	54.05	54.88	0.99	calcite
AT-PS-01	prograde skarn	124	0.02	0	2.73	51.88	54.63	1.00	calcite
AT-PS-01	prograde skarn	125	0.02	0.03	2.61	51.76	54.42	1.00	calcite
AT-PS-01	prograde skarn	127	0.02	0	2.49	51.93	54.44	1.00	calcite
AT-PS-01	prograde skarn	184	0.02	0	2.09	52.09	54.2	1.00	calcite
AT-PS-01	prograde skarn	185	0.02	0	2.45	51.66	54.13	1.00	calcite

CARBONATES

Sample	Rock group	anal. #	FeO	MnO	MgO	CaO	Total	XMg	mineral
AT-PS-01	prograde skarn	143	0.01	0.06	0.61	54.07	54.75	0.99	calcite
AT-PS-01	prograde skarn	129	0.01	0	0.13	55.13	55.27	0.96	calcite
AT-PS-01	prograde skarn	179	0	0.01	0.9	53.71	54.62	1.00	calcite
AT-PS-01	prograde skarn	128	0	0.04	0.12	55.18	55.34	1.00	calcite
AT-PS-01	prograde skarn	134	0	0	2.53	52.39	54.92	1.00	calcite
AT-PS-01	prograde skarn	140	0	0.08	0.78	53.9	54.76	1.00	calcite
AT-PS-01	prograde skarn	156	0	0.04	1.23	53.28	54.55	1.00	calcite
AT-PS-01	prograde skarn	164	0	0.04	1.46	53.08	54.58	1.00	calcite
AT-PS-01	prograde skarn	170	0	0	1.01	53.89	54.9	1.00	calcite
AT-PS-01	prograde skarn	176	0	0.02	0.7	54.43	55.15	1.00	calcite
AT-PS-01	prograde skarn	178	0	0.01	0.93	54.14	55.08	1.00	calcite
AT-PS-02	prograde skarn	11	0.17	0.07	0.24	54	54.48	0.72	calcite
AT-PS-02	prograde skarn	6	0.13	0.02	0.19	54.01	54.35	0.72	calcite
AT-PS-02	prograde skarn	3	0.12	0.05	0.28	54.04	54.49	0.81	calcite
AT-PS-02	prograde skarn	1	0.11	0.02	0.27	53.64	54.04	0.81	calcite
AT-PS-02	prograde skarn	4	0.11	0.02	0.19	54.14	54.46	0.75	calcite
AT-PS-02	prograde skarn	5	0.11	0.05	0.23	53.83	54.22	0.79	calcite
AT-PS-02	prograde skarn	8	0.11	0.05	0.15	54.06	54.37	0.71	calcite
AT-PS-02	prograde skarn	2	0.1	0.03	0.27	53.96	54.36	0.83	calcite
AT-PS-02	prograde skarn	12	0.09	0.05	0.29	54.3	54.73	0.85	calcite
AT-PS-02	prograde skarn	10	0.08	0.07	0.24	54.34	54.73	0.84	calcite
AT-PS-02	prograde skarn	7	0.07	0.1	0.17	54.04	54.38	0.81	calcite
AT-PS-02	prograde skarn	13	0.05	0.05	0.2	54.15	54.45	0.88	calcite
AT-PS-02	prograde skarn	9	0.01	0.01	0.14	54.2	54.36	0.96	calcite
DB-PS-01	prograde skarn	282	0.33	0.2	9.47	44.12	54.12	0.98	calcite
DB-PS-01	prograde skarn	277	0.3	0.12	10.93	42.07	53.42	0.98	calcite
DB-PS-01	prograde skarn	212	0.25	0.14	2.59	51.69	54.67	0.95	calcite
DB-PS-01	prograde skarn	238	0.24	0.13	3.63	51.14	55.14	0.96	calcite
DB-PS-01	prograde skarn	272	0.24	0.13	5.44	48.84	54.65	0.98	calcite
DB-PS-01	prograde skarn	192	0.23	0.08	2.32	52.43	55.06	0.95	calcite

CARBONATES

Sample	Rock group	anal. #	FeO	MnO	MgO	CaO	Total	XMg	mineral
DB-PS-01	prograde skarn	273	0.23	0.12	4.08	50.25	54.68	0.97	calcite
DB-PS-01	prograde skarn	278	0.23	0.14	8.03	46.31	54.71	0.98	calcite
DB-PS-01	prograde skarn	187	0.21	0.16	2.3	52.41	55.08	0.95	calcite
DB-PS-01	prograde skarn	216	0.21	0.14	2.18	52.02	54.55	0.95	calcite
DB-PS-01	prograde skarn	228	0.21	0.11	2.27	52.45	55.04	0.95	calcite
DB-PS-01	prograde skarn	246	0.21	0.13	4.1	50.55	54.99	0.97	calcite
DB-PS-01	prograde skarn	290	0.21	0.13	3.95	50.72	55.01	0.97	calcite
DB-PS-01	prograde skarn	188	0.2	0.15	2.38	52.98	55.71	0.95	calcite
DB-PS-01	prograde skarn	189	0.2	0.16	2.43	52.19	54.98	0.96	calcite
DB-PS-01	prograde skarn	191	0.2	0.06	2.45	52.51	55.22	0.96	calcite
DB-PS-01	prograde skarn	204	0.2	0.18	2.34	52.68	55.4	0.95	calcite
DB-PS-01	prograde skarn	220	0.2	0.18	1.64	53.21	55.23	0.94	calcite
DB-PS-01	prograde skarn	232	0.2	0.13	1.2	54.12	55.65	0.91	calcite
DB-PS-01	prograde skarn	294	0.2	0.08	5.19	48.88	54.35	0.98	calcite
DB-PS-01	prograde skarn	305	0.2	0.15	4.04	50.58	54.97	0.97	calcite
DB-PS-01	prograde skarn	314	0.2	0.23	5.1	49.59	55.12	0.98	calcite
DB-PS-01	prograde skarn	315	0.2	0.12	4.72	50.48	55.52	0.98	calcite
DB-PS-01	prograde skarn	190	0.19	0.11	2.54	51.84	54.68	0.96	calcite
DB-PS-01	prograde skarn	234	0.19	0.15	3.4	51.35	55.09	0.97	calcite
DB-PS-01	prograde skarn	281	0.19	0.18	7.43	46.84	54.64	0.99	calcite
DB-PS-01	prograde skarn	287	0.19	0.2	2.26	52.18	54.83	0.95	calcite
DB-PS-01	prograde skarn	289	0.19	0.11	2.25	52.88	55.43	0.95	calcite
DB-PS-01	prograde skarn	303	0.19	0.05	2.37	52.75	55.36	0.96	calcite
DB-PS-01	prograde skarn	202	0.18	0.12	1.67	53.27	55.24	0.94	calcite
DB-PS-01	prograde skarn	235	0.18	0.17	2.71	52.67	55.73	0.96	calcite
DB-PS-01	prograde skarn	237	0.18	0.16	2.01	52.96	55.31	0.95	calcite
DB-PS-01	prograde skarn	263	0.18	0.18	2.54	51.98	54.88	0.96	calcite
DB-PS-01	prograde skarn	266	0.18	0.09	2.45	51.35	54.07	0.96	calcite
DB-PS-01	prograde skarn	284	0.18	0.15	4.65	49.37	54.35	0.98	calcite
DB-PS-01	prograde skarn	193	0.17	0.11	2.52	52.37	55.17	0.96	calcite

CARBONATES

Sample	Rock group	anal. #	FeO	MnO	MgO	CaO	Total	XMg	mineral
DB-PS-01	prograde skarn	226	0.17	0.1	1.88	52.94	55.09	0.95	calcite
DB-PS-01	prograde skarn	248	0.17	0.15	2.7	51.66	54.68	0.97	calcite
DB-PS-01	prograde skarn	265	0.17	0.2	6.78	47.56	54.71	0.99	calcite
DB-PS-01	prograde skarn	269	0.17	0.09	2.08	52.72	55.06	0.96	calcite
DB-PS-01	prograde skarn	286	0.17	0.14	2.36	54.41	57.08	0.96	calcite
DB-PS-01	prograde skarn	215	0.16	0.04	2.02	52.39	54.61	0.96	calcite
DB-PS-01	prograde skarn	224	0.16	0.15	1.65	53.12	55.08	0.95	calcite
DB-PS-01	prograde skarn	295	0.16	0.18	4.66	50.1	55.1	0.98	calcite
DB-PS-01	prograde skarn	302	0.16	0.14	1.5	53.46	55.26	0.94	calcite
DB-PS-01	prograde skarn	205	0.15	0.14	2.51	52.9	55.7	0.97	calcite
DB-PS-01	prograde skarn	208	0.15	0.11	1.21	53.41	54.88	0.93	calcite
DB-PS-01	prograde skarn	210	0.15	0.08	2.08	52.71	55.02	0.96	calcite
DB-PS-01	prograde skarn	218	0.15	0.18	1.78	52.86	54.97	0.95	calcite
DB-PS-01	prograde skarn	222	0.15	0.14	1.63	52.64	54.56	0.95	calcite
DB-PS-01	prograde skarn	239	0.15	0.08	2.5	52.17	54.9	0.97	calcite
DB-PS-01	prograde skarn	244	0.15	0.23	1.85	52.78	55.01	0.96	calcite
DB-PS-01	prograde skarn	285	0.15	0.16	2.31	52.26	54.88	0.96	calcite
DB-PS-01	prograde skarn	298	0.15	0.15	3.31	51.98	55.59	0.98	calcite
DB-PS-01	prograde skarn	308	0.15	0.11	2.19	52.81	55.26	0.96	calcite
DB-PS-01	prograde skarn	313	0.15	0.09	2.06	52.51	54.81	0.96	calcite
DB-PS-01	prograde skarn	195	0.14	0.16	1.87	53.45	55.62	0.96	calcite
DB-PS-01	prograde skarn	198	0.14	0.13	2.14	52.54	54.95	0.96	calcite
DB-PS-01	prograde skarn	200	0.14	0.15	2.48	52.4	55.17	0.97	calcite
DB-PS-01	prograde skarn	209	0.14	0.1	1.81	52.55	54.6	0.96	calcite
DB-PS-01	prograde skarn	213	0.14	0.15	2.04	52.08	54.41	0.96	calcite
DB-PS-01	prograde skarn	217	0.14	0.05	2.21	52.26	54.66	0.97	calcite
DB-PS-01	prograde skarn	245	0.14	0.16	2.65	51.88	54.83	0.97	calcite
DB-PS-01	prograde skarn	247	0.14	0.1	2.84	52.23	55.31	0.97	calcite
DB-PS-01	prograde skarn	279	0.14	0.06	3.58	51.16	54.94	0.98	calcite
DB-PS-01	prograde skarn	293	0.14	0.13	4.92	49.54	54.73	0.98	calcite

CARBONATES

Sample	Rock group	anal. #	FeO	MnO	MgO	CaO	Total	XMg	mineral
DB-PS-01	prograde skarn	307	0.14	0.16	5.48	48.94	54.72	0.99	calcite
DB-PS-01	prograde skarn	194	0.13	0.15	1.56	53.43	55.27	0.96	calcite
DB-PS-01	prograde skarn	203	0.13	0.06	1.28	53.76	55.23	0.95	calcite
DB-PS-01	prograde skarn	240	0.13	0.06	2.64	52.07	54.9	0.97	calcite
DB-PS-01	prograde skarn	241	0.13	0.08	2.95	51.89	55.05	0.98	calcite
DB-PS-01	prograde skarn	255	0.13	0.14	2.12	52.64	55.03	0.97	calcite
DB-PS-01	prograde skarn	267	0.13	0.19	1.78	52.46	54.56	0.96	calcite
DB-PS-01	prograde skarn	288	0.13	0.17	1.97	52.42	54.69	0.96	calcite
DB-PS-01	prograde skarn	304	0.13	0.14	2.57	51.85	54.69	0.97	calcite
DB-PS-01	prograde skarn	214	0.12	0.11	2.75	51.85	54.83	0.98	calcite
DB-PS-01	prograde skarn	223	0.12	0.05	2.55	51.87	54.59	0.97	calcite
DB-PS-01	prograde skarn	229	0.12	0.06	1.91	53.77	55.86	0.97	calcite
DB-PS-01	prograde skarn	253	0.12	0.15	2.86	51.83	54.96	0.98	calcite
DB-PS-01	prograde skarn	259	0.12	0.12	3.93	50.37	54.54	0.98	calcite
DB-PS-01	prograde skarn	260	0.12	0.17	4.75	49.68	54.72	0.99	calcite
DB-PS-01	prograde skarn	268	0.12	0.07	2.04	52.71	54.94	0.97	calcite
DB-PS-01	prograde skarn	275	0.12	0.07	1.79	52.58	54.56	0.96	calcite
DB-PS-01	prograde skarn	309	0.12	0.13	3.28	51.42	54.95	0.98	calcite
DB-PS-01	prograde skarn	199	0.11	0.1	1.32	53.52	55.05	0.96	calcite
DB-PS-01	prograde skarn	201	0.11	0.12	1.77	52.65	54.65	0.97	calcite
DB-PS-01	prograde skarn	219	0.11	0.13	1.24	53.73	55.21	0.95	calcite
DB-PS-01	prograde skarn	221	0.11	0.11	1.62	52.78	54.62	0.96	calcite
DB-PS-01	prograde skarn	231	0.11	0.1	0.74	54.49	55.44	0.92	calcite
DB-PS-01	prograde skarn	257	0.11	0.1	2.64	52.07	54.92	0.98	calcite
DB-PS-01	prograde skarn	258	0.11	0.16	5.44	48.88	54.59	0.99	calcite
DB-PS-01	prograde skarn	262	0.11	0.1	1.28	53.24	54.73	0.95	calcite
DB-PS-01	prograde skarn	271	0.11	0.14	2.6	52.18	55.03	0.98	calcite
DB-PS-01	prograde skarn	296	0.11	0.09	4.25	50.2	54.65	0.99	calcite
DB-PS-01	prograde skarn	297	0.11	0.09	2.95	51.41	54.56	0.98	calcite
DB-PS-01	prograde skarn	306	0.11	0.18	4.73	50.11	55.13	0.99	calcite

CARBONATES

Sample	Rock group	anal. #	FeO	MnO	MgO	CaO	Total	XMg	mineral
DB-PS-01	prograde skarn	206	0.1	0.12	2.52	52.51	55.25	0.98	calcite
DB-PS-01	prograde skarn	236	0.1	0.04	2.09	52.83	55.06	0.97	calcite
DB-PS-01	prograde skarn	242	0.1	0.07	2.5	52.46	55.13	0.98	calcite
DB-PS-01	prograde skarn	252	0.1	0.11	2.73	52.87	55.81	0.98	calcite
DB-PS-01	prograde skarn	261	0.1	0.07	2.82	51.84	54.83	0.98	calcite
DB-PS-01	prograde skarn	274	0.1	0.08	1.29	53.69	55.16	0.96	calcite
DB-PS-01	prograde skarn	280	0.1	0.1	1.94	52.89	55.03	0.97	calcite
DB-PS-01	prograde skarn	312	0.1	0.09	3.53	50.89	54.61	0.98	calcite
DB-PS-01	prograde skarn	196	0.09	0.12	1.92	52.9	55.03	0.97	calcite
DB-PS-01	prograde skarn	249	0.09	0.1	2.54	52.3	55.03	0.98	calcite
DB-PS-01	prograde skarn	251	0.09	0.15	2.63	52.1	54.97	0.98	calcite
DB-PS-01	prograde skarn	270	0.09	0.15	2.33	52.24	54.81	0.98	calcite
DB-PS-01	prograde skarn	276	0.09	0.09	1.31	53.39	54.88	0.96	calcite
DB-PS-01	prograde skarn	301	0.09	0.1	1.62	53.27	55.08	0.97	calcite
DB-PS-01	prograde skarn	211	0.08	0.12	1.87	52.57	54.64	0.98	calcite
DB-PS-01	prograde skarn	207	0.07	0.11	2.12	52.63	54.93	0.98	calcite
DB-PS-01	prograde skarn	230	0.07	0.17	0.87	54.14	55.25	0.96	calcite
DB-PS-01	prograde skarn	243	0.07	0.1	2.17	52.72	55.06	0.98	calcite
DB-PS-01	prograde skarn	283	0.07	0.13	1.45	53.31	54.96	0.97	calcite
DB-PS-01	prograde skarn	292	0.07	0.08	1.97	52.73	54.85	0.98	calcite
DB-PS-01	prograde skarn	300	0.07	0.13	2.82	52.15	55.17	0.99	calcite
DB-PS-01	prograde skarn	256	0.06	0.18	2.13	53.02	55.39	0.98	calcite
DB-PS-01	prograde skarn	291	0.06	0.12	1.8	52.73	54.71	0.98	calcite
DB-PS-01	prograde skarn	311	0.06	0.14	4.57	50.17	54.94	0.99	calcite
DB-PS-01	prograde skarn	225	0.05	0.07	1.9	52.8	54.82	0.99	calcite
DB-PS-01	prograde skarn	254	0.05	0.15	2.75	52.41	55.36	0.99	calcite
DB-PS-01	prograde skarn	264	0.05	0.12	2.21	51.96	54.34	0.99	calcite
DB-PS-01	prograde skarn	227	0.04	0.2	0.95	54.38	55.57	0.98	calcite
DB-PS-01	prograde skarn	310	0.04	0.12	4.15	50.64	54.95	0.99	calcite
DB-PS-01	prograde skarn	233	0.03	0.12	1.74	53.01	54.9	0.99	calcite

CARBONATES

Sample	Rock group	anal. #	FeO	MnO	MgO	CaO	Total	XMg	mineral
DB-PS-01	prograde skarn	250	0.03	0.13	2.69	52.27	55.12	0.99	calcite
DB-PS-01	prograde skarn	197	0.01	0.08	2.61	52.15	54.85	1.00	calcite
DB-PS-01	prograde skarn	299	0	0.16	1.11	54.2	55.47	1.00	calcite
AT-PS-03	prograde skarn	69	0.21	0.03	2.74	51.52	54.5	0.96	calcite
AT-PS-03	prograde skarn	102	0.2	0.06	2.38	51.72	54.36	0.95	calcite
AT-PS-03	prograde skarn	114	0.2	0.03	2.04	52.25	54.52	0.95	calcite
AT-PS-03	prograde skarn	196	0.19	0.11	3.41	50.77	54.48	0.97	calcite
AT-PS-03	prograde skarn	198	0.19	0.04	2.86	51.09	54.18	0.96	calcite
AT-PS-03	prograde skarn	101	0.19	0.07	2.26	52.01	54.53	0.95	calcite
AT-PS-03	prograde skarn	191	0.18	0.09	3.55	50.22	54.04	0.97	calcite
AT-PS-03	prograde skarn	5	0.18	0.08	1.43	52.89	54.58	0.93	calcite
AT-PS-03	prograde skarn	78	0.18	0	2.47	51.79	54.44	0.96	calcite
AT-PS-03	prograde skarn	92	0.18	0.07	2.99	51.34	54.58	0.97	calcite
AT-PS-03	prograde skarn	93	0.18	0.03	3.08	51.33	54.62	0.97	calcite
AT-PS-03	prograde skarn	207	0.17	0.03	1.93	52.57	54.7	0.95	calcite
AT-PS-03	prograde skarn	71	0.17	0.04	2.67	51.49	54.37	0.97	calcite
AT-PS-03	prograde skarn	96	0.17	0.05	2.76	51.6	54.58	0.97	calcite
AT-PS-03	prograde skarn	197	0.17	0.04	4	49.89	54.1	0.98	calcite
AT-PS-03	prograde skarn	194	0.16	0.01	3.02	50.78	53.97	0.97	calcite
AT-PS-03	prograde skarn	190	0.16	0	2.75	51.35	54.26	0.97	calcite
AT-PS-03	prograde skarn	97	0.16	0.01	2.33	51.82	54.32	0.96	calcite
AT-PS-03	prograde skarn	113	0.16	0.07	2.44	51.85	54.52	0.96	calcite
AT-PS-03	prograde skarn	195	0.15	0.06	2.83	51.34	54.38	0.97	calcite
AT-PS-03	prograde skarn	6	0.15	0	1.49	52.75	54.39	0.95	calcite
AT-PS-03	prograde skarn	63	0.15	0.02	1.65	53.29	55.11	0.95	calcite
AT-PS-03	prograde skarn	85	0.15	0.04	2.25	51.92	54.36	0.96	calcite
AT-PS-03	prograde skarn	91	0.15	0.01	2.4	51.89	54.45	0.97	calcite
AT-PS-03	prograde skarn	98	0.15	0.02	2.42	52	54.59	0.97	calcite
AT-PS-03	prograde skarn	2	0.14	0.07	1.06	53.38	54.65	0.93	calcite
AT-PS-03	prograde skarn	56	0.14	0.02	1.55	53	54.71	0.95	calcite

CARBONATES

Sample	Rock group	anal. #	FeO	MnO	MgO	CaO	Total	XMg	mineral
AT-PS-03	prograde skarn	84	0.14	0.04	2.51	51.8	54.49	0.97	calcite
AT-PS-03	prograde skarn	109	0.14	0	2.48	51.81	54.43	0.97	calcite
AT-PS-03	prograde skarn	9	0.13	0.02	2	52.48	54.63	0.96	calcite
AT-PS-03	prograde skarn	62	0.13	0.06	1.97	52.36	54.52	0.96	calcite
AT-PS-03	prograde skarn	70	0.13	0.01	2.61	51.56	54.31	0.97	calcite
AT-PS-03	prograde skarn	80	0.13	0.01	2.27	52.25	54.66	0.97	calcite
AT-PS-03	prograde skarn	94	0.13	0.08	2.74	51.57	54.52	0.97	calcite
AT-PS-03	prograde skarn	106	0.13	0.02	2.2	51.66	54.01	0.97	calcite
AT-PS-03	prograde skarn	17	0.12	0.01	1.52	53	54.65	0.96	calcite
AT-PS-03	prograde skarn	82	0.12	0.04	2.69	52.01	54.86	0.98	calcite
AT-PS-03	prograde skarn	86	0.12	0.01	2.73	51.7	54.56	0.98	calcite
AT-PS-03	prograde skarn	88	0.12	0.01	2.37	52.01	54.51	0.97	calcite
AT-PS-03	prograde skarn	193	0.12	0	2.47	51.81	54.4	0.97	calcite
AT-PS-03	prograde skarn	210	0.11	0.02	3.79	50.54	54.46	0.98	calcite
AT-PS-03	prograde skarn	7	0.11	0.05	2.11	52.35	54.62	0.97	calcite
AT-PS-03	prograde skarn	34	0.11	0.04	2.52	51.48	54.15	0.98	calcite
AT-PS-03	prograde skarn	83	0.11	0.09	2.55	51.54	54.29	0.98	calcite
AT-PS-03	prograde skarn	87	0.11	0	2.68	51.67	54.46	0.98	calcite
AT-PS-03	prograde skarn	89	0.11	0.01	2.49	51.79	54.4	0.98	calcite
AT-PS-03	prograde skarn	103	0.11	0.03	2.05	51.96	54.15	0.97	calcite
AT-PS-03	prograde skarn	112	0.11	0	2.11	52.4	54.62	0.97	calcite
AT-PS-03	prograde skarn	116	0.11	0.01	2.38	51.86	54.36	0.97	calcite
AT-PS-03	prograde skarn	117	0.11	0.02	2.1	52.12	54.35	0.97	calcite
AT-PS-03	prograde skarn	192	0.11	0.04	2.8	51.29	54.24	0.98	calcite
AT-PS-03	prograde skarn	68	0.1	0.08	2.59	51.12	53.89	0.98	calcite
AT-PS-03	prograde skarn	79	0.1	0.05	2.34	52.1	54.59	0.98	calcite
AT-PS-03	prograde skarn	108	0.1	0.06	2.22	51.81	54.19	0.98	calcite
AT-PS-03	prograde skarn	20	0.09	0.07	1.2	52.55	53.91	0.96	calcite
AT-PS-03	prograde skarn	26	0.09	0.01	1.74	52.8	54.64	0.97	calcite
AT-PS-03	prograde skarn	31	0.09	0.1	1.83	52.34	54.36	0.97	calcite

CARBONATES

Sample	Rock group	anal. #	FeO	MnO	MgO	CaO	Total	XMg	mineral
AT-PS-03	prograde skarn	100	0.09	0.07	2.09	52.13	54.38	0.98	calcite
AT-PS-03	prograde skarn	206	0.09	0.05	2.58	52.15	54.87	0.98	calcite
AT-PS-03	prograde skarn	23	0.08	0.03	1.1	52.9	54.11	0.96	calcite
AT-PS-03	prograde skarn	24	0.08	0.03	0.91	53.05	54.07	0.95	calcite
AT-PS-03	prograde skarn	27	0.08	0.01	1.66	52.62	54.37	0.97	calcite
AT-PS-03	prograde skarn	29	0.08	0.05	1.44	52.85	54.42	0.97	calcite
AT-PS-03	prograde skarn	61	0.08	0.08	2.04	52.6	54.8	0.98	calcite
AT-PS-03	prograde skarn	64	0.08	0.04	1.29	53.31	54.72	0.97	calcite
AT-PS-03	prograde skarn	65	0.08	0.03	2.38	51.84	54.33	0.98	calcite
AT-PS-03	prograde skarn	67	0.08	0.05	2.97	51.12	54.22	0.99	calcite
AT-PS-03	prograde skarn	72	0.08	0.05	2.49	51.66	54.28	0.98	calcite
AT-PS-03	prograde skarn	81	0.08	0	2.56	51.7	54.34	0.98	calcite
AT-PS-03	prograde skarn	95	0.08	0.09	2.6	51.88	54.65	0.98	calcite
AT-PS-03	prograde skarn	118	0.08	0.05	2.18	51.85	54.16	0.98	calcite
AT-PS-03	prograde skarn	208	0.07	0.07	1.84	52.6	54.58	0.98	calcite
AT-PS-03	prograde skarn	16	0.07	0.1	1.36	53.19	54.72	0.97	calcite
AT-PS-03	prograde skarn	18	0.07	0.02	1.6	52.63	54.32	0.98	calcite
AT-PS-03	prograde skarn	33	0.07	0.08	1.62	52.32	54.09	0.98	calcite
AT-PS-03	prograde skarn	76	0.07	0.06	1.5	52.81	54.44	0.97	calcite
AT-PS-03	prograde skarn	90	0.07	0.06	2.34	51.95	54.42	0.98	calcite
AT-PS-03	prograde skarn	99	0.07	0.08	2.05	52.41	54.61	0.98	calcite
AT-PS-03	prograde skarn	104	0.07	0	2.02	52.34	54.43	0.98	calcite
AT-PS-03	prograde skarn	107	0.07	0.06	2.34	51.64	54.11	0.98	calcite
AT-PS-03	prograde skarn	3	0.06	0.07	1.55	52.87	54.55	0.98	calcite
AT-PS-03	prograde skarn	4	0.06	0.03	1.2	52.95	54.24	0.97	calcite
AT-PS-03	prograde skarn	28	0.06	0	1.35	53.03	54.44	0.98	calcite
AT-PS-03	prograde skarn	59	0.06	0	0.95	53.59	54.6	0.97	calcite
AT-PS-03	prograde skarn	111	0.06	0.07	2.41	51.84	54.38	0.99	calcite
AT-PS-03	prograde skarn	115	0.06	0.04	2.51	51.77	54.38	0.99	calcite
AT-PS-03	prograde skarn	21	0.05	0	1.11	52.91	54.07	0.98	calcite

CARBONATES

Sample	Rock group	anal. #	FeO	MnO	MgO	CaO	Total	XMg	mineral
AT-PS-03	prograde skarn	50	0.05	0	0.78	53.73	54.56	0.97	calcite
AT-PS-03	prograde skarn	60	0.05	0.03	2.04	52.17	54.29	0.99	calcite
AT-PS-03	prograde skarn	66	0.05	0.03	2.4	51.86	54.34	0.99	calcite
AT-PS-03	prograde skarn	8	0.04	0.05	2.27	51.74	54.1	0.99	calcite
AT-PS-03	prograde skarn	22	0.04	0.06	1.07	52.78	53.95	0.98	calcite
AT-PS-03	prograde skarn	51	0.04	0.05	1.27	52.99	54.35	0.98	calcite
AT-PS-03	prograde skarn	53	0.04	0.04	1.05	53.08	54.21	0.98	calcite
AT-PS-03	prograde skarn	55	0.04	0.04	1.5	53.04	54.62	0.99	calcite
AT-PS-03	prograde skarn	57	0.04	0.08	1.59	52.42	54.13	0.99	calcite
AT-PS-03	prograde skarn	73	0.04	0.02	1.81	52.58	54.45	0.99	calcite
AT-PS-03	prograde skarn	75	0.04	0	1.37	53.05	54.46	0.98	calcite
AT-PS-03	prograde skarn	77	0.04	0.07	1.66	52.52	54.29	0.99	calcite
AT-PS-03	prograde skarn	105	0.04	0.06	2.25	52.17	54.52	0.99	calcite
AT-PS-03	prograde skarn	110	0.04	0.03	2.6	51.52	54.19	0.99	calcite
AT-PS-03	prograde skarn	54	0.03	0.05	0.93	53.07	54.08	0.98	calcite
AT-PS-03	prograde skarn	58	0.03	0.02	0.82	53.65	54.52	0.98	calcite
AT-PS-03	prograde skarn	202	0.03	0.08	2	52.41	54.52	0.99	calcite
AT-PS-03	prograde skarn	19	0.02	0.01	1.26	53.28	54.57	0.99	calcite
AT-PS-03	prograde skarn	25	0.02	0.11	1.08	52.99	54.2	0.99	calcite
AT-PS-03	prograde skarn	52	0.02	0	1.09	53.31	54.42	0.99	calcite
AT-PS-03	prograde skarn	74	0.02	0.03	1.64	52.34	54.03	0.99	calcite
AT-PS-03	prograde skarn	1	0.01	0.03	1.03	53.58	54.65	0.99	calcite
AT-PS-03	prograde skarn	30	0.01	0	1.32	53.14	54.47	1.00	calcite
AT-PS-03	prograde skarn	32	0.01	0.07	0.95	53.82	54.85	0.99	calcite
AT-PS-03	prograde skarn	209	0	0	2.17	52.41	54.58	1.00	calcite
CL-PS-02	prograde skarn - sp skarn	72	0.84	0.2	5.41	47.45	53.9	0.92	calcite
CL-PS-02	prograde skarn - sp skarn	54	0.82	0.19	3.86	49.44	54.31	0.89	calcite
CL-PS-02	prograde skarn - sp skarn	53	0.81	0.19	3.89	49.42	54.31	0.90	calcite
CL-PS-02	prograde skarn - sp skarn	160	0.76	0.2	4.56	49.42	54.94	0.91	calcite
CL-PS-02	prograde skarn - sp skarn	39	0.75	0.17	3.72	49.64	54.28	0.90	calcite

CARBONATES

Sample	Rock group	anal. #	FeO	MnO	MgO	CaO	Total	XMg	mineral
CL-PS-02	prograde skarn - sp skarn	58	0.74	0.11	3.74	49.42	54.01	0.90	calcite
CL-PS-02	prograde skarn - sp skarn	76	0.74	0.14	3.78	48.93	53.59	0.90	calcite
CL-PS-02	prograde skarn - sp skarn	24	0.72	0.2	3.21	50	54.13	0.89	calcite
CL-PS-02	prograde skarn - sp skarn	52	0.72	0.24	3.63	49.39	53.98	0.90	calcite
CL-PS-02	prograde skarn - sp skarn	103	0.72	0.17	3.87	49.44	54.2	0.91	calcite
CL-PS-02	prograde skarn - sp skarn	7	0.71	0.21	3.25	49.99	54.16	0.89	calcite
CL-PS-02	prograde skarn - sp skarn	59	0.71	0.18	3.77	48.81	53.47	0.90	calcite
CL-PS-02	prograde skarn - sp skarn	70	0.71	0.16	3.29	49.42	53.58	0.89	calcite
CL-PS-02	prograde skarn - sp skarn	131	0.71	0.24	4.2	48.91	54.06	0.91	calcite
CL-PS-02	prograde skarn - sp skarn	61	0.7	0.22	3.25	51.07	55.24	0.89	calcite
CL-PS-02	prograde skarn - sp skarn	124	0.7	0.19	3.91	50.04	54.84	0.91	calcite
CL-PS-02	prograde skarn - sp skarn	156	0.69	0.23	5.05	47.78	53.75	0.93	calcite
CL-PS-02	prograde skarn - sp skarn	75	0.68	0.16	3.23	49.77	53.84	0.89	calcite
CL-PS-02	prograde skarn - sp skarn	51	0.67	0.23	3.3	50.1	54.3	0.90	calcite
CL-PS-02	prograde skarn - sp skarn	125	0.67	0.16	3.52	50.13	54.48	0.90	calcite
CL-PS-02	prograde skarn - sp skarn	130	0.67	0.15	3.12	50.09	54.03	0.89	calcite
CL-PS-02	prograde skarn - sp skarn	43	0.66	0.14	2.93	50.26	53.99	0.89	calcite
CL-PS-02	prograde skarn - sp skarn	44	0.66	0.11	3.08	50.29	54.14	0.89	calcite
CL-PS-02	prograde skarn - sp skarn	60	0.66	0.21	3.07	49.88	53.82	0.89	calcite
CL-PS-02	prograde skarn - sp skarn	64	0.66	0.16	3.6	49.7	54.12	0.91	calcite
CL-PS-02	prograde skarn - sp skarn	66	0.66	0.11	2.73	50.36	53.86	0.88	calcite
CL-PS-02	prograde skarn - sp skarn	56	0.65	0.1	3.64	49.69	54.08	0.91	calcite
CL-PS-02	prograde skarn - sp skarn	116	0.65	0.26	3.19	50.78	54.88	0.90	calcite
CL-PS-02	prograde skarn - sp skarn	9	0.64	0.15	3.51	49.07	53.37	0.91	calcite
CL-PS-02	prograde skarn - sp skarn	38	0.64	0.16	3.16	49.89	53.85	0.90	calcite
CL-PS-02	prograde skarn - sp skarn	55	0.64	0.15	3.51	49.8	54.1	0.91	calcite
CL-PS-02	prograde skarn - sp skarn	69	0.64	0.16	2.91	50.11	53.82	0.89	calcite
CL-PS-02	prograde skarn - sp skarn	132	0.64	0.14	3.81	49.51	54.1	0.91	calcite
CL-PS-02	prograde skarn - sp skarn	21	0.63	0.18	3.32	49.75	53.88	0.90	calcite
CL-PS-02	prograde skarn - sp skarn	30	0.63	0.18	3.44	49.5	53.75	0.91	calcite

CARBONATES

Sample	Rock group	anal. #	FeO	MnO	MgO	CaO	Total	XMg	mineral
CL-PS-02	prograde skarn - sp skarn	128	0.63	0.26	3.17	50.19	54.25	0.90	calcite
CL-PS-02	prograde skarn - sp skarn	155	0.63	0.19	4.96	48.63	54.41	0.93	calcite
CL-PS-02	prograde skarn - sp skarn	8	0.62	0.11	3.32	49.65	53.7	0.91	calcite
CL-PS-02	prograde skarn - sp skarn	34	0.62	0.21	2.7	50.23	53.76	0.89	calcite
CL-PS-02	prograde skarn - sp skarn	73	0.62	0.16	2.61	50.84	54.23	0.88	calcite
CL-PS-02	prograde skarn - sp skarn	96	0.62	0.16	2.87	50.32	53.97	0.89	calcite
CL-PS-02	prograde skarn - sp skarn	104	0.62	0.17	2.82	50.69	54.3	0.89	calcite
CL-PS-02	prograde skarn - sp skarn	174	0.62	0.17	2.93	50.92	54.64	0.89	calcite
CL-PS-02	prograde skarn - sp skarn	176	0.62	0.23	2.68	50.6	54.13	0.89	calcite
CL-PS-02	prograde skarn - sp skarn	42	0.61	0.2	2.92	50.09	53.82	0.90	calcite
CL-PS-02	prograde skarn - sp skarn	57	0.61	0.25	3.34	49.66	53.86	0.91	calcite
CL-PS-02	prograde skarn - sp skarn	129	0.61	0.24	2.94	50.59	54.38	0.90	calcite
CL-PS-02	prograde skarn - sp skarn	36	0.6	0.23	3.24	49.44	53.51	0.91	calcite
CL-PS-02	prograde skarn - sp skarn	37	0.6	0.14	3.07	49.93	53.74	0.90	calcite
CL-PS-02	prograde skarn - sp skarn	62	0.6	0.22	2.82	50.47	54.11	0.89	calcite
CL-PS-02	prograde skarn - sp skarn	109	0.6	0.24	2.26	51.62	54.72	0.87	calcite
CL-PS-02	prograde skarn - sp skarn	11	0.59	0.23	2.5	51.15	54.47	0.88	calcite
CL-PS-02	prograde skarn - sp skarn	20	0.59	0.23	2.96	50.02	53.8	0.90	calcite
CL-PS-02	prograde skarn - sp skarn	22	0.59	0.13	3.02	50.06	53.8	0.90	calcite
CL-PS-02	prograde skarn - sp skarn	25	0.59	0.19	2.16	51	53.94	0.87	calcite
CL-PS-02	prograde skarn - sp skarn	32	0.59	0.19	2.96	50.43	54.17	0.90	calcite
CL-PS-02	prograde skarn - sp skarn	171	0.59	0.21	3.73	49.89	54.42	0.92	calcite
CL-PS-02	prograde skarn - sp skarn	29	0.58	0.16	3.03	50.29	54.06	0.90	calcite
CL-PS-02	prograde skarn - sp skarn	49	0.58	0.15	2.18	51.51	54.42	0.87	calcite
CL-PS-02	prograde skarn - sp skarn	77	0.58	0.24	3.31	49.87	54	0.91	calcite
CL-PS-02	prograde skarn - sp skarn	81	0.58	0.13	3.5	49.75	53.96	0.91	calcite
CL-PS-02	prograde skarn - sp skarn	108	0.58	0.13	2.6	51.26	54.57	0.89	calcite
CL-PS-02	prograde skarn - sp skarn	134	0.58	0.15	2.98	50.74	54.45	0.90	calcite
CL-PS-02	prograde skarn - sp skarn	33	0.57	0.22	3.44	49.39	53.62	0.91	calcite
CL-PS-02	prograde skarn - sp skarn	71	0.57	0.12	3.48	49.74	53.91	0.92	calcite

CARBONATES

Sample	Rock group	anal. #	FeO	MnO	MgO	CaO	Total	XMg	mineral
CL-PS-02	prograde skarn - sp skarn	80	0.57	0.19	3.14	49.92	53.82	0.91	calcite
CL-PS-02	prograde skarn - sp skarn	106	0.57	0.15	3.35	50.29	54.36	0.91	calcite
CL-PS-02	prograde skarn - sp skarn	123	0.57	0.21	3.77	50.1	54.65	0.92	calcite
CL-PS-02	prograde skarn - sp skarn	175	0.57	0.15	4.03	49.09	53.84	0.93	calcite
CL-PS-02	prograde skarn - sp skarn	3	0.56	0.11	3.05	50.31	54.03	0.91	calcite
CL-PS-02	prograde skarn - sp skarn	14	0.56	0.13	3.06	50.18	53.93	0.91	calcite
CL-PS-02	prograde skarn - sp skarn	17	0.56	0.18	1.98	51.1	53.82	0.86	calcite
CL-PS-02	prograde skarn - sp skarn	48	0.56	0.2	2.53	50.94	54.23	0.89	calcite
CL-PS-02	prograde skarn - sp skarn	110	0.56	0.12	2.26	51.57	54.51	0.88	calcite
CL-PS-02	prograde skarn - sp skarn	19	0.55	0.21	2.45	50.75	53.96	0.89	calcite
CL-PS-02	prograde skarn - sp skarn	31	0.55	0.17	3.7	49.05	53.47	0.92	calcite
CL-PS-02	prograde skarn - sp skarn	45	0.55	0.2	2.62	51.23	54.6	0.89	calcite
CL-PS-02	prograde skarn - sp skarn	46	0.55	0.22	2.51	51.22	54.5	0.89	calcite
CL-PS-02	prograde skarn - sp skarn	119	0.55	0.13	2.08	52	54.76	0.87	calcite
CL-PS-02	prograde skarn - sp skarn	13	0.54	0.16	2.96	50.03	53.69	0.91	calcite
CL-PS-02	prograde skarn - sp skarn	27	0.54	0.11	2.58	50.57	53.8	0.89	calcite
CL-PS-02	prograde skarn - sp skarn	67	0.54	0.17	2.61	50.67	53.99	0.90	calcite
CL-PS-02	prograde skarn - sp skarn	105	0.54	0.17	3.13	50.36	54.2	0.91	calcite
CL-PS-02	prograde skarn - sp skarn	111	0.54	0.19	3.01	50.68	54.42	0.91	calcite
CL-PS-02	prograde skarn - sp skarn	6	0.53	0.1	2.55	51.03	54.21	0.90	calcite
CL-PS-02	prograde skarn - sp skarn	65	0.53	0.23	2.57	50.59	53.92	0.90	calcite
CL-PS-02	prograde skarn - sp skarn	79	0.53	0.14	2.9	50.01	53.58	0.91	calcite
CL-PS-02	prograde skarn - sp skarn	147	0.53	0.19	3.06	50.62	54.4	0.91	calcite
CL-PS-02	prograde skarn - sp skarn	178	0.53	0.11	1.98	51.96	54.58	0.87	calcite
CL-PS-02	prograde skarn - sp skarn	5	0.52	0.18	2.93	50.29	53.92	0.91	calcite
CL-PS-02	prograde skarn - sp skarn	40	0.52	0.18	2.5	50.92	54.12	0.90	calcite
CL-PS-02	prograde skarn - sp skarn	63	0.52	0.19	3.04	50.18	53.93	0.91	calcite
CL-PS-02	prograde skarn - sp skarn	78	0.52	0.15	2.3	51.3	54.27	0.89	calcite
CL-PS-02	prograde skarn - sp skarn	85	0.52	0.21	2.62	50.61	53.96	0.90	calcite
CL-PS-02	prograde skarn - sp skarn	126	0.52	0.12	2.53	51.47	54.64	0.90	calcite

CARBONATES

Sample	Rock group	anal. #	FeO	MnO	MgO	CaO	Total	XMg	mineral
CL-PS-02	prograde skarn - sp skarn	133	0.52	0.19	2.65	50.4	53.76	0.90	calcite
CL-PS-02	prograde skarn - sp skarn	173	0.52	0.13	2.9	50.31	53.86	0.91	calcite
CL-PS-02	prograde skarn - sp skarn	89	0.51	0.24	2.53	50.82	54.1	0.90	calcite
CL-PS-02	prograde skarn - sp skarn	98	0.51	0.13	2.29	51.59	54.52	0.89	calcite
CL-PS-02	prograde skarn - sp skarn	184	0.51	0.14	2.22	51.38	54.25	0.89	calcite
CL-PS-02	prograde skarn - sp skarn	2	0.5	0.17	2.37	51.35	54.39	0.89	calcite
CL-PS-02	prograde skarn - sp skarn	47	0.5	0.16	2.35	50.81	53.82	0.89	calcite
CL-PS-02	prograde skarn - sp skarn	74	0.5	0.14	2.31	50.88	53.83	0.89	calcite
CL-PS-02	prograde skarn - sp skarn	94	0.5	0.16	2.69	50.93	54.28	0.91	calcite
CL-PS-02	prograde skarn - sp skarn	164	0.5	0.14	2.52	51.08	54.24	0.90	calcite
CL-PS-02	prograde skarn - sp skarn	168	0.5	0.21	2.86	50.73	54.3	0.91	calcite
CL-PS-02	prograde skarn - sp skarn	177	0.5	0.19	2.08	51.52	54.29	0.88	calcite
CL-PS-02	prograde skarn - sp skarn	182	0.5	0.16	2.49	51.06	54.21	0.90	calcite
CL-PS-02	prograde skarn - sp skarn	23	0.49	0.18	2.79	50.27	53.73	0.91	calcite
CL-PS-02	prograde skarn - sp skarn	50	0.49	0.15	2.84	50.7	54.18	0.91	calcite
CL-PS-02	prograde skarn - sp skarn	102	0.49	0.17	3.06	50.53	54.25	0.92	calcite
CL-PS-02	prograde skarn - sp skarn	146	0.49	0.08	2.44	50.95	53.96	0.90	calcite
CL-PS-02	prograde skarn - sp skarn	83	0.48	0.21	2.6	50.56	53.85	0.91	calcite
CL-PS-02	prograde skarn - sp skarn	121	0.48	0.2	2.35	51.36	54.39	0.90	calcite
CL-PS-02	prograde skarn - sp skarn	149	0.48	0.17	2.4	51.56	54.61	0.90	calcite
CL-PS-02	prograde skarn - sp skarn	157	0.48	0.16	2.25	51.15	54.04	0.89	calcite
CL-PS-02	prograde skarn - sp skarn	172	0.48	0.17	2.48	50.9	54.03	0.90	calcite
CL-PS-02	prograde skarn - sp skarn	185	0.48	0.23	2.07	51.44	54.22	0.88	calcite
CL-PS-02	prograde skarn - sp skarn	16	0.47	0.23	2.07	51.55	54.32	0.89	calcite
CL-PS-02	prograde skarn - sp skarn	68	0.47	0.15	2.36	51.3	54.28	0.90	calcite
CL-PS-02	prograde skarn - sp skarn	82	0.47	0.1	1.92	51.75	54.24	0.88	calcite
CL-PS-02	prograde skarn - sp skarn	101	0.47	0.07	2.84	50.78	54.16	0.92	calcite
CL-PS-02	prograde skarn - sp skarn	141	0.47	0.19	3.11	50.66	54.43	0.92	calcite
CL-PS-02	prograde skarn - sp skarn	145	0.47	0.19	4.94	48.32	53.92	0.95	calcite
CL-PS-02	prograde skarn - sp skarn	161	0.47	0.12	1.96	51.56	54.11	0.88	calcite

CARBONATES

Sample	Rock group	anal. #	FeO	MnO	MgO	CaO	Total	XMg	mineral
CL-PS-02	prograde skarn - sp skarn	170	0.47	0.15	2.13	52.07	54.82	0.89	calcite
CL-PS-02	prograde skarn - sp skarn	1	0.46	0.21	2.68	50.52	53.87	0.91	calcite
CL-PS-02	prograde skarn - sp skarn	4	0.46	0.13	2.31	51.63	54.53	0.90	calcite
CL-PS-02	prograde skarn - sp skarn	35	0.46	0.21	2.54	50.39	53.6	0.91	calcite
CL-PS-02	prograde skarn - sp skarn	92	0.46	0.1	2.03	51.97	54.56	0.89	calcite
CL-PS-02	prograde skarn - sp skarn	114	0.46	0.17	2.34	52.05	55.02	0.90	calcite
CL-PS-02	prograde skarn - sp skarn	120	0.46	0.21	2	52.01	54.68	0.89	calcite
CL-PS-02	prograde skarn - sp skarn	159	0.46	0.16	2.02	51.88	54.52	0.89	calcite
CL-PS-02	prograde skarn - sp skarn	84	0.45	0.14	2.19	51.34	54.12	0.90	calcite
CL-PS-02	prograde skarn - sp skarn	91	0.45	0.17	2.83	50.83	54.28	0.92	calcite
CL-PS-02	prograde skarn - sp skarn	115	0.45	0.17	1.94	51.66	54.22	0.88	calcite
CL-PS-02	prograde skarn - sp skarn	148	0.45	0.1	2.36	51.37	54.28	0.90	calcite
CL-PS-02	prograde skarn - sp skarn	165	0.45	0.29	3.4	49.77	53.91	0.93	calcite
CL-PS-02	prograde skarn - sp skarn	41	0.44	0.09	2.7	50.84	54.07	0.92	calcite
CL-PS-02	prograde skarn - sp skarn	88	0.44	0.11	2.17	51.47	54.19	0.90	calcite
CL-PS-02	prograde skarn - sp skarn	100	0.44	0.25	1.61	52.82	55.12	0.87	calcite
CL-PS-02	prograde skarn - sp skarn	113	0.44	0.05	2.3	51.79	54.58	0.90	calcite
CL-PS-02	prograde skarn - sp skarn	136	0.44	0.1	1.6	52.67	54.81	0.87	calcite
CL-PS-02	prograde skarn - sp skarn	138	0.44	0.16	2.09	52.1	54.79	0.89	calcite
CL-PS-02	prograde skarn - sp skarn	150	0.44	0.16	2.35	51.54	54.49	0.90	calcite
CL-PS-02	prograde skarn - sp skarn	163	0.44	0.22	2.21	51.33	54.2	0.90	calcite
CL-PS-02	prograde skarn - sp skarn	179	0.44	0.14	2.1	51.38	54.06	0.89	calcite
CL-PS-02	prograde skarn - sp skarn	12	0.43	0.13	2.44	50.91	53.91	0.91	calcite
CL-PS-02	prograde skarn - sp skarn	107	0.43	0.17	2.47	51.53	54.6	0.91	calcite
CL-PS-02	prograde skarn - sp skarn	140	0.43	0.29	3.16	50.67	54.55	0.93	calcite
CL-PS-02	prograde skarn - sp skarn	142	0.43	0.17	2.05	51.56	54.21	0.89	calcite
CL-PS-02	prograde skarn - sp skarn	154	0.43	0.1	1.91	52.04	54.48	0.89	calcite
CL-PS-02	prograde skarn - sp skarn	169	0.43	0.19	2.22	51.49	54.33	0.90	calcite
CL-PS-02	prograde skarn - sp skarn	183	0.43	0.21	2.73	50.61	53.98	0.92	calcite
CL-PS-02	prograde skarn - sp skarn	10	0.42	0.18	2.05	51.27	53.92	0.90	calcite

CARBONATES

Sample	Rock group	anal. #	FeO	MnO	MgO	CaO	Total	XMg	mineral
CL-PS-02	prograde skarn - sp skarn	18	0.42	0.16	2.16	51.15	53.89	0.90	calcite
CL-PS-02	prograde skarn - sp skarn	153	0.42	0.09	2.47	51.22	54.2	0.91	calcite
CL-PS-02	prograde skarn - sp skarn	167	0.42	0.23	2.06	51.44	54.15	0.90	calcite
CL-PS-02	prograde skarn - sp skarn	97	0.41	0.13	2.16	51.54	54.24	0.90	calcite
CL-PS-02	prograde skarn - sp skarn	143	0.41	0.18	1.97	52.29	54.85	0.90	calcite
CL-PS-02	prograde skarn - sp skarn	144	0.41	0.19	2.18	52.98	55.76	0.90	calcite
CL-PS-02	prograde skarn - sp skarn	26	0.4	0.17	1.9	51.58	54.05	0.89	calcite
CL-PS-02	prograde skarn - sp skarn	99	0.4	0.17	1.3	52.95	54.82	0.85	calcite
CL-PS-02	prograde skarn - sp skarn	118	0.4	0.21	1.49	52.78	54.88	0.87	calcite
CL-PS-02	prograde skarn - sp skarn	127	0.4	0.18	2.46	51.59	54.63	0.92	calcite
CL-PS-02	prograde skarn - sp skarn	180	0.4	0.16	1.62	52.59	54.77	0.88	calcite
CL-PS-02	prograde skarn - sp skarn	15	0.39	0.15	1.91	52.08	54.53	0.90	calcite
CL-PS-02	prograde skarn - sp skarn	139	0.39	0.11	2.09	51.85	54.44	0.91	calcite
CL-PS-02	prograde skarn - sp skarn	158	0.39	0.17	2.41	51.14	54.11	0.92	calcite
CL-PS-02	prograde skarn - sp skarn	166	0.39	0.22	3.16	51.28	55.05	0.94	calcite
CL-PS-02	prograde skarn - sp skarn	28	0.38	0.36	0.57	53.7	55.01	0.73	calcite
CL-PS-02	prograde skarn - sp skarn	122	0.38	0.14	2.05	51.85	54.42	0.91	calcite
CL-PS-02	prograde skarn - sp skarn	152	0.38	0.13	2.55	51.6	54.66	0.92	calcite
CL-PS-02	prograde skarn - sp skarn	181	0.38	0.17	1.66	52.37	54.58	0.89	calcite
CL-PS-02	prograde skarn - sp skarn	87	0.37	0.05	1.97	51.61	54	0.90	calcite
CL-PS-02	prograde skarn - sp skarn	90	0.37	0.2	2.2	51.49	54.26	0.91	calcite
CL-PS-02	prograde skarn - sp skarn	162	0.37	0.12	2.05	51.56	54.1	0.91	calcite
CL-PS-02	prograde skarn - sp skarn	93	0.36	0.18	2.31	51.42	54.27	0.92	calcite
CL-PS-02	prograde skarn - sp skarn	137	0.35	0.13	2.63	51.14	54.25	0.93	calcite
CL-PS-02	prograde skarn - sp skarn	117	0.34	0.19	2.16	52.06	54.75	0.92	calcite
CL-PS-02	prograde skarn - sp skarn	112	0.33	0.18	2.2	51.84	54.55	0.92	calcite
CL-PS-02	prograde skarn - sp skarn	95	0.32	0.15	1.73	51.77	53.97	0.91	calcite
CL-PS-02	prograde skarn - sp skarn	135	0.32	0.18	1.08	52.98	54.56	0.86	calcite
CL-PS-02	prograde skarn - sp skarn	151	0.32	0.11	1.71	52.68	54.82	0.90	calcite
CL-PS-02	prograde skarn - sp skarn	86	0.28	0.13	1.67	52.77	54.85	0.91	calcite

CARBONATES

Sample	Rock group	anal. #	FeO	MnO	MgO	CaO	Total	XMg	mineral
CL-PS-02	prograde skarn - sp skarn	186	0.27	0.15	2.14	52.13	54.69	0.93	calcite
CL-PS-02A	prograde skarn - sp skarn	338	0.58	0.23	3.22	51	55.03	0.91	calcite
CL-RS-02	retrograde skarn	82	0.31	0.19	0.05	57.87	58.42	0.22	calcite
CL-PS-01B	prograde skarn	227	0.75	0.03	20.63	29.52	50.93	0.98	dolomite
CL-PS-01C	prograde skarn	256	0.6	0.04	21.12	29.87	51.63	0.98	dolomite
CL-PS-01C	prograde skarn	257	0.49	0.02	21.34	29.84	51.69	0.99	dolomite
AT-PS-03	prograde skarn	204	0.7	0	20.74	25.45	46.89	0.98	dolomite
AT-PS-03	prograde skarn	40	0.57	0.07	20.82	30.49	51.95	0.98	dolomite
AT-PS-03	prograde skarn	45	0.57	0.07	21.19	30.27	52.1	0.99	dolomite
AT-PS-03	prograde skarn	213	0.57	0.03	21.15	30.32	52.07	0.99	dolomite
AT-PS-03	prograde skarn	47	0.56	0.08	21.34	30.49	52.47	0.99	dolomite
AT-PS-03	prograde skarn	203	0.55	0.01	20.96	25.69	47.21	0.99	dolomite
AT-PS-03	prograde skarn	41	0.54	0.03	21.02	30.57	52.16	0.99	dolomite
AT-PS-03	prograde skarn	43	0.52	0.03	20.58	30.46	51.59	0.99	dolomite
AT-PS-03	prograde skarn	13	0.51	0.12	20.82	30.6	52.05	0.99	dolomite
AT-PS-03	prograde skarn	44	0.51	0.03	21.32	30.4	52.26	0.99	dolomite
AT-PS-03	prograde skarn	46	0.5	0.01	20.92	30.57	52	0.99	dolomite
AT-PS-03	prograde skarn	214	0.49	0.04	21.52	30.42	52.47	0.99	dolomite
AT-PS-03	prograde skarn	42	0.48	0.07	21.05	30.91	52.51	0.99	dolomite
AT-PS-03	prograde skarn	211	0.48	0.05	21.21	30.45	52.19	0.99	dolomite
AT-PS-03	prograde skarn	212	0.47	0.09	21.15	30.44	52.15	0.99	dolomite
AT-PS-03	prograde skarn	200	0.46	0.03	21.85	30.18	52.52	0.99	dolomite
AT-PS-03	prograde skarn	38	0.45	0	21.45	30.28	52.18	0.99	dolomite
AT-PS-03	prograde skarn	39	0.45	0	21.35	30.47	52.27	0.99	dolomite
AT-PS-03	prograde skarn	11	0.44	0.06	21.33	29.97	51.8	0.99	dolomite
AT-PS-03	prograde skarn	49	0.43	0.08	21.41	30.39	52.31	0.99	dolomite
AT-PS-03	prograde skarn	221	0.43	0.03	21.4	30.38	52.24	0.99	dolomite
AT-PS-03	prograde skarn	217	0.43	0.02	21.06	30.36	51.87	0.99	dolomite
AT-PS-03	prograde skarn	220	0.43	0.09	21.23	30.32	52.07	0.99	dolomite
AT-PS-03	prograde skarn	35	0.42	0.05	21.14	30.5	52.11	0.99	dolomite

CARBONATES

Sample	Rock group	anal. #	FeO	MnO	MgO	CaO	Total	XMg	mineral
AT-PS-03	prograde skarn	205	0.41	0	20.59	25.54	46.54	0.99	dolomite
AT-PS-03	prograde skarn	10	0.41	0.03	20.94	30.71	52.09	0.99	dolomite
AT-PS-03	prograde skarn	37	0.41	0.11	21.47	30.3	52.29	0.99	dolomite
AT-PS-03	prograde skarn	216	0.41	0.07	21.24	30.06	51.78	0.99	dolomite
AT-PS-03	prograde skarn	215	0.4	0.08	21.28	30.46	52.22	0.99	dolomite
AT-PS-03	prograde skarn	12	0.39	0.07	21.17	30.71	52.34	0.99	dolomite
AT-PS-03	prograde skarn	199	0.39	0.11	21.33	30.36	52.19	0.99	dolomite
AT-PS-03	prograde skarn	201	0.38	0.01	21.53	30.49	52.41	0.99	dolomite
AT-PS-03	prograde skarn	48	0.38	0.1	20.98	30.44	51.9	0.99	dolomite
AT-PS-03	prograde skarn	14	0.36	0.03	21.17	30.68	52.24	0.99	dolomite
AT-PS-03	prograde skarn	36	0.36	0.01	21.45	30.25	52.07	0.99	dolomite
AT-PS-03	prograde skarn	15	0.35	0.08	21.47	30.47	52.37	0.99	dolomite
AT-PS-03	prograde skarn	218	0.35	0.06	21.01	30.16	51.58	0.99	dolomite
AT-PS-03	prograde skarn	219	0.32	0.02	21.15	30.44	51.93	0.99	dolomite
CL-PS-02A	prograde skarn - sp skarn	346	1.68	0.24	20.36	29.31	51.59	0.96	dolomite
CL-PS-02A	prograde skarn - sp skarn	347	1.65	0.18	19.86	29.6	51.29	0.96	dolomite

CHLORITE

Sample	Rock group	anal. #	SiO2	TiO2	Al2O3	Cr2O3	FeO	MnO	MgO	CaO	Na2O	K2O	Total	Cr ppm	XMg
AT-MZ-02	igneous apophysis	29	28.52	0.13	18	0.03	23.95	0.12	16.47	0.16	0.01	0.02	87.41	205.26	0.55
AT-MZ-02	igneous apophysis	28	29.26	0.13	16.9	0	23.05	0.16	17.51	0.12	0	0	87.13		0.58
FD-SI-01	igneous apophysis	143	30.36	0.05	17.51	0.09	13.24	0.24	24.53	0.05	0	0.02	86.09	615.78	0.77
FD-SI-01	igneous apophysis	113	27.33	0.07	17.65	0.04	27.59	0.9	14.53	0.05	0	0.01	88.16	273.68	0.48
FD-SI-01	igneous apophysis	112	25.44	0.08	18.14	0.03	31.94	0.69	11.22	0	0	0	87.55	205.26	0.39
FD-SI-01	igneous apophysis	81	30.28	0	18.77	0.03	9.91	0.17	26.96	0	0	0	86.12	205.26	0.83
FD-SI-01	igneous apophysis	145	31.01	0.03	17.42	0.01	16.07	0.23	24.09	0.05	0.01	0.03	88.96	68.42	0.73
FD-SI-01	igneous apophysis	82	29.74	0.06	18.63	0.01	11.25	0.19	25.91	0.01	0.02	0	85.82	68.42	0.8
FD-SI-01	igneous apophysis	111	25.93	0.16	18.2	0	29.91	0.51	12.19	0.04	0	0.03	86.98		0.42
FD-SI-01	igneous apophysis	144	26.65	0.01	17.61	0	22.28	0.42	14.9	0.05	0	0.01	81.93		0.54
FD-SI-01	igneous apophysis	142	43.05	0	8.74	0	0.31	0.17	31.58	0.53	0.03	0.01	84.42		0.99
FD-SI-01	igneous apophysis	103	25.73	0.11	18.02		32.91	0.78	10.85	0.08	0	0.02	88.5		0.37
FD-SI-01	igneous apophysis	109	25.63	0.19	18.74		32.44	1.19	8.79	0.03	0	0.3	87.32		0.33
FD-SI-01	igneous apophysis	105	25.35	0.1	18.26		32.08	0.76	10.64	0.01	0	0.04	87.24		0.37
FD-SI-01	igneous apophysis	108	25.96	0.33	18.29		31.24	0.53	11.36	0.04	0.02	0.03	87.8		0.39
FD-SI-01	igneous apophysis	104	25.9	0.13	18.28		30.72	0.66	11.37	0	0.01	0.22	87.28		0.4
FD-SI-01	igneous apophysis	110	25.92	0.28	17.92		29.66	0.54	12.32	0.08	0	0.07	86.81		0.43
FD-SI-01	igneous apophysis	107	28.61	0.83	17.72		24.65	0.58	13.77	0.01	0.01	0.54	86.72		0.5
FD-SI-01	igneous apophysis	106	29.37	0.7	16.82		23.38	0.58	16.72	0.06	0.01	0.9	88.54		0.56
FD-SI-01	igneous apophysis	79	29.03	0.08	18.92		13.15	0.22	24.26	0.03	0	0	85.69		0.77
FD-SI-01	igneous apophysis	80	29.71	0.03	19.07		11.18	0.16	26.24	0.04	0.01	0.02	86.45		0.81
AT-MG-01	igneous apophysis	115	29.04	0.1	14.95	0.11	23.73	0.34	15.71	0.14	0.01	0.02	84.14	752.62	0.54
AT-MG-01	igneous apophysis	114	33.47	0.01	13.97	0.03	17.11	0.13	20.2	0.8	0.02	0.04	85.79	205.26	0.68
DB-PG-02	igneous apophysis - grt-leucogranite	93	24.75	0.2	16.56		38.26	1.48	5.95	0.04	0.06	0.03	87.31		0.22
DB-PG-02	igneous apophysis - grt-leucogranite	116	25.1	0.09	16.35		38.08	1.13	6.58	0.06	0.02	0.01	87.51		0.24
DB-PG-02	igneous apophysis - grt-leucogranite	36	25.48	0.13	20.26		35.5	1.02	5.88	0.01	0.02	0.01	88.39		0.23
DB-PG-02	igneous apophysis - grt-leucogranite	74	25.4	0.19	18.76		35.26	0.98	6.51	0.05	0.04	0.07	87.26		0.25
DB-PG-02	igneous apophysis - grt-leucogranite	50	25.13	0.09	20.85		34.11	0.49	6.23	0.05	0	0.02	87.16		0.25
DB-PG-02	igneous apophysis - grt-leucogranite	10	23.66	0.35	20.76		33.96	1.87	6.63	0.01	0.03	0.04	87.42		0.26
DB-PG-02	igneous apophysis - grt-leucogranite	83	26.84	0.26	14.22		33.63	0.73	8.85	0.06	0.04	0.07	84.7		0.32
DB-PG-02	igneous apophysis - grt-leucogranite	119	27.11	0.41	16.5		33.45	0.87	8.41	0.09	0.03	0.27	87.22		0.31
DB-PG-02	igneous apophysis - grt-leucogranite	85	27.37	0.71	18.89		32.75	0.28	7.78	0.09	0.04	0.6	88.58		0.3
DB-PG-02	igneous apophysis - grt-leucogranite	38	27.21	0.18	18.47		31.95	0.63	9.88	0.11	0.05	0.02	88.79		0.36
DB-PG-02	igneous apophysis - grt-leucogranite	101	28.34	0.77	16.96		30.94	0.81	9.61	0.09	0.03	1	88.76		0.36
DB-PG-02	igneous apophysis - grt-leucogranite	87	27.4	1.8	17.54		29.05	0.37	9.63	0.16	0.02	0.82	86.81		0.37
DB-PG-02	igneous apophysis - grt-leucogranite	161	32.26	2.06	18.12		28.63	0.74	7.2	1.53	0.07	0.51	91.12		0.31

CHLORITE

Sample	Rock group	anal. #	SiO2	TiO2	Al2O3	Cr2O3	FeO	MnO	MgO	CaO	Na2O	K2O	Total	Cr ppm	XMg
DB-PG-02	igneous apophysis - grt-leucogranite	122	28.9	0.19	15.7		25.97	0.47	15.79	0.21	0.04	0.14	87.41		0.52
DB-PG-02	igneous apophysis - grt-leucogranite	97	28.86	0.14	16.85		25.74	0.24	13.98	0.14	0.02	0.04	86.08		0.49
DB-PG-02	igneous apophysis - grt-leucogranite	40	29.71	1.04	14.35		22.28	0.41	16.31	0.07	0.09	0.5	84.75		0.57
DB-PG-02	igneous apophysis - grt-leucogranite	95	45.87	0.45	12.42		20.52	0.63	10	0.07	0.14	0.16	90.3		0.46
CL-PS-01C	prograde skarn	251	33.41	0.14	17.74	0.01	1.07	0.01	35.02	0.07	0.01	0.01	87.49	56.03	0.98
CL-PS-01C	prograde skarn	272	31.32	0.07	19.15	0	1.57	0	33.64	0.39	0.21	0.11	86.45	27.95	0.97
CL-PS-02A	prograde skarn - sp skarn	279	31.19	0.05	18.42	0.63	5.02	0.03	31.59	0.01	0.01	0	86.95	4286.96	0.92
CL-PS-02A	prograde skarn - sp skarn	278	31.32	0.06	18.07	0.56	5.08	0.03	31.93	0.02	0.01	0.03	87.11	3860.22	0.92
CL-PS-02A	prograde skarn - sp skarn	337	27.98	0.07	23.3	0.38	5.52	0	29.57	0.01	0	0.01	86.85	2616.05	0.91
CL-PS-02A	prograde skarn - sp skarn	328	28.09	0.07	22.76	0.36	5.47	0.04	29.83	0.02	0	0	86.63	2443.21	0.91
CL-PS-02A	prograde skarn - sp skarn	298	28.68	0.06	21.38	0.33	5.42	0.01	30.21	0.03	0	0	86.11	2227.75	0.91
CL-PS-02A	prograde skarn - sp skarn	276	29.58	0.08	20.9	0.31	5.27	0.04	30.33	0.04	0.02	0	86.57	2115.29	0.91
CL-PS-02A	prograde skarn - sp skarn	326	27.73	0.06	22.97	0.27	5.61	0	29.49	0.05	0.01	0.01	86.21	1837.62	0.9
CL-PS-02A	prograde skarn - sp skarn	280	31.44	0.06	17.74	0.25	5.02	0.08	32.23	0.01	0.02	0	86.85	1737.94	0.92
CL-PS-02A	prograde skarn - sp skarn	292	30.89	0.04	18.88	0.24	5.17	0.01	31.48	0.01	0.02	0.02	86.77	1672.93	0.92
CL-PS-02A	prograde skarn - sp skarn	335	29.02	0.07	21.97	0.21	5.47	0.04	29.95	0	0	0	86.74	1413.71	0.91
CL-PS-02A	prograde skarn - sp skarn	325	28.11	0.05	23.75	0.2	5.69	0.06	29.49	0	0	0	87.36	1343.56	0.9
CL-PS-02A	prograde skarn - sp skarn	281	30.5	0.07	19.56	0.19	5.22	0.03	31.1	0.1	0	0	86.78	1305.86	0.91
CL-PS-02A	prograde skarn - sp skarn	342	30.96	0.07	18.58	0.19	5.1	0.04	31.6	0.01	0	0.05	86.59	1288.73	0.92
CL-PS-02A	prograde skarn - sp skarn	340	28.84	0.08	22.48	0.19	5.66	0.05	29.77	0.02	0	0.02	87.12	1266.67	0.9
CL-PS-02A	prograde skarn - sp skarn	329	29.05	0.07	21.92	0.17	5.47	0.06	30.29	0.01	0	0	87.04	1180.54	0.91
CL-PS-02A	prograde skarn - sp skarn	341	28.51	0.08	22.89	0.17	5.64	0.05	29.93	0.04	0.03	0.09	87.42	1165.88	0.9
CL-PS-02A	prograde skarn - sp skarn	339	28.08	0.08	23.01	0.15	5.41	0.07	29.63	0.01	0	0.02	86.46	1025.03	0.91
CL-PS-02A	prograde skarn - sp skarn	282	28.4	0.06	22.76	0.15	5.58	0.02	29.92	0	0.01	0.01	86.93	1019.44	0.91
CL-PS-02A	prograde skarn - sp skarn	295	30.01	0.08	20.36	0.14	5.21	0.06	30.82	0.01	0.01	0	86.69	984.8	0.91
CL-PS-02A	prograde skarn - sp skarn	297	27.93	0.09	23	0.14	5.56	0	29.61	0.01	0	0	86.34	946.09	0.9
CL-PS-02A	prograde skarn - sp skarn	291	30.33	0.06	20.63	0.13	5.46	0.04	31.03	0.01	0	0	87.7	919.88	0.91
CL-PS-02A	prograde skarn - sp skarn	331	27.87	0.06	23.69	0.13	5.64	0.05	29.27	0	0	0	86.72	918.9	0.9
CL-PS-02A	prograde skarn - sp skarn	311	28.46	0.07	22.97	0.13	5.31	0.03	29.85	0	0	0	86.82	911.03	0.91
CL-PS-02A	prograde skarn - sp skarn	305	28.86	0.06	22.48	0.13	5.44	0.03	30.1	0.03	0.01	0	87.15	887.8	0.91
CL-PS-02A	prograde skarn - sp skarn	336	28.5	0.04	23.06	0.13	5.41	0.04	29.84	0.02	0	0	87.03	878.75	0.91
CL-PS-02A	prograde skarn - sp skarn	334	28.34	0.08	23.57	0.12	5.58	0.03	29.51	0	0	0	87.21	814.29	0.9
CL-PS-02A	prograde skarn - sp skarn	294	30.59	0.05	19.36	0.11	5.43	0.02	31.13	0.04	0	0.01	86.75	741.47	0.91
CL-PS-02A	prograde skarn - sp skarn	309	28.32	0.05	22.96	0.11	5.29	0.04	29.75	0.03	0.02	0	86.56	737.01	0.91
CL-PS-02A	prograde skarn - sp skarn	308	28.24	0.08	23.04	0.1	5.27	0.04	29.48	0.11	0	0	86.36	663.74	0.91
CL-PS-02A	prograde skarn - sp skarn	307	28.68	0.08	22.84	0.1	5.58	0.05	30.16	0.04	0	0	87.52	658.49	0.91

CHLORITE

Sample	Rock group	anal. #	SiO2	TiO2	Al2O3	Cr2O3	FeO	MnO	MgO	CaO	Na2O	K2O	Total	Cr ppm	XMg
CL-PS-02A	prograde skarn - sp skarn	330	27.73	0.06	22.98	0.09	5.36	0.07	29.42	0.58	0	0	86.31	636.27	0.91
CL-PS-02A	prograde skarn - sp skarn	324	28.99	0.04	22.52	0.08	5.58	0.03	30.03	0.01	0	0	87.28	580.87	0.91
CL-PS-02A	prograde skarn - sp skarn	290	31.47	0.05	17.99	0.08	4.97	0.02	31.88	0.02	0.02	0	86.51	536.84	0.92
CL-PS-02A	prograde skarn - sp skarn	310	28.87	0.05	22.7	0.07	5.4	0.04	30.13	0	0	0	87.25	471.37	0.91
CL-PS-02A	prograde skarn - sp skarn	293	30.24	0.06	19.61	0.07	5.3	0.05	30.92	0	0	0	86.26	462.62	0.91
CL-PS-02A	prograde skarn - sp skarn	322	30.1	0.07	20.13	0.07	5.15	0.06	31.03	0.06	0	0	86.67	453.88	0.91
CL-PS-02A	prograde skarn - sp skarn	306	28.59	0.06	22.92	0.06	5.24	0.04	30.17	0.03	0.01	0	87.1	407.59	0.91
CL-PS-02A	prograde skarn - sp skarn	296	31.17	0.04	18.39	0.05	4.95	0.04	31.96	0.02	0.01	0.01	86.65	353.35	0.92
CL-PS-02A	prograde skarn - sp skarn	327	30.01	0.08	20.05	0.02	5.28	0.06	30.66	0.02	0	0.07	86.26	160.31	0.91
CL-PS-02A	prograde skarn - sp skarn	321	28.29	0.07	23.01	0	5.59	0.05	29.89	0.04	0.02	0	86.96	0.1	0.91
CL-PS-02B	prograde skarn - sp skarn	352	29.46	0.07	20.38	0.38	5.37	0.03	29.96	0.03	0.01	0.01	85.71	2590.64	0.91
CL-PS-02B	prograde skarn - sp skarn	351	28.95	0.06	21.17	0.07	5.24	0.02	29.68	0.05	0.02	0	85.27	485.65	0.91
CL-PS-02B	prograde skarn - sp skarn	353	29.64	0.05	20.08	0.07	5.51	0.04	29.88	0.02	0	0.08	85.38	457.49	0.91
CL-PS-02B	prograde skarn - sp skarn	354	29.11	0.07	20.73	0.04	5.45	0.07	29.79	0.02	0.02	0.03	85.32	279.15	0.91
CL-RS-01	retrograde skarn	4	28.11	0.04	18.96	0.06	20.34	0.04	20.15	0	0	0.03	87.75	410.52	0.64
CL-RS-01	retrograde skarn	49	27.74	0	18.82	0.05	21.55	0.11	19.28	0.02	0	0.01	87.63	342.1	0.61
CL-RS-01	retrograde skarn	6	28.07	0.03	18.54	0.05	20.8	0.12	19.88	0.04	0	0	87.52	342.1	0.63
CL-RS-01	retrograde skarn	25	28.69	0.05	18.51	0.05	19.73	0.14	20.21	0.01	0	0	87.39	342.1	0.65
CL-RS-01	retrograde skarn	62	27.71	0.02	18.61	0.04	21.29	0.1	19.25	0.03	0	0	87.04	273.68	0.62
CL-RS-01	retrograde skarn	47	27.93	0.01	18.46	0.04	21.23	0.09	19.17	0.02	0	0.01	86.97	273.68	0.62
CL-RS-01	retrograde skarn	11	28.02	0.08	18.69	0.04	21.08	0.13	19.59	0.03	0	0	87.67	273.68	0.62
CL-RS-01	retrograde skarn	12	28.02	0.01	18.65	0.04	21.04	0.09	19.95	0.06	0.02	0.01	87.93	273.68	0.63
CL-RS-01	retrograde skarn	57	28.18	0.04	18.42	0.04	20.76	0.12	20.16	0.24	0	0.02	87.99	273.68	0.63
CL-RS-01	retrograde skarn	3	27.82	0.04	19.04	0.04	20.7	0.12	19.66	0.02	0	0	87.42	273.68	0.63
CL-RS-01	retrograde skarn	39	28.16	0.07	18.55	0.04	20.57	0.1	20.08	0.07	0	0	87.65	273.68	0.64
CL-RS-01	retrograde skarn	18	29.28	0.02	19.13	0.04	19.1	0.08	22.12	0.01	0.01	0	89.79	273.68	0.67
CL-RS-01	retrograde skarn	51	30.3	0.06	16.8	0.04	14.78	0.08	24.02	0.07	0	0	86.18	273.68	0.74
CL-RS-01	retrograde skarn	10	27.6	0.02	19.17	0.03	21.59	0.09	19.45	0.03	0	0.03	88	205.26	0.62
CL-RS-01	retrograde skarn	44	27.9	0.07	19.06	0.03	21.54	0.1	19.65	0.02	0.01	0.01	88.39	205.26	0.62
CL-RS-01	retrograde skarn	37	27.54	0.1	18.58	0.03	21.48	0.1	18.49	0.23	0.01	0	86.59	205.26	0.61
CL-RS-01	retrograde skarn	45	27.46	0.09	18.98	0.03	21.46	0.09	19.38	0.01	0.01	0	87.52	205.26	0.62
CL-RS-01	retrograde skarn	13	28.25	0.04	18.68	0.03	21.08	0.1	19.76	0.07	0	0.02	88.04	205.26	0.63
CL-RS-01	retrograde skarn	23	27.56	0	18.88	0.03	21.02	0.12	19.14	0.01	0.01	0.01	86.78	205.26	0.62
CL-RS-01	retrograde skarn	7	26.76	0.04	14.19	0.03	20.89	0.08	20.02	0.03	0	0	82.05	205.26	0.63
CL-RS-01	retrograde skarn	5	28.02	0.04	18.83	0.03	20.5	0.09	19.99	0	0	0.04	87.54	205.26	0.63
CL-RS-01	retrograde skarn	50	28.97	0.01	17.46	0.03	18.57	0.11	22.57	0.13	0	0.02	87.87	205.26	0.68

CHLORITE

Sample	Rock group	anal. #	SiO2	TiO2	Al2O3	Cr2O3	FeO	MnO	MgO	CaO	Na2O	K2O	Total	Cr ppm	XMg
CL-RS-01	retrograde skarn	36	30.34	0.06	17.14	0.03	12.52	0.04	25.08	0.05	0.01	0.02	85.28	205.26	0.78
CL-RS-01	retrograde skarn	70	27.55	0.04	19.19	0.02	21.41	0.12	19.59	0.01	0	0.01	87.95	136.84	0.62
CL-RS-01	retrograde skarn	38	27.45	0.04	18.56	0.02	21.39	0.06	19.07	0.31	0.02	0	86.92	136.84	0.61
CL-RS-01	retrograde skarn	24	27.64	0.05	18.79	0.02	21.31	0.08	19.51	0.01	0	0	87.45	136.84	0.62
CL-RS-01	retrograde skarn	19	28.14	0.02	19.19	0.02	21.28	0.13	19.87	0	0.01	0.01	88.67	136.84	0.62
CL-RS-01	retrograde skarn	2	28.07	0.05	19.56	0.02	21.12	0.13	19.86	0.04	0	0.01	88.85	136.84	0.63
CL-RS-01	retrograde skarn	68	27.77	0	19.4	0.02	21.07	0.08	19.9	0.02	0	0	88.27	136.84	0.63
CL-RS-01	retrograde skarn	69	27.9	0.04	19.1	0.02	21.05	0.1	19.61	0.02	0	0	87.85	136.84	0.62
CL-RS-01	retrograde skarn	43	27.7	0.03	19.01	0.02	21.03	0.09	19.39	0.08	0.01	0	87.36	136.84	0.62
CL-RS-01	retrograde skarn	63	27.88	0.03	18.71	0.02	20.98	0.14	19.44	0.01	0.02	0.01	87.28	136.84	0.62
CL-RS-01	retrograde skarn	27	27.77	0.02	18.8	0.02	20.92	0.12	19.71	0.01	0.01	0	87.4	136.84	0.63
CL-RS-01	retrograde skarn	26	28	0.05	19.35	0.02	20.83	0.11	19.73	0	0.02	0	88.12	136.84	0.63
CL-RS-01	retrograde skarn	33	28.02	0.06	19.44	0.02	20.58	0.13	19.74	0.04	0	0	88.02	136.84	0.63
CL-RS-01	retrograde skarn	71	27.65	0.05	18.87	0.01	22.17	0.14	18.84	0.02	0	0	87.73	68.42	0.6
CL-RS-01	retrograde skarn	9	27.72	0.06	19.12	0.01	22.15	0.09	19.19	0	0.01	0.01	88.37	68.42	0.61
CL-RS-01	retrograde skarn	42	27.77	0.03	18.82	0.01	21.48	0.12	19.15	0.18	0	0	87.57	68.42	0.61
CL-RS-01	retrograde skarn	1	27.95	0	19.36	0.01	20.96	0.12	19.48	0.04	0.01	0.02	87.95	68.42	0.62
CL-RS-01	retrograde skarn	28	27.91	0.03	18.81	0.01	20.73	0.15	19.41	0	0	0	87.04	68.42	0.63
CL-RS-01	retrograde skarn	61	27.54	0.11	18.61	0.01	20.67	0.1	19.64	0.32	0.02	0	87.02	68.42	0.63
CL-RS-01	retrograde skarn	40	28.55	0.02	18.36	0.01	19.72	0.05	21.61	0.06	0.01	0	88.4	68.42	0.66
CL-RS-01	retrograde skarn	56	28.82	0.04	17.7	0.01	17.93	0.07	21.45	0.26	0	0	86.3	68.42	0.68
CL-RS-01	retrograde skarn	34	29.2	0.03	17.99	0.01	16.91	0.07	22.1	0.02	0	0	86.33	68.42	0.7
CL-RS-01	retrograde skarn	73	27.33	0.09	18.95	0	22.4	0.17	18.86	0	0.02	0.01	87.83		0.6
CL-RS-01	retrograde skarn	72	28.09	0.06	19.12	0	22	0.15	19.33	0	0.01	0	88.76		0.61
CL-RS-01	retrograde skarn	41	27.5	0.03	18.27	0	21.84	0.13	18.59	0.31	0	0	86.68		0.6
CL-RS-01	retrograde skarn	20	28.18	0.06	18.56	0	21.48	0.08	19.66	0	0	0	88.02		0.62
CL-RS-01	retrograde skarn	46	27.85	0.04	18.84	0	21.44	0.08	19.01	0.03	0.02	0	87.32		0.61
CL-RS-01	retrograde skarn	64	27.92	0.01	18.58	0	21.39	0.11	19.84	0.01	0	0	87.87		0.62
CL-RS-01	retrograde skarn	67	27.86	0.01	19.26	0	21.39	0.08	19.4	0.02	0.01	0.01	88.04		0.62
CL-RS-01	retrograde skarn	48	27.74	0.05	18.9	0	21.38	0.08	19.65	0.03	0	0.01	87.84		0.62
CL-RS-01	retrograde skarn	21	27.84	0	18.84	0	21.35	0.12	19.37	0.02	0.01	0	87.55		0.62
CL-RS-01	retrograde skarn	8	27.91	0	19.01	0	21.29	0.13	19.14	0.02	0.02	0	87.54		0.62
CL-RS-01	retrograde skarn	65	27.72	0.09	19.07	0	21.26	0.06	19.87	0	0	0	88.1		0.62
CL-RS-01	retrograde skarn	15	26.21	0.05	16.13	0	21.2	0.09	18.47	0.04	0	0	82.18		0.61
CL-RS-01	retrograde skarn	31	27.89	0.02	18.13	0	21.09	0.06	19.5	0.01	0	0.01	86.71		0.62
CL-RS-01	retrograde skarn	29	27.96	0.03	18.77	0	20.98	0.11	19.63	0	0.01	0	87.5		0.63

CHLORITE

Sample	Rock group	anal. #	SiO2	TiO2	Al2O3	Cr2O3	FeO	MnO	MgO	CaO	Na2O	K2O	Total	Cr ppm	XMg
CL-RS-01	retrograde skarn	16	28.9	0.02	19.31	0	20.87	0.13	21.47	0.02	0	0	90.74		0.65
CL-RS-01	retrograde skarn	30	27.56	0.03	18.91	0	20.82	0.1	19.49	0.03	0.02	0.01	86.97		0.63
CL-RS-01	retrograde skarn	66	27.77	0.09	19.21	0	20.79	0.16	19.71	0.01	0.01	0.01	87.76		0.63
CL-RS-01	retrograde skarn	14	27.63	0.06	18.93	0	20.61	0.1	19.47	0.03	0	0	86.84		0.63
CL-RS-01	retrograde skarn	59	26.6	4.65	16.73	0	20.43	0.09	18.82	0.18	0.02	0	87.52		0.62
CL-RS-01	retrograde skarn	32	28.13	0.04	18.43	0	20.43	0.1	19.66	0.06	0	0.02	86.89		0.63
CL-RS-01	retrograde skarn	22	27.75	0.03	18.87	0	20.17	0.09	19.7	0	0.01	0	86.63		0.64
CL-RS-01	retrograde skarn	17	29.06	0.03	19.36	0	20.1	0.09	21.67	0.03	0	0	90.34		0.66
CL-RS-01	retrograde skarn	52	28.31	0.04	18.15	0	20.07	0.14	20.72	0.09	0.01	0	87.53		0.65
CL-RS-01	retrograde skarn	60	28.27	0.05	18.55	0	19.58	0.13	20.33	0.25	0	0	87.17		0.65
CL-RS-01	retrograde skarn	58	28.89	0.1	17.93	0	19.17	0.09	21.78	0.27	0.01	0	88.29		0.67
CL-RS-01	retrograde skarn	55	29.09	0.06	17.95	0	18.35	0.07	21.7	0.2	0.01	0.03	87.48		0.68
CL-RS-01	retrograde skarn	54	29.84	0.04	17.31	0	16.63	0.08	24.58	0.15	0	0	88.66		0.72
CL-RS-01	retrograde skarn	53	29.78	0.05	17.48	0	16.5	0.05	24.1	0.12	0.01	0	88.08		0.72
CL-RS-01	retrograde skarn	35	30.56	0.02	17.02	0	12.57	0.08	24.46	0.01	0.01	0.02	84.75		0.78
CL-RS-02	retrograde skarn	119	30	0.02	19.45	0.08	12.42	0.06	26.22	0	0.01	0.01	88.28	547.36	0.79
CL-RS-02	retrograde skarn	127	27.96	0.03	18.66	0.04	20.23	0.08	20.19	0.14	0	0	87.41	273.68	0.64
CL-RS-02	retrograde skarn	106	27.81	0.01	18.55	0.04	20	0.14	20.03	0.01	0	0	86.66	273.68	0.64
CL-RS-02	retrograde skarn	83	28.34	0.05	18.83	0.04	19.95	0.08	21.46	0.06	0	0	88.86	273.68	0.66
CL-RS-02	retrograde skarn	125	28.15	0	18.61	0.04	19.28	0.09	20.22	0.2	0.02	0.01	86.72	273.68	0.65
CL-RS-02	retrograde skarn	132	28.81	0.01	18.51	0.04	19.06	0.09	21.29	0.01	0.01	0	87.86	273.68	0.67
CL-RS-02	retrograde skarn	102	29.08	0.01	18.22	0.04	18.62	0.12	22	0.03	0	0	88.14	273.68	0.68
CL-RS-02	retrograde skarn	96	28.62	0	18.49	0.04	17.12	0.07	22.08	0.03	0	0	86.54	273.68	0.7
CL-RS-02	retrograde skarn	111	29.24	0.01	18.87	0.04	13.52	0.09	24.54	0.11	0	0	86.44	273.68	0.76
CL-RS-02	retrograde skarn	98	28.52	0.03	22.03	0.04	11.34	0.1	25.03	0.04	0.03	0.01	87.17	273.68	0.8
CL-RS-02	retrograde skarn	143	27.73	0.03	18.52	0.04	20.13	0.14	19.79	0.03	0	0	86.51	244.94	0.64
CL-RS-02	retrograde skarn	74	27.9	0.03	18.81	0.03	21.05	0.09	19.84	0.01	0	0	87.81	205.26	0.63
CL-RS-02	retrograde skarn	76	27.89	0.02	18.62	0.03	20.84	0.1	20.29	0.05	0.02	0.02	87.92	205.26	0.63
CL-RS-02	retrograde skarn	92	29.01	0.04	18.48	0.03	17.94	0.11	22.83	0.05	0.02	0	88.6	205.26	0.69
CL-RS-02	retrograde skarn	124	28.7	0.01	18.38	0.03	17.75	0.1	21.31	0.06	0.01	0	86.41	205.26	0.68
CL-RS-02	retrograde skarn	123	28.77	0.05	19.56	0.03	16.37	0.07	22.7	0.05	0	0.01	87.65	205.26	0.71
CL-RS-02	retrograde skarn	113	29.37	0.02	20.44	0.03	12.97	0.07	24.73	0.05	0.01	0	87.7	205.26	0.77
CL-RS-02	retrograde skarn	139	28.09	0	18.94	0.02	20.44	0.14	20.27	0.02	0.01	0	88.04	165.58	0.64
CL-RS-02	retrograde skarn	142	27.94	0.04	18.93	0.02	20.23	0.09	20.03	0.02	0.01	0	87.4	145.73	0.64
CL-RS-02	retrograde skarn	75	28.68	0.01	18.16	0.02	19.13	0.1	21.34	0.03	0	0.01	87.59	136.84	0.67
CL-RS-02	retrograde skarn	93	29.15	0.03	19.11	0.02	14.98	0.11	24.13	0.01	0.02	0	87.58	136.84	0.74

CHLORITE

Sample	Rock group	anal. #	SiO2	TiO2	Al2O3	Cr2O3	FeO	MnO	MgO	CaO	Na2O	K2O	Total	Cr ppm	XMg
CL-RS-02	retrograde skarn	108	29.53	0.03	18.86	0.02	14.31	0.08	24.24	0.06	0	0	87.17	136.84	0.75
CL-RS-02	retrograde skarn	84	30.77	0.02	5.3	0.02	12.72	0.02	19.86	13.51	0	0	82.82	136.84	0.74
CL-RS-02	retrograde skarn	121	28.92	0.06	21.32	0.02	12	0.09	24.8	0.05	0	0	87.31	136.84	0.79
CL-RS-02	retrograde skarn	117	28.77	0.02	19.68	0.02	11.97	0.07	24.37	0	0	0	84.95	136.84	0.78
CL-RS-02	retrograde skarn	136	28.24	0	18.18	0.02	18.57	0.09	21.2	0.03	0	0	86.41	133.42	0.67
CL-RS-02	retrograde skarn	140	28.15	0.04	19.06	0.01	20.67	0.09	20.39	0.04	0	0	88.5	79.37	0.64
CL-RS-02	retrograde skarn	134	29.19	0.01	17.96	0.01	18.97	0.12	21.78	0.05	0.01	0	88.17	68.42	0.67
CL-RS-02	retrograde skarn	130	28.64	0.01	18.38	0.01	17.64	0.07	22.23	0.03	0.02	0	87.03	68.42	0.69
CL-RS-02	retrograde skarn	81	34.89	0.04	10.97	0.01	14.97	0.05	22.59	0.64	0.12	0.02	85.02	68.42	0.73
CL-RS-02	retrograde skarn	110	29.06	0.03	19.15	0.01	14.42	0.09	23.28	0.04	0.01	0.01	86.18	68.42	0.74
CL-RS-02	retrograde skarn	94	28.64	0	20.28	0.01	12.67	0.12	24.04	0.05	0	0.01	85.86	68.42	0.77
CL-RS-02	retrograde skarn	116	29.08	0.02	22.29	0.01	11.68	0.13	25.06	0.03	0.01	0.02	88.32	68.42	0.79
CL-RS-02	retrograde skarn	91	28.64	0.02	21.6	0.01	11.64	0.08	25.47	0.03	0	0	87.51	68.42	0.8
CL-RS-02	retrograde skarn	120	29.21	0.05	21.54	0.01	11.6	0.07	25.41	0.01	0	0	87.95	68.42	0.8
CL-RS-02	retrograde skarn	100	28.55	0.07	20.46	0.01	10.94	0.1	24.86	0	0	0	85.01	68.42	0.8
CL-RS-02	retrograde skarn	138	29.2	0.04	18.23	0.01	18.55	0.12	21.23	0.07	0.03	0.03	87.62	60.21	0.67
CL-RS-02	retrograde skarn	126	27.61	0.05	18.74	0	20.92	0.09	19.78	0.16	0	0	87.43		0.63
CL-RS-02	retrograde skarn	137	28.03	0.04	19.27	0	20.77	0.1	20.4	0.08	0.05	0.01	88.76		0.64
CL-RS-02	retrograde skarn	128	28.08	0.06	18.55	0	20.67	0.16	20.69	0	0.03	0	88.33		0.64
CL-RS-02	retrograde skarn	141	28.13	0.03	19.05	0	20.47	0.15	20.36	0	0.01	0.01	88.29		0.64
CL-RS-02	retrograde skarn	144	28.19	0.03	18.82	0	20.15	0.1	20.13	0.03	0	0.01	87.56		0.64
CL-RS-02	retrograde skarn	129	28.29	0.03	18.69	0	20.08	0.11	20.55	0.03	0	0.02	87.9		0.65
CL-RS-02	retrograde skarn	85	28.56	0.02	18.33	0	19.55	0.08	20.62	0.06	0.01	0	87.31		0.65
CL-RS-02	retrograde skarn	77	27.72	0.01	18.44	0	19.45	0.14	19.85	0.23	0.01	0.04	86.02		0.65
CL-RS-02	retrograde skarn	78	28.51	0.02	18.47	0	18.66	0.07	21.42	0.2	0.03	0	87.42		0.67
CL-RS-02	retrograde skarn	135	28.21	0.05	18.07	0	18.53	0.06	21.21	0.04	0.01	0	86.26		0.67
CL-RS-02	retrograde skarn	79	29.02	0	18.9	0	18.48	0.07	21.93	0.22	0	0	88.7		0.68
CL-RS-02	retrograde skarn	97	27.89	0	18.35	0	18.16	0.13	20.55	0.12	0	0	85.28		0.67
CL-RS-02	retrograde skarn	101	28.91	0.03	18.56	0	18.04	0.12	22.17	0	0.02	0	87.89		0.69
CL-RS-02	retrograde skarn	105	28.33	0.01	18.47	0	17.98	0.13	21.28	0.04	0	0.01	86.32		0.68
CL-RS-02	retrograde skarn	104	28.7	0.07	18.59	0	17.95	0.12	22.09	0.02	0.02	0.01	87.6		0.69
CL-RS-02	retrograde skarn	80	33.59	0.02	11.42	0	17.95	0.07	22.45	0.74	0.13	0.01	86.79		0.69
CL-RS-02	retrograde skarn	131	28.93	0.02	18.37	0	17.71	0.1	21.93	0.03	0	0	87.24		0.69
CL-RS-02	retrograde skarn	95	28.53	0.04	18.75	0	17.33	0.12	21.18	0.04	0.02	0	86.11		0.69
CL-RS-02	retrograde skarn	133	30.51	0.03	14.94	0	17.32	0.02	21.82	0.14	0.01	0.03	85.27		0.69
CL-RS-02	retrograde skarn	103	28.75	0.02	18	0	17.24	0.11	22.14	0.01	0.01	0.01	86.28		0.7

CHLORITE

Sample	Rock group	anal. #	SiO2	TiO2	Al2O3	Cr2O3	FeO	MnO	MgO	CaO	Na2O	K2O	Total	Cr ppm	XMg
CL-RS-02	retrograde skarn	122	29.04	0	19.83	0	16.23	0.11	23.53	0.03	0	0.01	88.81		0.72
CL-RS-02	retrograde skarn	109	29.06	0.01	18.05	0	16.03	0.12	23.62	0.12	0	0	87.04		0.72
CL-RS-02	retrograde skarn	114	28.94	0.02	20.69	0	12.57	0.14	24.75	0.07	0	0	87.17		0.78
CL-RS-02	retrograde skarn	88	28.75	0.03	21.77	0	12.22	0.07	24.7	0.02	0	0	87.6		0.78
CL-RS-02	retrograde skarn	118	28.64	0.02	21.3	0	12.01	0.1	24.88	0.03	0	0	86.99		0.79
CL-RS-02	retrograde skarn	89	28.9	0.05	21.2	0	11.81	0.11	25.14	0.02	0	0	87.21		0.79
CL-RS-02	retrograde skarn	87	28.89	0.04	21.67	0	11.46	0.09	24.95	0	0.01	0	87.17		0.8
CL-RS-02	retrograde skarn	115	28.53	0.03	21.03	0	11.34	0.14	24.63	0.02	0	0.01	85.75		0.79
CL-RS-02	retrograde skarn	112	29.64	0.07	19.58	0	11.27	0.1	25.89	0.05	0	0	86.59		0.8
CL-RS-02	retrograde skarn	86	28.99	0.03	21.48	0	10.96	0.11	26.04	0	0	0	87.61		0.81
CL-RS-02	retrograde skarn	99	28.86	0.02	21.25	0	10.77	0.11	25.36	0.02	0.02	0	86.41		0.81
CL-RS-02	retrograde skarn	90	29.07	0.02	21.41	0	10.67	0.12	25.23	0.04	0.02	0	86.59		0.81
CL-RS-02	retrograde skarn	107	30.41	0.03	18.12	0	9.82	0.08	26.64	0.1	0	0.01	85.21		0.83
CL-RS-03	retrograde skarn	111	29.05	0	21.77	0.06	16.69	0.09	18.5	0.01	0	0	86.16	410.52	0.66
CL-RS-03	retrograde skarn	73	30.43	0	25.76	0.06	13.41	0.1	18.31	0.01	0	0	88.09	410.52	0.71
CL-RS-03	retrograde skarn	92	28.59	0.03	20.39	0.05	20.09	0.11	19.19	0.04	0.01	0	88.5	342.1	0.63
CL-RS-03	retrograde skarn	67	28.48	0	21.18	0.05	19.04	0.08	18.81	0	0	0.01	87.65	342.1	0.64
CL-RS-03	retrograde skarn	78	28.44	0.05	21.31	0.05	18.65	0.12	19.14	0	0	0	87.76	342.1	0.65
CL-RS-03	retrograde skarn	75	29.9	0.03	24.51	0.05	15.47	0.12	18.12	0.05	0	0	88.27	342.1	0.68
CL-RS-03	retrograde skarn	86	30.22	0.04	24.52	0.05	15.4	0.05	18.09	0.02	0	0	88.4	342.1	0.68
CL-RS-03	retrograde skarn	97	28.87	0.06	22.24	0.04	18.53	0.08	18.79	0.02	0.03	0	88.69	273.68	0.64
CL-RS-03	retrograde skarn	108	28.66	0	21.79	0.04	17.96	0.04	17.9	0.03	0.01	0.01	86.44	273.68	0.64
CL-RS-03	retrograde skarn	107	28.7	0.05	21.2	0.04	17.89	0.09	18.34	0.01	0	0	86.39	273.68	0.65
CL-RS-03	retrograde skarn	59	29.34	0.06	22.54	0.04	16.1	0.09	18.79	0.01	0.02	0	86.98	273.68	0.68
CL-RS-03	retrograde skarn	87	30.2	0.02	24.11	0.04	15.35	0.07	18.1	0	0.01	0.01	87.9	273.68	0.68
CL-RS-03	retrograde skarn	80	30.45	0.04	24.6	0.04	14.12	0.11	18.32	0.01	0.01	0	87.7	273.68	0.7
CL-RS-03	retrograde skarn	74	30.09	0.06	25.57	0.04	13.57	0.1	17.71	0	0	0.01	87.16	273.68	0.7
CL-RS-03	retrograde skarn	112	28.04	0.04	20.95	0.03	19.11	0.1	18.8	0	0	0	87.07	205.26	0.64
CL-RS-03	retrograde skarn	90	29.76	0	23.74	0.03	15.88	0.09	18.18	0.03	0.02	0.02	87.74	205.26	0.67
CL-RS-03	retrograde skarn	88	29.84	0.05	23.88	0.03	15.76	0.04	17.94	0.01	0	0	87.55	205.26	0.67
CL-RS-03	retrograde skarn	82	30.13	0.05	25.63	0.03	13.35	0.12	17.99	0.03	0	0	87.39	205.26	0.71
CL-RS-03	retrograde skarn	61	28.39	0.05	20.07	0.02	20.45	0.11	18.15	0.01	0.02	0.02	87.27	136.84	0.61
CL-RS-03	retrograde skarn	83	29.1	0.02	21.67	0.02	19.53	0.08	17.92	0.01	0	0	88.35	136.84	0.62
CL-RS-03	retrograde skarn	69	27.89	0.05	20.43	0.02	18.66	0.09	17.39	0	0	0	84.53	136.84	0.62
CL-RS-03	retrograde skarn	58	29.09	0.04	22.92	0.02	16.14	0.01	18.77	0	0	0	86.99	136.84	0.67
CL-RS-03	retrograde skarn	70	29.9	0.01	24.62	0.02	15.12	0.08	18.34	0.03	0.01	0.01	88.15	136.84	0.68

CHLORITE

Sample	Rock group	anal. #	SiO2	TiO2	Al2O3	Cr2O3	FeO	MnO	MgO	CaO	Na2O	K2O	Total	Cr ppm	XMg
CL-RS-03	retrograde skarn	71	29.87	0.04	25.13	0.02	13.45	0.1	18.27	0.03	0.01	0	86.91	136.84	0.71
CL-RS-03	retrograde skarn	84	28.13	0.05	19.58	0.01	21.02	0.17	18.27	0.01	0.01	0	87.29	68.42	0.61
CL-RS-03	retrograde skarn	94	27.92	0.09	19.9	0.01	20.75	0.04	19.03	0.07	0	0.01	87.82	68.42	0.62
CL-RS-03	retrograde skarn	106	28.31	0.09	19.67	0.01	19.97	0.1	18.43	0.01	0.02	0.02	86.65	68.42	0.62
CL-RS-03	retrograde skarn	103	29.4	0.05	22.73	0.01	16.81	0.04	18.16	0.03	0	0	87.24	68.42	0.66
CL-RS-03	retrograde skarn	85	29.75	0.03	23.47	0.01	16.54	0.08	17.94	0.05	0.07	0.01	87.96	68.42	0.66
CL-RS-03	retrograde skarn	98	29.74	0.06	25.09	0.01	14.4	0.1	18.82	0	0	0	88.21	68.42	0.7
CL-RS-03	retrograde skarn	81	29.96	0.03	25.45	0.01	13.93	0.09	18.6	0.01	0.03	0.01	88.13	68.42	0.7
CL-RS-03	retrograde skarn	54	27.75	0	19.1	0	21.18	0.14	18.48	0.03	0.02	0.01	86.72		0.61
CL-RS-03	retrograde skarn	64	28.26	0.06	20.24	0	20.93	0.12	18.67	0	0	0	88.29		0.61
CL-RS-03	retrograde skarn	91	27.85	0.01	19.5	0	20.86	0.15	18.89	0.03	0.01	0.01	87.36		0.62
CL-RS-03	retrograde skarn	77	27.99	0.05	19.94	0	20.63	0.09	18.99	0	0	0	87.73		0.62
CL-RS-03	retrograde skarn	93	28.3	0.04	19.99	0	20.6	0.1	18.8	0.01	0	0.01	87.92		0.62
CL-RS-03	retrograde skarn	62	28.43	0.02	20.11	0	20.55	0.15	18.22	0.01	0.02	0.02	87.56		0.61
CL-RS-03	retrograde skarn	100	28.36	0.02	20.31	0	20.35	0.15	18.67	0.01	0.01	0.03	87.95		0.62
CL-RS-03	retrograde skarn	63	28.45	0.05	19.91	0	20.33	0.09	17.84	0.01	0	0	86.72		0.61
CL-RS-03	retrograde skarn	96	28.26	0.03	20.12	0	20.09	0.09	18.74	0	0	0	87.34		0.62
CL-RS-03	retrograde skarn	76	28.21	0.03	20.4	0	20.06	0.1	19.09	0	0	0	87.93		0.63
CL-RS-03	retrograde skarn	95	28.29	0.01	20.38	0	20.01	0.09	18.88	0.03	0.01	0	87.71		0.63
CL-RS-03	retrograde skarn	52	28.41	0.01	20.39	0	19.57	0.1	18.78	0.06	0	0.01	87.33		0.63
CL-RS-03	retrograde skarn	53	28.35	0.03	20.65	0	19.44	0.13	18.86	0.01	0	0	87.48		0.63
CL-RS-03	retrograde skarn	104	28.35	0.01	20.34	0	19.37	0.12	18.69	0.03	0.01	0	86.93		0.63
CL-RS-03	retrograde skarn	68	28.56	0.01	20.78	0	19.08	0.08	18.56	0	0	0.02	87.08		0.63
CL-RS-03	retrograde skarn	65	29.5	0.08	23.84	0	18.36	0.11	18.32	0.02	0.03	0	90.26		0.64
CL-RS-03	retrograde skarn	110	28.45	0	21.61	0	17.82	0.08	18.11	0.01	0	0.02	86.1		0.64
CL-RS-03	retrograde skarn	102	29.41	0.02	22.98	0	17.71	0.08	17.97	0.01	0	0	88.22		0.64
CL-RS-03	retrograde skarn	105	29.14	0.06	22.64	0	17.59	0.07	18.3	0.03	0	0	87.82		0.65
CL-RS-03	retrograde skarn	60	28.64	0.05	21.81	0	17.22	0.08	19.06	0.01	0.01	0	86.89		0.66
CL-RS-03	retrograde skarn	109	29.31	0.09	22.59	0	16.95	0.09	18.09	0	0	0	87.14		0.66
CL-RS-03	retrograde skarn	101	29.06	0.08	22.39	0	16.82	0.05	18.59	0.06	0	0	87.08		0.66
CL-RS-03	retrograde skarn	55	28.73	0.06	22.21	0	16.78	0.1	18.49	0.06	0.02	0	86.51		0.66
CL-RS-03	retrograde skarn	56	29.08	0.06	22.27	0	16.51	0.09	18.45	0.03	0	0	86.5		0.67
CL-RS-03	retrograde skarn	57	29.24	0.07	22.89	0	16.46	0.07	18.57	0.03	0.01	0	87.36		0.67
CL-RS-03	retrograde skarn	89	30.1	0.04	23.86	0	15.63	0.06	17.73	0.01	0.04	0	87.5		0.67
CL-RS-03	retrograde skarn	79	30.1	0.05	24.38	0	14.85	0.06	18.14	0	0	0	87.58		0.69
CL-RS-03	retrograde skarn	72	29.95	0.07	23.67	0	14.67	0.08	18.13	0	0.01	0	86.61		0.69

CHLORITE

Sample	Rock group	anal. #	SiO2	TiO2	Al2O3	Cr2O3	FeO	MnO	MgO	CaO	Na2O	K2O	Total	Cr ppm	XMg
CL-RS-03	retrograde skarn	66	29.65	0.01	23.74	0	14.64	0.09	17.84	0.01	0	0.01	85.99		0.68
CL-RS-03	retrograde skarn	99	29.34	0.05	23.41	0	14.56	0.07	18.71	0.03	0	0	86.16		0.7
DB-PG-01	retrograde skarn	40	29.29	0.11	22.52	0.33	17	0.06	17.59	0.14	0.02	0	87.06	2257.86	0.65
DB-PG-01	retrograde skarn	17	29.5	0.04	22.72	0.21	15.95	0.09	17.55	0.08	0.02	0.01	86.21	1436.82	0.66
DB-PG-01	retrograde skarn	4	29.16	0.06	23.07	0.16	16.2	0.07	18.2	0	0.01	0	86.96	1094.72	0.67
DB-PG-01	retrograde skarn	26	29.87	0.06	23.3	0.15	16.01	0.11	17.96	0.02	0.01	0	87.48	1026.3	0.67
DB-PG-01	retrograde skarn	27	29.87	0.05	22.91	0.14	18	0.09	18.04	0.04	0.02	0	89.18	957.88	0.64
DB-PG-01	retrograde skarn	8	28.8	1.94	21.89	0.14	17.06	0.09	17.43	0.05	0	0	87.4	957.88	0.65
DB-PG-01	retrograde skarn	19	28.89	0.08	22.08	0.13	17.47	0.07	18.12	0.07	0.02	0	86.94	889.46	0.65
DB-PG-01	retrograde skarn	115	29.9	0.01	25.26	0.13	12.38	0.13	18.48	0.1	0	0	86.43	889.46	0.73
DB-PG-01	retrograde skarn	28	29.08	0.32	21.79	0.11	18.48	0.08	17.93	0.05	0	0.07	87.94	752.62	0.63
DB-PG-01	retrograde skarn	120	30.12	0.05	25.89	0.11	12.39	0.16	18.76	0.04	0.01	0.04	87.61	752.62	0.73
DB-PG-01	retrograde skarn	36	31.06	0.03	27.04	0.11	10.78	0.09	19.08	0.05	0	0.01	88.27	752.62	0.76
DB-PG-01	retrograde skarn	42	30.23	0.09	24.39	0.1	16.02	0.07	17.89	0.06	0.01	0.01	88.9	684.2	0.67
DB-PG-01	retrograde skarn	11	29.53	0.02	22.92	0.1	15.94	0.13	17.8	0	0.01	0.02	86.46	684.2	0.67
DB-PG-01	retrograde skarn	29	30.64	0.08	24.54	0.1	14.96	0.07	17.38	0.05	0.02	0	87.92	684.2	0.67
DB-PG-01	retrograde skarn	38	30.78	0.05	25.35	0.1	14.07	0.06	16.75	0.13	0.02	0	87.36	684.2	0.68
DB-PG-01	retrograde skarn	12	29.38	0.03	22.69	0.09	16.81	0.09	17.7	0.02	0	0	86.86	615.78	0.65
DB-PG-01	retrograde skarn	21	29.7	0.02	23.37	0.09	15.37	0.1	18.17	0.04	0	0	86.87	615.78	0.68
DB-PG-01	retrograde skarn	22	29.78	0	23.36	0.09	15.17	0.12	17.74	0.05	0	0.01	86.37	615.78	0.68
DB-PG-01	retrograde skarn	121	30.15	0.01	25.24	0.09	12.54	0.1	18.68	0.08	0	0.09	86.99	615.78	0.73
DB-PG-01	retrograde skarn	119	29.8	0.02	25.02	0.09	12.42	0.14	18.68	0.04	0	0.04	86.24	615.78	0.73
DB-PG-01	retrograde skarn	44	29.68	0.04	22.1	0.08	16.98	0.03	17.4	0.06	0	0	86.37	547.36	0.65
DB-PG-01	retrograde skarn	10	29.55	0.03	23.35	0.08	16.89	0.09	18.34	0.01	0.01	0.02	88.4	547.36	0.66
DB-PG-01	retrograde skarn	1	29.63	0.02	22.85	0.08	16.34	0.07	17.94	0.03	0	0	86.97	547.36	0.66
DB-PG-01	retrograde skarn	118	29.48	0.03	24.59	0.08	12.23	0.16	18.22	0.14	0	0.01	84.95	547.36	0.73
DB-PG-01	retrograde skarn	30	29.72	0.08	23.24	0.07	15.92	0.09	17.81	0	0	0	86.96	478.94	0.67
DB-PG-01	retrograde skarn	25	30.29	0.06	23.79	0.07	15.38	0.08	17.45	0.03	0	0.02	87.19	478.94	0.67
DB-PG-01	retrograde skarn	37	30.1	0.04	23.05	0.07	15.03	0.03	17.67	0.13	0.02	0.01	86.15	478.94	0.68
DB-PG-01	retrograde skarn	114	29.84	0.04	26.64	0.07	10.57	0.08	18.5	0.09	0	0.03	85.86	478.94	0.76
DB-PG-01	retrograde skarn	6	29.03	0.04	22.78	0.06	19.03	0.08	18.34	0.03	0	0	89.44	410.52	0.63
DB-PG-01	retrograde skarn	24	29.68	0	24.38	0.06	15.57	0.08	17.82	0.02	0.01	0.02	87.66	410.52	0.67
DB-PG-01	retrograde skarn	23	29.89	0.03	23.8	0.05	16.43	0.12	17.88	0	0.01	0	88.19	342.1	0.66
DB-PG-01	retrograde skarn	7	29.58	0	23.26	0.05	15.96	0.07	17.94	0	0.01	0	86.92	342.1	0.67
DB-PG-01	retrograde skarn	31	30.68	0.06	23.52	0.05	15.73	0.05	17.52	0.05	0	0	87.7	342.1	0.67
DB-PG-01	retrograde skarn	20	30.03	0.06	23.2	0.05	15.5	0.12	18.08	0.03	0.01	0.03	87.13	342.1	0.68

CHLORITE

Sample	Rock group	anal. #	SiO2	TiO2	Al2O3	Cr2O3	FeO	MnO	MgO	CaO	Na2O	K2O	Total	Cr ppm	XMg
DB-PG-01	retrograde skarn	9	29.64	0.03	24.09	0.05	14.83	0.04	17.73	0	0.01	0.03	86.45	342.1	0.68
DB-PG-01	retrograde skarn	18	30.26	0.01	23.87	0.04	15.44	0.09	17.59	0.03	0	0	87.37	273.68	0.67
DB-PG-01	retrograde skarn	2	30.79	0.03	25.54	0.04	13.32	0.02	17.73	0.02	0.01	0.01	87.58	273.68	0.7
DB-PG-01	retrograde skarn	117	29.5	0.04	25.23	0.03	12.35	0.12	19.15	0.29	0	0.02	86.73	205.26	0.73
DB-PG-01	retrograde skarn	116	29.75	0.03	25.46	0.03	12.22	0.19	19.06	0.23	0.01	0.02	87	205.26	0.74
DB-PG-01	retrograde skarn	35	30.84	0.04	26.42	0.03	11.67	0.12	18.38	0.06	0	0	87.61	205.26	0.74
DB-PG-01	retrograde skarn	43	29.23	0.17	20.58	0.02	19.8	0.06	17.45	0.15	0.01	0.02	87.49	136.84	0.61
DB-PG-01	retrograde skarn	34	29.21	0.05	21.87	0.02	17.65	0.1	17.98	0	0	0	86.91	136.84	0.64
DB-PG-01	retrograde skarn	33	29.03	0.01	23.16	0.02	15.46	0.05	17.92	0.01	0	0	85.69	136.84	0.67
DB-PG-01	retrograde skarn	45	30.66	0.14	24.44	0.02	15.14	0.1	17.96	0.09	0.01	0.02	88.58	136.84	0.68
DB-PG-01	retrograde skarn	113	30.6	0.85	25.32	0.02	12.62	0.11	17.87	0.19	0.04	0.01	87.62	136.84	0.72
DB-PG-01	retrograde skarn	39	29.78	0.12	22.21	0.01	17.17	0.08	18.58	0.16	0	0	88.15	68.42	0.66
DB-PG-01	retrograde skarn	46	30.94	0.22	24.35	0.01	14.78	0.08	17.96	0.12	0	0	88.47	68.42	0.68
DB-PG-01	retrograde skarn	41	29.34	0.13	21.01	0	18.34	0.06	17.16	0.08	0.01	0.01	86.14		0.63
DB-PG-01	retrograde skarn	32	29.09	0	22.33	0	16.22	0.07	18.13	0.01	0	0.01	85.86		0.67
DB-PG-01	retrograde skarn	3	30.45	0.03	24.97	0	13.95	0.06	18.13	0.03	0	0	87.64		0.7
DB-PG-01	retrograde skarn	5	29.88	0.08	26.34	0	10.94	0.09	19.82	0	0	0	87.18		0.76

SPINEL

Sample	Rock group	anal. #	SiO2	TiO2	Al2O3	Cr2O3	FeO	MnO	MgO	CaO	Na2O	K2O	Total	XMg
CL-PS-02A	prograde skarn - sp skarn	299	0.01	0.04	61.13	1.96	18.22	0.2	16.8	0	0.02	0	98.37	0.62
CL-PS-02A	prograde skarn - sp skarn	300	0	0.03	61.47	1.94	17.93	0.23	16.4	0.13	0.02	0	98.16	0.62
CL-PS-02A	prograde skarn - sp skarn	304	0.01	0.05	61.73	1.59	18.31	0.2	17.02	0.02	0.01	0	98.94	0.62
CL-PS-02A	prograde skarn - sp skarn	286	0.02	0.04	61.33	1.46	17.97	0.19	15.93	0.02	0.03	0	97	0.61
CL-PS-02A	prograde skarn - sp skarn	285	0	0.03	61.99	1.44	17.54	0.2	16.2	0	0.02	0	97.42	0.62
CL-PS-02A	prograde skarn - sp skarn	284	0.02	0.04	61.42	1.39	17.82	0.17	16.25	0.03	0.01	0.01	97.17	0.62
CL-PS-02A	prograde skarn - sp skarn	283	0.04	0.04	62.31	1.36	17.98	0.19	16.09	0	0.04	0.01	98.06	0.61
CL-PS-02A	prograde skarn - sp skarn	303	0	0.04	61.86	1.26	18.47	0.22	17.06	0.01	0.02	0	98.94	0.62
CL-PS-02A	prograde skarn - sp skarn	301	0	0.03	62.49	1.12	17.68	0.17	16.36	0.04	0.04	0	97.93	0.62
CL-PS-02A	prograde skarn - sp skarn	302	0	0.05	62.78	0.73	17.51	0.22	17.16	0.02	0.01	0	98.49	0.64

TABLE A.2 - SULFIDE TRACE ELEMENT DATA

Sample	Group	spot	Sulfide	Al27	Ti47	Ti49	Ti	V51	Cr52	Mn55	Co59	Ni60	Cu63	Zn66	As75	Se77	Sn118	Pb206	Pb208	Pb
CL-RS-01	retrograde skarn	31	ccp	224.62		329.15	329.15	0.42	70.37	19.86	9.51		193759.72	733.73	1.13		6.69	6.64	7.38	14.02
CL-RS-01	retrograde skarn	26	ccp	37.18	4.93	359.16	364.09	0.624	9.76	32.27	10.56		247334.48	3126.71	0.92		8.11	10.03	10.79	20.82
CL-RS-01	retrograde skarn	38	ccp	49.09	4.03	272.1	276.13	0.447	60.53	6.35	10.74		278652.72	1769.28	0.83		6.39	10.51	11.14	21.65
CL-RS-01	retrograde skarn	33	ccp	3499.33	6.06	303.47	309.53	0.53	75.08	55.9	9.19		203975.83	488.17	1.46		6.28	13.75	14.65	28.4
CL-RS-01	retrograde skarn	29	ccp	256.85	5.22	322.86	328.08	0.543	20.37	26.03	10.21	0.82	192582.56	3248.26	1.57		7.13	14.18	15.76	29.94
CL-RS-01	retrograde skarn	25	ccp	203.38		348.79	348.79	0.606	58.23	21.68	8.53		199349.2	1330.7	1.41		7.87	14.25	15.88	30.13
CL-RS-01	retrograde skarn	40	ccp	36		283.05	283.05	0.432	147.58	11.13	10.68		256279.66	881.59	0.42		8.92	15.47	17.07	32.54
CL-RS-01	retrograde skarn	37	ccp	1090.57	5.85	300.31	306.16	0.427	22.57	62.57	10.57	0.8	289226.53	2160.94	1.52		9.04	17.17	17.81	34.98
CL-RS-01	retrograde skarn	35	ccp	331.18	6.28	299.77	306.05	0.469	89.67	17.66	6.68	0.56	233310.86	894.87	0.65		9.55	20.41	21.52	41.93
CL-RS-01	retrograde skarn	30	ccp	1669.55	5.06	360.86	365.92	0.525	180.41	304.63	8.61	0.97	250312.97	764.45	1.22		8.23	20.24	22.11	42.35
CL-RS-01	retrograde skarn	27	ccp	3859.75		330.66	330.66	0.654	18.88	790.83	7.36		206573.11	1529.63	1		13.79	20.92	23.44	44.36
CL-RS-01	retrograde skarn	36	ccp	1006.71		286.41	286.41	0.562	70.07	64.11	24.22	1.14	313455.91	16136.94	0.94		11.93	25.71	27.22	52.93
CL-RS-01	retrograde skarn	28	ccp	740.33		339.2	339.2	0.555	218.87	455.02	27.43		249487.58	20775.87	0.93		11.41	34.15	38.61	72.76
CL-RS-01	retrograde skarn	34	ccp	592.42	4.21	322.92	327.13	0.475	77.38	433.61	10.41	0.45	214796.67	2344.12	1.14		7.53	36.67	39.31	75.98
CL-RS-01	retrograde skarn	39	ccp	126.17	3.46	278.73	282.19	0.439	97.77	9.18	12.83		225257.44	4876.4	0.66		5.72	41.02	46.11	87.13
CL-RS-02	retrograde skarn	11	ccp	4165.1		105.39	105.39	0.504	69.41	36.8	1.88		385386.78	5.46	1.34		4.06	16.78	17.86	34.64
CL-RS-02	retrograde skarn	12	ccp			103.22	103.22	0.098	65.05		31.99	19.02	374891.16	5.67	0.74		4.31	20.95	22.7	43.65
CL-RS-02	retrograde skarn	16	ccp			104.25	104.25	0.166	52.92	9.73	4.9	7.47	395018.53	5.99	0.94		3.93	24.5	26.47	50.97
CL-RS-02	retrograde skarn	9	ccp	111.93		109.36	109.36	0.151		7.59	0.377	1.92	377375.13	5.14	1.18		2.25	39.07	43.84	82.91
CL-RS-02	retrograde skarn	10	ccp	71.85		110.67	110.67	0.206	42.8		0.308	2.19	382510.03	5.81	0.84		3.98	41.43	45.09	86.52
CL-RS-02	retrograde skarn	8	ccp		7.01	117	124.01	0.181	52.66		0.614	1.22	396135.75	4.55	0.51		4.31	54.04	58.67	112.71
CL-RS-02	retrograde skarn	7	ccp	62.75		115.05	115.05	0.237	154.69	15.51	12.72	9.17	397465.66	7.33			5.08	67.24	75.15	142.39
CL-RS-02	retrograde skarn	13	ccp			106.73	106.73	0.2	101.75		10.57	3.58	398630.47	5.42	0.92		3.84	88.39	100.73	189.12
CL-RS-02	retrograde skarn	14	ccp			102.86	102.86	0.182	41.61		47.13	32.77	394090.31	5.53	1.15		7.69	95.8	105.95	201.75
CL-RS-02	retrograde skarn	15	ccp			99.72	99.72	0.194	60.6		0.395		389315.09	4.89	0.89		1.97	95.82	108.2	204.02
CL-RS-02	retrograde skarn	5	ccp	110.24	7.33	136.65	143.98	0.189	83.42	5.72	0.395	3.2	390350.47	5.51	1.43		3.77	103.51	108.26	211.77
CL-RS-02	retrograde skarn	6	ccp	540.32	4.16	128.2	132.36	0.156		49.94	31.7	38.83	387968	4.88	0.7		2.63	135.85	145.17	281.02
CL-PS-04	prograde skarn	25	ccp	501.16		97.01	97.01	0.136	91.48	135.69	0.544	12.11	388819.91	1011.34	0.69	-0.07	1.02	11.3	11.89	23.19
CL-PS-04	prograde skarn	28	ccp	53.3		92.14	92.14	0.114	50.8	15.1	0.949	9.36	379164.97	2657.79	0.88	-0.09	0.791	16.2	16.72	32.92
CL-PS-05	prograde skarn	18	ccp	3665.92	9.75	374.55	384.3	0.818	30.08	112.79	0.51	8.61	317909.44	546.2	0.71		9.23	5.51	5.69	11.2
CL-PS-05	prograde skarn	20	ccp	20.03	1.49	213.47	214.96	0.382	82.11	6.76	32.37	223.81	55251.43	395.75	0.362		2.36	6.95	7.2	14.15
CL-PS-05	prograde skarn	19	ccp	135.54		357.25	357.25	0.561	237.19	2309.2	0.772	15.56	235585.95	1058.61	0.92		8.72	12.02	11.92	23.94
CL-PS-05	prograde skarn	15	ccp	36.85	1.65	238.9	240.55	0.4	101.39	2451.2	28.48	166.23	98762.71	324.93	0.44		2.49	21.72	21.9	43.62
CL-PS-05	prograde skarn	17	ccp	82.12		370.56	370.56	0.707	19.37	16.15	3.11	15.03	88878.98	714.05	1.31		8.28	22.68	23.95	46.63
CL-PS-04	prograde skarn	31	py	41.74		92.34	92.34	0.166	46.18	15.72	134.71	442.75	15.12	2.96		0.042	0.111	1.42	1.45	2.87
CL-PS-04	prograde skarn	36	py	123.17		87.55	87.55	0.116	23.99	31.2	134.57	428.94	2.27	2.53	0.27	0.3	0.119	1.21	1.27	2.48
CL-PS-04	prograde skarn	37	py	74.29	2.88	85.02	87.9	0.072	70.42	17.65	137.8	438.59	1.35	3.23		0.028		8.82	9.9	18.72
CL-PS-04	prograde skarn	32	py	78.12	3.6	88.61	92.21	0.151	31.02	18.47	133.39	417.93	2.24	2.49	0.23	-0.023	0.108	2.1	2.18	4.28
CL-PS-04	prograde skarn	34	py	115.38		86.53	86.53	0.169	40.93	12.69	133.98	415.9	1.06	3.17			0.158	1.03	1.06	2.09

TABLE A.2 - SULFIDE TRACE ELEMENT DATA

Sample	Group	spot	Sulfide	Al27	Ti47	Ti49	Ti	V51	Cr52	Mn55	Co59	Ni60	Cu63	Zn66	As75	Se77	Sn118	Pb206	Pb208	Pb
CL-PS-04	prograde skarn	33	py	45.94	3.56	85.07	88.63	0.099	11.5	17.08	132.27	404.9		1.91	0.6	0.06	0.108	0.409	0.49	0.899
CL-PS-04	prograde skarn	40	py	173.13		77.14	77.14	0.139	18.73	8.93	134.39	404.42	3.9	2.69				215.8	226.13	441.93
CL-PS-04	prograde skarn	38	py			82.98	82.98	0.14		16.67	142.6	427.53	0.8	2.71	0.3	0.29		2.81	3.11	5.92
CL-PS-04	prograde skarn	35	py	73.86		82.21	82.21	0.178	33.36	13.47	140.6	401.42	4.54	3.69	0.23	0.18	0.223	0.98	1.06	2.04
CL-PS-04	prograde skarn	39	py	471.9	4.65	80.03	84.68	0.317	49.51	616.7	151.19	418.55	1.33	4.39		0.06	0.181	0.97	1.04	2.01
CL-PS-01	prograde skarn	27	py	48.48	2.29	353.54	355.83	0.592	36.06	9.81	197.04	335.99	1.91	5.78	0.36	0.97		1.39	1.43	2.82
CL-PS-01	prograde skarn	31	py	1575.24	2.41	305.78	308.19	0.522	33.93	42.44	186.67	315.99	1.088	4.96		0.06		9.75	10.43	20.18
CL-PS-01	prograde skarn	35	py	3547.88	10.32	308.22	318.54	0.8	72.21	43.32	192.38	320.36	2.18	6.35		0.7		7.55	8.14	15.69
CL-PS-01	prograde skarn	39	py	80.92	2.02	294.07	296.09	0.465	32.27	12.6	184.02	304.91	1.543	4.81	0.47	0.39		0.319	0.315	0.634
CL-PS-01	prograde skarn	37	py	339.63	2.57	281.02	283.59	0.487	40.8	10.48	185.64	307.09	1.751	4.59	0.27	0.13		0.373	0.461	0.834
CL-PS-01	prograde skarn	28	py	59.01	2.6	321.72	324.32	0.518	44.08	13.03	187.43	308.97	1.801	5.69	0.5	3.13	0.09	6.27	7	13.27
CL-PS-01	prograde skarn	25	py	73.75	1.89	326.24	328.13	0.479	89.61	10.49	178.11	292.74	3.08	5.78			0.159	0.67	0.737	1.407
CL-PS-01	prograde skarn	26	py	51.98	3.26	337.59	340.85	0.488	40.97		190.65	307.29	2.5	4.02			0.165	0.083	0.106	0.189
CL-PS-01	prograde skarn	40	py	75.39		284.64	284.64	0.468	35.69	20.9	191.71	307.54	3.53	9.26	0.9		0.106	1.38	1.48	2.86
CL-PS-01	prograde skarn	30	py	275.69	1.93	319.75	321.68	0.52	59.48	7.8	184.92	290.25	1.559	6.72	0.33	2.21	0.1	0.911	0.966	1.877
CL-PS-01	prograde skarn	36	py	172.98		298.08	298.08	0.508	24.49	13.09	196.97	307.04	2.93	5.45	0.61	1	0.095	5.37	5.59	10.96
CL-PS-01	prograde skarn	38	py	23.66		279.6	279.6	0.462	51.31	11.07	183.49	282.22	1.714	4.16	0.69		0.147	9.06	10.01	19.07
CL-PS-01	prograde skarn	29	py	465.45		336.14	336.14	0.575	65.85	9	192.41	293.61	1.617	5.11	0.39	1.79	0.089	13.59	14.55	28.14
DB-PS-01	prograde skarn	5	py		1.71	447.16	448.87	1.01	59	55.82	398.6	317.61	2.99	4.14	0.51	0.28	0.161	0.104	0.116	0.22
DB-PS-01	prograde skarn	6	py		2.17	430.54	432.71	0.774	46.68	486.21	438.09	361.72	70.17	4.04			0.154	0.585	0.697	1.282
DB-PS-01	prograde skarn	7	py		5.67	454.46	460.13	0.752	61.27	71.91	428.46	314.38	1.05	4.02	0.34		0.118	0.346	0.436	0.782
DB-PS-01	prograde skarn	8	py			441.09	441.09	0.93	46.56	139.67	414.1	310.7	7.98	4.14		0.36	0.107	0.345	0.354	0.699
DB-PS-01	prograde skarn	9	py			406.33	406.33	0.829	77.6	1761.63	412.88	295.35	28.4	3.87	0.41	0.94	0.085	0.063	0.225	0.288
DB-PS-01	prograde skarn	10	py		2.62	414.53	417.15	0.796	78.3	73.19	394.01	306.58	5.45	4.16	0.6		0.166	0.435	0.731	1.166
DB-PS-01	prograde skarn	11	py	85.85	1.71	410.42	412.13	1.33	22.67	917.18	521.18	331.23	48.83	5.31	0.54	0.65	0.282	0.552	0.829	1.381
DB-PS-01	prograde skarn	12	py	25.29	1.35	393.44	394.79	0.763	78.45	286.47	428.78	312.31	37.37	5.63		0.29	0.127	4.17	4.3	8.47
DB-PS-01	prograde skarn	13	py	1666.83		418.18	418.18	0.92	81.2	92.01	408.39	291.87	3.14	4.6	0.36		0.107	0.713	0.773	1.486
DB-PS-01	prograde skarn	14	py	363.07	1.87	391.04	392.91	2.36	80.27	1471.5	441.11	462.48	16.59	6.14	0.41	1.34	1.74	1.35	1.54	2.89
DB-PS-01	prograde skarn	16	py		3.55	409.55	413.1	0.99	77.03	246.33	409.22	379.73	28.33	4.48	0.36		0.093	6.3	7.17	13.47
DB-PS-01	prograde skarn	17	py	58.02	3.31	380.7	384.01	2	39.2	78.02	409.87	327.66	6.35	5.1			0.134	1.94	2.22	4.16
DB-PS-01	prograde skarn	18	py		1.85	381.81	383.66	0.91	56.23	175.47	417.12	293.93	6.26	3.86	0.67	0.48	0.119			0
DB-PS-01	prograde skarn	19	py		2.19	391.31	393.5	0.92	50.99	172.07	407.04	331.98	26.63	4.25	0.29	1.34	0.155	1.39	1.68	3.07
DB-PS-01	prograde skarn	20	py			373.2	373.2	0.92	47.71	138.47	421.49	321.84	1.56	4.35		0.8	0.07	0.427	0.503	0.93
CL-PS-05	prograde skarn	11	py		3.16	389.23	392.39	0.632	65.22	11.65	102.7	482.19	0.745	3.73	0.307		0.097	10.78	10.86	21.64
CL-PS-05	prograde skarn	5	py	53.48	2.66	441.47	444.13	0.72	94.55	7.77	107.65	458.72	2.45	6.96	0.59	5.82	0.088	7.82	8.24	16.06
CL-PS-05	prograde skarn	7	py	35.54	2.53	408.79	411.32	0.659	80.09	20.2	115.84	362.08	0.558	4.94	0.363	1.43	0.126	13.32	13.59	26.91
CL-PS-05	prograde skarn	9	py	2219.7	4.25	393.66	397.91	0.725	67.04	1141.17	119.05	368.99	1.266	5.32	0.216	3.8	0.072	19.42	20.27	39.69
CL-PS-05	prograde skarn	6	py	33.66		409.82	409.82	0.698	34	8.12	117.02	341.44	0.334	4.41	0.2	5.32	0.096	3.16	3.2	6.36
CL-PS-05	prograde skarn	12	py	1051.86	5.01	382.35	387.36	0.614	90.7	37.09	122.41	356.3	0.706	6.32	0.56	5.08	0.089	14.02	14.41	28.43

Se fecharmos a porta para todos os erros,
a verdade também ficará de fora.

ANEXO I

Título da Dissertação/Tese:

Metassomatismo polifásico em rochas carbonáticas: evolução e metalogênese dos escarnitos associados à intrusão do Complexo Granítico Caçapava do Sul (RS,Brasil)

Área de Concentração: Geoquímica

Autor: **GUILHERME SONNTAG HOERLLE**

Orientador: Prof. Dr. Marcus Vinicius Dorneles Remus

Examinador: Profa. Dra. **GLÁUCIA NASCIMENTO QUEIROGA**

Data: 22 de julho de 2021

Conceito: **A**

PARECER:

A tese apresentada é subdividida em cinco (05) capítulos, dos quais quatro (04) estão dispostos sob a forma de artigo científico submetido ou a ser submetido para revistas científicas internacionais (Qualis A1 & A2 na área de Geociências).

Trata-se de um trabalho extenso, muito bem escrito e de fácil leitura sobre um tema atual e que se baseou na utilização de várias técnicas analíticas, enriquecendo a tese.

Por todos os quesitos elencados acima, sugiro APROVAÇÃO COM CONCEITO **A.**

Assinatura: Data: 30 de julho de 2021

Ciente do Orientador:

Ciente do Aluno:

ANEXO I
Título da Dissertação/Tese:
Metassomatismo polifásico em rochas carbonáticas: evolução e metalogênese dos escarnitos associados à intrusão do Complexo Granítico Caçapava do Sul (RS, Brasil)
Área de Concentração: Geoquímica
Autor: **GUILHERME SONNTAG HOERLLE** □
Orientador: Prof. Dr. Marcus Vinicius Dorneles Remus
Examinador: Profa. Dra. **MOACIR JOSÉ BUENANO MACAMBIRA**
Data: 22/07/2021
Conceito: A, com Louvor
PARECER: A tese apresentada em quatro artigos científicos em Inglês submetidos e a serem submetidos a revistas com alto fator de impacto representa uma significativa contribuição para a geologia da região de Caçapava do Sul (RS, Brasil). Um capítulo introdutório em Português apresenta o estado da arte dos principais temas enfocados no estudo. Os artigos abrangem assuntos distintos da pesquisa, investigados através de variadas metodologias e enfoques científicos, suportados por um levantamento bibliográfico abrangente e atualizado. As ilustrações são de qualidade e adequadas, mas as tabelas de dados (material suplementar) necessitam de uniformização e complementação. Na apresentação e arguição, o candidato demonstrou domínio dos temas enfocados, respondendo com segurança às questões apresentadas. Enfim, sou favorável à aprovação da tese com conceito A, menção Com Louvor.
Assinatura: 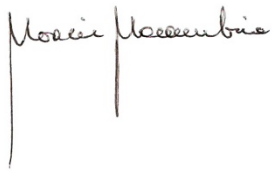 ` Data: 22/07/2021
Ciente do Orientador: Ciente do Aluno:

ANEXO I

Título da Dissertação/Tese:

Metassomatismo polifásico em rochas carbonáticas: evolução e metalogênese dos escarnitos associados à intrusão do Complexo Granítico Caçapava do Sul (RS,Brasil)

Área de Concentração: Geoquímica

Autor: **GUILHERME SONNTAG HOERLLE** □

Orientador: Prof. Dr. Marcus Vinicius Dorneles Remus

Examinador: Profa. Dra. **LÉO AFRANEO HARTMANN**

Data: 22/07/2021

Conceito: A – Excelente, com LOUVOR.

PARECER:

O doutorando Guilherme realizou uma excelente tese, com seleção de problema científico significativo, metodologia adequada e muito variada e de excelência internacional, obtenção de resultados muito significativos e de alta qualidade, e interpretação dos resultados em primeiro nível internacional. O documento da tese está bem apresentado; textos em português e inglês de boa qualidade; 3 artigos científicos submetidos a 3 periódicos internacionais de alto impacto e 1 um preparação. A tese se destaca pela excelência em todos os aspectos.

Assinatura:
Data: 22/07/20231

Ciente do Orientador:

Ciente do Aluno: